Time constraints on the formation of lithospheric mantle beneath cratons: a re-Os isotope and platinum group element study of peridotite xenoliths from northern Canada and Lesotho,

Gordon James Irvine

University of Durham

Time Constraints on the Formation of Lithospheric Mantle beneath Cratons: A Re-Os Isotope and Platinum Group Element Study of Peridotite Xenoliths from Northern Canada and Lesotho.

By

Gordon James Irvine
BSc (Hons) (Aberdeen)

A thesis submitted in partial fulfillment of
the requirements for the degree of Doctor of Philosophy

Department of Geological Sciences
University of Durham
November 2001

Declaration

I declare that this thesis, which I submit for the degree of Doctor of Philosophy at the University of Durham, is my own work and not substantially the same as any which has previously been submitted at this or another university.

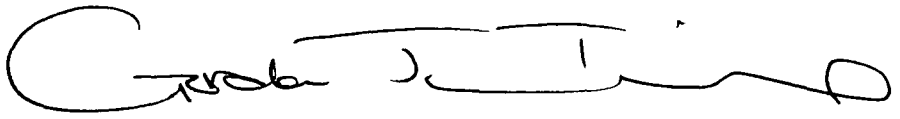

Gordon James Irvine

University of Durham
November 2001

Dedicated to the Memory of my Father

Peter A. Irvine

Abstract

Understanding the generation and evolution of cratonic lithospheric keels requires detailed knowledge of their age, timescale of formation, and the relationship between the crust and mantle part of the lithosphere. The Re-Os isotope system has been instrumental in providing an improved understanding of the timing of formation of cratonic lithospheric keels because of the large fractionation of Re from Os during mantle melting and the relative immunity of Os during mantle metasomatism. This study uses combined full PGE (Platinum Group Elements; Os, Ir, Ru, Pt, Pd) and Re-Os isotope analyses to place better constraints on the significance of Re-Os model ages in sub-continental lithospheric mantle suites from northern Canada and Lesotho, southern Africa. When combined with major-element studies, the coherence of major-elements with PGE fractionation trends, $(Pd/Ir)_n$, provide a firm basis for evaluating the significance of T_{RD} and T_{MA} model ages obtained from Re-Os isotope systematics. The fractionation of PGEs track melt depletion and melt enrichment end-member processes, and allow us to discern samples which have experienced Pd and Re enrichment at varying stages.

The Re-Os isotope and PGE analyses of peridotite xenoliths from the Jericho kimberlite clearly indicate the presence of Archean mantle beneath the Slave craton (T_{RD} range from 3.1 to 2.6 Ga), extending down into the high-temperature garnet facies. Archean ages are also evident in peridotite xenoliths from Somerset Island in the Churchill Province (oldest T_{RD} ca. 2.8 Ga). This is the first indication of Archean sub-continental lithosphere beneath this region that is characterised by early to mid-Proterozoic crustal ages. Some peridotites from the Jericho and Somerset Island peridotite suites have noticeably disturbed Re-Os isotope and PGE systematics and produce anomalously young model ages for cratonic lithospheric mantle overall. Many of the young model ages observed at Jericho and Somerset Island are coincident with major tectonomagmatic events manifested in the overlying crust and may represent new lithospheric mantle added at this time.

Depleted peridotite xenoliths from Lesotho (Kaapvaal craton) have very tightly clustered T_{RD} model ages (2.8 ± 0.1 Ga, $n = 26$). The model age of the lithospheric mantle beneath this region is significantly younger than the age of the oldest overlying crust on the Kaapvaal craton, but correlates well with the end of major crustal differentiation and stabilisation of the Kaapvaal craton. This indicates that large fractionation of lithospheric mantle beneath the Kaapvaal craton could have formed in the late-Archean.

Acknowledgements

I would like to express my gratitude to the following people for their help, guidance and companionship during this project. I shall be eternally grateful.

First of all I thank my supervisors, Dr. D. Graham Pearson and Prof. R. N. Thompson for all the words of advice they offered throughout the project. I also thank Graham for all his technical assistance in the lab and his patience with my rather poor grasp of written English. I would also like to thank my unofficial supervisors, Dr. Richard W. Carlson (Carnegie Institution of Washington) and Dr. Bruce A. Kjarsgaard (Geological Survey of Canada). Once again their advice and assistance was crucial in the completion of this project. Not only did they have to put up with my poor grasp of written English, but also my poor grasp of spoken English.

I would like to thank Dr. M. G. Kopylova (University of British Columbia) for access to the Jericho peridotite suite used in this project. My thanks also go to Bruce and John P. Armstrong (NWT Geology Division, *DIAND*, Canada) for access to further Somerset Island samples. Dr. G. Dreibus kindly provided sulfur analyses on the Lesotho, Jericho and Somerset Island peridotite suites.

Dr. Geoff Nowell, Graham and Bruce provided invaluable help in the field. They also proved to be excellent company whilst relaxing of an evening, supping a few ales down by the waterside in Cape Town, or touring the more colourful establishments of Yellowknife. An additional thanks must go out to the "gravel pit" in Bloemfontein for kindly taking care of my Lesotho field trip mug, and my supervisor!

Steve Shirey was freely available with his time when I needed assistance tackling the 15" DTM TIMS, or discussing my data, and for this I am indebted.

Thanks to Chris Ottley for tirelessly putting up with my many questions, and providing expert assistance with ICP-MS analyses at Durham.

I am grateful to Julie Southern, and latterly Dave Sales. They were always willing to give me access to saws, and diamond laps down in the rock prep area. They also made thin sections for me at a moment's notice with no questions asked.

Mary Horan and Tim Mock provided invaluable assistance in the lab at DTM and made my visits to DC very hospitable. I'd also like to thank Mr Batson in DC for looking after me during my visits to DTM. How he ever managed to understand me will remain an unsolved mystery.

Thanks go out to Sarah, Caroline, Phil, Dan, Sue, Abi, Dave and Rich for putting up with me, and in fact putting me up, at some stage during my time in Durham. I'd like to thank all the other postgrads for their support and friendship.

I would like to thank my parents for all their help, encouragement and support throughout my education, particularly my father who always encouraged me to "go further".

Finally I would like to thank my wife, Eilidh, for her encouragement and continual support, and putting up with my papers lying all over the house. I will clear them away.

This project was carried out under the tenure of a NERC postgraduate studentship, financed by NERC (GT04/97/73/ES). Further funding was provided by NSF grant EAR-9526840 for analyses at DTM, and Carnegie Canada for field-work in Somerset Island.

Contents

Appendix A

Appendix B

Appendix C

Appendix D

Appendix E

Appendix F

List of Figures

Chapter 4

Chapter 5

List of Tables

Chapter 2

Chapter 3

Chapter 4

Chapter 5

Chapter 6

List of Abbreviations Used

DTM: Department of Terrestrial Magnetism (Carnegie Institution, Washington DC, USA)
GSC: Geological Survey of Canada

ICP-MS: Inductively coupled plasma mass spectrometer
N-TIMS: Negative thermal ionisation mass spectrometer
INAA: Instrumental neutron activation analysis

x-flow: (Scott-type) Cross flow nebuliser
MCN: Micro-concentric nebuliser
MBCF: Mass bias correction factor
AMU: Atomic mass units
RSD: Relative standard deviation
2σ: 2 x RSD
Std.dev: standard deviation
MQ: Milli Q deionised, high-purity water
Conc: Concentrated
PTFE: Poly-tetrafluroethylene

PGE: Platinum group element
IPGEs: Ir-group of PGEs
PPGEs: Pd-group of PGEs
MSS: Mono-sulfide solution
BMS: Base Metal sulfide
HSE: Highly siderophile element
HFSE: High field strength element
REE: Rare earth element
LILE: Large ion lithophile element

D: Bulk partition coefficient

Ol: Olivine
OPX: Orthopyroxene
Sp: Spinel
Gnt: Garnet
CPX: Clinopyroxene
Ph: Phlogopite

T_{RD}: Rhenium depletion model age
T_{MA}: Mantle extraction model age

SCLM: Sub continental lithospheric mantle
CSBC: Central Slave Basement Complex
CSCG: Central Slave Cover Group

Chapter 1

Introduction

1.1 The Continental Lithospheric Mantle

The continental lithosphere can be described as the outer, rigid layer of the Earth. This layer cools by conduction and is distinct both mechanically and chemically from the convecting asthenosphere. The continental lithosphere itself is comprised of two components. The upper crustal component is represented by metamorphic, igneous and sedimentary rocks of varied compositions, and the lower mantle component by buoyant and refractory peridotite produced from the extraction of melt from a more fertile asthenospheric mantle.

To form an understanding of the mechanism and rate of formation of cratonic lithosphere, it is essential to understand the processes involved in the formation and evolution of both crustal and mantle components, and their inter-relationship. The evolution of continental crust is in general well constrained for most Archean cratons. However, the timing and processes involved in the stabilisation of the underlying sub-cratonic lithospheric mantle remain poorly understood.

Due to the incompatible nature of the elements in the Rb-Sr, Sm-Nd and U-Pb isotopic systems during partial melting, both mother and daughter isotopes are highly depleted in mantle residues. To obtain sufficient material for analysis requires extensive handpicking of mineral separates. In addition, the depleted nature of these elements results in these systems being susceptible to metasomatic alteration. This is exacerbated by the relatively cool nature of continental lithospheric mantle, where the low temperatures may act as a trap for incompatible element enriched partial melts or fluids. This may lead to the enrichment of the mantle peridotite and this process obscures the older, initial isotopic signature that recorded the original melt depletion event. A large portion of the lithospheric mantle is above the closure temperatures of many isotope systems. This will inevitably produce a diffusive exchange of isotopes between minerals within the peridotite. The resulting isochrons produced by minerals may therefore reflect the cooling of the peridotite during emplacement, as opposed to the time of extraction from the convecting mantle. Finally, during transport to the

surface and emplacement as xenoliths, the peridotites are free to interact with incompatible-element enriched fluids such as the host kimberlite or alkali basalt.

To investigate the timing of melt extraction and evolution of the lithospheric mantle therefore requires an isotopic system whose elements are either compatible, or not significantly enriched in metasomatic fluids. The Re-Os isotope system generally fulfils these conditions and has been utilised in many studies of continental lithospheric mantle underlying Archean cratons, using kimberlite hosted ultramafic xenoliths (Walker *et al.*, 1989; Carlson and Irving, 1994; Pearson *et al.*, 1995a; Pearson *et al.*, 1995b; Carlson *et al.*, 1999). Similar studies have been carried out on ultramafic xenoliths from regions of younger crustal ages (Pearson *et al.*, 1994; Meisel *et al.*, 1996; Handler *et al.*, 1997; Peslier *et al.*, 2000), and tectonically emplaced slices of mantle material (Reisberg *et al.*, 1991; Reisberg and Lorand, 1995).

1.2 The Re-Os Isotope System

Rhenium is a natural, but weak β-emitter with the primary isotope ^{187}Re decaying to a minor isotope of Osmium.

$$^{187}\mathrm{Re} \rightarrow {}^{187}Os + \beta^{-} + \bar{\nu} + Q$$

The half-life of ^{187}Re, ~ 43 Ga (Luck *et al.*, 1980; Luck and Allègre, 1983; Lindner *et al.*, 1986; Lindner *et al.*, 1989), falls within the range of the Rb-Sr, Sm-Nd and U-Pb systems and therefore makes it useful for applications in geochronology and cosmochronology. The geochemical behaviour of Re and Os however allows this system to provide unique insights into the processes affecting mantle rocks and mantle-derived partial melts.

1.2.1 Geochemical nature of Re and Os

Re and Os appear to be either siderophile or chalcophile under most conditions, though in detail their behaviour remains poorly understood. The chalcophile and siderophile behaviour means that the Re-Os isotope system can be employed to investigate processes that are inaccessible to other isotopic systems, due to either the low abundance of incompatible elements or later alteration. Re and Os also allow for the assessment of processes that produce differing effects on metal, sulfide and silicate phases. Osmium abundances in continental lithospheric mantle are relatively high compared to crustal rocks, and sulfides are generally present in all but the most depleted

harzburgitic peridotites (Lorand, 1991). The Re-Os isotope system is therefore ideal for analysing these processes within the lithospheric mantle.

1.2.2 Fractionation of Re and Os during mantle melting

In fertile, undepleted mantle material the ratio of Re to Os does not differ greatly from chondritic. During mantle melting however, the two elements behave quite differently resulting in the possibility of extreme fractionation. In general, during partial melting of the mantle, Re is mildly incompatible, with concentrations in the melt greater than those of the mantle source (see evolution of $^{187}Os/^{188}Os$ in Figure1.1).

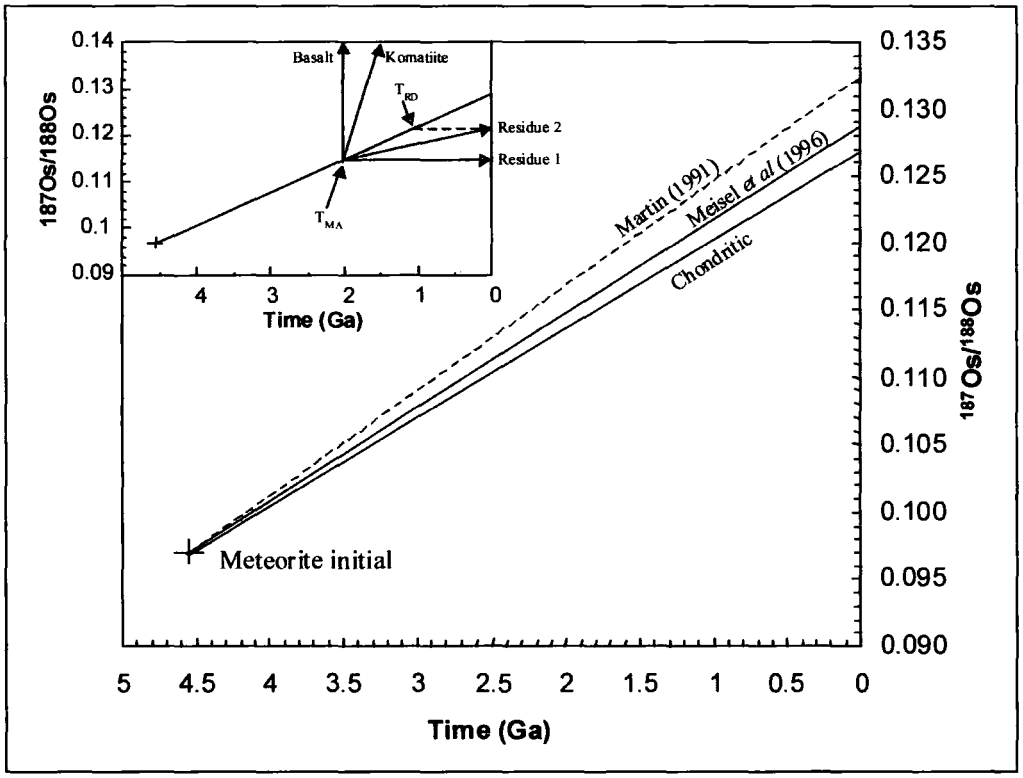

Figure 1.1 Mantle evolution of $^{187}Os/^{188}Os$ through time. Two single-stage evolutionary curves are illustrated; solid line, evolutionary curve of Meisel *et al* (1996), corresponding to a present day $^{187}Os/^{188}Os$ ratio of 0.1287 and $^{187}Re/^{188}Os$ ratio of 0.4243; dashed line, evolutionary curve for a plume-source mantle source (Martin, 1991), corresponding to a present day $^{187}Os/^{188}Os$ ratio of 0.1324 and $^{187}Re/^{188}Os$ ratio of 0.49. Chondritic line defines the average modern $^{187}Os/^{188}Os$ ratio of chondritic meteorites at 0.12700 (Luck and Allègre, 1983; Walker and Morgan, 1989). The inset diagram illustrates the calculated evolution of $^{187}Os/^{188}Os$ in two mantle melts formed at 2 Ga, and their mantle residues. The $^{187}Re/^{188}Os$ ratio of the basalt is 40, and the komatiite is 3.3. Residue 1 is wholly depleted in Re ($^{187}Re/^{188}Os$ = 0) and represents 30-40% extraction of komatiitic melt. Residue 2 formed from the extraction of approximately 15% basalt ($^{187}Re/^{188}Os$ = 0.24). Residue 2 demonstrates T_{RD} and T_{MA} model ages.

Osmium, by way of contrast, is highly compatible in the mantle residue during low to moderate degrees of partial melting and Os concentrations in the melt tend to be two

or three orders of magnitude less than the source (Shirey and Walker, 1998, and references therein). Oceanic and continental crust are ultimately formed from such melts, therefore almost all crustal rocks are distinguished by low Os concentrations and slightly higher Re concentrations relative to the mantle (Martin, 1990). Crustal rocks tend to have a higher Re/Os ratio than the mantle and therefore, with time, crustal Os becomes enriched in radiogenic ^{187}Os, compared to the mantle. The residual mantle, after partial melting, evolves with a Re/Os ratio less than that of the original source, and therefore a $^{187}Os/^{188}Os$ ratio less than that of the bulk earth (Figure 1.1). In the case of high degrees of melt extraction that typifies Archean sub-cratonic lithospheric mantle, Re may be removed wholly from the mantle source with a resulting lack of evolution of $^{187}Os/^{188}Os$ with time, thus preserving the initial value prior to melting.

The high abundances of Os in the lithospheric mantle compared to mantle-derived melts means that ultramafic xenoliths are relatively insensitive to contamination by their host magma, in contrast to incompatible elements such as Sr, Nd and Pb. Variations in the Os isotopic composition within mantle peridotites should therefore reflect previous periods of Re loss, possibly related to initial melt removal, rather than metasomatic alteration (Walker *et al.*, 1989).

1.2.3 Timing of lithospheric mantle formation

The timing of melt depletion in peridotites can be determined from the Re-Os systematics in one of several ways.

(i) the Re-Os isotopic compositions of the peridotites may produce isochrons defined by a line on a $^{187}Re/^{188}Os$ vs. $^{187}Os/^{188}Os$ diagram (Shirey, 1997), the slope of which equals the age of the melt event;

(ii) the correlation of melt depleted major elements such as Al with Os isotopic compositions can be used to infer the age of the melting event from the model age of the intercept on an Al_2O_3 vs. $^{187}Os/^{188}Os$ diagram (Reisberg and Lorand, 1995);

(iii) alternatively, model ages can be calculated directly for each peridotite sample by referencing the Os isotopic composition to upper mantle evolution curves.

Using the latter technique two model ages can be described (Figure 1.1), the mantle separation age (T_{MA}), and the Re-depletion age (T_{RD}). The T_{MA} model age assumes that

the Re/Os ratio of the sample has remained unchanged since its time of fractionation from a fertile mantle reservoir in a single-stage process. The measured $^{187}Re/^{188}Os$ is used to extrapolate the $^{187}Os/^{188}Os$ composition of the sample back to a chondritic reservoir, according to

$$T_{MA} = \frac{1}{\lambda_{Re}} \times \ln\left(\frac{(^{187}Os/^{188}Os)_{mantle} - (^{187}Os/^{188}Os)_{sample}}{(^{187}Re/^{188}Os)_{mantle} - (^{187}Re/^{188}Os)_{sample}} + 1\right)$$

where $(^{187}Os/^{188}Os)_{mantle} = 0.1287$ and $(^{187}Re/^{188}Os)_{mantle} = 0.4243$ (Meisel *et al.*, 1996), and λ_{Re} is the decay constant of $^{187}Re = 1.666 \times 10^{-11}$ (Smoliar *et al.*, 1996; Shirey and Walker, 1998).

The T_{RD} model age is similarly calculated but assumes that the initial $^{187}Re/^{188}Os$ ratio of the sample is zero (Walker *et al.*, 1989). This assumption is valid for mantle residues if the peridotite has experienced large degrees of partial melt extraction, depleting the sample wholly of Re. In this case, the T_{RD} and T_{MA} should approach one another. If the sample contains residual Re the T_{RD} represents a minimum age for the Re-depletion event.

The T_{MA} model ages produced for lithospheric mantle peridotites will be erroneous if the Re/Os ratio of the samples has changed more than once during the sample's evolution. Re enrichment through metasomatic processes would elevate the evolutionary trajectory of the Os isotopic composition resulting in a displacement of the intercept with fertile mantle to older ages. Re loss, as may be expected from weathering, would have the opposite effect, resulting in an underestimation of T_{MA} model ages. The T_{RD} model age, by contrast, will always provide a minimum age, as it is independent of the Re/Os ratio.

Previous studies of cratonic sub-continental lithospheric mantle have illustrated large discrepancies between T_{RD} and T_{MA} model ages for many samples (Walker *et al.*, 1989; Pearson *et al.*, 1995a; Pearson *et al.*, 1995b; Carlson *et al.*, 1999). If the systematics of the whole Platinum Group Element (PGE) suite are considered in conjunction with Re-Os age systematics it may be possible to evaluate the significance of T_{RD} and T_{MA} model ages and better constrain the age of the lithospheric mantle beneath cratons.

1.3 Platinum Group Elements in the mantle

The PGEs, including Os, are highly siderophile elements (HSEs), and are preferentially partitioned into metallic iron. In the absence of metallic iron, PGEs behave as chalcophiles and concentrate in sulfides. If we assume that the Earth accreted from chondritic material early in its history, during the formation of the core, separating metal and sulfide phases would have scavenged the HSEs leaving the upper mantle depleted in PGEs relative to chondrite (Chou *et al.*, 1983, Morgan *et al.*, 1981, Morgan, 1986).

HSEs in mantle xenoliths originating from the Earth's upper mantle are chondritic, and their abundances higher than expected from core-mantle equilibrium. It has been speculated that a chondritic component was added to the earth, following core formation, from late meteorite bombardment (Chou *et al.*, 1983, Morgan *et al.*, 1981, Morgan, 1986).

PGEs can be subdivided into two groups based upon their geochemical behaviour. The Ir group, or IPGEs, consists of the elements Ir, Os and Ru. The Pd group, or PPGEs comprise the elements Rh, Pt and Pd.

1.3.1 Location of PGEs in the mantle

PGEs are thought to reside predominantly in solid-solution in the intergranular base-metal sulfide phases present in the mantle (Mitchell and Keays, 1981). High measured abundances of PGEs in sulfides have been the main argument for sulfides being the primary host for PGEs in the mantle (Jagoutz *et al.*, 1979; Hart and Ravizza, 1996; Pattou *et al.*, 1996; Burton *et al.*, 1999; Alard *et al.*, 2000; Pearson *et al.*, 2000). From studies of Pyrenean orogenic lherzolites Lorand *et al* (1999) suggested that PGEs, although differing widely in chemical properties and geochemical behaviour, were strongly partitioned into the same phases based upon good PGE correlations.

It has often been speculated however that IPGEs are controlled by refractory phases such as Ir-Os alloys rather than sulfides (Mitchell and Keays, 1981; Fryer and Greenough, 1992; Garuti *et al.*, 1997; Brennan and Andrews, in press). Sulfides would normally be present as monosulfide solid solutions (*mss*) or molten sulfides under normal lithospheric mantle conditions but would re-equilibrate to low-temperature phases during emplacement of the xenolith (Keays *et al.*, 1981). Consensus in the literature suggests that IPGEs are controlled by separate phases to PPGEs, in peridotite samples collected at the surface. It does not exclude the possibility that within the

lithosphere or asthenosphere, PGEs and Re reside primarily in monosulfide solid solutions (*mss*) or sulfide liquid. Peridotites undergoing >30% partial melt removal will begin to lose their *mss* component. It has been suggested by Brennan and Andrews (in press), that *mss* in peridotites undergoing melt extraction may breakdown into micro-sulfides such as laurite or Ru-Os-Ir alloys with much higher solidi than *mss*. The existence of sulfide phases that are PGE specific, such as Pt in PtS and Ru in laurite, suggests that PGEs may not necessarily partition equally. This is consistent with the fractionation seen between IPGEs and PPGEs in depleted peridotites.

Os is considered to be somewhat heterogeneously distributed on a whole rock scale in the mantle (Martin, 1990). The root cause of the observed variability in absolute abundances of PGEs between individual samples of lithospheric mantle (a "nugget effect"), is likely to be from the heterogeneous distribution of sulfides or alloys and further detailed study is required to search for these samples.

1.3.2 Fractionation of PGEs during mantle melting

The differing chemical properties of IPGEs and PPGEs means that they fractionate differently during partial melting of the mantle. IPGEs, including Os, are compatible and remain in the residue whereas PPGEs, in contrast, are mildly incompatible and partition into the melt.

CI chondrite-normalised PGE abundances are plotted as recommended by Naldrett and Duke (1980), in order of decreasing melting point of the pure metal. Re is introduced to the PGE pattern and placed to the right of Pd due to the similarity in geochemical behaviour and similar compatibility. Chondrite-normalised PGE patterns present us with a method of assessing whether the Re-Os isotope system has remained closed since initial melt extraction and to what extent it has been disturbed by metasomatism. If melt/fluid enrichment or disturbance affects the peridotite subsequent to melt depletion, this should be reflected in the PGE pattern and PGE-major element systematics.

1.4 Inter-relationship of crust and lithospheric mantle

Previous Re-Os isotope studies of the sub-cratonic lithospheric mantle underlying the Archean Kaapvaal and Siberian cratons have demonstrated that the lithospheric mantle yields broadly similar ages to the age of the overlying crust (Pearson *et al.*, 1995a; Pearson *et al.*, 1995b; Carlson *et al.*, 1999). This evidence suggested that the

stabilisation of the lithospheric mantle possibly coincided with periods of crust formation, with a potential association between the generation of both mantle and crust in the Archean. Similar conclusions were arrived at from studies of Proterozoic circum-cratonic peridotite xenoliths and overlying Proterozoic crust in southern Africa (Pearson *et al.*, 1994).

1.5 Objectives of this study

Our present understanding of the timing of formation and stabilisation of Archean cratons, and their buoyant lithospheric mantle keels, is dominated by studies of kimberlite-hosted peridotite xenoliths from the Kaapvaal and Siberian cratons. One of the principle aims of this study was to expand the present database to include samples from other cratonic settings, specifically the Slave craton and Churchill province of Canada, to assess proposed models of craton formation and to allow better assessment of how representative samples from the Kaapvaal craton are as a whole. This comparison has only recently become possible because of the intense efforts in diamond exploration and mining taking place in northern Canada.

In addition to studying xenoliths from other cratonic settings, this study provides a very detailed examination of Re-Os isotope systematics of peridotite xenoliths from the SE part of the Kaapvaal craton; the Lesotho kimberlite field. These kimberlites contain exceptional xenolith inventories and provide an excellent opportunity to investigate the lithospheric mantle beneath the region. In addition, existing studies of xenoliths in the immediately adjacent off-craton area of E. Griqualand allow investigation of the nature of the lithosphere at the craton margin.

Previous studies of cratonic lithospheric mantle beneath the Kaapvaal and Siberian cratons were based upon well-constrained peridotite suites, biased towards xenoliths rich in garnet and clinopyroxene (CPX), which permit pressure-temperature calculations to be made. A further aim of this project was to focus on depleted Kaapvaal ultramafic xenoliths with lower garnet and CPX abundances, to examine whether such samples provide less disturbed Re-Os isotope systematics.

The over-riding theme of the study was to further constrain the link between ages recorded for crustal formation and modification, with Re-Os ages obtained for the lithospheric mantle, especially in the light of new geochronological data for lower crustal xenoliths from the regions studied.

Chapter 2

Analytical Techniques for the Determination of Re-Os isotopes and PGEs

2.1 Introduction

Numerous analytical techniques have been used to determine PGE abundances in geological samples, complemented by various chemical and pre-concentration techniques. Advances in inductively coupled mass spectrometry (ICP-MS) allow for pg/g detection limits for all PGEs. It has also been shown that negative ion thermal mass spectrometry (N-TIMS) is capable of determining pg/g levels of Os and Ir, together with Re (Creaser *et al.*, 1991; Völkening *et al.*, 1991; Walczyk and Heumann, 1993). The ease with which individual PGEs can be chemically separated from their matrices varies, and is related to their physical and chemical properties. The application of PGE analysis and instrumental techniques to geological samples is therefore limited by the ability to separate the PGEs at pg/g levels whilst retaining the low-level blanks necessary to match instrument detection levels.

2.2 Summary of analytical methods

In general, many of the PGE analytical techniques available do not allow for the determination of Re-Os isotopic compositions and other PGE abundances on the same aliquot. These methods are therefore unable to provide the geochronological information offered by the Re-Os decay system, and allow investigation of the relationship between Os isotope variations and PGE fractionation (Pearson and Woodland, 2000).

Ni-S fire assay

Ni-sulfide fire assay has been a favoured preconcentration method for PGEs for many analytical techniques including instrumental neutron activation analysis (INAA, Hoffman *et al.*, 1978; van Loon and Barefoot, 1991; McDonald *et al.*, 1994) and ICP-MS (Hall and Pelchat, 1994; Pattou *et al.*, 1996). The method has also been applied to Os-isotope analysis by N-TIMS (Martin, 1990; Hauri and Hart, 1993). This

preconcentration method is attractive because of the ability to use large sample aliquots (20g or more) to maximise the PGEs available for analysis, minimising PGE heterogeneity and "nugget effects".

The difficulty in obtaining high-purity nickel and reagents to allow determination of low-levels of PGEs in geological samples is a disadvantage of this method (Jarvis *et al.*, 1997b; Ravizza and Pyle, 1997; Woodland and Pearson, 1999). The blanks for nickel are both high and variable, and their contribution to the samples analysed is unclear (Woodland and Pearson, 1999). High Re blanks are common in flux materials (Martin, 1990), and the Ni-S fire assay technique does not quantitatively separate Re for analysis. Martin (1990) found that when fusions were spiked for isotope dilution, equilibrium of isotopes between the glass and bead was not accomplished. Re is therefore determined from separate aliquots and heterogeneity becomes an issue. Isolation of Os by aliquoting the concentrate reduces the sensitivity in low-level samples. Oxidising the Os to OsO_4 enhances ionisation (Gregoire, 1990), and also raises problems of memory effects if using ICP-MS (Pearson and Woodland, 2000). The nickel used in this method may also produce Ni-Ar interference on Ru, if Ni is carried over from the bead dissolution.

The Ni-S fire assay method, though useful for many applications, is not suitable for accurate geochronology or analysis of low-level PGE samples by ICP-MS.

Acid dissolution and sodium peroxide fusion

Acid dissolution techniques have very low-level blanks, and often employ isotope dilution (e.g. Enzweiller *et al.*, 1995). An advantage of this method is that the sample is in a suitable form for many preconcentration techniques. The method however often has poor recovery of PGEs due to refractory host phases (Hall and Pelchat, 1994), and may be susceptible to loss of volatile Os and Ru.

The fusion of samples with sodium peroxide can effectively dissolve refractory phases such as chromite. However, sample sizes are restricted (< 1g), and any heterogeneity of PGEs in the sample may cause serious analytical errors. Blank levels from the sodium peroxide or zirconium crucibles are also significant, particularly for Re-Os determinations (Morgan *et al.*, 1991), limiting this method and making it impossible for work on low-level Re samples (Pearson and Woodland, 2000).

2.3 Carius tube – Anion exchange chromatography preconcentration method

For combined Re-Os isotope and PGE studies, a low-blank, isotope dilution technique is required allowing analysis of Re, Os, Ir, Ru, Pt and Pd from the same aliquot. A new Carius tube – anion exchange chromatography method was developed at Durham University, and is described by Woodland (2000) and Pearson and Woodland (2000). A comparison of this technique with Ni-S fire assay is summarised by Woodland (1999).

2.3.1 Carius tube digestion of samples

Carius tube digestion is an old technique that has only recently been applied to the dissolution of geological samples, particularly for Re-Os isotope analysis (Shirey and Walker, 1994; Shirey and Walker, 1995). This method involves high-temperature (inverse) aqua regia digestion of geological samples between 220 and 240 °C (Shirey and Walker, 1995), in sealed carius tubes. Although silicates may not be completely digested by this method, under the highly oxidising conditions Re and Os are effectively and quantitatively released from refractory Pt-group phases (Shirey and Walker, 1995; Cohen and Waters, 1996). In recent studies, Rehkämper and Halliday (1997) demonstrated the effectiveness of carius tube digestion techniques in measuring other PGEs in geological samples. During digestion the aqua regia oxidises the Os to its highest valence state and creates the volatile OsO_4 (Shirey and Walker, 1995). The Os however is retained by the impervious, sealed carius tube and allows complete equilibration between spike and sample.

Carius tube method:

- Carius tubes pre-cleaned in boiling aqua regia
- Carius tubes chilled to –10°C in water-ethanol mix
- 1-2 g of sample weighed and transferred to carius tube via a funnel
- add pre-weighed spike to carius tube
- Add 2 ml conc. HCl to carius tube
- Add 5 ml conc. HNO_3 to carius tube
- Carius tube neck sealed using gas torch
- Carius tube warmed to room temperature and shaken to mix samples and acids
- Carius tube placed in steel jackets and heated in oven for 3 days

- Carius tube cooled to room temperature and then chilled before opening

A disadvantage of the carius tube technique is the small sample size. This is particularly a problem for the analysis of PGEs where heterogeneous distribution is possible (McDonald, 1998). This can be solved by replicate analyses of samples and ensuring that the samples are well powdered and homogenised. The advantage of this method, especially for low-level PGE analysis, is the low blank levels. Procedural blanks are dependent on reagents and are typically < 7pg for Os, < 1pg for Ir, < 10pg for Ru and Re, ~ 10pg for Pd and < 25pg for Pt (Woodland and Pearson, 1999; Pearson and Woodland, 2000).

2.3.2 Isotope dilution

Isotope dilution allows for accurate measurement of elemental abundances, providing isotope ratios can be measured accurately (Heumann, 1988). It is limited however by the requirement to find two isotopes that are unaffected by isobaric interferences (see review of isobaric interferences for PGEs in Pearson and Woodland, 2000), and the need to predict the sample concentration to optimise spikes. Rhodium, which is monoisotopic, is the only PGE not amenable to isotope dilution. All other PGEs have at least two isotopes, and a number of studies have used this method (Enzweiller *et al.*, 1995; Ravizza and Pyle, 1997; Rehkämper and Halliday, 1997).

To reduce weighing errors it is optimal to have a mixed single spike. The enriched isotopes chosen for the Durham peridotite spike were ^{99}Ru, ^{106}Pd, ^{185}Re, ^{190}Os, ^{191}Ir and ^{194}Pt (Pearson and Woodland, 2000). Spike concentrations are optimised so that approximately 0.1 ml of spike are required for each sample analysed.

2.3.3 Chemical separation of Re and PGEs

The Carius tube - anion exchange method allows the separation of all PGEs, and therefore maximises detection limits by reducing the number of masses that need to be measured. In addition, Re and Os are separated in the same dissolution. Preconcentration of samples removes most of the matrix, and thus minimises isobaric interferences and reduces matrix suppression in the plasma. The separation procedure comprises of several stages including solvent extraction and anion exchange columns, with yields rarely achieving 100%, and therefore isotope dilution is necessary.

2.3.3.a Solvent extraction of Os

The procedure of solvent extraction generally follows the methodology of Cohen and Waters (1996). Prior to opening, carius tubes are chilled to reduce internal pressure and prevent the escape of volatile OsO_4.

Os extraction

- The aqua regia solution and sample residue is removed and added to 4 ml chilled carbon tetrachloride. The mixture is allowed to warm and shaken for ~ 2 min to ensure thorough mixing.
- The organic fraction is separated from the aqua regia and added to 4 ml of chilled 9N HBr.
- Organic extraction of the aqua regia is repeated twice more to ensure consistent Os yields.
- After the final organic extraction and the maximum amount of CCl_4 has been removed from the aqua regia, the aqua regia is ready for further preconcentration of the other PGEs and Re.
- The HBr - CCl_4 mixture, with the Os, is sealed in its vial and allowed to warm to room temperature and then thoroughly shaken. This mixture is heated gently under a heat lamp for ~ 1 hour, or left overnight to ensure equilibration and transfer of the Os from the CCl_4 to the HBr.
- The HBr - CCl_4 mixture is allowed to cool and the HBr is pipetted from the organic phase and dried down. The Os is now ready for analysis by ICP-MS after being taken up in 1 ml of 3.5% HNO_3, or further purified for N-TIMS analysis.

The method for further purification of the Os for N-TIMS analysis follows the procedures of Roy-Barman and Allègre (1995) and Cohen and Waters (1996).

Micro-distillation of Os for N-TIMS analysis

- HBr and Os drydown taken up in 20 μl of chilled 9N H_2SO_4.
- Sample transferred to the cap of a 7 ml Savillex® teflon conical vial.
- 5 μl of 9N CrO_3 pipetted onto the sample and thoroughly mixed.
- 20 μl of 9N HBr pipetted into the bottom of the conical vial. PTFE tape is applied to the thread of the vial.
- Conical vial carefully inverted and screwed onto the cap taking care not to dislodge the HBr.
- Teflon vial wrapped in foil leaving a gap below HBr to avoid overheating.

- Vial heated at 80 °C for 2 hours. Os is oxidised by CrO_3 and causes a micro-distillation of the Os into the HBr.
- Vials are removed from the hotplate and the cap unscrewed before inverting the base to the upright position
- The HBr is dried down and the sample is ready for N-TIMS analysis.

2.3.3.b Chromatographic separation of Ir, Ru, Pt, Pd and Re

To improve sensitivity and for effective analysis of PGEs by ICP-MS it is advantageous to separate the individual elements into different fractions. As a result of the differing behaviour of individual PGEs on anion resin (Korkisch and Klakl, 1989), ion-exchange chromatography is an ideal method for separating the PGEs. This method of separation has been used widely for analysis of combinations of PGEs (e.g. Morgan *et al.*, 1991), and Rehkämper and Halliday (1997) proposed a method for the separation of PGEs and Re using mixed acid elutions. Unfortunately, the method presented by Rehkämper and Halliday (1997) did not include the ability to separate Os. Pearson and Woodland (2000) presented an anion-exchange separation technique that compliments the extraction of Os. PGEs have an affinity for anion-exchange resin and therefore chromatography is an obvious means of PGE separation. Application of this method however requires isotope dilution because of difficulties in quantitative elution from the resin (Jarvis *et al.*, 1997b; Jarvis *et al.*, 1997a).

Sample preparation

The residual aqua regia and silicate residue from the Os extraction procedure contains the other PGEs, and requires preparation for column chemistry.

- The aqua regia is dried down under a heat lamp in a clean environment.
- 1 ml conc. HNO_3 is added to the drydown, refluxed and dried down again to remove residual CCl_4.
- 2 ml conc. HF and 0.5 ml conc. HNO_3 are added to the sample and refluxed. Residual SiO_2 is removed as SiF_4, reducing the matrix before adding to the column and freeing PGEs from silicate phases. Sample dried down.
- 2 ml conc. HNO_3 added to the samples to remove residual HF. Sample dried down.
- 2 ml conc. HCl added to the sample to convert PGEs to a chloride form necessary for the column chemistry. Sample dried down.

- Sample taken up in 10 ml of 0.5N HCl and centrifuged to remove insoluble precipitate.
- Cl_2 is bubbled through the sample solution and it is left overnight to ensure oxidation of PGEs (after Anbar *et al.*, 1997).

The valence state of the PGEs is important for their adsorption onto the anion-exchange resin (Korkisch and Klakl, 1989), in particular Ir which is more strongly retained as $IrCl_6^{2-}$. Chlorine gas is used as a strong oxidant to achieve this oxidation state of Ir, as it has the advantage of introducing no matrix to the sample and minimises the blanks.

Anion-exchange separation method

- 1 ml pre-cleaned (Pearson and Woodland, 2000) Biorad® AG1-X8 100-200# resin is loaded into a standard Biorad® column with 2 ml resin capacity and 10 ml reservoir.
- Resin cleaned with 20ml warm 12N HNO_3 followed by 35 ml MQ water.
- Resin conditioned with 30 ml 6N HCl followed by 35 ml chlorinated 0.5N HCl to ensure oxidation of resin.
- Sample loaded onto column.
- 5 ml 0.8N HNO_3 added to column to elute transition elements, e.g. Zn (after Rehkämper and Halliday, 1997), followed by 10 ml 1N HF/HCl to elute Hf and Zr.
- 20 ml of 0.1M H_2SO_3 are eluted to reduce Ir (after Anbar *et al.*, 1997).
- 30 ml of MQ water are eluted to remove traces of H_2SO_3.
- Ir is eluted and collected in 20 ml of 2N HCl.
- Pt is eluted and collected in 20 ml of 6N HCl.
- 5 ml of MQ water is eluted to remove traces of HCl.
- Re and Ru are eluted and collected in 20 ml of 4N HNO_3.
- Pd is eluted and collected in 20 ml of warm 12N HNO_3

This procedure allows the separation of five fractions. The yields for Os are between 70 and 90% (Cohen and Waters, 1996). Yields for Re are ~ 90%, yields for Ir, Pt and Pd are between 60-70% and yields for Ru are variable between 30 and 60% (Pearson and Woodland, 2000).

2.4 Mass Spectrometry

Analyses of Re and PGEs were performed at Durham University using a Perkin Elmer Sciex Elan 6000 quadrupole ICP-MS. Analyses of Os by N-TIMS were performed at the Carnegie Institution of Washington using their in-house 15" magnetic sector thermal ionisation mass spectrometer.

2.4.1 Re and PGE analyses by ICP-MS

2.4.1.a Nebulisation

Two types of nebuliser were used in conjunction with the ICP-MS during measurement of PGE data.

i. A standard cross-flow nebuliser with Scott-type double pass spray chamber.

ii. CETAC Technologies Aridus® de-solvating micro-concentric nebuliser.

The instrument was optimised prior to PGE analysis, and performance monitored, by a daily check solution from which oxide production and machine sensitivity could be assessed.

The standard cross-flow nebuliser was used to obtain Re and occasionally Ir, Ru, Pt and Pd abundance data. The standard rate of up-take for this nebuliser was ca. 1 ml/min. Detection limits were controlled by the requirement to dilute samples to ca. 1.5 – 2 ml. The cross-flow nebuliser has a low memory for PGEs, and oxide production for elements producing isobaric interferences range from 0.8 to 2.5% as metal-oxide to metal ratio (Pearson and Woodland, 2000).

The CETAC Aridus® nebuliser was used to obtain Ir, Ru, Pt and Pd data. Sample up-take rates ranged from 45 – 70 μl/min, dependant on optimisation of the ICP-MS, and oxide production was generally < 0.03%. The Aridus nebuliser produces a higher magnitude of signal than the cross-flow nebuliser. Additionally, sensitivity can be enhanced by the low up-take rate of the Aridus, which permits better pre-concentration of samples by taking up in smaller volumes of liquid.

2.4.1.b Instrument mass-bias and precision

Throughout PGE data collection, mass bias was estimated using standard solutions, ranging in concentration from 0.1 to 10 ppb, dependant on the approximate concentration of the element within the sample. Typical mass bias correction factors for the measured ratios are illustrated in Table 2.1.

Element	**Ir**	**Ru**	**Pt**	**Pd**	**Re**
Ratio Measured	**193/191**	**101/99**	**195/194**	**105/106**	**187/185**
Natural Ratio	1.681	1.346	1.027	0.817	1.674
Measured Ratio	1.717	1.421	1.04	0.794	1.692
2σ error	0.008	0.02	0.006	0.029	0.005
MBCF	0.979	0.947	0.988	1.029	0.989

Table 2.1 Typical mass bias correction factors for PGEs (2σ errors based on approximately 20 individual analyses).

The mass bias effects for the ratios measured are summarised in Figure 2.1. The lower atomic mass PGEs, Ru and Pd, show the largest mass bias (Figure 2.1) at ca. 2.5 % per atomic mass unit (AMU^{-1}). The mass bias, though variable between analytical sessions, is reproducible within individual sessions, 2σ relative standard deviations (RSDs) ranging between 0.1 and 0.4 %. The variability of mass bias for Ru (2.41 ± 0.61 % AMU^{-1}) is more than three times that of Pd (2.49 ± 0.19 % AMU^{-1}). This may be attributable to errors induced by the lower signals measured for Ru compared to Pd, or greater isobaric interferences (see review by Pearson and Woodland, 2000).

The higher atomic mass PGEs (Re, Ir and Pt) produce lower mass bias values, with all elements lower than 1.5 % AMU^{-1} (Figure 2.1). Within individual sessions 2σ RSDs were generally less than 0.4 %. Elements that are close in mass, such as Ir and Re, do not necessarily show the same degree of mass bias on the ICP-MS e.g. 0.91 ± 0.24 % AMU^{-1} for Ir vs. 0.82 ± 0.25 % AMU^{-1} for Re. For this reason the Re standard is not used as a mass-bias for Ir, nor spiking with non-PGEs of similar atomic mass. The long-term mass-bias for Pt is higher than both Ir and Re at 1.14 ± 0.36 % AMU^{-1}. The quality of standard reproducibility for mass-bias means the error from correction in the isotope dilution calculation is negligible.

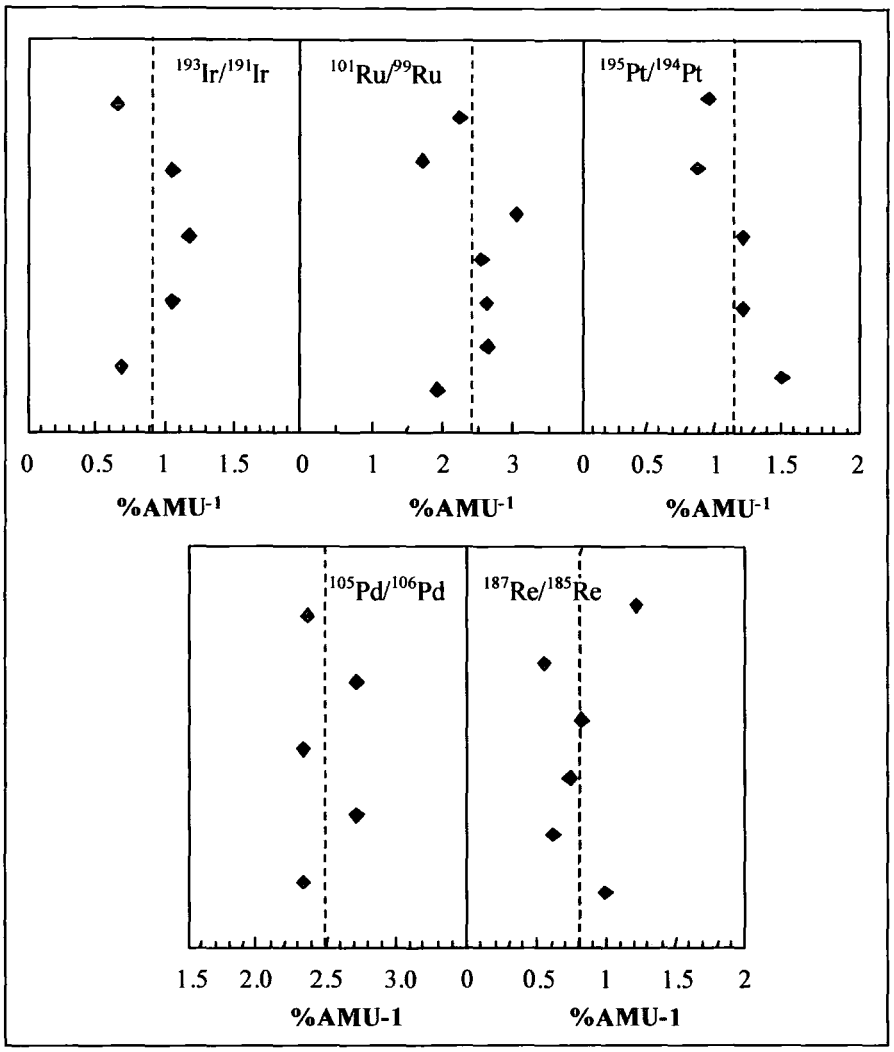

Figure 2.1 Mass bias per atomic mass unit for measured PGE isotope ratios. Each data point represents between 15 and 25 separate analyses of standard solutions in the 0.1 to 10 ng/g concentration range. Two-sigma error bars of the mean standard for each analysis are smaller than symbols. Dashed line represents the overall mean for the plotted values.

2.4.1.c Analytical procedure

The RF power for the ICP-MS during analysis of PGEs ranged from 1200 to 1300 W, dependant on nebulisation. The cross-flow nebuliser generally requires higher power settings than the CETAC Aridus® desolvating nebuliser. Twenty-five to thirty mass sweeps were performed for one isotopic ratio measurement, with 25 to 30 replicates. Peak dwell time ranged from 20 to 40 ms. Ion-lens settings were optimised for the mass-range being measured during any given session, and during individual sessions normally only one element was measured. Elemental and oxide interferences were corrected on-line.

The dried-down column cuts were taken up in 3.5 % HNO_3, up to 3 hrs prior to analysis, and refluxed to ensure the PGEs were taken up into solution. The samples

were then transferred to micro-centrifuge tubes for analysis and storage. The volume of diluent used to take the samples up into solution is dependant on the element being analysed and the number of masses that are required to be measured, and which nebuliser is used.

Prior to sample analysis PGE standard solutions were run to establish mass-bias corrections, and oxide generation levels were monitored using pure element solutions of Hf, Mo, Zr and Y. The corrections for oxide production were updated in the software for on-line correction. During sample analysis, the samples were interspersed with standard and pure element solution to monitor oxide-production, sensitivity and mass-bias drift. All further data reduction was performed off-line with spreadsheets.

2.4.1.d Accuracy and precision

Before investigating the PGE results for samples, it is useful to perform replicate analyses on appropriate standards to characterise inter-element fractionation (McDonald, 1998), and outline accuracy and reproducibility. Eight replicate analyses were performed on the in-house Durham University peridotite PGE standard, sample GP13, a spinel lherzolite from the Beni Bousera peridotite massif (Table 2.2).

Sample	Os (ppb)	Ir (ppb)	Ru (ppb)	Pt (ppb)	Pd (ppb)	Re (ppb)
GP13 (1)	3.72	3.22	7.04	6.70	5.92	0.33
GP13 (2)	3.67	3.23	6.72	6.38	5.36	0.33
GP13 (3)	3.85	3.41	6.95	7.46	5.44	0.34
GP13 (4)	4.15	4.09	7.34	7.28	5.28	0.33
GP13 (5)	3.72	3.28	6.71	6.49	5.87	0.32
GP13 (6)	3.83	3.75	6.76	7.19	5.68	0.33
GP13 (7)	3.99	3.86	7.00	6.66	5.31	0.32
GP13 (8)	4.02	3.67	7.23	7.85	6.27	0.33
Mean	3.87	3.56	6.97	7.00	5.64	0.33
stdev	0.17	0.33	0.23	0.52	0.35	0.01
2σ % RSD	8.77	18.36	6.66	14.89	12.56	3.23
Primitive mantle	3.4	3.2	5.0	7.1	3.9	0.28
CI chondrite	490	455	710	1010	550	40

Table 2.2 Replicate analyses of Durham peridotite standard GP13. CI chondrite values from McDonough and Sun (1995). Primitive mantle values taken as 0.007 x CI chondrite after method of McDonough and Sun (1995).

The data in Table 2.2 are based on the analyses of either 1 or 2 g sample aliquots. In general elements show reproducibility better than 15 % (2σ RSD), except Ir which is slightly higher at 18.36 % (Figure 2.2).

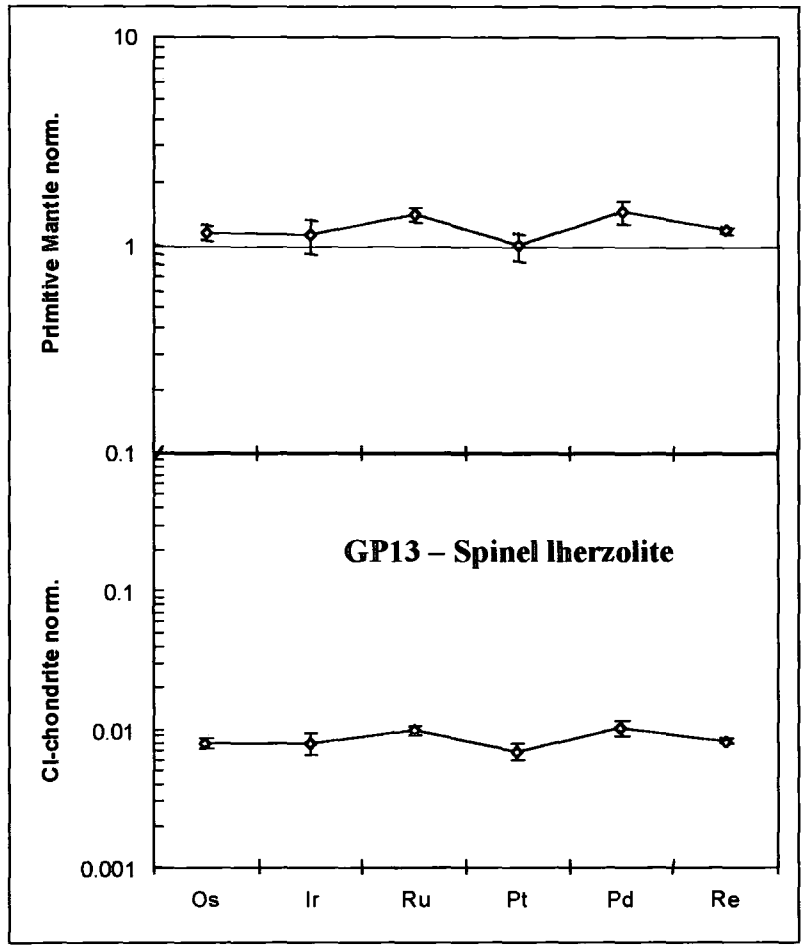

Figure 2.2 Chondrite and primitive mantle normalised PGE abundances for replicate analyses of sample GP13 (a spinel lherzolite form the Beni Bousera orogenic massif), from Table 2.2. Normalising factors after Table 2.2 (McDonough and Sun, 1995). Error bars are 2σ RSD.

The variation observed between the individual analyses may originate from incomplete digestion of refractory phases such as spinel during Carius tube digestion. Two groups of elements are apparent in sample GP13, those with exceptional reproducibility less than 10 %, i.e., Os, Ru and Re (8.77, 6.66 and 3.23 % 2σ RSD), and those with reproducibility between 10 and 20%, i.e. Ir, Pt and Pd. Although there is a variation in the reproducibility between IPGEs in standard GP13, such as Os and Ir, the mean concentrations of Os and Ir produce a chondritic ratio overall (Figure 2.3a). Analysis of peridotite samples during this study consistently produced near chondritic Os/Ir ratios (Figure 2.3b), suggesting good access to all PGE phases during digestion using the carius tube technique.

The PGE abundances in GP13 are comparable to those of typical orogenic spinel lherzolites analysed by other methods (e.g. Pattou *et al.*, 1996). The levels of

reproducibility, and similarity of PGE values for GP13 with those expected for this type of rock indicate that the technique gives accurate and precise PGE data for peridotites.

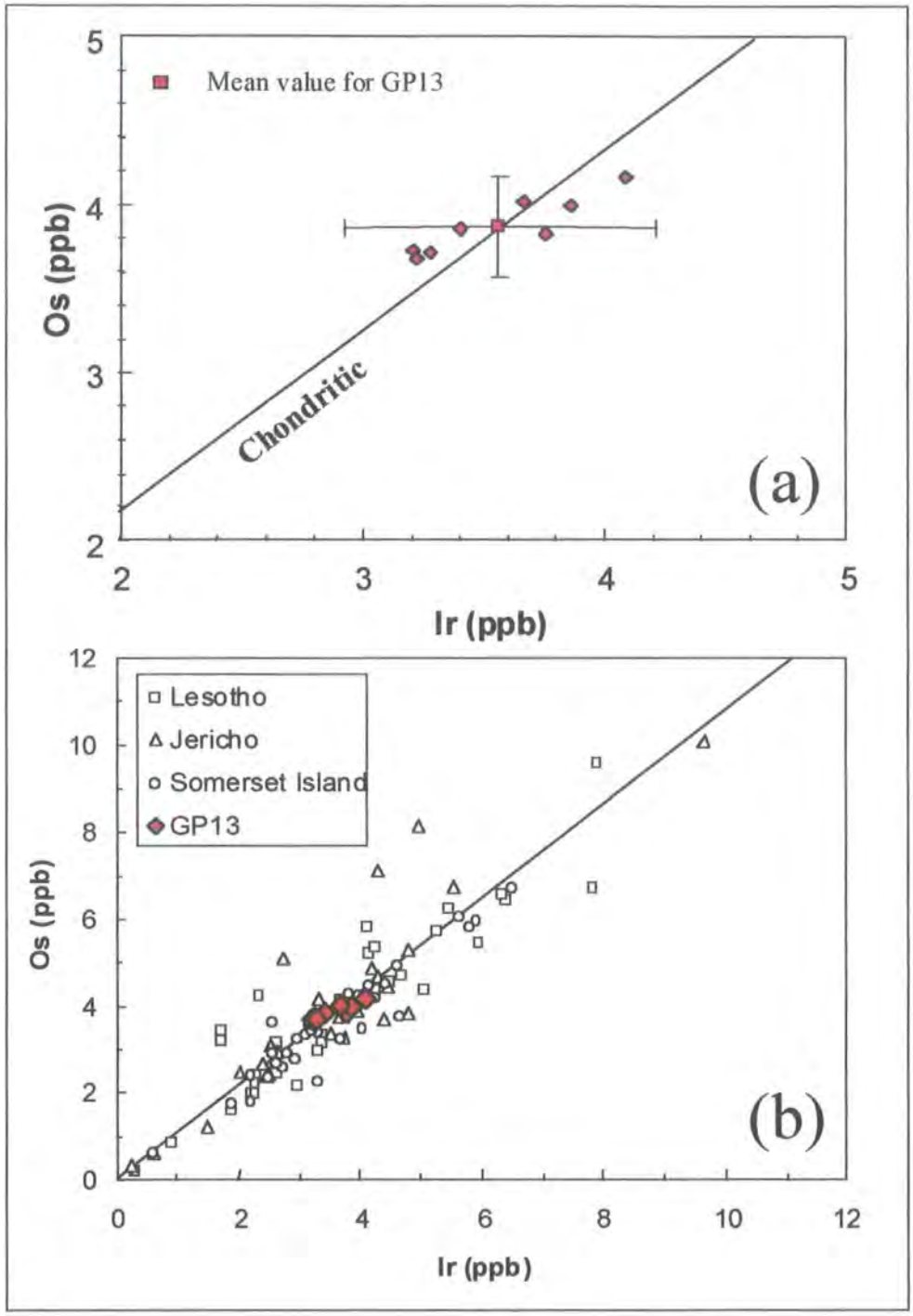

Figure 2.3 Plot of Os vs. Ir for GP13 and peridotites from the Lesotho, Jericho and Somerset Island peridotite suites. (a) Os and Ir data for GP13, from Table 2.2, with 2σ RSD% error bars. (b) Os and Ir data for GP13 and 98 peridotite samples from the Lesotho, Jericho and Somerset Island suites. Line represents the chondritic ratio (McDonough and Sun, 1995).

2.4.2 Os analyses by N-TIMS

2.4.2.a Sample preparation

For analysis of Os by N-TIMS, samples are loaded onto Pt filaments. The Pt filament is prepared from Pt-ribbon, rolled from a high-purity Pt-wire. The Pt ribbon is pre-cleaned by heating for 1 to 4 hrs in molten sodium carbonate or potassium pyrosulfate and leaching in 8N HNO_3. Dried down Os samples are taken-up in 9N HBr and loaded onto the Pt filaments. The HBr, with Os sample, are then dried-down under heatlamps and placed in an outgasser. Osmium samples are metalised for 3 hrs at a pressure $< 10^{-6}$ torr, and filament temperatures of 300-400 °C. After removal of the filaments from the outgasser, 20 μg $Ba(NO_3)_2$ are loaded and dried onto the filaments at the location of the Os sample to act as an electron-donor. The samples are then ready for loading into the mass-spectrometer.

2.4.2.b Operating conditions

Os is run as OsO_3^- ions (after Creaser *et al.*, 1991; and Völkening *et al.*, 1991) on the 15", 60° sector DTM mass spectrometer. Os is run on Pt filaments at temperatures of between 800 and 900 °C, and an oxygen leak degrading the vacuum to approximately 8 x 10^{-5} Pa, maintained by an oxygen bleed valve. ^{192}Os beams are maintained at less than 500 Kcps for 4 to 6 hours, during which time all Os isotopes are measured (masses 240, 238, 237, 236, 235 and 234), along with mass 233 ($^{185}Re^{16}O_3$). These are peak-hopped into the single electron-multiplier detector. Osmium isotope compositions are corrected for mass-dependant isotope fractionation using a linear law, normalised to $^{192}Os/^{188}Os = 3.082614$ (Creaser *et al.*, 1991). Osmium isotopic compositions are corrected for oxygen interference using the accepted values of Nier (1950), $^{17}O/^{16}O = 0.0003708$ and $^{18}O/^{16}O = 0.002085$.

2.4.2.c Accuracy and precision

To investigate the reproducibility of individual Os isotope ratios determined by N-TIMS, repeat analyses of the DTM Os standard were made during the period of this study. The standards were run under normal operating conditions applied to the samples. The fractionation and oxide corrected Os isotope ratios for the standards are presented in Table 2.3. Replicate determinations of the in-house DTM Os standard

gave external reproducibility for $^{187}Os/^{188}Os$ of less than ± 2.4 ‰ at the 2σ level (Table 2.3).

Sample	$^{192}Os/^{188}Os$	$^{190}Os/^{188}Os$	$^{189}Os/^{188}Os$	$^{187}Os/^{188}Os$	$^{186}Os/^{188}Os$
DTM std.	3.082614	1.98314	1.22029	0.17391	0.12031
DTM std.	3.082614	1.98487	1.21998	0.17448	0.11962
DTM std.	3.082614	1.98322	1.22071	0.17426	0.11997
DTM std.	3.082614	1.98262	1.21853	0.17445	0.12009
DTM std.	3.082614	1.98373	1.21969	0.17412	0.12011
DTM std.	3.082614	1.98245	1.21958	0.17413	0.12025
DTM std.	3.082614	1.98278	1.22089	0.17405	0.11985
Average	3.082614	1.98326	1.21995	0.17420	0.12003
2σ		0.00166	0.00159	0.00042	0.00048
DTM std.[a]	3.082614	1.9832 ± 12	1.2196 ± 10	0.17396 ± 38	0.1203 ± 29
DTM std.[b]	3.082614	1.9842 ± 54	1.2197 ± 39	0.17429 ± 55	0.1202 ± 16

Table 2.3 Replicate analyses of DTM Os standard solution over period of study. Blanks during analysis ranged from 1 to 5 pg. Os isotopic compositions are corrected for Oxygen interference using accepted values (Nier, 1950) and for mass fractionation to $^{192}Os/^{188}Os$ of 3.082614 (Creaser *et al.*, 1991). For comparative purposes, analyses of the DTM Os standard by Shirey (1997) are presented, [a] 13 samples analysed using analog counting, [b] 22 samples analysed using pulse counting, with 2σ errors of the population of measurements.

Chapter 3

Peridotite Xenoliths from the Lesotho Kimberlite Field

3.1 Introduction

Tomographic studies have shown that Archean cratons are underlain by thick, cold lithospheric mantle roots with high seismic velocities (Jordan, 1988; James *et al.*, 2001). The low-density, residual peridotite root contributes to the long-term stability of Archean continental lithosphere (Boyd and McCallister, 1976; Jordan, 1979). Samples of sub-cratonic mantle, erupted by kimberlitic magmatism, are dominated by xenoliths from both the Kaapvaal and Siberian cratons (Boyd and Mertzman, 1987; Boyd, 1989). These xenoliths have highlighted the refractory nature of mantle roots beneath Archean cratons i.e., residues depleted in fusible major elements from melt extraction (Nixon, 1987a; Herzberg, 1993; Boyd *et al.*, 1997), and similarities between mantle samples from these two areas have dominated thoughts on the evolution of cratonic lithospheric mantle (Boyd *et al.*, 1997).

Initial work on the Sr-Nd isotope chemistry of Kaapvaal peridotites indicated their antiquity (Menzies and Murthy, 1980; Richardson *et al.*, 1985). Previous Re-Os isotope studies of Kaapvaal lithospheric peridotites erupted by kimberlites have shown that the mantle part of the lithospheric keel is very ancient (generally > 2.5 Ga) over large areas (Walker *et al.*, 1989; Pearson *et al.*, 1995a; Carlson *et al.*, 1999), with the oldest ages being broadly coincident with major crust building. However, the xenoliths analysed in these studies produced a large variation in both Re-Os T_{RD} and T_{MA} model ages, and the cause and significance of this variation in age is not obvious. In the initial studies, peridotites were analysed that had been selected from a group of samples previously examined for their mineral composition in order to deduce their pressure and temperature of origin. As the technique of geothermobarometry is based on chemical exchange reactions between garnet, pyroxene and olivine, the samples selected for geothermobarometry, and thereafter Re-Os analysis, were among the more garnet and diopside-rich, and hence fertile, peridotites from South African kimberlites. Recent

studies suggest that some of the garnet and diopside may have been re-introduced by melt interaction following initial melt-depletion (Keleman *et al.*, 1992; Pearson *et al.*, 2001). This could result in widely varying Re-Os model age systematics that are difficult to specifically correlate with geological events recorded in the overlying crust.

In this study we have concentrated on depleted xenoliths from 4 kimberlites in Lesotho, on the SE margin of the Kaapvaal craton (Figure 3.1). Samples were selected with generally low abundances of garnet and diopside compared to some of the previously studied lherzolites, in an attempt to filter out some of the "noise" that may be associated with new, post melt-depletion growth of these phases. The aim of this study is to determine the time of melt depletion from the Kaapvaal lithospheric mantle, since this event(s) resulted in the creation of the chemically buoyant residual peridotites that may be essential to the long-term survival of continental lithosphere (Jordan, 1988). The study also allows us to compare age systematics in the Lesotho lithospheric mantle with those of other locations beneath the Kaapvaal craton, and also the lithospheric mantle as sampled by nearby off-craton kimberlites such as those in East Griqualand (Figure 3.1).

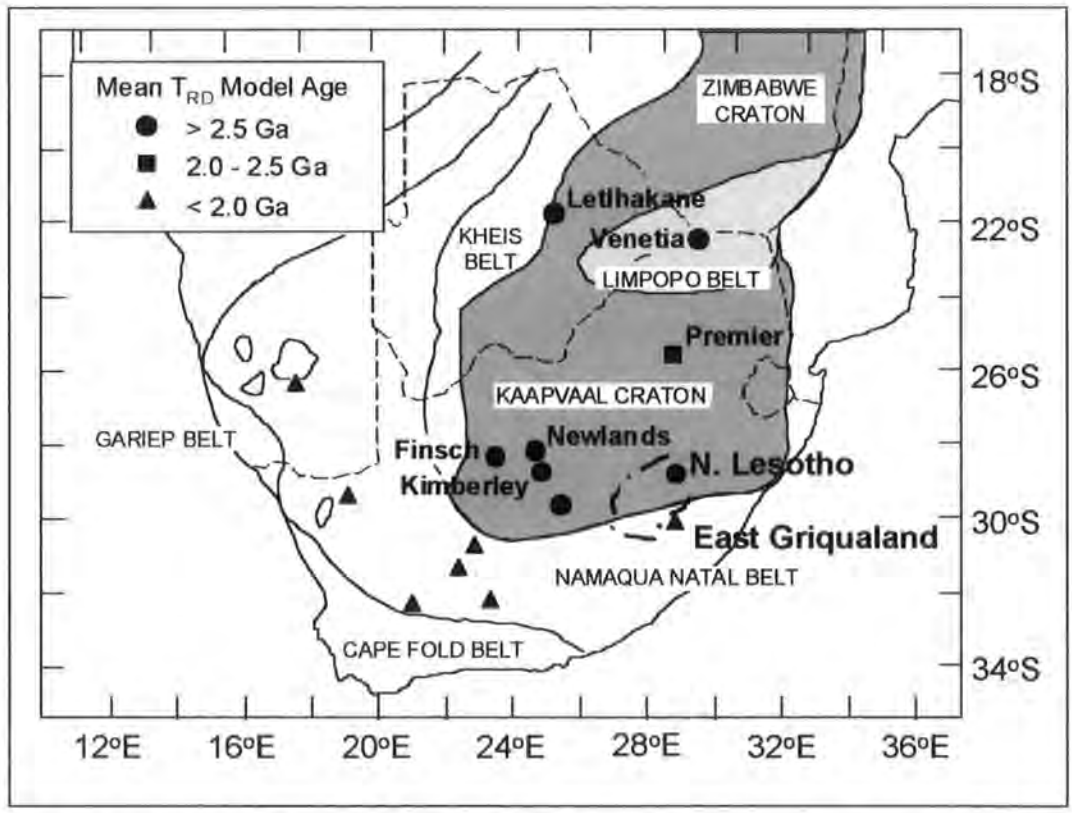

Figure 3.1 Geological sketch map of southern Africa showing tectonic elements. Dark grey shading indicates area underlain by Archean basement. Light grey shading indicates the Limpopo belt separating the Kaapvaal and Zimbabwe cratons. Lesotho, indicated in bold outline, is on the southern margin of the Kaapvaal craton. Re-Os T_{RD} model ages of kimberlite hosted peridotite xenoliths.

3.2 Geological Setting

3.2.1 Regional Geology

Lesotho and the Kaapvaal craton have a long geological history, rooted in the Archean during craton formation and stabilisation, and continuing through to the Cretaceous. The geological record for Lesotho and the Kaapvaal craton is summarised in Table 3.1.

3.2.1.a The Kaapvaal craton

The Kaapvaal craton covers an area of approximately 1.2 x 10^6 km^2 (Figure 3.1), with the outer limits defined largely by geological mapping and geochronology (de Wit *et al.*, 1992), aided by geophysics and image processing (Corner, 1991; Chicowich and Green, 1992). The craton is bounded to the north by the Zimbabwean craton; to the west and south by Proterozoic mobile belts; and to the east by the Lebombo monocline composed of Jurassic volcanic rocks associated with the break-up of Gondwana.

The Kaapvaal craton formed between 3.7 and 2.7 Gyr ago, and its Archean history of approximately 1 Gyr can be conveniently separated into two distinct periods (de Wit *et al.*, 1992). The first period between 3.7 and 3.1 Ga records the initial formation of the Kaapvaal shield and may represent processes resembling those of modern-day oceanic basins, though at shallower depths (de Wit *et al.*, 1992). The second period of Archean history between 3.1 and 2.7 Ga appears to represent intra-continental and continent-margin processes with growth of the craton through tectonic accretion and subduction-related igneous processes ending with the final stabilisation of the craton (de Wit *et al.*, 1992).

Early Archean History

The Kaapvaal craton is not a homogeneous province, but is composed of several sub-domains or terrains (Figure 3.2). The oldest, core domain is located in the eastern part of the craton. This Ancient Gneiss terrain, containing tonalitic intrusions as old as 3.644 Ga (Compston and Kröner, 1988; Hunter, 1991; Helmstaedt and Gurney, 2001), is tectonically juxtaposed next to the Barberton greenstone belt. The Onverwacht Group, part of the southern Barberton greenstone terrain, has been dated at ca. 3.5 Ga (de Wit *et al.*, 1992; Helmstaedt and Gurney, 2001). This group, known as the Jamestown ophiolite (de Wit *et al.*, 1992), has been compared to Phanerozoic ophiolites and is thought to represent the remnants of an early oceanic lithosphere (de Wit *et al.*,

Table 3.1 Summary of Geological events for the Kaapvaal craton and Lesotho.

Type	Geology	Age	Comments	Reference
Early Archean				
Basement	Gneisses and intrusives	3.65 - 3.55 Ga	Ancient Gneiss terrain and trodhjemite-tonalite basement.	1, 2, 3, 4
Mafic and ultramafic rock with associated sediments	Greenstone belts	3.5 – 3.3 Ga	Barberton greenstone belts (or ophiolite) and Natal granite-greenstone terrain.	4, 5, 6
Syntectonic intrusives	Trodhjemite-tonalite	3.3 – 3.2 Ga	Thrusting and amalgamation of Ancient Gneiss, Barberton and Natal terrains.	5
Syntectonic intrusives	Granite sheets	3.15 – 3.07 Ga	Transcurrent shearing across amalgamated terrains and last major anatexis affecting central Kaapvaal 3.08 +/- 0.01 Ga.	7, 8
Western Kaapvaal				
Diamonds	Harzburgitic inclusions	3.2 Ga	Diamonds from Finsch and Kimberley.	9
Mafic and ultramafic rocks with associated sediments	Greenstone belts	3.0 – 2.8 Ga	Colesberg, Amalia and Kraaipan greenstone terrains.	10
Deformation	Crustal shortening	2.84 – 2.72 Ga	East-west shortening during amalgamation of terrains.	11
Late Archean				
Volcano-sedimentary sequence	Basalts - rhyolite and fluvial shelf sediments	~ 2.94 Ga	Pongola supergroup. Extensional rift basin?	12
Volcano-sedimentary sequence	Alkali basalts - rhyolite and flysch-type to molasse-type sediments.	3.07 - 2.71 Ga	Witwatersrand supergroup incl. Dominion group. Dominion possibly continental rift, Lower Wits continental shelf and Upper Wits foreland compressional basin.	7, 12, 13
Flood basalt volcanism	Mafic to intermediate volcanics.	2.71 – 2.55 Ga	Ventersdorp supergroup. Major extension forming northeast trending grabens.	13, 14
Metamorphism	Transient thermal pulse	2723 Ma	Granulite xenoliths from kimberlites record transient thermal pulse >1000°C at 1.0-1.5 GPa. Synchronous with Ventersdorp.	14, 15, 16
Proterozoic				
Sedimentary rocks	Quartzite and shallow water carbonates.	~ 2.56 Ga	Transvaal supergroup. Tectonic and thermal subsidence.	
Metamorphism	Zircon growth	1114-1000 Ma	Metamorphic zircon growth in lower crustal xenoliths from southern Kaapvaal suggests major thermal modification, possibly related to the Namaqua-Natal orogeny	17, 18

Table 3.1 (Continued)

Type	Geology	Age	Comments	Reference
Lesotho- Karroo				
Sedimentary rocks		Permian	The *Ecca* series. These unconformably overlie the crystalline basement.	19
Sedimentary rocks	Shales, mudstones and sandstones	Triassic	The *Beaufort* series. Plant and reptile remains.	19, 20
Sedimentary rocks	Arkoses, sandstones, shales, mudstones	Triassic	The *Stormberg* series	19
Extrusive volcanics – flood basalts	Explosive intrusive vents, basalts, ash, tuff and agglomerates	Jurassic	The *Drakensberg* beds. Explosive intrusive vents precede Drakensberg basalts (190 - 150 Ma). Ash, tuff and agglomerates occur locally.	12, 19
Intrusives	Dolerites	Jurassic	Dolerite sheets occur throughout the Karroo as vertical dykes and horizontal sheets	19
Lesotho- kimberlites				
Kimberlite magmatism	Kimberlite pipes and dykes.	Cretaceous (~ 87.1 Ma.)	Kimberlite dykes and pipes intrude the Karoo sequence. Kimberlite pipes appear to post-date kimberlite dyke emplacement. Controlled by WNW-trending fractures and occasionally WSW-fractures.	19, 20

1 - Compston and Kröner (1988), 2 - Hunter (1991), 3 - Helmstaedt and Gurney (2001), 4 -Armstrong *et al.* (1990), 5 - de Wit (1991), 6 - Hunter (1991), 7 - de Wit *et al.* (1992), 8 - Moser *et al.* (2001), 9 - Richardson *et al.* (1984), 10 - Poujol *et al.* (2000), 11 - Carney *et al.* (1994), 12 - Windley (1995), 13 - Cheney and Winter (1995), 14 - Armstrong *et al.* (1991), 15 - Dawson *et al.* (1997), 16 - Schmitz *et al.* (1998), 17 - Schmitz and Bowring (1999), 18 - Schmitz and Bowring (2000), 19 - Dempster and Richard (1973), 20 - Turner (1972), 20 - Davis (1977).

1992). During the period 3.46 to 3.43 Ga this group was thrust onto an active arc-like terrain with a 3.54 trodhjemite-tonalite basement (Armstrong *et al.*, 1990). Between 3.3 and 3.2 Ga, a second thrusting event resulted in the amalgamation of the southern and northern Barberton Greenstone terrains, and the Ancient Gneiss terrain (Armstrong *et al.*, 1990; de Wit *et al.*, 1992). All three of these terrains were intruded by chemically similar tronhjemitic intrusions at this time (de Wit, 1991). During the period of 3.15 to 3.07 Ga, transcurrent shearing occurred and regionally extensive granite sheets were emplaced across the three terrains (de Wit *et al.*, 1992).

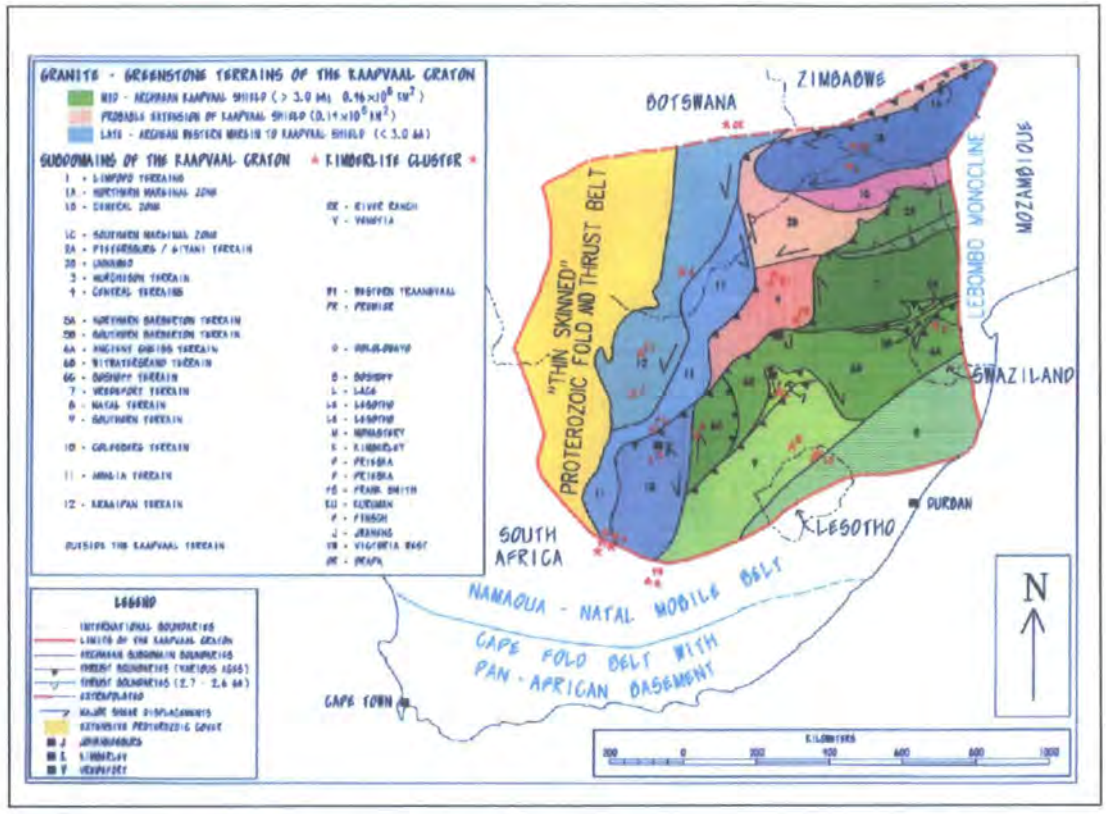

Figure 3.2 Detailed schematic map of the Kaapvaal craton showing Archean crustal domains, from de Wit *et al* (1992).

The ancient core of the Kaapvaal craton was enlarged to the south by the amalgamation of the 3.4-3.2 Ga Natal granite-greenstone terrain. This terrain has sedimentary rocks of shallow marine affinities (Hunter, 1991). Widespread tonalitic plutonism within this terrain is the same age and composition, and corresponds to, the second trondhjemite-tonalite episode (3.3-3.2 Ga) experienced by the ancient core. This was followed by the post-tectonic granitic sheets at ca. 3.0 Ga (de Wit *et al.*, 1992). The ancient gneiss and Natal greenstone terrains are unconformably overlain by relatively undeformed volcano-sedimentary sequences of the Pongola basin ca. 2.95 Ga (Hunter,

1991). Amalgamation of the Natal terrain with the Barberton-Ancient Gneiss core is likely to have occurred by 3.2 Ga with final stabilisation by 3.0 Ga.

To the north of the ancient core, greenstone terrains including the Murchison, Giyani and Pietersburg Greenstone terrains, and possibly high-grade metamorphic greenstone remnants in the southern margin of the Limpopo Province (de Wit *et al.*, 1992), are believed to include some rocks as old as those of the Barberton Greenstone terrain (Poujol and Anhaeusser, 2001). It is uncertain when these terrains amalgamated with each other and with the ancient core to the south, but they were securely joined by 3.1 Ga (Helmstaedt and Gurney, 2001).

Although obscured by Late Archean and younger strata, the east-west trending terrains of the ancient core are believed to continue as far west as the Vredefort structure (de Wit *et al.*, 1992; Helmstaedt and Gurney, 2001), and are probably truncated by the north-south trending Colesberg lineament. To the west of this lineament are the north-south trending Colesberg, Amalia and Kraaipan granite-greenstone terrains which are considerably younger (Helmstaedt and Gurney, 2001). Crust-lithosphere coupling and the last major anatexis affecting the crust of the central Kaapvaal has been dated at 3.08 +/- 0.01 Ga in the Vredefort section (Moser *et al.*, 2001).

Western Kaapvaal Province

The Colesberg, Amalia and Kraaipan granite-greenstone terrains in the west of the Kaapvaal craton yield young Archean ages between 3.01 and 2.79 Ga (Poujol *et al.*, 2000). The Kraaipan Greenstone terrain, which occurs in highly deformed gneisses, extends into Botswana where it is intruded by the Gabarone granite at 2.83 Ga (Helmstaedt and Gurney, 2001). East-west shortening related to the amalgamation of the north trending terrains has been dated between 2.84 and 2.72 Ga by Carney *et al* (1994).

The oldest crustal ages of ca. 3.0 Ga are younger than harzburgitic garnet inclusions of diamonds from Finsch and Kimberley at ca. 3.2 Ga (Richardson *et al.*, 1984), both located in the western part of the Kaapvaal province. This may indicate that the lithospheric root of the older eastern part of the province extends under the younger crust of the western part of the province.

Late Archean History

Following stabilisation of the Kaapvaal shield, the craton became a basement for a series of unconformity bounded volcano-sedimentary sequences. These include the Pongola, Dominion, Witwatersrand, Ventersdorp, Transvaal, Soutpansberg and

Waterberg sequences (Cheney and Winter, 1995). The oldest sequences (older than 2.714 Ga), including the Dominion, Witwatersrand and Lower Ventersdorp are confined to the southeastern Kaapvaal. The Middle Ventersdorp, which is older than 2.709 Ga, partly covers the northern and western areas of the province. The Upper Ventersdorp, post 2.709 Ga and pre 2.552 Ga, covers much of the western province and is the first sequence that overlaps the boundary between the younger western and older eastern parts of the Kaapvaal province (Cheney and Winter, 1995). The history of deformation in these sequences suggest that the basement rocks at first overthrust the Dominion and Witwatersrand sequences followed by the Lower and Middle Ventersdorp. The Upper Ventersdorp sequence unconformably overlaps the earliest east-verging thrusts. The sedimentary record is consistent with tectonic accretion of the western over the eastern part of the province (Helmstaedt and Gurney, 2001).

The Lower Witwatersrand basin probably formed as a continental platform on a passive margin facing open-ocean to the south and west (de Wit *et al.*, 1992). The Upper Witwatersrand basin is interpreted as a foreland compressional basin possibly related to the convergence of the Kaapvaal and Zimbabwe cratons (de Wit *et al.*, 1992), or alternatively the convergence of the eastern and western parts of the Kaapvaal province (Helmstaedt and Gurney, 2001). The Central Rand deposition, 2.84-2.71 Ga (Armstrong *et al.*, 1991), overlaps with 2.9-2.7 Ga north-directed overthrusting of the Kaapvaal over the Limpopo province (Helmstaedt and Gurney, 2001), suggesting that the Witwatersrand basin was in the hinterland of the thrust belt. Westerly accretion supports the westerly provenance of Upper Witwatersrand sediments (Helmstaedt and Gurney, 2001), a problem for a Limpopo foreland basin model (de Wit *et al.*, 1992).

Sapphirine granulite xenoliths from the Lace, Voorspoed and Star kimberlites preserve evidence of a transient thermal pulse in the deep crust of the southwestern Kaapvaal craton. Thermobarometry indicate peak temperatures > 1100°C at pressures of 1.0 to 1.5 GPa (Dawson *et al.*, 1997), and Zircon and Monazite produce U-Pb ages recording early cooling ages of 2723 Ma (Schmitz *et al.*, 1998). This episode of ultra-high temperature metamorphism in the lower crust appears to be synchronous with the initiation of Ventersdorp flood basalt volcanism (Armstrong *et al.*, 1991). The combined western and eastern parts of the province to the south of the Thabazimbi-Murchison lineament experienced major extension resulting in the deposition of the volcano-sedimentary Upper Ventersdorp sequence, deposited between 2.7 and 2.6 Ga in a series of northeast trending grabens (Armstrong *et al.*, 1991). The origin of this extension episode is uncertain and may represent oblique convergence between the

Kaapavaal and Zimbabwe cratons (Helmstaedt and Gurney, 2001), or the failed arm of a triple-junction related to the speculated rifting of the Kaapvaal and Pilbara provinces (Nelson *et al.*, 1992).

Proterozoic Evolution

Tectonic and thermal subsidence in the early Proterozoic formed the Transvaal sedimentary basins. The Transvaal supergroup overlies the Ventersdorp group unconformably. The basal quartzite grades up into shallow water carbonates that dominate the sequence (Eriksson *et al.*, 1993). Dating of stromatilitic carbonates provide an age of 2.56 Ga for the Transvaal Dolomite (Jahn *et al.*, 1990). The Bushveld Igneous complex was emplaced into the Upper Transvaal sediments at 2.05 Ga (Eales and Cawthorn, 1996).

Garnet bearing granulite and upper amphibolite facies lower crustal xenoliths from the Markt kimberlite on the southwestern margin of the Kaapvaal craton yield Mesoproterozoic metamorphic zircon U-Pb ages ranging from 1114 to 1092 Ma (Schmitz and Bowring, 2000). Similarly felsic and mafic granulite xenoliths from the northern Lesotho kimberlites on the southern margin of the craton produce metamorphic zircon and monazite U-Pb ages of 1050-1000 Ma (Schmitz and Bowring, 1999). This suggests that lower parts of the thickened crust along the southern and eastern margins of the Kaapvaal craton underwent major thermal modification in the Mesoproterozoic. This indicates a metamorphic history post-dating cratonisation and possibly related to the Namaqua-Natal orogeny (Schmitz and Bowring, 1999).

3.2.1.b Lesotho

Sedimentary and Igneous Geology

The crystalline basement underlying Lesotho does not outcrop at surface and the rocks in Lesotho mainly belong to the overlying Karroo system. The Karroo overlie a large part of southern Africa as relatively flat-lying sandstone and shale sequences. The Karroo system consists of four large series ranging in age from Carboniferous to lower Jurassic, the Dwyka, Ecca, Beaufort and Stormberg. The Stormberg sediments are overlain by a thick succession of tholeiitic lavas, the Drakensberg Beds (Dempster and Richard, 1973).

Borehole data (SOEKOR hole W1/1/72) from neighbouring parts of South Africa, in the Ficksburg area (Figure 3.3), suggest that the Carboniferous Dwyka series is absent from northern Lesotho and that lower parts of the Ecca series are attenuated (Dempster

and Richard, 1973). The Permian Ecca series is deposited on the crystalline gneissose basement, which it overlaps unconformably.

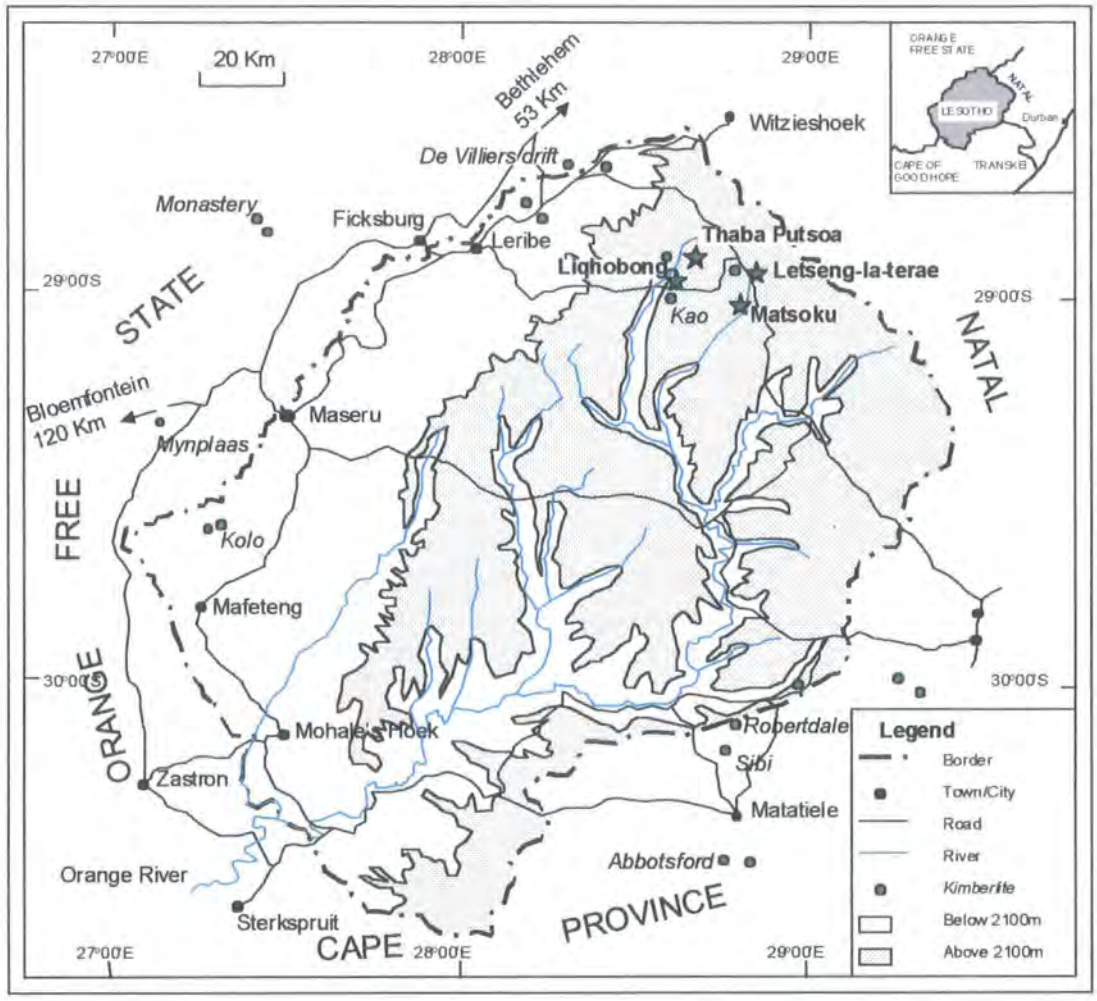

Figure 3.3 Map of Lesotho (after Dempster and Richard, 1973) showing location of kimberlites. Peridotite xenoliths from kimberlites highlighted with stars and bold type were used in this study.

The uppermost, Triassic Beaufort beds outcrop along the Caledon River and are represented by 35-40 m of purple shales and mudstones, and buff sandstones (Dempster and Richard, 1973).

Rocks of the Stormberg series underlie most of Lesotho. The sediments are Triassic to Rhaetic in age (Dempster and Richard, 1973). The lowermost *Molteno Beds* form a stratigraphic wedge which thins and overlaps the Upper Beaufort series towards the north (Turner, 1972). It is represented by up to 50 m of massive and coarse arkosic grits and sandstones, which are locally pebbly. Occasional shales and mudstones occur. The *Red Beds* overlie the Molteno Beds conformably and are similarly attenuated towards the north (Dempster and Richard, 1973). These consist of 65-70 m of pink, buff and greenish sandstones alternating with red, green and purple shales and mudstones. The *Cave Sandstone* beds lie conformably on the Red Beds and are composed of an upper,

massive cream-coloured fine grain sandstone 70-75 m thick, and a lower succession of finer-grained red, green and purple sandstones and mudstones 60-65 m thick.

The early Jurassic Drakensberg basalts were preceded by the explosive intrusion of vents in the sedimentary sequence and basal lavas in the lowlands (Dempster and Richard, 1973). Thin beds of ash, tuff and agglomerate are found in the south of Lesotho. The vents occur generally northeast of Leribe (Figure 3.3) and occur both singularly and in groups, with no evidence of tectonic control (Dempster and Richard, 1973). No lavas appear to be associated with the vents. The largest group of vents (over 400 m diameter) penetrate not only the Cave sandstone but also the lowermost lava flows. The throat is filled with a volcanic agglomerate composed of sandstone fragments and lapilli of vesicular basalt grading into a tuff indistinguishable from fine-grained sandstone (Dempster and Richard, 1973). The Drakensberg beds are a series of monotonous lava flows of varying thickness, erupted between 190 and 150 Ma (Windley, 1995), or 183.7 +/- 0.6 Ma (Encarnacion *et al.*, 1996). Occasional sandstone beds form bands and lenses in the lowermost lava flows indicating the continuation of sedimentation after the first outpouring of lava. The Drakensberg basalts are flood basalts that represent a remnant of a more extensive lava field that once covered a large area of southern Africa. The remaining basalts in Lesotho exceed 1600 m in places (Dempster and Richard, 1973).

Dolerites occur throughout the upper Karroo and form horizontal sheets and vertical dykes.

Kimberlite Geology

The Geology of Lesotho kimberlites has been summarised by Nixon (1973b). Kimberlite dykes and pipes were intruded into the Karroo sequences and are situated on WNW-trending fracture zones (Dempster and Richard, 1973). Emplacement of kimberlite pipes appears to post-date emplacement of dykes, as no dyke crosscuts the pipe-country-rock contact. Kimberlite emplacement has produced little disturbance or deformation of the country-rock and what fracturing exists is limited in extent to a few metres from the contact (Dempster and Richard, 1973).

Although the kimberlites are controlled by WNW-trending fractures, several pipes are located at the intersection with WSW-fractures and in several cases these contain kimberlite dykes

Kimberlite pipes in northern Lesotho form four main clusters at Butha-Buthe (north of Leribe), Kao, Letseng and Robert (to the east of Letseng). The tendency for

kimberlites to form clusters is common and may relate to favourable tensional crustal fractures (Dempster and Richard, 1973).

Cretaceous ages have been determined for the kimberlite pipes in Lesotho, the Mothae kimberlite pipe produces a U-Pb zircon age of 87.1 Ma (Davis, 1977).

3.2.2 Geological setting of the Lesotho kimberlites

The Letseng-la-terae kimberlite complex lies adjacent to the Drakensberg road, 82 km from Leribe (29°00'S, 28°52'E; Figures 3.3 and 3.4), and consists of two pipes and three varieties of kimberlite dyke. The pipes penetrate 1.5 km of *Stormberg basaltic lavas* and contain xenoliths of Karroo (Trias-Jurassic) sediments, basement gneiss, granulites and ultrabasic nodules. The kimberlite pipes are composite bodies with several generations of kimberlite, but in both cases the main kimberlite unit is of tuffaceous diatreme facies (Bloomer and Nixon, 1973), or tuffaceous kimberlitic breccia.

Figure 3.4 Photograph of the Letseng-la-terrae kimberlite open pit.

The Thaba Putsoa kimberlite is located high in the mountains of northern Lesotho, at an elevation of 2928 m (28°54'S, 28°40'E; Figure 3.3). The kimberlite is a typical blow, approximately 100 m long and lenticular in shape resulting from the expansion of a dyke (Nixon, 1973a).

The Matsoku pipe is a small diatreme outcropping on the side of a ridge at an elevation of 2840 m, above the Lipitsaneng River between that river and the Matsoku

River (28°59'S, 28°44'E; Figures 3.3). This kimberlite pipe is notable for the quantity, size and variety of xenoliths of deep origin. (Cox *et al.*, 1973)

The Liqhobong kimberlite consists of a main pipe connected to a satellite pipe by a dyke. The main pipe, located at the head of Liqhobong valley at 2650 m (29°04'S, 28°37'E; Figures 3.3 and 3.5), is circular (300 m in diameter) and consists of a single intrusive phase of diatreme facies kimberlite (Nixon and Boyd, 1973b). The satellite pipe lies 300 m upslope to the WNW, is circular (90 m in diameter) and consists of three kimberlite phases of diatreme and hypabyssal facies kimberlite. The dyke can be traced 1.3 km to the SE on a bearing of 125°, near to the source of the Liqhobong River at an elevation of 2950 m, where it expands into a blow of hypabyssal facies kimberlite; the SE blow of Nixon and Boyd (Nixon and Boyd, 1973b).

Figure 3.5 Photograph of the Liqhobong kimberlite (centre), and prospecting camp (foreground).

3.3 Sample selection and Analytical Methods

Mantle xenoliths are common in several southern African kimberlites erupting through the Kaapvaal craton. These are dominantly spinel, spinel-garnet and garnet lherzolites, with minor harzburgites, dunites, eclogites and pyroxenites, which are locally abundant (Boyd and Gurney, 1986). A representative selection of thirty six peridotite xenoliths were chosen for this study from various kimberlite bodies in Lesotho, on the southern margin of the Kaapvaal craton (Figure 3.3). The xenoliths studied were chosen from the University of Durham collection, collected during the 7th

International Kimberlite Conference Lesotho field trip (1998). Petrological and textural summaries are provided in Appendix A.

All samples were selected so that large, 500g (minimum) bulk samples could be cut and powdered to provide representative bulk compositions. In addition, sufficient material remained to allow further petrological and geochemical studies. The methods of sample preparation and whole-rock analysis are described in detail in Appendix B. Large sample sizes were used to obtain representative analyses of both major and trace elements. Major elements were analysed by wavelength-dispersive X-ray fluorescence, the precision determined by replicate analysis of internal standard and reference materials. Trace elements and REE were determined by ICP-MS. The precision was estimated from duplicate analyses of rock standards.

3.3.1 Letseng-la-terae

The xenolith samples used in this study were collected from the former Letseng-la-terae mine stockpile (Figure 3.3), and are a subset of 70 peridotite xenoliths. The Letseng kimberlite hosts a well-preserved suite of, generally large ovoid (10 to 20 cm), mantle-derived xenoliths. Garnet peridotite predominates over spinel peridotite in the collection and over 60% of samples analysed were garnet peridotite with the remainder garnet-spinel (17%) and spinel peridotite (22%). The xenoliths are mainly lherzolites with minor harzburgite. Using the textural nomenclature of Harte (1977), most xenoliths are classified as coarse equant to coarse tabular. However, subordinate porphyroclastic examples do occur. Eighteen representative samples were chosen for different textural types, facies and degrees of alteration.

3.3.2 Matsoku

The Matsoku kimberlite hosts a well-preserved suite of mantle-derived xenoliths, with mantle xenoliths up to $^1/_8$ m^3 volume recorded (Cox *et al.*, 1973). The Matsoku pipe contains on average 20-30% xenolithic material (Dawson, 1968), with up to 45% of xenoliths represented by mantle-derived rocks. Six representative samples were selected from different facies (3 spinel, 2 spinel-garnet and one garnet peridotite) and textural types. The majority of the peridotite xenoliths analysed have coarse equant to coarse tabular textures, based on the textural classification of mantle-derived rocks by Harte (1977). Minor examples of porphyroclastic textures occur. The xenoliths analysed are mainly lherzolites but harzburgites also occur. Composite xenoliths or

those showing obvious signs of compositional banding, which are common at Matsoku (Cox *et al.*, 1973), we specifically avoided.

3.3.3 Liqhobong

The SE blow of the Liqhobong kimberlite intrusion hosts a well-preserved suite of, generally large ovoid-rounded (10 to 30 cm), mantle-derived xenoliths. These can be assigned to five groups based on mineralogy: i) spinel harzburgite (2%), ii) garnet-spinel lherzolite (4%), iii) garnet harzburgite (8%), iv) garnet lherzolite (56%), and v) garnet lherzolite with phlogopite (30%, Nixon and Boyd, 1973b). The Durham peridotite xenolith collection from Liqhobong is dominated by garnet lherzolites with minor phlogopite bearing samples. Five representative samples were selected for analysis. Using the textural nomenclature of Harte (1977), the xenoliths analysed are classified as coarse equant to coarse tabular, with one example of a porphyroclastic peridotite.

3.3.4 Thaba Putsoa

The xenoliths used in this study were collected from the surface workings of the Thaba Putsoa kimberlite blow (Figure 3.3). Four representative samples were selected from different facies (1 spinel, 3 spinel-garnet) and textural types. The majority of the peridotite xenoliths analysed have coarse equant to coarse tabular textures, based on the textural classification of mantle-derived rocks by Harte (1977) with one example of a porphyroclastic peridotite. The xenoliths analysed are generally lherzolitic but harzburgites also occur.

3.4 Petrology of Lesotho lithospheric mantle xenoliths

3.4.1 Xenolith Petrography

Polished thin sections were prepared for all Lesotho peridotite samples analysed in this study. Petrographical descriptions for each sample are summarised in Appendix A.

3.4.1.a Letseng-la-terae

Coarse Peridotite

Coarse peridotite xenoliths from the Letseng kimberlite are composed of olivine (50-70%), and lesser amounts of OPX (20-40%), CPX (0-4%), spinel (0-1%) and/or garnet (0-8%). The peridotites are predominantly lherzolitic, but harzburgite is also prominent. Coarse peridotite occurs in spinel, spinel-garnet and garnet facies. The coarse texture of the peridotites derives from early crystallisation of large subhedral olivine (up to 12 mm) and OPX (3-8 mm) and these dominate the mineral assemblage (Figure 3.6a). Clinopyroxene occurs as equant, emerald-green anhedral crystals (0.5-3 mm). Clinopyroxene also occurs in close association with garnet, and as narrow, late stage interstitial veins. Reddish-brown to opaque spinel forms late anhedral, irregular crystals up to 1 mm in size. These are interstitial and sometimes show poikilitic/symplectic intergrowth with OPX (Figure 3.6b). Garnet is lilac coloured, 3-8 mm in size, subhedral to anhedral and is variably surrounded by kelyphitic rims containing spinel and occasional phlogopite. The kelyphitic alteration rims show complex zonation patterns with various distinct zones (Figure 3.6c). Two kelyphite zones are generally apparent in the Letseng garnets. An inner zone of fibrous or feathery aggregates, and an outer zone of small equant pyroxene crystals. Reid and Dawson (1970) have described similar kelyphitic coronas in xenoliths from the Lashaine volcano in Tanzania. Phlogopite occurs, with CPX, in close association with garnet. Possibly these grew from garnet during hydrous reaction, alternatively garnet may have grown from phlogopite during dehydration.

The majority of peridotite specimens show coarse tabular, and occasionally coarse equant, texture (Figure 3.6a) based on the classification of Harte (1977).

Olivine crystals in sample LET25 form long laths that appear to form an orientated texture within the sample. Application of a red-tint indicates that the crystal axes are aligned (Figure 3.6d). Rarely OPX shows exsolution lamellae of CPX aligned along the cleavage in tabular sections. Secondary alteration includes serpentine after olivine and OPX.

Porphyroclastic Peridotites

Low-temperature peridotite xenoliths from the Letseng kimberlite occasionally exhibit non-fluidal porphyroclastic textures (Figure 3.6e). The porphyroclastic non-fluidal peridotites comprise olivine (60-65%), OPX (30-35%), with minor CPX (2-4%), spinel (0-1%) and / or garnet (0-3%). Olivine porphyroclasts (5-7 mm) show undulose

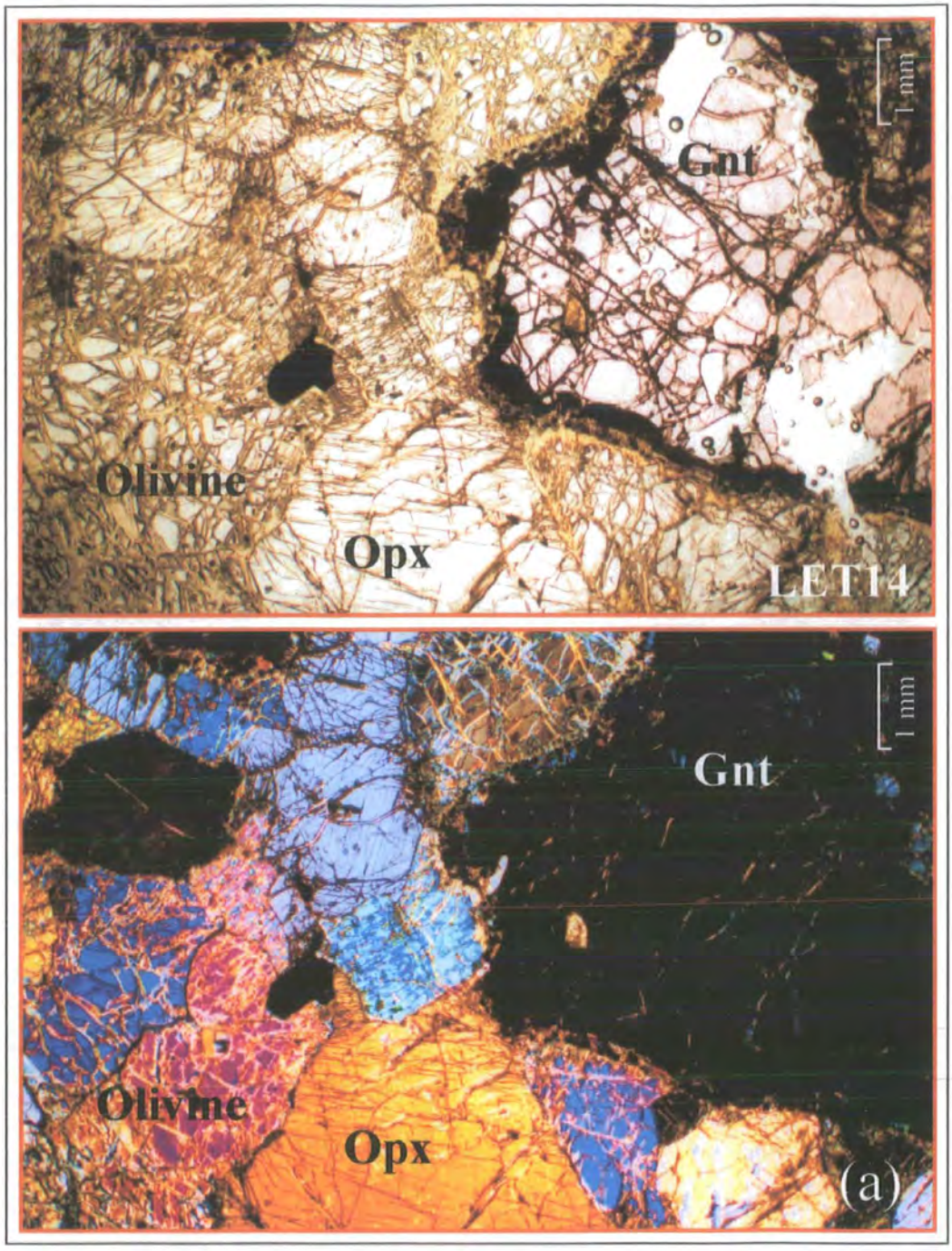

Figure 3.6a Photomicrograph of a low-T garnet-spinel harzburgite, sample LET14 from the Letseng-la-terae kimberlite, showing coarse equant texture.

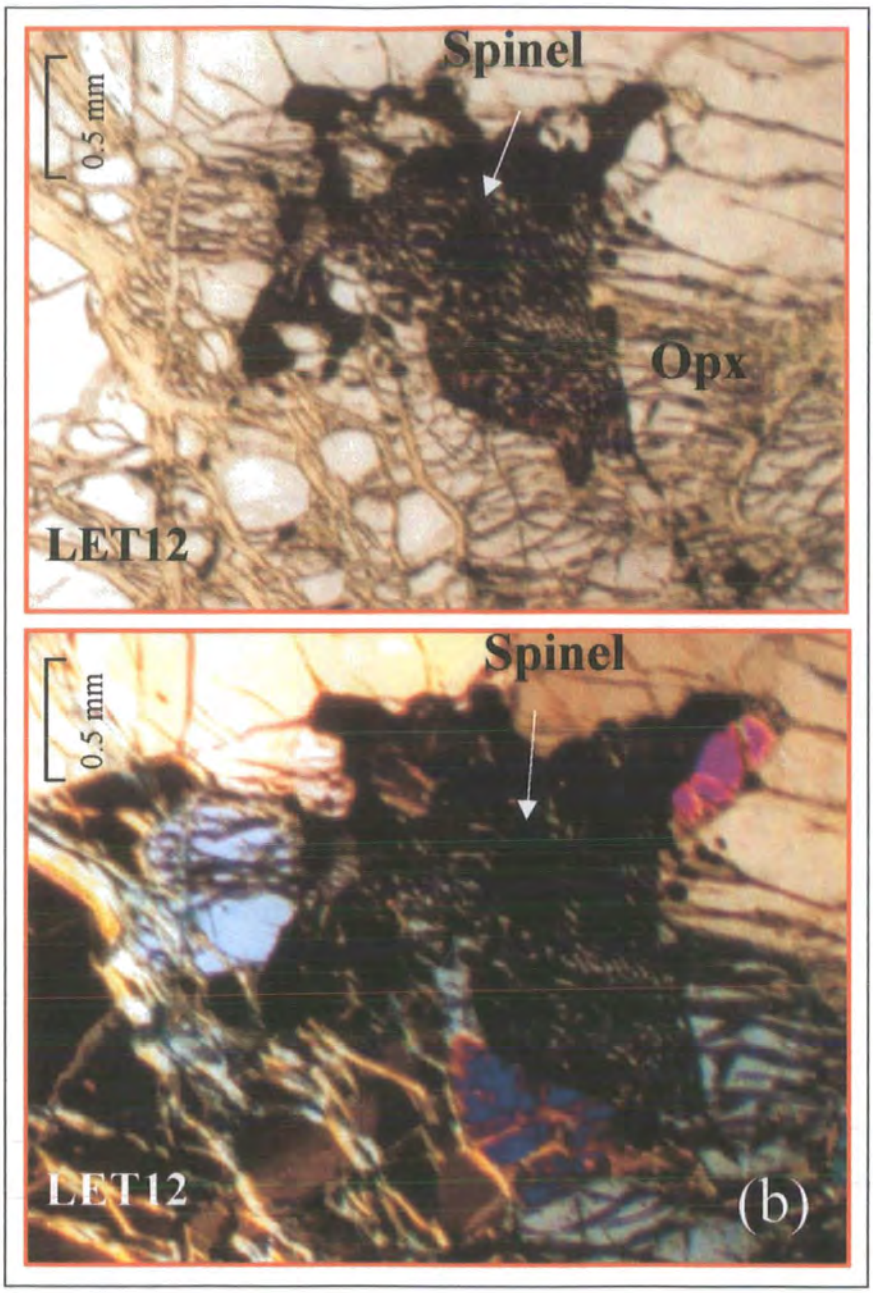

Figure 3.6b Photomicrograph of a low-T coarse garnet harzburgite, sample LET12 from the Letseng-la-terae kimberlite, showing interstitial spinel forming poikilitic intergrowth texture with OPX.

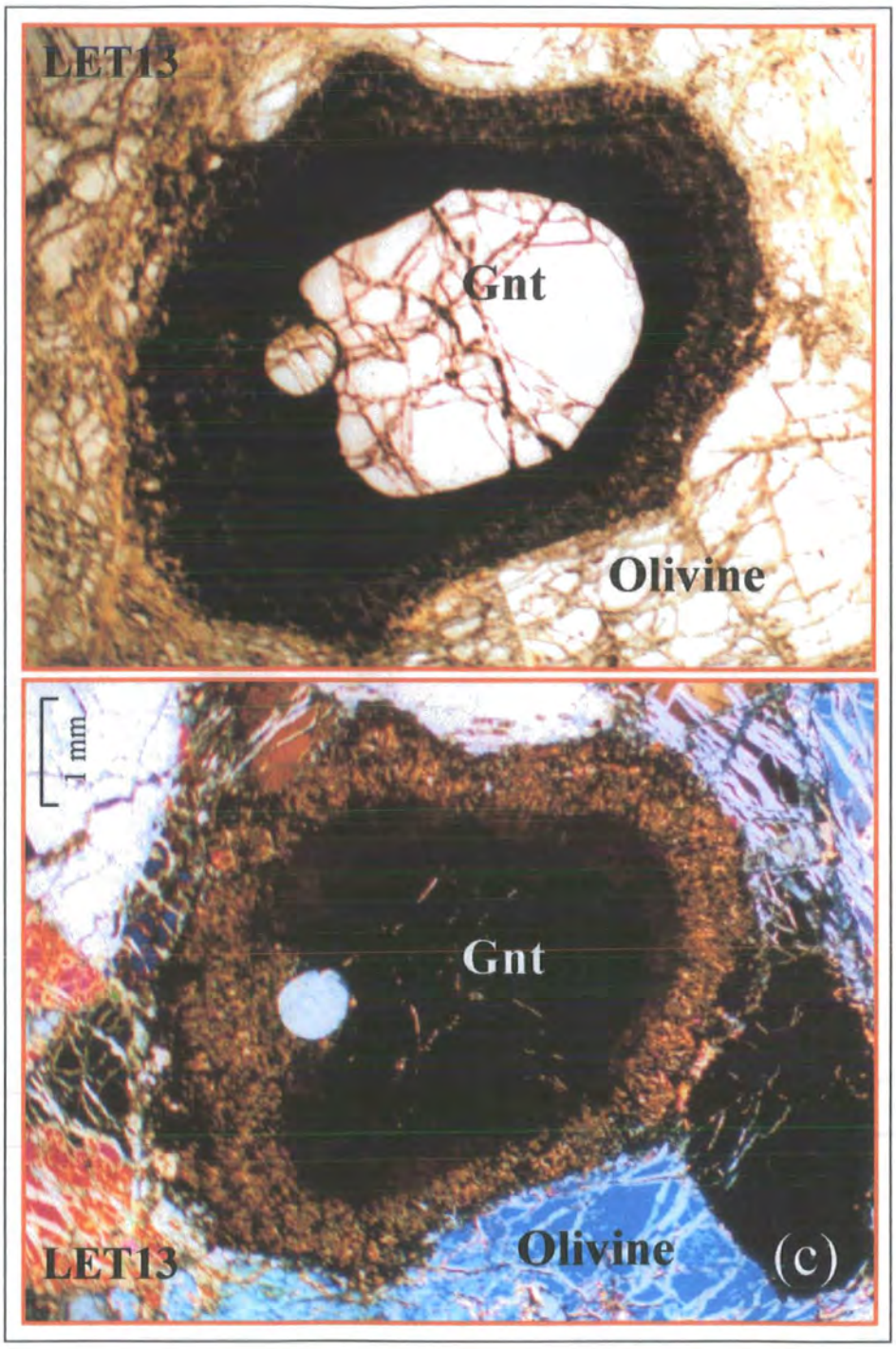

Figure 3.6c Photomicrograph of low-T coarse garnet-spinel harzburgite, sample LET13 from the Letseng-la-terae kimberlite, showing zoned kelyphitic "corona" around garnet crystal.

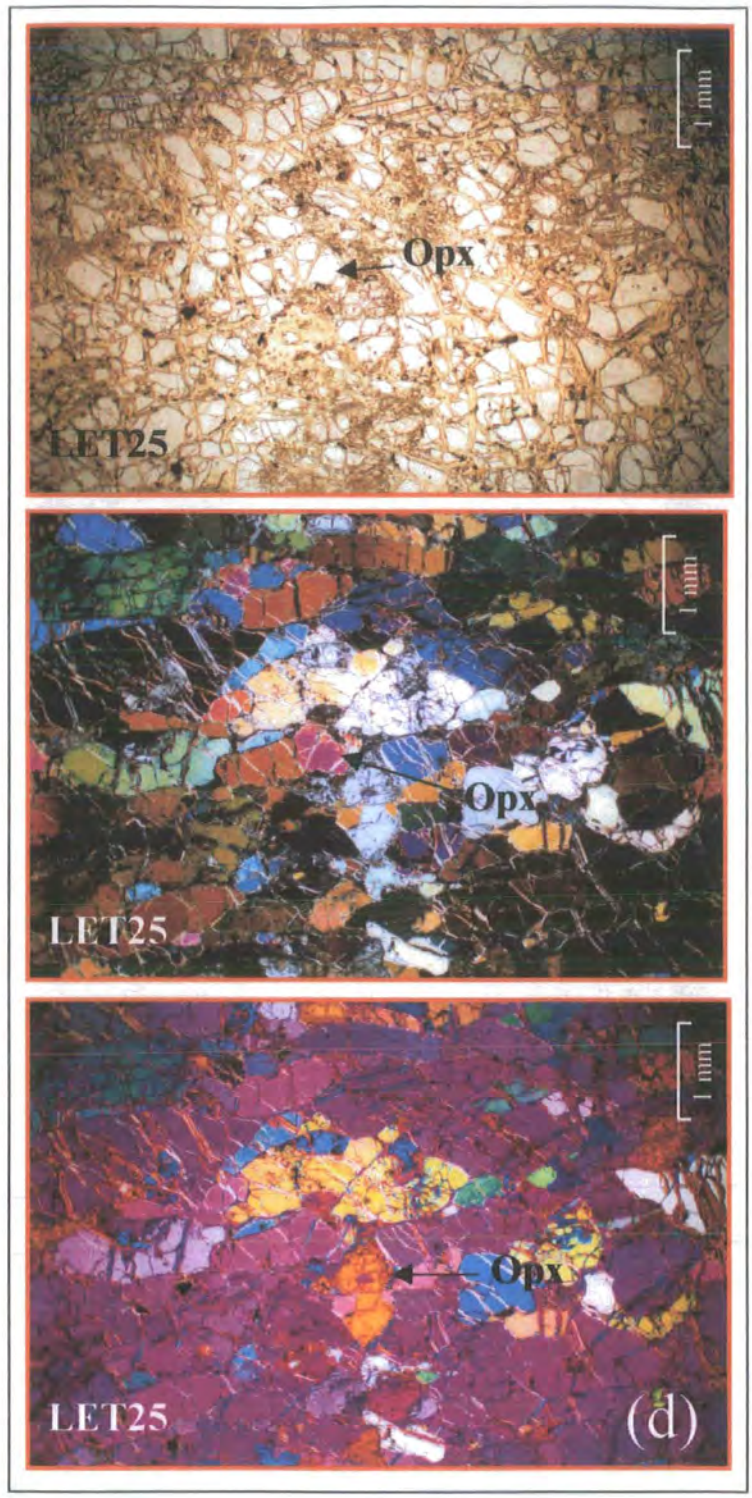

Figure 3.6d Photomicrograph of low-T spinel lherzolite, sample LET25 from the Letseng-la-terae kimberlite, showing aligned axes in olivine crystals (see text for details).

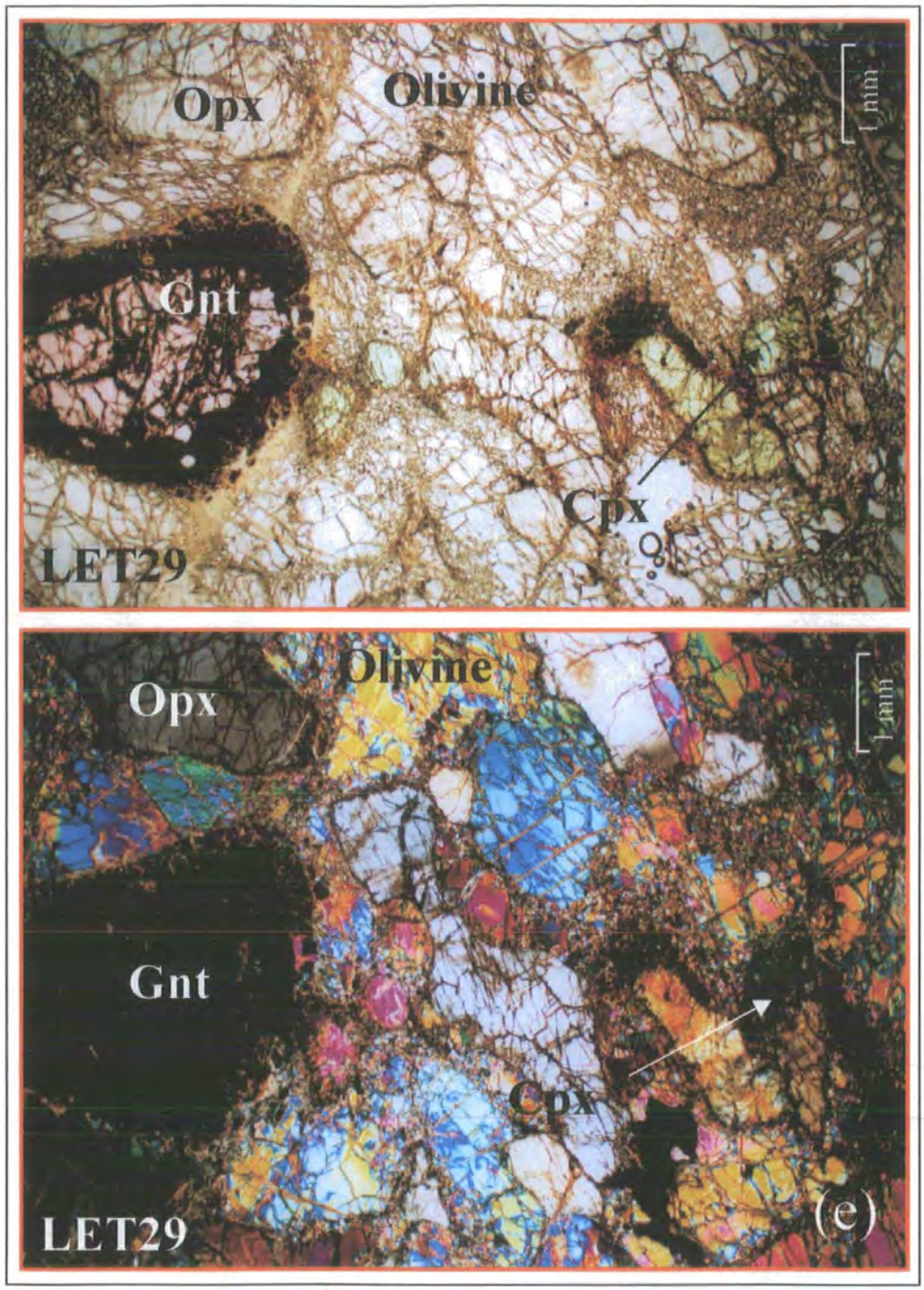

Figure 3.6e Photomicrograph of low-T garnet lherzolite, sample LET29 from the Letseng-la-terae kimberlite, showing porphyroclastic non-fluidal texture.

extinction and kink banding, and are associated with strain-free olivine neoblasts (0.1-0.5 mm). Orthopyroxene occurs as large porphyroclasts (up to 6 mm), and show undulose extinction and kink banding. CPX (up to 3mm), spinel (up to 0.5 mm) and garnet (up to 5mm) are optically similar to those found in coarse peridotites. Phlogopite occasionally forms subhedral tabular crystals that may be in textural equilibrium with the primary mantle mineralogy, which would suggest a primary metasomatic origin (e.g. (Winterburn *et al.*, 1990). Generally phlogopite is found in close relationship with CPX.

3.4.1.b Thaba Putsoa

Coarse Peridotite

Nixon and Boyd (1973c) have previously described numerous ultrabasic nodules from Thaba Putsoa. Within the Durham collection, xenoliths of coarse spinel-garnet facies lherzolite are composed of olivine (65-68%), and lesser amounts of OPX (28-30%), CPX (up to 1%), spinel (up to 1%) and/or garnet (3-4%). The coarse texture derives from early crystallisation of large subhedral olivine (up to 7 mm) and OPX (3-7 mm), which dominate the mineral assemblage (Figure 3.7a). Clinopyroxene occurs as discrete emerald-green anhedral equant crystals (1-2.5 mm). Clinopyroxene also occurs in close association with garnet and as narrow, late stage interstitial veins. Reddish-brown to opaque spinel forms late, interstitial anhedral crystals up to 2 mm in size, and sometimes show poikilitic/symplectic intergrowth with OPX (Figure 3.7a). Subhedral to anhedral, lilac coloured garnet (1-2 mm) is variably surrounded by kelyphitic rims, which contain phlogopite and spinel. Orthopyroxenes often show exsolution lamellae of CPX aligned along the cleavage.

The peridotite xenoliths have a coarse tabular texture and show similar features as xenoliths from Letseng. Secondary alteration includes serpentine after olivine and OPX.

Porphyroclastic Peridotites

One of the low-temperature xenoliths from Thaba Putsoa analysed in this study exhibits a non-fluidal porphyroclastic texture (Figure 3.7b). This peridotite comprises olivine (61%), OPX (30%), CPX (1%), spinel (1%) and garnet (7%). Olivine porphyroclasts (up to 3 mm) show undulose extinction and kink banding. These are associated with strain-free olivine neoblasts (up to 0.5 mm). Orthopyroxene occurs as

large porphyroclasts (up to 3 mm) and show slight evidence of strain. Spinel (up to 1 mm) and garnet (up to 4 mm) are optically similar to those found in coarse peridotites.

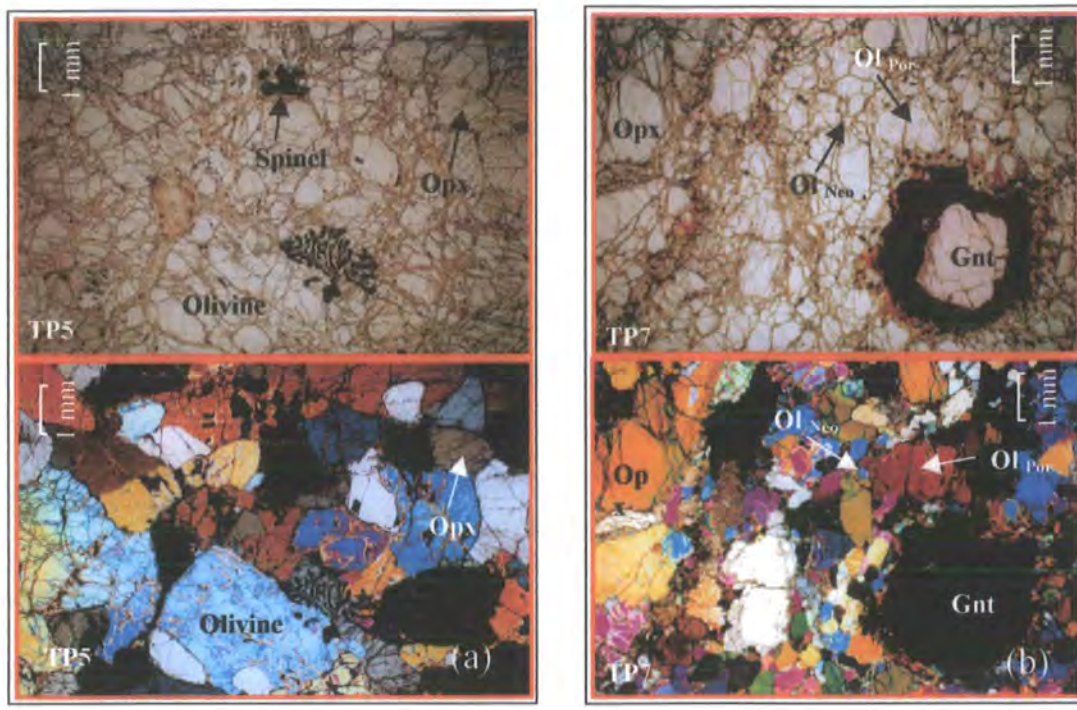

Figure 3.7 Photomicrographs of peridotite xenoliths from the Thaba Putsoa kimberlite, showing (a) coarse textured peridotite showing late stage interstitial spinel forming poikilitic intergrowth texture with OPX, (b) porphyroclastic non-fluidal texture in peridotite.

3.4.1.c Matsoku

Coarse Peridotite

Low-temperature coarse peridotite xenoliths are composed of olivine (55-65%), and lesser amounts of OPX (30-35%), CPX (2-4%), spinel (up to 1%) and/or garnet (0-5%). This is a similar range to that reported from previous studies of Matsoku peridotite suites (Cox *et al.*, 1973; Harte *et al.*, 1987). Large subhedral olivine (up to 5 mm) and OPX (2-5 mm) dominate the mineral assemblage (Figure 3.8a). Clinopyroxene occurs as discrete emerald-green anhedral equant crystals (up to 2 mm). Clinopyroxene also occurs in close association with garnet and phlogopite. Spinel forms late, interstitial anhedral crystals up to 1 mm in size. Subhedral to anhedral garnet (up to 4 mm) is lilac coloured, with small kelyphitic rims. Phlogopite occurs, with CPX, in close association with garnet. Possibly these grew from garnet during hydrous reaction, alternatively garnet may have grown from phlogopite during dehydration. Phlogopite also occurs as a discrete phase forming subhedral interstitial crystals (up to 2.5 mm) that may be in

textural equilibrium with the primary mantle mineralogy (Figure 3.8a), and therefore may be of a primary metasomatic origin (Winterburn *et al.*, 1990).

The peridotite xenoliths generally have a coarse equant texture (Figure 3.8a), or are occasionally coarse tabular, and show similar features to xenoliths from Letseng.

Porphyroclastic Peridotites

Matsoku peridotite xenoliths occasionally exhibit non-fluidal porphyroclastic textures (Figure 3.8b). These comprise of olivine (55-65%), OPX (30-40%), CPX (1-2%), spinel (up to 1%) and garnet (3%). Strained olivine porphyroclasts (Ol_{Por}, up to 3 mm) show undulose extinction and kink banding and are associated with strain-free olivine neoblasts (Ol_{Neo}, up to 0.2 mm). Strained OPX occurs as large porphyroclasts (up to 3 mm). Spinel (up to 0.5 mm) and garnet (up to 1 mm) are optically similar to those found in coarse peridotites.

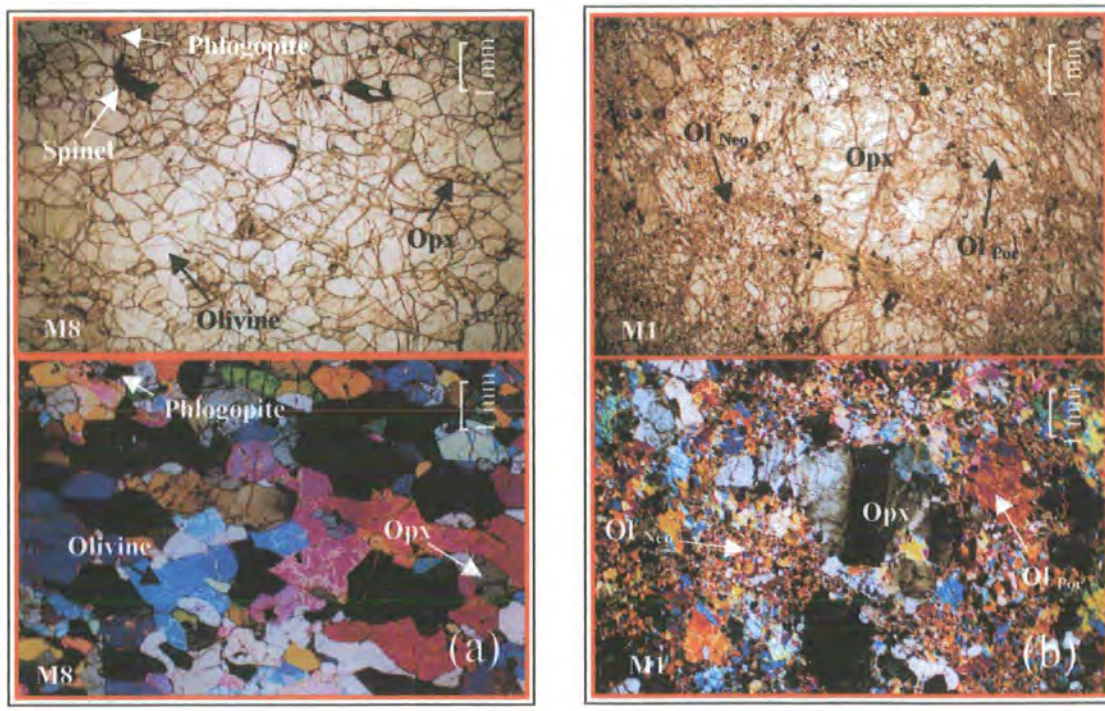

Figure 3.8 Photomicrographs of peridotite xenoliths from the Matsoku kimberlite, showing (a) coarse texture in peridotite with phlogopite, (b) porphyroclastic non-fluidal texture in peridotite.

3.4.1.d Liqhobong

Coarse Peridotite

Coarse tabular, garnet facies lherzolites are composed of olivine (50-70%), and lesser amounts of OPX (25-40%), CPX (0-2%), and garnet (5-7%), similar to that reported by Nixon and Boyd (1973b). Large subhedral olivine (up to 9 mm) and OPX (3-5 mm) dominate the mineral assemblage. The coarse texture of the peridotites

derives from early crystallisation of these phases. Clinopyroxene occurs as emerald-green anhedral equant crystals (0.5-3 mm), and occasionally interstitially as small veins. Clinopyroxene also occurs in close association with garnet. Garnet forms subhedral to anhedral, lilac coloured (1-2 mm) crystals and shows varying degrees of kelyphitisation. Kelyphite rims are variably zoned (inner fibrous and outer crystalline), and are often associated with phlogopite and spinel. Orthopyroxenes often show exsolution lamellae of CPX aligned along the cleavage. The peridotite xenoliths show many similar features to xenoliths from Letseng.

Porphyroclastic Peridotites

One xenolith from Liqhobong analysed in this study exhibits a non-fluidal porphyroclastic texture. This peridotite comprises olivine (55%), OPX (40%), CPX (1%), and garnet (4%). Strained olivine porphyroclasts (up to 7 mm) show undulose extinction and kink banding, and these are associated with strain-free olivine neoblasts (0.1-0.3 mm). Strained OPX occurs as large porphyroclasts (up to 6 mm). Clinopyroxene (up to 2mm) and garnet (up to 4mm) are optically similar to those found in coarse peridotites.

3.4.2 Mineral Chemistry

Electron-microprobe analyses of olivine, OPX, CPX and garnet mineral compositions were performed at the Carnegie Institution of Washington using a JEOL JXA-8900L electron probe (see Appendix C for operating conditions). Mineral analyses are listed in Tables 3.2 to 3.5.

3.4.2.a Olivine

Representative olivine analyses for the Lesotho low-temperature peridotite suite are presented in Table 3.2. In general, compositions are comparable to those reported in Nixon (1973b). Individual olivine crystals appear to be homogenous in thin section but show slight evidence of chemical zonation. Serpentine veins crosscut many individual olivine crystals, but grains generally have fresh cores.

Olivine from the Lesotho peridotites is magnesium rich and ranges in magnesium number ($Mg^{\#}$ = Mg/{Mg+Fe}) from 0.914 to 0.937 (average 0.928), with one example from Matsoku having a $Mg^{\#}$ of 0.886 (Figure 3.9). This is comparable to the reported range of 0.92 to 0.93 (average 0.926), from previous studies of Kaapvaal peridotite xenoliths (Boyd, 1989). The most magnesian olivine (Fo_{92-93}) in Lesotho peridotite

Table 3.2 Representative olivine analyses for Lesotho peridotites. These yield cation totals, based on 4 oxygens, between 3.008 and 3.017 (average 3.012), comparable with a theoretical 3.000 cation total. Olivines from lherzolites and harzburgites produce a range and average in cation totals identical to that for the whole suite. Silicon per formula unit is also variable ranging from 0.983 to 0.992 (average 0.988) atoms per formula unit (AFU) in lherzolites, and 0.983 to 0.989 (average 0.987) AFU for harzburgites. The sum of octahedrally co-ordinated cations within the Kaapvaal suite is approximately 2.016, close to the theoretical value of 2.

Sample	**LET2**	**LET2**	**LET6**	**LET6**	**LET8**	**LET8**	**LET12**	**LET12**	**LET13**	**LET13**	**LET14**	**LET14**	**LET25**	**LET25**
Type	core	rim	core	rim	core	rim	core	rim	core	rim	core	rim	core	rim
Analyses	16	13	13	15	15	15	16	17	12	13	11	11	11	11
SiO_2	40.77	40.83	40.64	40.60	40.79	40.79	40.59	40.54	40.77	40.85	40.81	40.83	40.68	40.71
TiO_2	0.01	0.01	0.03	0.03	0.00	0.00	0.00	0.09	0.01	0.01	0.00	0.00	0.00	0.00
Al_2O_3	0.00	0.01	0.00	0.01	0.00	0.01	0.01	0.04	0.00	0.01	0.01	0.01	0.00	0.01
Cr_2O_3	0.02	0.02	0.04	0.04	0.01	0.01	0.02	0.05	0.01	0.02	0.01	0.02	0.00	0.01
FeO	6.51	6.50	7.24	7.24	6.45	6.45	7.25	7.24	6.63	6.63	6.23	6.23	7.04	7.06
MnO	0.08	0.08	0.10	0.10	0.07	0.08	0.08	0.14	0.08	0.08	0.08	0.08	0.08	0.09
MgO	52.13	52.08	51.50	51.52	52.21	52.17	51.56	51.28	52.03	51.92	52.38	52.35	51.73	51.63
CaO	0.02	0.02	0.02	0.02	0.01	0.01	0.02	0.06	0.02	0.02	0.02	0.02	0.01	0.01
Na_2O	0.01	0.01	0.01	0.01	0.01	0.01	0.01	0.06	0.00	0.01	0.01	0.00	0.00	0.00
NiO	0.46	0.46	0.42	0.42	0.46	0.47	0.46	0.50	0.44	0.44	0.46	0.46	0.44	0.46
Cations O =4														
Si	0.987	0.988	0.987	0.986	0.987	0.987	0.986	0.986	0.988	0.989	0.987	0.987	0.987	0.988
Al	0.000	0.000	0.000	0.000	0.000	0.000	0.000	0.001	0.000	0.000	0.000	0.000	0.000	0.000
Ti	0.000	0.000	0.000	0.000	0.000	0.000	0.000	0.002	0.000	0.000	0.000	0.000	0.000	0.000
Fe	0.132	0.132	0.147	0.147	0.131	0.131	0.147	0.147	0.134	0.134	0.126	0.126	0.143	0.143
Mn	0.002	0.002	0.002	0.002	0.001	0.002	0.002	0.003	0.002	0.002	0.002	0.002	0.002	0.002
Mg	1.882	1.879	1.865	1.866	1.884	1.883	1.868	1.859	1.879	1.874	1.888	1.887	1.872	1.868
Ca	0.000	0.000	0.001	0.001	0.000	0.000	0.000	0.002	0.000	0.001	0.000	0.000	0.000	0.000
Na	0.001	0.000	0.001	0.000	0.000	0.000	0.000	0.003	0.000	0.001	0.000	0.000	0.000	0.000
Cr	0.000	0.000	0.001	0.001	0.000	0.000	0.000	0.001	0.000	0.000	0.000	0.000	0.000	0.000
Ni	0.009	0.009	0.008	0.008	0.009	0.009	0.009	0.010	0.009	0.009	0.009	0.009	0.009	0.009
Sum	3.013	3.011	3.012	3.013	3.013	3.012	3.013	3.013	3.012	3.010	3.013	3.012	3.013	3.012
Mg#	0.935	0.935	0.927	0.927	0.935	0.935	0.927	0.927	0.933	0.933	0.937	0.937	0.929	0.929

Table 3.2 (continued) Olivine analyses.

Sample	**LET28**	**LET28**	**LET29**	**LET29**	**LET30**	**LET30**	**LET31**	**LET31**	**LET38**	**LET38**	**LET47**	**LET47**	**LET48**	**LET48**
Type	core	rim	core	rim	core	rim	core	rim	core	rim	core	rim	core	rim
Analyses	12	12	13	12	10	14	11	10	10	15	12	12	11	11
SiO_2	40.53	40.62	40.48	40.48	40.44	40.56	40.47	40.42	40.79	40.71	40.55	40.73	40.66	40.72
TiO_2	0.00	0.00	0.00	0.00	0.00	0.01	0.01	0.01	0.00	0.01	0.00	0.00	0.00	0.01
Al_2O_3	0.00	0.01	0.01	0.01	0.01	0.01	0.01	0.01	0.01	0.01	0.01	0.01	0.01	0.01
Cr_2O_3	0.00	0.01	0.02	0.03	0.02	0.03	0.02	0.03	0.02	0.02	0.03	0.03	0.02	0.03
FeO	6.70	6.72	7.07	7.11	7.10	7.12	7.32	7.34	6.64	6.71	7.28	7.30	7.05	7.05
MnO	0.08	0.08	0.08	0.09	0.08	0.09	0.09	0.09	0.08	0.09	0.09	0.09	0.09	0.09
MgO	52.17	52.05	51.84	51.77	51.86	51.70	51.59	51.58	51.97	51.95	51.58	51.38	51.71	51.63
CaO	0.01	0.01	0.02	0.03	0.02	0.03	0.02	0.03	0.02	0.03	0.02	0.03	0.02	0.02
Na_2O	0.00	0.01	0.02	0.01	0.01	0.01	0.01	0.01	0.01	0.01	0.00	0.01	0.01	0.01
NiO	0.50	0.50	0.47	0.48	0.44	0.44	0.46	0.48	0.46	0.46	0.43	0.42	0.43	0.43
Cations O =4														
Si	0.983	0.985	0.983	0.984	0.983	0.985	0.984	0.983	0.988	0.987	0.985	0.989	0.987	0.988
Al	0.000	0.000	0.000	0.000	0.000	0.000	0.000	0.000	0.000	0.000	0.000	0.000	0.000	0.000
Ti	0.000	0.000	0.000	0.000	0.000	0.000	0.000	0.000	0.000	0.000	0.000	0.000	0.000	0.000
Fe	0.136	0.136	0.144	0.144	0.144	0.145	0.149	0.149	0.135	0.136	0.148	0.148	0.143	0.143
Mn	0.002	0.002	0.002	0.002	0.002	0.002	0.002	0.002	0.002	0.002	0.002	0.002	0.002	0.002
Mg	1.886	1.881	1.877	1.875	1.878	1.872	1.870	1.870	1.877	1.877	1.869	1.861	1.871	1.868
Ca	0.000	0.000	0.001	0.001	0.001	0.001	0.000	0.001	0.001	0.001	0.001	0.001	0.001	0.001
Na	0.000	0.001	0.001	0.001	0.001	0.001	0.000	0.000	0.000	0.001	0.000	0.000	0.001	0.001
Cr	0.000	0.000	0.000	0.001	0.000	0.001	0.000	0.001	0.000	0.000	0.001	0.001	0.000	0.001
Ni	0.010	0.010	0.009	0.009	0.009	0.009	0.009	0.009	0.009	0.009	0.008	0.008	0.008	0.008
Sum	3.017	3.015	3.017	3.016	3.017	3.014	3.016	3.016	3.012	3.013	3.014	3.010	3.013	3.011
Mg#	0.933	0.933	0.929	0.928	0.929	0.928	0.926	0.926	0.933	0.932	0.927	0.926	0.929	0.929

Table 3.2 (continued) Olivine analyses.

Sample	LET49	LET49	LET58	LET58	LET64	LET64	LQ5	LQ5	M1	M1	M5	M5	M9	M9	TP9	TP9
Type	core	rim	core	rim	core	rim	core	rim	core	rim	core	rim	core	rim	core	rim
Analyses	12	12	10	10	8	8	11	12	12	13	14	12	15	11	9	10
SiO_2	40.44	40.45	40.61	40.68	40.92	40.73	40.89	40.90	39.86	39.99	40.68	40.78	40.74	40.73	40.84	40.85
TiO_2	0.00	0.01	0.00	0.01	0.01	0.01	0.00	0.01	0.03	0.04	0.00	0.01	0.03	0.04	0.00	0.00
Al_2O_3	0.02	0.02	0.01	0.01	0.01	0.01	0.01	0.03	0.01	0.02	0.00	0.00	0.01	0.01	0.00	0.00
Cr_2O_3	0.04	0.04	0.02	0.03	0.03	0.03	0.02	0.02	0.01	0.02	0.00	0.00	0.02	0.03	0.01	0.02
FeO	8.39	8.43	7.74	7.77	6.94	6.99	6.92	6.95	11.04	11.07	7.55	7.59	7.52	7.54	7.14	7.17
MnO	0.11	0.10	0.10	0.10	0.09	0.10	0.08	0.08	0.10	0.11	0.10	0.10	0.09	0.10	0.08	0.09
MgO	50.53	50.48	51.10	50.98	51.63	51.75	51.58	51.52	48.51	48.32	51.23	51.08	51.12	51.06	51.49	51.43
CaO	0.05	0.05	0.03	0.03	0.02	0.02	0.03	0.04	0.03	0.04	0.01	0.01	0.02	0.02	0.02	0.02
Na_2O	0.02	0.02	0.01	0.01	0.01	0.01	0.01	0.02	0.04	0.03	0.01	0.01	0.01	0.01	0.00	0.01
NiO	0.41	0.39	0.39	0.38	0.35	0.36	0.46	0.44	0.37	0.38	0.43	0.42	0.46	0.46	0.41	0.41
Cations O =4																
Si	0.988	0.988	0.988	0.990	0.992	0.988	0.991	0.992	0.985	0.989	0.989	0.992	0.990	0.991	0.991	0.991
Al	0.001	0.001	0.000	0.000	0.000	0.000	0.000	0.001	0.000	0.000	0.000	0.000	0.000	0.000	0.000	0.000
Ti	0.000	0.000	0.000	0.000	0.000	0.000	0.000	0.000	0.001	0.001	0.000	0.000	0.000	0.001	0.000	0.000
Fe	0.171	0.172	0.158	0.158	0.141	0.142	0.140	0.141	0.228	0.229	0.153	0.154	0.153	0.153	0.145	0.146
Mn	0.002	0.002	0.002	0.002	0.002	0.002	0.002	0.002	0.002	0.002	0.002	0.002	0.002	0.002	0.002	0.002
Mg	1.839	1.838	1.854	1.850	1.865	1.871	1.864	1.862	1.788	1.780	1.857	1.851	1.853	1.851	1.862	1.860
Ca	0.001	0.001	0.001	0.001	0.001	0.001	0.001	0.001	0.001	0.001	0.000	0.000	0.001	0.001	0.000	0.000
Na	0.001	0.001	0.000	0.000	0.001	0.001	0.000	0.001	0.002	0.001	0.000	0.000	0.001	0.001	0.000	0.000
Cr	0.001	0.001	0.000	0.001	0.000	0.001	0.000	0.000	0.000	0.000	0.000	0.000	0.000	0.001	0.000	0.000
Ni	0.008	0.008	0.008	0.008	0.007	0.007	0.009	0.009	0.007	0.007	0.008	0.008	0.009	0.009	0.008	0.008
Sum	3.012	3.012	3.011	3.010	3.008	3.012	3.008	3.008	3.015	3.011	3.011	3.008	3.009	3.009	3.009	3.009
Mg#	0.915	0.914	0.922	0.921	0.930	0.930	0.930	0.930	0.887	0.886	0.924	0.923	0.924	0.924	0.928	0.927

occurs in harzburgitic xenoliths (Figure 3.9), and ranges in $Mg^{\#}$ from 0.927 to 0.937 (average 0.933). The $Mg^{\#}$ for lherzolites ranges from 0.914 to 0.933 (average 0.927), implying that higher values of $Mg^{\#}$ occur in the more refractory, harzburgitic peridotites (Figure 3.9). If we compare the xenoliths in terms of facies, peridotites from the spinel facies (0.923-0.935, average 0.929) and garnet-spinel facies (0.926-0.937, average 0.931) are only slightly more magnesian rich than those from garnet facies (0.914-0.935, average 0.927). Low-temperature porphyroclastic samples analysed lie within the range for coarse peridotites suggesting that there is no compositional difference between textural types.

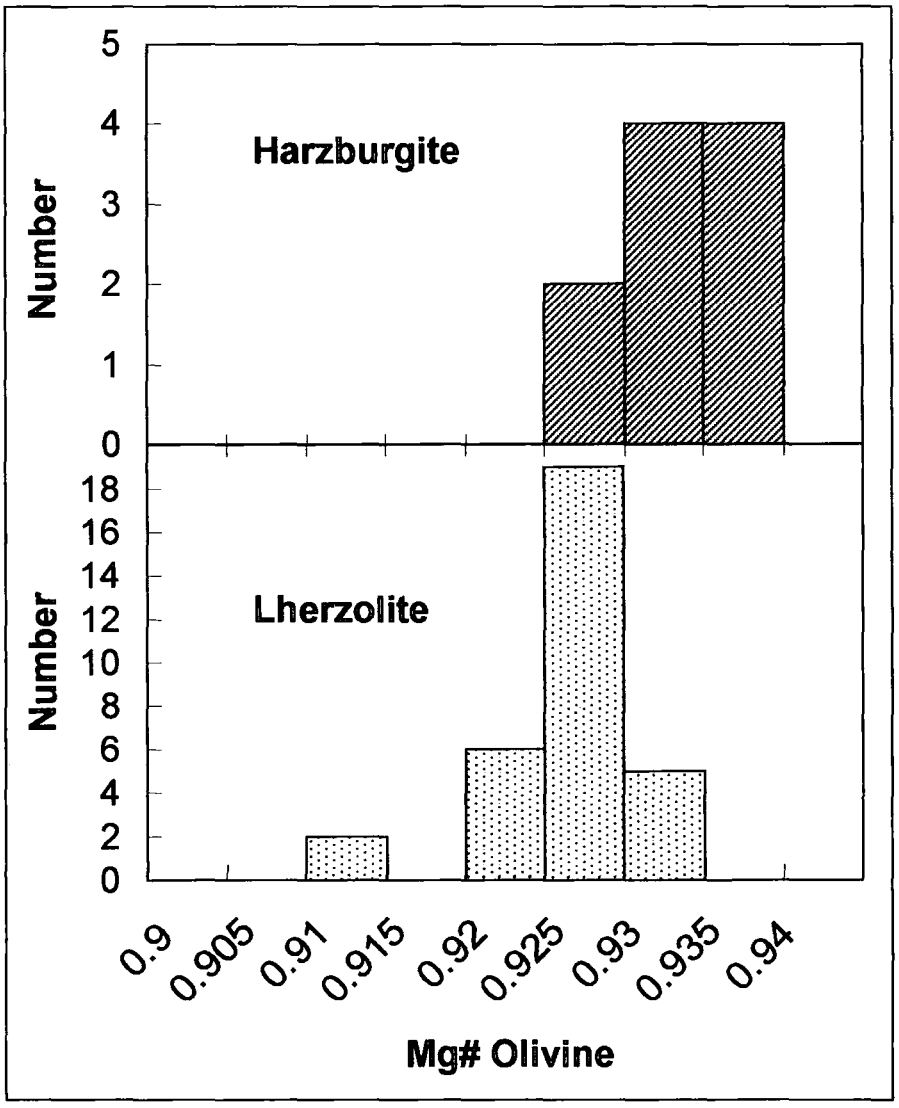

Figure 3.9 Histograms of $Mg^{\#}$ of olivine {Mg/(Mg+Fe)} for Lesotho peridotites.

The average Lesotho olivine $Mg^{\#}$ for this study at 0.928 +/- 0.005 is slightly higher, but within error of that reported for the Kaapvaal low-T peridotite suite as a whole by

Boyd (1989) at 0.926. Concentrations of Ni in olivine range from 0.35 to 0.5 wt% (average 0.44 wt% NiO). Ni concentrations in olivines from harzburgites (0.46-0.5 wt% NiO, average 0.47 wt%) tend to be more Ni-rich than olivines from lherzolites (0.35-0.48 wt% NiO, average 0.43 wt%). Ni concentrations in olivines from spinel, spinel-garnet and garnet facies span similar ranges. A negative correlation exists between MnO and MgO.

Olivines from the Lesotho peridotites contain negligible levels of Al, Cr, Ca and Ti. Extended counting times were not used to quantify these elements. In general olivines appear to be unzoned, but rims may have slightly elevated concentrations of Al, Cr, Ca, Fe and Ti. No systematic variation was observed for these elements in relation to other oxide components within the mineral.

3.4.2.b Orthopyroxene

Representative OPX analyses for the Lesotho peridotite suite are presented in Table 3.3. Although OPX crystals appear to be homogenous in thin section they show slight evidence of chemical zonation.

Orthopyroxene composition varies little within the Lesotho peridotite suite and is generally characterised by high $Mg^{\#}$, ranging from 0.922 to 0.945 (average 0.936). If we compare the xenoliths in terms of facies, the $Mg^{\#}$ of spinel facies peridotites (0.925-0.939, average 0.933) is slightly lower than garnet-spinel (0.933-0.945, average 0.938) and garnet facies peridotites (0.922-0.942, average 0.936). The most magnesian OPX in the Lesotho peridotite suite occurs in harzburgitic xenoliths, and ranges in $Mg^{\#}$ from 0.936 to 0.945 (average 0.940). The $Mg^{\#}$ for lherzolites ranges from 0.922 to 0.941 (average 0.934), implying that higher values of $Mg^{\#}$ occur in the more refractory peridotites. In all cases OPX in the peridotites is more Mg-rich than co-existing olivine, and suggests that the parageneses are equilibrated (Boyd, 1970).

Within the Lesotho low-T peridotite suite OPX generally has low CaO content. However, OPX often shows evidence of CPX exsolution suggesting that they were saturated with respect to diopside at high-temperature. This either suggests that partial melting did not progress far past the four-phase field of Ol-OPX-CPX and an Al-phase, or that the OPX was subjected to later Ca enrichment prior to eruption.

Orthopyroxenes appear to show slight zonation with slightly elevated concentrations of Al, Cr, Ca, Fe and Ti in the rims.

Table 3.3 Representative OPX analyses for Lesotho peridotites. These yield cation totals, based on 6 oxygens, between 4.004 and 4.016 (average 4.009), comparable with a theoretical 4.000 cation total. OPX from lherzolites and harzburgites produce a range and average in cation totals identical to that for the whole suite.

Sample	**LET2**	**LET2**	**LET6**	**LET6**	**LET8**	**LET8**	**LET12**	**LET12**	**LET13**	**LET13**	**LET14**	**LET14**	**LET25**	**LET25**
Type	core	rim	core	rim	core	rim	core	rim	core	rim	core	rim	core	rim
Analyses	12	12	12	15	11	10	8	10	13	11	10	12	11	12
SiO_2	57.796	57.757	57.689	57.674	57.356	57.338	57.680	57.805	57.653	57.704	57.740	57.836	57.160	57.019
TiO_2	0.005	0.010	0.110	0.115	0.003	0.008	0.006	0.009	0.018	0.021	0.009	0.020	0.009	0.010
Al_2O_3	0.794	0.843	0.541	0.558	1.362	1.373	0.685	0.690	0.770	0.799	0.752	0.777	1.593	1.764
Cr_2O_3	0.351	0.376	0.420	0.429	0.378	0.422	0.353	0.356	0.265	0.271	0.301	0.310	0.315	0.342
FeO	3.973	3.988	4.381	4.411	4.211	4.211	4.363	4.366	4.133	4.111	3.848	3.819	4.673	4.702
MnO	0.092	0.096	0.113	0.119	0.094	0.098	0.107	0.101	0.097	0.091	0.093	0.089	0.111	0.111
MgO	36.527	36.379	36.055	35.976	36.156	36.103	36.161	36.028	36.626	36.535	36.859	36.744	35.762	35.560
CaO	0.268	0.311	0.423	0.439	0.322	0.326	0.464	0.467	0.293	0.305	0.243	0.245	0.272	0.370
Na_2O	0.094	0.130	0.155	0.165	0.032	0.027	0.065	0.064	0.045	0.051	0.037	0.032	0.024	0.033
NiO	0.100	0.111	0.113	0.113	0.085	0.093	0.116	0.115	0.099	0.111	0.118	0.127	0.082	0.088
Cation O = 6														
Si	1.973	1.973	1.976	1.976	1.961	1.960	1.974	1.978	1.970	1.971	1.970	1.973	1.957	1.954
Al	0.032	0.034	0.022	0.023	0.055	0.055	0.028	0.028	0.031	0.032	0.030	0.031	0.064	0.071
Ti	0.000	0.000	0.003	0.003	0.000	0.000	0.000	0.000	0.000	0.001	0.000	0.001	0.000	0.000
Fe	0.113	0.114	0.125	0.126	0.120	0.120	0.125	0.125	0.118	0.117	0.110	0.109	0.134	0.135
Mn	0.003	0.003	0.003	0.003	0.003	0.003	0.003	0.003	0.003	0.003	0.003	0.003	0.003	0.003
Mg	1.859	1.852	1.841	1.837	1.842	1.840	1.845	1.838	1.866	1.861	1.875	1.869	1.826	1.816
Ca	0.010	0.011	0.016	0.016	0.012	0.012	0.017	0.017	0.011	0.011	0.009	0.009	0.010	0.014
Na	0.006	0.009	0.010	0.011	0.002	0.002	0.004	0.004	0.003	0.003	0.002	0.002	0.002	0.002
Cr	0.009	0.010	0.011	0.012	0.010	0.011	0.010	0.010	0.007	0.007	0.008	0.008	0.009	0.009
Ni	0.003	0.003	0.003	0.003	0.002	0.003	0.003	0.003	0.003	0.003	0.003	0.003	0.002	0.002
Sum	4.009	4.009	4.010	4.010	4.008	4.007	4.009	4.005	4.012	4.010	4.011	4.008	4.007	4.007
Mg#	0.942	0.942	0.936	0.936	0.939	0.939	0.937	0.936	0.940	0.941	0.945	0.945	0.932	0.931

Table 3.3 (continued) OPX analyses.

Sample	LET28	LET28	LET29	LET29	LET30	LET30	LET31	LET31	LET38	LET38	LET47	LET47	LET48	LET48
Type	core	rim	core	rim	core	rim	core	rim	core	rim	core	rim	core	rim
Analyses	11	11	10	13	11	11	11	11	10	10	9	8	9	10
SiO_2	56.969	56.928	57.454	57.485	57.477	57.564	57.502	57.470	57.921	57.858	57.680	57.721	57.741	57.756
TiO_2	0.001	0.003	0.007	0.008	0.008	0.020	0.030	0.039	0.004	0.010	0.005	0.010	0.017	0.025
Al_2O_3	1.519	1.609	0.833	0.849	0.723	0.744	0.827	0.838	0.772	0.794	0.737	0.749	0.710	0.802
Cr_2O_3	0.355	0.385	0.332	0.360	0.343	0.356	0.313	0.355	0.279	0.314	0.361	0.365	0.348	0.398
FeO	4.403	4.448	4.307	4.302	4.253	4.250	4.430	4.437	4.199	4.189	4.542	4.569	4.417	4.416
MnO	0.109	0.101	0.100	0.095	0.104	0.105	0.101	0.106	0.092	0.096	0.105	0.105	0.104	0.109
MgO	36.179	36.046	36.288	36.199	36.449	36.318	36.061	36.012	36.069	36.048	35.933	35.832	36.003	35.782
CaO	0.357	0.385	0.428	0.446	0.441	0.447	0.462	0.465	0.453	0.467	0.438	0.448	0.414	0.442
Na_2O	0.005	0.007	0.144	0.139	0.083	0.086	0.153	0.154	0.097	0.101	0.074	0.080	0.117	0.150
NiO	0.103	0.087	0.107	0.117	0.119	0.109	0.120	0.124	0.115	0.122	0.125	0.121	0.131	0.120
Cation O = 6														
Si	1.951	1.950	1.967	1.968	1.968	1.970	1.970	1.969	1.979	1.978	1.975	1.977	1.976	1.977
Al	0.061	0.065	0.034	0.034	0.029	0.030	0.033	0.034	0.031	0.032	0.030	0.030	0.029	0.032
Ti	0.000	0.000	0.000	0.000	0.000	0.001	0.001	0.001	0.000	0.000	0.000	0.000	0.000	0.001
Fe	0.126	0.127	0.123	0.123	0.122	0.122	0.127	0.127	0.120	0.120	0.130	0.131	0.126	0.126
Mn	0.003	0.003	0.003	0.003	0.003	0.003	0.003	0.003	0.003	0.003	0.003	0.003	0.003	0.003
Mg	1.847	1.840	1.852	1.847	1.860	1.853	1.841	1.839	1.837	1.837	1.835	1.829	1.837	1.826
Ca	0.013	0.014	0.016	0.016	0.016	0.016	0.017	0.017	0.017	0.017	0.016	0.016	0.015	0.016
Na	0.000	0.000	0.010	0.009	0.006	0.006	0.010	0.010	0.006	0.007	0.005	0.005	0.008	0.010
Cr	0.010	0.010	0.009	0.010	0.009	0.010	0.008	0.010	0.008	0.008	0.010	0.010	0.009	0.011
Ni	0.003	0.002	0.003	0.003	0.003	0.003	0.003	0.003	0.003	0.003	0.003	0.003	0.004	0.003
Sum	4.014	4.013	4.016	4.014	4.016	4.013	4.014	4.013	4.004	4.005	4.007	4.006	4.008	4.006
Mg#	0.936	0.936	0.938	0.938	0.939	0.938	0.936	0.935	0.939	0.939	0.934	0.933	0.936	0.935

Table 3.3 (continued) OPX analyses.

Sample	LET49	LET49	LET58	LET58	LET64	LET64	LQ5	LQ5	M1	M1	M5	M5	M9	M9	TP9	TP9
Type	core	rim	core	rim	core	rim	core	rim	core	rim	core	rim	core	rim	core	rim
Analyses	10	9	9	11	10	10	11	12	10	10	10	11	11	11	10	9
SiO_2	57.419	57.457	57.767	57.652	57.942	57.875	57.649	57.652	56.895	56.931	56.562	56.427	57.500	57.512	57.654	57.673
TiO_2	0.029	0.040	0.004	0.023	0.012	0.031	0.004	0.010	0.148	0.159	0.018	0.033	0.119	0.146	0.003	0.009
Al_2O_3	0.870	0.867	0.739	0.754	0.759	0.815	0.785	0.799	0.860	0.872	2.124	2.241	0.838	0.841	0.866	0.869
Cr_2O_3	0.326	0.332	0.334	0.365	0.298	0.325	0.251	0.257	0.193	0.204	0.279	0.308	0.300	0.312	0.308	0.318
FeO	5.215	5.235	4.714	4.751	4.110	4.132	4.253	4.254	6.672	6.685	5.081	5.125	4.593	4.609	4.454	4.482
MnO	0.124	0.115	0.107	0.108	0.102	0.102	0.092	0.088	0.116	0.121	0.124	0.126	0.101	0.104	0.101	0.106
MgO	34.677	34.619	35.635	35.628	36.079	35.988	36.294	36.273	34.336	34.188	35.527	35.410	35.855	35.766	36.146	36.045
CaO	1.041	1.019	0.499	0.506	0.474	0.481	0.429	0.438	0.494	0.513	0.198	0.231	0.431	0.437	0.328	0.344
Na_2O	0.173	0.179	0.095	0.099	0.119	0.149	0.125	0.119	0.190	0.218	0.020	0.023	0.144	0.157	0.048	0.050
NiO	0.126	0.137	0.106	0.115	0.106	0.103	0.118	0.110	0.097	0.108	0.067	0.075	0.118	0.117	0.094	0.103
Cation O = 6																
Si	1.976	1.977	1.979	1.977	1.980	1.978	1.972	1.972	1.969	1.970	1.941	1.938	1.970	1.971	1.973	1.973
Al	0.035	0.035	0.030	0.030	0.031	0.033	0.032	0.032	0.035	0.036	0.086	0.091	0.034	0.034	0.035	0.035
Ti	0.001	0.001	0.000	0.001	0.000	0.001	0.000	0.000	0.004	0.004	0.000	0.001	0.003	0.004	0.000	0.000
Fe	0.150	0.151	0.135	0.136	0.117	0.118	0.122	0.122	0.193	0.193	0.146	0.147	0.132	0.132	0.127	0.128
Mn	0.004	0.003	0.003	0.003	0.003	0.003	0.003	0.003	0.003	0.004	0.004	0.004	0.003	0.003	0.003	0.003
Mg	1.779	1.776	1.820	1.821	1.838	1.834	1.851	1.850	1.771	1.764	1.817	1.812	1.832	1.827	1.843	1.839
Ca	0.038	0.038	0.018	0.019	0.017	0.018	0.016	0.016	0.018	0.019	0.007	0.009	0.016	0.016	0.012	0.013
Na	0.012	0.012	0.006	0.007	0.008	0.010	0.008	0.008	0.013	0.015	0.001	0.002	0.010	0.010	0.003	0.003
Cr	0.009	0.009	0.009	0.010	0.008	0.009	0.007	0.007	0.005	0.006	0.008	0.008	0.008	0.008	0.008	0.009
Ni	0.004	0.004	0.003	0.003	0.003	0.003	0.003	0.003	0.003	0.003	0.002	0.002	0.003	0.003	0.003	0.003
Sum	4.007	4.006	4.004	4.006	4.005	4.005	4.013	4.012	4.014	4.013	4.012	4.013	4.010	4.009	4.007	4.006
Mg#	0.922	0.922	0.931	0.930	0.940	0.939	0.938	0.938	0.902	0.901	0.926	0.925	0.933	0.933	0.935	0.935

3.4.2.c Clinopyroxene

Representative CPX analyses for the Lesotho peridotite suite are presented in Table 3.4. Within the Lesotho peridotite suite CPXs have variable compositions, probably reflecting the multiple generations of CPX in a given sample. All CPXs in the Lesotho peridotite suite have a high Cr_2O_3 content, ranging from 0.6 to 3.6 wt% (average 1.49 wt%), and are therefore classified as Cr-diopside (Figure 3.10).

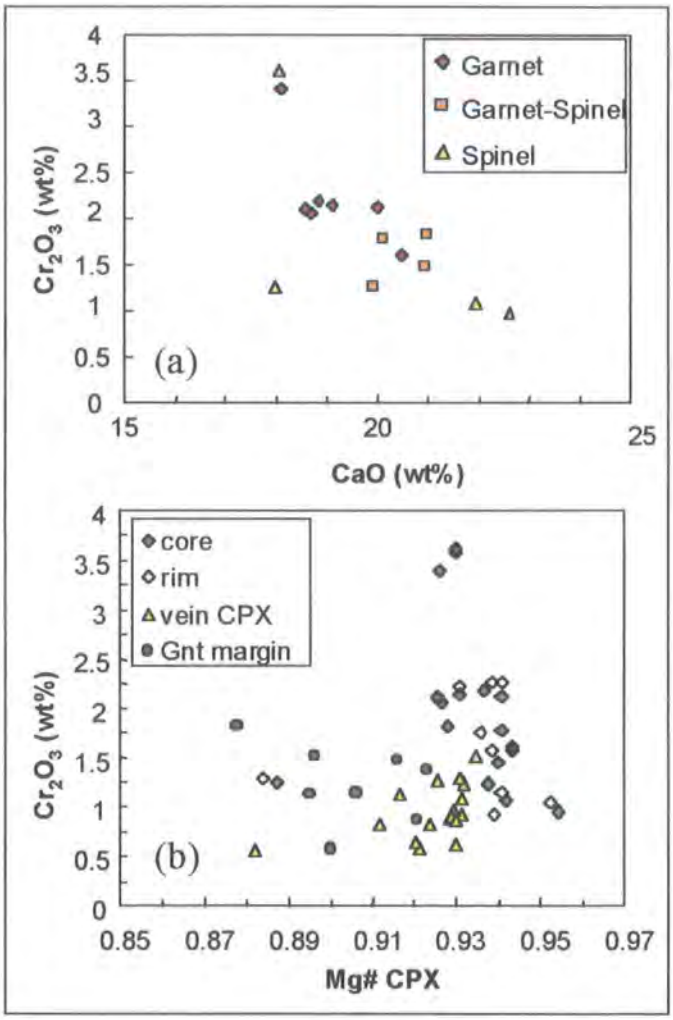

Figure 3.10 Composition of CPX in low-T Lesotho peridotites as (a) Cr_2O_3 vs. CaO for CPX core compositions, (b) Cr_2O_3 vs. Mg# CPX for all CPXs.

The composition of large discrete CPXs is magnesian rich and is characterised by high $Mg^{\#}$, ranging from 0.925 to 0.954 (average 0.936). Al_2O_3 ranges from 1.51 to 3.89 wt% (average 2.55 wt%), FeO from 1.48 to 3.65 wt% (average 2.13 wt%), Na_2O from 1.19 to 2.98 wt% (average 2.17 wt%), and TiO_2 from 0 to 0.39 wt% (average 0.1 wt%). In the large discrete CPXs there is a slight decrease from core to rim in both Al_2O_3 (0.04 wt% range) and Na_2O (0.12 wt% range) content which may be related to sub-solidus re-

Table 3.4 Representative CPX analyses for Lesotho peridotites. These yield cation totals, based on 6 oxygens, between 4.005 and 4.031 (average 4.017), slightly higher than the theoretical 4.000 cation total.

Sample	LET2	LET2	LET6	LET6	LET8	LET12	LET13	LET13	LET14	LET25	LET25	LET28	LET29	LET29
Type	vein	Gnt rim	core	rim	vein	vein	vein	Gnt rim	Gnt rim	core	rim	vein	core	rim
Analyses	15	3	12	12	18	23	14	1	9	9	9	25	10	6
SiO_2	54.87	49.65	54.94	54.88	54.88	54.66	53.78	49.94	49.19	54.25	54.23	54.63	54.64	54.65
TiO_2	0.38	0.73	0.28	0.30	0.36	0.37	0.71	1.23	1.05	0.00	0.01	0.12	0.01	0.03
Al_2O_3	1.07	8.49	2.09	2.09	1.57	1.84	1.76	6.88	8.92	2.38	2.38	0.91	2.62	2.65
Cr_2O_3	1.26	1.15	3.60	3.63	0.95	0.99	0.86	0.60	1.54	0.98	1.06	1.53	2.16	2.25
FeO	2.61	3.39	2.14	2.15	2.50	2.66	3.37	3.37	3.26	1.48	1.52	2.45	2.23	2.22
MnO	0.10	0.25	0.09	0.08	0.09	0.12	0.12	0.19	0.21	0.06	0.06	0.09	0.07	0.08
MgO	19.78	16.14	15.90	15.89	18.91	19.46	19.43	16.96	15.76	17.01	16.99	19.45	16.72	16.61
CaO	19.01	19.13	18.04	18.03	19.48	18.89	19.11	20.28	18.71	22.61	22.56	19.62	19.10	19.00
Na_2O	0.89	1.05	2.88	2.91	1.19	0.98	0.81	0.53	1.34	1.19	1.16	1.13	2.38	2.44
NiO	0.04	0.01	0.04	0.04	0.06	0.05	0.05	0.02	0.01	0.03	0.04	0.05	0.06	0.06
Cation O = 6														
Si	1.975	1.801	1.986	1.984	1.976	1.966	1.944	1.815	1.785	1.962	1.961	1.972	1.973	1.973
Al	0.045	0.363	0.089	0.089	0.067	0.078	0.075	0.295	0.382	0.101	0.101	0.039	0.112	0.113
Ti	0.010	0.020	0.008	0.008	0.010	0.010	0.019	0.034	0.029	0.000	0.000	0.003	0.000	0.001
Fe	0.079	0.103	0.065	0.065	0.075	0.080	0.102	0.102	0.099	0.045	0.046	0.074	0.067	0.067
Mn	0.003	0.008	0.003	0.002	0.003	0.004	0.004	0.006	0.007	0.002	0.002	0.003	0.002	0.002
Mg	1.061	0.873	0.857	0.857	1.015	1.043	1.047	0.919	0.853	0.917	0.916	1.047	0.900	0.894
Ca	0.733	0.743	0.699	0.699	0.751	0.728	0.740	0.789	0.728	0.876	0.874	0.759	0.739	0.735
Na	0.062	0.074	0.202	0.204	0.083	0.069	0.057	0.037	0.094	0.084	0.081	0.079	0.166	0.171
Cr	0.036	0.033	0.103	0.104	0.027	0.028	0.025	0.017	0.044	0.028	0.030	0.044	0.062	0.064
Ni	0.001	0.000	0.001	0.001	0.002	0.001	0.002	0.001	0.000	0.001	0.001	0.001	0.002	0.002
Sum	4.005	4.018	4.011	4.013	4.009	4.006	4.015	4.014	4.020	4.015	4.013	4.022	4.023	4.023
Mg#	0.931	0.895	0.930	0.929	0.931	0.929	0.911	0.900	0.896	0.954	0.952	0.934	0.930	0.930

Table 3.4 (continued) CPX analyses.

Sample	LET29	LET29	LET30	LET30	LET30	LET30	LET31	LET31	LET38	LET38	LET38	LET38	LET47	LET47
Type	vein	Gnt rim	core	rim	vein	Gnt rim	core	vein	core	rim	vein	Gnt rim	core	rim
Analyses	12	3	7	7	4	4	2	1	6	6	4	2	5	18
SiO_2	54.41	52.75	54.61	54.55	53.78	51.82	54.91	54.72	54.74	54.70	54.22	53.06	54.55	54.78
TiO_2	0.21	0.20	0.03	0.04	0.40	0.27	0.09	0.17	0.01	0.01	0.20	0.16	0.00	0.21
Al_2O_3	1.65	4.50	2.14	2.16	2.25	5.83	2.68	1.21	2.04	2.06	2.04	4.38	1.53	0.88
Cr_2O_3	0.91	1.51	2.14	2.28	0.84	1.17	2.07	0.93	1.60	1.64	0.90	0.89	1.83	0.95
FeO	2.77	3.18	1.94	1.91	2.92	3.40	2.37	2.76	1.89	1.87	2.78	2.98	2.04	2.82
MnO	0.10	0.21	0.07	0.07	0.12	0.27	0.07	0.11	0.06	0.08	0.13	0.17	0.08	0.11
MgO	20.05	19.30	17.07	16.99	19.69	18.34	16.59	19.98	17.43	17.42	20.46	19.23	17.44	20.12
CaO	18.90	17.25	20.03	19.94	19.05	17.98	18.69	19.07	20.49	20.48	18.53	18.15	21.01	19.24
Na_2O	0.95	1.08	1.93	1.99	0.88	0.91	2.48	1.02	1.69	1.68	0.74	0.96	1.46	0.84
NiO	0.05	0.02	0.04	0.05	0.05	0.02	0.06	0.04	0.04	0.06	0.02	0.02	0.05	0.05
Cation O = 6														
Si	1.959	1.899	1.973	1.972	1.940	1.869	1.980	1.971	1.975	1.974	1.949	1.908	1.975	1.974
Al	0.070	0.191	0.091	0.092	0.096	0.248	0.114	0.051	0.087	0.088	0.086	0.185	0.065	0.037
Ti	0.006	0.005	0.001	0.001	0.011	0.007	0.002	0.005	0.000	0.000	0.005	0.004	0.000	0.006
Fe	0.083	0.096	0.059	0.058	0.088	0.103	0.071	0.083	0.057	0.056	0.083	0.090	0.062	0.085
Mn	0.003	0.006	0.002	0.002	0.004	0.008	0.002	0.003	0.002	0.002	0.004	0.005	0.002	0.003
Mg	1.076	1.036	0.919	0.915	1.059	0.986	0.892	1.073	0.938	0.937	1.096	1.031	0.941	1.081
Ca	0.729	0.665	0.775	0.772	0.736	0.695	0.722	0.736	0.792	0.792	0.714	0.699	0.815	0.743
Na	0.066	0.075	0.135	0.140	0.061	0.063	0.173	0.071	0.118	0.118	0.052	0.067	0.103	0.059
Cr	0.026	0.043	0.061	0.065	0.024	0.033	0.059	0.026	0.046	0.047	0.025	0.025	0.052	0.027
Ni	0.001	0.001	0.001	0.002	0.002	0.001	0.002	0.001	0.001	0.002	0.001	0.001	0.002	0.001
Sum	4.020	4.017	4.018	4.019	4.020	4.014	4.018	4.021	4.017	4.017	4.016	4.016	4.018	4.017
Mg#	0.928	0.916	0.940	0.941	0.923	0.906	0.926	0.928	0.943	0.943	0.929	0.920	0.927	0.939

Table 3.4 (continued) CPX analyses.

Sample	LET48	LET48	LET49	LET49	LET58	LET58	LET58	LET64	LET64	LET64	LQ5	LQ5
Type	core	vein	vein	Gnt rim	core	rim	vein	core	vein	Gnt rim	core	rim
Analyses	8	15	25	2	7	8	5	10	7	3	3	3
SiO_2	54.49	54.57	55.00	48.24	54.91	54.93	54.04	54.92	53.95	52.52	54.93	54.79
TiO_2	0.07	0.14	0.05	0.98	0.03	0.03	0.57	0.13	0.63	0.70	0.01	0.05
Al_2O_3	2.87	1.47	1.71	9.97	1.51	1.73	2.00	2.93	2.13	3.95	2.37	2.60
Cr_2O_3	3.41	1.32	1.14	1.85	1.48	1.58	1.29	2.19	1.11	1.40	1.27	1.78
FeO	2.25	2.63	3.12	3.67	2.01	2.03	2.71	1.97	2.51	2.71	2.08	2.11
MnO	0.08	0.10	0.11	0.20	0.07	0.07	0.12	0.08	0.13	0.12	0.07	0.08
MgO	15.70	19.70	19.12	14.74	17.53	17.32	18.78	16.30	18.94	18.09	17.35	17.05
CaO	18.09	18.93	18.33	19.14	20.96	20.66	19.44	18.85	19.64	19.26	19.92	19.49
Na_2O	2.98	1.07	1.36	1.18	1.45	1.59	1.01	2.58	0.94	1.21	1.93	2.04
NiO	0.06	0.05	0.06	0.01	0.06	0.05	0.04	0.05	0.03	0.05	0.06	0.02
Cation O = 6												
Si	1.971	1.966	1.980	1.758	1.984	1.984	1.951	1.978	1.946	1.899	1.979	1.975
Al	0.122	0.063	0.073	0.428	0.064	0.074	0.085	0.124	0.090	0.168	0.100	0.110
Ti	0.002	0.004	0.001	0.027	0.001	0.001	0.015	0.003	0.017	0.019	0.000	0.001
Fe	0.068	0.079	0.094	0.112	0.061	0.061	0.082	0.059	0.076	0.082	0.063	0.064
Mn	0.003	0.003	0.003	0.006	0.002	0.002	0.004	0.002	0.004	0.004	0.002	0.002
Mg	0.846	1.058	1.026	0.801	0.944	0.932	1.011	0.875	1.018	0.975	0.932	0.916
Ca	0.701	0.731	0.707	0.747	0.812	0.799	0.752	0.727	0.759	0.746	0.769	0.753
Na	0.209	0.075	0.095	0.084	0.101	0.111	0.071	0.180	0.066	0.085	0.135	0.142
Cr	0.097	0.037	0.032	0.053	0.042	0.045	0.037	0.062	0.032	0.040	0.036	0.051
Ni	0.002	0.002	0.002	0.000	0.002	0.002	0.001	0.001	0.001	0.001	0.002	0.001
Sum	4.022	4.018	4.013	4.016	4.013	4.012	4.008	4.015	4.009	4.020	4.019	4.015
Mg#	0.926	0.930	0.916	0.877	0.940	0.938	0.925	0.936	0.931	0.923	0.937	0.935

Table 3.4 (continued) CPX analyses.

Sample	LQ5	M1	M1	M1	M5	M5	M9	M9	M9	TP9	TP9	TP9
Type	vein	core	rim	vein	core	rim	core	rim	vein	core	rim	vein
Analyses	12	6	7	1	7	11	6	8	2	6	9	5
SiO_2	54.98	54.53	54.42	53.19	53.67	53.62	54.74	54.67	54.59	54.72	54.58	54.05
TiO_2	0.20	0.39	0.40	1.16	0.14	0.15	0.30	0.32	0.46	0.00	0.01	0.82
Al_2O_3	1.28	3.20	3.32	2.93	3.89	3.98	2.88	2.94	1.64	3.18	3.30	1.31
Cr_2O_3	0.64	1.27	1.30	0.59	1.09	1.16	2.12	2.14	0.60	1.78	2.29	0.67
FeO	2.73	3.65	3.75	4.37	1.74	1.77	2.35	2.34	3.00	1.81	1.82	2.85
MnO	0.12	0.10	0.09	0.15	0.06	0.06	0.08	0.08	0.12	0.07	0.07	0.10
MgO	20.17	16.05	15.90	18.21	15.67	15.64	16.26	16.21	19.46	15.92	15.53	18.41
CaO	18.90	17.98	17.86	17.83	21.94	21.79	18.56	18.57	18.91	20.12	19.81	20.82
Na_2O	0.96	2.79	2.90	1.56	1.77	1.80	2.67	2.70	1.17	2.36	2.56	0.95
NiO	0.03	0.06	0.05	0.01	0.04	0.03	0.05	0.04	0.06	0.04	0.04	0.03
Cation O = 6												
Si	1.976	1.972	1.970	1.928	1.942	1.940	1.975	1.973	1.967	1.974	1.971	1.958
Al	0.054	0.136	0.141	0.125	0.166	0.170	0.123	0.125	0.069	0.135	0.140	0.056
Ti	0.005	0.010	0.011	0.032	0.004	0.004	0.008	0.009	0.013	0.000	0.000	0.022
Fe	0.082	0.111	0.113	0.133	0.053	0.054	0.071	0.070	0.090	0.055	0.055	0.086
Mn	0.004	0.003	0.003	0.005	0.002	0.002	0.002	0.002	0.004	0.002	0.002	0.003
Mg	1.080	0.866	0.858	0.984	0.845	0.843	0.874	0.872	1.045	0.856	0.836	0.995
Ca	0.728	0.697	0.693	0.693	0.851	0.845	0.718	0.718	0.730	0.778	0.766	0.808
Na	0.067	0.195	0.203	0.110	0.124	0.126	0.187	0.189	0.082	0.165	0.179	0.066
Cr	0.018	0.036	0.037	0.017	0.031	0.033	0.060	0.061	0.017	0.051	0.065	0.019
Ni	0.001	0.002	0.002	0.000	0.001	0.001	0.001	0.001	0.002	0.001	0.001	0.001
Sum	4.015	4.029	4.031	4.025	4.018	4.017	4.019	4.020	4.018	4.016	4.016	4.015
Mg#	0.929	0.887	0.883	0.881	0.941	0.940	0.925	0.925	0.920	0.940	0.938	0.920

equilibration. TiO_2 and FeO are slightly enriched towards the margins. The CPXs show a negative correlation between CaO and Cr_2O_3 (Figure 3.10a).

Clinopyroxene associated with garnet is less magnesium rich, $Mg^{\#}$ ranging from 0.877 to 0.923 (average 0.904), than the discrete CPX (Figure 3.10b). These CPXs also tend to be more enriched in Al_2O_3 (average 6.14 wt%), TiO_2 (average 0.62 wt%), FeO (average 3.18 wt%) and MgO (average 17.69 wt%), whilst lower in SiO_2 (average 51.28 wt%), Cr_2O_3 (average 1.18 wt%), and Na_2O (average 1.01 wt%). No clear correlation exists between CaO and Cr_2O_3.

Late stage vein-like CPX is magnesium rich, $Mg^{\#}$ ranging from 0.911 to 0.934 (average 0.926), but less Mg-rich than the discrete CPX. These CPXs also tend to be more enriched in TiO_2 (average 0.41 wt%), FeO (average 2.87 wt%) and MgO (average 19.41 wt%), whilst lower in Al_2O_3 (average 1.69 wt%), Cr_2O_3 (average 0.97 wt%), and Na_2O (average 1.04 wt%). No clear correlation exists between CaO and Cr_2O_3.

3.4.2.d Garnet

The garnet from Lesotho peridotites is a chromium pyrope with high MgO, low CaO and $Mg^{\#}$ ranging from 0.821 to 0.865 (Table 3.5). The pyrope content of the garnet ranges from 71 to 87%. A summary of the end-member compositions is given in Table 3.5. The garnets are generally homogeneous and exhibit only minor chemical zoning on a thin-section scale. The Cr_2O_3 content within the garnets ranges from 4.2 to 8.3 wt%. On average, garnet from harzburgites is more Cr_2O_3 rich (6.59 +/- 0.5 wt%) than garnet from lherzolites (5.55 +/- 1.25 wt%). Very little variation is observed between garnet from peridotites of different facies or textures. The garnets can generally be classified as group 9 (G9) garnets in the statistical classification scheme of Dawson and Stephens (1975). Plotted as Cr_2O_3 vs. CaO (Figure 3.11), G9 compositions predominate but some harzburgitic sub-calcic G10 garnets are also present. Garnets appear to show slight zonation with slightly elevated concentrations of Al, Fe and Ti in the rims and lower concentrations of Ca and Cr.

The composition of garnet is significant. In previous studies of Lesotho peridotite xenoliths, the oldest Re-Os T_{RD} model age measured was for sub-calcic sample PHN2825, from Liqhobong, at 3.3 Ga (Pearson *et al.*, 1995a). In this study the sub-calcic samples produce Re-Os T_{RD} model ages within the range of calcium saturated samples, at 2.8 Ga, and are therefore not significantly older.

Table 3.5 Representative garnet analyses for Low-T Lesotho peridotites.

Sample	LET2	LET2	LET12	LET12	LET13	LET13	LET14	LET14	LET29	LET29	LET30	LET30	LET31	LET31
Type	core	rim	core	rim	core	rim	core	rim	core	rim	core	rim	core	rim
Analyses	9	11	12	14	9	11	9	12	13	11	11	11	11	14
SiO_2	41.40	41.52	41.30	41.38	41.21	41.45	41.67	42.03	41.29	41.51	41.12	41.11	41.45	41.51
TiO_2	0.03	0.03	0.04	0.04	0.05	0.06	0.03	0.04	0.03	0.03	0.02	0.02	0.09	0.11
Al_2O_3	18.71	18.72	19.18	19.19	18.90	18.93	19.18	19.20	19.60	19.72	18.69	18.77	19.92	19.96
Cr_2O_3	7.27	7.14	6.38	6.36	6.35	6.20	6.35	6.03	6.01	5.72	7.16	7.02	5.53	5.33
FeO	6.33	6.34	6.56	6.54	6.68	6.68	6.20	6.16	6.39	6.41	6.40	6.37	6.57	6.64
MnO	0.37	0.37	0.35	0.35	0.42	0.41	0.35	0.34	0.34	0.33	0.36	0.35	0.33	0.33
MgO	21.29	21.31	20.03	20.00	19.50	19.43	22.15	22.20	20.74	20.91	20.33	20.17	21.12	21.07
CaO	4.56	4.53	6.15	6.13	6.87	6.82	4.07	3.99	5.56	5.33	5.89	6.18	4.97	5.02
Na_2O	0.02	0.02	0.01	0.01	0.02	0.03	0.00	0.01	0.03	0.03	0.01	0.01	0.03	0.03
NiO	0.02	0.01	0.01	0.01	0.01	0.00	0.01	0.01	0.01	0.01	0.01	0.00	0.00	0.01
Si	2.978	2.985	2.979	2.983	2.982	2.996	2.982	3.002	2.968	2.978	2.971	2.970	2.971	2.975
Al	1.586	1.587	1.631	1.631	1.612	1.613	1.618	1.616	1.661	1.667	1.592	1.599	1.683	1.686
Ti	0.002	0.002	0.002	0.002	0.003	0.003	0.002	0.002	0.001	0.002	0.001	0.001	0.005	0.006
Fe	0.381	0.381	0.396	0.394	0.405	0.404	0.371	0.368	0.384	0.385	0.387	0.385	0.394	0.398
Mn	0.023	0.022	0.021	0.022	0.026	0.025	0.021	0.021	0.020	0.020	0.022	0.021	0.020	0.020
Mg	2.283	2.284	2.154	2.149	2.103	2.093	2.363	2.363	2.222	2.236	2.190	2.172	2.257	2.251
Ca	0.352	0.349	0.475	0.474	0.533	0.528	0.312	0.305	0.428	0.410	0.456	0.479	0.381	0.385
Na	0.003	0.003	0.001	0.001	0.002	0.004	0.000	0.001	0.004	0.004	0.002	0.002	0.004	0.004
Cr	0.413	0.406	0.364	0.362	0.363	0.354	0.359	0.340	0.342	0.324	0.409	0.401	0.313	0.302
Ni	0.001	0.001	0.000	0.000	0.001	0.000	0.001	0.001	0.001	0.000	0.001	0.000	0.000	0.000
Sum	8.022	8.019	8.023	8.018	8.029	8.020	8.028	8.019	8.031	8.027	8.029	8.030	8.028	8.027
Mg#	0.857	0.857	0.845	0.845	0.839	0.838	0.864	0.865	0.853	0.853	0.850	0.850	0.851	0.850
Almandine	2.69	2.69	9.29	9.43	9.81	10.21	1.56	1.46	8.51	8.40	6.19	7.12	8.52	8.85
Andradite	0.00	0.00	0.00	0.00	0.00	0.00	0.00	0.00	0.00	0.00	0.00	0.00	0.00	0.00
Grossular	0.00	0.00	0.00	0.00	0.00	0.00	0.00	0.00	0.00	0.00	0.00	0.00	0.00	0.00
Pyrope	83.60	83.70	73.72	73.61	71.27	71.03	86.29	86.60	76.12	76.83	77.01	75.50	77.67	77.25
Spessartine	0.83	0.82	0.73	0.74	0.86	0.85	0.77	0.76	0.70	0.69	0.77	0.74	0.69	0.69
Uvarovite	12.87	12.79	16.26	16.22	18.05	17.91	11.38	11.18	14.67	14.09	16.03	16.63	13.13	13.21

Table 3.5 (continued) Garnet analyses.

Sample	LET38	LET38	LET47	LET47	LET49	LET49	LET64	LET64	LQ5	LQ5	M9	M9	TP9	TP9	TP9
Type	core	rim	core	rim	core	rim	core	rim	core	rim	core	rim	Hi-Cr core	Hi-Cr rim	Lo-Cr rim
Analyses	8	7	9	10	3	4	10	10	11	16	17	18	7	9	3
SiO_2	41.66	41.74	40.73	40.88	41.58	41.65	41.60	41.78	41.72	41.74	41.38	41.63	40.71	40.68	41.53
TiO_2	0.01	0.02	0.01	0.01	0.22	0.20	0.01	0.02	0.01	0.02	0.25	0.33	0.00	0.01	0.00
Al_2O_3	20.68	20.70	17.73	17.73	19.96	20.05	20.88	20.83	20.95	20.96	20.33	20.49	17.90	18.02	20.65
Cr_2O_3	4.76	4.70	8.32	8.27	4.85	4.80	4.56	4.54	4.30	4.24	4.85	4.40	8.02	7.86	4.65
FeO	6.21	6.21	6.79	6.78	6.91	6.88	6.32	6.27	6.28	6.32	6.82	6.87	6.87	6.89	6.92
MnO	0.31	0.31	0.38	0.38	0.29	0.29	0.32	0.32	0.31	0.30	0.33	0.34	0.44	0.43	0.39
MgO	20.98	20.98	18.91	18.80	21.00	20.96	20.96	20.89	21.08	21.15	20.85	21.04	17.67	17.91	19.59
CaO	5.35	5.32	7.11	7.13	5.15	5.13	5.32	5.33	5.32	5.22	5.12	4.81	8.37	8.18	6.27
Na_2O	0.02	0.02	0.01	0.01	0.02	0.03	0.02	0.02	0.02	0.04	0.06	0.08	0.01	0.02	0.01
NiO	0.01	0.01	0.01	0.01	0.03	0.01	0.01	0.01	0.01	0.01	0.01	0.01	0.01	0.01	0.00
Si	2.975	2.979	2.971	2.980	2.980	2.983	2.970	2.981	2.976	2.976	2.965	2.976	2.979	2.974	2.982
Al	1.741	1.741	1.524	1.524	1.686	1.693	1.757	1.752	1.761	1.761	1.718	1.727	1.543	1.553	1.748
Ti	0.001	0.001	0.000	0.001	0.012	0.011	0.001	0.001	0.000	0.001	0.014	0.018	0.000	0.001	0.000
Fe	0.371	0.371	0.415	0.414	0.414	0.412	0.378	0.374	0.374	0.377	0.409	0.411	0.420	0.421	0.415
Mn	0.019	0.019	0.023	0.023	0.017	0.018	0.019	0.019	0.018	0.018	0.020	0.020	0.027	0.027	0.024
Mg	2.233	2.232	2.057	2.044	2.244	2.239	2.231	2.222	2.241	2.248	2.227	2.243	1.927	1.952	2.097
Ca	0.409	0.407	0.556	0.557	0.395	0.393	0.407	0.407	0.406	0.398	0.393	0.369	0.657	0.641	0.482
Na	0.002	0.002	0.001	0.001	0.003	0.004	0.003	0.002	0.002	0.005	0.008	0.011	0.001	0.002	0.001
Cr	0.269	0.265	0.480	0.476	0.275	0.272	0.257	0.256	0.243	0.239	0.275	0.249	0.464	0.454	0.264
Ni	0.001	0.001	0.001	0.001	0.002	0.000	0.000	0.000	0.001	0.001	0.001	0.001	0.000	0.001	0.000
Sum	8.021	8.018	8.027	8.020	8.029	8.026	8.023	8.015	8.023	8.025	8.029	8.024	8.019	8.024	8.013
Mg#	0.858	0.858	0.832	0.832	0.844	0.844	0.855	0.856	0.857	0.856	0.845	0.845	0.821	0.823	0.835
Almandine	10.52	10.79	7.26	7.68	9.17	9.66	10.56	11.15	10.40	10.46	10.95	11.07	12.12	11.81	12.69
Andradite	0.21	0.29	0.00	0.00	0.00	0.00	0.70	0.49	1.00	1.08	0.00	0.00	0.00	0.00	0.33
Grossular	0.00	0.00	0.00	0.00	0.00	0.00	0.00	0.29	0.43	0.27	0.00	0.00	0.00	0.00	2.58
Pyrope	75.08	74.92	72.37	71.91	76.72	76.32	75.09	74.54	75.32	75.54	75.11	75.78	64.87	65.72	70.33
Spessartine	0.63	0.63	0.82	0.82	0.60	0.60	0.65	0.64	0.62	0.61	0.67	0.69	0.91	0.90	0.80
Uvarovite	13.56	13.37	19.55	19.58	13.51	13.42	12.99	12.88	12.24	12.04	13.26	12.46	22.10	21.57	13.27

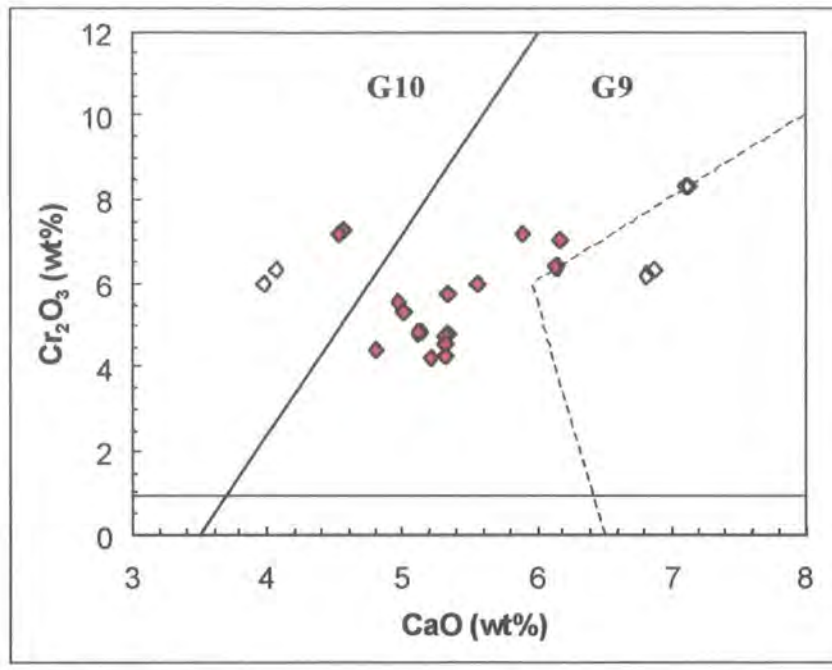

Figure 3.11 A Cr_2O_3 vs. CaO plot for garnet in Lesotho peridotites. Fields shown for garnets (e.g. G9, G10 and all non-peridotitic garnets) are from Dawson and Stephens (1975). Red diamonds = garnets from garnet peridotites; white diamonds = garnets from garnet-spinel peridotites.

3.4.3 Pressure-Temperature Calculations

As discussed above, peridotite xenoliths from the Lesotho suite contain minerals that show between–grain variations, particularly CPX. The compositions of the cores of "primary" minerals demonstrate the smallest variance. The use of thermobarometric calculations has been limited to mineral grains that show homogeneous core compositions. Based on these restrictions up to 14 *P-T* estimates for Lesotho peridotites have been obtained (Table 3.6).

Sample	p (GPa) BK	T (°C) BK	p (GPa) BK	T (°C) O'Neill	p (GPa) BK	T (°C) Harley
LET12			4.4	1022	4.0	964
LET13			3.4	869	3.4	866
LET14			3.4	911	3.4	917
LET2			3.0	898	3.0	884
LET29	2.7	1023	2.3	941	2.0	867
LET30	4.1	1032	4.0	1011	3.6	942
LET31	2.9	1072	2.4	955	2.0	876
LET38	4.0	1023	3.8	981	3.8	985
LET47	3.9	988	3.7	934	3.6	920
LET49	0.0		3.1	1106	2.7	1015
LET64	4.3	1063	4.0	1021	3.6	948
LQ5	3.0	1033	2.7	969	2.3	897
M9	4.3	1074	4.0	1019	3.7	975
TP9	3.5	896	3.4	879	3.3	860

Table 3.6 Pressure and Temperature estimates for Lesotho peridotites, calculated iteratively using geothermobarometric solutions of (i) Brey & Köhler (1990), (ii) Brey & Köhler (1990) and O'Neill (1980), and (iii) Brey & Köhler (1990) and Harley (1984).

Equilibrium *P-T* estimates were computed for CPX-bearing lherzolites based on the compositions of coexisting garnet, OPX and CPX. Several geothermobarometric solutions have been applied to the peridotite suite. Temperature estimates were made using the geothermometers of Harley (1984), O'Neill (1980) and Brey & Köhler (1990). Pressure was estimated using the geobarometer of Brey & Köhler (1990). These methods were coupled in the three different combinations and *P-T* estimates were calculated iteratively (Table 3.6); the BK-BK solution, the BK-ON solution and the BK-Harley solution (Figure 3.12).

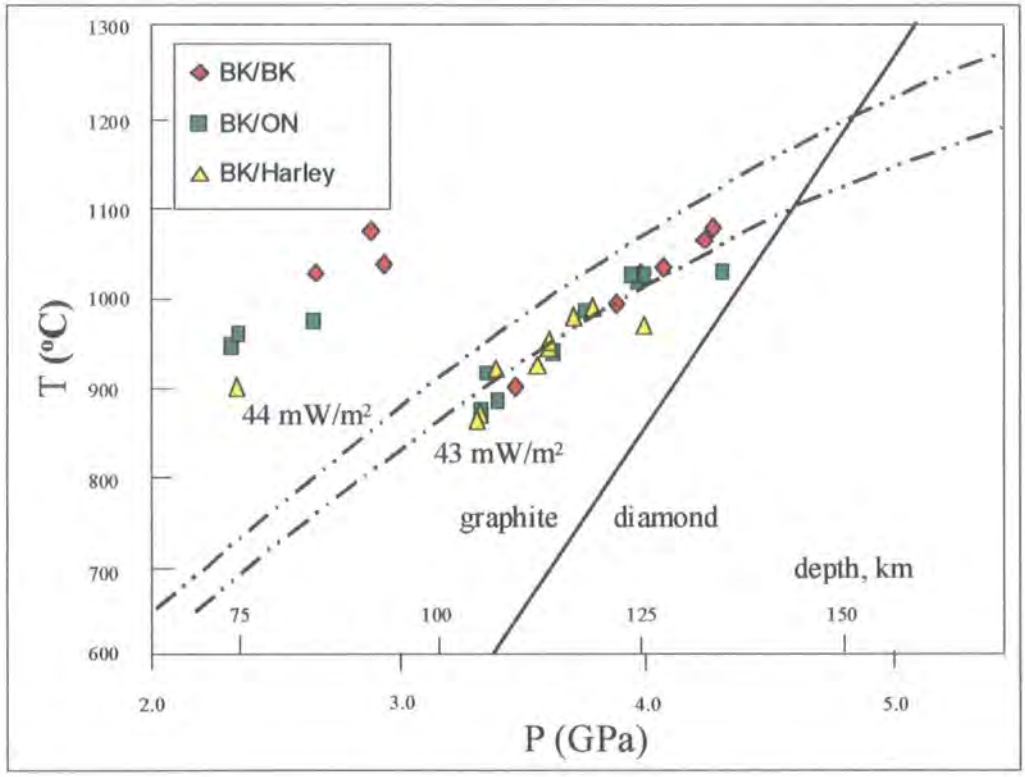

Figure 3.12 Equilibrium pressure-temperature estimates for Lesotho peridotites calculated iteratively according to (i) Brey & Köhler (1990), (ii) O'Neill (1980) and Brey & Köhler (1990), and (iii) Brey & Köhler (1990) and Harley (1984).

The three solutions define a steady-state geotherm for the lithospheric mantle beneath Lesotho of approximately 43 mW/m^2. The temperature of equilibration for the Lesotho peridotites in this study, where data is available, range from 860 to 1100 °C, and corresponding pressures range from 2.3 to 4.4 GPa.

Several samples (LET29, LET31 and LQ5) are consistently displaced from the steady-state geotherm, irrespective of the geobarometer and geothermometer solution used, suggesting disequilibrium between minerals within these peridotites.

3.4.4 Discussion of mineral textures and chemistry

The lithospheric mantle beneath Lesotho possesses many features that have been commonly reported for cratonic mantle elsewhere. The peridotites are coarse textured in general, and rarely display disrupted textures. The most dominant rock type is peridotite, with Mg-enriched mineral compositions, similar to that reported previously for peridotites from Lesotho (Nixon *et al.*, 1963; Nixon and Boyd, 1973a), other parts of the Kaapvaal craton (Nixon, 1987a) and from the Siberian craton (Boyd *et al.*, 1997). Peridotites from Lesotho are depleted in fusible elements compared to primitive mantle. A similarity in olivine composition between peridotites from Lesotho and other cratonic settings indicates a comparable degree of depletion. The range in $Mg^{\#}$ of olivine (0.92 to 0.94) parallels the average range for peridotites from previous studies of Kaapvaal peridotites, as well as the Siberian (Udachnaya) and Slave cratons (Boyd and Canil, 1997; Boyd *et al.*, 1997; MacKenzie and Canil, 1998; Kopylova *et al.*, 1999b). This reflects the highly refractory nature of the Lesotho peridotites.

A shared feature of both the Lesotho peridotites and those from Siberia and the Slave craton is the presence of a late-stage Na-, Al- and Cr-depleted CPX. This CPX occurs as fine-grained veins at grain boundaries within the xenoliths. Boyd *et al* (1997) and Kopylova *et al* (1999b) attributed this feature, in the Siberian and Slave peridotites respectively, to secondary crystallisation during eruption.

The negative trend between Cr_2O_3 and CaO in CPX may relate to equilibration with spinel. If the partitioning of Cr and Ca into silicates is controlled by the presence of spinel with a constant Cr-Ca ratio, a negative Ca-Cr correlation in contemporaneous silicate phases might be expected.

The compositional range found in the peridotitic garnet of the Lesotho peridotite suite, like those previously reported for the Kaapvaal craton, lie predominantly within the G9 field with few G10 (harzburgitic) garnet compositions, even within harzburgites. The scarcity of G10 garnets within peridotites from the Kaapvaal craton has been attributed to equilibration of harzburgite assemblages with lherzolite-dominated mantle (Boyd and Nixon, 1978), but may also be related to disruption of low-Ca rocks because of the presence of carbonate (Canil, 1990). Garnet within most harzburgites is saturated in Ca despite an absence of CPX.

The Lesotho xenoliths record a wide range of equilibration conditions in the lithospheric mantle, indicating a derivation from depths of 100 to 135 km, and have provided a reasonable section through the lithosphere beneath Lesotho.

3.5 Xenolith whole-rock Major and Trace element geochemistry

3.5.1 Introduction

Studies of the peridotitic mantle underlying Archean cratons have shown that it is chemically distinctive from the mantle underlying younger sub-continental and sub-oceanic settings (Boyd, 1989). Cratonic peridotites have undergone melt extraction resulting in the depletion of fusible elements such as Fe, Al and Ca (Nixon, 1987a; Herzberg, 1993; Boyd *et al.*, 1997). This depletion results in a buoyant low-density mantle-root, contributing to the long-term stability of Archean continental lithosphere (Boyd and McCallister, 1976; Jordan, 1979). Although depleted in major elements the shallow cratonic lithospheric mantle is enriched in light rare earth elements (LREE) and modal OPX (Menzies *et al.*, 1987; Boyd, 1989; McDonough, 1990). Hawkesworth *et al* (1983) and Menzies *et al* (1987) interpreted this enrichment in LREE as the result of interaction of metasomatising, percolating fluids with the lithospheric mantle.

Before the Re-Os system can be applied to the interpretation of the formation of the lithospheric mantle, it is essential to assess the role of melting and re-enrichment processes. Using elemental data the chemical composition of the Lesotho peridotite suite will be discussed, and models proposed for the observed range in compositions.

Major element analyses have been re-calculated as anhydrous compositions to correct for serpentinisation, reflected in the loss on ignition. The data were normalised to 100% after subtraction of loss on ignition. This procedure is based on the assumption that serpentinisation is an isochemical process, with only water being added to the system. Uncorrected major element data are presented in Table 3.7, and corrected anhydrous data in Table 3.8. Rare earth element data are presented in Table 3.9.

3.5.2 Whole-Rock Elemental Data

3.5.2.a Major element composition

Whole-rock analyses for the Lesotho peridotite suite show that they are strongly depleted in the fusible elements Fe, Ti, Ca, Al and Na compared to estimates of fertile

Table 3.7 Major element compositions for low-T Lesotho peridotites. LOI: loss on ignition.

Sample	LET2	LET6	LET8	LET12	LET13	LET14	LET25	LET27	LET28	LET29	LET30	LET31	LET38	LET47	LET48	LET49
Major Elements in wt%																
SiO_2	43.35	43.04	44.12	44.41	44.07	44.88	43.13	44.32	43.60	44.32	44.04	44.55	46.41	43.96	44.47	41.86
TiO_2	0.04	0.14	0.01	0.02	0.07	0.04	0.04	0.10	0.01	0.02	0.04	0.05	0.02	0.01	0.03	0.07
Al_2O_3	0.57	0.83	0.55	0.84	0.91	0.73	0.67	1.30	0.57	1.00	1.26	1.02	1.51	0.83	0.85	1.49
FeO	3.64	3.75	4.63	4.46	4.22	3.24	4.50	3.78	3.74	4.23	4.07	5.00	4.98	4.42	3.67	4.90
Fe_2O_3	2.55	2.78	1.11	2.05	2.08	2.63	2.32	2.69	2.65	2.16	2.40	1.40	0.85	2.20	2.89	3.14
MnO	0.10	0.12	0.10	0.11	0.12	0.10	0.11	0.12	0.11	0.11	0.12	0.12	0.12	0.12	0.12	0.14
MgO	44.65	42.66	44.75	41.21	43.20	42.51	44.16	41.38	43.72	42.98	42.57	41.21	41.55	42.15	41.84	41.84
CaO	0.36	0.67	0.17	0.86	0.46	0.35	0.39	0.78	0.26	0.75	0.74	0.74	0.78	0.47	0.75	1.15
Na_2O	0.07	0.12	0.04	0.05	0.05	0.05	0.05	0.10	0.05	0.08	0.07	0.10	0.08	0.06	0.09	0.10
K_2O	0.02	0.37	0.01	0.01	0.03	0.01	0.02	0.12	0.00	0.01	0.02	0.03	0.01	0.01	0.07	0.02
P_2O_5	0.03	0.01	0.02	0.02	0.02	0.02	0.02	0.03	0.03	0.02	0.03	0.03	0.02	0.02	0.04	0.02
LOI	4.87	5.60	4.69	6.18	4.80	5.62	4.76	5.44	5.43	4.49	4.81	5.74	3.80	5.76	5.24	5.26
Total	100.24	100.09	100.19	100.22	100.03	100.19	100.18	100.16	100.17	100.17	100.17	100.00	100.14	100.01	100.05	99.99

Sample	LET58	LET64	TP6	TP7	TP9	LQ1	LQ5	LQ6	LQ8	LQ9	M1	M5	M6	M8	M9	M11	M13
Major Elements in wt%																	
SiO_2	43.39	45.63	44.45	44.64	45.02	43.52	46.90	46.02	46.69	46.99	43.71	45.64	44.60	45.99	46.82	46.27	45.39
TiO_2	0.09	0.08	0.01	0.20	0.01	0.04	0.01	0.03	0.01	0.03	0.56	0.03	0.04	0.04	0.11	0.06	0.07
Al_2O_3	1.00	1.71	0.65	1.03	0.86	1.13	1.71	1.44	1.20	1.44	0.80	1.46	1.41	1.44	1.42	1.30	0.85
FeO	4.70	4.14	5.42	6.82	5.49	4.29	4.22	5.62	4.93	4.41	7.94	5.58	5.89	6.06	5.84	4.90	5.38
Fe_2O_3	2.61	1.92	1.23	0.85	1.05	2.38	1.87	0.62	1.08	1.67	1.90	1.25	0.83	0.72	0.47	1.49	1.38
MnO	0.13	0.12	0.12	0.12	0.12	0.11	0.12	0.12	0.11	0.11	0.14	0.12	0.12	0.13	0.13	0.12	0.12
MgO	42.02	40.49	44.62	42.69	43.94	44.26	41.56	42.12	43.12	42.40	41.35	43.09	42.86	43.15	41.59	42.94	44.29
CaO	1.00	0.86	0.44	0.86	0.53	0.49	0.89	0.91	0.71	0.74	0.56	0.86	0.88	0.80	0.91	0.82	0.62
Na_2O	0.08	0.09	0.06	0.10	0.07	0.08	0.09	0.12	0.11	0.11	0.12	0.09	0.10	0.09	0.14	0.12	0.10
K_2O	0.04	0.07	0.00	0.02	0.00	0.01	0.03	0.10	0.05	0.07	0.07	0.10	0.09	0.10	0.08	0.05	0.05
P_2O_5	0.04	0.03	0.02	0.03	0.02	0.03	0.02	0.02	0.02	0.03	0.02	0.03	0.03	0.03	0.02	0.03	0.03
LOI	4.94	4.90	3.16	2.82	3.00	3.93	2.81	3.09	1.81	2.19	3.02	1.57	2.73	1.59	2.63	2.05	1.91
Total	100.04	100.04	100.18	100.17	100.11	100.26	100.24	100.21	99.84	100.19	100.19	99.82	99.57	100.14	100.16	100.15	100.19

Table 3.8 Anhydrous major element and selected trace element data for low-T Lesotho peridotites. $Mg^{\#}$ = Mg/(Mg+Fe). Modes were calculated using whole-rock compositions and converting to an equivalent modal mineralogy using mass balance relationships implied by observed mineralogy in Kaapvaal peridotites.

Sample	LET2	LET6	LET8	LET12	LET13	LET14	LET25	LET27	LET28	LET29	LET30	LET31	LET38	LET47	LET48	LET49	LET58
Major Elements in wt%																	
SiO_2	45.45	45.55	46.20	47.22	46.28	47.46	45.20	46.79	46.02	46.32	46.18	47.26	48.18	46.64	46.90	44.19	45.63
TiO_2	0.04	0.15	0.01	0.02	0.07	0.04	0.04	0.11	0.01	0.02	0.04	0.05	0.02	0.01	0.03	0.07	0.09
Al_2O_3	0.60	0.88	0.58	0.89	0.96	0.77	0.70	1.37	0.60	1.05	1.32	1.08	1.57	0.88	0.90	1.57	1.05
FeO	3.82	3.97	4.85	4.74	4.43	3.43	4.72	3.99	3.95	4.42	4.27	5.30	5.17	4.69	3.87	5.17	4.94
Fe_2O_3	2.67	2.94	1.16	2.18	2.18	2.78	2.43	2.84	2.80	2.26	2.52	1.49	0.88	2.33	3.05	3.31	2.74
MnO	0.10	0.13	0.10	0.12	0.13	0.11	0.12	0.13	0.12	0.11	0.13	0.13	0.12	0.13	0.13	0.15	0.14
MgO	46.82	45.15	46.86	43.82	45.37	44.95	46.28	43.69	46.15	44.92	44.64	43.72	43.13	44.72	44.13	44.17	44.19
CaO	0.38	0.71	0.18	0.91	0.48	0.37	0.41	0.82	0.27	0.78	0.78	0.79	0.81	0.50	0.79	1.21	1.05
Na_2O	0.07	0.13	0.04	0.05	0.05	0.06	0.05	0.11	0.05	0.08	0.08	0.11	0.08	0.06	0.09	0.11	0.09
K_2O	0.02	0.39	0.01	0.01	0.03	0.01	0.03	0.12	0.00	0.01	0.02	0.04	0.01	0.01	0.07	0.02	0.04
P_2O_5	0.03	0.01	0.02	0.02	0.02	0.02	0.02	0.03	0.03	0.02	0.03	0.03	0.02	0.02	0.04	0.02	0.04
Ca/Al	0.85	1.09	0.42	1.38	0.68	0.65	0.79	0.81	0.62	1.01	0.79	0.98	0.70	0.76	1.19	1.04	1.35
Mg No	0.931	0.924	0.934	0.921	0.927	0.931	0.923	0.922	0.927	0.925	0.924	0.921	0.928	0.922	0.922	0.906	0.914
Trace Elements in ppm																	
Ni	2647	2365	2601	2539	2418	2450	2541	2304	2683	2508	2362	2361	2215	2358	2346	2495	2403
Cr	1458	2157	959	2301	2218	1888	1834	2332	1351	2347	3581	2284	2765	2536	2840	2863	2415
Co	96	94	96	102	97	92	101	97	101	98	96	95	88	97	95	109	102
V	16.1	20.5	13.0	24.1	23.4	20.6	20.1	29.8	18.1	23.3	31.8	27.3	32.6	25.8	28.1	37.0	30.6
Sr	13.2	10.0	8.6	16.5	12.4	19.1	11.1	18.3	25.1	20.4	14.4	25.5	8.6	11.7	30.3	10.4	27.6
Nd	1.35	0.84	0.85	2.02	1.28	1.31	1.51	2.07	2.42	1.18	1.90	2.32	1.41	0.87	2.63	1.29	2.9
Calculated modes in wt%																	
Ol	67.89	65.96	64.65	54.70	62.33	57.09	68.85	53.71	62.85	61.92	60.81	56.06	51.44	60.84	59.15	67.10	64.74
OPX	26.57	29.86	31.99	36.96	31.76	38.64	28.78	37.14	35.05	31.64	31.50	37.28	40.74	34.59	34.51	21.12	26.72
CPX	2.16	3.26	3.10	2.19	0.71	0.72	1.40	2.18	1.39	2.03	1.18	2.02	1.23	trace	2.36	2.32	2.92
Sp		0.92	0.26		trace	trace	0.97		0.71					trace			
Gnt	3.38			6.15	5.21	3.55		6.97		4.41	6.51	4.64	6.59	4.57	3.98	9.46	5.62

Table 3.8 (continued) Anhydrous major element and selected trace element data for low-T Lesotho peridotites.

Sample	LET64	TP6	TP7	TP9	LQ1	LQ5	LQ6	LQ8	LQ9	M1	M5	M6	M8	M9	M11	M13
Major Elements in wt%																
SiO_2	47.96	45.82	45.85	46.36	45.18	48.14	47.38	47.63	47.95	44.98	46.45	46.05	46.67	48.01	47.16	46.18
TiO_2	0.08	0.01	0.21	0.01	0.04	0.01	0.03	0.01	0.03	0.58	0.03	0.04	0.04	0.11	0.06	0.07
Al_2O_3	1.80	0.67	1.06	0.89	1.17	1.76	1.48	1.22	1.47	0.82	1.49	1.46	1.46	1.46	1.33	0.86
FeO	4.35	5.59	7.01	5.65	4.45	4.33	5.79	5.03	4.50	8.17	5.68	6.08	6.15	5.99	4.99	5.47
Fe_2O_3	2.02	1.27	0.87	1.08	2.47	1.92	0.64	1.10	1.70	1.96	1.27	0.86	0.73	0.48	1.52	1.40
MnO	0.13	0.12	0.12	0.12	0.11	0.12	0.12	0.11	0.11	0.14	0.12	0.12	0.13	0.13	0.12	0.12
MgO	42.56	45.99	43.85	45.25	45.94	42.66	43.37	43.99	43.26	42.55	43.86	44.26	43.79	42.65	43.77	45.06
CaO	0.90	0.45	0.88	0.55	0.51	0.91	0.94	0.72	0.76	0.58	0.88	0.91	0.81	0.93	0.84	0.63
Na_2O	0.10	0.07	0.10	0.07	0.09	0.09	0.13	0.11	0.11	0.12	0.10	0.10	0.09	0.14	0.12	0.11
K_2O	0.08	0.00	0.02	0.00	0.01	0.03	0.10	0.05	0.07	0.07	0.10	0.09	0.10	0.08	0.06	0.05
P_2O_5	0.03	0.02	0.03	0.02	0.03	0.02	0.02	0.02	0.03	0.02	0.03	0.03	0.03	0.02	0.03	0.03
Ca/Al	0.68	0.91	1.13	0.83	0.59	0.70	0.85	0.80	0.69	0.95	0.80	0.84	0.75	0.87	0.85	0.99
Mg No	0.925	0.924	0.909	0.924	0.925	0.926	0.924	0.929	0.927	0.884	0.920	0.920	0.920	0.922	0.925	0.923
Trace Elements in ppm																
Ni	2091	2621	2337	2508	2615	2161	2367	2338	2275	2316	2404	2386	2388	2198	2358	2419
Cr	2917	1408	2266	2271	2111	2577	2487	2390	2468	1019	2617	1957	2227	2575	2150	2590
Co	88	104	101	102	105	88	97	95	92	121	101	97	100	91	94	101
V	35.4	20.4	33.1	26.4	20.7	30.1	33.4	28.4	32.0	44.9	37.6	33.5	36.0	30.5	26.7	28.0
Sr	12.5	8.4	21.3	10.3	8.2	14.2	14.0	16.4	19.1	14.4	22.9	28.0	18.5	24.5	23.1	27.4
Nd	1.8	0.6	1.6	0.8	1.1	1.3	1.2	1.2	1.8	0.8	1.8	2.4	1.6	1.4	2.0	2.2
Calculated modes in wt%																
Ol	51.23	68.06	61.28	64.14	69.34	50.45	55.28	56.11	51.25	64.76	59.00	61.72	58.82	52.16	58.17	64.19
OPX	39.43	28.35	29.91	31.33	24.69	40.61	36.12	37.80	40.68	30.05	36.25	33.44	35.03	39.81	34.91	32.67
CPX	1.55	0.31	0.43	0.32	0.49	1.71	2.13	1.52	1.50	1.46	3.67	3.86	2.58	2.49	2.31	2.51
Sp		trace	0.52	trace						0.17	1.08	0.99	0.19			0.33
Gnt	7.79	3.28	7.86	4.21	5.48	7.23	6.47	4.57	6.58	3.56			3.38	5.53	4.60	0.30

mantle composition (Nixon and Boyd, 1973c; McDonough, 1990). This is in keeping with the magnesian nature of their olivines. The removal of a basaltic fraction from fertile mantle will deplete magmaphile elements such as Al, but Mg will remain primarily within the residue. Plotting the ratio of Mg/Si against the ratio of Al/Si gives a strongly anti-correlated trend that is indicative of the degree of depletion (Figure 3.13).

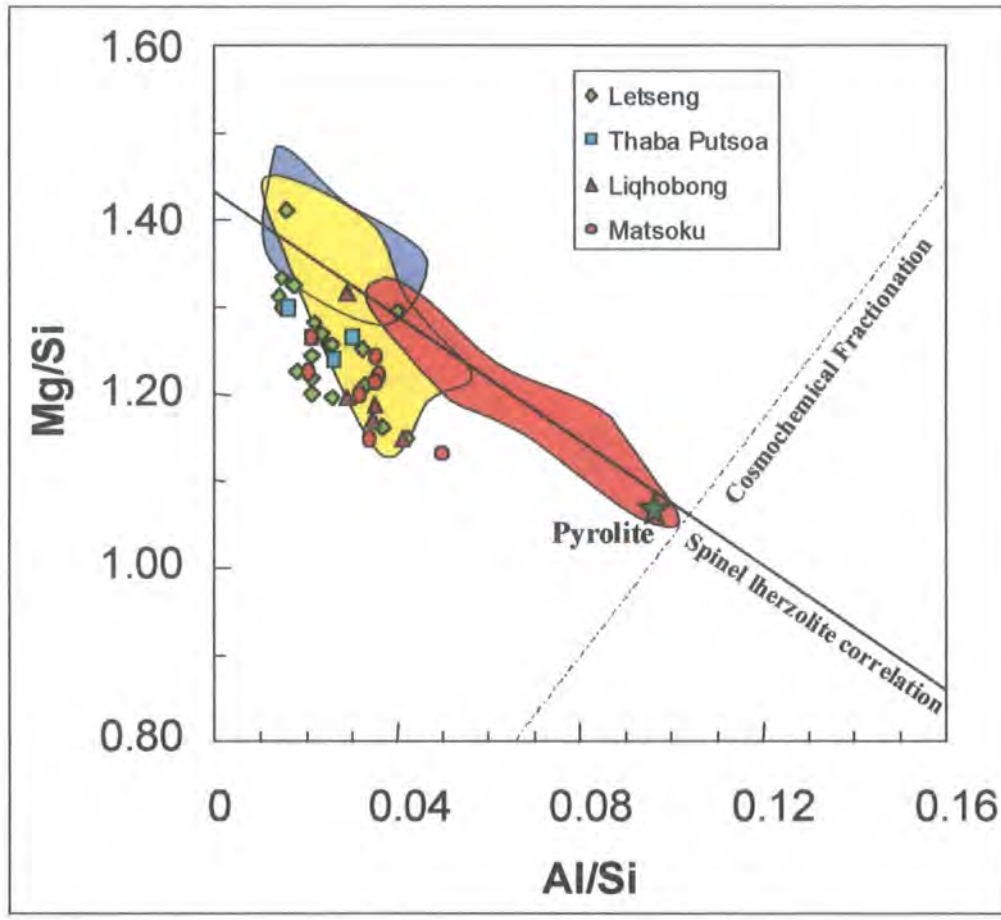

Figure 3.13 Mg/Si vs. Al/Si wt ratios of Lesotho peridotites compared to the range for primitive spinel lherzolites erupted off craton (Morgan, 1986), represented by the red field. Kaapvaal low-T peridotites from previous studies represented by yellow field, Siberian by the blue-grey field. Kaapvaal and Siberian data from Boyd and Mertzman (1987) and Boyd *et al* (1997). Additional data from Jagoutz (1979).

Spinel peridotites show a linear depletion trend on such a diagram (Morgan, 1986), intersecting the cosmochemical fractionation line of Jagoutz (1979) near to the value of pyrolite (Ringwood, 1975). The Lesotho low-T peridotites are highly depleted in Al and enriched in Mg (Figure 3.13), but a secondary, overlying trend of Mg depletion relative to Al, or Si enrichment, causes many of the samples to deviate from the spinel lherzolite array. A similar observation has been made for peridotite xenoliths from

other Kaapvaal localities (Pearson *et al.*, 1995a) and is essentially a manifestation of the enrichment in OPX identified by Boyd (1989). The MgO content of the Lesotho peridotites ranges from 42.6 to 46.9 wt%. Whole rock magnesium numbers $Mg^{\#}$ (Figure 3.14) for lherzolites (average 0.923) and harzburgites (average 0.926) imply that higher values of $Mg^{\#}$ occur in the more refractory peridotites. The average whole rock $Mg^{\#}$ for the Lesotho low-T peridotite suite is 0.923, lower than the average olivine $Mg^{\#}$ (0.928), and may suggest that the whole-rock has been enriched in Fe, lowering the bulk $Mg^{\#}$.

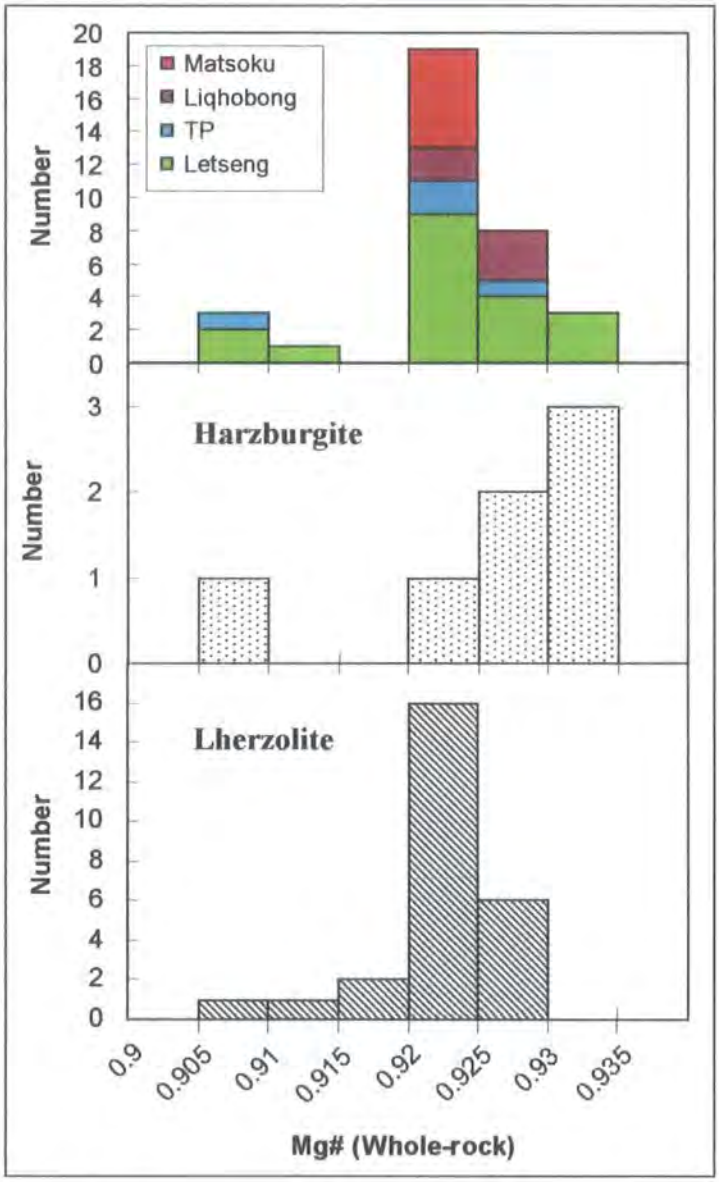

Figure 3.14 Histogram of whole rock $Mg^{\#}$ of low-T Lesotho peridotites.

Bivariate oxide-MgO plots for the major element composition of Lesotho peridotites display several systematic trends. As MgO content increases, Al_2O_3 and CaO contents are shown to decrease (Figure 3.15). A similar but very poorly defined negative trend appears to exist between MgO and TiO_2. No systematic correlation exists between MgO and FeO. Both FeO and TiO_2 may have initially formed a better correlation with MgO, with later scattering of data from metasomatic alteration. SiO_2 displays a negative trend with MgO, however Lesotho peridotites are generally enriched relative to primitive mantle compositions (Figure 3.15).

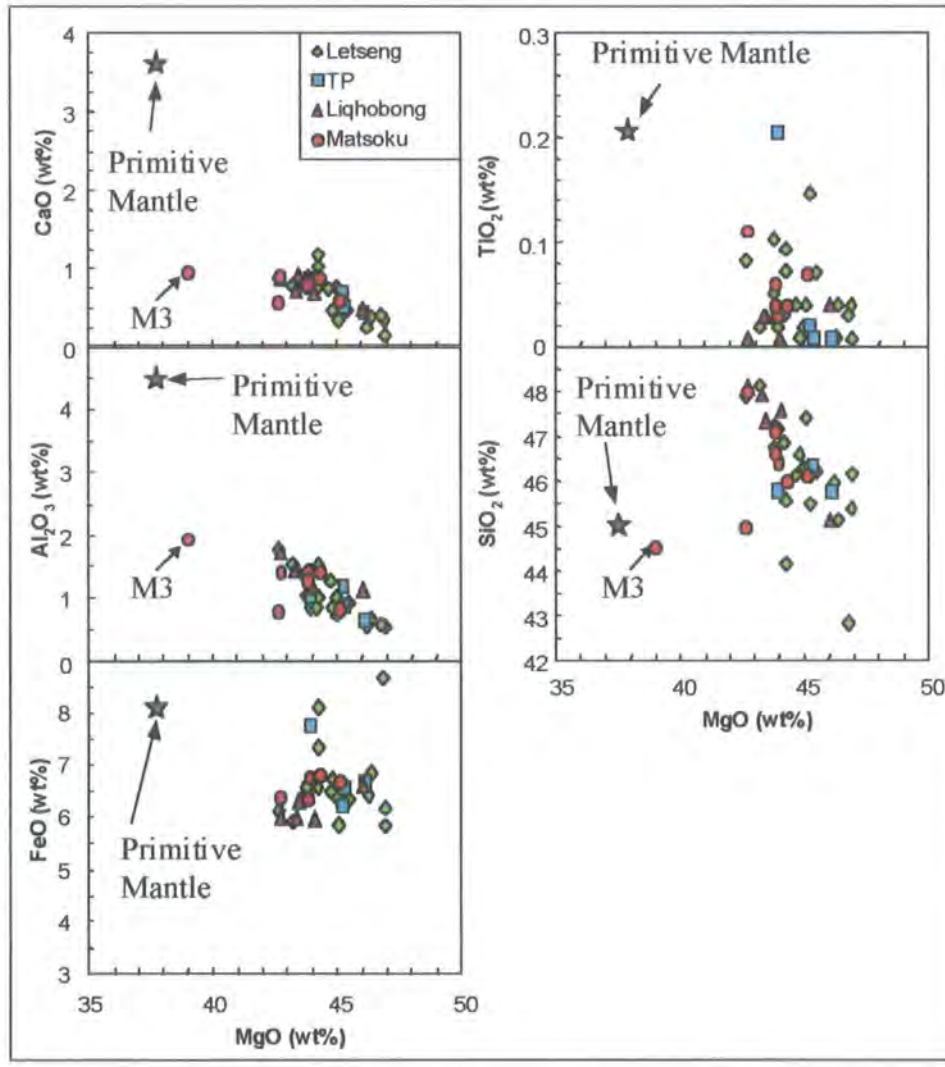

Figure 3.15 Variation of major elements with MgO (wt%) for low-T Lesotho peridotites. Primitive mantle, denoted by the star, after McDonough (1990).

The Lesotho peridotites are depleted in Ca relative to abyssal peridotites but range from being depleted, to slightly more fertile in terms of Al (Figure 3.16). In general the Lesotho peridotites lie below the oceanic trend, with Ca/Al values ranging from 0.42 to 1.38 (mean = 0.85; Table 3.8). This is slightly higher than previously reported for

peridotites from the Kaapvaal craton (average 0.73, Boyd, 1989). No systematic variation exists between peridotites from different facies or textural types for the Lesotho suite.

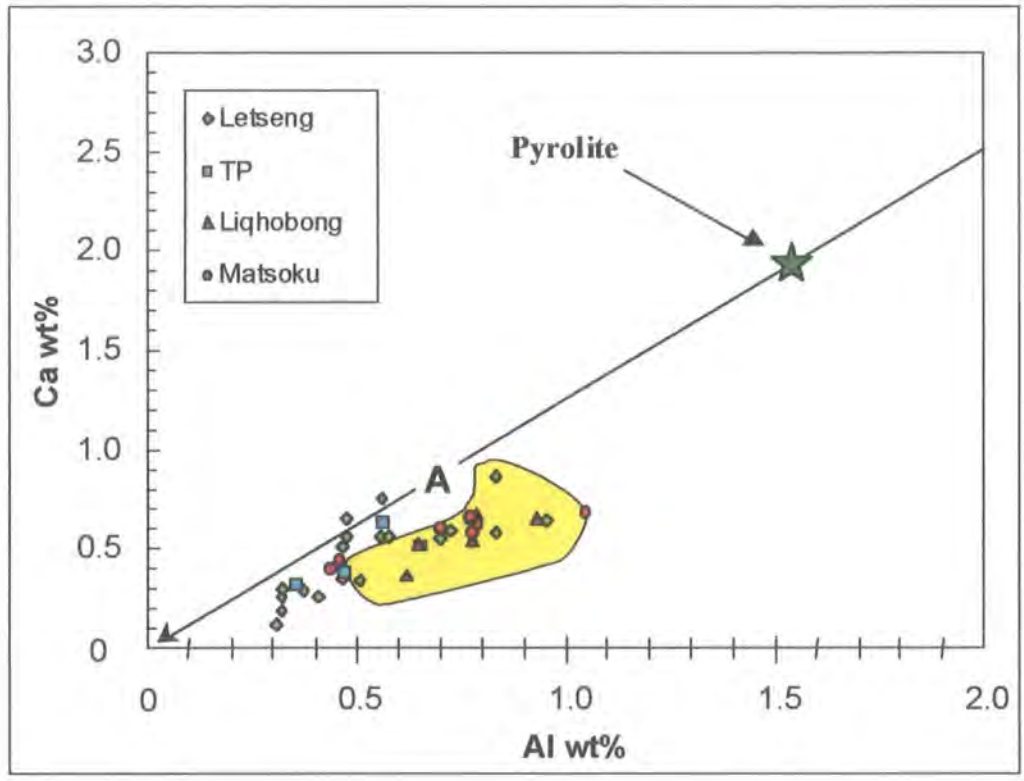

Figure 3.16 Composition of Lesotho peridotites as wt% Ca vs. wt% Al. Line represents overall trend expected for the depletion of oceanic peridotite (Boyd, 1989). Also shown are average compositions for abyssal peridotite (Dick *et al.*, 1984), indicated by the letter A and pyrolite (Ringwood, 1979), indicated by star. Field represents low-T Kaapvaal peridotite (Boyd, 1989).

3.5.2.b Mineral Modes

Modal mineral proportions for the Lesotho peridotite xenoliths were calculated using whole rock compositions and converting to an equivalent modal mineralogy using mass balance relationships implied by observed mineralogy in the peridotites (Table 3.8). The methodology is described in Appendix D. Mineral compositions from Nixon (1973b) were used along with data from this study during the calculations.

The modal abundance of olivine in the Lesotho peridotites ranges from 50% to 69%, with an average of 60%. This is similar to an average overall modal abundances for olivine in low-T peridotites from the Kaapvaal craton of 61% (Boyd, 1989). When plotted as olivine $Mg^{\#}$ vs. modal olivine content (Figure 3.17), the chemical signature of the Lesotho suite is identical to that previously reported for low-T peridotites from the

whole of the Kaapvaal craton and similar to the Siberian cratons, but clearly distinct from oceanic domains.

The average modal OPX content of Lesotho peridotites is 33% (range of 21 to 41%). This is slightly higher than the overall Kaapvaal average of 31% (Boyd, 1989). The low modal abundances of olivine relative to the refractory nature of the peridotites is reflected in the high modal abundance of OPX. The average modal CPX content of the Lesotho peridotites (1.9%) is slightly higher than the overall Kaapvaal average (1.8%, Boyd, 1989).

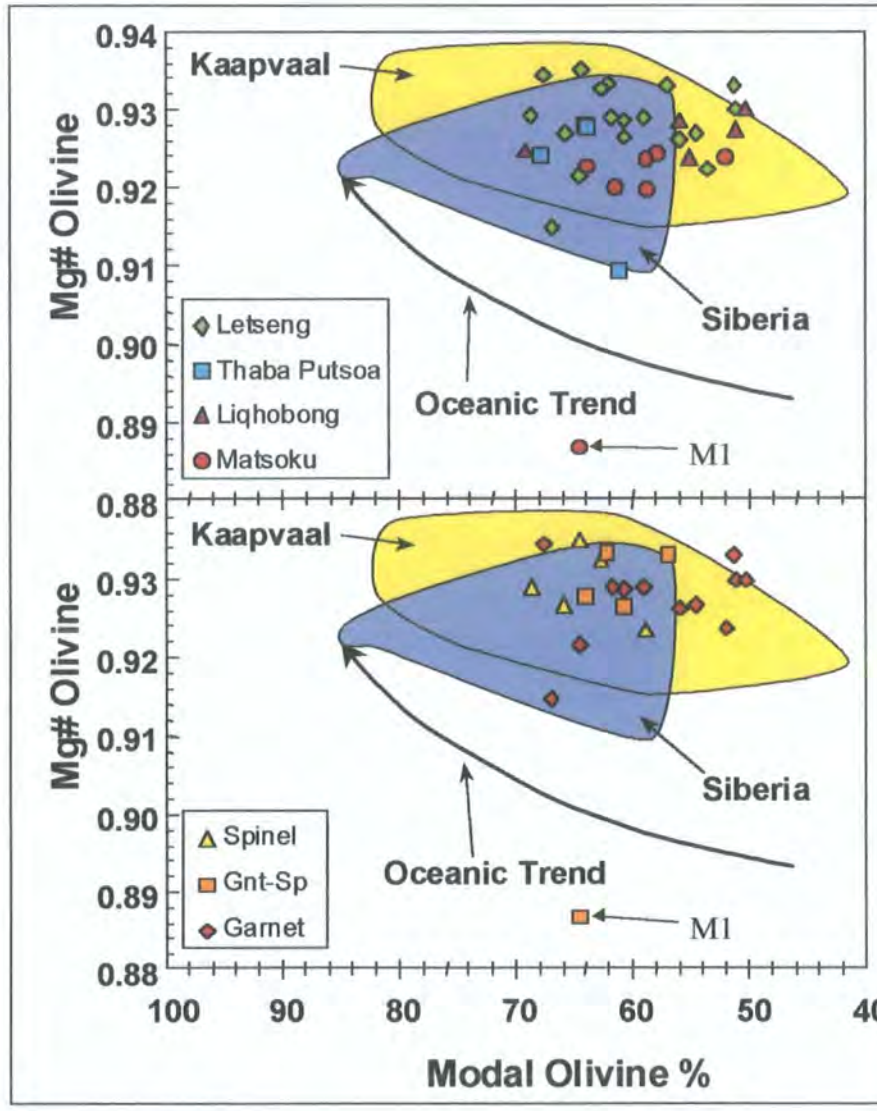

Figure 3.17 Olivine $Mg^{\#}$ vs. modal olivine content (%) for low-T Lesotho peridotites. Fields for Low-T peridotites from the Kaapvaal and Siberian cratons (Boyd, 1989; Boyd *et al.*, 1997). Trend defined by oceanic peridotites after Boyd (1989).

3.5.2.c Trace elements

Transition metal trace elements

Nickel behaves compatibly within the Lesotho peridotite samples, showing a positive correlation with MgO (Figure 3.18). Cobalt also appears as though it may behave compatibly, but the data is more scattered. Although producing an approximately positive correlation Co is generally depleted relative to primitive mantle compositions (Figure 3.18). In contrast, vanadium abundances are inversely correlated demonstrating its incompatibility in the peridotites. Canil (1997) attributed the decreasing vanadium content to the removal of CPX and spinel with the melt. The contrasting behaviour of these elements agrees with the observed compatibilities from melt systems (Frey and Prinz, 1978). Cr abundances also appear to be inversely correlated, and this behaviour may also relate to the removal of CPX and spinel with the melt. The correlation however is not so well defined and the data is more scattered. This may be the result of later metasomatism from melts passing through the peridotite, or patent metasomatism as CPX and some garnet is introduced (Pearson *et al.*, 2001).

Nickel variation within the Lesotho peridotite suite ranges from 2091 to 2683 ppm. The variation of Ni with MgO is relatively large, up to 200ppm (10%). The lack of any well defined correlation and the scatter in data may indicate a cumulate component within the peridotites, rather than being solely a residue from partial melting (Pearson, 1989). Cryptic metasomatism from melts passing through the peridotite, patent metasomatism as CPX and garnet introduced (Pearson *et al.*, 2001), or serpentinisation (Coleman, 1977) may be an alternative source for the scatter in Ni concentration.

Rare earth elements

The Lesotho peridotite suite considered as a whole shows consistent trace element characteristics (Table 3.9). Chondrite normalised whole-rock REE abundances for the peridotites are shown in Figure 3.19. They are strikingly similar over the entire suite. HREE are, in the main, subchondritic with values ranging from 0.08 to 0.69 x chondrite and relatively flat Ho to Lu profiles showing little evidence of fractionation or enrichment. An exception to this is sample M3 from Matsoku with superchondritic HREE values of 2 x chondrite and a relatively flat profile overall. This sample also has a whole-rock $Mg^{\#}$ of 0.868 and may represent a highly modified, metasomatised peridotite such as those recognised by Harte *et al* (1987) from this locality. Sample M1 appears to be intermediate between sample M3 and the Lesotho suite as a whole, with subchondritic HREE, but LREE mirroring those of sample M3 (Figure 3.19).

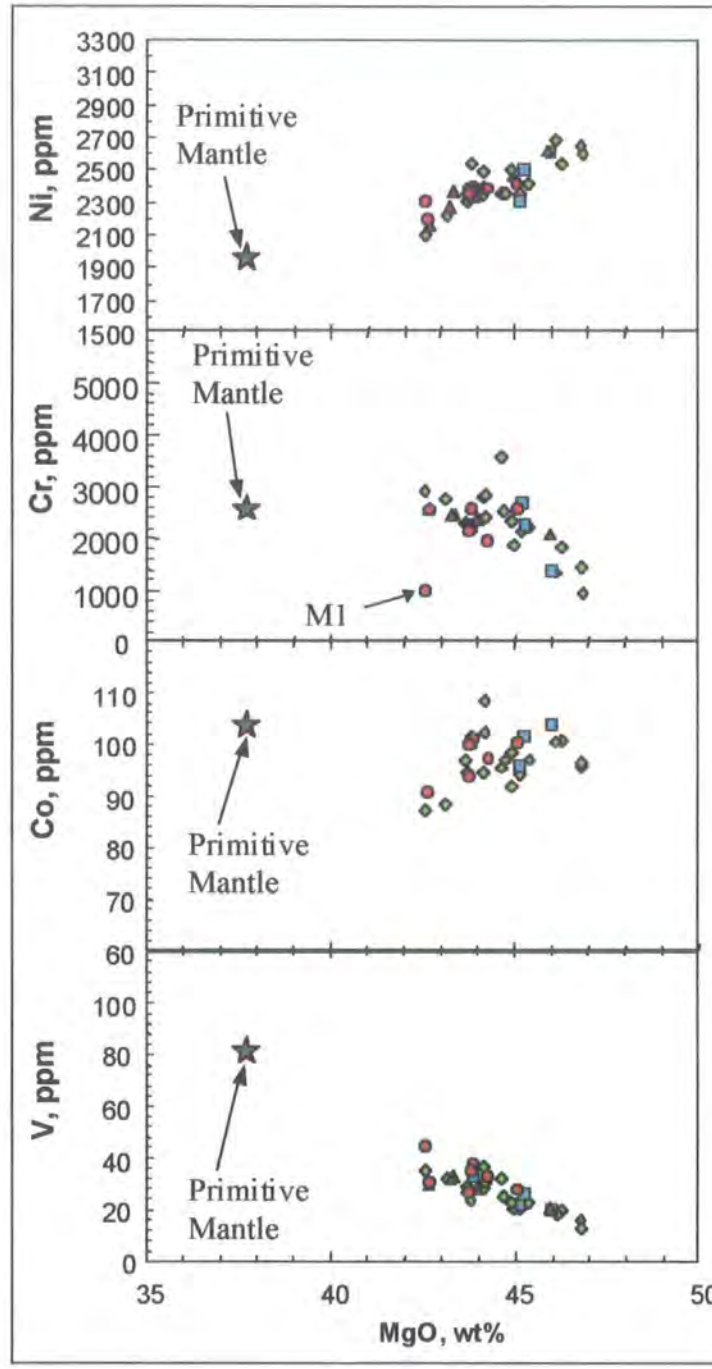

Figure 3.18 Variations of trace elements (ppm) with MgO (wt%) for low-T Lesotho peridotites. Primitive mantle after McDonough and Sun (1995).

Table 3.9 Rare earth element data for low-T Lesotho peridotites. Chondrite normalised using normalisation values of M^{c}Donough and Sun (1995).

Sample	LET2	LET6	LET8	LET12	LET13	LET14	LET25	LET27	LET28	LET29	LET30	LET31	LET38	LET47	LET48	LET49	LET58	LET63
REE concentrations in ppm																		
La	2.41	0.44	0.93	2.56	1.36	1.36	1.46	2.14	2.98	1.17	1.84	2.66	1.35	0.74	2.90	1.30	3.06	0.32
Ce	4.93	1.07	1.72	4.72	2.58	2.62	3.01	4.10	5.57	2.25	3.59	5.04	2.63	1.45	5.59	2.55	5.94	0.59
Pr	0.64	0.18	0.23	0.57	0.33	0.35	0.40	0.52	0.68	0.30	0.48	0.62	0.35	0.21	0.70	0.34	0.74	0.07
Nd	2.27	0.85	0.86	2.03	1.29	1.32	1.52	2.08	2.43	1.19	1.91	2.33	1.42	0.89	2.64	1.30	2.88	0.29
Sm	0.32	0.16	0.16	0.28	0.23	0.19	0.22	0.36	0.35	0.24	0.35	0.38	0.26	0.15	0.45	0.21	0.47	0.07
Eu	0.09	0.05	0.04	0.07	0.07	0.05	0.05	0.10	0.08	0.07	0.09	0.11	0.07	0.04	0.13	0.06	0.12	0.02
Gd	0.23	0.12	0.11	0.18	0.18	0.13	0.15	0.26	0.21	0.23	0.24	0.31	0.19	0.09	0.34	0.18	0.32	0.07
Tb	0.03	0.01	0.01	0.02	0.02	0.01	0.02	0.03	0.02	0.03	0.03	0.04	0.02	0.01	0.04	0.03	0.03	0.01
Dy	0.16	0.06	0.05	0.07	0.08	0.06	0.06	0.14	0.09	0.14	0.13	0.17	0.09	0.03	0.22	0.14	0.15	0.05
Ho	0.03	0.01	0.01	0.01	0.01	0.01	0.01	0.02	0.01	0.02	0.02	0.03	0.01	0.00	0.04	0.03	0.02	0.01
Er	0.09	0.02	0.01	0.02	0.02	0.02	0.02	0.05	0.03	0.04	0.04	0.05	0.02	0.01	0.07	0.08	0.05	0.03
Tm	0.02	0.00	0.00	0.00	0.00	0.00	0.00	0.01	0.00	0.01	0.01	0.01	0.00	0.00	0.01	0.01	0.01	0.01
Yb	0.10	0.01	0.01	0.02	0.02	0.01	0.02	0.04	0.02	0.03	0.03	0.03	0.02	0.01	0.04	0.09	0.04	0.03
Lu	0.02	0.00	0.00	0.00	0.00	0.00	0.00	0.01	0.00	0.00	0.01	0.01	0.00	0.00	0.01	0.02	0.01	0.01
Chondrite normalised REE																		
La	10.16	1.87	3.93	10.82	5.75	5.75	6.15	9.02	12.57	4.92	7.77	11.22	5.69	3.13	12.23	5.48	12.91	1.34
Ce	8.04	1.74	2.81	7.70	4.21	4.27	4.91	6.69	9.09	3.67	5.86	8.22	4.29	2.37	9.12	4.16	9.68	0.96
Pr	6.86	1.96	2.43	6.19	3.59	3.73	4.30	5.63	7.33	3.18	5.15	6.72	3.77	2.21	7.57	3.65	7.96	0.80
Nd	4.96	1.86	1.88	4.43	2.82	2.89	3.32	4.55	5.31	2.61	4.17	5.11	3.10	1.94	5.78	2.85	6.29	0.64
Sm	2.16	1.11	1.09	1.89	1.56	1.30	1.51	2.44	2.34	1.65	2.34	2.60	1.78	1.00	3.03	1.42	3.18	0.45
Eu	1.51	0.84	0.77	1.25	1.23	0.88	0.97	1.77	1.45	1.32	1.59	2.02	1.31	0.65	2.26	1.06	2.17	0.39
Gd	1.15	0.61	0.57	0.89	0.92	0.64	0.75	1.30	1.06	1.17	1.20	1.58	0.98	0.43	1.70	0.88	1.58	0.34
Tb	0.86	0.40	0.35	0.51	0.54	0.37	0.43	0.90	0.62	0.82	0.79	1.09	0.62	0.26	1.23	0.71	0.94	0.22
Dy	0.65	0.26	0.20	0.30	0.32	0.23	0.26	0.56	0.38	0.57	0.54	0.70	0.37	0.14	0.90	0.59	0.61	0.19
Ho	0.59	0.18	0.13	0.22	0.20	0.16	0.16	0.40	0.24	0.38	0.37	0.48	0.26	0.07	0.64	0.53	0.40	0.16
Er	0.56	0.13	0.09	0.14	0.14	0.11	0.12	0.31	0.17	0.26	0.27	0.31	0.14	0.05	0.45	0.50	0.29	0.18
Tm	0.61	0.12	0.04	0.08	0.12	0.08	0.08	0.28	0.16	0.20	0.24	0.24	0.12	0.04	0.32	0.53	0.24	0.20
Yb	0.63	0.08	0.06	0.10	0.10	0.08	0.09	0.25	0.10	0.17	0.18	0.20	0.10	0.04	0.26	0.55	0.22	0.21
Lu	0.69	0.08	0.08	0.12	0.12	0.08	0.08	0.24	0.08	0.16	0.20	0.20	0.12	0.04	0.24	0.61	0.20	0.28
Chondrite nomalised REE ratios																		
La/Yb	16.12	23.58	61.67	103.97	55.30	75.56	64.93	36.55	128.51	28.53	42.75	56.00	54.73	87.72	47.75	10.06	58.54	6.26
Sm/Yb	3.42	14.06	17.06	18.14	15.02	17.12	15.96	9.87	23.95	9.57	12.88	12.98	17.10	27.95	11.82	2.61	14.40	2.10
Dy/Yb	1.04	3.31	3.19	2.87	3.05	3.07	2.75	2.27	3.86	3.33	2.96	3.47	3.58	3.81	3.51	1.07	2.77	0.87

Table 3.9 (continued) REE data for low-T Lesotho peridotites

Sample	LET64	TP5	TP6	TP7	TP9	LQ1	LQ5	LQ6	LQ8	LQ9	M1	M3	M5	M6	M8	M9	M11	M13
REE in ppm																		
La	1.73	1.35	0.49	1.69	0.54	1.13	1.18	1.00	1.07	1.92	0.75	0.67	2.39	3.03	1.88	1.38	2.08	2.50
Ce	3.39	2.85	1.06	3.26	1.25	2.22	2.37	2.09	2.19	3.79	1.52	1.44	4.36	5.68	3.56	2.77	4.14	4.95
Pr	0.44	0.41	0.15	0.41	0.18	0.28	0.32	0.29	0.29	0.48	0.20	0.20	0.51	0.67	0.43	0.36	0.51	0.60
Nd	1.78	1.70	0.65	1.61	0.83	1.09	1.35	1.19	1.17	1.84	0.80	0.87	1.82	2.41	1.59	1.43	1.99	2.22
Sm	0.33	0.28	0.13	0.28	0.18	0.22	0.26	0.24	0.23	0.31	0.15	0.23	0.30	0.40	0.27	0.29	0.35	0.33
Eu	0.10	0.08	0.04	0.08	0.06	0.07	0.08	0.08	0.07	0.09	0.05	0.09	0.08	0.11	0.08	0.09	0.10	0.09
Gd	0.26	0.21	0.12	0.22	0.18	0.24	0.20	0.25	0.20	0.23	0.17	0.34	0.23	0.29	0.21	0.27	0.28	0.23
Tb	0.03	0.03	0.02	0.03	0.03	0.04	0.03	0.04	0.02	0.03	0.03	0.07	0.03	0.03	0.02	0.04	0.03	0.02
Dy	0.14	0.09	0.09	0.13	0.14	0.20	0.10	0.23	0.12	0.13	0.17	0.47	0.12	0.14	0.11	0.20	0.14	0.09
Ho	0.02	0.01	0.02	0.02	0.02	0.03	0.02	0.04	0.02	0.02	0.04	0.11	0.02	0.02	0.02	0.03	0.02	0.02
Er	0.05	0.03	0.03	0.05	0.05	0.07	0.03	0.09	0.03	0.04	0.09	0.30	0.04	0.05	0.04	0.08	0.04	0.03
Tm	0.01	0.00	0.01	0.01	0.01	0.01	0.00	0.01	0.00	0.01	0.01	0.05	0.01	0.01	0.01	0.01	0.01	0.00
Yb	0.04	0.02	0.02	0.04	0.03	0.04	0.02	0.07	0.03	0.02	0.08	0.30	0.04	0.04	0.03	0.06	0.03	0.02
Lu	0.01	0.00	0.00	0.01	0.01	0.01	0.00	0.01	0.00	0.00	0.01	0.05	0.01	0.01	0.01	0.01	0.00	0.00
Chondrite normalised REE																		
La	7.28	5.69	2.08	7.14	2.29	4.77	5.00	4.21	4.52	8.11	3.14	2.83	10.07	12.79	7.94	5.83	8.79	10.53
Ce	5.53	4.65	1.73	5.31	2.03	3.62	3.86	3.40	3.57	6.19	2.48	2.35	7.12	9.27	5.81	4.52	6.75	8.07
Pr	4.71	4.36	1.65	4.43	1.96	2.97	3.44	3.07	3.10	5.18	2.10	2.19	5.54	7.18	4.59	3.87	5.46	6.51
Nd	3.89	3.71	1.41	3.51	1.81	2.39	2.94	2.61	2.56	4.04	1.75	1.91	3.97	5.27	3.48	3.14	4.35	4.85
Sm	2.26	1.92	0.90	1.88	1.23	1.46	1.74	1.65	1.54	2.09	1.04	1.53	2.04	2.72	1.83	1.95	2.34	2.24
Eu	1.72	1.40	0.71	1.37	1.03	1.31	1.35	1.49	1.24	1.60	0.91	1.56	1.46	1.88	1.42	1.67	1.78	1.65
Gd	1.30	1.07	0.62	1.10	0.92	1.22	1.02	1.27	1.01	1.15	0.83	1.71	1.18	1.44	1.04	1.36	1.38	1.15
Tb	0.83	0.69	0.47	0.75	0.69	1.02	0.72	1.11	0.66	0.83	0.75	1.86	0.69	0.91	0.66	1.08	0.89	0.61
Dy	0.55	0.38	0.36	0.53	0.56	0.81	0.42	0.92	0.48	0.52	0.68	1.91	0.47	0.58	0.45	0.82	0.59	0.38
Ho	0.40	0.24	0.27	0.37	0.42	0.59	0.27	0.73	0.31	0.33	0.64	1.94	0.33	0.42	0.31	0.62	0.40	0.27
Er	0.30	0.17	0.20	0.28	0.31	0.41	0.20	0.56	0.21	0.24	0.57	1.89	0.26	0.29	0.25	0.50	0.28	0.18
Tm	0.28	0.16	0.20	0.24	0.24	0.32	0.16	0.53	0.16	0.20	0.57	2.11	0.24	0.28	0.24	0.49	0.20	0.16
Yb	0.27	0.15	0.11	0.24	0.20	0.26	0.15	0.41	0.16	0.15	0.50	1.89	0.25	0.28	0.21	0.36	0.20	0.14
Lu	0.28	0.16	0.12	0.20	0.20	0.24	0.16	0.41	0.16	0.16	0.49	1.95	0.28	0.28	0.24	0.37	0.16	0.12
Chondrite nomalised REE ratios																		
La/Yb	27.25	39.00	18.61	30.27	11.51	18.50	34.23	10.18	28.01	55.59	6.29	1.50	40.54	46.29	37.60	16.05	44.94	73.72
Sm/Yb	8.45	13.17	8.01	7.97	6.19	5.68	11.90	4.00	9.52	14.35	2.07	0.81	8.20	9.83	8.67	5.37	11.95	15.68
Dy/Yb	2.06	2.60	3.20	2.25	2.82	3.13	2.90	2.22	2.95	3.58	1.37	1.01	1.88	2.11	2.13	2.27	2.99	2.67

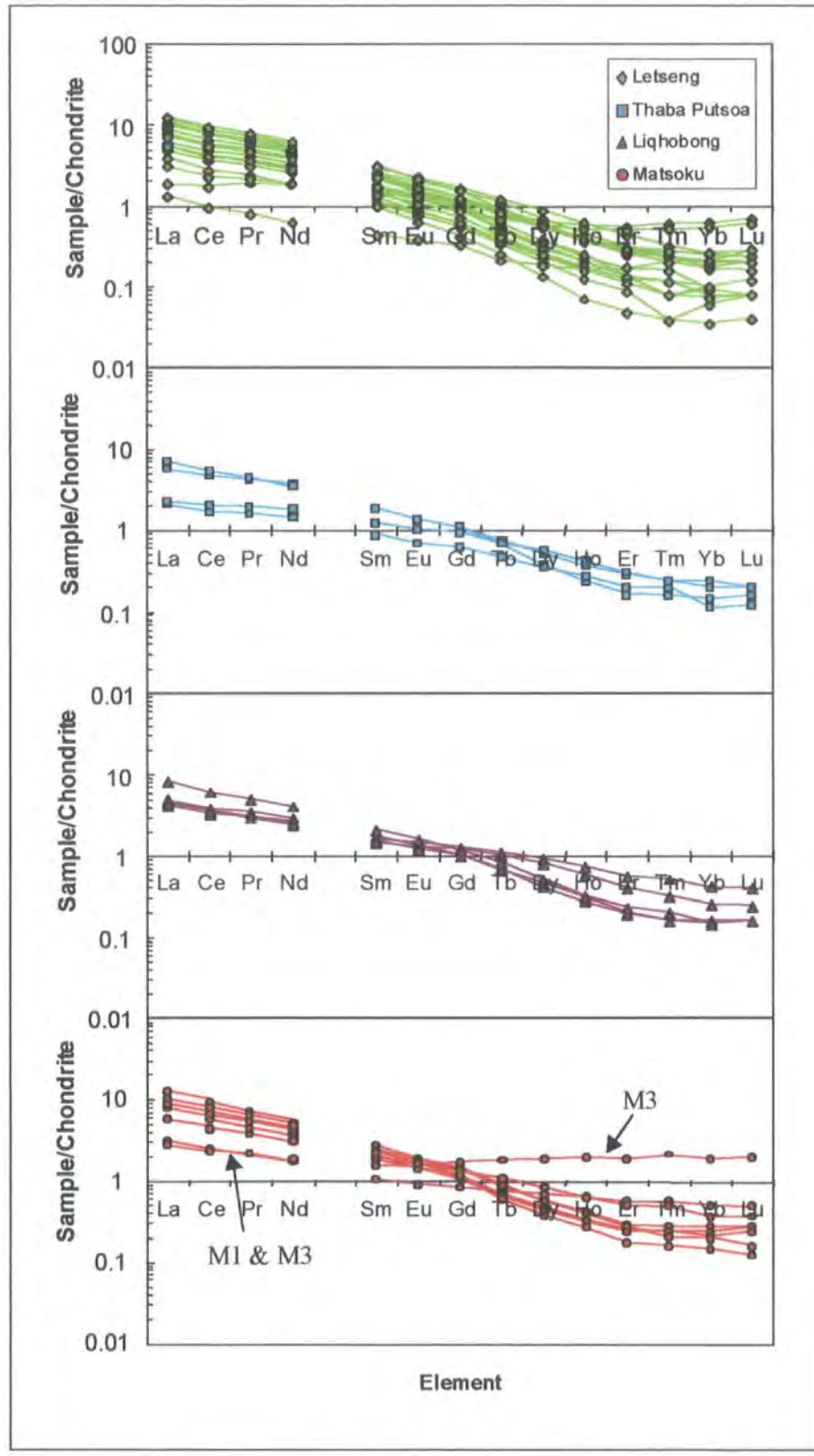

Figure 3.19 Chondrite normalised REE profiles for low-T Lesotho peridotites using normalisation values of M^{c}Donough and Sun (1995).

Excluding the anomalous sample (M3), all samples have high chondrite normalised La/Yb (6 to 129, mean = 42.8) and Sm/Yb (2 to 28, mean = 11.3) ratios. This may suggest the equilibration of the source of incompatible elements with garnet. The subchondritic nature of HREE is characteristic of melt depletion removing garnet from the residue completely, or melt removal at shallower depth in the absence of residual garnet. All samples, excluding the anomalous Matsoku sample, show enrichment in LREE from 1.3 to 12.9 x chondrite. The overall LREE enrichment seen in the Lesotho low-T peridotites is identical to that previously reported for low-T peridotites from the Kaapvaal craton (Nixon *et al.*, 1981), and also the Slave craton (Kopylova and Russell, 2000). Enrichment of LREE within the Lesotho peridotites is not consistent with the major element depletion recorded in the xenoliths. This would suggest that the processes creating these chemical signatures are decoupled (Nixon, 1987b). This may therefore represent melt addition with LREE enrichment, or cryptic metasomatism from fluids passing through the mantle.

3.5.3 Interpretation of whole-rock major element data

By the comparison of compositional data for naturally occurring residual peridotite samples with the residues of experimental melting, Walter (1999) found it possible to infer pressure and temperature conditions for the melt depletion event. To make such a comparison for dry melting, $FeO_{(T)}$, SiO_2, MgO and Al_2O_3 contents have been used (Figure 3.20). The parameters inferred for dry melting are also applicable to high pressure melting in the presence of 4-5 wt% H_2O (Walter, 1999).

If the FeO, Al_2O_3 and MgO contents are primary, they would indicate very high degrees as well as pressures of melting (Walter, 1998). The majority of Lesotho peridotite compositions can be explained by dry 40-60% isobaric batch-melting of pyrolite at pressures ranging from 4 GPa to in excess of 7 GPa (Figure 3.20), or 20-40% polybaric batch-melting at an average pressure of 5 GPa. However, if we are mindful of the fact that late-stage introduction of diopside and some garnet (Simon *et al.*, 2001) may have altered bulk-rock FeO and Al_2O_3 contents, these estimates will not be accurate.

Over 80% of the Lesotho xenoliths have SiO_2 contents higher than model residues and can not be reconciled with melt extraction from pyrolite at any pressure. Even the average SiO_2 content (46.5 wt%) would require a significantly enriched source relative to pyrolite. The apparently negative correlation between SiO_2 and FeO can not be

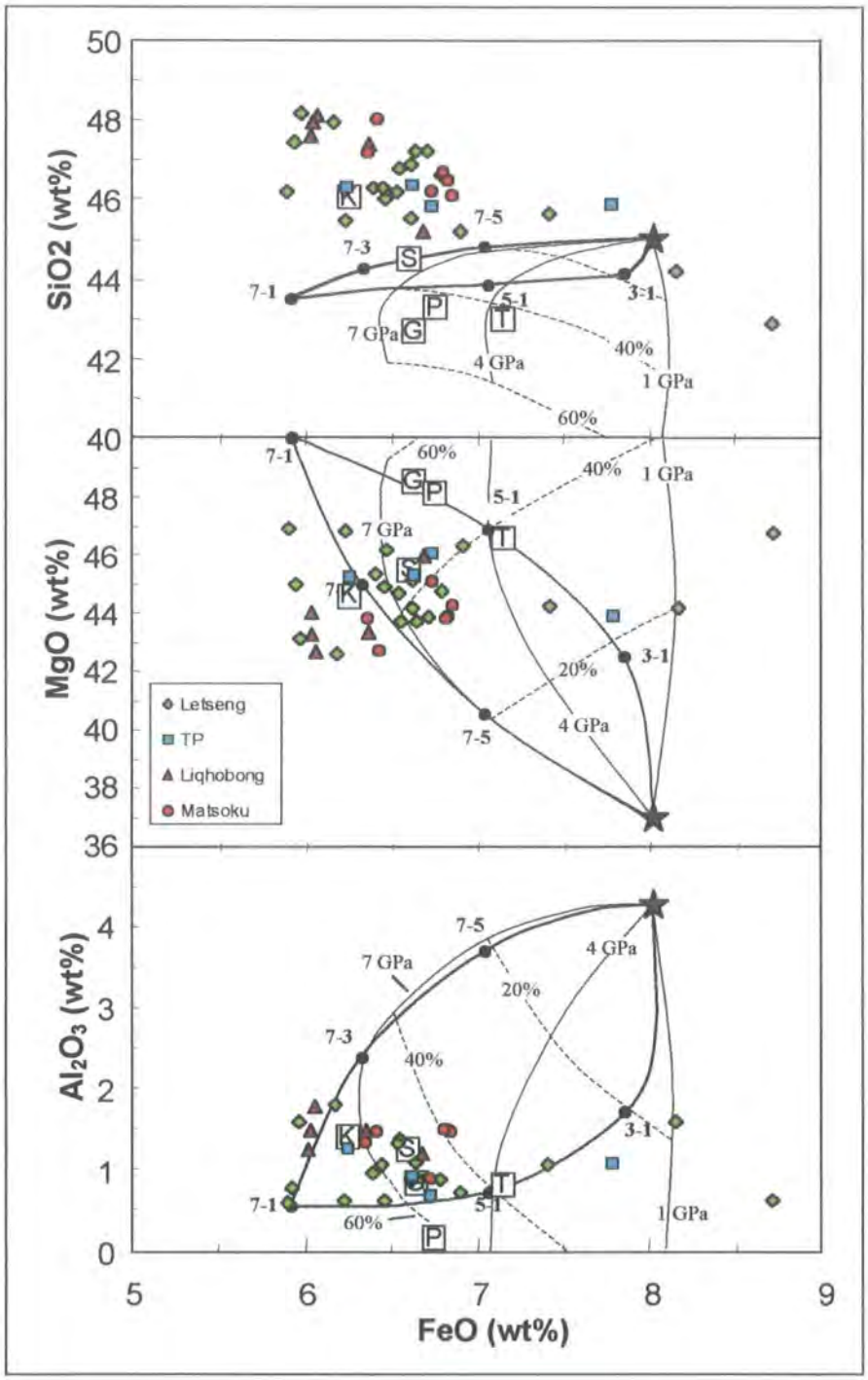

Figure 3.20 Oxide variation diagrams (wt%) for residues of batch and polybaric near-fractional melt extraction, after the method of Walter (1999). Thin solid lines are isobaric batch melt extraction contours and dashed lines give percent batch melt extraction. The filled circles connected by thick solid contours are residues of polybaric near-fractional melt extraction and are labelled according to the pressure range of melt extraction (see Appendix E). Open squares show average low-temperature cratonic peridotites from Kaapvaal (K), Siberia (S), Tanzania (T), Papua New Guinea (P) and East Greenland (G). Additional data from Walter (1999). Fertile mantle denoted by star symbol..

easily reconciled with melt extraction. The Lesotho peridotites are too rich in Si and modal OPX, and too low in olivine to be comparable to high-pressure experimental residues. This inconsistency has been reported for low-temperature peridotites from the Kaapvaal craton before (Maaloe and Aoki, 1977; Boyd and Mertzman, 1987; Boyd, 1989). Low-T peridotites from the Siberian craton have also been found to have high modal OPX concentrations (Boyd *et al.*, 1997).

The mechanism enriching SiO_2 may also alter other oxides as well. If the SiO_2 enrichment is the consequence of OPX addition (Boyd, 1989; Keleman *et al.*, 1998), this will also increase Al_2O_3 and decrease FeO and MgO. The high pressure of melt extraction indicated by the data may therefore be an artefact. A few Lesotho peridotite samples have $FeO_{(T)}$ contents higher than experimental residues of experimental melting at 1 GPa. This may be the result of metasomatism, enriching the sample in Fe as proposed for other peridotite suites (Harte and Hawkesworth, 1989).

3.5.4 Melt extraction

3.5.4.a Major element modelling of melt residues

Even though the Lesotho low-T peridotite suite may have experienced some disturbance to its major element composition, it can be useful to compare the xenolith data to melting models. As discussed above, the depleted nature of the Lesotho lithospheric mantle can be attributed to variable, but large, degrees of melting of a primitive mantle source. The observed variance in major element trends may result from the varying degrees of melt extraction, plus superimposed modification by later metasomatism. By applying geochemical modelling techniques such as those developed by Hanson and Langmuir (1978), this hypothesis can be investigated (see Appendix E for details). The modelling of major elements is constrained by known partition coefficients (K_D) for $Mg_{(Ol/melt)}$ and $Fe_{(Ol/melt)}$ as a function of composition, pressure and temperature, and solid phase stoichiometry. This information can be applied to a model homogeneous mantle source, and used to calculate MgO and FeO contents of peridotite residues from varying degrees of melting. The degree of melt extraction experienced by the Lesotho peridotites can be estimated by assuming that they formed from partial melting of a pyrolitic source (MgO = 47.8 mol%, FeO = 5.35 mol%, Ringwood, 1975). Experimental partition coefficient data from Bickle *et al* (1977), at pressures 3.0 GPa, were used in conjunction with the equations of Hanson and Langmuir (1978) to produce a residue grid (Figure 3.21). From this type

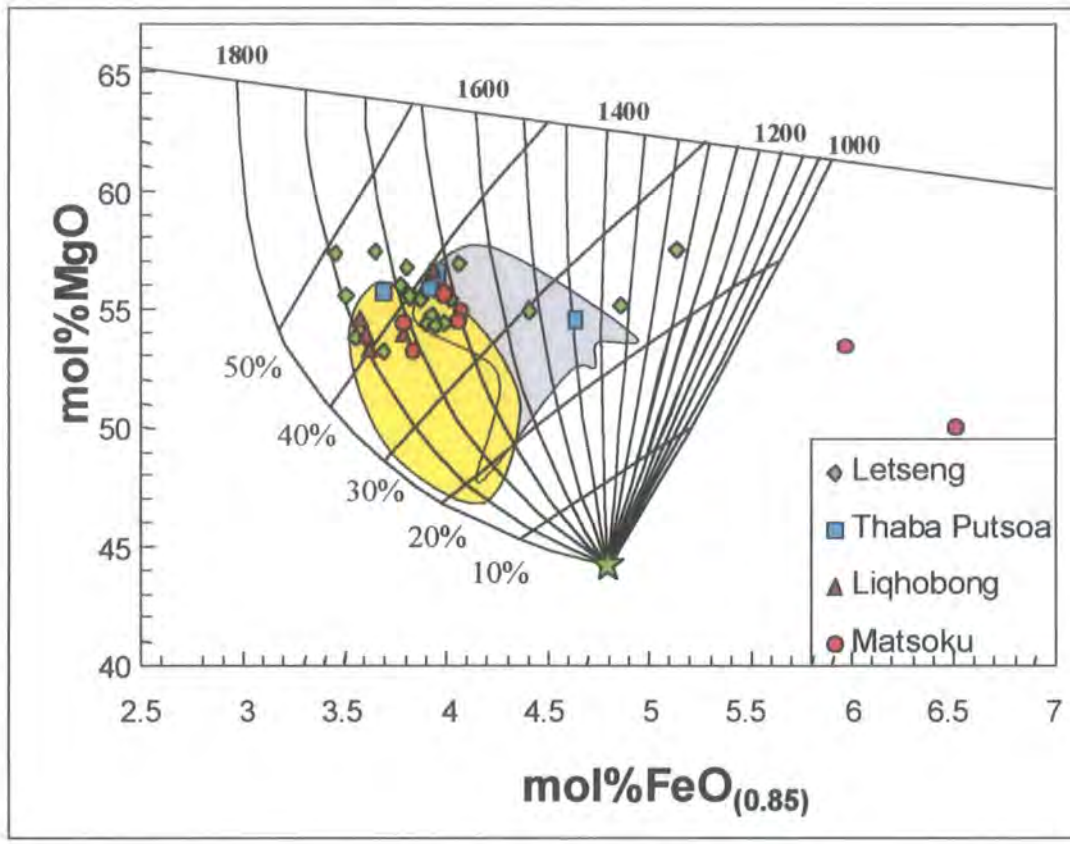

Figure 3.21 FeO-MgO diagram for Kaapvaal peridotites. The diagram is contoured for temperature and degree of batch melting of pyrolitic mantle (Ringwood, 1975) at 3 GPa using method described by Hanson and Langmuir (1978). Field for Kaapvaal and Siberian peridotites from Pearson *et al* (1995a). Kaapvaal low-T peridotites represented by yellow field, Siberian by the light grey field. Pyrolite denoted by star symbol..

of modelling (Figure 3.21) the Lesotho peridotites appear to represent ~35 to 50% batch melting of a pyrolitic mantle source. This is a minimum value if bulk FeO has been enriched. No overall correlation exists between facies and degree of melting, but harzburgites from the Letseng kimberlite display higher degrees of melting (40-50%) than lherzolites (30-40%). The liquidus temperature of 4-phase lherzolites increases with pressure (Thompson, 1984), and if this is combined with the pressure dependence of K_D, high-pressure residues will shift to the left (lower mol% FeO) on Figure 3.21, whilst low-pressure residues will shift to the right (higher mol% FeO). Although the temperature at which residues form will vary with pressure, the degree of melting remains approximately constant (Hanson and Langmuir, 1978). It is apparent from Figure 3.21 that some peridotites show anomalously high FeO contents. This may indicate that the samples represent low-pressure melt residue, or alternatively may be indicative of their later enrichment of Fe after melt extraction. Trace element data for these samples does not appear to deviate from that seen for other peridotite samples,

with the exception of samples M1 and M3, and therefore FeO is not increasing with the observed LREE enrichment.

From Figure 3.21 it would appear as though the Lesotho low-T peridotites generally represent similar degrees of melting to that previously reported for a suite of low-T Kaapvaal peridotites (Pearson *et al.*, 1995a), with a few samples indicating higher degrees of melt extraction. Several samples overlap the field for low-T Siberian peridotite xenoliths but this may be the result of Fe-enrichment. Boyd *et al* (1997) found clear evidence of late-stage enrichment of Ca and Fe in the Siberian suite.

3.5.4.b HREE modelling

Although REE abundances in the whole-rock peridotites are obviously disturbed, the low HREE contents may be indicative of the melt removal processes rather than melt addition. The fractionation of HREE as a function of HREE abundances can be modelled to estimate the degree of melting (Figure 3.22), after the method of Bodinier *et al* (1988). As well as providing evidence for the degree of melting, the fractionation of HREE can also distinguish between the presence and absence of garnet, owing to the buffering of HREE by garnet.

On a plot of Dy/Yb ratio against Yb (Figure 3.22), calculated ratios for model melting of a peridotite source of variable garnet content are presented for up to 20% batch and fractional melting, after Burnham (1995). See Appendix E for a detailed explanation of modelling parameters. The Lesotho peridotites show little evidence of a decrease in Dy/Yb with a decrease in Yb, but instead tend to show an increase in the Dy/Yb ratio for a given Yb abundance. The Lesotho peridotites therefore, do not match the trajectories of the predicted model melts and this would suggest that the samples have undergone Dy addition after the melt depletion event. The HREE also appear to be overprinted by later metasomatic events. The modelling of REEs provides no evidence of the initial melt depletion event, or the composition of the source mantle. However, within the Lesotho peridotite suite absolute Yb abundances are generally sub-chondritic (Figure 3.19), and this would suggests that melting either occurred within spinel facies or was sufficient to remove all garnet from the residue.

3.5.5 Summary of peridotite petrogenesis

Based on the experimental models of Walter (1999), a general model for the origin of the cratonic mantle underlying Lesotho is illustrated in Figure 3.23. Primary melt

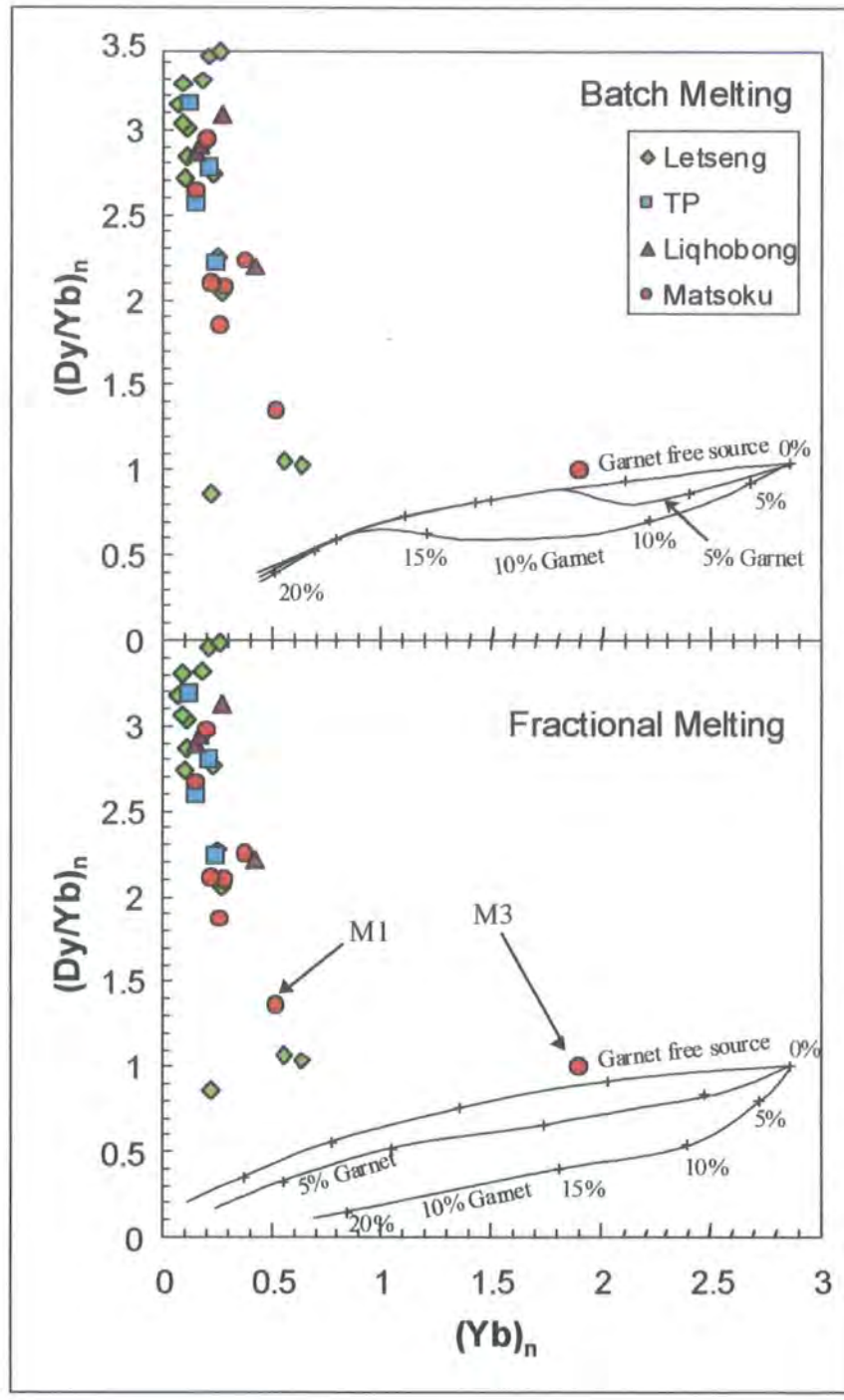

Figure 3.22 Variation of Dy/Yb ratio with Yb abundances in low-T Lesotho peridotites, superimposed on calculated variations of Dy/Yb ratios with Yb calculated for up to 25% melting of a peridotite source containing variable quantities of garnet, after Burnham (1995). Crosses at 5% melting intervals.

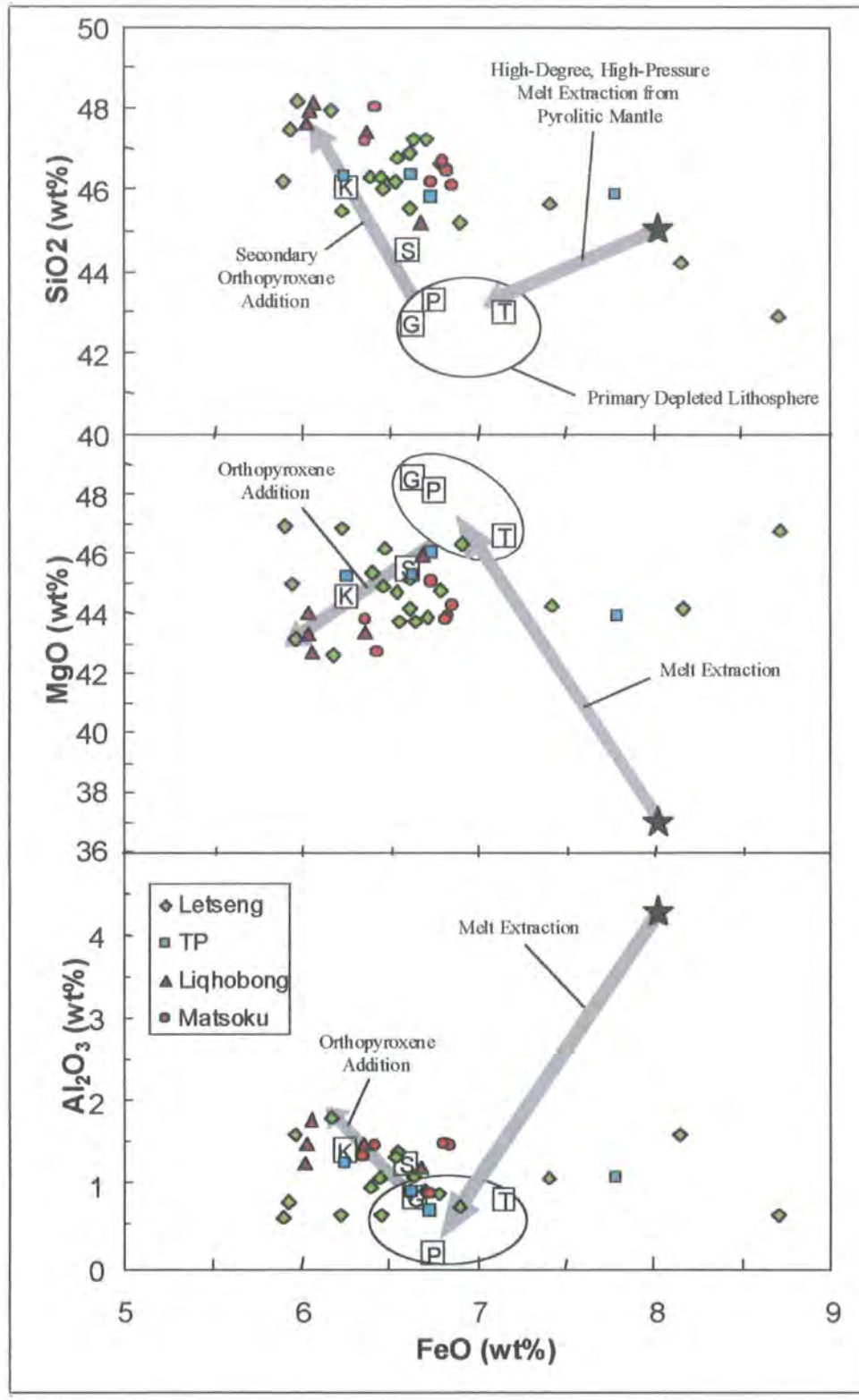

Figure 3.23 Oxide variation diagrams (wt%) showing a general model for the origin of cratonic lithosphere, after Walter (1999). Primary melt extraction from pyrolitic mantle (star symbol) of about 40-50% melt at pressures of 3-4 GPa produce a residue with compositions within a field encompassing Tanzania, Greenland and Papua New Guinea. Addition of OPX to Siberian and Kaapvaal lithosphere has caused enrichment in SiO_2 and Al_2O_3, and depletion in MgO and FeO.

extraction from a pyrolitic source produces a harzburgitic lithosphere (melt extraction vector of Figure 3.23). The average values illustrated for Greenland, Tanzania and Papua New Guinea approximate residues of 40 to 50% melt extraction at an average of 3-4 GPa (Walter, 1999). This is consistent with the $Mg^{\#}$ of olivine in the Lesotho peridotites. Subsequent to melt extraction, the addition of secondary SiO_2 and Al_2O_3, reflected in the high modal OPX content of the peridotites, moves the average composition along a vector parallel to the OPX addition compositional vector for the Kaapvaal and Siberian cratons, shown in Figure 3.23. The addition of SiO_2 and Al_2O_3 is associated with depletion of MgO. The addition of silica to the peridotites may be the result of melt-mantle reaction (Keleman *et al.*, 1998), cumulate mixing (Herzberg, 1993; Herzberg, 1999) or a combination of both. Several apparently depleted Lesotho samples (high MgO and low Al_2O_3) have FeO contents higher than the model pyrolitic source, and therefore suggest Fe metasomatism, as previously noted from studies of other cratonic peridotite suites (Harte *et al.*, 1987; Menzies *et al.*, 1987). Iron-enrichment from metasomatism would shift the sample to the right on Figure 3.23, if the Fe is preferentially mobilised relative to Mg and Al. This may account for any inconsistencies between modal mineralogy, mineral chemistry and whole-rock major element modelling in the Lesotho suite. The enrichment in Fe would appear to be generally unrelated to LREE enrichment, and no systematic relationship between Fe enrichment and trace elements can be seen. An exception to this may be samples M1 and M3 from Matsoku. These samples appear to show possible HREE enrichment as well as Fe enrichment, which may relate to a separate episode of metasomatism.

Trace element enrichment of the Lesotho peridotite xenoliths is not systematically related to major-element chemistry. Subsequent to melt depletion, all Kaapvaal samples have undergone consistent LREE enrichment. This suggests that the lithospheric mantle has undergone episodic and variable metasomatism from varying metasomatic fluids of different character (see summary by Menzies and Hawkesworth, 1987).

3.6 Re-Os Isotopic Study of Lesotho Peridotite Xenoliths

3.6.1 Introduction

To understand the generation and evolution of the cratonic lithospheric mantle beneath Lesotho would require knowledge of the age, time-scale of formation and relationship between the crustal and mantle section of the lithosphere.

The major and trace element data presented in previous sections for the Lesotho peridotite suite have suggested that the continental lithosphere underlying Lesotho has a complex history involving melt depletion with refertilisation, or metasomatism associated with the passage of later mantle-derived melts/fluids. Previous isotopic studies of Kaapvaal peridotite xenoliths using the Rb-Sr, Sm-Nd and U-Pb isotope systems have afforded a great insight into the processes modifying lithospheric mantle keels (see reviews by, Menzies and Hawkesworth, 1987; Menzies, 1990; Pearson, 1999a; Pearson, 1999b). These systems have provided little information on estimating the age of formation, as they primarily track metasomatic enrichment events rather than melt depletion.

A critical step in producing compositional buoyancy in the lithospheric mantle keel, vital for lithosphere formation and craton stabilisation, is the extraction of melt from the lithospheric mantle (Walker *et al.*, 1989; Pearson, 1999b). Osmium is a compatible element during partial melting of the mantle, and consequently the Os content of most magmatic fluids is low. Metasomatic alteration of the mantle by these magmatic fluids should have a negligible effect on mantle $^{187}Os/^{188}Os$ ratios. The Re-Os isotope system therefore provides an opportunity to help constrain the timing of, and processes concerned in, the formation of the continental lithospheric mantle underlying Lesotho. This information should be less subject to the effects of metasomatism and the alteration processes that obscure the results of other isotope systems.

3.6.2 Re and Os Abundances and Isotopic Compositions

3.6.2.a Re variation

Rhenium abundances in the low-T Lesotho peridotite xenoliths (Table 3.10) show a considerable scatter (0.01 to 0.60 ppb), extending over a range similar to that previously reported for Archean cratonic peridotite xenoliths from the Kaapvaal and Siberian cratons (Walker *et al.*, 1989; Pearson *et al.*, 1995a; Pearson *et al.*, 1995b; Carlson *et al.*, 1999), and also the Slave craton (Chapter 4). The scatter in Re concentrations for the Lesotho samples however is larger than that seen in post-Archean cratonic peridotite xenoliths (Carlson and Irving, 1994; Meisel *et al.*, 1996; Handler *et al.*, 1997; Peslier *et al.*, 2000). The mean Re concentration for all Lesotho peridotite xenoliths in this study is 0.141 ppb (std.dev. = 0.128) with a median of 0.101 ppb (n = 35), compared to an estimated 0.26 ppb for fertile mantle (Morgan, 1986). This demonstrates that peridotite xenoliths from Lesotho are, in general, depleted in Re relative to fertile

Table 3.10 Re-Os Isotopic data for Lesotho peridotites. γOs, T_{RD} and T_{MA} calculated with respect to chondrite ($^{187}Os/^{188}Os$ = 0.3972 and $^{187}Re/^{188}Os$ = 0.1276; Walker *et al.*, 1989) and fertile mantle ($^{187}Os/^{188}Os$ = 0.4243 and $^{187}Re/^{188}Os$ = 0.1287; Meisel *et al.*, 1996) with ^{187}Re decay constant of 1.666 x 10^{-11} yr^{-1}. γOs is the difference (in %) in $^{187}Os/^{188}Os$ between the sample and fertile mantle/chondrite at the eruption age of the kimberlite. Errors are 2σ within run. T_{RD} and T_{MA} expressed in Ga.

Samples	Re (ppb)	Os (ppb)	$^{187}Re/^{188}Os$	$^{187}Os/^{188}Os$(m)	+/-	$^{187}Os/^{188}Os$(i)	γOs	T_{RD}	T_{MA}	$^{187}Os/^{188}Os$(i)	γOs	T_{RD}	T_{MA}
						Chondrite				*Fertile Mantle*			
(Letseng)													
LET2	0.330	5.71	0.2772	0.10864	12	0.10820	-14.80	2.86		0.10820	-15.49	2.83	
LET6	0.137	3.18	0.2065	0.10878	15	0.10846	-14.60	2.82		0.10846	-15.29	2.80	
LET8	0.251	1.60	0.7526	0.10864	9	0.10746	-15.38	2.96		0.10746	-16.07	2.93	
LET12	0.153	3.16	0.2319	0.10954	10	0.10918	-14.03	2.72		0.10918	-14.73	2.70	
LET13	0.041	3.31	0.0593	0.10864	13	0.10854	-14.53	2.81	3.27	0.10854	-15.22	2.79	3.21
LET14	0.089	4.70	0.0906	0.10858	12	0.10844	-14.61	2.82	3.61	0.10844	-15.30	2.80	3.51
LET25	0.150	1.98	0.3644	0.10830	10	0.10773	-15.18	2.93	2.77	0.10773	-15.86	2.90	
LET27	0.367	6.25	0.2822	0.10903	14	0.10859	-14.50	2.80		0.10859	-15.19	2.78	
LET28	0.096	3.88	0.1187	0.10793	10	0.10775	-15.16	2.92	4.09	0.10775	-15.85	2.90	3.95
LET29	0.260	3.44	0.3625	0.11007	8	0.10950	-13.78	2.67		0.10950	-14.48	2.66	
LET30	0.217	2.37	0.4385	0.11302	9	0.11233	-11.55	2.26		0.11233	-12.26	2.27	
LET31	0.200	5.82	0.1656	0.10966	13	0.10940	-13.85	2.68	4.47	0.10940	-14.55	2.67	4.26
LET38	0.090	13.73	0.0314	0.10904	9	0.10899	-14.18	2.74	2.97	0.10899	-14.87	2.73	2.93
LET47	0.192	4.35	0.2124	0.10947	11	0.10914	-14.07	2.72		0.10914	-14.76	2705.67	
LET48	0.225	1.99	0.5448	0.11617	8	0.11531	-9.20	1.83		0.11531	-9.94	1.86	
LET49	0.113	3.86	0.1405	0.11909	9	0.11887	-6.40	1.30	1.95	0.11887	-7.16	1.37	2.0
LET58	0.332	5.22	0.3056	0.10788	12	0.10740	-15.43	2.97		0.10740	-16.11	2.94	
LET63	0.089	4.13	0.1039	0.11908	11	0.11892	-6.36	1.29	1.71	0.11892	-7.12	1.37	1.77
LET64	0.598	6.42	0.4476	0.11000	10	0.10930	-13.94	2.70		0.10930	-14.63	2.68	

Table 3.10 (continued) Re-Os Isotopic data for Lesotho peridotites.

Samples	Re (ppb)	Os (ppb)	$^{187}Re/^{188}Os$	$^{187}Os/^{188}Os(m)$	+/-	$^{187}Os/^{188}Os(i)$	γOs	T_{RD}	T_{MA}	$^{187}Os/^{188}Os(i)$	γOs	T_{RD}	T_{MA}
						Chondrite				*Fertile Mantle*			
(Thaba Putsoa)													
TP6	0.021	5.46	0.0185	0.10734	12	0.10731	-15.53	2.99	3.12	0.10731	-16.21	2.95	3.08
TP7	0.032	2.44	0.0637	0.10821	17	0.10812	-14.89	2.87	3.39	0.10812	-15.57	2.84	3.32
TP9	0.024	4.57	0.0254	0.10768	12	0.10764	-15.26	2.94	3.13	0.10764	-15.95	2.91	3.08
(Liqhobong)													
LQ1	0.013	0.20	0.3041	0.11252	15	0.11207	-11.78	2.30		0.11207	-12.49	2.31	
LQ5	0.012	6.56	0.0090	0.10908	12	0.10907	-14.14	2.73	2.79	0.10907	-14.83	2.71	2.77
LQ6	0.105	2.17	0.2331	0.10949	17	0.10915	-14.08	2.72		0.10915	-14.77	2.70	
LQ8	0.010	3.82	0.0120	0.10804	12	0.10802	-14.96	2.88	2.97	0.10802	-15.65	2.86	2.93
LQ9	0.016	6.68	0.0113	0.10827	12	0.10826	-14.78	2.85	2.93	0.10826	-15.47	2.82	2.90
(Matsoku)													
M1	0.164	2.20	0.3571	0.12204	10	0.12151	-4.35	0.91		0.12151	-5.12	1.01	
M3	0.260	0.82	1.5161	0.12516	10	0.12290	-3.25	0.70		0.12290	-4.04	0.82	
M5	0.090	3.16	0.1371	0.11179	17	0.11158	-12.16	2.37	3.54	0.11158	-12.87	2.37	3.43
M6	0.079	2.95	0.1280	0.11100	17	0.11081	-12.77	2.48	3.58	0.11081	-13.47	2.48	3.48
M8	0.077	4.38	0.0847	0.11300	9	0.11288	-11.14	2.18	2.74	0.11288	-11.86	2.20	2.71
M9	0.015	9.55	0.0075	0.10851	9	0.10850	-14.59	2.82	2.87	0.10850	-15.28	2.79	2.84
M11	0.033	4.24	0.0377	0.10976	8	0.10970	-13.64	2.64	2.90	0.10970	-14.34	2.63	2.87
M13	0.031	5.36	0.0276	0.10950	15	0.10946	-13.83	2.68	2.87	0.10946	-14.53	2.66	2.84

mantle compositions (Figure 3.24), with only a few samples showing enriched concentrations. If the samples depleted relative to fertile mantle are considered alone (Table 3.10), the mean Re content is 0.096 ppb (std.dev. = 0.072) with a median of 0.089 ppb (n = 30). This becomes more comparable to the mean Re concentration of 0.084 ppb (std.dev. = 0.078) and median of 0.072 ppb for previous studies of Kaapvaal peridotites (Carlson *et al.*, 1999).

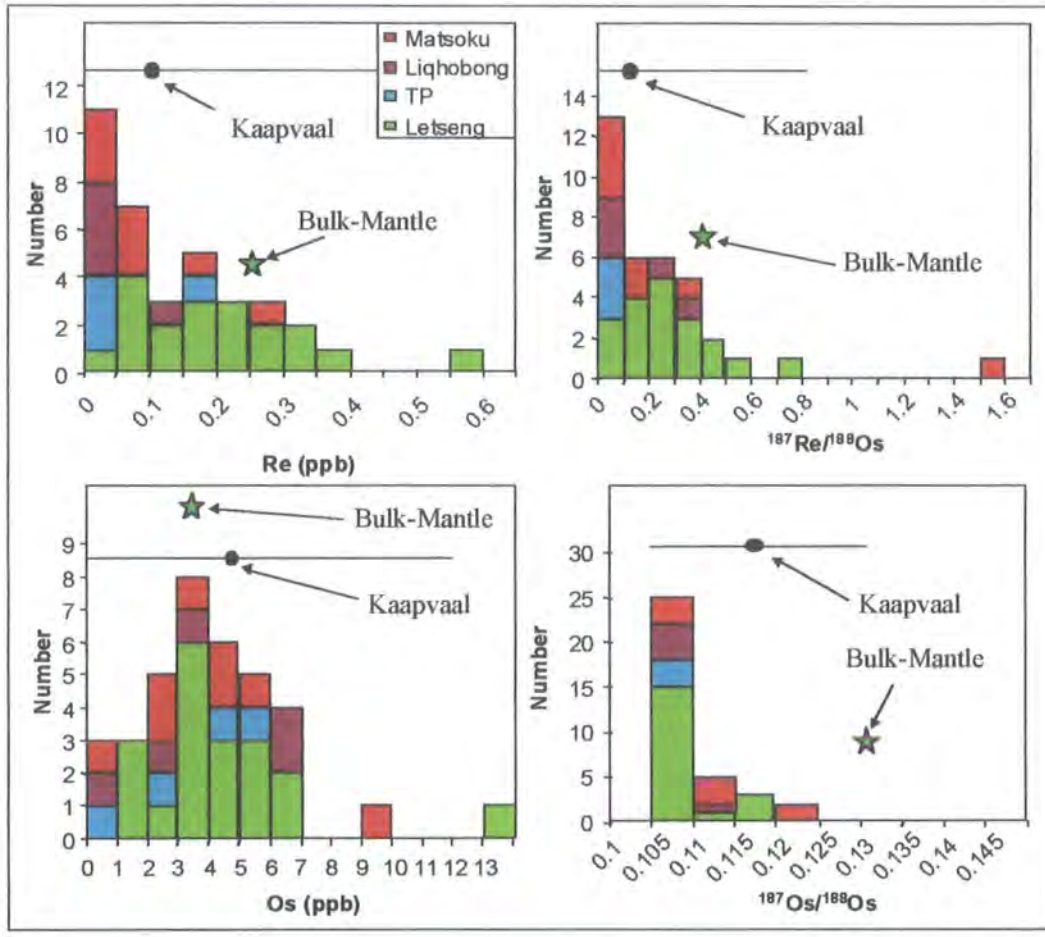

Figure 3.24 Histograms of Re and Os concentration (ng/g or ppb), $^{187}Re/^{188}Os$ and $^{187}Os/^{188}Os$ for low-T Lesotho peridotite xenoliths. Mean Kaapvaal values and range after Carlson *et al* (1999) and Bulk-Mantle after Morgan (1986).

A summary of mean and median Re concentrations is presented in Table 3.11. Peridotite xenoliths from Thaba Putsoa generally have the lowest Re contents in the Lesotho peridotite suite. Peridotite xenoliths from the Liqhobong kimberlite complex and Matsoku kimberlite have slightly higher Re concentrations, whilst xenoliths from the Letseng-la-terae kimberlite pipes have the highest Re abundances. If samples enriched in Re relative to fertile mantle estimates are excluded, the mean and median Re concentrations for peridotites from Thaba Putsoa and Liqhobong remain unchanged, and are the most depleted peridotites. The mean and median Re abundance for samples

from the Matsoku kimberlite now appear to be more depleted (Table 3.11), and more similar to typical values reported for Archean and post-Archean peridotite xenoliths (Handler *et al.*, 1997; Carlson *et al.*, 1999). The mean Re content of peridotites from the Letseng kimberlite, though still high relative to the other kimberlite locations, now appear to be more depleted (Table 3.11). This suggests that the continental lithospheric mantle beneath Lesotho is generally depleted in Re, as typically seen in Archean and post-Archean regions, but many samples have probably undergone later, localised Re enrichment.

Location	Mean (ppb)	+/-	Median (ppb)	n
Lesotho	0.141	0.128	0.101	35
Lesotho†	0.096	0.072	0.089	30
Letseng-la-terae	0.207	0.133	0.192	19
Letseng-la-terae†	0.147	0.063	0.144	14
Thaba Putsoa	0.026	0.006	0.024	3
Liqhobong	0.045	0.05	0.014	5
Matsoku	0.094	0.082	0.078	8
Matsoku†	0.07	0.05	0.077	7

Table 3.11 Summary of the mean and Median Re concentrations in peridotites from the Lesotho suite and individual Lesotho kimberlite locations.

† calculated mean and median for peridotite xenoliths depleted in Re relative to fertile mantle compositions (0.26 ppb, Morgan, 1986).

3.6.2.b Os variation

Osmium concentrations for the Lesotho peridotite suite (Table 3.10), show a considerable range (0.20 ppb to 13.7 ppb), similar to that previously reported for Kaapvaal and Siberian peridotites (Walker *et al.*, 1989; Pearson *et al.*, 1995a; Pearson *et al.*, 1995b; Carlson *et al.*, 1999). The Os abundances of Lesotho peridotites, on average (mean = 4.27 ppb; Table 3.12), are higher than estimates for fertile mantle (3.4 ppb, Morgan, 1986). This is consistent with the depleted nature of the xenoliths (Figure 3.24), and the compatible nature of Os. The Os concentrations of peridotite xenoliths from previous studies of the Kaapvaal craton (mean = 4.61 ppb, median = 4.05 ppb, Carlson *et al.*, 1999) and from studies of Alpine peridotites (mean = 3.74 ppb, median = 3.84 ppb, Reisberg and Lorand, 1995), are also higher than fertile mantle. The Os content of the Lesotho xenolith suite tends to lie between these two groups. In contrast,

rift related spinel peridotite xenoliths (McBride *et al.*, 1996; Meisel *et al.*, 1996; Handler *et al.*, 1997; Chesley *et al.*, 1999; Peslier *et al.*, 2000), arc related spinel peridotite xenoliths (Brandon *et al.*, 1996) and Abyssal peridotites (Snow and Reisberg, 1995) have Os contents lower than fertile mantle estimates.

A summary of mean and median Os concentrations is presented in Table 3.12. The Os concentrations for peridotite xenoliths from Letseng, Thaba Putsoa, Liqhobong and Matsoku are generally similar, and all higher than fertile mantle estimates. This suggests that there is little, if any, spatial distribution in differences within the Os systematics of the Lesotho continental lithospheric mantle.

Location	Mean (ppb)	+/-	Median (ppb)	n
Lesotho	4.27	2.5	3.87	35
Letseng-la-terae	4.47	2.68	3.88	19
Thaba Putsoa	4.15	1.55	4.57	3
Liqhobong	3.91	2.79	3.82	5
Matsoku	4.08	2.62	3.7	8

Table 3.12 Summary of the mean and Median Os concentrations in peridotites from the Lesotho suite and individual Lesotho kimberlite locations.

3.6.2.c Re/Os isotopic variation

Cratonic peridotites have amongst the lowest $^{187}Re/^{188}Os$ ratios of any peridotite suites, though in general most peridotites worldwide have $^{187}Re/^{188}Os$ ratios less than fertile mantle estimates ($^{187}Re/^{188}Os = 0.4243$, Meisel *et al.*, 1996). The overall range in both Re and Os concentrations within the Lesotho peridotite xenolith suite presented in Table 3.10 results in a large range in $^{187}Re/^{188}Os$ ratios from 0.007 to 1.52 (subchondritic to suprachondritic), with a mean of 0.233 (Table 3.13). This is higher than $^{187}Re/^{188}Os$ ratios reported in previous studies of peridotites from the Kaapvaal craton (mean $^{187}Re/^{188}Os = 0.109$, Carlson *et al.*, 1999), and slightly higher than Alpine peridotites (mean $^{187}Re/^{188}Os = 0.207$, Reisberg and Lorand, 1995). Of the 35 Lesotho samples analysed in this study (Table 3.10), five have $^{187}Re/^{188}Os$ ratios greater than fertile mantle. If we exclude these five samples from the suite, the average $^{187}Re/^{188}Os$ ratio is reduced considerably to 0.15 (Table 3.13). This is more comparable to the

studies of Kaapvaal and Alpine peridotite xenoliths, and is consistent with the moderately incompatible nature of Re during partial melting.

Location	Mean	+/-	Median	n
Lesotho	0.233	0.28	0.153	35
Lesotho†	0.15	0.122	0.128	30
Letseng-la-terae	0.273	0.186	0.232	19
Letseng-la-terae†	0.2	0.113	0.207	15
Thaba Putsoa	0.036	0.024	0.025	3
Liqhobong	0.115	0.145	0.012	5
Matsoku	0.287	0.509	0.106	8
Matsoku†	0.111	0.119	0.085	7

Table 3.13 Summary of the mean and Median $^{187}Re/^{188}Os$ ratios in peridotites from the Lesotho suite and individual Lesotho kimberlite locations.

† calculated mean and median for peridotite xenoliths with $^{187}Re/^{188}Os$ ratios lower than fertile mantle estimates only (0.4243, Meisel *et al.*, 1996).

The mean $^{187}Re/^{188}Os$ ratio for peridotite xenoliths from Thaba Putsoa (Table 3.13) is lower than that previously reported for Kaapvaal peridotites (Carlson *et al.*, 1999), whereas the mean $^{187}Re/^{188}Os$ ratio of peridotite xenoliths from Liqhobong is comparable. The mean $^{187}Re/^{188}Os$ for peridotites from Letseng and Matsoku are higher than both Kaapvaal and Alpine peridotites. If we exclude samples with $^{187}Re/^{188}Os$ ratios higher than fertile mantle, the peridotite xenoliths from the Thaba Putsoa and Liqhobong remain unchanged, but the mean $^{187}Re/^{188}Os$ ratio for those from Matsoku is lowered (Table 3.13), and more comparable to the overall Kaapvaal mean (Carlson *et al.*, 1999). The mean $^{187}Re/^{188}Os$ ratio of peridotites from the Letseng is also reduced (Table 3.13), but is more comparable to the mean of Alpine peridotites (Reisberg and Lorand, 1995). This evidence supports the observation that the lithospheric mantle beneath Lesotho is depleted relative to fertile mantle, as typically seen in Archean and post-Archean regions, but locally enriched.

3.6.2.d Os isotopic variation

It has been shown that the clearest distinction between cratonic peridotites and peridotites from other tectonic settings is provided by Os isotopic composition (Carlson *et al.*, 1999). The Os isotopic composition of Lesotho peridotite xenoliths ranges from $^{187}Os/^{188}Os$ of 0.1073 to 0.1229 (Table 3.10), i.e. from significantly more depleted than

chondritic to near chondritic (Figure 3.24). This is similar to the range for other Kaapvaal, and Siberian peridotite xenolith suites (Pearson *et al.*, 1995a; Pearson *et al.*, 1995b; Carlson *et al.*, 1999). The range in Re/Os for Lesotho peridotites overlaps that of peridotites from other tectonic settings. The low unradiogenic $^{187}Os/^{188}Os$ values present in the Lesotho suite however are distinctive from these other peridotite groups (Figure 3.24). The Lesotho peridotites are highly unradiogenic relative to both chondritic and fertile mantle estimates (Table 3.10). The unradiogenic isotopic characteristic of the Lesotho peridotites indicates a long-term Re depletion, and isolation from the convecting mantle, which occurred earlier than in the non-cratonic peridotite groups. This is comparable to the observed $^{187}Os/^{188}Os$ isotopic values for peridotites from other cratonic peridotite suites.

Location	Mean	+/-	Median	N
Kaapvaal†	0.1115	0.0032	0.1105	38
Lesotho	0.1106	0.004	0.1091	35
Letseng-la-terae	0.1102	0.0036	0.109	19
Thaba Putsoa	0.1077	0.0004	0.1076	3
Liqhobong	0.1094	0.0016	0.1091	5
Matsoku	0.1134	0.0056	0.1112	8

Table 3.14 Summary of the mean and Median $^{187}Os/^{188}Os$ ratios in peridotites from the Lesotho suite and individual Lesotho kimberlite locations.

† Mean and median $^{187}Os/^{188}Os$ ratios for Kaapvaal craton from Carlson *et al* (1999).

The $^{187}Os/^{188}Os$ isotopic composition of peridotite xenoliths from Lesotho (Table 3.14), are on average slightly less radiogenic than other Kaapvaal craton suites (Carlson *et al.*, 1999). Peridotites from Thaba Putsoa are the most unradiogenic within the Lesotho suite, with the average $^{187}Os/^{188}Os$ compositions of peridotites from Liqhobong and Letseng only slightly more radiogenic (Table 3.14). The peridotite xenoliths from Matsoku are the most radiogenic within the Lesotho suite.

3.6.3 PGE geochemistry of the Lesotho peridotites

3.6.3.a Whole-rock PGE abundances

If the Lesotho peridotite suite is considered as a whole, it shows a large variation in PGE and Re abundances (Table 3.15). This range in PGE concentrations is much larger than has been observed for Pyrenean orogenic lherzolites (Lorand *et al.*, 1999), or

Table 3.15 PGE, Re and selected major and trace element abundances for Lesotho peridotites. CI chondrite values from McDonough and Sun (1995). Primitive mantle values taken as 0.007 x CI chondrite after method of McDonough and Sun (1995).

Samples	S (ppm)	Al_2O_3 (wt%)	(La/Yb)n	Ba (ppm)	Nb (ppm)	Os (ppb)	Ir (ppb)	Ru (ppb)	Pt (ppb)	Pd (ppb)	Re (ppb)
Letseng											
LET2	202.75	0.60	16.12	27.48	3.37	5.71	5.26	8.17	3.76	0.73	0.33
LET6	345.00	0.88	23.58	20.51	1.42	3.18	1.72	1.42	0.18	0.04	0.14
LET8	161.00	0.58	61.67	30.98	2.06	1.60	1.89	2.16	0.29	0.09	0.25
LET12	188.00	0.89	103.97	17.08	3.33	3.16	2.65	4.44	0.54	0.07	0.15
LET13	158.00	0.96	55.30	48.00	2.92	3.31	3.37	4.70	0.89	0.02	0.04
LET14	130.25	0.77	75.56	18.70	2.43	4.70	4.69	6.19	1.50	0.38	0.09
LET25	350.50	0.70	64.93	28.60	1.81	1.98	2.22	3.65	2.11	0.12	0.15
LET27	273.75	1.37	36.55	31.15	3.95	6.25	5.44	8.12	3.92	0.10	0.37
LET28	380.75	0.60	128.51	30.75	3.74	3.88	3.33	5.41	2.40	0.03	0.10
LET29	128.40	1.05	28.53	9.29	2.06	3.44	1.71	2.45	1.41	0.21	0.26
LET30	145.00	1.32	42.75	18.90	3.24	2.37	2.33	2.38	0.22	0.11	0.22
LET31	266.00	1.08	56.00	28.50	3.81	5.82	4.12	7.74	2.69	0.52	0.20
LET38	84.22	1.57	54.73	12.54	2.27	13.73	8.54	15.51	9.63	0.04	0.09
LET47	127.00	0.88	87.72	12.68	1.76	4.35	4.27	6.39	3.32	0.03	0.19
LET48	86.00	0.90	47.75	59.21	4.92	1.99	2.27	9.73	3.16	1.76	0.23
LET49	196.80	1.57	10.06	31.93	2.08	3.86	3.81	7.44	6.75	5.92	0.11
LET58	91.75	1.05	58.54	27.23	5.30	5.22	4.17	5.71	4.29	0.85	0.33
LET63	332.50	0.61	6.26	6.87	0.77	4.13	3.67	6.88	3.70	1.76	0.09
LET64	121.00	1.80	27.25	25.44	3.15	6.42	6.41	10.05	7.48	0.24	0.60

Table 3.15 (continued) PGE, Re and selected major and trace element abundances for Lesotho peridotites.

Samples	S (ppm)	Al_2O_3 (wt%)	(La/Yb)n	Ba (ppm)	Nb (ppm)	Os (ppb)	Ir (ppb)	Ru (ppb)	Pt (ppb)	Pd (ppb)	Re (ppb)
Thaba Putsoa											
TP6	90.00	0.67	18.61	4.87	1.50	5.46	5.95	9.98	4.00	0.06	0.02
TP7	73.00	1.06	30.27	19.09	3.75	2.44	2.63	2.95	0.80	0.21	0.03
TP9	57.00	0.89	11.51	6.82	1.55	4.57	4.51	7.25	4.28	0.10	0.02
Liqhobong											
LQ1	294.75	1.17	18.50	52.10	2.02	0.20	0.33	4.64	0.17	0.03	0.01
LQ5	28.00	1.76	34.23	7.62	1.89	6.56	6.34	8.78	2.28	0.09	0.01
LQ6	60.00	1.48	10.18	15.60	1.79	2.17	2.98	3.93	2.42	0.30	0.11
LQ8	19.00	1.22	28.01	19.87	1.90	3.82	3.75	5.36	2.47	0.17	0.01
LQ9	60.00	1.47	55.59	19.40	3.10	6.68	7.83	12.42	4.30	0.07	0.02
Matsoku											
M1	122.00	0.82	6.29	13.06	10.00	2.21	2.27	4.23	3.37	2.69	0.16
M3	274.50	1.98	1.50	9.38	33.34	0.82	0.94	1.56	1.50	1.36	0.26
M5	60.00	1.49	40.54	29.46	2.81	3.16	3.36	5.47	3.41	1.31	0.09
M6	42.50	1.46	46.29	26.08	4.00	2.95	3.29	5.21	2.79	1.02	0.08
M8	97.00	1.46	37.60	25.21	2.77	4.38	5.04	7.23	5.50	2.10	0.08
M9	22.25	1.46	16.05	16.84	1.90	9.55	7.89	9.56	6.50	0.06	0.01
M11	56.00	1.33	44.94	18.13	3.42	4.24	2.35	6.03	2.26	0.33	0.03
M13	83.00	0.86	73.72	27.73	2.26	5.36	4.28	4.56	1.90	0.09	0.03
Primative mantle	250	4.44	1.47	6.6	0.658	3.4	3.2	5	7.1	3.9	0.28
CI chondrite	54,000	1.62	1.47	2.41	0.24	490	455	710	1,010	550	40
Lesotho Range						13.73 - 0.2	8.54 - 0.33	15.51 - 1.42	9.63 - 0.17	5.92 - 0.02	0.6 - 0.01
Lesotho Average						4.28	3.87	6.22	3.03	0.66	0.14

alkali-basalt hosted spinel peridotites (Morgan *et al.*, 1981; Handler and Bennett, 1999). Overall, IPGE (Ir, Os, Ru) abundances for Lesotho peridotites are higher than primitive mantle estimates (McDonough and Sun, 1995, Table 3.15), whereas the PPGE (Pt, Pd) abundances are depleted. This is consistent with the major-element depleted nature of the Lesotho peridotites and suggests that the PGEs have been fractionated during melt extraction, as would be expected from their differing compatibilities (Rehkämper *et al.*, 1999b). IPGEs from the Lesotho peridotites have similar abundances to those for orogenic massifs (Pattou *et al.*, 1996; Lorand *et al.*, 1999), but tend to be higher than those of spinel peridotites (Morgan *et al.*, 1981; Handler and Bennett, 1999). In contrast, PPGE abundances within the Lesotho samples are depleted relative to both orogenic massifs and alkali-basalt hosted spinel peridotites.

3.6.3.b Covariation of PGEs in Lesotho peridotites

Iridium shows good positive correlations with Os and Ru, at close to chondritic ratios (Figure 3.25). Correlation coefficients for Os, and Ru, with Ir for the entire Lesotho suite are r = 0.90 and 0.86 respectively. Xenoliths from individual kimberlite pipes within the suite show different levels of correlation (Table 3.16).

Location	Correlation coefficients		
	Os-Ir	Ru-Ir	n
Lesotho	0.90	0.86	35
Letseng-la-terae	0.92	0.86	19
Thaba Putsoa	0.99	1	3
Liqhobong	0.98	0.89	5
Matsoku	0.93	0.9	8

Table 3.16 Summary of correlation coefficients for IPGEs within the Lesotho low-T peridotite suite, and individual kimberlites.

Those from the Letseng kimberlite mirror the overall correlation of the Lesotho sample set, with xenoliths from Thaba Putsoa, Liqhobong and Matsoku showing better correlations. This is probably a reflection of the number of samples from the individual kimberlites and their overall contribution to the Lesotho data-set. The mean chondrite normalised Os/Ir ratio, $(Os/Ir)_n$, for the Lesotho peridotites is marginally superchondritic at 1.01, whilst $(Ru/Ir)_n$ is clearly superchondritic at 1.37 (Table 3.17). The PPGEs, in contrast to the IPGEs, show very little overall systematic correlation with Ir (Figure 3.25). The Ir-Pt variation for the whole suite has a correlation coefficient of r = 0.77. No correlation exists at all for both Pd and Re. The mean chondrite normalised ratios for Pt, Pd and Re with Ir, $(Pt/Ir)_n$, $(Pd/Ir)_n$ and $(Re/Ir)_n$, are subchondritic (Table 3.17).

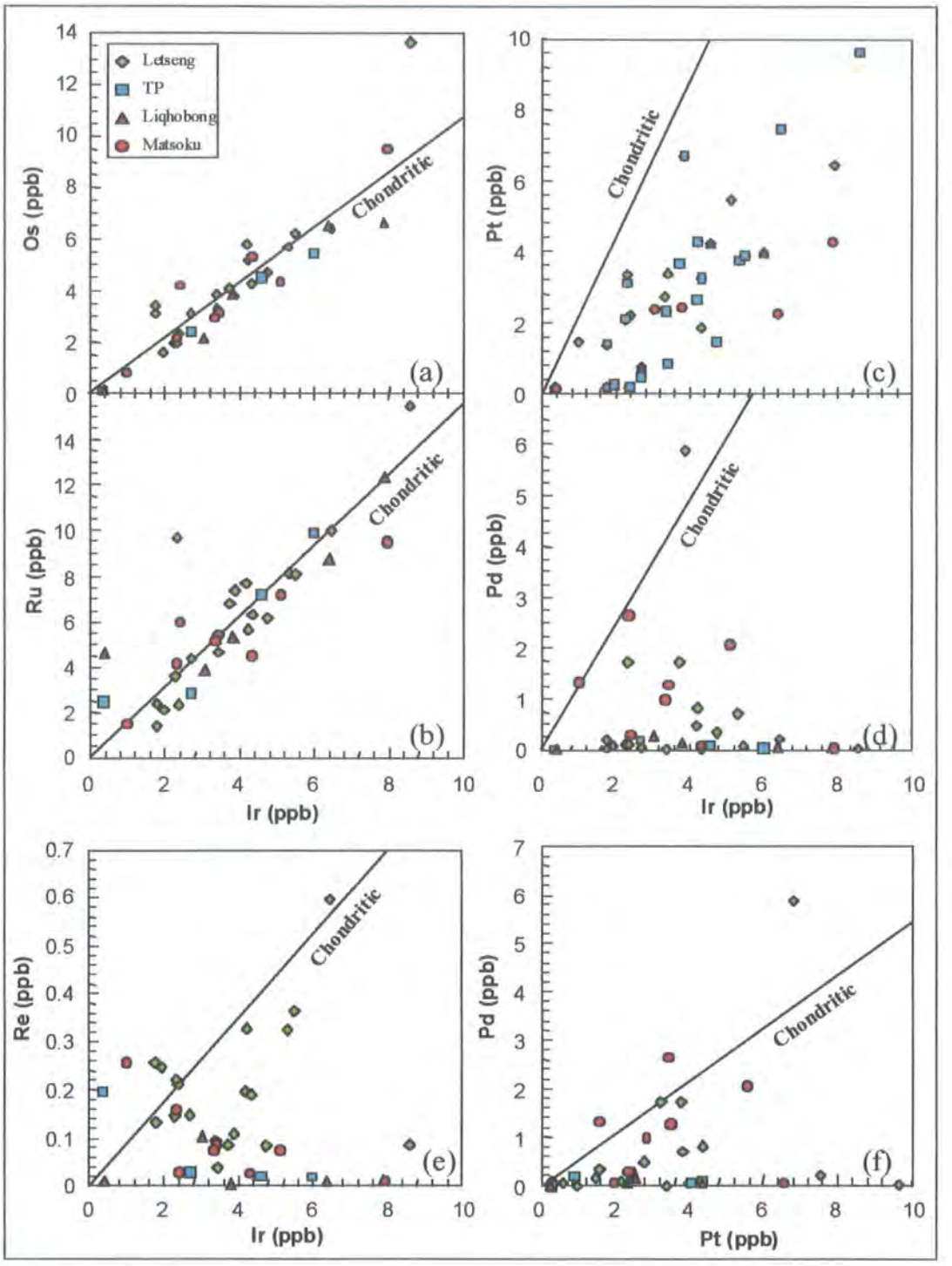

Figure 3.25 Bivariate PGE abundance plots for the Lesotho peridotite suite. (a-e) Os, Ru, Pt, Pd and Re versus Ir. (f) Pd versus Pt. The positive correlation between Os, Ru and Ir (r = 0.90 and 0.86 respectively), may suggest these elements are controlled by the same phases in the xenoliths. None of the remaining PGEs or Re correlate with Ir or each other. Chondritic ratio from McDonough and Sun (1995).

Table 3.17 Cl-chondrite normalised PGEs and PGE ratios for the Lesotho peridotite suite. Chondrite normalised using normalisation values of M^{c}Donough and Sun (1995).

Samples	Os	Ir	Ru	Pt	Pd	Re	(Os/Ir)n	(Ru/Ir)n	(Pt/Ir)n	(Pd/Ir)n	(Re/Ir)n
Letseng											
LET2	0.0117	0.0116	0.0115	0.0037	0.0013	0.0082	1.01	1.00	0.32	0.12	0.71
LET6	0.0065	0.0038	0.0020	0.0002	0.0001	0.0034	1.72	0.53	0.05	0.02	0.90
LET8	0.0033	0.0042	0.0030	0.0003	0.0002	0.0063	0.79	0.73	0.07	0.04	1.51
LET12	0.0064	0.0058	0.0062	0.0005	0.0001	0.0038	1.11	1.07	0.09	0.02	0.65
LET13	0.0068	0.0074	0.0066	0.0009	0.0000	0.0010	0.91	0.89	0.12	0.01	0.14
LET14	0.0096	0.0103	0.0087	0.0015	0.0007	0.0022	0.93	0.85	0.14	0.07	0.21
LET25	0.0040	0.0049	0.0051	0.0021	0.0002	0.0038	0.83	1.06	0.43	0.05	0.77
LET27	0.0128	0.0120	0.0114	0.0039	0.0002	0.0092	1.07	0.96	0.32	0.02	0.77
LET28	0.0079	0.0073	0.0076	0.0024	0.0001	0.0024	1.08	1.04	0.32	0.01	0.33
LET29	0.0070	0.0038	0.0035	0.0014	0.0004	0.0065	1.86	0.92	0.37	0.10	1.72
LET30	0.0048	0.0051	0.0033	0.0002	0.0002	0.0054	0.95	0.65	0.04	0.04	1.06
LET31	0.0119	0.0091	0.0109	0.0027	0.0009	0.0050	1.31	1.20	0.29	0.10	0.55
LET38	0.0280	0.0188	0.0219	0.0095	0.0001	0.0022	1.49	1.16	0.51	0.00	0.12
LET47	0.0089	0.0094	0.0090	0.0033	0.0001	0.0048	0.95	0.96	0.35	0.01	0.51
LET48	0.0041	0.0050	0.0137	0.0031	0.0032	0.0056	0.81	2.75	0.63	0.64	1.13
LET49	0.0079	0.0084	0.0105	0.0067	0.0108	0.0028	0.94	1.25	0.80	1.28	0.34
LET58	0.0107	0.0092	0.0080	0.0042	0.0015	0.0083	1.16	0.88	0.46	0.17	0.91
LET63	0.0084	0.0081	0.0097	0.0037	0.0032	0.0022	1.04	1.20	0.45	0.40	0.28
LET64	0.0131	0.0141	0.0142	0.0074	0.0004	0.0149	0.93	1.00	0.53	0.03	1.06

Table 3.17 (continued) CI-chondrite normalised PGEs and PGE ratios for the Lesotho peridotite suite.

Samples	Os	Ir	Ru	Pt	Pd	Re	(Os/Ir)n	(Ru/Ir)n	(Pt/Ir)n	(Pd/Ir)n	(Re/Ir)n
Thaba Putsoa											
TP6	0.0111	0.0131	0.0141	0.0040	0.0001	0.0005	0.85	1.07	0.30	0.01	0.04
TP7	0.0050	0.0058	0.0041	0.0008	0.0004	0.0008	0.86	0.72	0.14	0.06	0.14
TP9	0.0093	0.0099	0.0102	0.0042	0.0002	0.0006	0.94	1.03	0.43	0.02	0.06
Liqhobong											
LQ1	0.0004	0.0007	0.0065	0.0002	0.0001	0.0003	0.57	8.96	0.23	0.08	0.44
LQ5	0.0134	0.0139	0.0124	0.0023	0.0002	0.0003	0.96	0.89	0.16	0.01	0.02
LQ6	0.0044	0.0066	0.0055	0.0024	0.0006	0.0026	0.67	0.84	0.37	0.08	0.40
LQ8	0.0078	0.0082	0.0075	0.0024	0.0003	0.0002	0.95	0.92	0.30	0.04	0.03
LQ9	0.0136	0.0172	0.0175	0.0043	0.0001	0.0004	0.79	1.02	0.25	0.01	0.02
Matsoku											
M1	0.0045	0.0050	0.0060	0.0033	0.0049	0.0041	0.90	1.19	0.67	0.98	0.82
M3	0.0017	0.0021	0.0022	0.0015	0.0025	0.0065	0.82	1.07	0.72	1.19	3.15
M5	0.0064	0.0074	0.0077	0.0034	0.0024	0.0023	0.87	1.04	0.46	0.32	0.30
M6	0.0060	0.0072	0.0073	0.0028	0.0018	0.0020	0.83	1.01	0.38	0.26	0.27
M8	0.0089	0.0111	0.0102	0.0054	0.0038	0.0019	0.81	0.92	0.49	0.34	0.17
M9	0.0195	0.0173	0.0135	0.0064	0.0001	0.0004	1.12	0.78	0.37	0.01	0.02
M11	0.0086	0.0052	0.0085	0.0022	0.0006	0.0008	1.67	1.64	0.43	0.12	0.16
M13	0.0109	0.0094	0.0064	0.0019	0.0002	0.0008	1.16	0.68	0.20	0.02	0.08

3.6.3.c PGE patterns of Lesotho peridotites

Chondrite normalised PGE patterns track melt depletion and enrichment events in peridotites, similar to the way REEs mirror these processes (Lorand *et al.*, 1999; Rehkämper *et al.*, 1999a), and therefore provide a useful means for interpreting the Re-Os isotope systematics.

IPGEs within the Lesotho peridotites range from 0.0004 to 0.028 x CI chondrite (mean = 0.0087 x CI chondrite), and show flat chondrite normalised pattern with little intra-element fractionation (Figure 3.26; Table 3.17). This is considered by O'Neill (1991) to be characteristic of PGE patterns for upper-mantle peridotites. Such behaviour displays the compatible nature of the IPGEs (Os, Ir and Ru) in mantle melting processes (Barnes *et al.*, 1985; Brügmann *et al.*, 1987; Barnes and Picard, 1993; Reisberg and Lorand, 1995). The overall range in IPGE abundances within the suite may be the reflection of a heterogeneous ("nugget effect") distribution of PGEs within the mantle. Several samples show non-chondrititic Os/Ru and Ir/Ru ratios, which again may be attributable to "nugget effects" of different PGE host minerals.

PPGEs in the Lesotho peridotites are highly variable, with samples showing strongly fractionated, rather than flat chondritic patterns (cf. O'Neill, 1991). This behaviour is essentially consistent with the moderately incompatible nature of PPGEs. On the basis of the shape of the PPGE part of the PGE patterns, five groups of peridotites have been ascertained in the Lesotho peridotite suite (Figure 3.26a-e) which will be outlined below.

3.6.3.d Fractionation of PGEs within the Lesotho peridotites

PPGE depleted peridotites (Group A)

One sample from Liqhobong, sample LQ8, has highly fractionated PPGEs (Figure 3.26a), with marked depletions in Pd and Re, an intermediate depletion in Pt and $(Pd/Ir)_n$ of 0.037 (Tables 3.17 and 3.18). This pattern is that expected for a peridotite having undergone extensive degrees of melt extraction, and in the Lesotho suite this depletion trend is much more apparent than in harzburgitic residues from Pyrenean orogenic massifs (cf. Lorand *et al.*, 1999). The depleted PGE pattern of LQ8 suggests that the system has remained closed with respect to PGEs since the time of melt extraction and that melt extraction was sufficient to exhaust residual sulfides.

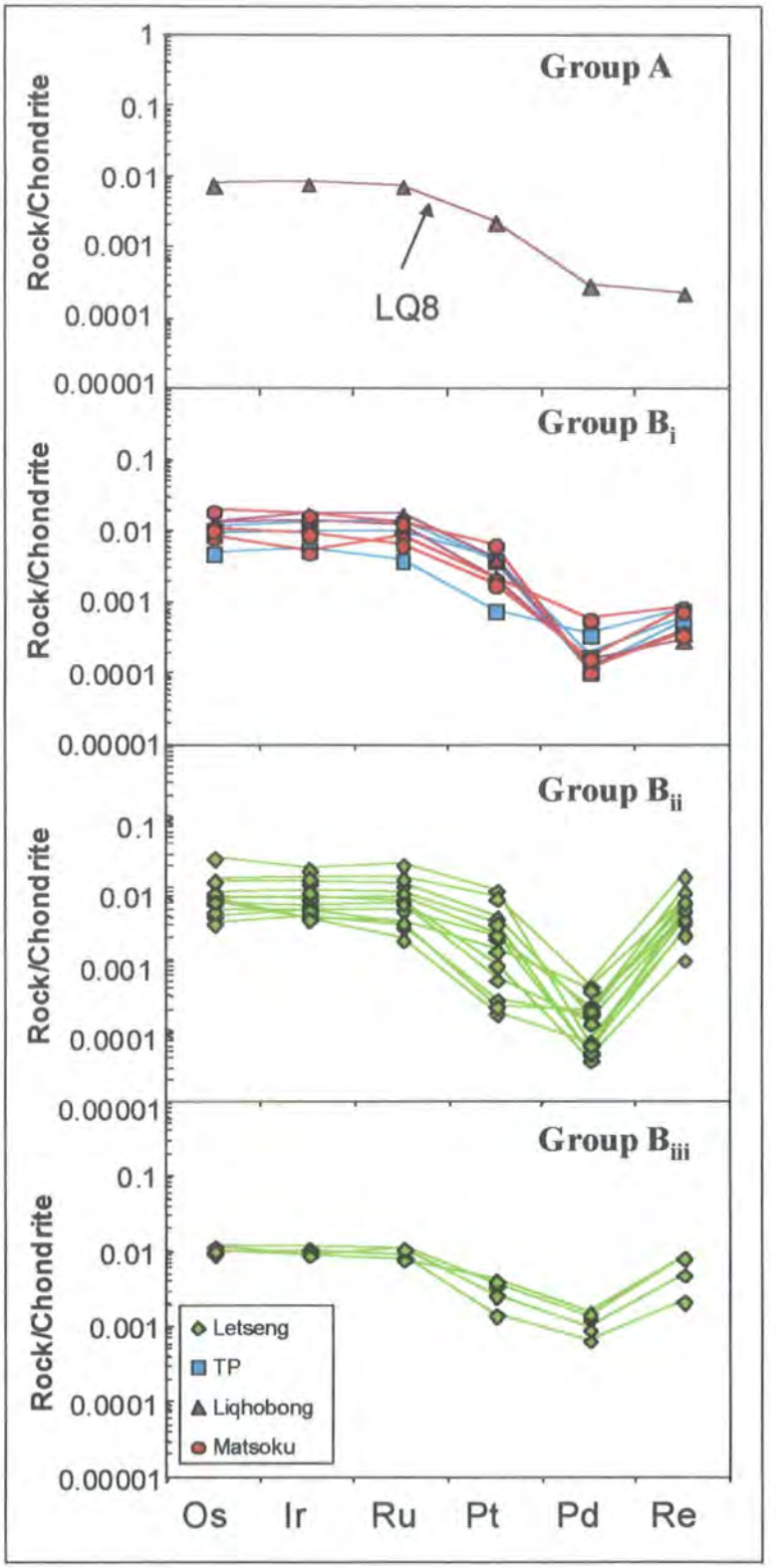

Figure 3.26 CI-chondrite normalised PGE patterns for the Lesotho peridotite suite. Group A - PPGE depleted pattern, Group Bi - PPGE depleted pattern with Re enrichment, Group Bii - PPGE depleted pattern with more pronounced Re enrichment, and Group Biii - PPGE depleted pattern with pronounced Re and possible Pd enrichment. CI chondrite values from McDonough and Sun (1995).

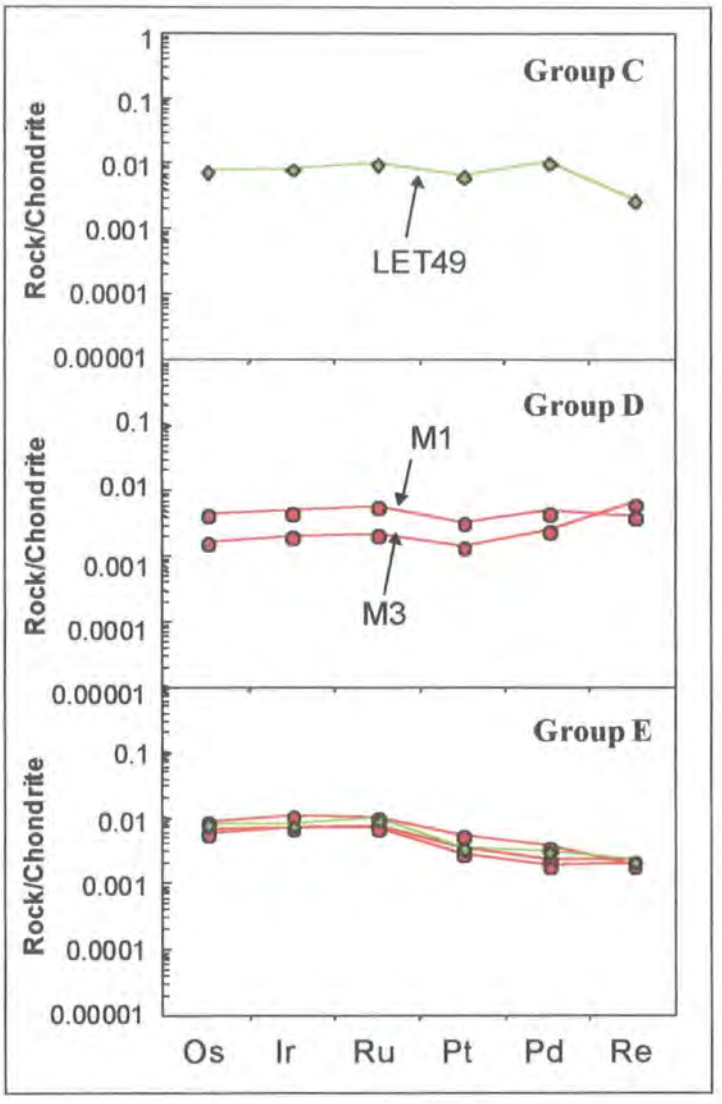

Figure 3.26 (continued) CI-chondrite normalised PGE abundances for the Lesotho peridotite suite. Group C - Re and Pd enriched peridotites, Group D - Re and Pd enriched peridotites, and Group E - moderately depleted peridotites?

PPGE depleted peridotites with Re enrichment (Group B)

This group of samples also has a marked depletion in PPGEs (Figure 3.26b_{i-iii}), but has varying Re contents with a marked upwards inflections in the extended chondrite-normalised PGE patterns. This may reflect secondary Re addition to the peridotite, perhaps by the host kimberlite. This group has been further divided into 3 sub-groups (i to iii) related to the degree of Re inflection, and for group {iii} possible Pd addition to the peridotite samples. Low $(Pd/Ir)_n$ for subgroups {i} (0.007 to 0.117) and {ii} (0.004 to 0.102) support the notion that these samples represent variably but extensively depleted peridotites and hence suggests that the samples have experienced later Re introduction (Tables 3.17 and 3.18). The low $(Pd/Ir)_n$ for subgroup iii (0.067 to 0.169)

Table 3.18 Summary of PGE behaviour within the Lesotho peridotites, on the basis of the shape of the PPGE part of the PGE patterns. Average whole-rock elemental abundances and PGE ratios on the basis of PPGE determined groups.

Group	PGE Pattern	Pd (ppb)	Re (ppb)	S (ppm)	Al_2O_3 (wt%)	Ba (ppm)	Nb (ppm)	$(Pd/Ir)_n$	$(Re/Ir)_n$	$(Re/Pt)_n$
A	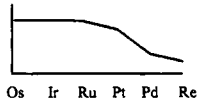	0.17	0.01	19	1.22	19.9	1.9	0.04	0.03	0.10
B_i	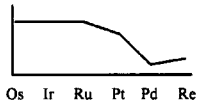	0.13	0.02	58.7	1.19	15.1	2.4	0.03	0.07	0.30
B_{ii}	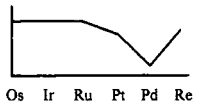	0.09	0.21	205	1.05	23.8	2.6	0.03	0.8	7.27
B_{iii}	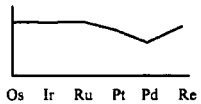	0.62	0.24	173	0.88	25.5	3.7	0.11	0.6	1.89
C	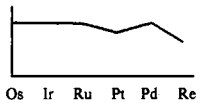	5.92	0.11	197	1.57	31.9	2.1	1.28	0.34	0.42
D	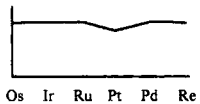	2.02	0.21	198	1.40	11.2	21.7	1.09	1.98	2.81
E	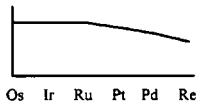	1.54	0.08	133	1.25	21.9	2.6	0.33	0.26	0.59

also suggests that these peridotites represent variably depleted peridotites, but these have either undergone lower degrees of melt extraction, or alternatively they have experienced later Pd enrichment. Sub-groups ii and iii have experienced a greater degree of Re enrichment in comparison to sub-group i, and show greater inflections in their chondrite-normalised PGE patterns.

PPGE depleted peridotites with Pd enrichment (Group C)

One sample from Letseng, LET49, shows a noticeable depletion in Pt similar to that seen in the other groups. However Pd is considerably more enriched (Figure 3.26c) in this sample and this may be an indication that Pd has been re-introduced to the peridotites after the melt extraction event. Re appears to be depleted in this sample and has not obviously been enriched along with Pd. The chondrite-normalised Pd/Ir ratio for this sample is 1.28 (Tables 3.17), and indicates that $(Pd/Ir)_n$ may be a poor indicator of depletion within these peridotites without consideration of Pt, and more particularly Re. This emphasises the value of having both PGE and Re data, which most PGE analytical methods do not achieve.

The enrichment of Pd in this group of peridotites suggests that Re and Pd may be decoupled in metasomatising fluids, i.e. the Re and Pd may have been disturbed or re-introduced by separate events. Without Pd as a reference within the PGE pattern it is difficult to ascertain whether Re has been enriched to any degree, or whether the system has remained closed with respect to Re.

PPGE depleted peridotites with Pd and Re enrichment (Group D)

Two samples from Matsoku, M1 and M3, show marked depletion in Pt, as seen for all other Lesotho peridotites (Figure 3.26d). Both Re and Pd within these samples has clearly been enriched and they have chondrite-normalised Re/Pt ratios > 1 (Tables 3.17 and 3.18).

Moderately fractionated PPGE peridotites? (Group E)

This group of peridotites display what could be interpreted as moderately fractionated PPGEs relative to IPGEs, in response to melt depletion (Figure 3.26e). Fractionation of the PPGEs is not so marked and this is reflected in $(Pd/Ir)_n$ ranging from 0.26 to 0.40 (Tables 3.17 and 3.18). These samples may represent the residues of relatively low degrees of melting, and as such may retain higher abundances of PPGEs in the residua. Alternatively, such patterns could originate from highly PPGE depleted samples that have experienced some later PPGE addition. It is therefore difficult to ascertain whether the system has remained closed with respect to Re infiltration without further knowledge of the degree of melt removal and the mobility of sulfides and PGEs. Slight

inflections in the chondrite-normalised PGE pattern for samples M5 and M6 at Re would make the latter model more likely. Likewise, sample LET63 appears to have a nominal inflection in its PGE pattern at Pd.

PGE fractionation

The depletion of PPGEs in the Lesotho peridotite xenoliths is consistent with their major-element-depleted nature, and suggests that the PGEs have been fractionated during melt extraction. Relative compatibility of PGEs during fractionation, through melt extraction, based on the evidence from the chondrite-normalised patterns of peridotites from Lesotho, is in the order Os ~ Ir ~ Ru > Pt > Pd ≥ Re. This is consistent with the order of fractionation seen in melts derived from the mantle (Barnes *et al.*, 1985; Woodland, 2000), and supports the order in which these elements are placed on chondrite-normalised patterns.

In contrast to the ubiquitous enrichment of LREEs in whole-rock peridotites, PGEs invariably have PPGE depleted patterns, generally retaining some vestiges of a depleted character with sub-chondritic abundances of Pt and Pd, i.e. the incompatible PGEs. Some samples retain very PPGE and Re depleted characters, even when showing typical LREE enrichment. Thus, lithophile elements are largely decoupled from chalcophile/siderophile elements, as seen in their isotopic signatures (Pearson *et al.*, 1995a).

3.6.4 PGE variation with whole-rock chemistry

3.6.4.a Variation of PGEs with sulfur

High abundances of PGEs measured in sulfides (Jagoutz *et al.*, 1979; Hart and Ravizza, 1996; Pattou *et al.*, 1996; Pearson *et al.*, 1998b; Burton *et al.*, 1999; Alard *et al.*, 2000; Pearson *et al.*, 2000) have been the main argument for sulfides being the primary hosts for PGEs in the mantle. It has often been speculated however that the IPGEs are controlled by refractory phases such as Ir-Os alloys rather that sulfides (Mitchell and Keays, 1981; Fryer and Greenough, 1992, Garuti, 1997 #1558; Brennan and Andrews, in press). Sulfides would normally be present as *mss* or molten sulfides under normal lithospheric mantle conditions but would re-equilibrate to low temperature phases during emplacement of the xenolith (Keays *et al.*, 1981). The existence of sulfide phases that are PGE specific, such as Pt in PtS and Ru in Laurite, suggests that PGEs do not necessarily partition equally if such phases exist.

The control that sulfides have on PGEs within the Lesotho peridotites can be assessed through comparison of PGE and S abundances. Within the mantle sulfur is a moderately incompatible element and behaves coherently during mantle melting processes (Lorand, 1989; Lorand, 1991; Garuti *et al.*, 1997). In contrast PGEs have high partition coefficients into sulfides, of the order $D_{sulf} \sim 2500$ to 310000 (Peach *et al.*, 1994; Fleet *et al.*, 1996). Unless all sulfide within the mantle is consumed (~25% melting) and the melt nears saturation (Keays, 1995), no correlation between S and PGEs should necessarily exist for the peridotites.

Estimates for the abundance of S in fertile mantle vary, but are normally less than 300 ppm (Peach and Mathez, 1996). Sulfur concentrations within Lesotho peridotites range from 19 to 381 ppm, i.e. from highly depleted, to enriched relative to a fertile mantle source. Little overall correlation appears to exist between PGEs and S in the Lesotho peridotite suite (Figure 3.27).

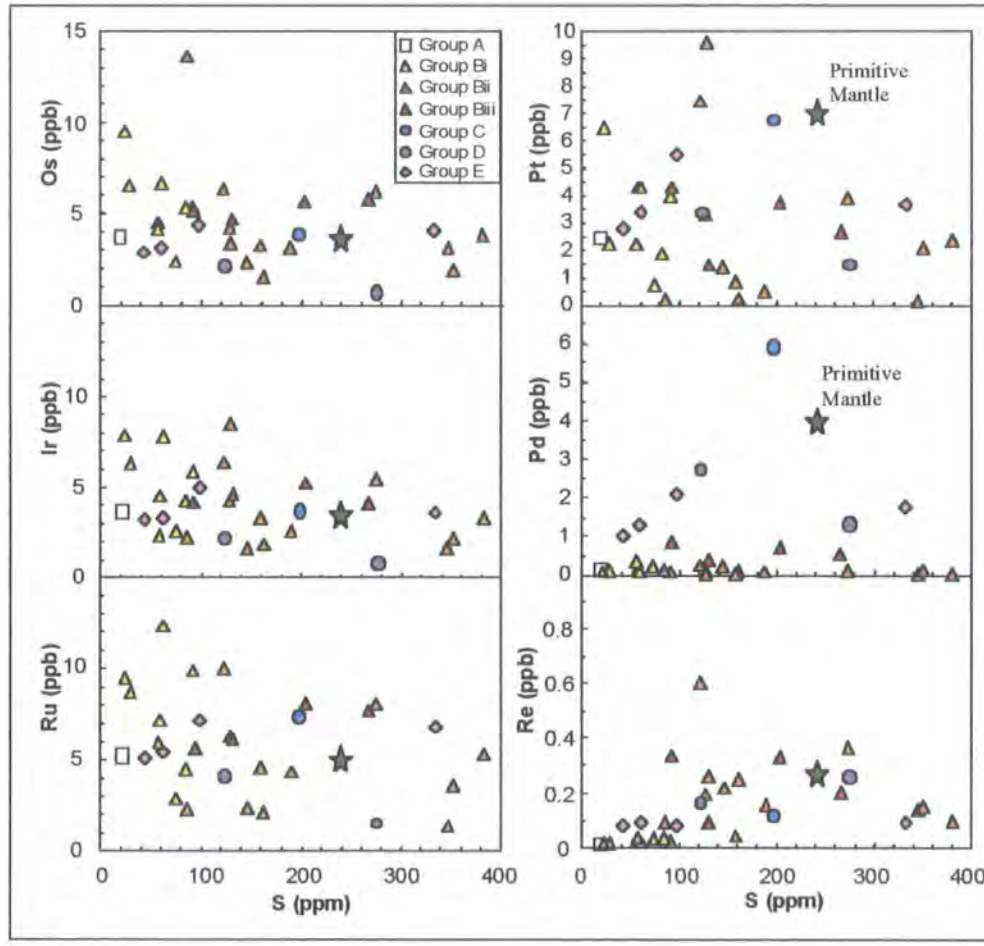

Figure 3.27 PGE and Re abundances versus S content for the Lesotho peridotite suite. Primitive mantle represented by star, after McDonough and Sun (1995).

The Lesotho peridotites show flat chondritic IPGE patterns, but also show varying absolute abundances within individual peridotites. If the individual peridotite xenoliths do not derive from the same homogeneous source, it would not be surprising that they show no positive correlations with sulfur overall. Alternatively, poor PGE-S correlations may simply reflect metasomatism, as observed for Pyrenean peridotites by Lorand *et al* (1999). IPGEs would appear to be less susceptible to melt-related metasomatism than PPGEs, on the basis of their higher compatibility and chondritic behaviour.

In detail, systematic correlations between PPGE variations and sulfur exist in the Lesotho suite, particularly when considered in terms of their overall PGE patterns (Figure 3.28; Table 3.18). Group A peridotites represent melt depleted peridotites from extensive degrees of melt extraction and have low Pd, Re and Al_2O_3 abundances (Figure 3.28a; Table 3.18). Group B peridotites show variable amounts of Re enrichment associated with an enrichment in S (Figure 3.28a and 3.28b). The sub-group B_{iii} also has elevated Pd abundances associated with S enrichment (Figure 3.28b; Table 3.18). The third group of peridotites, Group C (Table 3.18), show Pd enrichment associated with an enrichment of S (Figure 3.28c). These samples also appear to have elevated Re abundances, also associated with S enrichment. The fourth group, Group D peridotites, show Pd enrichment but with a much more prominent Re enrichment (Figure 3.28c). Group E Lesotho peridotites show moderately fractionated PGE patterns that may represent the residues of relatively low degrees of partial melting. The peridotites in this group are poorly correlated however with respect to Pd, Re and S (Figure 3.28d). This group may represent the removal of Pd, Re and S with the melt fraction, and a perturbed depletion trend from a common homogeneous source. Alternatively the poor correlation of Pd, Re and S within the group may reflect initial depletion followed by variable enrichment in Pd, Re and S. This is supported by the S concentration of sample LET63, which is more enriched than fertile mantle at 333 ppm and suggests likely sulfide addition (Figure 3.28d). Higher Pd abundances in these samples do not necessarily correlate with higher S. This may simply represent higher initial abundances in the source rock rather than enrichment.

3.6.4.b Variation of PGEs with major elements

No overall systematic variation is observed between major elements, such as Al_2O_3, and PGE abundance for the Lesotho peridotites (Figure 3.29; Table 3.15), despite the

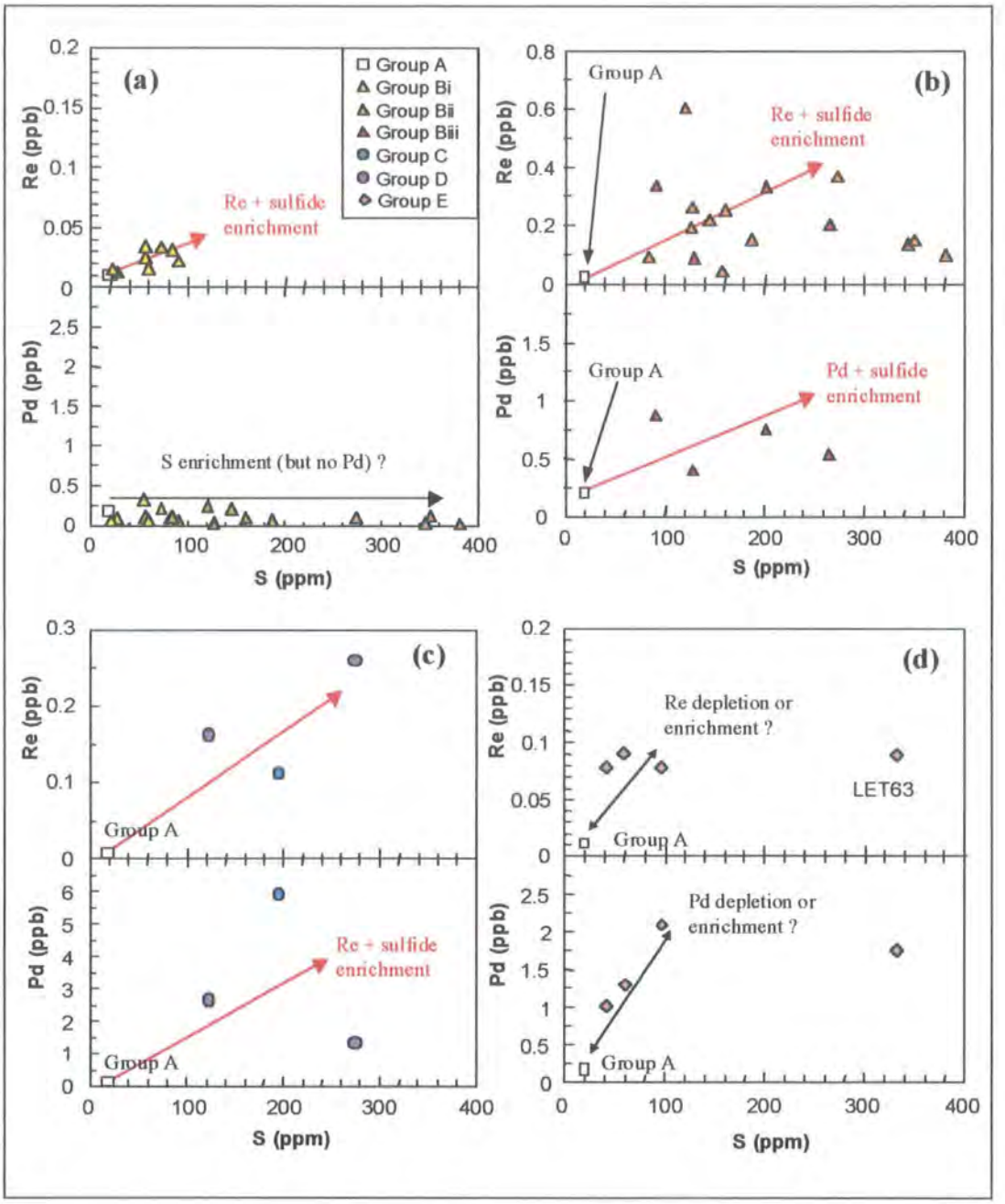

Figure 3.28 Pd and Re abundances versus S content for individual Lesotho peridotite groups, based on CI-chondrite normalised PGE patterns. (a) Group A and B peridotites, (b) Group B peridotites, (c) Group C and D peridotites and (d) Group E peridotites.

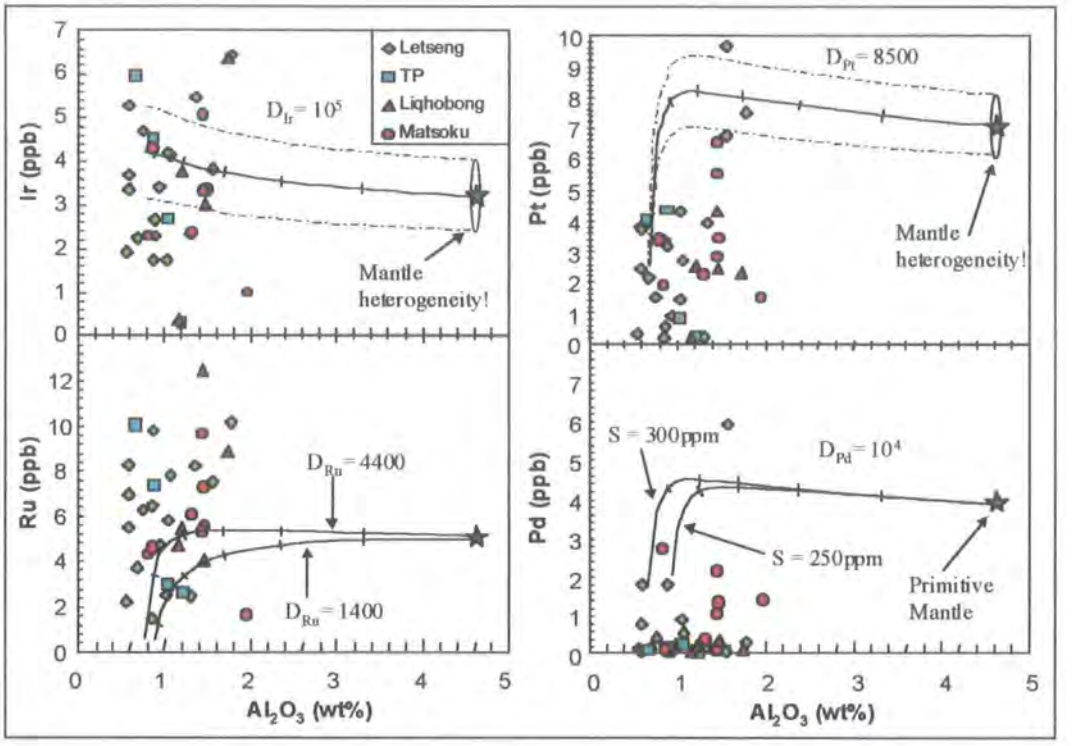

Figure 3.29 PGE abundances versus Al_2O_3. Predicted residue compositions are based on non-modal fractional melting models using a primitive mantle source ppm (represented by star symbol) with sulfur compositions of 250-300 ppm, and the extracted melts have a sulfur capacity of 1000 ppm S. The range of partition coefficients for PGEs, $D_{PGE(sul\ell melt)}$ is large (Stone *et al.*, 1990; Bezmen *et al.*, 1994; Peach *et al.*, 1994; Fleet *et al.*, 1996). A value of 10^4 for D_{Pd} has been used to model Pd based upon the good correlation found by Lorand *et al*(1999) in Pyrenean orogenic lherzolites. The value D_{Ir} was assumed to be an order of magnitude higher based upon contrasting behaviour of these two elements in the same study. D_{Ru} was modelled using values of 1400 and 4400, D_{Pt} a value of 8500. For comparison of models with xenolith data, F values were re-calculated as Al_2O_3 wt%. Varying S content of the source or S capacity of the melt does not significantly alter the melt extraction trends. Marks indicate 5% increments of melting.

large range in Al_2O_3 depletion. Due to their highly compatible nature, it is not surprising that IPGEs show no clear relationship with Al_2O_3. The PPGEs, which are moderately incompatible, also show no distinct correlations (Figure 3.29).

Correlations between the shapes of PGE patterns and bulk-rock Al_2O_3 contents are evident (Figure 3.30). These trends for Al_2O_3 mirror those observed for Sulfur-PGE relationships. Group A peridotites represent melt-depleted peridotites from extensive degrees of melt extraction, and have low Pd, Re and S abundances (Tables 3.15 and 3.18). Sample LQ8 of Group A seems to have experienced a degree of melt addition, reflected in an enhanced Al_2O_3 abundance for its PPGE and S content. The melt addition to this sample does not appear to have disturbed the PGE systematics of the peridotite, but merely displaces the sample to higher Al_2O_3 values (Figure 3.30a). Group B peridotites show no overall systematic correlation between Re and Al_2O_3 (Figure 3.30a and 3.30b). However, enrichment in Re is variably associated with enrichment in Al_2O_3. Peridotites from Group B_{iii} also show enrichment in Pd associated

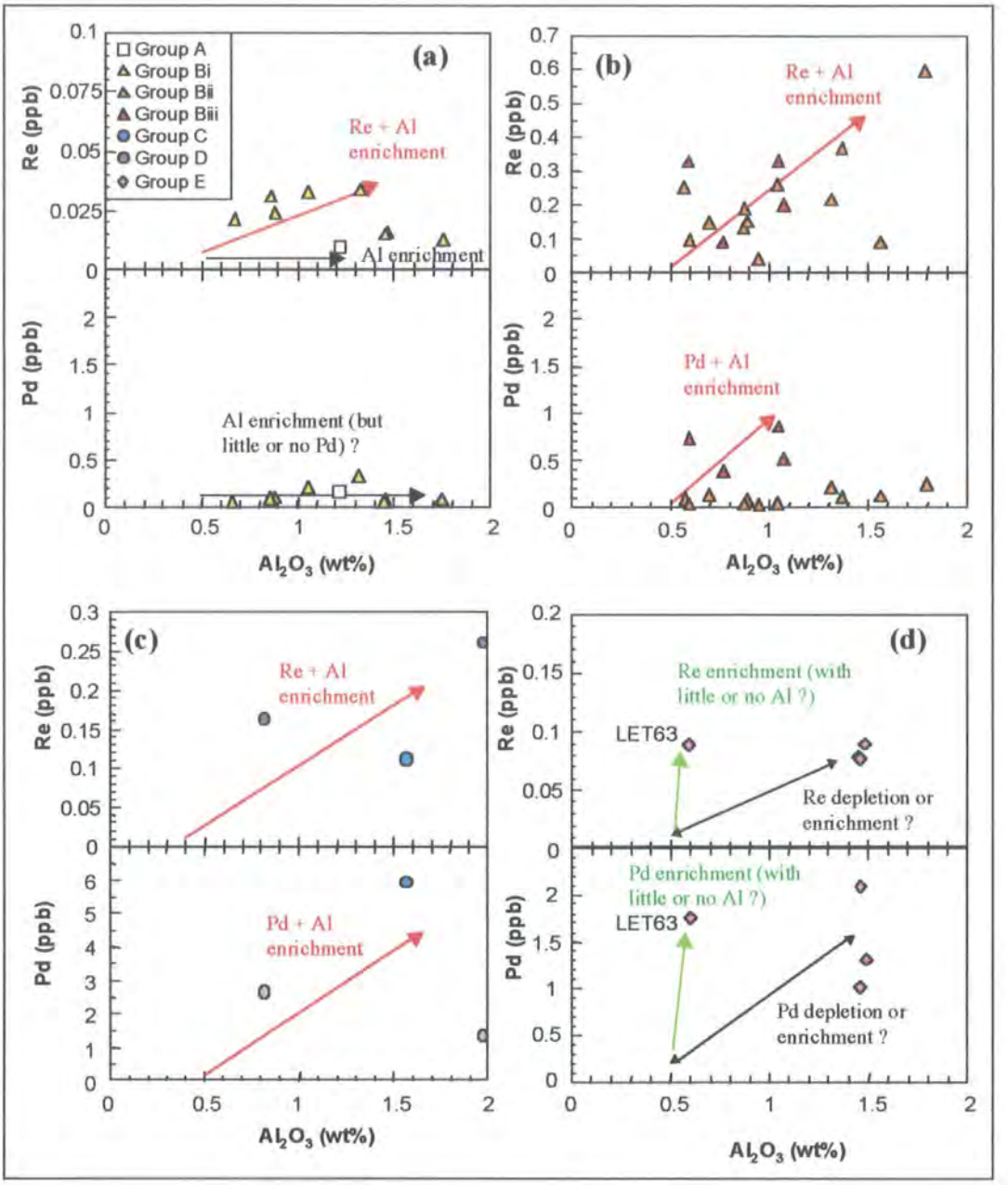

Figure 3.30 Pd and Re abundances versus Al_2O_3 content for the Lesotho peridotite, based on CI-chondrite normalised PGE patterns. (a) Group A and B peridotites, (b) Group B peridotites, (c) Group C and D peridotites, and (d) Group E peridotites.

with Al_2O_3 enrichment (Figure 3.30b). Group C peridotites show a pronounced enrichment in Pd associated with enrichment of Al_2O_3 (Figure 3.30c; Table 3.18), and a slight enrichment in Re. Peridotites from Group D show marked enrichments in both Pd and Re associated with Al_2O_3 (Figure 3.30d; Table 3.18). The samples designated as Group E peridotites, with moderately fractionated PGE patterns, show very little correlation between Pd, Re and Al_2O_3 (Figure 3.30d). Although the chondrite-normalised PGE patterns suggest that these samples may represent the removal of Pd and Re during small degrees of partial melting, the overall lack of correlation with Al_2O_3 would suggest that these samples represent depleted samples that have been variably enriched in Pd, Re and Al_2O_3. This is supported by elevated abundances of Al_2O_3 up to 1.49 wt%.

3.6.4.c Variation of PGEs with trace elements

In contrast to IPGEs, PPGEs are incompatible and fractionate during mantle melting and subsequent metasomatism. It is therefore more likely that trace elements will track the behaviour of PPGEs and may help to constrain the relative roles of fluid enrichment versus melt depletion.

PGE variation with REE: La and Yb

As observed in previous sections, the variation of PGEs within the Lesotho peridotite suite is not consistent with a single stage melt-extraction event alone, but suggests a more complex history. The CI-chondrite normalised PGE patterns from most Lesotho peridotites display the remnants of the original fractionation associated with melt extraction, manifested in the depletion of Pt and/or Pd abundances relative to IPGEs. Incompatible trace elements in contrast show strong enrichment rather than depletion. Neither abundances nor ratios of PGEs correlate with (La/Yb)n ratios. This is consistent with other studies which find that LILE-enriching processes do not significantly enrich chalcophile PGEs (Mitchell and Keays, 1981; Morgan *et al.*, 1981; Lorand, 1989).

PGE variation with hydrous fluid mobile elements

Both Re and Pd show a wide scatter when plotted against Ba, with no overall systematics or correlations discernible. If separated on the basis of CI-chondrite normalised PGE patterns, correlations are still generally poor, but it may be possible to derive systematics from the data. The variation in Pd and Re with Ba generally tends to mirror the variation of Pd and Re with Al_2O_3.

PGE variation with fluid immobile incompatible elements: Nb

Re and Pd also show a lack of correlation with high field strength elements such as Nb. Separated on the basis of CI-chondrite normalised PGE patterns, the variation in Pd and Re with Nb generally tends to reflect the variation of Pd and Re with Al_2O_3.

3.6.5 Re-Os and PGE systematics for Lesotho peridotite xenoliths

3.6.5.a Effects of alteration on Re and Os abundances

The alteration of peridotites through weathering processes may contribute to the modification of Os concentrations within the peridotites, by the possible leaching of sulfides (Lorand, 1990; Handler *et al.*, 1997). This process however will tend to reduce the Os concentrations within peridotites if primary sulfides are present. The Lesotho peridotites are relatively fresh, for cratonic peridotites, and even samples showing higher degrees of alteration, such as LET63 (up to 20% serpentinisation), have Re and Os concentrations close to the average for the Lesotho peridotite suite (Table 3.10). This has been observed before for peridotite xenoliths from the Kaapvaal craton, where samples showing up to 60% serpentinisation (FRB 1302) have Os concentrations indistinguishable from the average (Carlson *et al.*, 1999). As suggested by Lorand (1990) and Handler *et al* (1997), post-eruptive oxidation of xenoliths would be liable to remove the base metal sulfide (BMS) phase. Under such oxidising conditions, Burnham (1995) proposed that both Re and Os would be unstable as sulfide species. ReS_2 and OsS_2 would react with oxidising fluids and sulfur would be released in solution as sulfate ions. Rhenium would be soluble in the oxidising fluids and therefore lost, whilst Os remains as either metal or hydrated oxide grains (Burnham, 1995). This process does not explain the scatter seen in Os abundances within the Lesotho suite, nor does it explain the wide scatter to high Re abundances (Figure 3.24 and 3.31).

The spread in Os concentration as a function of major element depletion (Figure 3.31) may be related to the exsolution of the element from the mantle BMS phase under reducing conditions. This could result in the heterogeneous distribution of Os-bearing minerals such as Os-Ir alloys or laurite (Burnham, 1995).

Handler *et al* (1999) observed fractionation between Ir and Os within alkali-basalt hosted spinel peridotites, from Australia. This was attributed to the breakdown of sulfides and late stage Os mobility (Handler *et al.*, 1999). From Figure 3.32 it can be seen that the Ir/Os ratio of Lesotho peridotites tends to be near-chondritic with a mean of 0.99 +/- 0.27 (cf. Chondritic Ir/Os = 0.95, Anders and Grevesse, 1989; Jochum,

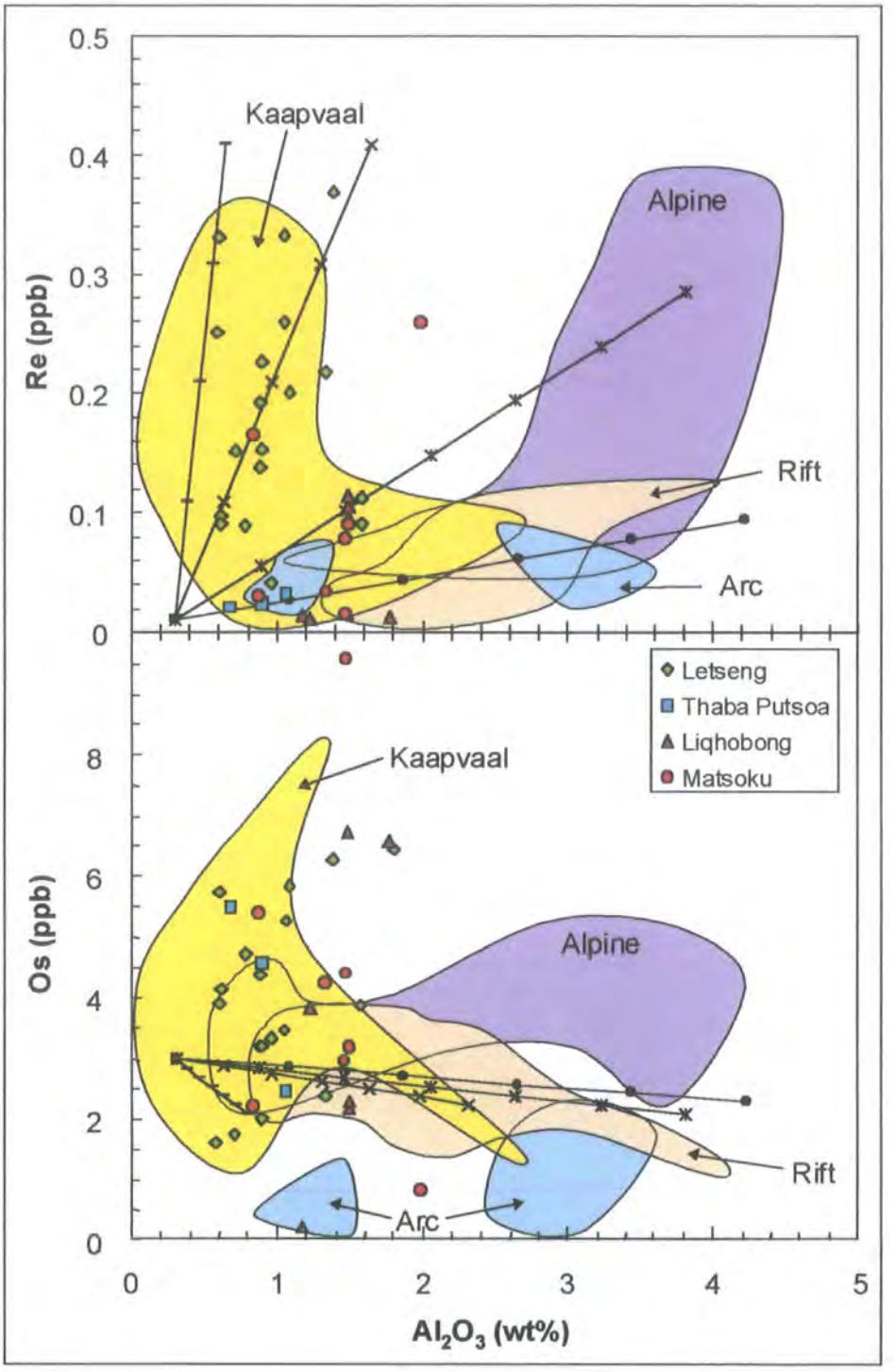

Figure 3.31 Re and Os concentrations (in ppb), plotted against Al_2O_3 content (in wt%). Cratonic peridotites from the Kaapvaal craton (Carlson *et al.*, 1999) represented by the yellow field. Alpine peridotite data (Reisberg *et al.*, 1991; Reisberg and Lorand, 1995) are shown by the purple field and rift-related spinel peridotites (Meisel *et al.*, 1996; Handler *et al.*, 1997) by the beige field. Spinel peridotites from "arc" settings are shown by the blue fields, one each for samples from the Simcoe volcano in the Cascades and the Itchinomegata volcano in the back arc of the Japanese convergent margin (Brandon *et al.*, 1996). The lines represent model mixing lines between an end-member depleted peridotite (Al_2O_3 = 0.3%, Re = 0.01ppb, Os = 3ppb, $^{187}Os/^{188}Os$ = 0.109) and possible metasomatising magmas, marks indicate 5% increments in the addition of magma. Carbonatite (horizontal hatching; Al_2O_3 = 2%, Re = 2ppb, Os = 0.002ppb, $^{187}Os/^{188}Os$ = 0.13; Shank *et al* (1992)), kimberlite (x; Al_2O_3 = 7%, Re = 2ppb, Os = 0.5ppb, $^{187}Os/^{188}Os$ = 0.13; Walker *et al* (1989)), average OIB (star; Al_2O_3 = 12%, Re = 0.35ppb, Os = 0.2ppb, $^{187}Os/^{188}Os$ = 0.135; Reisberg *et al* (1993), Roy-Barman and Allègre (1995), Hauri and Hart (1996) and Hauri *et al* (1996)) and average MORB (circle; Al_2O_3 = 16%, Re = 0.93ppb, Os = 0.002ppb, $^{187}Os/^{188}Os$ = 0.125; Roy-Barman and Allègre (1994) and Hauri and Hart (1996)).

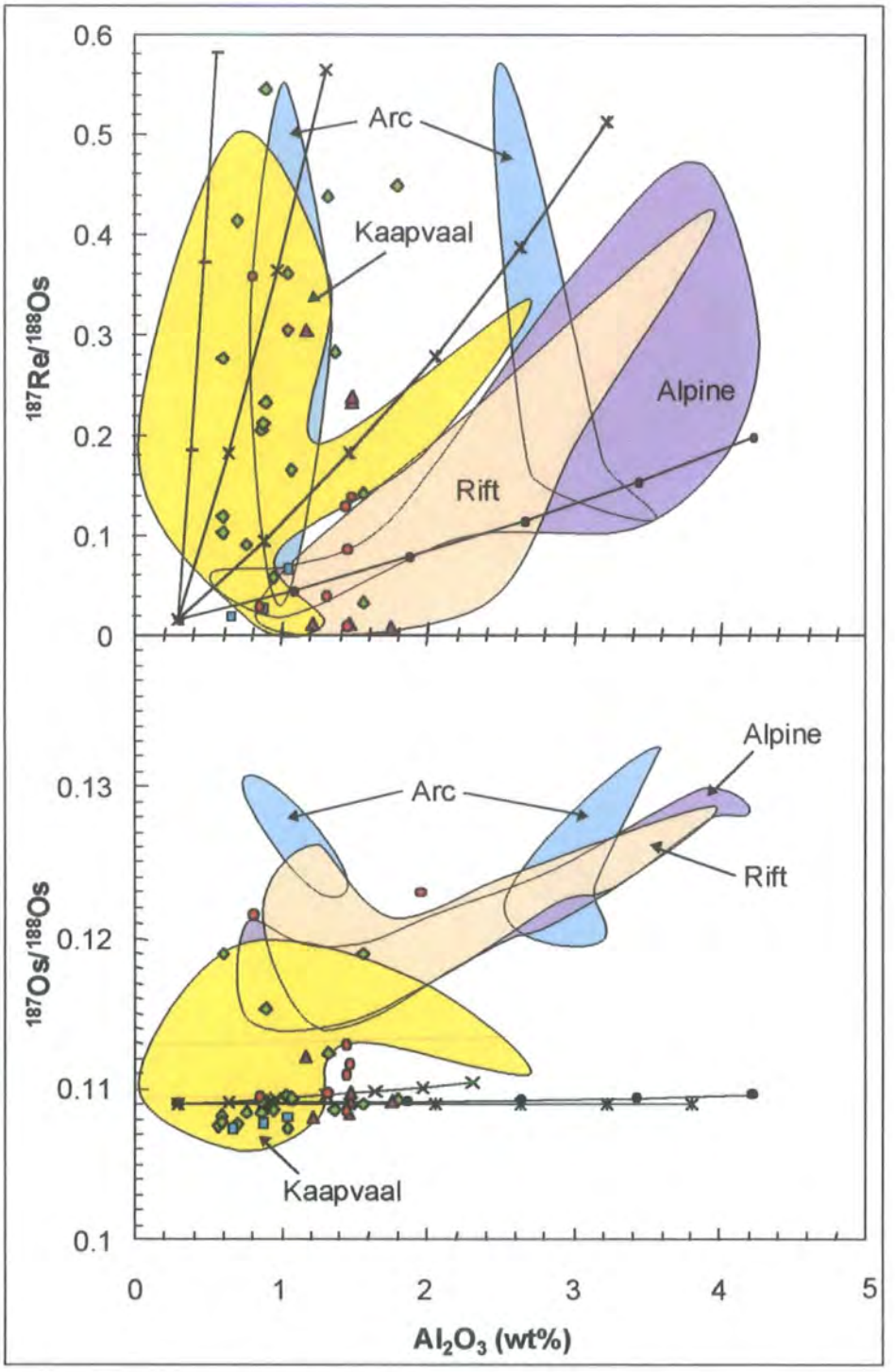

Figure 3.31 (continued) $^{187}Re/^{188}Os$ and $^{187}Os/^{188}Os$ plotted against Al_2O_3 content (in wt%).

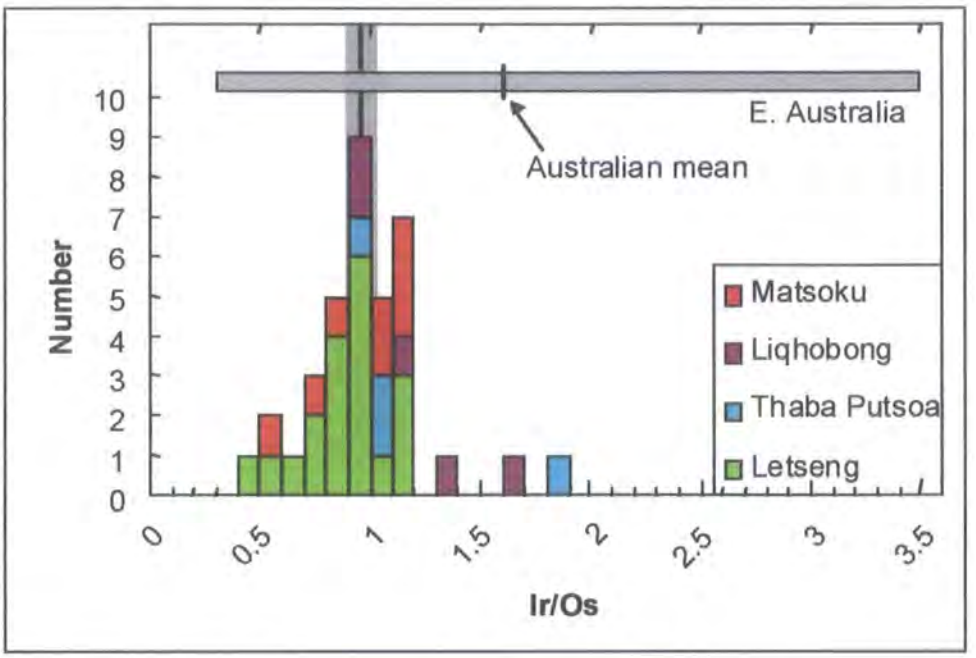

Figure 3.32 Histogram of Ir/Os ratios for Lesotho peridotites. Vertical line represents CI-chondrite Ir/Os and grey band represents 2σ error on mean from Anders and Grevesse (1989) and Jochum (1996). Australian xenolith data from Handler *et al* (1999).

1996), and there would appear to be little evidence for late stage Os loss through weathering in this suite.

Both these lines of evidence would suggest that Os and other IPGEs are not situated in sulfides, in the Lesotho peridotites.

3.6.5.b Behaviour of Re, Os and PGEs during partial melt extraction

Re behaviour during melt extraction

Rhenium concentrations should correlate with indices of melt extraction, such as Al_2O_3, if the Re characteristics of the xenoliths simply reflect partial melting processes operating on a homogeneous mantle source. Previous studies on Alpine peridotites have proposed that Re partitions into melts with a distribution coefficient similar to that of Al (Reisberg and Lorand, 1995), as seen by the simple correlation in Figure 3.31. Rift-related spinel peridotites erupted in alkali basalts show similar, though shallower, correlations (Meisel *et al.*, 1996; Handler *et al.*, 1997). Arc-related spinel peridotites, by way of contrast, show little correlation between Re and Al (Brandon *et al.*, 1996). Cratonic peridotite xenoliths from Lesotho show no correlation between Re and Al_2O_3, which confirms that the Re variation is not exclusively controlled by partial melt extraction (Figure 3.31). Previous studies of cratonic peridotite xenoliths from the Kaapvaal craton found no correlation between Re and melt-extraction indices and

suggested that the large variation in Re may have been caused by "metasomatism" (Pearson *et al.*, 1995a; Carlson *et al.*, 1999).

Lesotho peridotites show no apparent correlation between Re/Os and Al_2O_3 (Figure 3.31). Peridotites from Alpine and rift-related settings by comparison show good correlations between Re/Os and Al content and this would suggest that they behave in a manner more consistent with melt extraction, or simple mixing with melts. Only "arc" related spinel peridotites show behaviour that is more comparable to that of cratonic peridotites.

Os and other PGE behaviour during partial melt extraction

PGEs within mantle melting residues are strongly buffered by residual sulfides (Lorand *et al.*, 1993; Keays, 1995; Snow and Schmidt, 1998). If PGEs are modelled as a function of Al_2O_3, this allows us to investigate the buffering effect of sulfides and the behaviour of PGEs and Re during partial melting. It was argued by Lorand *et al* (1989) that the positive correlations between S and Al_2O_3 within unmetasomatised peridotites from the Pyrenees were evidence of a residual origin for sulfides. From Figure 3.33 it can be seen that no correlation appears to exists between S and Al_2O_3 for the Lesotho peridotites. This lack of correlation however, may be attributable to later metasomatism disrupting any original systematics that may have been present.

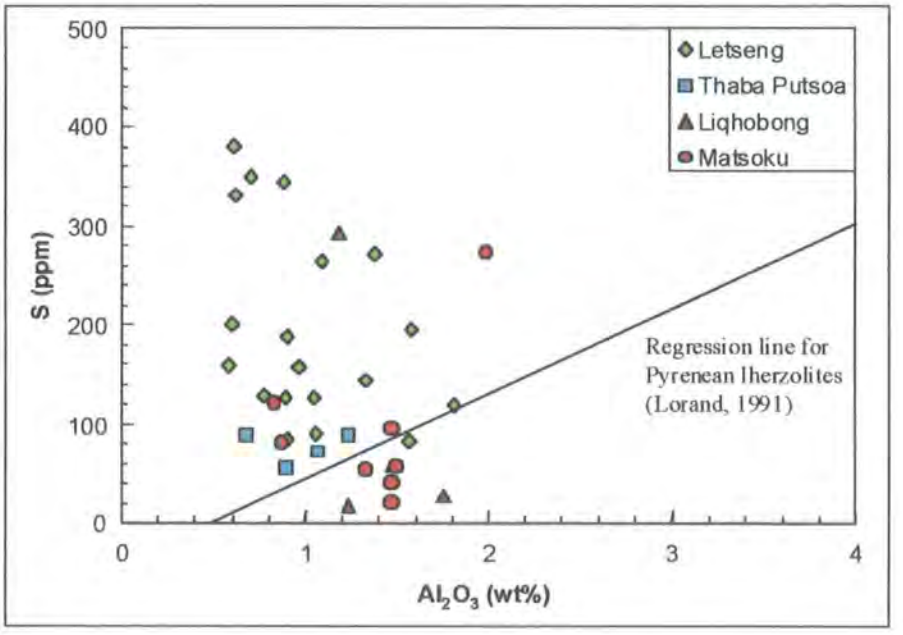

Figure 3.33 Variations of S (ppm) as a function of Al_2O_3 (wt%) in the low-T Lesotho peridotites.

The application of single-stage melt extraction models to the Lesotho peridotites fail to account for the variation in PGEs with S (Tables 3.15 and 3.18), and therefore do not

place strong constraints on the role of sulfides in hosting PGEs (Figure 3.34). The vertical distribution of data in Figure 3.34, may be consistent with a non-homogeneous source mantle. In terms of control by sulfides, the distribution of S within the Lesotho samples is more complex. Several samples with very low-level Pd concentrations are enriched in sulfur.

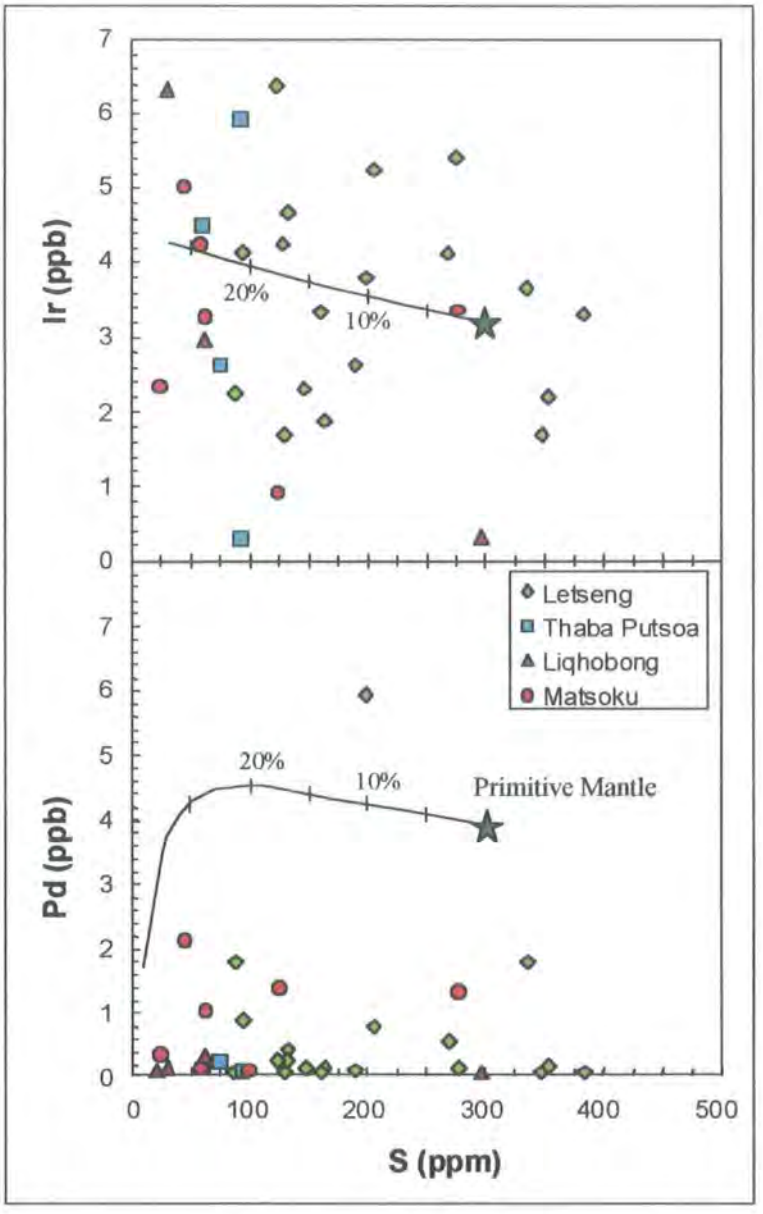

Figure 3.34 Predicted residue compositions are based on non-modal fractional melting models using a primitive mantle source with sulfur compositions of 300 ppm (represented by star symbol), and the extracted melts have a sulfur capacity of 1000 ppm S. The range of partition coefficients for PGEs, $D_{PGE(sulf/melt)}$ is large (Stone *et al.*, 1990; Bezmen *et al.*, 1994; Peach *et al.*, 1994; Fleet *et al.*, 1996). As for Figure 3.29 a value of 10^4 for D_{Pd} has been used to model Pd and the value D_{Ir} was assumed to be an order of magnitude higher based upon contrasting behaviour of these two elements. Varying S content of the source or S capacity of the melt does not significantly alter the melt extraction trends.

Non-modal fractional melting, melt extraction models were created for PGEs for comparison to the Lesotho peridotites (Figure 3.29). Values of F for the models were recalculated as Al_2O_3 using the inverse method of Bodinier (1988). Very little overall correlation seems to exist between PGEs and Al_2O_3, or the predicted models of melt extraction (Figures 3.29 and 3.31). Several samples appear to display both low Pd and Al_2O_3 abundances, and thus are consistent with >25% melt extraction. If the S content of the source is varied, this does not significantly alter the melt extraction trends for the models and therefore cannot explain the spread in the Lesotho data. Using varied partition coefficients ($D_{PGE(sulf/melt)}$), also fails to account for the spread in data. As Os and Ir are compatible elements during mantle melting processes, plots of Os and Ir against melt-indices such as Al_2O_3 should produce sub-horizontal trends. This is the case for peridotites from most tectonic settings (Figure 3.31). Peridotites from Lesotho, together with peridotites from other locales in the Kaapvaal craton (Pearson *et al.*, 1995a; Carlson *et al.*, 1999) show a wide, non-systematic variation in Os concentrations with a near vertical trend, at generally low Al_2O_3 (wt%) contents. Even the most extreme cases of melt extraction and sulfide breakdown would not produce such a range in Os, or Ir, contents (Figures 3.29 and 3.31). If all Os were to remain in the residue, 50% melt extraction would increase the Os concentration by a factor of two only. Assuming that experimental bulk partition coefficient data ($D_{PGE(sulf/melt)}$) for Os and Ir are correct, another factor must influence the variation seen in their concentrations. As illustrated for Os and Ir, some of the vertical spread in Figures 3.29 and 3.31, over and above that expected for simple melt extraction, may be consistent with a non-homogeneous mantle source, and reflects the heterogeneous distribution of sulfides or ultra-trace Os-Ir alloys within the Lesotho lithospheric mantle. Why this trait should be exclusive to cratonic lithospheric peridotites, as seen at Lesotho and the Kaapvaal craton overall, and not peridotites from other tectonic settings remains unclear. One alternative is that the variations observed in the IPGE contents of cratonic peridotites are produced from some process other than melt removal. This alternative is not supported by the general features of PGE patterns of these rocks. Another possibility is that the variations in Ir and Os abundances are related to very large degrees of depletion completely removing primary sulfides and stabilising alloy phases. Heterogeneously distributed alloy phases, rich in Ir and Os, may then cause substantial whole rock heterogeneity that is not encountered in non-cratonic peridotites.

If PGE ratios are considered as a function of Al_2O_3, as opposed to individual abundances, this should negate heterogeneities in the source, on the assumption that

chondritic ratios are present to begin with. If we consider Pd and Ir, as examples of incompatible and compatible PGEs respectively, the theoretical models of melt extraction should constrain the behaviour and fractionation of these groups. Limited correlation still seems to exist between the theoretical and actual behaviour of Pd/Ir and Al_2O_3 for melt extraction models in the Lesotho suite (Figure 3.35), but some systematics emerge.

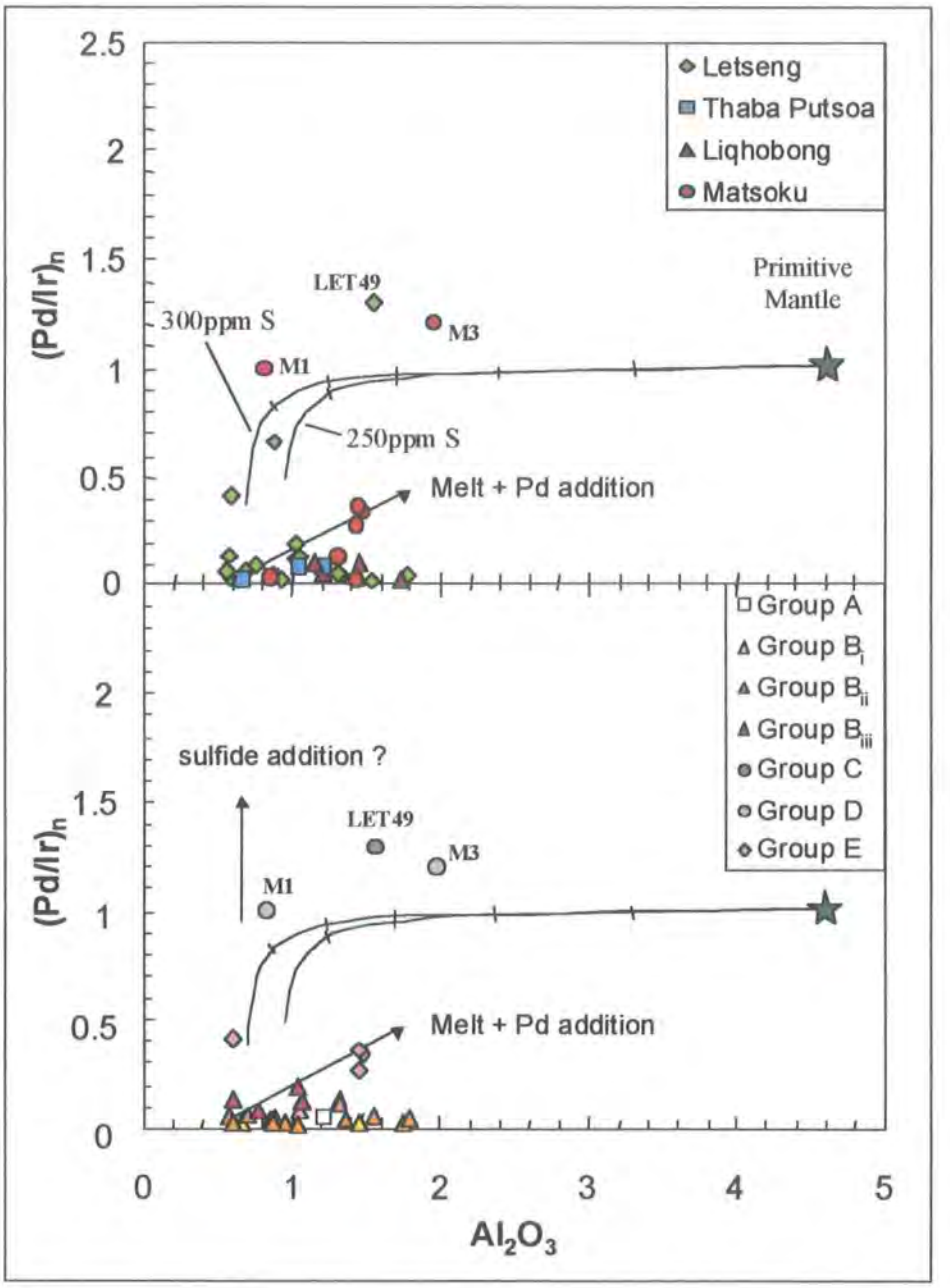

Figure 3.35 Variation of chondrite-normalised Pd/Ir as a function of whole-rock Al_2O_3 content (wt%). Lines represent the theoretical evolution of Pd/Ir in a peridotite residuum submitted to increasing degrees of equilibrium partial melting. Marks indicate 5% increments of melting. Primitive mantle represented by the star symbol. The two curves depict starting compositions with 250ppm and 300ppm total sulfur.

For several of the Lesotho peridotites, depleted bulk-rock Al_2O_3 contents correlate well with samples showing depleted Pd signatures, i.e. low $(Pd/Ir)_n$ (Groups A and B, Table 3.18, Figures 3.26a and 3.26b), and this would suggest that the PGE systematics for these samples have remained closed since the time of initial melt extraction. Displacement of other samples from the theoretical model is consistent with their disturbed PGE patterns. These samples plot on vectors that may be attributable to either or both sulfide and melt addition (Figure 3.35).

3.6.5.c Effects of metasomatism and melt infiltration

Metasomatism

Studies of mantle sulfides have shown that multiple generations of sulfides can exist within individual peridotites (Burton *et al.*, 1999; Alard *et al.*, 2000; Pearson *et al.*, 2000). Precipitation of secondary sulfides along intergranular boundaries may account for the observed variation in Os abundances, PGE systematics and isotope ratios within the Lesotho peridotite suite. In general, melt and sulfide addition in Lesotho peridotites associated with Re enrichment only (Group B in Table 3.18), appears to have little or no effect on Os abundance or $^{187}Os/^{188}Os$ ratios (Table 3.19). Peridotites with more complex PGE patterns that show enrichment in Pd as well as Re tend to have more radiogenic $^{187}Os/^{188}Os$ ratios (Tables 3.18 and 3.19), and therefore Os isotopic compositions may be a reflection of secondary sulfide addition in these samples. However, in terms of Os abundance there is no clear evidence to suggest Os enrichment (Table 3.19). An alternative explanation therefore may be that the radiogenic Os isotopic compositions indicate residual Re in only moderately depleted peridotites (Group E of Table 3.18), or Re addition occurring earlier in the history of the sample.

The variation in absolute and relative abundances of PGEs and their co-variation with S and Al_2O_3 (Table 3.18) suggest that the Lesotho peridotites have a complex history of melt extraction, followed by post melt-extraction enrichment. However, the nature of this enrichment in PGEs and Re is variable suggesting that the peridotites have either been affected by different generations of fluid, varying degrees of PGE precipitation from sulfide introduction, or else there is a spatial distribution to PGE precipitation. Rb-Sr, Sm-Nd and U-Th-Pb isotope studies on mantle peridotites support the idea of ubiquitous, multi-stage metasomatism (Stosch *et al.*, 1980; Richardson *et al.*, 1985, Carlson, 1994; Pearson *et al.*, 1995a).

Group	Sample	S (ppm)	Os (ppb)	$(Pd/Ir)_n$	$^{187}Os/^{188}Os(i)$
A	LQ8	19	3.82	0.037	0.10802
B_i	TP6	90	5.46	0.009	0.10731
	TP7	73	2.44	0.065	0.10812
	TP9	57	4.57	0.019	0.10764
	LQ5	28	6.56	0.011	0.10907
	LQ9	60	6.68	0.007	0.10826
	M9	22.25	9.55	0.007	0.10850
	M11	56	4.24	0.116	0.10970
	M13	83	5.36	0.018	0.10946
B_{ii}	LET6	345	3.18	0.017	0.10846
	LET8	161	1.60	0.040	0.10746
	LET12	188	3.16	0.023	0.10918
	LET13	158	3.31	0.005	0.10854
	LET25	350.5	1.98	0.045	0.10773
	LET27	273.75	6.25	0.015	0.10859
	LET28	380.75	3.88	0.007	0.10775
	LET29	128.4	13.73	0.004	0.10950
	LET30	145	3.44	0.102	0.11233
	LET38	84.22	2.37	0.039	0.10899
	LET47	127	4.35	0.005	0.10914
	LET64	121	6.42	0.031	0.10930
B_{iii}	LET2	202.75	5.71	0.115	0.10820
	LET14	130.25	4.70	0.067	0.10844
	LET31	266	5.82	0.104	0.10940
	LET58	91.75	5.22	0.169	0.10740
C	LET49	196.8	3.86	1.28	0.11887
D	M1	122	2.21	0.980	0.12151
	M3	274.5	0.82	1.19	0.12290
E	LET63	332.5	4.13	0.396	0.11892
	M5	60	3.16	0.322	0.11158
	M6	42.5	2.95	0.255	0.11081
	M8	97	4.38	0.344	0.11288

Table 3.19 Summary of S and Os abundances, PGE systematics and $^{187}Os/^{188}Os$ isotope ratios for Lesotho peridotites, on the basis of the PGE patterns.

The high Re abundance and Re/Os ratio of mantle derived melts and fluids relative to residual peridotite, renders the peridotite susceptible to Re contamination by processes such as metasomatism and melt infiltration. No single magma or fluid type however can be invoked to produce the wide spread seen in Re and Os abundances, or $^{187}Re/^{188}Os$ and $^{187}Os/^{188}Os$ ratios observed in the Lesotho peridotites, and several types or generations of fluids may be necessary e.g. carbonatite, kimberlite, OIB or MORB (Figure 3.31).

The small variation in Al_2O_3 concentration seen within the Lesotho peridotites (Table 3.10) would limit the metasomatising fluid to one with a relatively high Re/Al and

Os/Al ratio (Figure 3.31). In terms of Re, this tends to rule out basaltic fluids and it has been suggested that either carbonatitic and high Re kimberlitic melts (Figure 3.31, Pearson *et al.*, 1995a; Carlson *et al.*, 1999), or Re-rich, Al-poor hydrous fluids from the de-watering of subducted slabs (Brandon *et al.*, 1996) may be the responsible metasomatising mediums. The mean Os concentration for Lesotho peridotites is higher than bulk-mantle, compared to lower than bulk-mantle for those from arc settings. Brandon *et al* (1996) suggested that the low Os concentrations of arc peridotites were the result of oxidation by hydrous fluids, and therefore this process seems unlikely to account for the generally high Os content within Lesotho peridotites. Alternatively, another type of fluid associated with subduction zones may be responsible.

Tonalites and trondhjemites have been invoked as an explanation for the high SiO_2 content of cratonic peridotites from the Kaapvaal craton (Rudnick, 1995). Their high Al and low Os compositions make them an unlikely metasomatising agent. Os-rich alloys or sulfides precipitated from fluids or magmas percolating through the lithospheric mantle however, may be responsible for raising Os concentrations (Pearson *et al.*, 1998b).

Observations from off-craton spinel lherzolite and orogenic massif suites show simple correlations between $^{187}Os/^{188}Os$ and Al_2O_3 (Reisberg and Lorand, 1995; Handler *et al.*, 1997). In contrast, the Lesotho peridotite suite shows no apparent correlation between $^{187}Os/^{188}Os$ and Al_2O_3 (Figure 3.31). This lack of correlation has also been observed in other cratonic and circum-cratonic xenoliths suites such as Namibia and East Griqualand (Pearson, 1999a). The mixing lines in Figure 3.31 suggest that infiltration by common magmatic fluids could account for the horizontal distribution in $^{187}Os/^{188}Os$ data but can not for the vertical, unless the infiltration of metasomatising fluids was accompanied by precipitation of Os-rich sulfides or alloys.

The scatter in Re content in the Lesotho peridotites (Figure 3.31) can be accounted for by the addition of 0-20% kimberlite or 0-15% carbonatite to the lithospheric peridotites, though this fails to account for all samples. The remaining spread in Re data can be accounted for by the addition of 0-10% OIB or MORB. The bulk addition of carbonatite or kimberlite to the peridotites should be apparent from enrichment in elements such as Ba and Sr. However, there is no overall systematic correlation between Re and Ba (Figure 3.36). The spread in Re and Ba can be variously accounted for by the addition of 0-5% carbonatite, 0-5% kimberlite or 0-25% OIB, but again this does not account for all samples, e.g. the enrichment in Al_2O_3 seen in some. If the composition of the modelled end-member depleted peridotite in Figure 3.31 is

sequentially modified, the model mixing lines better correspond with some of the scattered data. One explanation for this may be that the peridotites are not sourced from a single homogeneous depleted mantle source, but instead may be sourced from a variably depleted mantle. This model is overly simplistic however and does not account for the possibility of several generations of metasomatic alteration by various fluid types.

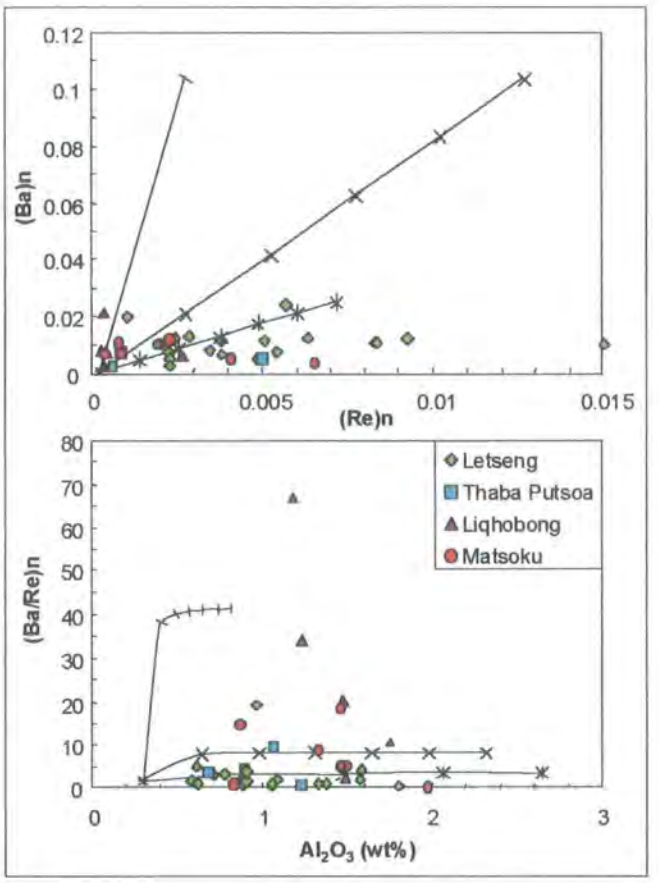

Figure 3.36 A) Chondrite normalised plot of Ba vs. Re content for Lesotho peridotites. B) Chondrite normalised Ba/Re ratio vs. Al_2O_3. The lines represent model mixing lines between an end-member depleted peridotite (Re = 0.01ppb, Ba = 1ppm) and possible metasomatising magmas, marks indicate 5% increments in the addition of magma. Carbonatite (hatching; Re = 2ppb, Ba = 5000ppm; Tuttle and Gittins (1966), kimberlite (x; Re = 2ppb, Ba = 1000ppm; Bergman (1987) and Smith *et al* (1985), average OIB (star; Re = 0.35ppb, Ba = 200ppm; Basaltic Volcanism Studies Project (1981).

Cumulate processes

Herzberg (1993) proposed that the OPX rich nature of cratonic peridotites in the Kaapvaal craton could be explained by the crystallisation of OPX cumulates, the result of mixing between an ascending komatiitic magma and an olivine-rich residue of komatiite extraction. An alternative mechanism to explain the spread in Re and Os abundances is that they contain a cumulate component (Herzberg, 1993; Pearson *et al.*, 1995a; Herzberg, 1999). The modal volume of OPX in peridotites from the Lesotho

suite mirrors that of peridotites from other parts of the Kaapvaal craton (Table 3.8), and therefore this model may apply. However, the Re concentration within OPX may be low (Hart and Ravizza, 1996), and therefore the addition of OPX is unlikely to produce the observed scatter in Re concentration. If the deep crystallisation of the komatiite and cumulate component is accompanied by the precipitation of sulfides or alloys rich in Re and Os though, this may contribute to the scatter observed (Pearson *et al.*, 1998b).

3.7 Timing of lithospheric mantle differentiation

The rationale behind extracting Re-Os age information from peridotites is outlined in Chapter 1.2.

3.7.1 Re-Os Isochrons

If the Kaapvaal lithospheric mantle, as sampled by the Lesotho kimberlites, was formed from a common source with constant isotopic composition, in a single melt-extraction event, and the residues left with varying Re/Os ratios, the samples would define an isochron whose slope defines the age of melt extraction. From Figure 3.37, it can be seen that this is not the case and the data are widely scattered, due to the processes discussed in chapter 3.6. For comparative purposes, reference isochrons have been added to Figure 3.37. Some samples lie close to these isochrons, and define linear arrays. Four out of seven samples from the Matsoku kimberlite appear to define a linear array that corresponds to an age of 2.2 Ga with an initial Os isotopic composition of 0.1083 (γOs = -13.36), with the other three Matsoku samples slightly displaced from the array. However four out of seven peridotites from Matsoku also produce an age of 3.4 Ga with an initial Os isotopic composition of 0.108 (γOs = -13.6). From the overall scatter in data, it is doubtful whether these ages have any real significance. Many of the samples from Letseng define a shallow slope that most likely reflects Re-addition near the time of kimberlite eruption.

The lack of isochronous behaviour argues against the variation in Re and Os being produced by cumulate processes close to the time of melt extraction, and instead suggests that Re/Os was fractionated, more than once, following initial formation. This is consistent with other studies that show evidence of recent Re and Os addition in mantle xenoliths (Walker *et al.*, 1989; Meisel *et al.*, 1996; Chesley *et al.*, 1999) and massif peridotites (Reisberg *et al.*, 1991; Reisberg and Lorand, 1995).

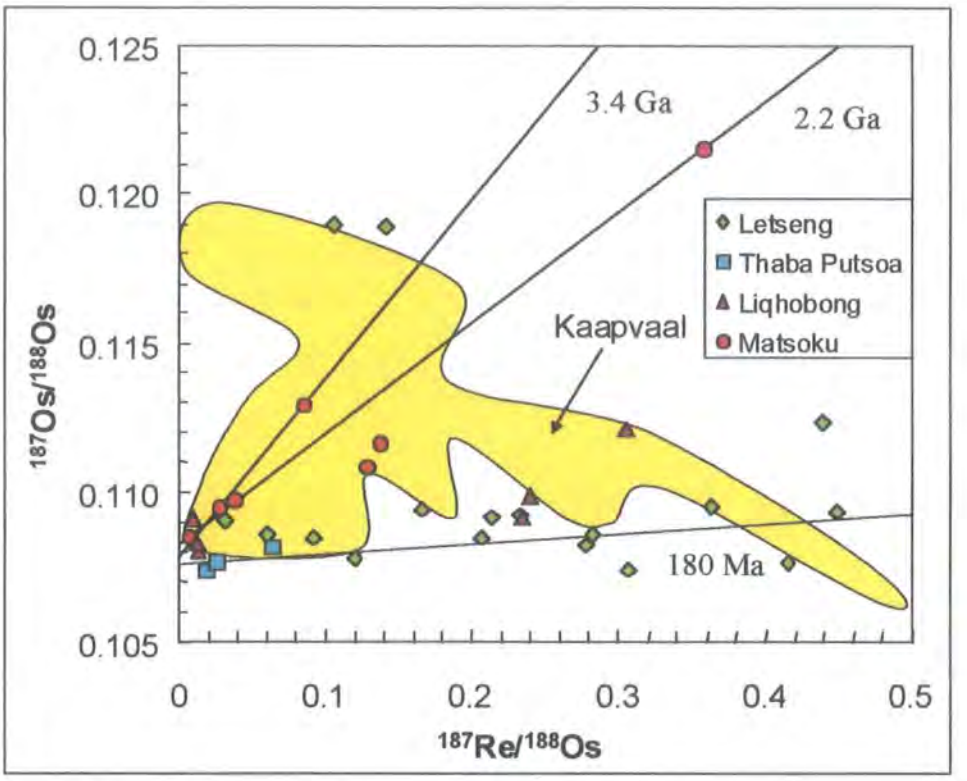

Figure 3.37 Re-Os isochron diagram for the Lesotho data shown in Table 3.10. Reference isochrons passing through the Lesotho data are shown. Isochrons were calculated using a decay constant (λ) of 1.666×10^{-11}. Kaapvaal data, shown by yellow field, from Carlson *et al* (1999).

3.7.2 Age determination from Al_2O_3 - $^{187}Os/^{188}Os$ relationships

Studies on massif peridotites have noted correlations between fertility indices, such as Al_2O_3, and $^{187}Os/^{188}Os$ and this has been attributed to either melt depletion (Reisberg *et al.*, 1991; Reisberg and Lorand, 1995), or mixing between harzburgite and a basaltic melt (Reisberg *et al.*, 1991). If this correlation formed due to the process of melt extraction, the intercept point on the y-axis could be used to establish the initial Os isotopic composition of the peridotites. From this intercept, the time of melt extraction and lithosphere formation can be determined using model age arguments. This method assumes that the peridotites were derived from a primitive mantle source with a narrowly defined composition (McDonough and Sun, 1995; Shirey and Walker, 1998). There is a lack of good correlation between Al_2O_3 and $^{187}Os/^{188}Os$ for the Lesotho peridotites (Figure 3.38). The dispersion of the data is too great for any useful age information to be obtained from this approach for the Lesotho samples.

The lack of correlation between Al_2O_3 and Os isotopes is not surprising given the known variations in $^{187}Os/^{188}Os$ composition over a small range in Al_2O_3 and the likely metasomatic alteration to both.

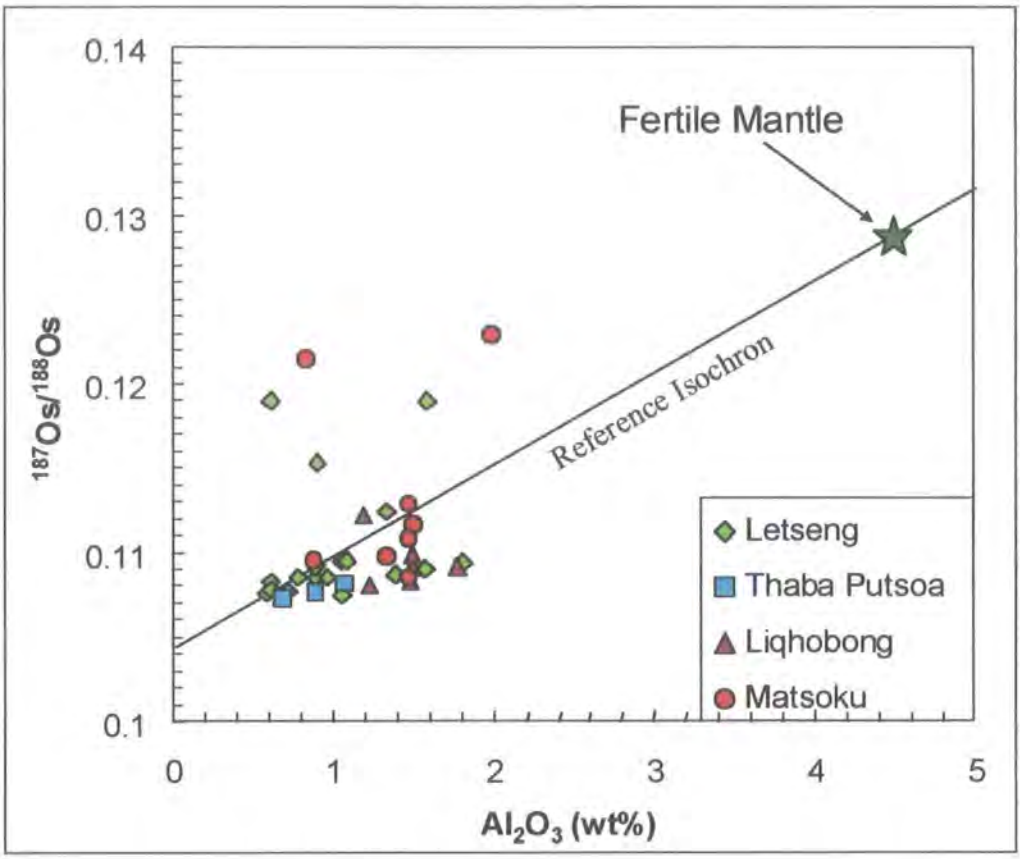

Figure 3.38 $^{187}Os/^{188}Os$ ratios plotted against Al_2O_3 content (in wt%) for low-T Lesotho peridotites. Line represents a reference "isochron" passing through fertile mantle and the most depleted Lesotho samples. $^{187}Os/^{188}Os(i)$ for the isochron is 0.1045, which equates to an age of 3.33Ga.

3.7.3 Os isotope model ages for Kaapvaal peridotites

Rhenium depletion model ages (T_{RD})

In trying to assess the age significance of the variation in Os isotopic composition for the Kaapvaal peridotites we can take a simplistic end-member model that assumes the peridotite represents a residue of melt extraction, free of Re prior to capture by the kimberlite. The rhenium depletion age (T_{RD}) calculates the isotopic composition of both the sample and model reservoir at the time of kimberlite eruption, and calculates a model age assuming the Re content of the sample is zero (Walker *et al.*, 1989). This provides a minimum age only for a sample and will underestimate the true age of samples if it was not completely free of Re. The T_{RD} model age will only overestimate the true formation age of a sample if the sample formed from, or interacted with, a melt of lower $^{187}Os/^{188}Os$ than the bulk mantle. Peridotites tend to have higher Os concentrations than most magmas, therefore infiltration by any melt is unlikely to greatly alter the Os isotopic composition. T_{RD} model ages are presented here as T_{RD} eruption ages, where Os in-growth from possible Re addition at the time of kimberlite

eruption is removed. It is assumed that the Re content of the peridotite xenoliths represents the addition of Re from the kimberlite during entrainment.

The observed range in Os isotopic compositions for the Lesotho peridotites (Table 3.10) equates to T_{RD} model ages of 2.9 to 0.8 Ga (Figure 3.39). Twenty-six samples have T_{RD} model ages between 2.5 Ga and 3.0 Ga, and 10 samples have T_{RD} ages < 2.5Ga. Three features stand out in the distribution of T_{RD} model ages shown in Figure 3.39; (i) no samples with T_{RD} > 3.0 Ga, (ii) the large peak in ages between 2.5 and 3.0 Ga, and (iii) the scattering of T_{RD} to younger, post-Archean ages. The mean T_{RD} model age for all Lesotho peridotite samples in this study is 2.5 +/- 0.5 Ga (1 std.dev.) with a median of 2.7 Ga. This is similar to that reported from previous studies of Kaapvaal peridotites with a mean of 2.5 +/- 0.4 Ga and median of 2.6 Ga (Carlson *et al.*, 1999; Menzies *et al.*, 1999), although the spread in ages is larger than at most localities.

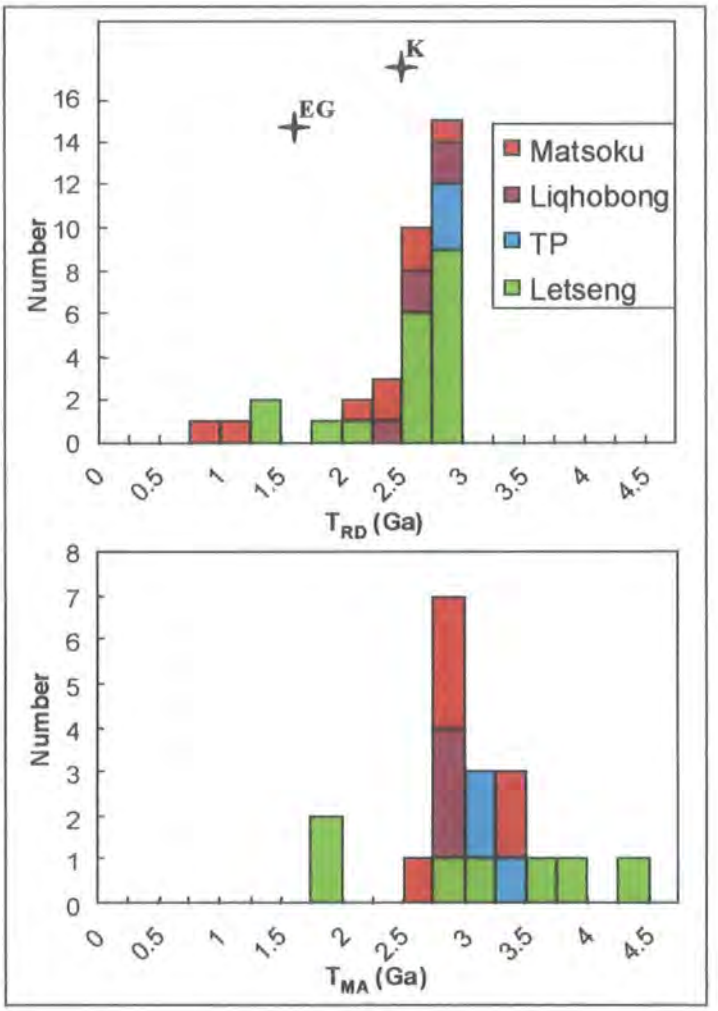

Figure 3.39 Histograms of Re-depletion (T_{RD}) and mantle extraction (T_{MA}) Re-Os model ages for Lesotho peridotites. Also shown are mean T_{RD} values for K – Kaapvaal from Carlson *et al* (1999) at 2.5 Ga, and EG - East Griqualand from Pearson *et al* (1998a) at 1.5 Ga.

Previous studies of samples from Lesotho produce a similarly wide spread in data (Pearson *et al.*, 1995a). Despite the wide spread, peridotite samples from this study that give T_{RD} ages in the range 2.5 to 3.0 Ga are very tightly clustered around a mean of 2.8 +/- 0.1 Ga, n = 26. PHN2825, a sub-calcic garnet harzburgite from Liqhobong, gives a T_{RD} model age of 3.1 Ga (Pearson *et al.*, 1995a). No peridotite xenoliths as old as this sample were found in the new data set. In general, peridotites from individual kimberlite localities in Lesotho show a similar distribution in T_{RD} ages compared to the overall distribution seen in Figure 3.39. Peridotites from Letseng have a mean T_{RD} model age of 2.6 +/- 0.5 Ga with a median of 2.7 Ga and peridotites from Liqhobong have a mean of 2.5 +/- 0.2 Ga with a median of 2.7 Ga. Peridotites from Matsoku have a slightly lower mean T_{RD} model age, at 2.1 +/- 0.8 Ga. Peridotites from Thaba Putsoa have slightly higher mean T_{RD} model age of 2.9 +/- 0.1 Ga, based on a limited data-set of three samples.

There is no clear overall correlation between T_{RD} and depth of origin for the Lesotho peridotite suite (Figure 3.40), although there may be a weak correlation at the Letseng kimberlite where there appears to be a possible younging with depth. If we consider spinel peridotites alone, these have a mean T_{RD} of 2.7 +/- 0.2 Ga with a median of 2.8 Ga, which is comparable to the overall mean for Lesotho. The mean for garnet-spinel peridotites is 2.5 +/- 0.6 Ga with a median of 2.8 Ga, and garnet peridotites 2.6 +/- 0.4 Ga with a median of 2.7 Ga. The mean T_{RD} ages of garnet-spinel and garnet peridotites are skewed by several anomalously young peridotites, samples LET48, LET49 and M1. If these samples are excluded, the mean for garnet-spinel peridotites is 2.7 +/- 0.2 Ga with a median of 2.8 Ga, and garnet peridotites 2.7 +/- 0.2 Ga with a median of 2.7 Ga. The age of the Lesotho lithospheric mantle within the individual facies would therefore appear to be the same, within error. The maximum T_{RD} model ages for spinel peridotites, garnet-spinel peridotites and garnet peridotites are all 2.9 Ga. It would therefore suggest that ancient Archean lithospheric mantle persisted to depth at Lesotho, and that younger ages either reflect modification by reworking at a later stage or younger mantle has been added to the lithospheres stratigraphic column.

Mantle separation model ages (T_{MA})

T_{MA} ages for the Lesotho peridotites (Table 3.10) range from 4.3 to 1.8 Ga (Figure 3.39), excluding those that produce future ages or ages greater than the age of the Earth. Nine samples have T_{MA} ages >3.0 Ga, eight samples have T_{MA} model ages between 2.5 Ga and 3.0 Ga, and two samples have T_{MA} ages < 2.5Ga. Two features are prominent in Figure 3.39; (i) main peak in samples between 2.5 and 3.0 Ga, and (ii) the scattering

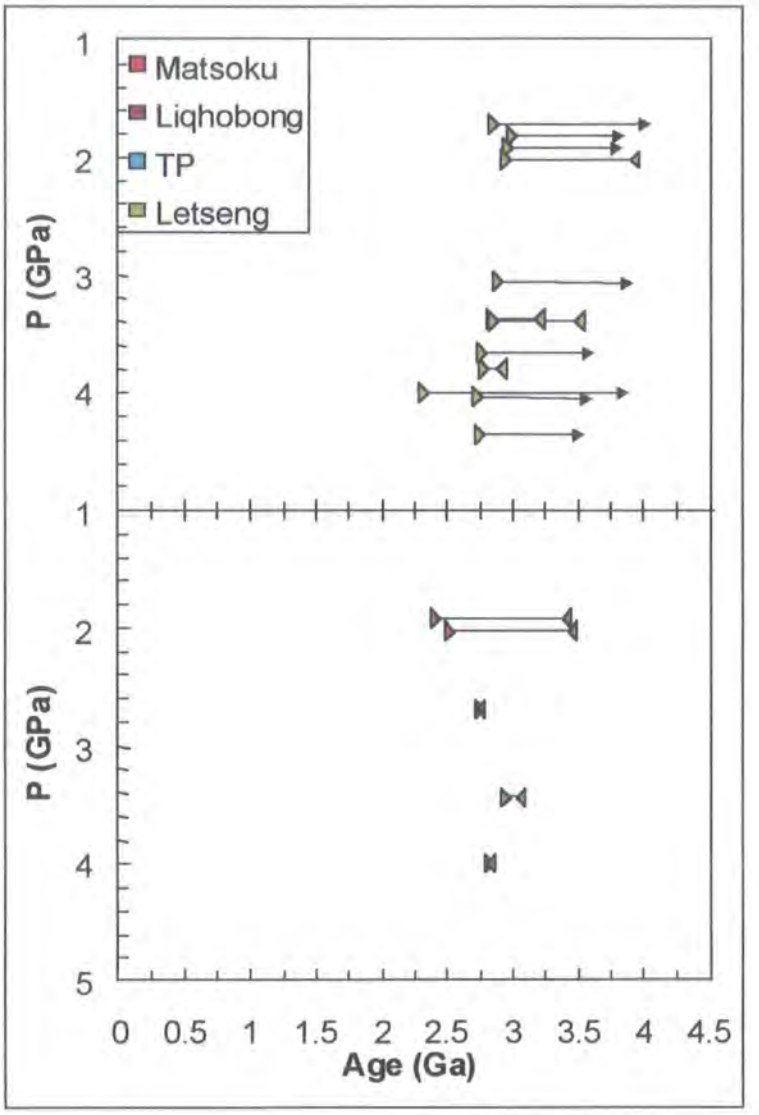

Figure 3.40 T_{RD} (right facing triangles) and T_{MA} (left facing triangles) model ages for peridotite xenoliths from individual kimberlite pipes plotted against the pressure of equilibration as determined by mineral geothermobarometry. All samples plotting at pressures less than 2 GPa are spinel peridotites (pressure arbitrarily assigned in 0.2 GPa increments up to 2 GPa). Samples with arrows have T_{MA} ages in excess of the age of the Earth.

of T_{MA} to older > 3.0 Ga, Archean ages. The mean T_{MA} model age for all Lesotho peridotite samples shown in Figure 3.39 is 3.0 +/- 0.6 Ga (1 std.dev.) with a median of 2.9 Ga. In general, peridotites from individual kimberlite localities in Lesotho show a similar distribution in T_{MA} ages compared to the overall distribution seen in Figure 3.39. Peridotites from Letseng have a mean T_{MA} model age of 3.0 +/- 0.6 Ga with a median of 2.9 Ga, Thaba Putsoa a mean T_{MA} model age of 3.1 +/- 0.9 Ga with a median of 3.2 Ga, Liqhobong a mean T_{MA} model age of 2.9 +/- 0.09 Ga with a median of 2.9 Ga and Matsoku a mean of 3.0 +/- 0.3 Ga with a median of 2.9 Ga.

Again there is no clear correlation between T_{MA} model ages and depth of origin for the Lesotho peridotites (Figure 3.40). If we consider spinel peridotites alone, these have

a mean T_{MA} of 3.6 +/- 0.3 Ga with a median of 3.5 Ga, but this is poorly constrained. The mean T_{MA} for garnet-spinel peridotites (3.1 +/- 0.3 Ga with a median of 3.1 Ga) and garnet peridotites (2.9 +/- 0.6 Ga with a median of 2.9 Ga) are generally lower than for coarse spinel peridotites and these are better constrained. The maximum T_{MA} model age for spinel peridotites at Kaapvaal is 3.9 Ga, garnet-spinel peridotites 3.5 Ga, and garnet peridotites 4.2 Ga. Again this would suggest that the lithospheric mantle beneath Kaapvaal has persisted since the Archean, throughout its stratigraphic column.

Spurious mantle separation ages will be produced if the Re/Os ratio of the Lesotho samples has changed at all during the evolution of the sample. If we consider infiltration by the host kimberlite (Figures 3.31), this will produce an increase in the Re/Os ratio without greatly affecting the $^{187}Os/^{188}Os$ composition. The calculated evolutionary trajectory of the Os isotopic composition through time will be erroneously steepened, displacing the intercept with fertile mantle towards higher ages thereby overestimating the true melt extraction age. A loss of Re, possibly produced by weathering and consequent sulfide removal, would result in an underestimated T_{MA}. Many T_{MA} model ages deviate greatly from their T_{RD} model ages (Figure 3.41), as expected for samples that have experienced recent Re addition with no changes in $^{187}Os/^{188}Os$, e.g. sample LET8 (Table 3.10). Even though T_{MA} model ages are susceptible to Re addition, occasionally T_{MA} model ages for Lesotho peridotites are within a few 100 Ma of their T_{RD} ages, and suggest relatively little disturbance, e.g. LQ8.

3.7.4 Constraints from PGE systematics on the significance of model ages for the lithospheric mantle beneath Kaapvaal

If PGE systematics of Lesotho peridotites are considered in conjunction with the Re-Os age systematics we can evaluate the significance of T_{RD} vs. T_{MA} model ages and therefore better constrain the age of the lithospheric mantle beneath the Lesotho section of the Kaapvaal craton.

A single peridotite sample from Liqhobong, LQ8, displays an extremely fractionated CI-chondrite normalised PGE pattern (Figure 3.26a). This pattern would be expected for a residue of extensive melting where loss of most of the primary sulfide has occurred (>25% melting). This is also reflected in the depleted major element compositions (Table 3.8). The very depleted Re content of LQ8 is reflected in the close agreement seen between T_{RD} and T_{MA} model ages (both 2.9 Ga). The low bulk-rock

Al_2O_3, low $(Pd/Ir)_n$ of 0.04, depleted PGE profile and close agreement in model ages suggest that the Re-Os isotope systematics for at least some of the Lesotho peridotites have remained closed since initial melt extraction. REE enrichment of this sample (Table 3.9) indicates that the sample has undergone a degree of metasomatism, but this is not accompanied by significant Re enrichment and hence the Re-Os isotope systematics remain undisturbed. The T_{MA} model age of sample LQ8 therefore is a likely approximation of the age of melting and provides a substantiated maximum age for the lithospheric mantle as sampled by the Lesotho kimberlites from the present sample suite. The small difference between T_{RD} and T_{MA} model ages shows that, although T_{RD} represents the minimum age of the sample, in this case it is a good approximation of the actual age for PPGE depleted samples, because Re was mostly removed during the intense melt extraction.

Many Lesotho samples display highly fractionated PGE patterns but show marked inflections in the Re abundance (Figure 3.26a and 3.26b). (Pd/Ir)n values for these samples (mean = 0.01 +/- 0.004) suggest these samples have undergone melt extraction and give little indication of the disturbed nature of the PGE profiles. The extended PGE pattern for samples such as LET8 show a marked inflection at Re and this leads to a considerable difference between T_{RD} (2.9 Ga) and T_{MA} (future) model ages. The Re enrichment was accompanied by S enrichment (Figure 3.28b) but limited enrichment in Al_2O_3 (Figure 3.30c). This suggests enrichment by sulfides with a limited addition of any silicate phases. Sample LET8 has an identical T_{RD} model age to sample LQ8, consistent with a major melt extraction event at 2.9 Ga, and this may suggest that Os was not transported by the infiltrating sulfide phases.

Several Lesotho peridotites display moderately fractionated chondrite normalised PGE patterns (Figure 3.26e). These patterns would be expected for peridotites that have experienced low degrees of partial melting, where Re may still be residual in the sample e.g. sample LET63 (Table 3.17), with only moderate depletion of Pt, Pd and Re. This is consistent with the model $(Pd/Ir)_n$ vs. Al_2O_3 evolutionary trend (Figure 3.35). The PGE profile for this sample shows little evidence of disturbance to the PPGEs, or open-system behaviour. In comparison to more depleted Lesotho samples, the chondrite normalised Pd and Re abundances are almost a magnitude greater, which may suggest that primary sulfides are still resident within this section of the mantle and melting never reached the point of total sulfide breakdown. The model ages for LET63 provide a T_{RD} model age of 1.4 Ga and a T_{MA} of 1.8 Ga respectively. The model ages are in

close agreement, and therefore the T_{MA} model age may better reflect the true age of the sample.

Using combined PGE characteristics with the Re-Os isotope systematics, and examination of the correlation between PGEs and magmaphile elements to Lesotho peridotites, we can gain better insights into the age systematics of the Kaapvaal lithospheric mantle beneath Lesotho. This allows us to improve our understanding of initial differentiation and subsequent modification of the lithosphere. From the CI-chondrite normalised extended PGE patterns it is evident that the majority of samples have undergone a degree of Re enrichment. T_{MA} model ages quite often produce anomalously old ages of formation compared with T_{RD} (Figure 3.41), and frequently produce future ages. As all Lesotho peridotites show some vestiges of major-element and PPGE melt depletion, T_{RD} model ages might be regarded as a more reliable indicator of the age of a particular sample. The systematic behaviour of melt-depleted extended PGE patterns, agreement of $(Pd/Ir)_n$ vs. Al_2O_3 and coincidence of T_{MA} and T_{RD} ages for some of the samples give us confidence that they are recording mainly the timing of melt depletion and lithospheric formation.

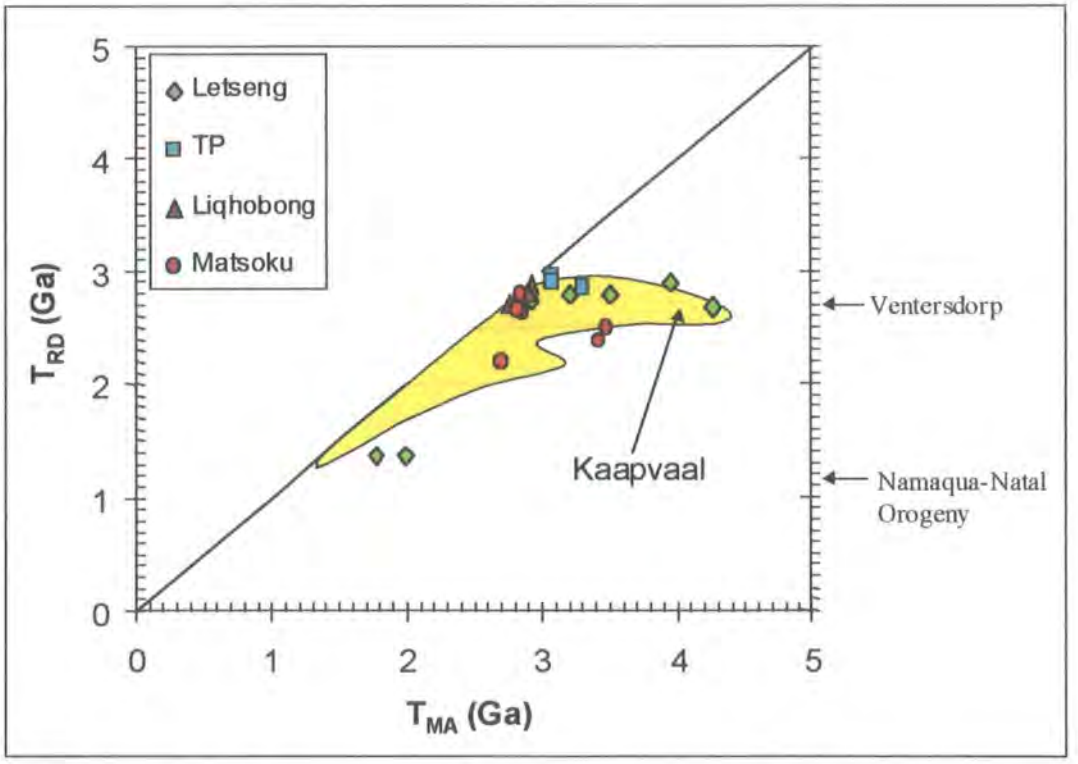

Figure 3.41 Plot of T_{RD} vs. T_{MA} model ages for peridotites from individual Lesotho kimberlites. The line in the figure represents the $T_{RD} = T_{MA}$ line. Data for peridotites from the Kaapvaal craton (Carlson *et al.*, 1999).

3.8 Evolution of the lithospheric mantle beneath the Kaapvaal Craton

Lesotho

The Ancient Gneiss terrain of the Kaapvaal craton contains elements as old as 3.644 Ga (Compston and Kröner, 1988; Hunter, 1991; Helmstaedt and Gurney, 2001), and is tectonically juxtaposed next to the ca. 3.5 Ga Barberton greenstone belt (de Wit et al., 1992; Helmstaedt and Gurney, 2001). This ancient core of the Kaapvaal craton was enlarged to the south by the amalgamation of the 3.4-3.2 Ga Natal granite-greenstone terrain (Hunter, 1991), which underlies Lesotho. Previous Re-Os studies of peridotites from Liqhobong have produced T_{RD} model ages of up to 3.3 Ga (Pearson et al., 1995a), consistent with the formation of the lithospheric mantle at this time. In contrast, no peridotite in this latest study has produced T_{RD} model ages as old as this. An isochron from 4 Matsoku samples also produces an age of 3.4 Ga, but this may be coincidental considering the scatter in data. Similarly a correlation of Al_2O_3 vs. $^{187}Os/^{188}Os$ gives a slope equal to an Al-Os model age of 3.3 Ga using the most depleted of the Lesotho peridotites, though scatter in the data makes this an uncertain age.

New data from lower crustal xenoliths indicate a very widespread, craton-wide differentiation event that affected the entire crustal thickness at ca. 3.1 Ga (Moser *et al.*, 2001). Such a widespread crustal differentiation event is inconsistent with the presence of a thick (>150 km), protective lithospheric mantle keel beneath the craton at this time and Moser *et al* (2001) have suggested that this event represents a maximum age for the establishment of a protective lithospheric mantle root. This does not preclude the prior existence of significantly older lithospheric mantle beneath the Kaapvaal craton, and some lithospheric xenoliths do yield meso-Archean T_{RD} model ages (Pearson *et al.*, 1995a; Carlson *et al.*, 1999; Menzies *et al.*, 1999), but the majority do not and this requires an amalgamation of terranes in the neo-Archean. The Ancient Gneiss and Natal greenstone terrains are unconformably overlain by relatively undeformed volcano-sedimentary sequences of the Pongola basin ca. 2.95 Ga (Hunter, 1991). Several samples from the Lesotho peridotite suite produce T_{RD} model ages of 2.9 Ga, particularly at Thaba Putsoa. The mean T_{MA} model age for peridotites in the Lesotho suite is 3.0 Ga, consistent with the addition of material to, or modification of the Lithospheric mantle at this time. These ages may relate to either the final stabilisation of the lithospheric keel after the crustal differentiation event of Moser *et al* (2001), or the tectonic and magmatic processes forming the Pongola basin.

The Kaapvaal shield, after it had stabilised, became a basement for a series of unconformity-bounded volcano-sedimentary sequences, including the Dominion,

Witwatersrand and Ventersdorp. The Central Rand deposition has been dated at 2.84-2.71 Ga (Armstrong *et al.*, 1991). The Middle Ventersdorp, which is older than 2.709 Ga, covers part of the northern and western part of the province. Lower crustal xenoliths from Lace and Voorspoed kimberlites preserve evidence of a transient thermal pulse in the deep crust of the southwestern Kaapvaal craton. Zircon and Monazite produce U-Pb growth and early cooling ages of 2723 Ma (Schmitz *et al.*, 1998). This episode of ultra-high temperature metamorphism appears to coincide with the initiation of Ventersdorp flood basalt volcanism (Armstrong *et al.*, 1991). The combined western and eastern parts of the province to the south of the Thabazimbi-Murchison lineament experienced major extension resulting in the deposition of the volcano-sedimentary Upper Ventersdorp sequence, deposited between 2.7 and 2.6 Ga (Armstrong *et al.*, 1991). The origin of this extension episode is still unknown and may represent oblique convergence between the Kaapavaal and Zimbabwe cratons (Helmstaedt and Gurney, 2001), or the failed arm of a triple-junction related to the speculated rifting of the Kaapvaal and Pilbara provinces (Nelson *et al.*, 1992). The mean T_{RD} model age for all Lesotho peridotites is 2.5 Ga with a median of 2.6 Ga. If the dataset is filtered to look at samples with ages between 2.5 and 3.0 Ga, the Lesotho dataset is tightly clustered at 2.8 +/- 0.1 Ga. This suggests that the lithospheric mantle beneath Lesotho may have formed, or been greatly modified by the convergence or extension tectonics and magmatic processes forming these volcano-sedimentary basins.

The Archean age of zircon cores from Lesotho lower crustal xenoliths, analysed by Schmitz and Bowring (1999), is very close to the mean and median values for the lithospheric mantle Os model age data. Some mantle samples however are significantly older and give T_{RD} model ages that are not represented in the lower crustal zircon population. The lower crustal xenolith data set is limited at present, and the lack of older zircon ages may be simply a function of inadequate sampling. Alternatively, the 2.6 Ga zircon ages for the Lesotho samples (Schmitz and Bowring, 1999) may be a reflection of cooling the lower crust below the U-Pb blocking temperature and so evidence of older crustal differentiation events are no longer recorded. In evaluating these hypotheses, it would be unusual that U-Pb zircon ages resulting from such cooling would coincide with the main peak of T_{RD} model ages in the underlying mantle, since the Re-Os ages reflect bulk-rock chemical changes that are unlikely to be reset by subsolidus diffusion at the whole-rock size scale. Zircon cores from five crystals give mid-Proterozoic ages (1.7 Ga), consistent with T_{RD} model ages seen within the cratonic

lithospheric mantle at these localities. It is unclear whether this is coincidence or related to this event.

Recent geochronological studies of the lower crust in and around the Kaapvaal craton define events between 1114 and 1000 Ma (Schmitz and Bowring, 1999; Schmitz and Bowring, 2000, Table 3.1). This suggests that lower parts of the thickened crust along the southern and eastern margins of the Kaapvaal craton were modified in the Mesoproterozoic, indicating a metamorphic history post-dating cratonisation and possibly related to the Namaqua-Natal orogeny (Schmitz and Bowring, 1999). It is striking that these relatively young events recorded in the lower crust appear to be represented in the mantle section of the lithosphere, within error, at Matsoku (1.0 Ga) and possibly Letseng (1.4 Ga), as similarly young T_{RD} model ages. Such young T_{RD} model ages in the Lesotho lithospheric mantle raise the question as to whether this represents new material added to the Lesotho lithosphere during the Namaqua-Natal orogen, hence providing the heat for granulite metamorphism. Alternatively this thermal/tectonic event may reflect melts introduced into the lithospheric mantle that significantly overprinted and modified previously existing lithospheric mantle.

The Lesotho kimberlites erupt through the Drakensberg beds, which were erupted themselves between 190 and 150 Ma (Windley, 1995) as part of the Karroo flood basalts. No evidence of this event is apparent in the Re-Os model ages of the Lesotho peridotite suite. However, on the Re-Os isochron diagram (Figure 3.37) the Lesotho data produce a near horizontal spread in data which relates to a young disturbance, generally attributed to kimberlite infiltration but possibly related to this Karroo event.

The Kaapvaal Craton

Os isotopic data for peridotite xenoliths from the Letlhakane kimberlite, towards the north-western margin of the craton (Figure 3.1) give very consistent T_{RD} model ages, between 2.8 and 2.5 Ga for the majority of samples (mean = 2.6 +/- 0.2 Ga, median = 2.6 Ga, n = 10, Carlson *et al.*, 1999). Peridotites from the Newlands kimberlite, in the southern part of the craton, provide a similar average, and tight range, in Re-Os model ages (Menzies *et al.*, 1999). Peridotite xenoliths from the Kimberley area, which lies towards the south-west margin of the craton, show a range in T_{RD} ages from 2.4 to 2.8 (mean = 2.6 +/- 0.2) Ga, with a bi-modal distribution (Carlson *et al.*, 1999). Of 7 samples analysed, 4 had T_{RD} ages between 2.7 and 2.8 Ga, which is comparable to the peak seen in the Lesotho data set (Figure 3.39). The mean T_{RD} age for the Lesotho peridotite xenoliths (2.5 +/- 0.5 Ga) is very similar to the mean peridotite ages from these other, widely dispersed localities, but the Lesotho samples show a greater overall

range, scattering primarily to younger ages. A similar scatter in ages is seen in peridotites from the Venetia kimberlite, which lies at the northern boundary of the craton, erupting through the Archaean Limpopo metamorphic belt that is often interpreted as the suture between the Kaapvaal and Zimbabwean cratons. Of the on-craton localities, only the Premier kimberlite shows a significantly younger average Re-Os T_{RD} model age of 2.2 Ga (Carlson *et al.*, 1999). Of the localities so far studied, Premier is the only kimberlite erupted near the 2.05 Ga Bushveld igneous intrusion. The offset of the Premier xenolith data to circa 2.0, rather than 2.6 Ga ages, may indicate that the mantle beneath Premier was affected by the Bushveld magmatic event (Carlson *et al.*, 1999).

In contrast to on-craton areas, peridotite xenolith suites from off-craton areas surrounding the Kaapvaal craton yield significantly younger T_{RD} models ages (Pearson *et al.*, 1998a; Pearson, 1999b), indicating younger, Proterozoic formation ages for circum-cratonic lithospheric mantle. The East Griqualand kimberlite field is immediately adjacent to the south-east margin of the Kaapvaal craton (Figure 3.1), ca. 170 km from the Lesotho kimberlite field. Xenoliths from East Griqualand kimberlites have T_{RD} model ages of up to 2.35 Ga with no evidence of Archean ages (mean = 1.7 +/- 0.4 Ga, median = 1.7 Ga, n = 14). Maximum T_{RD} model ages for off-craton peridotites also appear to decrease as a function of distance from the craton (Janney *et al.*, 1999).

The various end-member models of craton generation that have been proposed (de Wit *et al.*, 1992; Kröner and Layer, 1992; Pearson, 1999a; Pearson, 1999b) may produce different lateral variations in lithospheric mantle age over the craton to which we can compare the observed variation in peridotite xenolith ages. The results of this study raise several interesting questions and possibilities concerning the evolution of the Kaapvaal lithospheric mantle and have implications for the varying models of craton generation. One model suggests that the lithospheric mantle beneath the Kaapvaal craton is ultimately Hadean in age (4.5 – 4.0 Ga) and may have crystallised from an early magma ocean (Herzberg, 1993). Over 100 samples of this lithospheric mantle have now been analysed, none of which appear to record any vestiges of a Hadean age. Plumes have also been invoked for forming the large volumes of Archean craton (Kröner and Layer, 1992; Herzberg, 1993). The very large number of T_{RD} model ages for the whole Kaapvaal lithospheric mantle that cluster in the 2.7 Ga area may provide support for a large, single mantle differentiation event that formed the bulk of the lithospheric keel beneath the craton; such as may be associated with plume activity.

Unfortunately, Re-Os T_{RD} model ages are not sufficiently precise to distinguish between an essentially instantaneous formation for the Kaapvaal lithosphere, i.e. plume model, compared to a more prolonged formation process, for example by subduction or imbricate stacking of oceanic lithosphere (de Wit *et al.*, 1992). In any case, the ca. 2.6 Ga mean ages for the peridotites is considerably younger than the main 3.5 to 3.2 Ga crust-building event recorded over large parts of the Kaapvaal craton (Herzberg, 1993). If the late Archean T_{RD} model ages recorded by most Kaapvaal xenoliths are a true reflection of their ages, a large lithospheric mantle stabilisation event would appear to be coincidental with the generation of the voluminous Ventersdorp lava sequence (de Wit *et al.*, 1992).

Chapter 4

The Slave Craton – Peridotite Xenoliths from the Jericho Kimberlite

4.1 Introduction

Our present knowledge regarding the nature and origin of 'continental roots' is based on a limited sample set. Until comparatively recently, samples of sub-cratonic mantle, erupted by kimberlitic magmatism, were dominated by xenoliths from South Africa, with up to 70% of cratonic mantle material described coming from the Kaapvaal craton (Boyd and Mertzman, 1987; Boyd, 1989; Griffin *et al.*, 1999a). Much of the remaining sub-cratonic mantle samples analysed originate from the Udachnaya kimberlite (Siberian craton). There are several similarities between mantle samples from these two areas (Boyd *et al.*, 1997) and together they have dominated our thinking when it comes to understanding the evolution of cratonic lithospheric mantle. More recent prospecting has led to the discovery of kimberlites on other cratons, producing a more characteristic/representative collection of cratonic peridotites from around the world.

The Slave Structural Province in the Northwest Territories of Canada (Padgham and Fyson, 1992) is one of several Archean nuclei that form the North American Craton (Figure 4.1). Until the discovery of kimberlites in the Slave craton in the 1990's, the lithospheric mantle underlying this craton was inaccessible to studies other than geophysical. The first kimberlite occurrences in the craton were discovered in the Lac de Gras region in 1991, at Lac de Gras (Pell, 1997). In the wake of these initial discoveries more than 250 kimberlite pipes have now been recorded (Pell, 1997). Peridotite xenoliths from these kimberlites have provided the first insights into the lithospheric mantle underlying this craton and therefore provide the prospect of further expanding our view of lithosphere formation. This allows us to examine the validity of models of cratonic growth developed for the Kaapvaal and Siberian cratons by analysing the evolution and growth of a third Archean craton, the Slave craton.

4.2 Geological Setting

4.2.1 Regional Geology

The Slave craton has a long geological history with its origin in the Archean and the formation the Canadian Shield, but continuing through to the Tertiary with kimberlite magmatism. The geological record for the Slave craton is summarised in Table 4.1.

The Archean Slave Province is a small Archean granite-greenstone terrane, approximately 190,000 km^2 (Hoffman, 1989) to 210,000 km^2 (Isachsen and Bowring, 1994) in area, located in the Northwest and Nunavut Territories of Canada, on the northwest margin of the Canadian Shield (Figure 4.1).

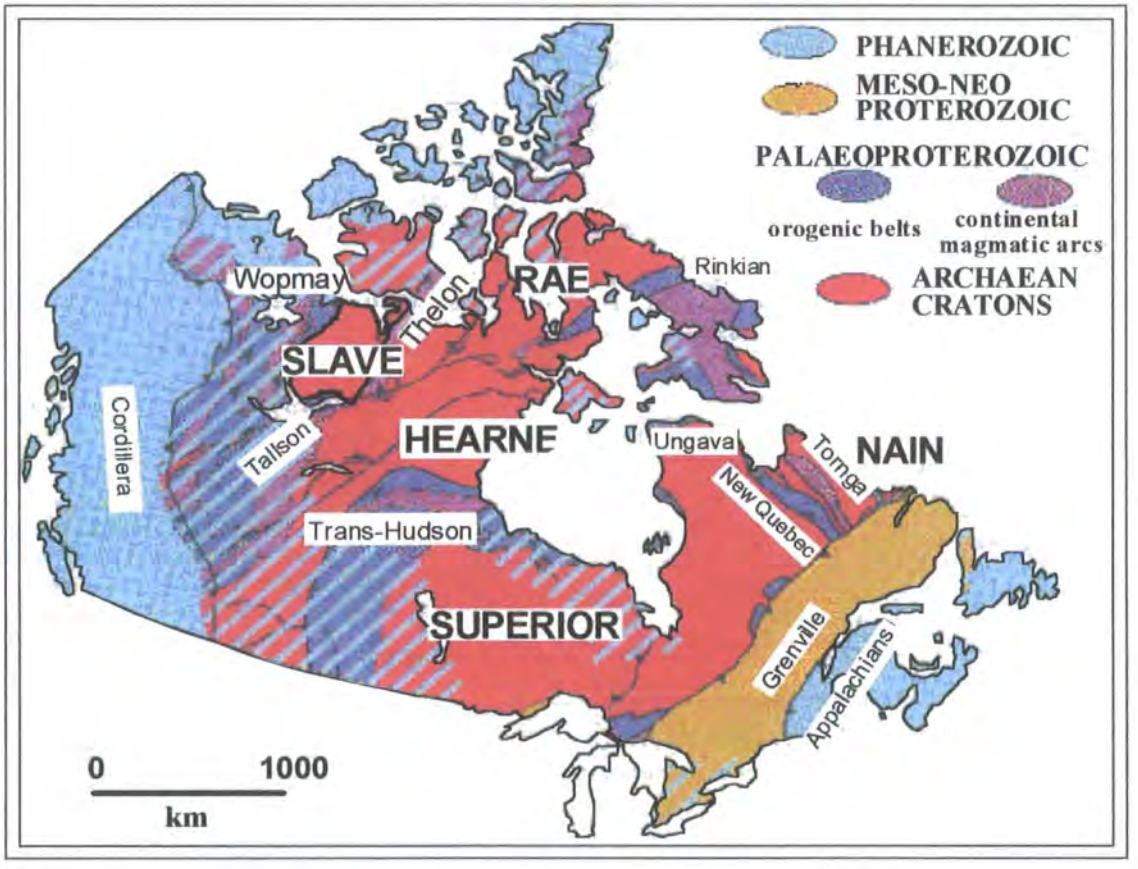

Figure 4.1 Precambrian tectonic elements of the North American craton in Canada, modified after Percival (1996). Slave craton highlighted with heavy border. Upper case names represent Archean Provinces; lower case names represent Proterozoic and Phanerozoic orogens. Blue diagonal stripes represent areas where the Precambrian basement is covered by Phanerozoic platformal cover.

Like many Archean cratons around the world, the Slave craton is comprised of mainly granitoid intrusive rocks (up to 65% of current exposure) with greenstone belts

Table 4.1 Summary of Geological events for the Slave craton.

Type	Geology	Age	Comments	Reference
Archean				
Basement rocks	Gneisses, migmatites and deformed granitoids	> 2.9 Ga	Central Slave Basement Complex (Anton terrane and Sleepy Dragon complex) including the 3.96-4.0 Ga Acasta Gneiss.	1, 2, 3, 4
Early cover	Mafic rocks, Quartzite, BIF, felsic volcanics	2.92 – 2.73	Central Slave Cover Group. Stratigraphically beneath the Yellowknife Supergroup.	1, 2, 4
Mafic to intermediate volcanics	Greenstone Belts	2.73 – 2.61 Ga		1, 2
Sedimentary rocks	Basalts and Metaturbidites	2.71 – 2.61 Ga	Yellowknife Supergroup e.g. Contwoyto and Itchen formations.	1, 2
Synvolcanic intrusives	High and low Al_2O_3 trondhjemite and diorite.	2.72 – 2.65 Ga	Associated with volcanism. Calc-alkaline.	1, 2, 5
Syn-deformational intrusives	trondhjemites, monzodiorites and granodiorites	2.62 - 2.59 Ga	Metaluminous, calc-alkaline.	1, 2, 5
Post-deformation/collision intrusives	biotite and 2 mica granite	2.59 - 2.58 Ga	Partial melting of metasedimentary protoliths.	1, 2, 5
Metamorphism and deformation	Amphibolite and Greenschist	2.62 – 2.59 Ga	2 – 6 kbar	6
Alkaline Intrusions	Carbonatites	2.6 – 2.59 Ga	Two loclaities recorded.	7
Proterozoic				
Dyke swarm	Diabase	2.23 Ga	Malley dyke swarm. NE trending.	8
Dyke swarm	Diabase	2.21 Ga	Mackay dyke swarm. E trending.	8
Intrusives	Peralkaline granite-syenite, alkaline-carbonatite complex	2.18 Ga		9
Dyke swarm	Diabase	2.03 – 2.02 Ga	Lac de Gras dyke swarm. NNE trending.	8
Orogen		2.2 - 1.92 Ga	Thelon Orogen which formed when the craton was involved in a continent-continent collision with the Churchill Province (Rae sub-province)	10, 11
Orogen		1.97 - 1.84 Ga	Wopmay Orogen bounds the Slave Province on the western margin and developed as a result of collision between the Slave and a buried Nahanni continental block to the West.	12, 13
Sedimentary cover	Foredeep and Shelf sediments	2.2 – 1.86 Ga	Kilohigok Basin associated with Thelon oroceny, central and north. Wopmay sediments in west.	12, 13, 14

Table 4.1 (Continued) Summary of Geological events for the Slave craton.

Type	Geology	Age	Comments	Reference
Dyke swarm	Diabase/gabbro	1.27 Ga	Mackenzie dyke swarm	15, 16
Dyke swarm	Diabase	0.78 Ga	Gunbarrel dyke swarm	15
Dyke swarm	Diabase	0.72 Ga	Franklin dyke swarm	15
Phanerozoic				
Paleozoic cover	Platform carbonates	Mid-Devonian	Known from xenoliths. Possibly craton wide	9
Mesozoic cover	Marine and minor (late) terrestrial sediments	Cretaceous	Known from xenoliths. Possibly craton wide	17
Cenozoic	terrestrial sediments	Tertiary		17
Kimberlites:				
Drybones		440 Ma		18
Jericho		172 Ma		18
Lac de Gras		84 to 47 Ma		19

1 - Kusky (1989), 2 - Padgham and Fyson (1992), 3 - Bowring *et al.* (1990), 4 -Bleeker *et al.* (1999), 5 - Davis *et a.l* (1994), 6 - King *et al.* (1992), 7 - Relf *et al.* (1995), 8 - Le Cheminant *et al.* (1996), 9 - Pell. (1997), 10 - Hoffman. (1987), 11 - Hanmer *et al.* (1992), 12 - Hoffman (1989), 13 - Bowring and Grotzinger (1992), 14 - Tirrul and Grotzinger. (1990), 15 - Fahrig. (1987), 16 - Le Cheminant and Heaman (1987), 17 - Cookenboo (1999), 18 - Heaman *et al* (1997), 19 - Davis and Kjarsgaard (1997).

of mafic to felsic volcanic rocks (2.73-2.61 Ga) and flysch-type supracrustal metaturbidites (Padgham and Fyson, 1992). The Slave Province has some unique features compared with other cratons. It contains a higher proportion of metasedimentary and felsic volcanic rocks, a large number of evolved high-K granitoids and limited occurrences of ultramafic igneous rocks with no alkalic lavas known (Padgham and Fyson, 1992). Komatiites are rare and occur only in the extreme southern and northern part of the craton (Bleeker *et al.*, 1999a, B.A. Kjarsgaard, pers. comm., 2000), and are believed absent elsewhere.

The Slave craton is suggested to have grown by the amalgamation of an ancient micro-continent, the Anton Terrane, with younger convergent margin material through eastward subduction (Hoffman, 1989; Kusky, 1989; Griffin *et al.*, 1999b, Figure 4.2). The convergent margin material that docked with the Anton Terrane comprises the Contwoyto Terrane, believed to be an accretionary wedge, and the Hackett River magmatic arc. The adjoining deformed continental margin is represented by the Sleepy Dragon terrane (Fyson and Helmstaedt, 1988; Kusky, 1989). However, recent isotopic and mapping studies (Bleeker *et al.*, 1999a; Bleeker *et al.*, 1999b) have proposed a rifting and plume origin for many of the sequences attributed to the accretionary model, though these studies have not yet ruled out a subduction process.

The ancient 2.9-4.0 Ga Anton Terrane basement, more recently termed the Central Slave Basement Complex (CSBC) along with the Sleepy Dragon terrane by Bleeker *et al.* (1999), consists of quartzofeldspathic gneisses, migmatites and deformed granitoids. This complex includes some of the oldest known rocks on Earth, the 3.96-4.0 Ga Acasta gneiss (Bowring *et al.*, 1990; Bowring and Housh, 1995). The Hackett River Terrane is composed of volcanic rocks, predominantly felsic-intermediate calc-alkaline pyroclastics, and associated sub-volcanic trondhjemite and diorite plutons (2.72-2.65 Ga). Turbidite deposits to the SW of this magmatic arc have been interpreted as submarine fans in a fore-arc setting (King *et al.*, 1992). To the NE of the arc greywackes have been interpreted as back-arc basin deposits. The Contwoyto Terrane consists of greywacke-mudstone turbidites with tectonic slivers of iron formations and mafic volcanics.

The basement rocks of the Sleepy Dragon terrane are overlapped by an ancient stable shelf assemblage consisting of mafic rocks at the base, overlain by quartz arenites and sandstones of basement provenance (2.9-3.7 Ga detrital zircon ages, Padgham and Fyson, 1992; Isachsen and Bowring, 1997) and associated with iron formations. These are overlain by felsic volcanics. This basement cover has the earliest known sediments

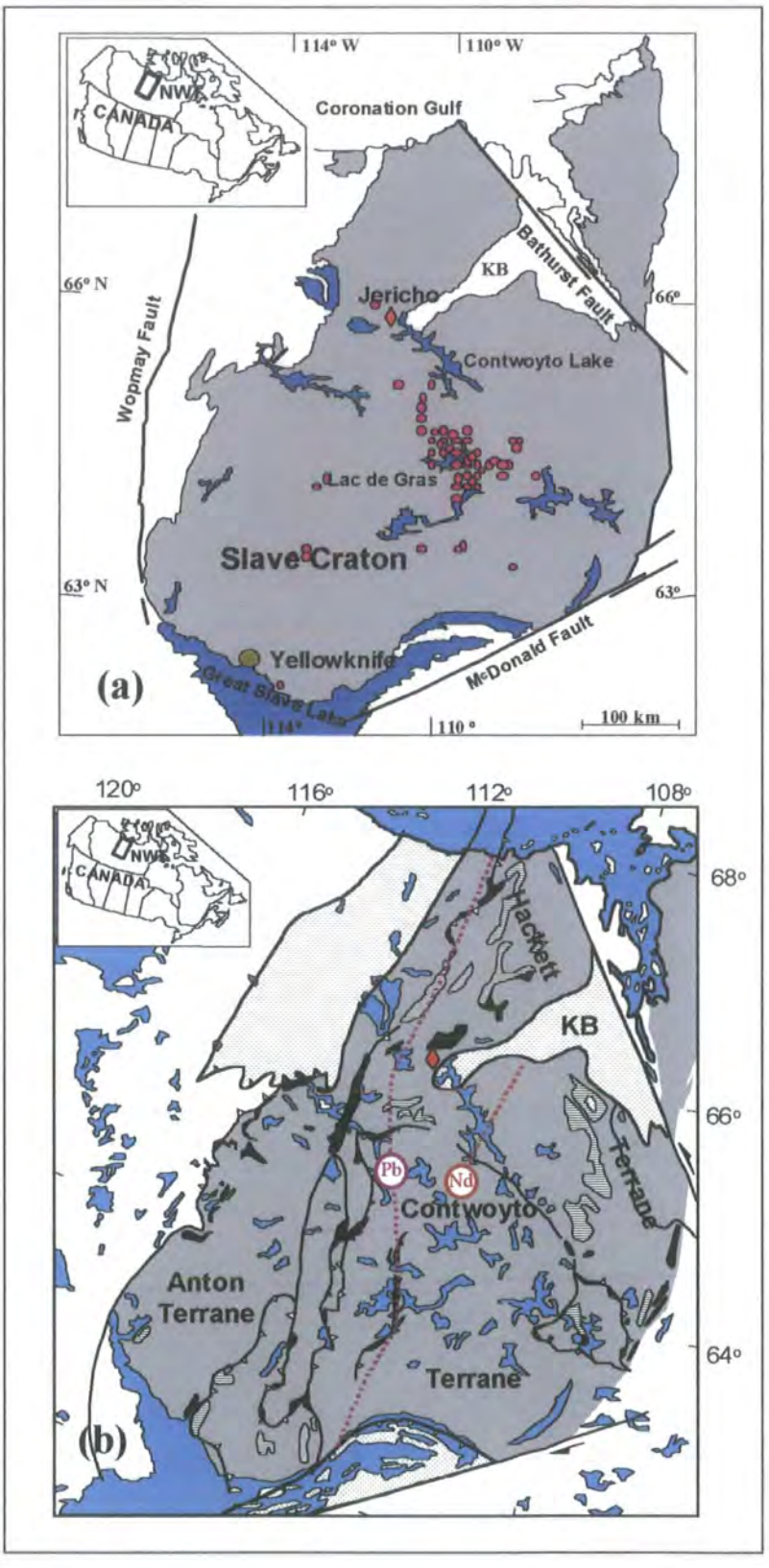

Figure 4.2 Schematic map of the Slave craton, Northwest Territories, Canada, modified after Kopylova *et al.* (1999b) and Padgham and Fyson (1992). (a) Distribution of kimberlites (purple circles) within the Slave craton. Location of the territorial capital, Yellowknife, marked by yellow, striped circle. Location of Jericho kimberlite marked by a red diamond. Faults indicated by bold lines. (b) Terrane map of the Slave craton showing felsic volcanics (horizontal lines), mafic volcanics (black) and Proterozoic sediments (stippled). Purple dashed line represents the Thorpe (1992) Pb isotopic boundary and brown dashed line represents the Nd isotopic boundary of Davis and Hegner (1992). KB – Kilohigok Basin.

in the province and has been collectively termed the Central Slave Cover Group (CSCG) by Bleeker *et al.* (1999a). This cover sequence is believed to be younger than ca. 2924 Ma but older than ca. 2734 Ma, the oldest recorded age of mafic magmatism related to the Yellowknife Supergroup (Bleeker *et al.*, 1999a; Bleeker *et al.*, 1999b). The supracrustal rocks of the Slave craton, in general, are collectively grouped together within the Yellowknife supergroup (2.73-2.61 Ga) due to overall similarities. The most dominant units, occurring within the Yellowknife supergroup, are the greywacke-mudstone turbidites with volcaniclastic debris, which are widespread in all parts of the craton. These are derived from and interbedded with felsic, basaltic and andesitic volcanic rocks. A large proportion of the volcanic rocks are felsic to intermediate in composition (up to 45%) and the basalts are SiO_2 rich (>50%) (Padgham and Fyson, 1992).

Recent studies have suggested that the Anton Terrane may represent the remnants of a rifted continental block (Yamashita *et al.*, 1998; Doyle *et al.*, 1999). It has also been suggested that mafic-intermediate volcanic rocks in this terrane may have been generated in a single back-arc system. The Hackett Terrane with its dominantly felsic volcanic rocks may represent a fore-arc setting. The size and composition of these settings has been likened to the present-day Sino-Korea/Japan system (Yamashita *et al.*, 1998). This setting of continent and back/fore-arcs also has significant turbidite deposits in the associated basins, comparable to the Contwoyto Terrane.

The final stabilisation and cratonisation of the Slave craton was marked by the emplacement of voluminous granitoid intrusions ca. 2.62-2.58 Ga during and after collision (Davis *et al.*, 1994). These include the group 2 syn-deformational trondhjemites, monzodiorites and granodiorites (2.62-2.59 Ga) and group 3 post-deformation/collision biotite and 2 mica granite (2.59-2.58 Ga) of Davis *et al.* (1994). The group 2 granitoids have calc-alkaline chemistry and trace element patterns which are suggestive of modern subduction related igneous suites. The group 3 granitoids in contrast resemble K-U-Th rich Phanerozoic post-orogenic suites.

Pb and Nd isotope studies indicate a fundamental division between the western and eastern Slave craton (Davis and Hegner, 1992; Thorpe *et al.*, 1992; Bleeker *et al.*, 1999a). Pb isotope studies on volcanogenic massive sulfide deposits indicate a major boundary approximately co-incident with the 112°W meridian (Figure 4.2). The Pb to the West of the line is more radiogenic indicating a derivation in part from older felsic crust. To the East the Pb indicates a more juvenile source (Thorpe *et al.*, 1992). This boundary also approximately delineates the eastern limit of basement rock exposures,

and basal quartz arenite occurrences of the CSCG. The Nd isotopic composition of group 3 granitoids produces a similar boundary, offset to the East of the Pb line by approximately 100km (Davis and Hegner, 1992, Figure 4.2). The isotopic signatures correspond to a significant boundary within the Slave craton related to crustal volumes of different ages, and it has been suggested this represents the accretion of younger portions of the craton in the East to an older western continent at ca. 2.7 Ga.

Geological evolution of the Slave craton continued into the Proterozoic. The Province was welded together with other Archean cratons, including the Superior and Nain Provinces in the Paleoproterozoic (2.5 – 1.6 Ga) to form the North American craton (Percival, 1996, Figure 4.1). The Slave Province is bounded to the East by the Thelon Orogen (ca. 2.2-1.92 Ga) which formed when the craton was involved in a continent-continent collision with the Churchill Province (Rae sub-province). The southern margin is bounded by the Great Slave Lake shear zone, interpreted as a 1.9 Ga intracontinental transform fault related to the eastward indentation of the Slave craton into the Churchill Province (Hoffman, 1987; Hanmer *et al.*, 1992). Remnants of an East facing passive margin shelf sequence are preserved within the Kilohigok basin, which was formed by flexure in the lithosphere related to the collision (Tirrul and Grotzinger, 1990). The Wopmay Orogen (ca. 1.97-1.84 Ga) bounds the Slave Province on the western margin and developed as a result of collision between the Slave and a buried Nahanni continental block to the West. Commencing at ca. 1.97 Ga Proterozoic island arcs were accreted to the rifted western margin of the province, thrusting foredeep and shelf sediments onto the margin (Hoffman, 1989; Bowring and Grotzinger, 1992). The Hottah magmatic arc formed between 1.94 and 1.9 Ga and was thereafter overlain by back-arc rift sequences. Subsequent to this the Great Bear continental arc (1.88-1.86 Ga) formed over the eastward subduction beneath the craton and eventually stitched the Hottah arc to the Slave craton. The terminal collision with the Nahanni terrane occurred ca. 1.8 Ga. Most geological activity involving the Slave craton ended by 1.65 Ga when the craton was incorporated into Laurentia (Hoffman, 1989).

Intrusive Igneous Geology

The Slave craton is notable for its abundance of Proterozoic dyke swarms with at least five recorded (Le Cheminant *et al.*, 1996). It is suggested that each emplacement episode represents either mantle plumes or rifting events along the margins of Laurentia and the Slave craton (Fahrig, 1987). The swarms include three old swarms, the Malley diabase dykes (2.23 Ga), the MacKay diabase dykes (2.21 Ga) and the Lac de Gras diabase dykes (2.03 and 2.02 Ga). Probably the most significant event is the younger

1.27 Ga MacKenzie diabase dykes and gabbros, which resulted in the Coppermine River flood basalts and Muskox intrusion (Le Cheminant and Heaman, 1989). The dykes extend over 2300km from a focus slightly to the west of Victoria Island, which has been interpreted as a plume head (Fahrig, 1987, Figure 4.3).

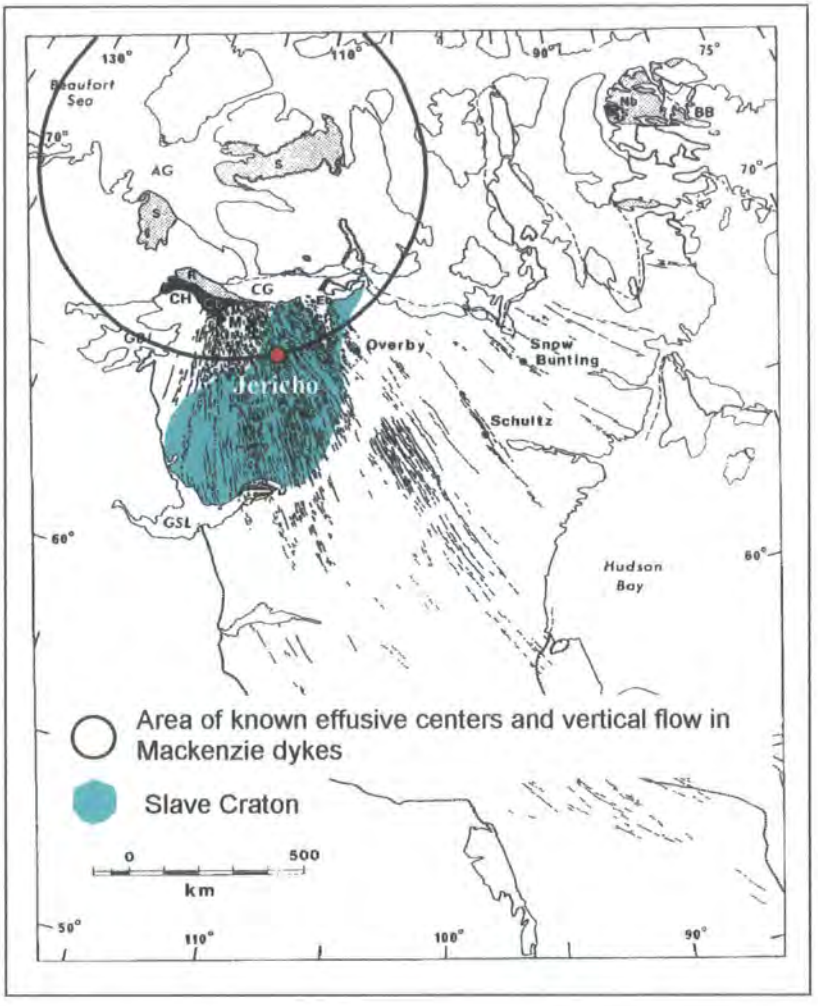

Figure 4.3 Regional distribution of MacKenzie dyke swarm and related igneous rocks, modified after LeCheminant and Heaman (1989). Large circle indicates area of vertical flow within dykes and known effusive centres. Slave craton shaded in green. M = Muskox intrusion, Cb = Coppermine River basalts. Small red circle represents the Jericho kimberlite.

At distances less than 500km from the focus, including the northern extremities of the Slave craton, dykes have been emplaced vertically but at distances greater than 500km the dykes appear to be dominated by horizontal flow fabrics (Ernst and Baragar, 1992). Other notable events include the Gunbarrel and Franklin diabase dyke swarms at 0.78 and 0.72 Ga respectively (Fahrig, 1987). In addition to the dyke swarms there were carbonatites emplaced at 2.6-2.59 Ga (Relf *et al.*, 1995) and peralkaline granite-syenite and alkaline-carbonatitic complexes emplaced at 2.18 Ga (Pell, 1997). The emplacement of diamondiferous kimberlites in the late Cretaceous and Eocene

would suggest that these Paleo- and Meso-proterozoic magmatic events did not significantly remove diamond bearing lithospheric mantle or raise the geotherm for prolonged periods.

Sedimentary Cover

Phanerozoic cover rocks are absent in the Slave craton and are known only from xenoliths contained within some kimberlites (Pell, 1997). Middle Devonian fossiliferous limestones, Cretaceous to Tertiary mudstones and other Paleozoic limestones have all been reported (Cookenboo, 1999, and references therein), and these are commonly exposed in the areas surrounding the Slave craton.

Kimberlite Activity

Kimberlite has been intruded into the Slave craton episodically from the Cambrian through to the Tertiary (Heaman *et al.*, 1997). The Lac de Gras area kimberlite pipes in general are aligned in a NNW trend with subordinate pipes orthogonal to the main trend, both NNE and ENE in alignment (Kjarsgaard, 1996). The majority of kimberlite occurrences discovered in the Slave craton are concentrated in the Lac de Gras region, in the centre of the craton, and there may be several generations. These range in age from 47 to 84 Ma, though older kimberlites activity has been suggested (Davis and Kjarsgaard, 1997). These Eocene ages are consistent with the occurrence of Paleocene and Cretaceous fossils within kimberlites. Outwith the central Slave, older kimberlite pipes have been dated, with Jericho in the Northwest yielding Jurassic Rb-Sr and U-Pb ages of 172 +/- 2 Ma (Heaman *et al.*, 1997; Kopylova *et al.*, 1999b) and in the Southwest the Drybones pipe dated at 440Ma by U-Pb and the AK5035 pipe at 539 Ma (Davis and Kjarsgaard, 1997; Heaman *et al.*, 1997). Most kimberlites are small and do not outcrop at the surface but are instead covered by glacial till or lakes. They are usually carrot-shaped like classic South African kimberlites but much smaller in size, and invariably eroded (Kjarsgaard, 1996).

4.2.2 Geological setting of the Jericho kimberlite

The mid-Jurassic (172 + 2 Ma, Heaman *et al.*, 1997) Jericho kimberlite is located approximately 400 km north-northeast of Yellowknife, NWT, near the northern end of Contwoyto Lake and 60 km south of the Arctic circle in the barrenlands of northern Canada (65°59'55"N, 111°28'45"W; (Kopylova *et al.*, 1999b, Figures 4.2 and 4.4a). The Jericho kimberlite is a diamondiferous group Ia multiphase kimberlite with a precursor dyke and at least two pipes (Cookenboo, 1998; Kopylova *et al.*, 1998a). The

Jericho Pipe (JD-1) was discovered in 1995, 135 km north of the Ekati cluster of kimberlite pipes near Lac de Gras (Figure 4.4b), beneath 10-35 m overburden. A second satellite pipe, JD-2, was discovered 250m north of the first kimberlite, and together these form the Tahera Corporation Jericho Diamond Project (Figure 4.4c).

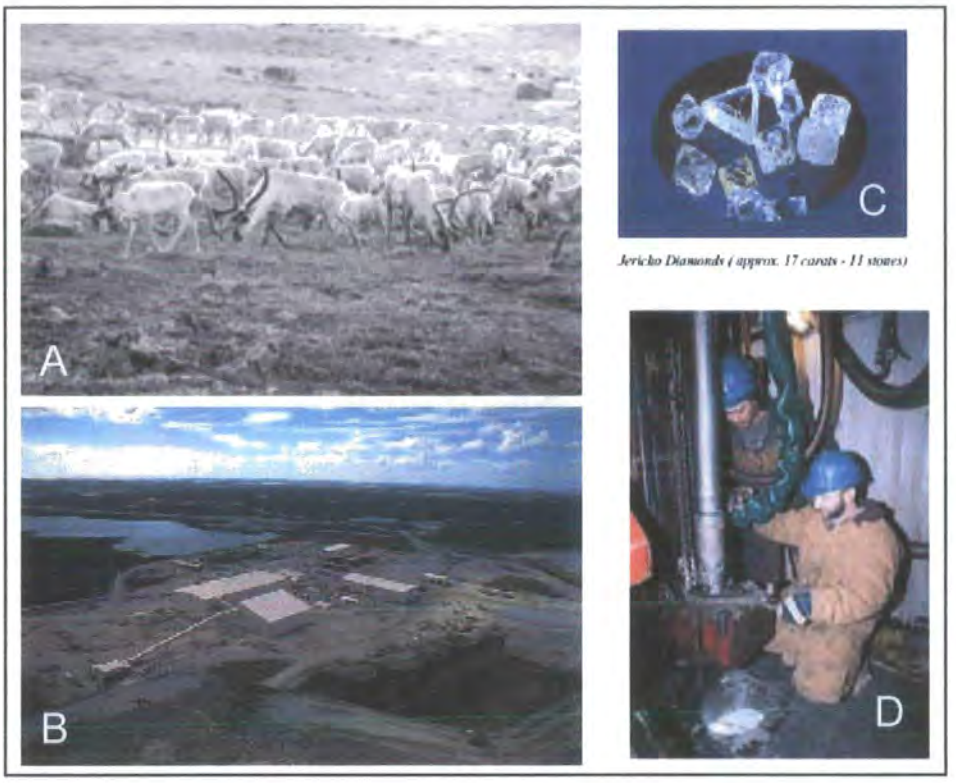

Figure 4.4 Photographs from diamond prospecting of the Slave craton (Tahera Corporation web page, 2001). A) The barrenlands of Canada. Typical flora and fauna taken at the Jericho kimberlite site. B) Mining activity at the Ekati kimberlite displaying typical features of the barrenlands of Canada. C) Diamonds from the Jericho kimberlite pipe, recovered during bulk sampling and coring of the kimberlite. D) Drilling operations to recover cores from the Jericho kimberlite.

The Jericho pipe intrudes Archean granitic basement rocks of the 2.58–2.59 Ga Contwoyto batholith (van Breeman *et al.*, 1989; Bowie, 1994) and at depth intrudes older Precambrian dykes. The Jericho kimberlite is located to the East of the Thorpe (1992) Pb-isotope boundary but to the West of the Nd-isotope boundary of Davis and Hegner (1992, Figure 4.2). The main Jericho pipe, JD-1, is located in a topographic low between two parallel mafic Mackenzie dykes; the first located 40m to the east with a strike of 335° and the second 250 m to the west (Cookenboo, 1999). Pipe JD-2 is located on the shore of nearby Carat lake and is connected to JD-1 by a kimberlite dyke with a strike parallel to that of the Mackenzie dykes. Archean metaturbidite and banded iron formation, belonging to the Contwoyto formation of the Yellowknife Supergroup, outcrop 8 km to the south of the Jericho kimberlite (King *et al.*, 1992). The western margin of the Kilohigok basin lies 1 km to the southeast of Jericho, and sediments from

this basin form cliffs above the Archean basement. These sediments thicken towards the centre of the basin in the east where younger gabbroic sills can be found. The Jericho kimberlite hosts peridotite xenoliths from the underlying mantle. Griffin *et al.* (1999b) and Kopylova and Russell (2000) have suggested that the Jericho kimberlite erupts through the Hackett Terrane. The Jericho kimberlite was also located to the east of the published Thorpe (1992) Pb-isotope boundary (Figure 4.2), and west of the Nd-isotope boundary of Davis and Hegner (1992). However, the Hackett terrane does not extend this far west, and recent unpublished GSC Pb-data on Galena from the Lupin Mine (east of Jericho) suggest it is "old". Jericho therefore lies to the west of the Pb-isotope boundary (Kjarsgaard, pers. comm., 2001; Figure 4.2). The mantle underlying the Jericho kimberlite therefore belongs to either the CSBC, or Contwoyto terrane.

4.3 Sample selection and Summary of previous studies

4.3.1 Jericho sample selection

A representative selection of thirty peridotite xenoliths was chosen for this study from the collection of M.G. Kopylova at the University of British Columbia. A sample list with textural summaries is provided in Appendix A. The Jericho collection has been well characterised petrologically and for major element whole rock geochemistry by Kopylova *et al.* (1999b) and Kopylova and Russell (2000).

A comprehensive suite of approximately 200 mantle xenoliths was available from test boreholes and a large tonnage underground bulk sample of the Jericho kimberlite (Figure 4.4d). The xenoliths are normally less than 15 cm in diameter but can be upwards of 30 cm in size (Kopylova *et al.*, 1999b). The Jericho kimberlite contains a variety of mantle xenoliths that can be assigned to five groups based on mineralogy and texture: i) coarse peridotite, ii) porphyroclastic peridotite (fluidal and non-fluidal), iii) eclogite (massive and anisotropic), iv) megacrystalline pyroxenite, and v) ilmenite-garnet wehrlite and clinopyroxenite (Kopylova *et al.*, 1999a). The xenolith suite has the following proportion of rock types: 36% coarse peridotite, 23% porphyroclastic peridotite, 25% eclogite, 12% megacrystalline pyroxenite and 4% wehrlite and clinopyroxenite. In general the mantle beneath the Jericho kimberlite resembles cratonic mantle elsewhere in terms of proportions, petrography and mineralogy, with distinct low-temperature and high-temperature suites. Eclogite appears to be more common at Jericho than in most South African pipes.

The Jericho xenolith suite at present represents the largest sized and best-studied xenolith suite to come from the Slave craton to date. Pearson *et al.* (1999) have studied large numbers of small samples (<5 cm in size) but modes and bulk-chemical data are not considered reliable.

The methods of sample preparation and whole-rock analysis are described in detail in Appendix B. Trace elements and REE were determined by ICP-MS. The precision was estimated from duplicate analyses of rock standards.

4.3.2 Xenolith Petrography

Kopylova *et al.* (1999b) carried out extensive petrographical studies on the Jericho suite of mantle xenoliths analysed in this study, hence all samples have been previously well characterised.

4.3.2.a Coarse Peridotites

The coarse peridotites are predominantly equilibrated lherzolites and harzburgites of both spinel and garnet facies and show mainly equant and tabular textures in the nomenclature of Harte (1977). These peridotites are composed of 55-90% olivine, 0.5-10% orthopyroxene, 0-10% clinopyroxene, 0-5% Garnet, and 0-1% spinel. Early crystallisation of large subhedral olivine (3-10 mm) and orthopyroxene (0.8-5 mm) and late crystallisation of anhedral clinopyroxene (1-7 mm), garnet and spinel produce the coarse textures of these peridotites (Figure 4.5a). Evidence of secondary alteration includes serpentinisation, carbonate pseudomorphs and phlogopite growth, though some Jericho samples appear to contain primary-metasomatic phlogopite and amphibole as defined by Winterburn *et al.* (1990).

4.3.2.b Porphyroclastic Peridotites

Deformation textures in porphyroclastic peridotites from Jericho subdivide these peridotites into non-fluidal (Figure 4.5b) and fluidal porphyroclastic peridotites (Figure 4.5c).

Non-fluidal Porphyroclastic

The non-fluidal porphyroclastic peridotites comprise 40-90% strained olivine porphyroclasts (1.5-7 mm), 3-40% euhedral, tabular or equant olivine neoblasts (0.05-0.5 mm), 5-12% orthopyroxene porphyroclasts (up to 4 mm), 0-10% subhedral clinopyroxene (≤ 4 mm), and 2-10% euhedral colourless garnet (0.5-3 mm).

Fluidal Porphyroclastic

Fluidal porphyroclastic peridotites can be subdivided into non-disrupted and disrupted peridotites. The non-disrupted peridotites comprise 20-45% strained olivine porphyroclasts, 35-70% equant or tabular olivine neoblasts (0.5 mm), 1-5% clinopyroxene (bands of neoblasts with few porphyroclasts), 1-15% orthopyroxene (both strained porphyroclasts and fine neoblasts), and 1-3% garnet.

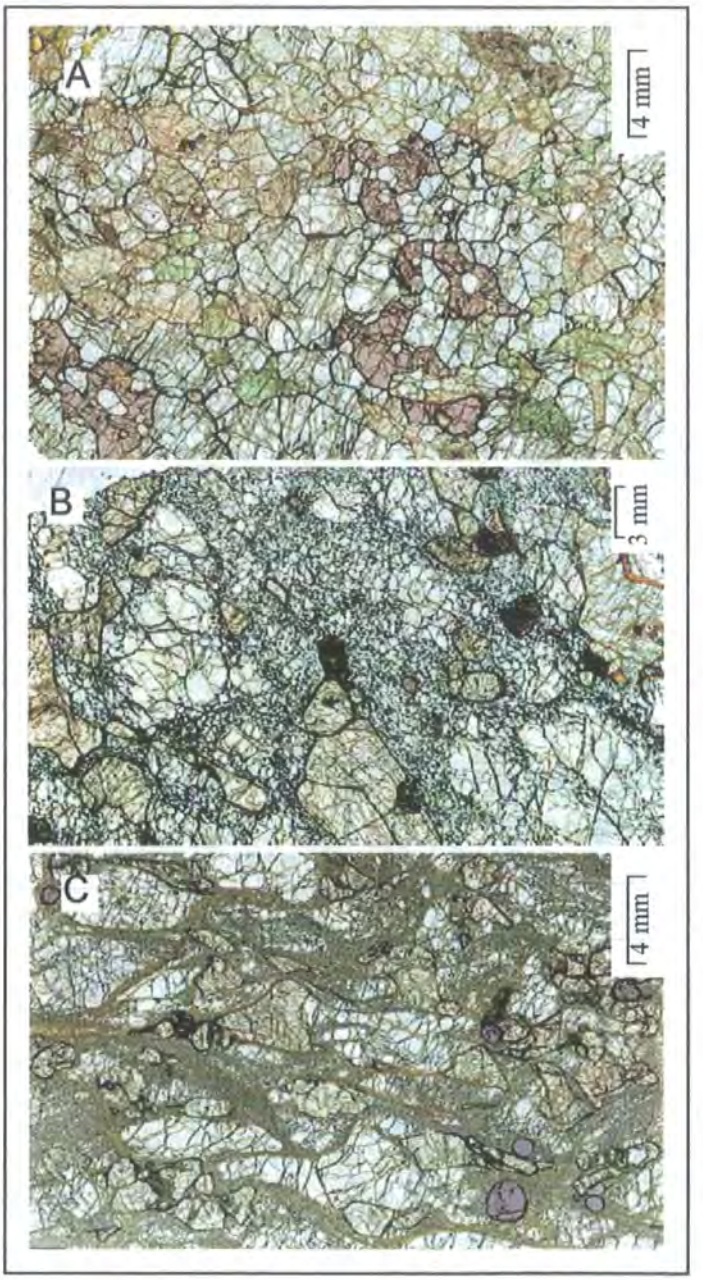

Figure 4.5 Photomicrographs of peridotite xenoliths from the Jericho kimberlite (Kopylova *et al.*, 1999b), showing (a) coarse equant texture in a garnet lherzolite, (b) porphyroclastic non-fluidal texture of a garnet harzburgite, and (c) porphyroclastic non-disrupted fluidal texture of garnet harzburgite.

The disrupted peridotites comprise of up to 70% olivine neoblasts (0.03-0.05 mm), 10-15% orthopyroxene neoblasts in banded layers (with few porphyroclasts), 1-5%

clinopyroxene neoblasts, and contain stringers and layers of disrupted garnet (0-3%) much of which is replaced by phlogopite.

4.3.3 Mineral Chemistry

Petrological studies of Jericho peridotites by Kopylova *et al.* (1999b) have shown shared features between the Slave cratonic mantle and cratonic mantle elsewhere. Low temperature peridotites from Jericho have Mg-enriched mineral compositions comparable to peridotites from other cratons. Similarity in olivine compositions show corresponding degrees of melt depletion, with modal magnesium numbers ($Mg^{\#}$ = 0.91-0.93) parallel to the average for Kaapvaal and Udachnaya (Boyd *et al.*, 1997). High temperature peridotites from Jericho show Fe, Ca and Ti-enriched mineral chemistry which is a common feature in cratonic suites world-wide (Boyd and Mertzman, 1987; Smith and Boyd, 1987; Harte and Hawkesworth, 1989). Harzburgites from Jericho lack sub-calcic (G10) garnet, which is a feature shared with some harzburgites of the Kaapvaal craton; this has been accredited to equilibration within lherzolite dominated mantle (Boyd and Nixon, 1978). Late stage Na, Al and Cr-depleted clinopyroxene along orthopyroxene grain boundaries in Jericho peridotites has counterparts in Udachnaya peridotites. This has been attributed to secondary crystallisation upon eruption (Boyd *et al.*, 1997).

Three unique trends are apparent within Jericho peridotite xenoliths: i) a high proportion of texturally unequilibrated samples, ii) Cr-enriched mineral chemistry in porphyroclastic peridotite relative to coarse, and iii) a compositional trend in pyrope garnets that is less Cr-enriched than the common "lherzolitic" trend (Kopylova *et al.*, 1999b).

Minerals in unequilibrated samples show patchy zoning, which is generally restricted to rims. Clinopyroxene and garnet are the most heterogeneous minerals, with garnet showing depletion in CaO and Cr_2O_3 towards rims. Clinopyroxene shows three distinct zoning patterns that are superimposed on a common decrease in Al_2O_3 and Na_2O towards the rim: i) Ca-enrichment with Cr-depletion, ii) Ca-enrichment with little or no Cr-enrichment, and iii) Fe-Ti enrichment (Kopylova *et al.*, 1999b). Three processes are required to explain this mineral disequilibrium. Garnet growth at the expense of clinopyroxene may explain redistribution of Ca and Al (Sautter and Harte, 1988) between these minerals. Clinopyroxene trends i) and ii) are normally related to cooling but these are more pronounced in high-temperature peridotites. Clinopyroxene trend iii)

is consistent with an increase in temperature and may be related to mantle-melt metasomatism (Harte *et al.*, 1987; Smith and Boyd, 1987). Trend iii) is uncommon at Jericho but cryptic metasomatism is evident from Y and Zr contents of garnets (Kopylova *et al.*, 1998b).

Compared to undeformed coarse peridotites, minerals from porphyroclastic samples are Cr-rich or show Cr-zonation. Olivine and orthopyroxene is Cr and Ca-enriched, and garnet higher in Cr_2O_3. Cr-enrichment is not evident in clinopyroxene from porphyroclastic peridotites. These may be primary features associated with an absence of spinel, relating to depth. Alternatively the variation may be secondary and related to deformation. Kopylova *et al.* (1999b) found Cr-enrichment in rims of clinopyroxene porphyroclasts and neoblasts and rare olivine porphyroclasts that retained early depletion of Cr and Ca.

Garnet from spinel bearing peridotites display an "unusual" Cr-Ca trend that is less Cr-enriched than the common lherzolitic trend. This has been attributed to equilibration with a lherzolitic mineral assemblage containing spinel, though the rarity of this trend may allude to an unknown contributing factor (Kopylova *et al.*, 1999b). Garnets from spinel-free peridotites plot on a lherzolitic trend.

4.3.4 Geothermobarometry

Using the geothermometers of Finnerty & Boyd (1987), O'Neill & Wood (1979), Brey & Köhler (1990) and geobarometers of MacGregor (1974), and Brey & Köhler (1990), Kopylova *et al.* (1998c; 1999b) constructed a pressure-temperature (P-T) array for the paleo-geothermal regime of the cratonic mantle beneath Jericho. This was derived from coexisting garnet-clinopyroxene-orthopyroxene compositions within peridotite samples, using only homogenous core compositions. Geothermobarometry separates the Jericho peridotites into low- and high-temperature suites. Samples consistent with the steady-state conductive geotherm are considered low-temperature whilst peridotites shifted from the geotherm to higher temperatures were defined as the high-temperature suite. Low temperature peridotites are generally coarse textured, and only rarely porphyroclastic. High temperature peridotites are exclusively porphyroclastic and garnet is always non-disrupted. Disrupted garnet only occurs in low-temperature samples. This relationship between equilibration temperature and texture is similar to that of the Kaapvaal xenolith suite. Coarse peridotite equilibrated at depths between 45 and 190 km and temperatures approximately 500-1000°C. High-T

porphyroclastic peridotite derives from below 190 km and at temperatures 1100-1300°C. Kopylova *et al.* (1999b) interpreted this disturbance in the P-T array and loss of coarse peridotite at 190 km as the petrological transition from lithosphere to asthenosphere. However, this may not be strictly correct, as the proposed high-T samples do not appear to be fertile enough.

Evidence from thermobarometry suggest that the mantle beneath the central Slave craton in the region of the Jericho kimberlite is cooler than the cratonic upper mantle beneath the Kaapvaal and Siberian cratons, with a mantle heat flow of 40mW/m^2, and represents a cool end-member to cratonic mantle regimes (Kopylova *et al.*, 1999b). The mantle beneath the central Slave craton is also colder than surrounding mantle from the periphery of the North American craton as sampled by kimberlites in Somerset Island, Montana, Colorado-Wyoming and Kentucky (Kjarsgaard and Peterson, 1992; Meyer *et al.*, 1994). This supports the theory proposed by Finnerty and Boyd (1987) that the lithosphere-asthenosphere boundary shallows towards the North and South of the North American craton.

4.4 Xenolith whole-rock Major and Trace element Geochemistry

4.4.1 Introduction

Based on Kaapvaal-dominated studies, a key distinguishing feature of cratonic lithospheric peridotites is a deficiency in magmaphile major elements such as Ca, Al and Fe compared to estimates of fertile mantle (Boyd and Mertzman, 1987; Nixon, 1987a; Herzberg, 1993). This was attributed to their residual nature from past partial melting and extraction events. The deficiency in Fe and Al results in compositional buoyancy, which is important for the long-term survival of lithospheric mantle keels (Boyd and McCallister, 1976; Jordan, 1979). In contradiction to the depleted nature of major elements, shallow cratonic lithospheric mantle is enriched in light rare earth elements (LREE) and modal orthopyroxene (Menzies *et al.*, 1987; Boyd, 1989; McDonough, 1990). LREE enrichment has been attributed to the interaction of lithospheric mantle with metasomatising, percolating fluids (Hawkesworth *et al.*, 1983; Menzies *et al.*, 1987).

In order to compare major element analyses, the data was recalculated as anhydrous compositions to correct for serpentinisation, reflected in the loss on ignition. The data were normalised to 100% after subtraction of loss on ignition. Uncorrected major element data are presented in Table 4.2, and corrected anhydrous data in Table 4.3.

Table 4.2 Major element compositions for Jericho peridotites. LOI: loss on ignition. Por: porphyroclastic. Major element data from Kopylova and Russell (2000), and this study.

	Low-T Coarse Spinel									Low-T Coarse Garnet					
Sample	**8-7**	**9-12**	**10-11**	**10-12A**	**10-12B**	**11-18**	**23-9**	**39-23**	**44-12**	**9-2**	**10-456'**	**11-22**	**13-2**	**21-1**	**22-1**
Major Elements in wt%															
SiO_2	45.97	42.51	43.39	44.26	44.57	43.68	45.64	42.09	41.39	42.67	44.36	44.13	41.86	45.84	45.72
TiO_2	0.02	0.04	0.05	0.04	0.02	0.02	0.02	0.04	0.02	0.05	0.05	0.08	0.05	0.03	0.032
Al_2O_3	0.64	1.79	1.21	1.24	0.53	0.41	0.67	1.28	1.05	0.34	0.95	1.6	0.47	0.66	0.84
FeO	5.33	5.48	5.76	5.72	5.34	5.25	5.07	5.46	4.63	5.28	5.94	6.03	5.95	5.48	
Fe_2O_3	0.51	2.01	1.03	0.95	0.96	0.9	0.89	1.36	2.02	1.22	1.32	1.34	2.19	1.28	7.82
MnO	0.1	0.12	0.11	0.11	0.1	0.1	0.1	0.1	0.08	0.1	0.12	0.14	0.12	0.12	0.098
MgO	45.55	41.35	45.51	43.97	45.43	47.56	44.63	46.44	42.85	46.85	42.36	41.1	44.25	43.54	44.66
CaO	0.6	1.75	0.95	0.9	0.54	0.25	0.28	0.92	0.25	0.35	1.75	1.77	0.79	0.54	0.6
Na_2O	0.24	0.33	0.17	0.22	0.2	0.09	0.09	0.26	0.13	0.18	0.2	0.25	0.24	0.22	0.06
K_2O	0.1	0.15	0.06	0.19	0.06	0.06	0.08	0.07	0.12	0.12	0.27	0.15	0.11	0.18	0.133
P_2O_5	0.018	0.037	0.023	0.023	0.018	0.013	0.014	0.013	0.019	0.025	0.06	0.047	0.025	0.028	0.011
Cr_20_3	0.277	0.386	0.383	0.387	0.324	0.198	0.384	0.526	0.405	0.327	0.411	0.843	0.288	0.434	
NiO	0.261	0.286	0.283	0.275	0.258	0.313	0.295	0.312	0.311	0.306	0.268	0.257	0.303	0.275	0.23
LOI	0.35	3.58	0.72	1.28	1.88	0.83	1.86	1.36	6.68	2.27	2.09	1.77	3.58	1.28	
Total	99.93	99.82	99.61	99.56	100.23	99.67	100.02	100.02	99.96	100.06	100.14	99.5	100.22	99.9	99.97

Table 4.2 (continued) Major element compositions for Jericho peridotites.

	Low-T Coarse Garnet							Low-T Por Gnt	High-T Por Garnet						
Sample	**22-4**	**25-4**	**26-11**	**28-15**	**41-4**	**51-2**	**53-10**	**21-3**	**21-2**	**23-1**	**26-9**	**39-3**	**40-9**	**40-20**	**40-21**
Major Elements in wt%															
SiO_2	44.7	44.26	45.32	44.18	43.65	39.63	38.87	41.97	41.59	42.45	41.31	41.01	42.19	44.69	42.18
TiO_2	0.04	0.05	0.041	0.1	0.04	0.14	0.06	0.15	0.08	0.05	0.18	0.12	0.06	0.1	0.08
Al_2O_3	1.4	1.03	0.95	1.49	0.72	5.29	0.64	1.53	0.81	0.82	2.51	1.33	0.72	1.14	0.91
FeO	5.94			5.36	5.77	5.78	5.28	5.98	6.31	6.1	7.13	5.71	6.81	5.33	6.87
Fe_2O_3	1.1	8.34	7.9	1.94	1.45	2.95	3.07	2.11	1.94	1.75	2.34	1.65	1.63	2.87	1.7
MnO	0.12	0.114	0.109	0.12	0.12	0.13	0.09	0.12	0.12	0.12	0.15	0.12	0.13	0.12	0.13
MgO	42.47	44.49	44.84	41.85	44.45	34.15	42.06	42.51	45.49	44.61	38.82	43.2	45.05	38.58	44.57
CaO	1.2	0.98	0.68	0.84	0.67	2.33	0.74	1.5	0.47	0.65	3.11	1.45	0.57	1.16	0.74
Na_2O	0.14	0.16	0.08	0.25	0.22	0.16	0.13	0.39	0.17	0.2	0.32	0.39	0.15	0.19	0.16
K_2O	0.23	0.218	0.257	0.37	0.22	0.36	0.16	0.48	0.09	0.12	0.59	0.52	0.09	0.11	0.16
P_2O_5	0.035	0.04	0.033	0.034	0.03	0.043	0.026	0.061	0.027	0.027	0.083	0.09	0.025	0.014	0.027
Cr_2O_3	0.477			0.408	0.371	0.513	0.409	0.303	0.424	0.476	0.397	0.439	0.325	0.507	0.409
NiO	0.271	0.24	0.24	0.28	0.304	0.242	0.37	0.293	0.322	0.314	0.226	0.305	0.309	0.338	0.329
LOI	0.99			2.79	1.49	8.72	8.28	2.43	1.76	1.85	2.11	3.08	0.96	5.29	1.46
Total	99.12	99.68	100.21	100.01	99.5	100.44	100.19	99.82	99.6	99.54	99.27	99.41	99.01	100.44	99.72

Table 4.3 Anhydrous major element and selected trace element data for Jericho peridotites. Abbreviations as Table 4.2. $Mg^{\#}$ = Mg/(Mg+Fe). Modes were calculated using whole-rock compositions and converting to an equivalent modal mineralogy using mass balance relationships implied by observed mineralogy in Kaapvaal peridotites.

	Low-T Coarse Spinel									Low-T Coarse Garnet					
Sample	**8-7**	**9-12**	**10-11**	**10-12A**	**10-12B**	**11-18**	**23-9**	**39-23**	**44-12**	**9-2**	**10-456'**	**11-22**	**13-2**	**21-1**	**22-1**
Major Elements in wt%															
SiO_2	46.16	44.17	43.88	45.03	45.32	44.19	46.50	42.66	44.37	43.63	45.24	45.16	43.32	46.48	45.73
TiO_2	0.02	0.04	0.05	0.04	0.02	0.02	0.02	0.04	0.02	0.05	0.05	0.08	0.05	0.03	0.03
Al_2O_3	0.64	1.86	1.22	1.26	0.54	0.41	0.68	1.30	1.13	0.35	0.97	1.64	0.49	0.67	0.84
FeO	5.35	5.69	5.82	5.82	5.43	5.31	5.17	5.53	4.96	5.40	6.06	6.17	6.16	5.56	
Fe_2O_3	0.51	2.09	1.04	0.97	0.98	0.91	0.91	1.38	2.17	1.25	1.35	1.37	2.27	1.30	7.82
MnO	0.10	0.12	0.11	0.11	0.10	0.10	0.10	0.10	0.09	0.10	0.12	0.14	0.12	0.12	0.10
MgO	45.74	42.97	46.02	44.74	46.19	48.12	45.47	47.07	45.94	47.91	43.20	42.05	45.79	44.15	44.67
CaO	0.60	1.82	0.96	0.92	0.55	0.25	0.29	0.93	0.27	0.36	1.78	1.81	0.82	0.55	0.60
Na_2O	0.24	0.34	0.17	0.22	0.20	0.09	0.09	0.26	0.14	0.18	0.20	0.26	0.25	0.22	0.06
K_2O	0.10	0.16	0.06	0.19	0.06	0.06	0.08	0.07	0.13	0.12	0.28	0.15	0.11	0.18	0.13
P_2O_5	0.02	0.04	0.02	0.02	0.02	0.01	0.01	0.01	0.02	0.03	0.06	0.05	0.03	0.03	0.01
Cr_20_3	0.28	0.40	0.39	0.39	0.33	0.20	0.39	0.53	0.43	0.33	0.42	0.86	0.30	0.44	
NiO	0.26	0.30	0.29	0.28	0.26	0.32	0.30	0.32	0.33	0.31	0.27	0.26	0.31	0.28	
Ca/Al	1.27	0.98	1.39	1.06	1.38	0.82	0.56	0.97	0.32	1.32	2.49	1.49	2.27	1.10	0.99
Mg#	0.933	0.910	0.924	0.923	0.929	0.933	0.931	0.925	0.922	0.929	0.914	0.910	0.909	0.921	0.919
Trace Elements in ppm															
Ni	2060	2459	2249	2199	2061	2488	2362	2485	2620	2335	2148	2066	2464	2191	2300
Cr	1903	2288	2650	2694	2254	1371	2677	3648	2971	2744	2868	5902	2039	3011	2245
Co	98	103	103	92	99	106	109	105	104	102	104	105	109	97	103
V	15.8	12.1	28.6	34.9	19.1	12.7	61.8	37.5	22.6	44.3	43.1	48.5	33.3	22.9	24.5

Table 4.3 (continued) Anhydrous major element and selected trace element data for Jericho peridotites.

	Low-T Coarse Garnet							Low-T Por Gnt	High-T Por Garnet						
Sample	22-4	25-4	26-11	28-15	41-4	51-2	53-10	21-3	21-2	23-1	26-9	39-3	40-9	40-20	40-21
Major Elements in wt%															
SiO_2	45.55	44.40	45.23	45.44	44.54	43.21	42.29	43.09	42.51	43.45	42.52	42.57	43.03	46.97	42.93
TiO_2	0.04	0.05	0.04	0.10	0.04	0.15	0.07	0.15	0.08	0.05	0.19	0.12	0.06	0.11	0.08
Al_2O_3	1.43	1.03	0.95	1.53	0.73	5.77	0.70	1.57	0.83	0.84	2.58	1.38	0.73	1.20	0.93
FeO	6.05			5.51	5.89	6.30	5.74	6.14	6.45	6.24	7.34	5.93	6.95	5.60	6.99
Fe_2O_3	1.12	8.37	7.88	2.00	1.48	3.22	3.34	2.17	1.98	1.79	2.41	1.71	1.66	3.02	1.73
MnO	0.12	0.11	0.11	0.12	0.12	0.14	0.10	0.12	0.12	0.12	0.15	0.12	0.13	0.13	0.13
MgO	43.28	44.63	44.75	43.05	45.35	37.23	45.76	43.65	46.49	45.66	39.95	44.85	45.95	40.55	45.36
CaO	1.22	0.98	0.68	0.86	0.68	2.54	0.81	1.54	0.48	0.67	3.20	1.51	0.58	1.22	0.75
Na_2O	0.14	0.16	0.08	0.26	0.22	0.17	0.14	0.40	0.17	0.20	0.33	0.40	0.15	0.20	0.16
K_2O	0.23	0.22	0.26	0.38	0.22	0.39	0.17	0.49	0.09	0.12	0.61	0.54	0.09	0.12	0.16
P_2O_5	0.04	0.04	0.03	0.03	0.03	0.05	0.03	0.06	0.03	0.03	0.09	0.09	0.03	0.01	0.03
Cr_20_3	0.49			0.42	0.38	0.56	0.45	0.31	0.43	0.49	0.41	0.46	0.33	0.53	0.42
NiO	0.28			0.29	0.31	0.26	0.40	0.30	0.33	0.32	0.23	0.32	0.32	0.36	0.33
Ca/Al	1.16	1.20	0.97	0.76	1.26	0.59	1.56	1.32	0.78	1.07	1.67	1.47	1.07	1.37	1.10
Mg#	0.916	0.913	0.918	0.913	0.918	0.878	0.903	0.906	0.910	0.912	0.882	0.915	0.907	0.897	0.904
Trace Elements in ppm															
Ni	2170	2400	2400	2263	2437	2073	3163	2364	2586	2526	1828	2488	2476	2791	2631
Cr	2210	1975	3326	2871	2590	3827	3045	2129	2965	3334	2796	3118	2268	3646	2848
Co	101	96	104	107	108	105	128	106	117	110	101	108	114	114	116
V	39.7	16.4	31.2	34.7	18.4	98.7	21.3	49.0	27.3	28.9	26.6	37.2	31.4	31.3	26.8

4.4.2 Whole-Rock Elemental Data

4.4.2.a Major element composition

Whole rock analyses of Jericho peridotites (Kopylova and Russell, 2000) indicate that they are strongly depleted in fusible elements such as Al and Ca (Table 4.2). Removal of a basaltic fraction from fertile mantle depletes magmaphile elements such as Al, whilst Mg remains primarily in the residue. Plotting Al/Si against Mg/Si for residues should therefore produce a strongly anti-correlated trend indicative of the degree of depletion (Figure 4.6).

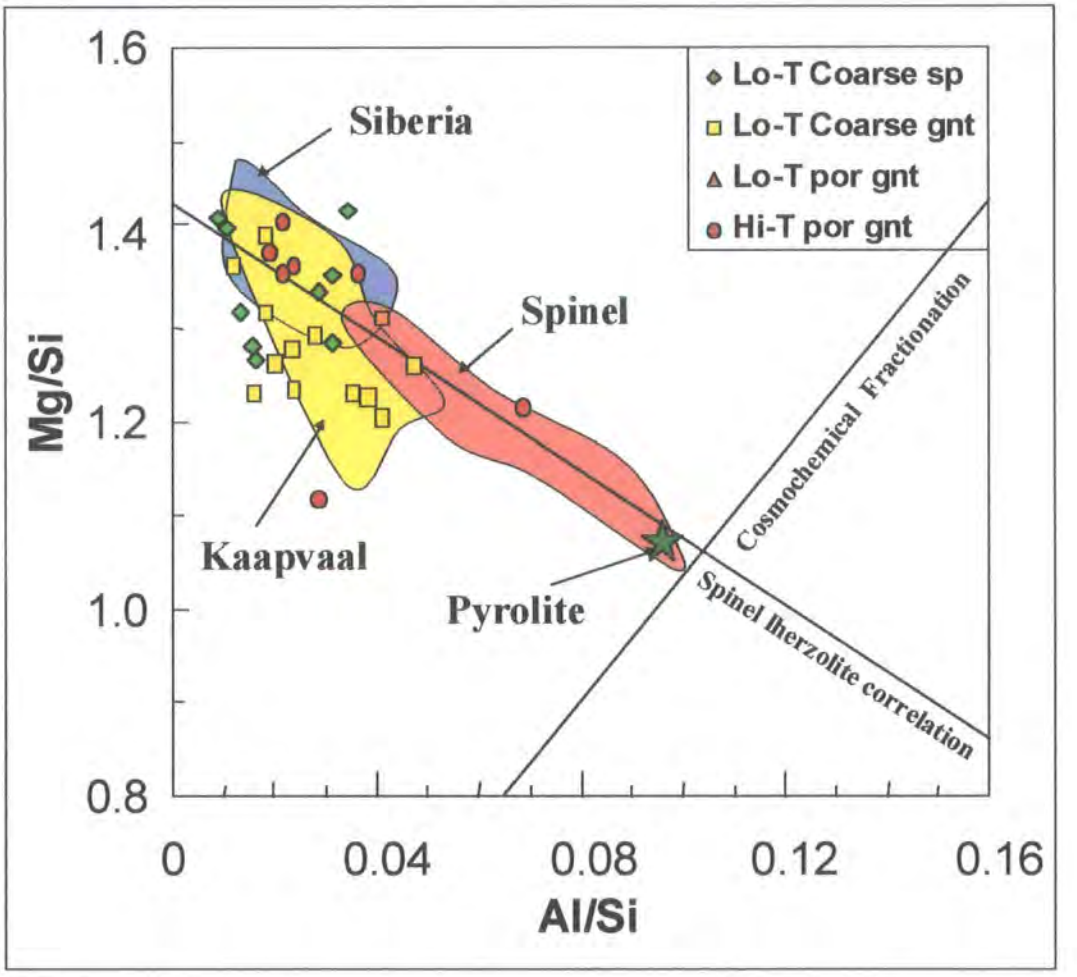

Figure 4.6 Mg/Si vs. Al/Si wt% ratios of Jericho peridotites compared to the range for primitive spinel lherzolites erupted off craton (Morgan, 1986), represented by the red field. Kaapvaal low-T peridotites represented by yellow field, Siberian low-T peridotites by the blue-grey field. Kaapvaal and Siberian data from Boyd and Mertzman (1987) and Boyd *et al.* (1997). Additional data from Jagoutz (1979).

Off-craton spinel peridotites describe a linear array or depletion trend (Morgan, 1986) that intersects the cosmochemical fractionation line of Jagoutz *et al.* (1979) close to the value for pyrolite (Ringwood, 1975). The Jericho peridotites are highly depleted in Al and enriched in Mg relative to off-craton spinel peridotites (Figure 4.6). Many

samples display an overlying trend of Al depletion, or possibly Si enrichment, relative to Mg which causes them to deviate from the spinel lherzolite array of Morgan (1986), in a manner characteristic of Kaapvaal OPX-enriched peridotites (Boyd, 1989; Pearson *et al.*, 1995a). Coarse spinel, low temperature garnet and high temperature garnet peridotites overlap the compositional fields of low temperature peridotites from Kaapvaal and Siberia (Figure 4.6).

The bulk composition of Slave peridotites from the Jericho kimberlite range from those characteristic of depleted harzburgites to compositions more fertile than abyssal peridotites (Figure 4.7).

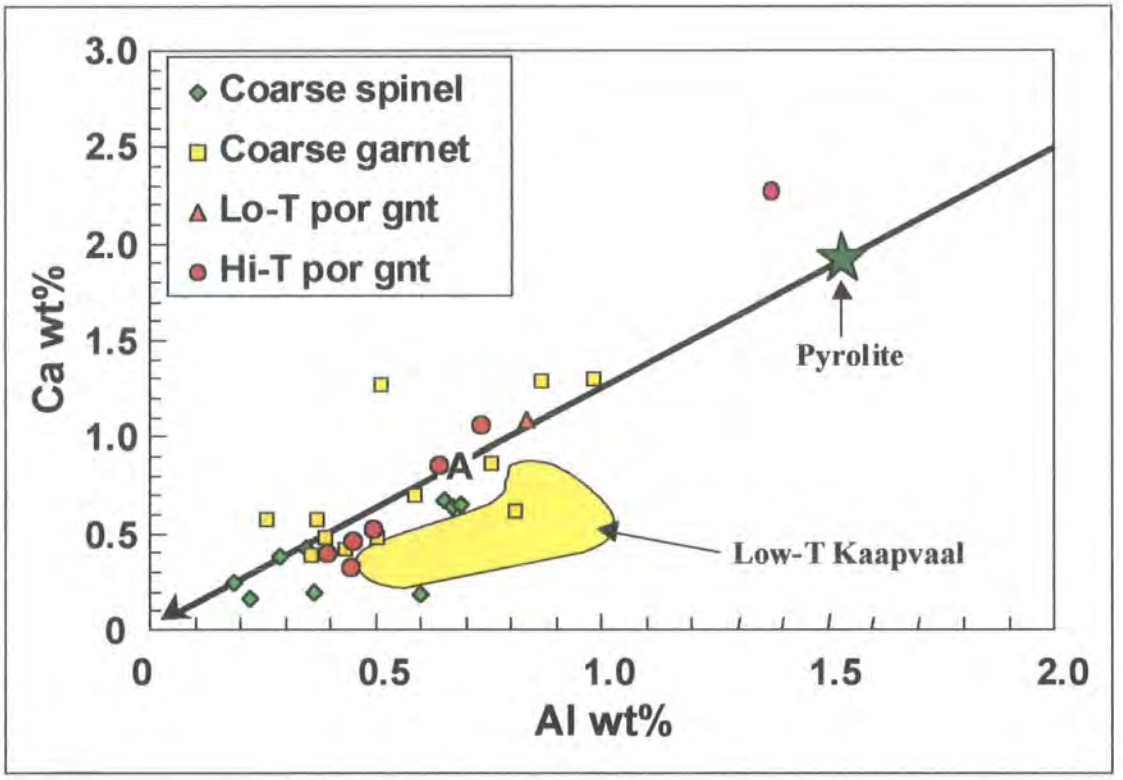

Figure 4.7 Composition of Jericho peridotites as Ca wt% vs. Al wt%. Line represents overall trend expected for the depletion of oceanic peridotite (Boyd, 1989). Also shown are average compositions for abyssal peridotite (Dick *et al.*, 1984), indicated by the letter A, and pyrolite (Ringwood, 1979), indicated by star. Jericho data from Kopylova and Russell (2000). Field represents low-T Kaapvaal peridotite (Boyd, 1989).

Some high temperature garnet peridotites have compositions as fertile as pyrolite (cf. Ringwood, 1975), although these fertile samples tend to differ in their Ca/Al ratios (Kopylova and Russell, 2000). Comparing the Jericho peridotites with samples of cratonic peridotite from the Kaapvaal craton it is apparent that Slave peridotites in general have higher Ca/Al ratios (range = 0.32 - 2.49) with a mean of 1.19, compared to 0.73 for Kaapvaal peridotites (Boyd, 1989). The Jericho suite of peridotites can be subdivided on the basis of Ca/Al ratio. Low-T coarse spinel peridotites have a mean

Ca/Al ratio of 0.97 compared with ratios of 1.32 and 1.22 for low-T coarse garnet and high-T prophyroclastic non-disrupted garnet peridotites respectively (Table 4.3).

The negative correlation observed between FeO and SiO_2 for the Jericho samples (Figure 4.8) is opposite to what would be expected for the normal magmaphile behaviour of residues (Boyd *et al.*, 1997), and may indicate a secondary process.

4.4.2.b Mineral Modes

Kopylova and Russell (2000) compared the $Mg^{\#}$ (olivine and whole rock) and olivine modes from Jericho peridotites with those of the Kaapvaal and Siberian cratons (Figure 4.9). Within the Jericho xenolith suite the coarse spinel peridotites are distinct from coarse garnet and high temperature garnet peridotites using these parameters. Coarse spinel peridotites with mean $Mg^{\#}$ of 0.93 overlap the compositional field of low temperature Siberian and Kaapvaal peridotites (Figure 4.9). However, the Jericho spinel peridotites have less modal pyroxene (OPX + CPX) and are more enriched in olivine than Kaapvaal and Siberian peridotites (Kopylova and Russell, 2000). Low temperature garnet peridotites from Jericho generally have less magnesium rich olivines than those from Siberia or Kaapvaal ($Mg^{\#}$ of 0.91-0.92 compared to 0.93), contain more modal olivine (67% compared to 61%, Kopylova and Russell, 2000), and are closer in composition to high temperature peridotites from other cratons (Figure 4.9). High temperature garnet peridotites from Jericho are similar to high temperature peridotites from other cratons but have higher olivine modes (84-68% compared to 84-64% for Kaapvaal and Siberia) and olivines in the Jericho samples are less Mg-rich ($Mg^{\#}$ of 0.90 compared to 0.915), more similar to oceanic mantle (0.908). Both the low and high temperature garnet peridotites from Jericho overlap the oceanic trend of Boyd (1989).

The decrease in $Mg^{\#}$ of olivine with depth at Jericho, from low-T peridotites to high-T peridotites, is reflected in an increase in $FeO_{(T)}$, which shows progressive enrichment with depth, from low-T spinel to high-T garnet peridotites (Figure 4.8). $FeO_{(T)}$ also seems to define a stratigraphic boundary between low temperature spinel and low temperature garnet peridotite. Modal orthopyroxene in Jericho peridotites also decreases with depth from an average of 26 vol% in spinel peridotites to 15 vol% in high temperature garnet peridotites (Kopylova and Russell, 2000). This is reflected in a decrease in SiO_2 with depth, on going from low-T spinel peridotites through low-T garnet to high-T garnet peridotites (Figure 4.8), and may be attributed to an increase

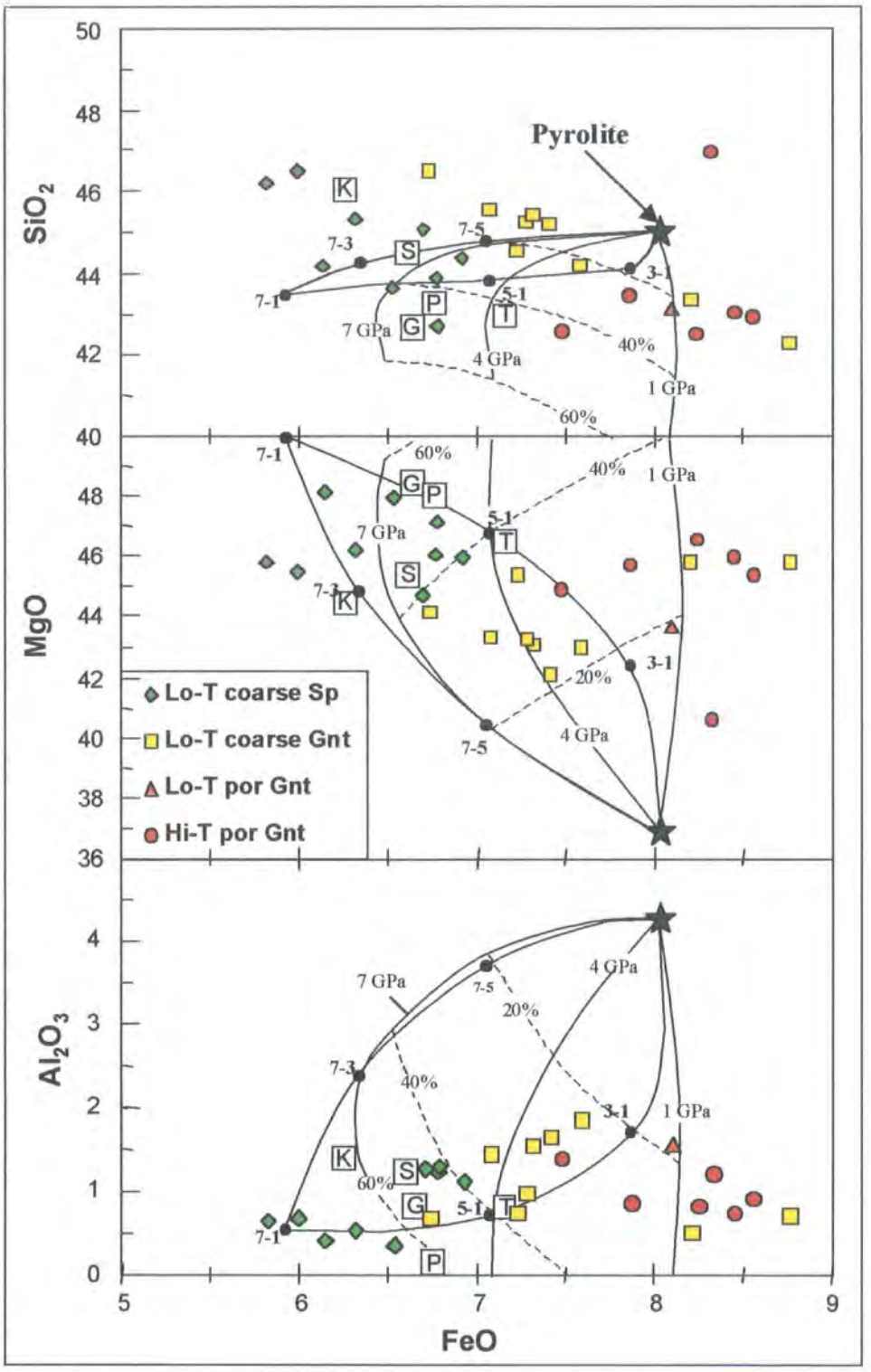

Figure 4.8 Oxide variation diagrams (wt%). Residues of batch and polybaric near-fractional melt extraction, after the method of Walter (1999). Thin solid lines are isobaric batch melt extraction contours and dashed lines give percent batch melt extraction. The filled circles connected by thick solid contours are residues of polybaric near-fractional melt extraction and are labelled according to the pressure range of melt extraction (see Appendix E). Open squares show average low-temperature cratonic peridotites from Kaapvaal (K), Siberia (S), Tanzania (T), Papua New Guinea (P) and East Greenland (G). Additional data from Walter (1999). Fertile mantle denoted by star symbol.

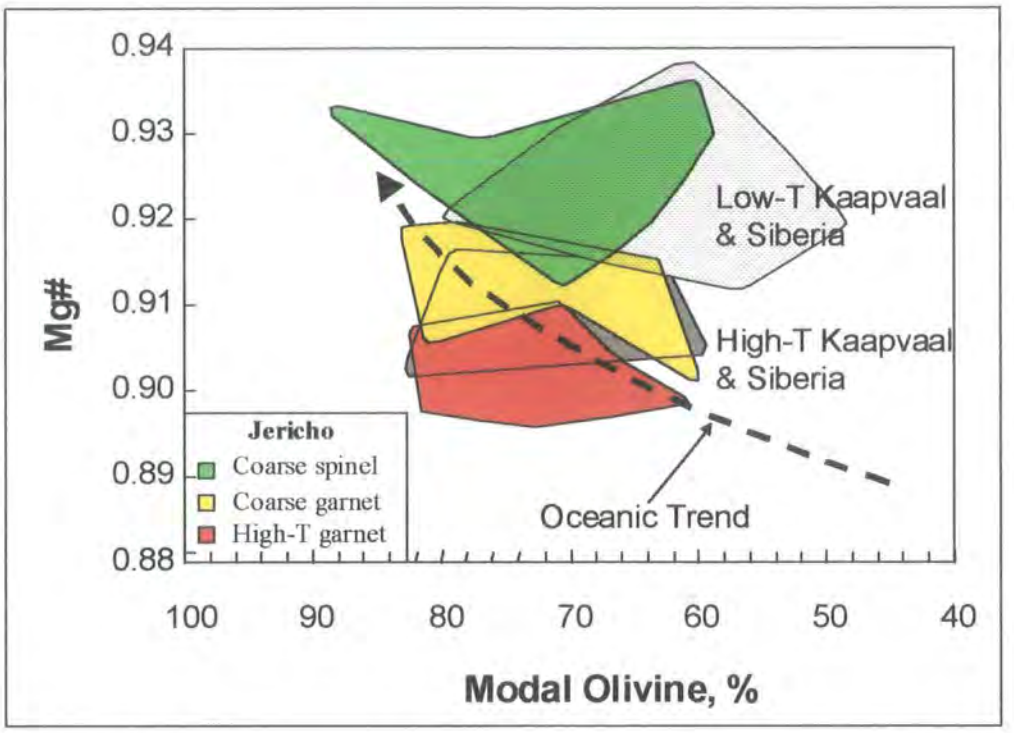

Figure 4.9 Olivine $Mg^{\#}$ vs. modal olivine content (%) for Jericho peridotites. Jericho data from Kopylova and Russell (2000). Fields for Low-T peridotites from the Kaapvaal and Siberian cratons (Boyd, 1989; Boyd *et al.*, 1997). Trend defined by oceanic peridotites after Boyd (1989).

in garnet content and probably a decrease in orthopyroxene. The low temperature lithospheric mantle beneath Jericho contains on average less orthopyroxene (19-26 vol%) than Kaapvaal (31 vol%) lithospheric mantle but is comparable to Siberia (20 vol%) (Boyd *et al.*, 1997; Kopylova and Russell, 2000).

The higher Ca/Al ratios noted within the Jericho low-T garnet peridotites may be attributed to their high average modal clinopyroxene content of 7.1%, compared to 1.8% in Kaapvaal peridotites (Boyd, 1989; Kopylova and Russell, 2000). The depleted nature of the Jericho low-T peridotites (high $Mg^{\#}$ and high modal olivine) would suggest that the high modal abundance of clinopyroxene in low-T garnet peridotites may be related to patent metasomatism and CPX addition to the samples (Pearson *et al.*, 2001).

4.4.2.c Trace elements

Transition metal trace elements

Nickel behaves compatibly within the Jericho peridotites, showing a positive correlation with MgO content (Figure 4.10). In contrast, vanadium abundances are negatively correlated with MgO (Figure 4.10), suggesting partition coefficients of less than unity, and indicative of vanadium's incompatibility in the peridotites. The

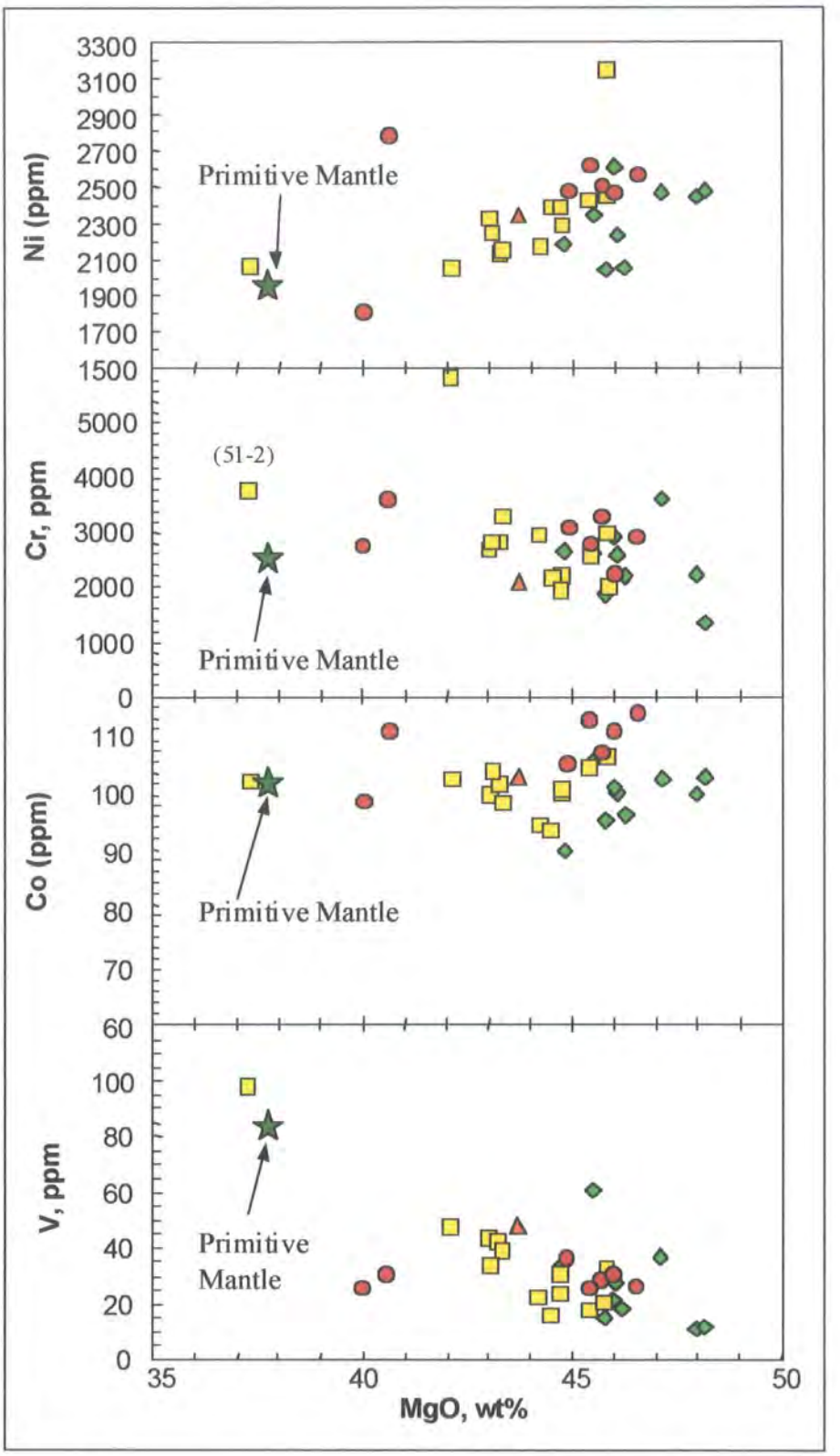

Figure 4.10 Variations of trace elements (ppm) with MgO (wt%) for Jericho peridotites. Primitive mantle after McDonough and Sun (1995). Symbols same as Figure 4.8.

contrasting behaviour of Ni and V agrees with the previously observed compatibilities from melt systems (Frey and Prinz, 1978). Cobalt and Cr show little correlation with MgO content (Figure 4.10). Frey *et al.* (1985) attributed a similar incoherent Cr-MgO relationship in peridotites from the Ronda massif to heterogeneous Cr distribution (contained mainly in minerals such as spinel). Maaloe and Aoki (1977) found similar lack of correlation in peridotites from continental alkali basalts. Elthon (1992) attributed the lack of variation of Cr to a partition coefficient of $K_D \sim 1$, therefore resulting in no variation with melting.

The total Ni variation in the Jericho peridotite suite is 1828 to 3163 ppm (Table 4.4). This is consistent with derivation of the peridotites from residues of varying degrees of partial melting. The correlation generally appears to be better for low temperature and high temperature garnet peridotites, with spinel peridotites tending to show a larger degree of scatter. The variation of Ni with MgO is large, up to 400ppm (20%). The observed scatter in data may be indicative of a cumulate component within the peridotites rather than solely a residue of partial melting (Pearson, 1989). Alternatively, the scatter in Ni concentration may be the result of serpentinisation (Coleman, 1977), or cryptic metasomatism from melts passing through the peridotite, patent metasomatism by the introduction of clinopyroxene and garnet (Pearson *et al.*, 2001). The latter argument is supported by the high values of modal CPX observed in some Jericho peridotites.

The negative correlation of V with MgO may reflect a decrease in clinopyroxene and spinel, which are removed with the melt (Canil, 1997). Sample 51-2 is very enriched in V (98.7 ppm) and this may reflect later CPX or melt addition (Figure 4.10).

Kopylova and Russell (2000) report that Sr abundances in the Jericho peridotites are higher (40-50 ppm) than Sr abundances in Siberian and Kaapvaal peridotites (Boyd *et al.*, 1997), which may be a reflection of the higher clinopyroxene contents. Sr/Nd ratios are variable and are lowest in garnet peridotite at 11 to 24, with spinel peridotite higher at 26 to 33. The Sr/Nd ratios of garnet peridotite are similar to primitive mantle and in general most other continental mantle. The Sr/Nd ratios of spinel peridotites from the Slave craton in contrast may be related to a residual origin at a convergent margin (McDonough, 1990).

Rare earth elements

All samples of the Slave mantle as sampled by the Jericho kimberlite show a similar trace element character (Table 4.4). Chondrite normalised REE patterns for Jericho peridotites are remarkably similar over the entire suite (Figure 4.11), and show 7x to

Table 4.4 Rare earth element data for Jericho peridotites. Chondrite normalised using normalisation values of M^{c}Donough and Sun (1995).

	Low-T Coarse Spinel									Low-T Coarse Garnet						
Sample	**8-7**	**9-2**	**10-11**	**10-12A**	**10-12B**	**11-18**	**23-9**	**39-23**	**44-12**	**9-12**	**10-456**	**11-22**	**13-2**	**21-1**	**22-1**	**22-4**
REE in ppm																
La	3.498	3.761	3.315	5.713	1.840	1.466	1.037	1.465	4.189	3.973	8.616	5.102	4.964	2.460	1.685	4.890
Ce	4.942	7.305	5.411	8.205	2.559	1.993	1.768	2.723	4.547	5.721	12.990	7.567	7.255	3.926	2.578	7.637
Pr	0.484	0.993	0.586	0.821	0.243	0.190	0.197	0.342	0.406	0.557	1.389	0.755	0.701	0.412	0.259	0.826
Nd	1.514	4.063	1.919	2.674	0.786	0.580	0.707	1.300	1.238	1.739	4.875	2.549	2.316	1.428	0.871	3.082
Sm	0.168	0.578	0.228	0.330	0.097	0.000	0.000	0.627	0.572	0.204	0.000	0.441	0.000	0.000	0.000	0.751
Eu	0.040	0.159	0.059	0.085	0.024	0.018	0.023	0.070	0.106	0.050	0.163	0.111	0.079	0.058	0.031	0.156
Gd	0.097	0.337	0.144	0.203	0.058	0.048	0.048	0.211	0.084	0.115	0.399	0.276	0.223	0.156	0.079	0.361
Tb	0.008	0.034	0.014	0.018	0.005	0.006	0.005	0.030	0.010	0.011	0.035	0.036	0.021	0.017	0.007	0.035
Dy	0.037	0.155	0.058	0.079	0.026	0.000	0.000	0.083	0.159	0.046	0.000	0.049	0.000	0.000	0.000	0.165
Ho	0.005	0.027	0.011	0.012	0.004	0.003	0.004	0.036	0.007	0.007	0.021	0.030	0.019	0.010	0.005	0.021
Er	0.010	0.077	0.023	0.026	0.009	0.000	0.000	8.844	5.265	0.012	0.000	11.981	0.000	0.000	0.000	7.552
Tm	0.001	0.015	0.004	0.004	0.001	0.001	0.001	0.016	0.002	0.001	0.007	0.010	0.006	0.002	0.002	0.008
Yb	0.006	0.097	0.022	0.024	0.007	0.000	0.000	0.000	0.000	0.009	0.000	0.000	0.000	0.000	0.000	0.000
Lu	0.001	0.018	0.004	0.005	0.001	0.001	0.001	0.016	0.002	0.001	0.005	0.010	0.006	0.002	0.002	0.007
Chondrite normalised REE																
La	14.76	15.87	13.99	24.10	7.76	6.19	4.38	6.18	17.68	16.76	36.35	21.53	20.95	10.38	7.11	20.63
Ce	8.06	11.92	8.83	13.38	4.17	3.25	2.88	4.44	7.42	9.33	21.19	12.34	11.84	6.40	4.21	12.46
Pr	5.21	10.70	6.31	8.85	2.62	2.05	2.12	3.69	4.38	6.00	14.97	8.14	7.55	4.44	2.79	8.90
Nd	3.31	8.89	4.20	5.85	1.72	1.27	1.55	2.84	2.71	3.81	10.67	5.58	5.07	3.12	1.91	6.74
Sm	1.13	3.90	1.54	2.23	0.65	0.41	0.58	1.65	1.03	1.38	4.18	2.50	1.97	1.48	0.77	3.52
Eu	0.71	2.82	1.04	1.51	0.43	0.32	0.41	1.24	1.88	0.89	2.90	1.97	1.40	1.03	0.55	2.77
Gd	0.49	1.69	0.72	1.02	0.29	0.24	0.24	1.06	0.42	0.58	2.01	1.39	1.12	0.78	0.40	1.81
Tb	0.22	0.93	0.37	0.48	0.12	0.17	0.14	0.83	0.28	0.30	0.97	1.00	0.58	0.47	0.19	0.97
Dy	0.15	0.63	0.24	0.32	0.11	0.08	0.10	0.76	0.17	0.18	0.61	0.69	0.46	0.30	0.16	0.60
Ho	0.08	0.49	0.19	0.22	0.06	0.05	0.07	0.66	0.13	0.12	0.38	0.55	0.35	0.18	0.09	0.38
Er	0.06	0.48	0.14	0.16	0.05	0.03	0.04	0.65	0.09	0.08	0.28	0.43	0.28	0.10	0.07	0.31
Tm	0.04	0.59	0.14	0.16	0.04	0.04	0.04	0.65	0.08	0.04	0.28	0.40	0.24	0.08	0.08	0.32
Yb	0.04	0.60	0.14	0.15	0.04	0.03	0.03	0.60	0.08	0.06	0.23	0.38	0.25	0.08	0.07	0.27
Lu	0.02	0.73	0.16	0.18	0.04	0.04	0.04	0.65	0.08	0.04	0.20	0.41	0.24	0.08	0.08	0.28
Chondrite nomalised REE ratios																
La/Yb	413.27	26.34	103.54	163.40	185.13	181.07	128.08	10.37	227.66	291.78	160.36	56.82	84.30	123.79	95.39	75.50
Sm/Yb	31.69	6.48	11.40	15.10	15.59	11.97	17.11	2.76	13.32	23.96	18.45	6.59	7.91	17.69	10.33	12.87
Dy/Yb	4.21	1.05	1.75	2.16	2.55	2.38	2.80	1.28	2.17	3.22	2.69	1.83	1.84	3.59	2.13	2.20

Table 4.4 (continued) REE data for Jericho peridotites

	Low-T Coarse Garnet						Low-T Por Gnt	High-T Por Garnet						
Sample	**25-4**	**26-11**	**28-15**	**41-4**	**51-2**	**53-10**	**21-3**	**21-2**	**23-1**	**26-9**	**39-3**	**40-9**	**40-20**	**40-21**
REE in ppm														
La	5.663	5.025	3.887	3.355	11.620	9.123	13.724	3.269	3.670	4.707	14.848	2.128	1.646	2.908
Ce	8.741	8.025	5.860	5.226	20.044	12.618	21.407	4.684	5.689	7.783	23.386	3.112	2.551	4.307
Pr	0.919	0.834	0.583	0.575	2.195	1.128	2.142	0.453	0.575	0.860	2.325	0.316	0.266	0.422
Nd	3.312	2.848	2.024	2.017	7.816	3.409	7.192	1.531	1.909	3.032	7.641	1.059	0.890	1.390
Sm	0.207	0.204	1.192	1.392	0.190	1.323	0.000	0.549	0.000	1.487	0.851	0.630	2.481	0.295
Eu	0.154	0.096	0.110	0.083	0.313	0.210	0.225	0.059	0.070	0.137	0.247	0.051	0.050	0.058
Gd	0.328	0.215	0.281	0.219	0.561	0.175	0.607	0.146	0.156	0.403	0.637	0.136	0.119	0.165
Tb	0.036	0.021	0.034	0.022	0.076	0.016	0.069	0.019	0.013	0.057	0.070	0.023	0.017	0.024
Dy	0.041	0.037	0.393	0.279	0.037	0.148	0.000	0.149	0.000	0.215	0.246	0.235	0.977	0.078
Ho	0.017	0.011	0.020	0.014	0.118	0.011	0.064	0.015	0.010	0.063	0.055	0.022	0.017	0.026
Er	7.796	5.983	3.295	6.434	8.554	9.839	0.000	5.702	0.000	9.224	3.957	2.928	3.193	5.167
Tm	0.004	0.003	0.006	0.003	0.068	0.002	0.024	0.005	0.004	0.028	0.019	0.008	0.006	0.011
Yb	0.000	0.000	0.000	0.000	0.000	0.000	6.752	0.000	0.000	0.000	0.000	0.000	0.000	0.000
Lu	0.003	0.003	0.005	0.004	0.074	0.002	0.025	0.006	0.004	0.025	0.019	0.009	0.006	0.010
Chondrite normalised REE														
La	23.89	21.20	16.40	14.16	49.03	38.49	57.91	13.79	15.49	19.86	62.65	8.98	6.95	12.27
Ce	14.26	13.09	9.56	8.53	32.70	20.58	34.92	7.64	9.28	12.70	38.15	5.08	4.16	7.03
Pr	9.90	8.99	6.28	6.20	23.65	12.16	23.08	4.88	6.20	9.27	25.05	3.41	2.87	4.55
Nd	7.25	6.23	4.43	4.41	17.10	7.46	15.74	3.35	4.18	6.63	16.72	2.32	1.95	3.04
Sm	3.42	2.56	2.43	2.00	5.62	2.02	5.99	1.33	1.64	3.19	6.58	1.11	0.91	1.25
Eu	2.74	1.71	1.95	1.47	5.56	3.73	4.00	1.05	1.24	2.43	4.39	0.91	0.89	1.03
Gd	1.65	1.08	1.41	1.10	2.82	0.88	3.05	0.73	0.78	2.03	3.20	0.68	0.60	0.83
Tb	1.00	0.58	0.94	0.61	2.11	0.44	1.91	0.53	0.36	1.58	1.94	0.64	0.47	0.66
Dy	0.55	0.34	0.56	0.43	2.16	0.30	1.40	0.37	0.26	1.31	1.32	0.47	0.37	0.56
Ho	0.31	0.20	0.37	0.26	2.16	0.20	1.17	0.27	0.18	1.15	1.01	0.40	0.31	0.48
Er	0.22	0.13	0.29	0.18	2.41	0.12	1.02	0.26	0.13	1.06	0.82	0.40	0.25	0.41
Tm	0.16	0.12	0.24	0.12	2.75	0.08	0.97	0.20	0.16	1.13	0.77	0.32	0.24	0.45
Yb	0.17	0.10	0.22	0.14	2.74	0.09	0.94	0.23	0.16	0.98	0.75	0.36	0.23	0.35
Lu	0.12	0.12	0.20	0.16	3.01	0.08	1.02	0.24	0.16	1.02	0.77	0.37	0.24	0.41
Chondrite nomalised REE ratios														
La/Yb	137.39	206.89	75.44	103.60	17.90	442.68	61.74	60.84	99.72	20.37	83.71	24.71	29.82	34.66
Sm/Yb	19.68	25.02	11.19	14.61	2.05	23.23	6.39	5.86	10.53	3.27	8.79	3.07	3.90	3.52
Dy/Yb	3.17	3.29	2.58	3.17	0.79	3.41	1.49	1.61	1.66	1.35	1.77	1.28	1.58	1.58

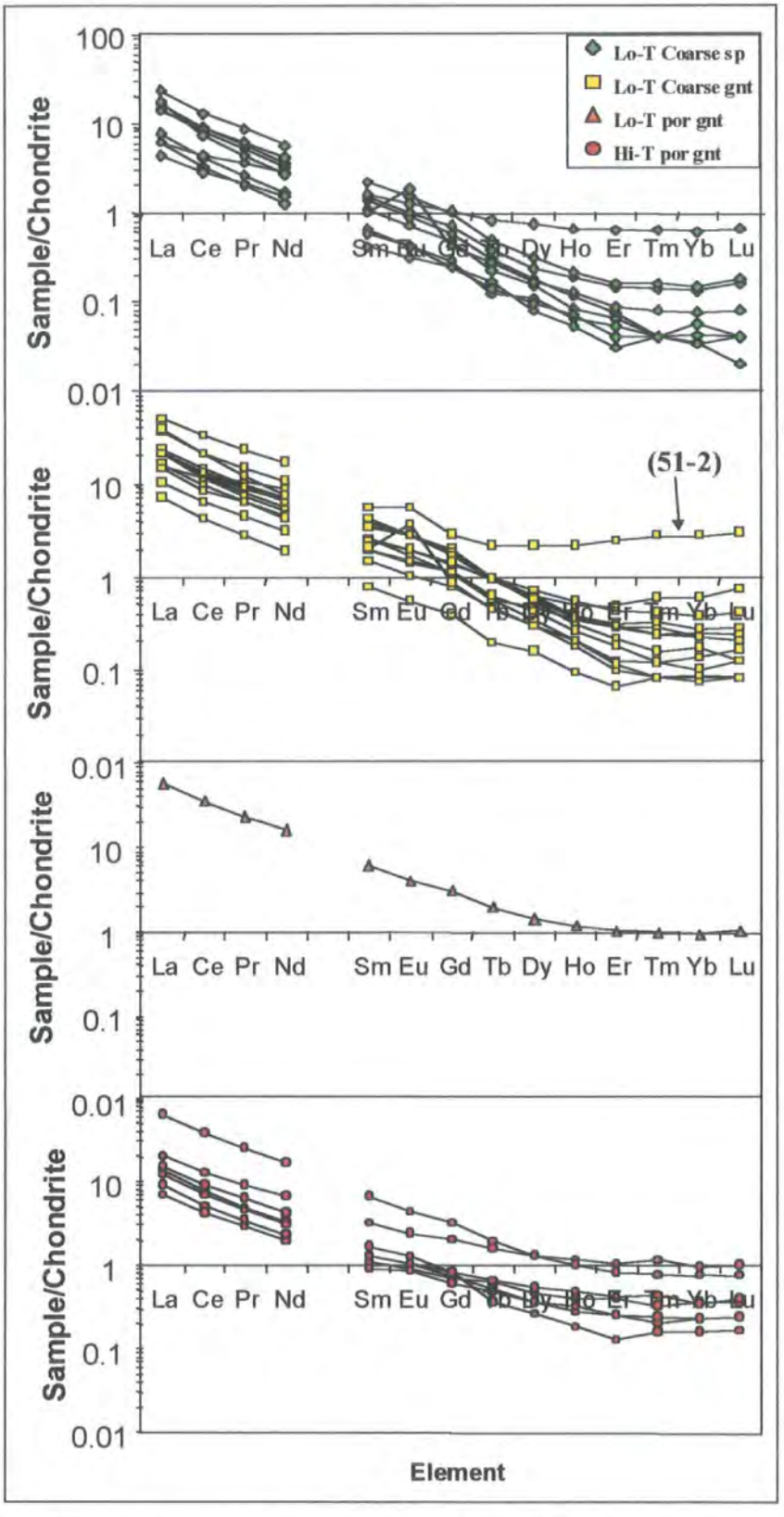

Figure 4.11 Chondrite normalised REE profiles for Jericho peridotites using normalisation values of M^{c}Donough and Sun (1995).

70x enrichment of LREE (La). HREE (Er to Lu) tend to have flat subchondritic profiles with little evidence of fractionation or enrichment. The HREE tend to be sub-chondritic and vary from 0.02 to 0.9 x chondrite. As reported by Kopylova and Russell (2000), the REE distribution of Slave mantle is similar to median garnet bearing Archean lithospheric mantle. All samples have high Sm/Yb ratios (chondrite normalised Sm/Yb from 1.98 to 31.69, mean = 11.52) suggesting equilibration of the source of incompatible elements with garnet.

The LREE enrichment of the Jericho peridotite suite is similar to that noted in peridotites from other cratons such as the Kaapvaal craton (Nixon *et al.*, 1981) and Lesotho peridotite suite (Chapter3), but tends to be more pronounced in the Slave samples with a greater fractionation of LREE/HREE. The LREE enrichment within the Jericho peridotites is not consistent with the major element depletion recorded in the xenoliths. In the Jericho peridotite suite, the processes creating these distinct chemical signatures must be decoupled as noted in Nixon (1987b). This LREE enrichment must therefore represent melt addition or cryptic metasomatism from fluids passing through the mantle.

The subchondritic character of the HREE may be attributable to melt depletion removing all residual garnet. Alternatively melt depletion may have occurred at shallower depths in the absence of residual garnet. Sample 51-2 is an exception to the general case, and shows HREE values of 2 to 3 x chondrite. This sample however has enriched major element chemistry, more fertile than pyrolite (Ringwood, 1975). The whole-rock $Mg^{\#}$ of this sample is 0.878 (Table 4.3) and may represent highly modified, metasomatised peridotite such as those recognised at Matsoku (Chapter 3, Harte *et al.*, 1987).

4.4.3 Interpretation of whole-rock major element data

By comparing the compositional data of the naturally occurring Jericho peridotites to residues of experimental melting, P-T conditions can be inferred for the melt depletion events forming these peridotites (Walter, 1999). For such a comparison on dry melting Walter (1999) used $FeO_{(T)}$, SiO_2, MgO and Al_2O_3 (Figure 4.8). The parameters inferred for dry melting are also applicable for high pressure melting in the presence of 4-5 wt% H_2O (Walter, 1999). We must be heedful of the fact that late-stage introduction of diopside to Jericho peridotites would alter whole-rock FeO and Al_2O_3 contents and therefore the estimates will not be accurate.

The majority of high-T garnet peridotite compositions can be explained by the dry batch melting of pyrolite at pressures of 1 to 4 GPa (Figure 4.8). Kopylova and Russell (2000) however, noted that the $Mg^{\#}$ of olivines from the high temperature peridotites were lower than those found in equivalent low-pressure oceanic residues. $FeO_{(T)}$ contents also seem to be higher than experimental residues of experimental melting at 1 GPa which Kopylova and Russell (2000) suggested may result from asthenospheric metasomatism enriching Na, Ti and Fe, as proposed for other peridotite suites by Harte and Hawkesworth (1989).

On the basis of major element chemistry, Jericho low temperature garnet peridotites can be explained by ~20 to 55% batch melting of pyrolite at pressures of 1 to 7 GPa (Figure 4.8). Compositions in terms of $Mg^{\#}$ and modes as described by Kopylova and Russell (2000) are similar to experimentally produced residues of high pressure isobaric melting.

The spinel peridotites can in general be explained by 40 to 60% batch melting at 4 to 7 GPa (Figure 4.8). The most Si poor compositions resemble residues of 20 to 60% isobaric batch melting at 7 GPa, but the majority of spinel peridotites tend to be too rich in Si and modal orthopyroxene, and too low in modal olivine to be comparable to high pressure experimental residues (Kopylova and Russell, 2000, Figure 4.8). This inconsistency is similar to the high modal orthopyroxene concentrations reported for low-T Kaapvaal and Siberian peridotites (Maaloe and Aoki, 1977; Boyd and Mertzman, 1987).

4.4.4 Melt extraction

4.4.4.a Major element modelling of melt residues

As discussed above the Jericho peridotite suite may have experienced some disturbance to its major element systematics. It can still be useful however to compare the xenolith data to melting models. Overall, the depleted nature of the Jericho peridotites has been attributed to varying but large degrees of melting of a primitive mantle source. The variation in major element trends may be the result of varying degrees of melt extraction, with overlying modification by later metasomatism. Assuming that Al and Ca variation is not the result of later garnet and diopside addition, using geochemical modelling techniques such as those developed by Hanson and Langmuir (1978) can help test this hypothesis (For details see Appendix E). The degree of melt extraction experienced by the Jericho samples is estimated by assuming that

they formed from a pyrolitic source (MgO = 47.8 mol%, FeO = 5.35 mol%; (Ringwood, 1975). The partition coefficient data of Bickle *et al.* (1977) at 3.0 GPa have been used in combination with the equations of Hanson and Langmuir (1978) to produce a residue grid (Figure 4.12).

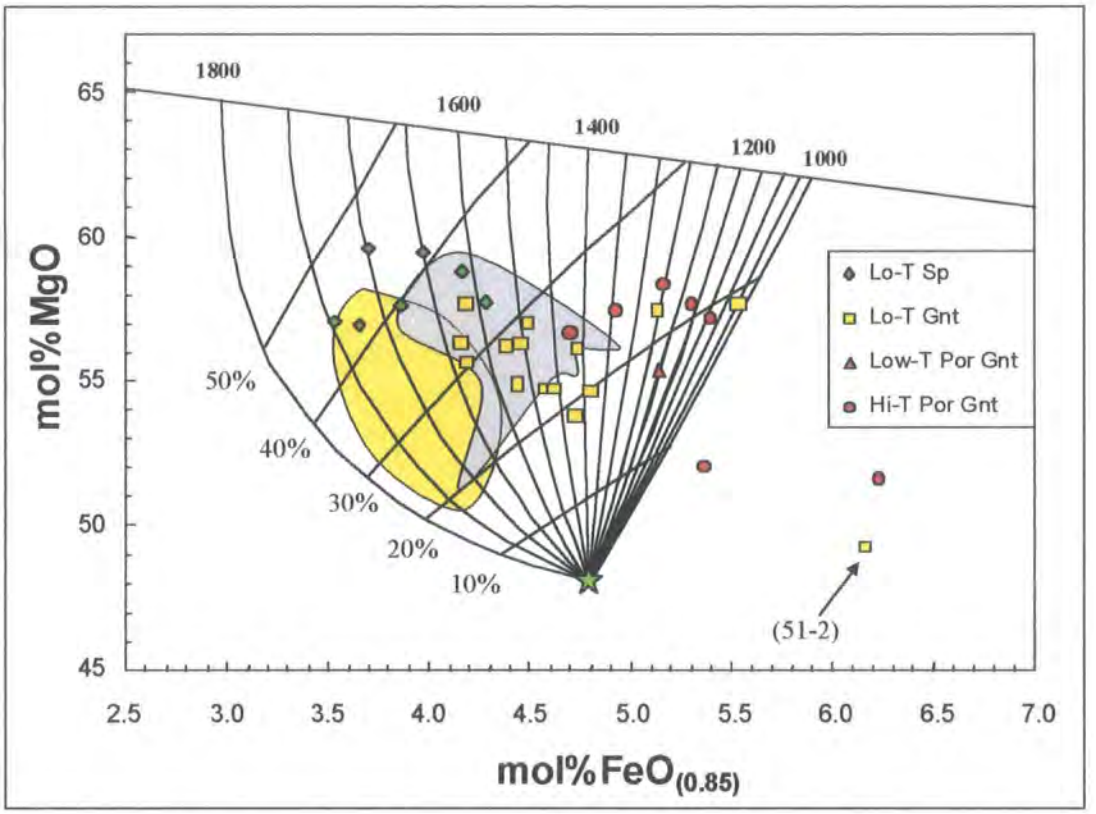

Figure 4.12 FeO-MgO diagram for Jericho peridotites. The diagram is contoured for temperature and degree of batch melting of pyrolitic mantle (Ringwood, 1975) at 3 GPa using method described by Hanson and Langmuir (1978). Field for Kaapvaal and Siberian peridotites from Pearson *et al.* (1995a). Kaapvaal low-T peridotites represented by yellow field, Siberian by the blue-grey field. Pyrolite denoted by star symbol.

By using this type of modelling (Figure 4.12), it can seen that spinel peridotites may represent ~30 to 45% batch melting of a pyrolitic source. It is also apparent that low temperature and high temperature garnet peridotites represent lower degrees of batch melting (~ 18 to 35 %) than spinel peridotites. If bulk FeO has been enriched this value represents a minimum. This is consistent with the higher $Mg^{\#}$ of olivine in low-T spinel peridotites, relative to low-T and high-T garnet peridotites. It should be noted that the liquidus temperature of 4-phase lherzolite increases with pressure (Thompson, 1984). Combining this with the pressure dependence of K_D, high-pressure melt residues will be shifted to the left on Figure 4.12 (lower mol% FeO), low-pressure residues will be shifted to the right (higher mol% FeO). Whilst the temperatures at which the residues were formed will vary with pressure, the degree of melting remains approximately the

same (Hanson and Langmuir, 1978). From Figure 4.12 it is also apparent that some low and high temperature garnet peridotites have anomalously high FeO contents. This is either related to enrichment of Fe after melt extraction, or the samples could represent low-pressure melt residues. Trace element data for these samples does not appear to differ from that noted for other peridotite samples, with the exception of 51-2, and therefore FeO is not increasing with the observed LREE enrichment.

Several Jericho low-T spinel peridotites overlap the composition field for Kaapvaal low-T peridotites and this would suggest they represent similar degrees of melting (Figure 4.12). Several Jericho low-T spinel peridotites and many of the low-T garnet peridotites overlap the field for Siberian low-T spinel peridotites. This is worthy of note because Boyd *et al* (1997) found clear indication of late-stage introduction of Ca and Fe to the Siberian suite.

4.4.4.b HREE modelling

REE abundances in the Jericho whole-rock peridotites are obviously disturbed (Figure 4.11). However, the low HREE abundances may be indicative of the melt depletion event rather than later melt addition. As most metasomatic melts are LREE enriched and HREE depleted, HREE are in general relatively undisturbed during metasomatism and therefore may be of use during modelling. The fractionation of HREE as a function of HREE abundances (Figure 4.13) may be used to estimate the degree of melting, after the method of Bodinier *et al.* (1988). The fractionation of HREE can also help differentiate between the presence and absence of garnet, due to the buffering of HREE by garnet.

On a plot of Dy/Yb ratio against Yb (Figure 4.13), calculated ratios for model melting of a peridotite source of variable garnet content are presented for up to 20% batch and fractional melting, after Burnham (1995). Details of modelling parameters can be found in Appendix E. The Jericho peridotites give no indication of a decrease in the Dy/Yb ratio with a decrease in Yb, but instead for a given Yb abundance show an increase in the Dy/Yb ratio. The HREE of Jericho peridotites do not match the trajectories of model melts, and this would suggest that the samples have undergone Dy addition after the initial melt depletion event. No evidence of the initial melt depletion event or the composition of the source mantle can be ascertained by the modelling of REEs, as these appear to be completely overprinted by later metasomatic events. However, absolute Yb abundances for the Jericho peridotites are generally sub-

chondritic (Figure 4.11), and this would suggest that melting either occurred within spinel facies or was sufficient to remove all garnet from the residue.

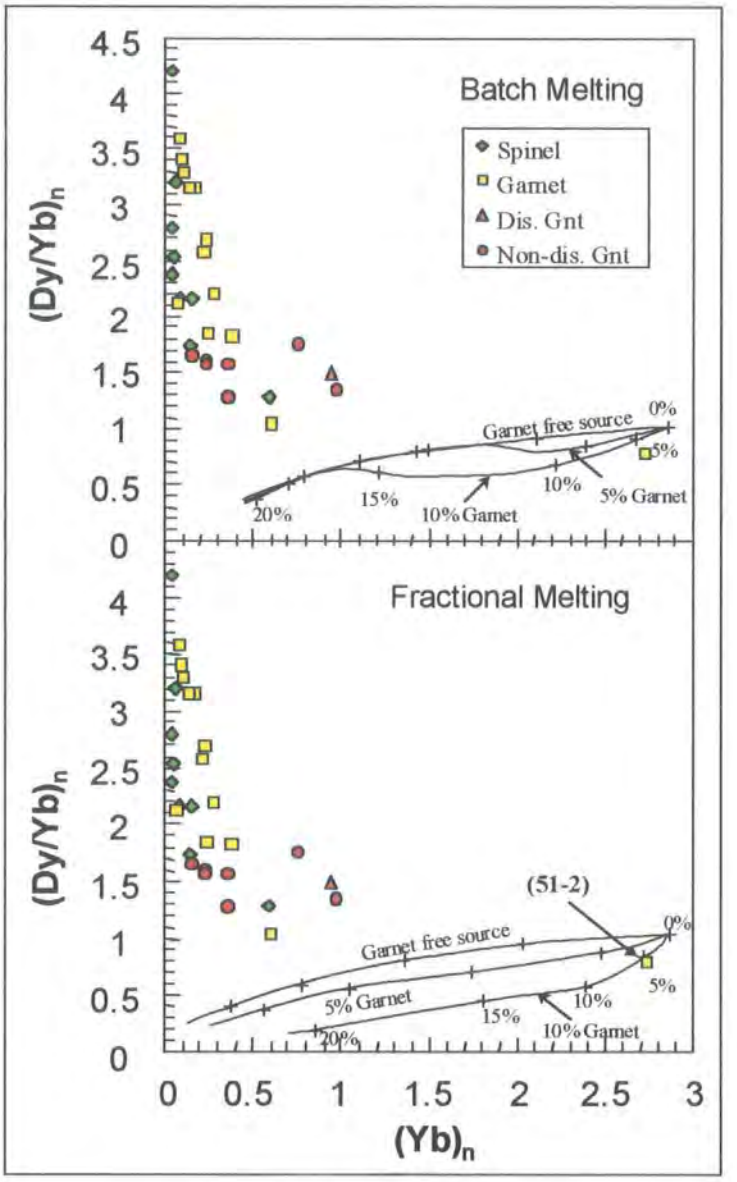

Figure 4.13 Variation of Dy/Yb ratio with Yb abundances in peridotites from Jericho, superimposed on calculated variations of Dy/Yb ratios with Yb calculated for up to 25% melting of a peridotite source containing variable quantities of garnet, after Burnham (1995). Crosses at 5% melting intervals.

4.4.5 Summary of peridotite petrogenesis

A model for the origin of Slave cratonic mantle, based on the experimental model of Walter (1999), is illustrated in Figure 4.14. The average values illustrated for Greenland spinel predicate xenoliths, Tanzanian xenoliths and Papua New Guinea ophiolites approximate a residue of 40 to 50% melt extraction at an average of 3 to 4GPa (Walter, 1999).

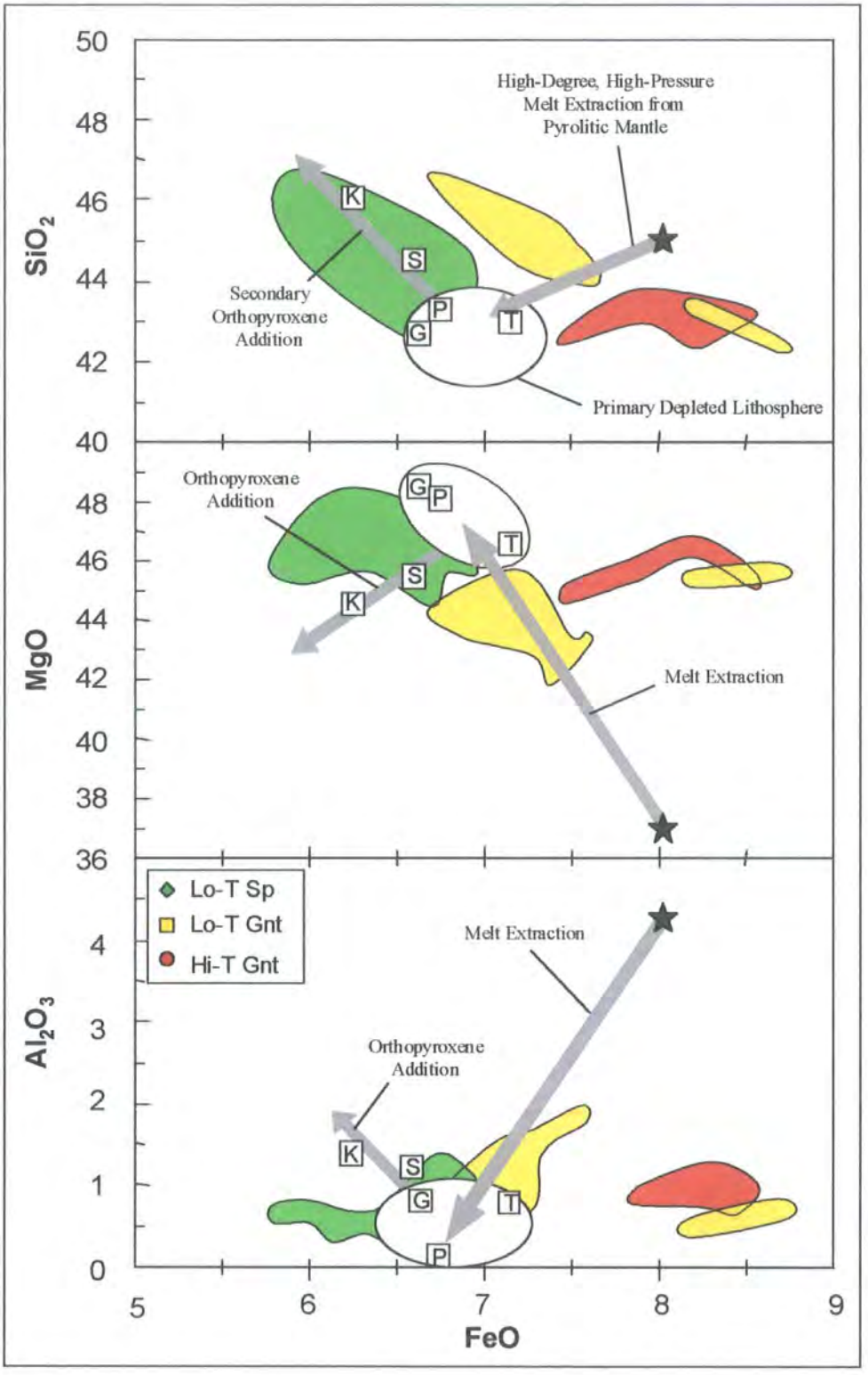

Figure 4.14 Oxide variation diagrams (wt%) showing a general model for the origin of cratonic lithosphere, after Walter (1999). Primary melt extraction from pyrolitic mantle (star symbol) of about 40-50% melt at pressures of 3-4 GPa produce a residue with compositions within a field encompassing Tanzania, Greenland and Papua New Guinea. Addition of OPX to Siberian and Kaapvaal lithosphere has caused enrichment in SiO_2 and Al_2O_3, and depletion in MgO and FeO. Green field - Jericho low-T spinel peridotites; yellow field – low-T Jericho garnet peridotites; and red field – Jericho high-T garnet peridotites.

For Jericho low-T spinel peridotites, primary melt extraction from a pyrolitic mantle produces harzburgitic lithosphere (primary melt extraction vector on Figure 4.14). This is consistent with the $Mg^{\#}$ of olivine in the Jericho spinel peridotites. Subsequent addition of orthopyroxene has moved the average composition of Jericho spinel peridotites along a secondary OPX addition compositional vector, as shown in Figure 4.14. This may be the consequence of cumulate mixing (Herzberg, 1993; Herzberg, 1999), melt-mantle reaction (Keleman *et al.*, 1998) or a combination of both.

For low-T coarse garnet and high-T garnet peridotites the picture is not as clear. For the majority of low-T garnet peridotites, these appear to lie on the vector of melt extraction but are generally more fertile than the harzburgitic residues from Greenland, Tanzania and Papua New Guinea, suggesting that they were formed from lower degrees of melt. The low-T garnet peridotites however, appear to have an overlying and secondary trend parallel to the vector for secondary OPX addition, and the addition of SiO_2 (Figure 4.14). Again this may be the result of cumulate mixing (Herzberg, 1993; Herzberg, 1999) and / or melt-mantle reaction (Keleman *et al.*, 1998). Several low-T garnet peridotites also have FeO contents higher than the model pyrolitic source. This may be further evidence that the low-T garnet peridotites have suffered Fe enrichment. The Al_2O_3 content of these samples suggest that they are depleted in nature, therefore Fe may have been preferentially mobilised in the metasomatising fluid. If Fe is preferentially mobilised relative to Mg and Al, this would shift samples to the right on Figure 4.14. This may explain inconsistencies observed between modal mineralogy, mineral chemistry and whole-rock major element modelling. The Fe enrichment appears to be generally unrelated to REE enrichment. An exception to this may be sample 51-2. This sample shows possible HREE enrichment as well as Fe enrichment, which may relate to a separate metasomatic episode. Many of the high temperature garnet peridotites also have FeO compositions higher than that of a pyrolitic source. As noted previously these samples may have suffered from asthenospheric metasomatism, which has resulted in Fe enrichment and a shift to the right in Figure 4.14. The late-stage introduction of secondary diopside, as suggested by the high modal abundance of CPX, would also contribute to higher bulk-rock FeO and Al_2O_3 contents.

Trace element enrichment in Jericho peridotite xenoliths does not appear to be systematically related to major-element chemistry. Subsequent to melt depletion, all Jericho peridotites have undergone a consistent LREE enrichment. In addition some samples show SiO_2 or OPX enrichment, and many samples show FeO enrichment. This may suggest that the lithospheric mantle has undergone episodic and variable

metasomatism from varying metasomatic fluids of different character (review by Menzies and Hawkesworth, 1987).

4.5 Re-Os Isotopic Study of Jericho Peridotite Xenoliths

4.5.1 Introduction

To understand the generation and evolution of the cratonic lithospheric keel beneath the Slave craton, detailed knowledge of the age, time-scale of formation and the relationship between the crust and mantle part of the lithosphere are required.

It has been suggested that the lithospheric mantle underlying the Slave craton, as sampled by the Jericho kimberlite, has a complicated history that involves episodes of melt depletion, and possible refertilisation or metasomatic alteration related to the passage of mantle-derived fluids. Osmium is compatible during partial melting of the mantle and the Os content of magmatic fluids is consequently low. Metasomatic alteration by magmatic fluids should therefore have a negligible effect on $^{187}Os/^{188}Os$ ratios within the lithospheric mantle. Re-Os isotope analyses of peridotite xenoliths from the Jericho kimberlite give an opportunity to constrain the timing of the melt extraction events that formed these peridotites. This is the critical step producing their compositional buoyancy and the key to their role in lithosphere formation and craton stabilisation (Walker *et al.*, 1989; Pearson, 1999b).

4.5.2 Re and Os Abundances and Isotopic Compositions

4.5.2.a Re variation

Rhenium abundances in the Jericho peridotite suite (Table 4.5) show a considerable scatter (0.0052 to 0.29 ppb), spanning a similar range to that reported from other cratonic peridotite xenolith suites (Walker *et al.*, 1989; Pearson *et al.*, 1995a; Pearson *et al.*, 1995b; Carlson *et al.*, 1999). The mean Re concentration for all Jericho peridotite samples listed in this study is 0.075 ppb (std.dev. = 0.064) with a median of 0.06 ppb (n = 29), compared to an estimated Re content of 0.26 ppb for fertile mantle (Morgan, 1986). This illustrates that lithospheric mantle peridotites from the central Slave craton beneath Jericho are highly depleted in Re relative to fertile mantle compositions (Figure 4.15). This is comparable to an average Re concentration of 0.084 (std.dev.

Table 4.5 Re-Os Isotopic data for Jericho peridotites. γOs, T_{RD} and T_{MA} calculated with respect to chondrite ($^{187}Os/^{188}Os$ = 0.3972 and $^{187}Re/^{188}Os$ = 0.1276; Walker *et al.*, 1989) and fertile mantle ($^{187}Os/^{188}Os$ = 0.4243 and $^{187}Re/^{188}Os$ = 0.1287; Meisel *et al.*, 1996) with ^{187}Re decay constant of 1.666 x 10^{-11} yr^{-1}. γOs is the difference (in %) in $^{187}Os/^{188}Os$ between the sample and fertile mantle/chondrite at the eruption age of the kimberlite. Errors are 2σ within run. T_{RD} and T_{MA} expressed in Ga. P-T estimates from Kopylova *et al* (1999b).

Samples	T (°C)	P (GPa)	Re (ppb)	Os (ppb)	$^{187}Re/^{188}Os$	$^{187}Os/^{188}Os$(m)	+/-	$^{187}Os/^{188}Os$(i)	γOs	T_{RD}	T_{MA}	$^{187}Os/^{188}Os$(i)	γOs	T_{RD}	T_{MA}
								Chondrite				*Fertile Mantle*			
Low-T Coarse Spinel															
8-7			0.006	2.47	0.0117	0.10679	16	0.10676	-15.60	3.07	3.15	0.10676	-16.26	3.03	3.11
9-12			0.013	4.86	0.0125	0.10660	13	0.10656	-15.75	3.09	3.19	0.10656	-16.41	3.05	3.14
10-11			0.033	3.30	0.0483	0.10798	17	0.10784	-14.74	2.91	3.28	0.10784	-15.41	2.88	3.22
10-12A			0.036	3.10	0.0561	0.10742	16	0.10726	-15.20	2.99	3.45	0.10726	-15.87	2.96	3.37
10-12B			0.008	4.20	0.0092	0.10839	19	0.10836	-14.32	2.83	2.90	0.10836	-15.00	2.81	2.87
11-18			0.012	5.10	0.0108	0.10872	14	0.10869	-14.07	2.79	2.86	0.10869	-14.75	2.77	2.83
23-9			0.005	1.23	0.0203	0.10759	26	0.10754	-14.98	2.95	3.10	0.10754	-15.65	2.92	3.06
39-23			0.146	2.65	0.2650	0.11890	17	0.11814	-6.59	1.41	3.81	0.11814	-7.33	1.48	3.58
44-12			0.075	2.40	0.1502	0.11077	26	0.11034	-12.76	2.55	3.95	0.11034	-13.45	2.54	3.80
Low-T Coarse Garnet															
9-2	809	3.28	0.103	3.75	0.1328	0.11987	21	0.11949	-5.53	1.21	1.72	0.11949	-6.27	1.29	1.79
10-456'			0.056	3.38	0.0804	0.11861	16	0.11838	-6.40	1.37	1.67	0.11838	-7.14	1.44	1.74
11-22			0.023	21.53	0.0052	0.12462	11	0.12460	-1.49	0.45	0.45	0.12460	-2.26	0.58	0.58
13-2			0.290	0.32	4.3138	0.13055	20	0.11821	-6.54	1.40	0.05	0.11821	-7.27	1.47	0.03
21-1	811	3.08	0.061	7.15	0.0410	0.11467	14	0.11455	-9.44	1.94	2.14	0.11455	-10.15	1.97	2.16
22-1	690	2.67	0.064	4.46	0.0689	0.11002	18	0.10982	-13.17	2.62	3.13	0.10982	-13.86	2.61	3.07
22-4	833	3.6	0.127	3.83	0.1599	0.11468	14	0.11422	-9.69	1.98	3.18	0.11422	-10.40	2.01	3.10
25-4	975	4.77	0.060	3.88	0.0746	0.11300	12	0.11278	-10.83	2.19	2.65	0.11278	-11.53	2.21	2.64
26-11	944	4.27	0.059	6.74	0.0419	0.11503	16	0.11491	-9.15	1.88	2.08	0.11491	-9.87	1.92	2.11
28-15			0.086	8.17	0.0507	0.11736	13	0.11722	-7.32	1.54	1.74	0.11722	-8.05	1.60	1.79

Table 4.5 (continued) Re-Os Isotopic data for Jericho peridotites.

Samples	T (°C)	P (GPa)	Re (ppb)	Os (ppb)	$^{187}Re/^{188}Os$	$^{187}Os/^{188}Os(m)$	+/-	$^{187}Os/^{188}Os(i)$	γOs	T_{RD}	T_{MA}	$^{187}Os/^{188}Os(i)$	γOs	T_{RD}	T_{MA}
								Chondrite				*Fertile Mantle*			
Low-T Coarse Garnet															
41-4	648	2.52	0.037	4.19	0.0430	0.11389	15	0.11377	-10.05	2.05	2.27	0.11377	-10.76	2.08	2.29
51-2			0.082	3.71	0.1059	0.11772	23	0.11742	-7.17	1.52	2.00	0.11742	-7.90	1.58	2.03
53-10			0.170	10.10	0.0809	0.10819	9	0.10796	-14.65	2.89	3.57	0.10796	-15.32	2.87	3.48
Low-T Por Gnt															
21-3	1088	5.12	0.078	4.66	0.0799	0.11309	16	0.11286	-10.77	2.18	2.68	0.11286	-11.47	2.20	2.66
High-T Por Garnet															
21-2	1335	5.77	0.197	5.31	0.1786	0.11222	13	0.11171	-11.68	2.35	4.07	0.11171	-12.38	2.36	3.90
23-1			0.137	0.31	2.1157	0.12255	37	0.11650	-7.89	1.65	-0.18	0.11650	-8.62	1.70	-0.22
26-9			0.069	2.95	0.1127	0.11570	17	0.11538	-8.78	1.81	2.45	0.11538	-9.50	1.86	2.45
39-3			0.111	3.97	0.1350	0.11542	23	0.11503	-9.05	1.87	2.72	0.11503	-9.77	1.90	2.69
40-9	1297	5.6	0.025	0.61	0.1965	0.12042	18	0.11986	-5.23	1.15	2.10	0.11986	-5.98	1.24	2.14
40-20			0.093	4.36	0.1026	0.11039	15	0.11010	-12.95	2.58	3.40	0.11010	-13.64	2.58	3.32
40-21	1273	5.47	0.034	2.43	0.0668	0.11837	22	0.11818	-6.57	1.40	1.65	0.11818	-7.30	1.47	1.71

= 0.078) and median of 0.072 ppb for Kaapvaal peridotite xenoliths analysed by Carlson *et al.* (1999).

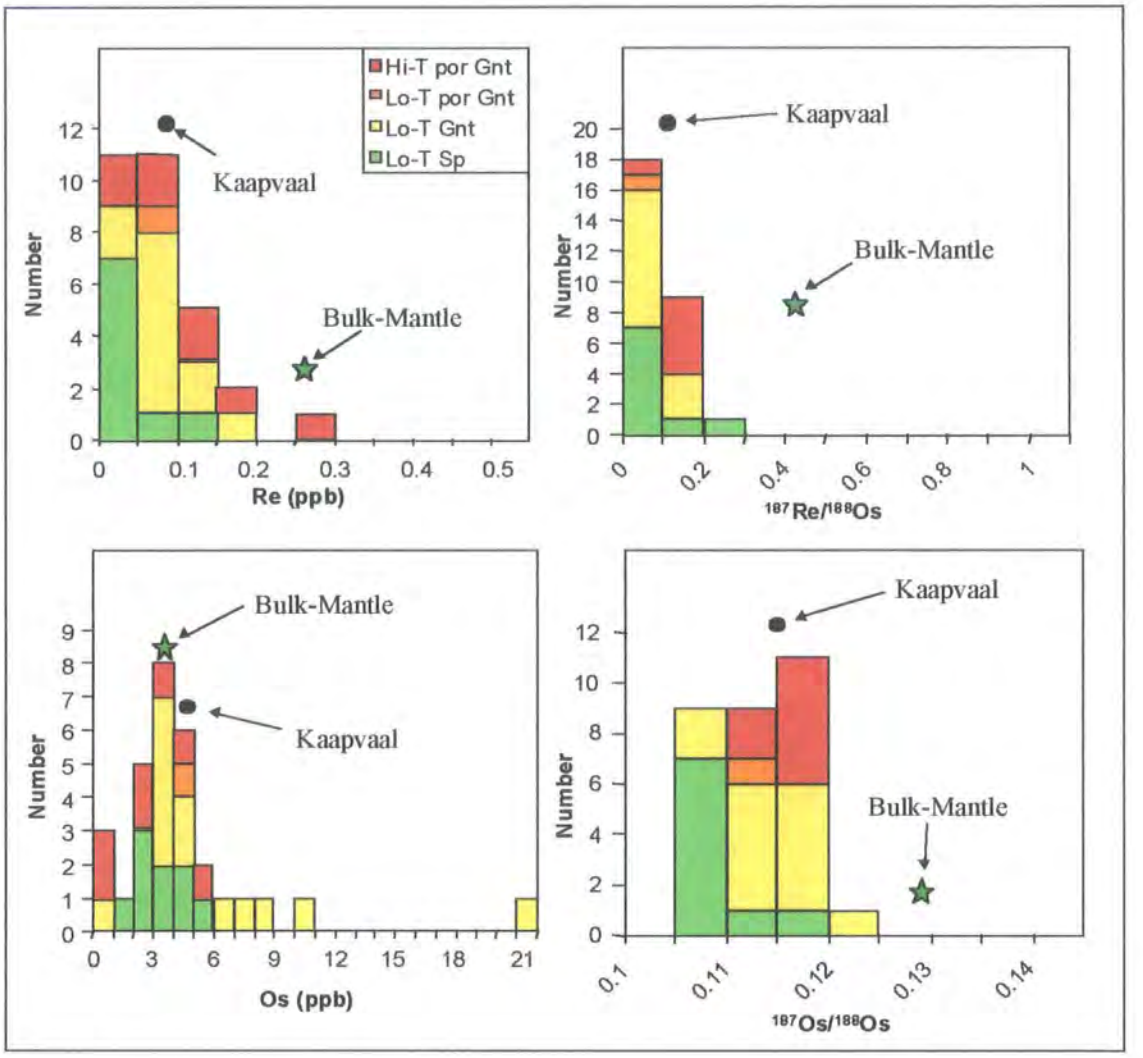

Figure 4.15 Histograms of Re and Os concentration (ng/g or ppb), $^{187}Re/^{188}Os$ and $^{187}Os/^{188}Os$ for Jericho peridotite xenoliths. Mean Kaapvaal values after Carlson *et al.* (1999) and Bulk-Mantle after Morgan (1986).

A summary of mean and median Re concentrations is presented in Table 4.6. Coarse spinel peridotites from the Jericho suite generally have lower Re concentrations than low-T coarse garnet and high-T porphyroclastic non-disrupted garnet peridotites. The Re data also suggests that there may be an increase in Re content with depth at Jericho, either related to lower degrees of partial melting or later Re enrichment. Several peridotites from Jericho have Re concentrations enriched relative to fertile mantle, and this is supporting evidence for enrichment.

Location and Facies	Mean (ppb)	+/-	Median (ppb)	n
Jericho	0.077	0.064	0.062	30
Low-T Spinel	0.037	0.047	0.013	9
Low-T Garnet	0.094	0.070	0.064	13
Low-T Garnet†	0.077	0.040	0.062	12
High-T Garnet	0.095	0.060	0.093	7
High-T Garnet†	0.088	0.063	0.081	6

Table 4.6 Summary of the mean and Median Re concentrations in peridotites from the Jericho suite and individual facies.
† calculated mean and median for peridotite xenoliths depleted in Re relative to fertile mantle compositions (0.26 ppb, Morgan, 1986).

4.5.2.b Os variation

Osmium concentrations for the Jericho peridotite suite (Table 4.5) are similar to those reported for Kaapvaal and Siberian peridotites (Walker *et al.*, 1989; Pearson *et al.*, 1995a; Pearson *et al.*, 1995b; Carlson *et al.*, 1999), showing a considerable range (0.33 ppb to 21.5 ppb). The Os abundances of Jericho peridotites are, on average (4.5 ppb; Table 4.7), higher than estimates for fertile mantle (3.4 ppb, Morgan, 1986). This is consistent with the melt-depleted nature of the xenoliths and high distribution coefficient for Os into the solid (Figure 4.15). Os concentrations reported from studies of Kaapvaal peridotite xenoliths (mean = 4.61 ppb, median = 4.05 ppb, Carlson *et al.*, 1999) and Alpine peridotites (mean = 3.74 ppb, median = 3.84 ppb, Reisberg *et al.*, 1991; Reisberg and Lorand, 1995) also tend to be higher than estimates for fertile mantle. Abyssal peridotites (Snow and Reisberg, 1995), rift related spinel peridotite xenoliths (McBride *et al.*, 1996; Meisel *et al.*, 1996; Handler *et al.*, 1997) and arc related spinel peridotite xenoliths (Brandon *et al.*, 1996), in contrast, have Os concentrations lower than fertile mantle.

Location and Facies	Mean (ppb)	+/-	Median (ppb)	n
Jericho	4.50	3.87	3.86	30
Low-T Spinel	3.26	1.26	3.10	9
Low-T Garnet	6.25	5.23	4.19	13
High-T Garnet	3.27	1.66	3.46	6

Table 4.7 Summary of the mean and Median Os concentrations in peridotites from the Jericho suite and individual facies.

A summary of mean and median Os abundances is presented in Table 4.7. The Os concentrations for coarse spinel peridotite xenoliths from the Jericho kimberlite, although on average lower than fertile mantle estimates, are generally higher than those reported for rift related spinel peridotite xenoliths (Handler *et al.*, 1997; Peslier *et al.*, 2000). In contrast, the Os contents of low-T coarse garnet peridotites are higher than fertile mantle estimates, and generally higher than Kaapvaal peridotite xenoliths. The Os concentrations of High-T garnet peridotites also tends to be lower than fertile mantle, but again are higher than rift related spinel peridotite xenoliths (Handler *et al.*, 1997; Peslier *et al.*, 2000). The variation observed within the Jericho peridotite suite may be the result of a heterogeneous distribution of Os within the lithospheric mantle or an artefact of the selected sample-set. Alternatively it may indicate vertical variations within the stratigraphic section of the lithospheric mantle.

4.5.2.c Re/Os isotopic variation

In general, the Re/Os ratios of cratonic peridotites are amongst the lowest for any peridotites. Most peridotites tend towards lower Re/Os than estimated fertile mantle however ($^{187}Re/^{188}Os$ = 0.4243, Meisel *et al.*, 1996). The range in Re and Os concentrations for the Jericho peridotites (Table 4.5) produce a large range in $^{187}Re/^{188}Os$ from 0.005 to 4.31 (i.e. subchondritic to suprachondritic, Figure 4.15), resulting in an average $^{187}Re/^{188}Os$ ratio of 0.292 (Table 4.8). Overall this is higher than peridotites from the Kaapvaal craton (average $^{187}Re/^{188}Os$ = 0.109, Carlson *et al.*, 1999) and higher than Alpine peridotites (mean $^{187}Re/^{188}Os$ = 0.207, Reisberg and Lorand, 1995). However, the Jericho peridotites have lower $^{187}Re/^{188}Os$ than that reported for spinel peridotite xenoliths from the Northern Canadian Cordillera (mean $^{187}Re/^{188}Os$ = 0.537, Peslier *et al.*, 2000). Of the 30 peridotites analysed (Table 4.5), only two samples have $^{187}Re/^{188}Os$ greater than fertile mantle. The data from Jericho are skewed greatly by these high Re, low Os samples (13-2 and 23-1). If we exclude these samples the average $^{187}Re/^{188}Os$ for Jericho peridotites is substantially reduced to 0.084 (Table 4.8), even lower than the mean for Kaapvaal peridotites. This is more consistent with the incompatible nature of Re in a residua during partial melting.

The mean $^{187}Re/^{188}Os$ ratio for low-T spinel peridotite xenoliths is lower than that reported for Kaapvaal peridotites (Table 4.8). The mean $^{187}Re/^{188}Os$ ratio for both low-T garnet and high-T garnet peridotites are higher than both Kaapvaal and Alpine peridotites, and similar to fertile mantle. If we exclude samples with $^{187}Re/^{188}Os$ higher

than fertile mantle, the mean $^{187}Re/^{188}Os$ for low-T garnet peridotites is lowered and more comparable to the Jericho spinel peridotites and those from the Kaapvaal craton. The $^{187}Re/^{188}Os$ ratio for high-T peridotites is also reduced but remains higher than Kaapvaal peridotites but lower than that for Alpine peridotites (Table 4.8). This evidence supports the observation that the lithospheric mantle beneath Jericho is depleted relative to fertile mantle, as typically seen in Archean and post-Archean regions, but it is also apparent that there is an increase in Re concentration with increasing depth in the lithospheric mantle beneath Jericho.

Location and facies	Mean	+/-	Median	n
Jericho	0.292	0.85	0.077	30
Jericho†	0.084	0.064	0.072	28
Low-T Spinel	0.065	0.088	0.020	9
Low-T Garnet	0.400	1.177	0.075	13
Low-T Garnet†	0.074	0.043	0.072	12
High-T Garnet	0.415	0.751	0.135	7
High-T Garnet†	0.132	0.049	0.124	6

Table 4.8 Summary of the mean and Median $^{187}Re/^{188}Os$ concentrations in peridotites from the Jericho suite and individual facies.

† calculated mean and median for peridotite xenoliths with $^{187}Re/^{188}Os$ ratios lower than fertile mantle estimates only (0.4243, Meisel *et al.*, 1996).

4.5.2.d Os isotopic variation

Os isotopic compositions provide the clearest difference between cratonic peridotites and peridotites from other tectonic settings. Os isotopic compositions of the Jericho peridotite xenoliths range from $^{187}Os/^{188}Os$ values of 0.1066 to 0.1246 values (Table 4.5; Figure 4.15), i.e. from significantly more depleted than chondritic to near chondritic. This is comparable to the range for Kaapvaal and Siberian peridotite suites (Pearson *et al.*, 1995a; Pearson *et al.*, 1995b; Carlson *et al.*, 1999). Though there is an overlap in the range of Re/Os for Jericho peridotites and peridotites from other tectonic settings, the very low, unradiogenic $^{187}Os/^{188}Os$ values present at Jericho (particularly coarse spinel peridotites) are distinct from other peridotite groups (Figure 4.15). The Jericho peridotites are highly unradiogenic relative to both chondritic and fertile mantle estimates (Table 4.5). The unradiogenic isotopic nature of the Jericho peridotite suite is comparable to other cratonic peridotites (Walker *et al.*, 1989; Pearson *et al.*, 1995a; Pearson *et al.*, 1995b; Carlson *et al.*, 1999; Pearson, 1999a). This indicates that long-

term Re depletion and isolation from the convecting mantle occurred much earlier than in the non-cratonic peridotite groups. By inference magmaphile element depletion must also have occurred in Jericho peridotites long before that of other peridotite groups from other tectonic settings.

Location	Mean	+/-	Median	N
Kaapvaal†	0.1115	0.0032	0.1105	38
Jericho	0.1135	0.005	0.1114	30
Low-T Spinel	0.1091	0.0036	0.1078	9
Low-T Garnet	0.1154	0.0044	0.1147	12
High-T Garnet	0.1150	0.0037	0.1152	5

Table 4.9 Summary of the mean and Median $^{187}Os/^{188}Os$ ratios in peridotites from the Jericho suite and individual Jericho facies.
† Mean and median $^{187}Os/^{188}Os$ ratios for Kaapvaal craton from Carlson *et al* (1999).

The $^{187}Os/^{188}Os$ isotopic composition of Jericho peridotite xenoliths is on average more radiogenic than those from the Kaapvaal craton (Carlson *et al.*, 1999). However, on average the low-T spinel peridotites from Jericho are more unradiogenic than Kaapvaal peridotites (Table 4.9). Coarse spinel peridotites from the Jericho suite generally have lower $^{187}Os/^{188}Os$ ratios than low-T coarse garnet peridotites and high-T porphyroclastic garnet peridotites (Table 4.9). This suggests that Os isotope ratios of peridotites become more radiogenic at depth in the lithospheric mantle beneath Jericho.

4.5.3 PGE geochemistry of the Jericho peridotite suite

4.5.3.a Whole-rock PGE abundances

Considered as a whole, the Jericho peridotite suite shows a large variation in PGEs and Re (Table 4.10). This range is larger than that recorded for Pyrenean orogenic lherzolites (Lorand *et al.*, 1999), or for spinel peridotites from alkali basalts (Morgan *et al.*, 1981; Handler and Bennett, 1999). On average the IPGE (Ir, Os, Ru) concentrations for Jericho samples are higher than primitive mantle estimates (McDonough and Sun, 1995, Table 4.10), whilst the PPGE (Pt, Pd) abundances are depleted. This is consistent with the major-element depleted nature of the Jericho peridotites and suggests the PGEs have fractionated during melt extraction, as expected from their different compatibilities (Rehkämper *et al.*, 1999b). In comparison to peridotites from other tectonic settings, the IPGEs from the Jericho suite have similar abundances to those reported for orogenic massifs (Pattou *et al.*, 1996; Lorand *et al.*, 1999) and higher than those reported for

Table 4.10 PGE, Re and selected major and trace element abundances for Jericho peridotites. CI chondrite values from McDonough and Sun (1995). Primitive mantle values taken as 0.007 x CI chondrite after method of McDonough and Sun (1995).

Samples	S (ppm)	Al2O3 (wt%)	(La/Yb)n	Ba (ppm)	Nb (ppm)	Os (ppb)	Ir (ppb)	Ru (ppb)	Pt (ppb)	Pd (ppb)	Re (ppb)
Low-T Coarse Spinel											
8-7	47	0.64	413.27	27.45	3.01	2.47	2.03	3.47	0.25	0.05	0.01
9-12	108	0.35	291.78	101.86	12.70	4.86	4.20	7.44	4.22	0.25	0.01
10-11	164	1.22	103.54	45.16	3.99	3.30	3.75	5.75	0.79	0.05	0.03
10-12A	109	1.26	163.40	101.92	6.33	3.10	2.53	4.16	0.34	0.07	0.04
10-12B	51	0.54	185.13	10.60	1.22	4.20	4.03	5.91	1.00	0.03	0.01
11-18	50	0.41	181.07	19.49	1.34	5.10	2.73	5.13	0.78	0.18	0.01
23-9	66	0.68	128.08	11.93	1.13	1.23	1.50	6.78	0.03	0.02	0.01
39-23	115	1.30	10.37	24.03	1.34	2.65	2.40	5.43	2.83	2.57	0.15
44-12	599	1.13	227.66	22.88	1.36	2.40	2.49	5.68	0.05	0.05	0.08
Low-T Coarse Garnet											
9-2	221	1.86	26.34	83.92	3.40	3.75	3.65	7.52	8.20	6.14	0.10
10-456'	141	0.97	160.36	182.98	6.58	3.38	3.50	5.68	6.79	2.31	0.06
11-22	128	1.64	56.82	70.16	5.95	21.53	19.74	19.60	21.30	9.01	0.02
13-2	157	0.49	84.30	48.63	5.81	0.32	0.27	0.57	0.24	0.17	0.29
21-1	76	0.67	123.79	47.90	2.64	7.15	4.30	5.87	1.42	0.06	0.06
22-1	73	0.81	95.39	29.97	2.44	4.46	4.47	8.15	3.87	0.10	0.06
22-4	78	1.43	75.50	86.37	5.99	3.83	4.79	8.60	5.36	1.97	0.13
25-4	107	1.11	137.39	68.96	5.99	3.88	3.97	5.63	5.03	1.51	0.06
26-11	76	0.95	206.89	48.58	5.51	6.74	5.52	4.73	5.63	6.78	0.06
28-15	131	1.53	75.44	64.44	11.58	8.17	4.95	7.71	6.28	2.66	0.09
41-4	77	0.73	103.60	97.97	3.46	4.19	3.30	6.57	3.27	0.75	0.04
51-2	545	5.77	17.90	80.44	10.76	3.71	4.39	6.95	4.56	3.72	0.08
53-10	791	0.70	442.68	112.63	2.82	10.10	9.66	15.02	12.38	2.22	0.17

Table 4.10 (continued) PGE, Re and selected major and trace element abundances for Jericho peridotites.

Samples	S (ppm)	Al2O3 (wt%)	(La/Yb)n	Ba (ppm)	Nb (ppm)	Os (ppb)	Ir (ppb)	Ru (ppb)	Pt (ppb)	Pd (ppb)	Re (ppb)
Low-T Por Garnet											
21-3	283	1.57	61.74	258.68	19.40	4.66	4.30	7.93	5.25	2.94	0.08
High-T Por Garnet											
21-2	171	0.83	60.84	68.22	3.78	5.31	4.79	13.11	9.74	5.19	0.20
23-1	68	0.84	99.72	26.17	4.39	0.31	0.26	0.30	0.09	0.13	0.14
26-9	167	2.58	20.37	58.66	7.29	2.95	2.65	5.34	1.94	1.72	0.07
39-3	235	1.38	83.71	202.09	23.18	3.97	3.88	7.56	4.09	2.24	0.11
40-9	128	0.73	24.71	34.98	2.69	0.61	0.63	2.29	1.55	0.81	0.02
40-20	96	1.20	29.82	12.47	2.41	4.36	4.13	6.41	3.19	0.12	0.09
40-21	107	0.93	34.66	23.52	3.48	2.43	2.51	5.47	2.26	0.86	0.03
Primative mantle	250	4.44	1.47	6.6	0.658	3.4	3.2	5	7.1	3.9	0.28
CI chondrite	54,000	1.62	1.47	2.41	0.24	490	455	710	1,010	550	40
Jericho Range						21.53 - 0.31	19.74 - 0.26	19.6 - 0.3	21.3 - 0.03	11.76 - 0.02	0.29 - 0.01
Jericho Average						4.56	4.10	6.89	4.54	2.27	0.08

spinel peridotites (Morgan *et al.*, 1981; Handler and Bennett, 1999). The PPGEs in the Jericho suite however, are depleted relative to both alkali basalt hosted peridotites and orogenic massifs.

4.5.3.b Covariation of PGEs in Jericho peridotites

Osmium and Ru both show good positive correlations with Ir, at close to chondritic ratios (Figure 4.16). Correlation coefficients for Os, and Ru, with Ir for the Jericho peridotite suite are 0.97 and 0.88 respectively. Xenoliths from different facies show varying levels of correlation (Table 4.11).

Location	Correlation coefficients		
	Os-Ir	Ru-Ir	n
Jericho	0.97	0.88	28
Low-T Spinel	0.76	0.41	9
Low-T Garnet	0.97	0.93	11
High-T Garnet	1.0	0.92	7

Table 4.11 Summary of correlation coefficients for IPGEs within the Jericho peridotite suite, and individual facies.

Low-T garnet and high-T garnet peridotites show the best correlation within the suite. The low-T spinel peridotites show poor correlation. These samples are the most depleted peridotites within the suite, and this may therefore be a reflection of a heterogeneous distribution of residual IPGEs.

The mean chondrite normalised Os/Ir ratio, $(Os/Ir)_n$, for Jericho peridotites is slightly superchondritic at 1.04, and $(Ru/Ir)_n$ is superchondritic at 1.21 (Table 4.12). The PPGEs, in contrast, show poor systematic correlations with Ir (Figure 4.16). The Pt-Ir variation for the entire suite has a correlation coefficients of 0.9. The correlation for Pd is 0.68, but no correlation exists for Re. The mean chondrite normalised ratios of Pt, Pd and Re with Ir, $(Pt/Ir)_n$, $(Pd/Ir)_n$, and $(Re/Ir)_n$ are subchondritic (Table 4.12).

4.5.3.c PGE patterns of Jericho peridotites

IPGEs in the Jericho peridotites range from 0.0012 to 0.021 x CI chondrite, and generally have flat chondrite-normalised patterns displaying little inter-element fractionation (Figure 4.17; Table 4.12). This is regarded as a characteristic feature of upper-mantle peridotites (cf. O'Neill, 1991), and reflects the compatible behaviour of

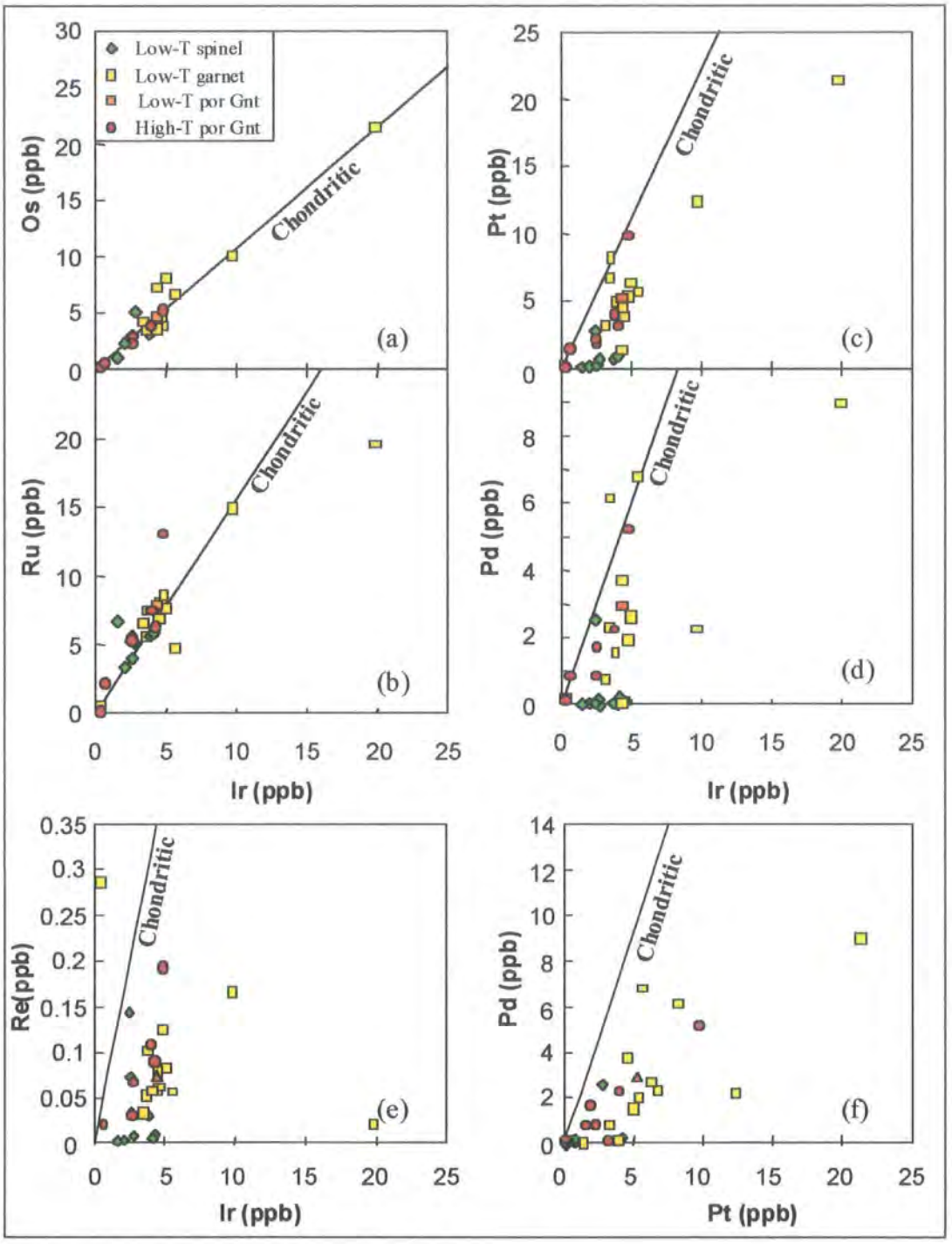

Figure 4.16 Bivariate PGE abundance plots for the Jericho peridotite suite. (a-e) Os, Ru, Pt, Pd and Re versus Ir. (f) Pd versus Pt. The positive correlation between Os, Ru and Ir ($r = 0.97$ and 0.88 respectively), may suggest these elements are controlled by the same phases in the xenoliths. None of the remaining PGEs or Re correlate with Ir or each other. Chondritic ratios from McDonough and Sun (1995).

Table 4.12 CI-chondrite normalised PGEs and PGE ratios for the Jericho peridotite suite. Chondrite normalised using normalisation values of M^{c}Donough and Sun (1995).

Samples	Os	Ir	Ru	Pt	Pd	Re	(Os/Ir)n	(Ru/Ir)n	(Pt/Ir)n	(Pd/Ir)n	(Re/Ir)n
Low-T Coarse Spinel											
8-7	0.00504	0.00445	0.00489	0.00025	0.00009	0.00015	1.13	1.10	0.06	0.02	0.03
9-12	0.00992	0.00923	0.01048	0.00417	0.00045	0.00032	1.07	1.14	0.45	0.05	0.03
10-11	0.00673	0.00823	0.00810	0.00078	0.00009	0.00083	0.82	0.98	0.10	0.01	0.10
10-12A	0.00633	0.00557	0.00586	0.00033	0.00013	0.00091	1.14	1.05	0.06	0.02	0.16
10-12B	0.00857	0.00886	0.00832	0.00099	0.00005	0.00020	0.97	0.94	0.11	0.01	0.02
11-18	0.01042	0.00600	0.00723	0.00077	0.00033	0.00029	1.73	1.20	0.13	0.06	0.05
23-9	0.00250	0.00330	0.00955	0.00003	0.00004	0.00013	0.76	2.89	0.01	0.01	0.04
39-23	0.00541	0.00528	0.00765	0.00280	0.00468	0.00365	1.02	1.45	0.53	0.89	0.69
44-12	0.00490	0.00548	0.00801	0.00004	0.00010	0.00188	0.90	1.46	0.01	0.02	0.34
Low-T Coarse Garnet											
9-2	0.00765	0.00801	0.01059	0.00812	0.01116	0.00259	0.95	1.32	1.01	1.39	0.32
10-456'	0.00690	0.00768	0.00800	0.00672	0.00420	0.00141	0.90	1.04	0.88	0.55	0.18
11-22	0.04393	0.04338	0.02761	0.02109	0.01639	0.00058	1.01	0.64	0.49	0.38	0.01
13-2	0.00066	0.00060	0.00081	0.00023	0.00031	0.00725	1.11	1.35	0.39	0.52	12.17
21-1	0.01459	0.00945	0.00827	0.00141	0.00011	0.00152	1.54	0.87	0.15	0.01	0.16
22-1	0.00909	0.00982	0.01149	0.00383	0.00018	0.00160	0.93	1.17	0.39	0.02	0.16
22-4	0.00781	0.01053	0.01211	0.00531	0.00359	0.00318	0.74	1.15	0.50	0.34	0.30
25-4	0.00793	0.00872	0.00793	0.00498	0.00275	0.00151	0.91	0.91	0.57	0.32	0.17
26-11	0.01375	0.01213	0.00666	0.00558	0.01233	0.00147	1.13	0.55	0.46	1.02	0.12

Table 4.12 (continued) CI-chondrite normalised PGEs and PGE ratios for the Jericho peridotite suite.

Samples	Os	Ir	Ru	Pt	Pd	Re	(Os/Ir)n	(Ru/Ir)n	(Pt/Ir)n	(Pd/Ir)n	(Re/Ir)n
Low-T Coarse Garnet											
28-15	0.01666	0.01089	0.01086	0.00622	0.00484	0.00215	1.53	1.00	0.57	0.44	0.20
41-4	0.00855	0.00725	0.00926	0.00323	0.00137	0.00094	1.18	1.28	0.45	0.19	0.13
51-2	0.00756	0.00965	0.00978	0.00451	0.00676	0.00204	0.78	1.01	0.47	0.70	0.21
53-10	0.02061	0.02123	0.02115	0.01226	0.00403	0.00425	0.97	1.00	0.58	0.19	0.20
54-9	0.01455	0.01437	0.01748	0.01550	0.02139	0.00675	1.01	1.22	1.08	1.49	0.47
56-1	0.00739	0.00750	0.01035	0.00683	0.01122	0.00340	0.98	1.38	0.91	1.50	0.45
Low-T Por Garnet											
21-3	0.00952	0.00945	0.01117	0.00520	0.00534	0.00194	1.01	1.18	0.55	0.56	0.21
High-T Por Garnet											
21-2	0.01084	0.01053	0.01298	0.00965	0.00943	0.00493	1.03	1.23	0.92	0.90	0.47
26-9	0.00601	0.00581	0.00529	0.00192	0.00312	0.00173	1.03	0.91	0.33	0.54	0.30
39-3	0.00809	0.00853	0.00749	0.00405	0.00406	0.00278	0.95	0.88	0.47	0.48	0.33
40-9	0.00124	0.00138	0.00227	0.00154	0.00148	0.00062	0.90	1.65	1.12	1.08	0.45
40-20	0.00890	0.00908	0.00635	0.00316	0.00023	0.00233	0.98	0.70	0.35	0.02	0.26
40-21	0.00496	0.00553	0.00541	0.00223	0.00156	0.00084	0.90	0.98	0.40	0.28	0.15

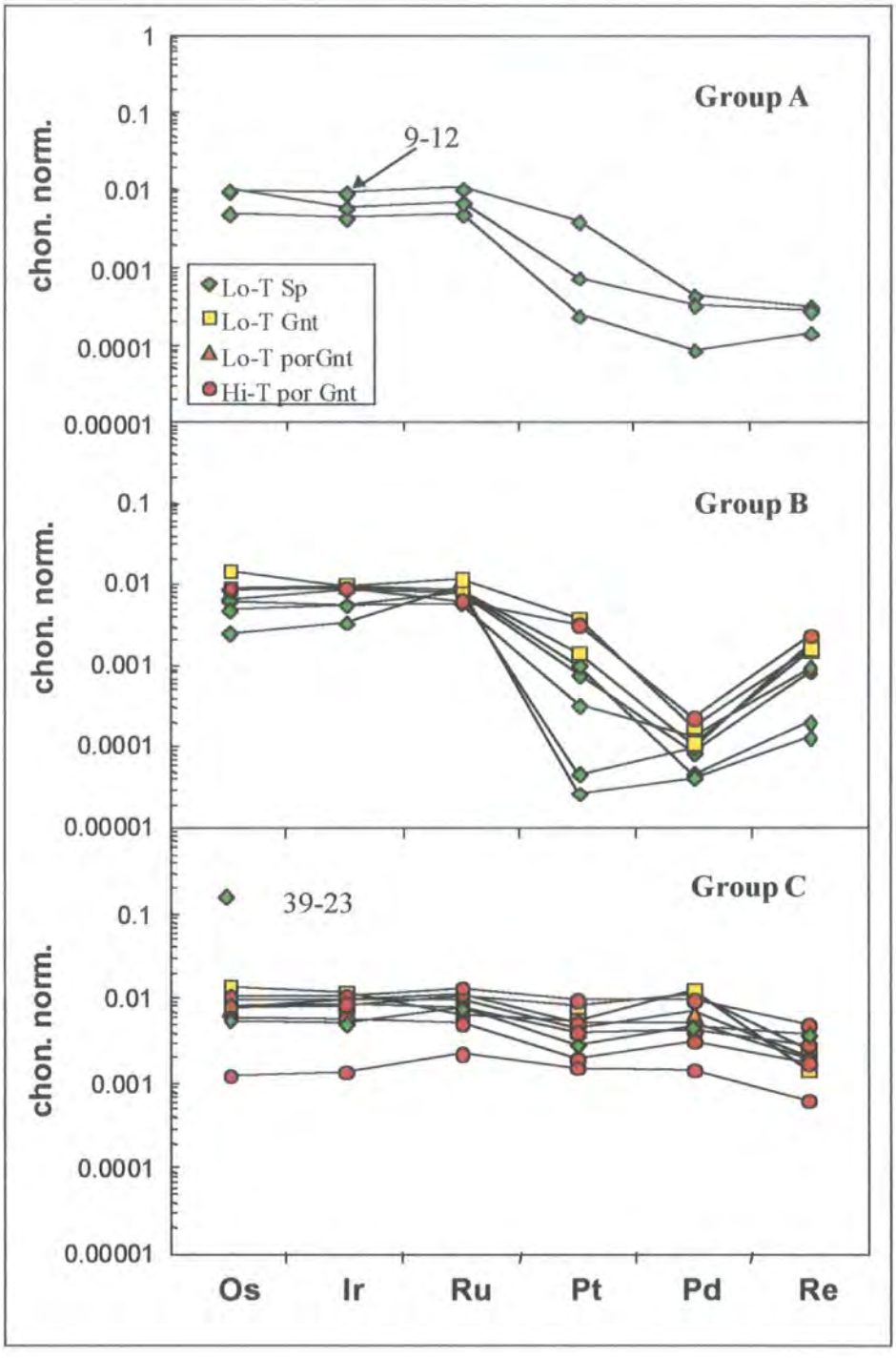

Figure 4.17 CI-chondrite normalised PGE abundances for the Jericho peridotite suite: Group A - PPGE depleted pattern, Group B - PPGE depleted pattern with Re enrichment, and Group C - PPGE depleted pattern with Pd and possible Re enrichment. CI chondrite values from McDonough and Sun (1995).

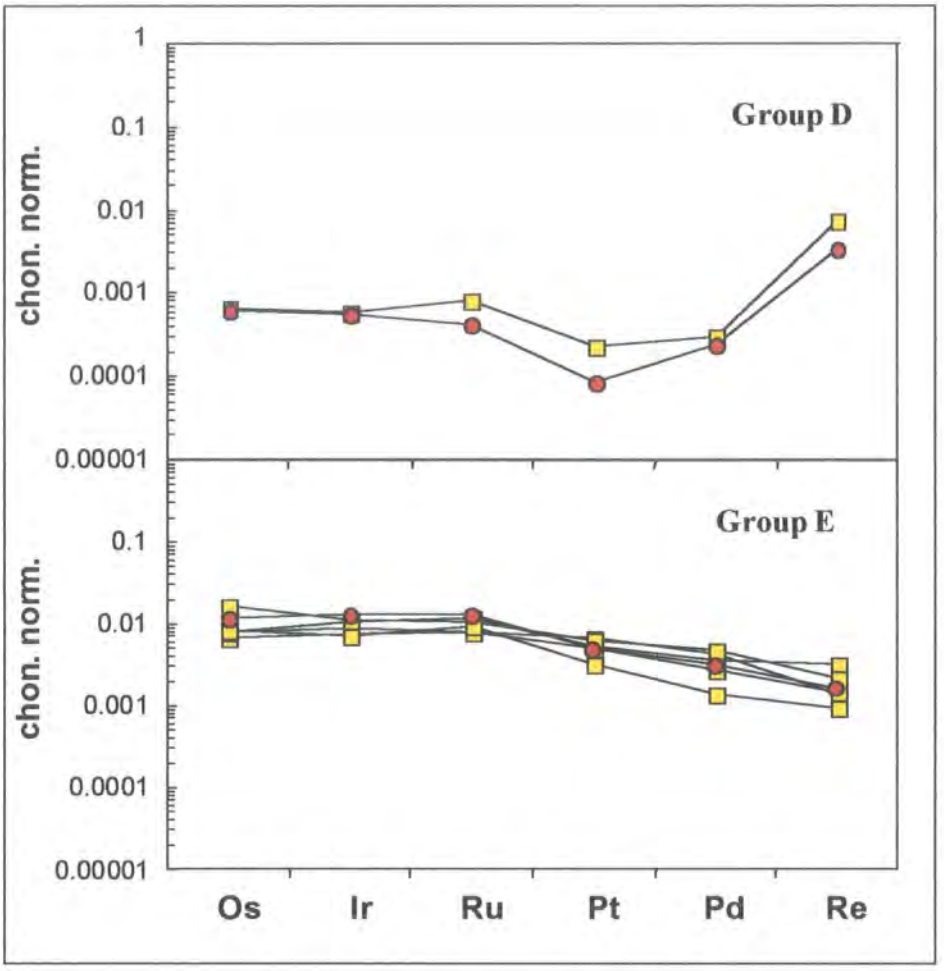

Figure 4.17 (continued) CI-chondrite normalised PGE abundances for the Jericho peridotite suite: Group D - PPGE depleted pattern with Pd and Re enrichment, and Group E - Moderately fractionated PGE patterns?

melting processes (Barnes *et al.*, 1985; Brügmann *et al.*, 1987; Barnes and Picard, 1993; Reisberg and Lorand, 1995).

Variations exist between peridotites from different facies. Peridotites from the low-T garnet facies exhibit a more uniform IPGE distribution at ~ 0.001 x CI chondrite (Figure 4.17). Peridotites from the low-T spinel and high-T garnet facies are more variable ranging from 0.001 to 0.01 x CI chondrite. Occasionally samples have unchondritic Os/Ir or Ru/Ir (e.g. 23-9). The large range in IPGE concentrations within the Jericho peridotites, in addition to unchondritic IPGE ratios, may be extreme examples of the heterogeneous distribution of IPGEs ("nugget effects") and PGMs.

The PPGEs within the Jericho peridotite suite are very variable, with many samples showing strongly fractionated patterns in contrast to the IPGEs. This is consistent with moderately incompatible behaviour of PPGEs. The Jericho coarse garnet peridotites have much more variable chondrite-normalised patterns than the coarse spinel

peridotites. On the basis of their chondrite-normalised PGE patterns, several distinct groups of peridotites have been recognised within the Jericho suite, (Figure 4.17a-e), summarised below.

4.5.3.d Fractionation of PGEs within the Jericho peridotites

PPGE depleted peridotites (Group A)

Three spinel peridotites have highly fractionated PPGEs (Figure 4.17a), with marked depletions in Pt, Pd and Re. This pattern is characteristic of that expected for a peridotite that has undergone extensive melt extraction. This depletion trend is much more marked than the PGE patterns of harzburgitic residues from Pyrenean orogenic massifs (Lorand *et al.*, 1999). Chondrite normalised Pd/Ir ratios for these samples range from $(Pd/Ir)_n$ of 0.02 to 0.055 (Table 4.12 and 4.13). These depleted PGE patterns suggest that the system has remained closed with respect to PGEs after initial melt-extraction, and the melt extraction was enough to exhaust sulfides.

PPGE depleted peridotites with Re enrichment (Group B)

This group of samples (Figure 4.17b) produce a fractionated PGE pattern with marked depletion in Pt and Pd, but with varying Re contents which results in a marked upward inflection in the PGE patterns. This reflects secondary introduction of Re to the system, perhaps by infiltration of the host kimberlite. Low $(Pd/Ir)_n$ ratios within spinel (0.005 to 0.017), low-T garnet (0.011 to 0.019) and high-T garnet peridotites (0.025) of this group support the notion that these samples represent highly depleted peridotites, and. The samples have therefore experienced later Re addition, and the Re-Os system has not remained closed since the time of melt extraction.

PPGE depleted peridotites with Pd enrichment (Group C)

This group of peridotites has a moderately fractionated PGE pattern (Figure 4.17c). These samples appear to show depletion in Pt relative to IPGEs, but have an inflection in the pattern at Pd, in many cases accentuating the depletion of Re. This may indicate that Pd has been enriched in the peridotites following melt extraction. If we consider sample 39-23, superimposing the PGE pattern of this samples onto that of sample 9-12 (group A), the IPGE and Pt abundances correlate well indicating that the 39-23 may have been depleted in PPGEs but later enriched.

The enrichment of Pd indicates the potential risk of using $(Pd/Ir)_n$ as an indicator for the degree of depletion, without also considering Pt and Re. The degree of Pd enrichment in these samples, relative to Re, suggests the elements may be decoupled in

Table 4.13 Summary of PGE behaviour within the Jericho peridotites, on the basis of the shape of the PPGE part of the PGE patterns. Average whole-rock elemental abundances and PGE ratios on the basis of PPGE determined groups.

Group	PGE Pattern	Pd (ppb)	Re (ppb)	S (ppm)	Al_2O_3 (wt%)	Ba (ppm)	Nb (ppm)	$(Pd/Ir)_n$	$(Re/Ir)_n$	$(Re/Pt)_n$
A	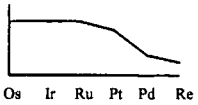	0.16	0.01	68.5	0.46	49.6	5.7	0.04	0.04	0.35
B_i	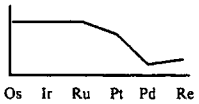	0.06	0.05	154.3	0.86	35.4	2.7	0.02	0.16	6.59
C	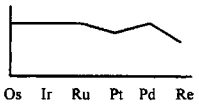	3.29	0.09	204.6	1.75	88.3	8.1	0.78	0.32	0.56
D	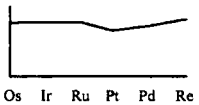	0.15	0.21	112	0.65	37.4	5.1	0.47	9.10	35.31
E	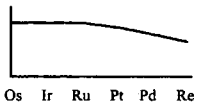	1.84	0.07	106.5	1.13	100.1	6.7	0.37	0.20	0.35

metasomatising fluids, and therefore may have been disturbed by separate events. The $(Pd/Ir)_n$ for the two low-T coarse garnet peridotites within this group are super-chondritic at 1.02 and 1.34 respectively (Table 4.12), and may suggest melt-rock reaction processes such as those proposed by Rehkämper *et al.* (1999).

PPGE depleted peridotites with Pd and Re enrichment (Group D)

These samples show a marked depletion in Pt (Figure 4.17d), but both Re and Pd are clearly enriched with respect to Pt with $(Re/Pt)_n$ ranging from ~ 31 to 40.

Moderately fractionated PPGE peridotites (Group E)

This group of peridotites are predominantly from the low-T coarse garnet facies (Figure 4.17e), and display moderately fractionated PPGEs relative to IPGEs. Fractionation of the PPGEs is not so marked as in group A peridotites and this is reflected in $(Pd/Ir)_n$ ranging from 0.2 to 0.5. These Jericho samples may represent the residues of low degree melts, and as such retain higher abundances of PPGEs in the residua. Alternatively the samples may represent peridotites that have experienced a larger degree of melt extraction, but have subsequently been enriched in PPGEs, masking the initial depletion event. Slight inflections in the PGE pattern at Pd and Re and depleted major-element chemistry for several samples in this group may make the latter argument more likely. It is therefore difficult to ascertain whether the system has remained closed with respect to Re infiltration without further knowledge of the degree of melt and the mobility of sulfides and PGEs

PGE fractionation

Depletion of PPGEs is consistent with the major-element depleted nature of the Slave lithospheric mantle and suggests that the PGEs were fractionated during melt extraction. Relative compatibility during the fractionation of PGEs as a result melt extraction, based upon the evidence from the chondrite-normalised patterns of Jericho peridotites is in the order Os ~ Ir ~ Ru > Pt > Pd ≥ Re. This is consistent with the order of fractionation observed in melts derived from the mantle (Barnes *et al.*, 1985).

In contrast to the pervasive enrichment of LREEs experienced by the Jericho peridotite suite, PGEs consistently have PPGE depleted patterns, in general retaining remnants of a depleted nature with sub-chondritic abundances of incompatible PGEs, i.e. Pt and Pd. This is consistent with the decoupling of lithophile elements from chalcophile/siderophile elements as observed from isotopic signatures in studies of Kaapvaal cratonic peridotites (Pearson *et al.*, 1995a).

4.5.4 PGE variation with whole-rock chemistry

4.5.4.a Variation of PGEs with sulfur

The role of sulfides on the control of PGEs within the Jericho peridotites can be assessed through comparison of PGE and S abundances. Sulfur is a moderately incompatible element within the mantle, and behaves coherently in mantle melting processes (Lorand, 1989; Lorand, 1991). However, PGEs have high partition coefficients into sulfides, and unless all sulfide within the mantle is consumed (~ 25% melting), and the melt nears saturation (Keays, 1995), no correlation between S and PGEs should necessarily exist.

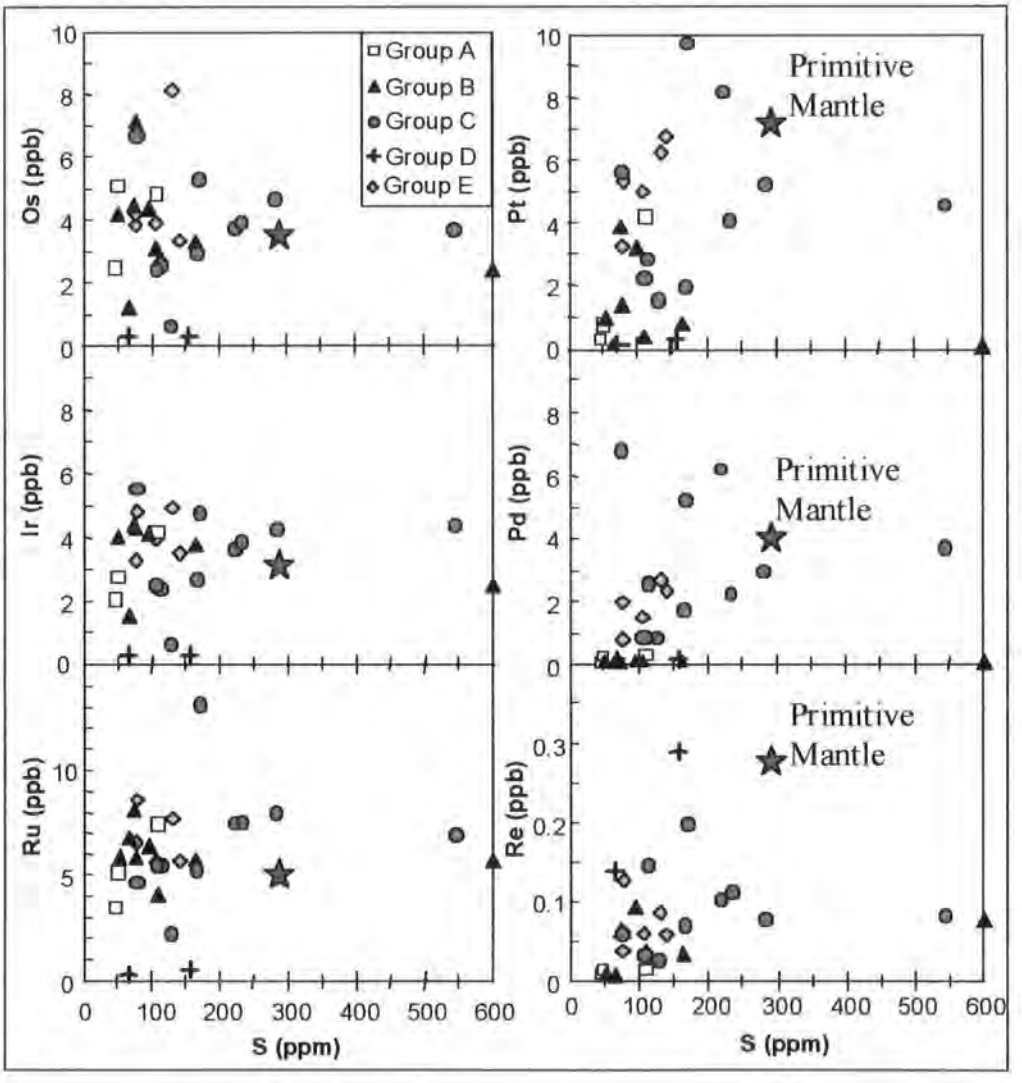

Figure 4.18 PGE and Re abundances versus S content for the Jericho peridotite suite. Primitive mantle, represented by star, after McDonough and Sun (1995).

Present estimates for the S content of fertile mantle vary but are generally less than 300ppm (Peach and Mathez, 1996). The S contents within the Jericho samples ranges from 47 to 600 ppm, from depleted to enriched relative to a fertile mantle source. Very little correlation exists between the PGEs and S within the Jericho peridotite suite (Figure 4.18). The Jericho peridotites in general show flat chondritic IPGE patterns, but with varying absolute abundances within individual peridotites. If the individual peridotite xenoliths were not derived from the same homogeneous source, it would not be surprising that they show no positive correlations with sulfur overall. An alternative explanation however, is that the poor PGE-S correlations may simply reflect metasomatism, as observed for Pyrenean peridotites by Lorand *et al* (1999). IPGEs would appear to be less susceptible to melt-related metasomatism than PPGEs, on the basis of their higher compatibility and chondritic behaviour.

When studied in detail, correlations between PGEs and S become evident in the Jericho peridotite suite, particularly when considered in terms of PGE patterns. Within the Jericho suite there appears to be five distinct groups (Figure 4.19; Table 4.13). Group A peridotites have highly depleted PGE patterns with low Pd, Re and S concentrations and represent extensive degrees of melt extraction (Figure 4.19a; Table 4.13). The Group B peridotites represent residual peridotites, but show variable degrees of Re enrichment, associated with a slight enrichment S (Figure 4.19b) through possible metasomatism or melt addition with variable degrees of Sulfide addition. The group C peridotites show a prominent enrichment in Pd associated with enrichment in S (Figure 4.19c). These samples also appear to have elevated Re abundances associated with the enrichment in S. The fourth group, Group D peridotites, show Pd enrichment, but more particularly a prominent Re enrichment, associated with S enrichment (Figure 4.19d). Group E peridotites show a moderately fractionated PGE pattern and may therefore represent the residues of relatively low degrees of partial melting. A good correlation exists between Pd, Re and S within this group ($r = 0.74$ for Pd), and may represent the removal of Pd, Re and S with the melt fraction, and a depletion trend from a common homogeneous source with minor perturbations. Alternatively the samples may represent depleted peridotites that have experienced a similar degree of enrichment in Pd and Re. Sample 22-4, which shows a slight inflection in Re abundance, would support the argument for enrichment.

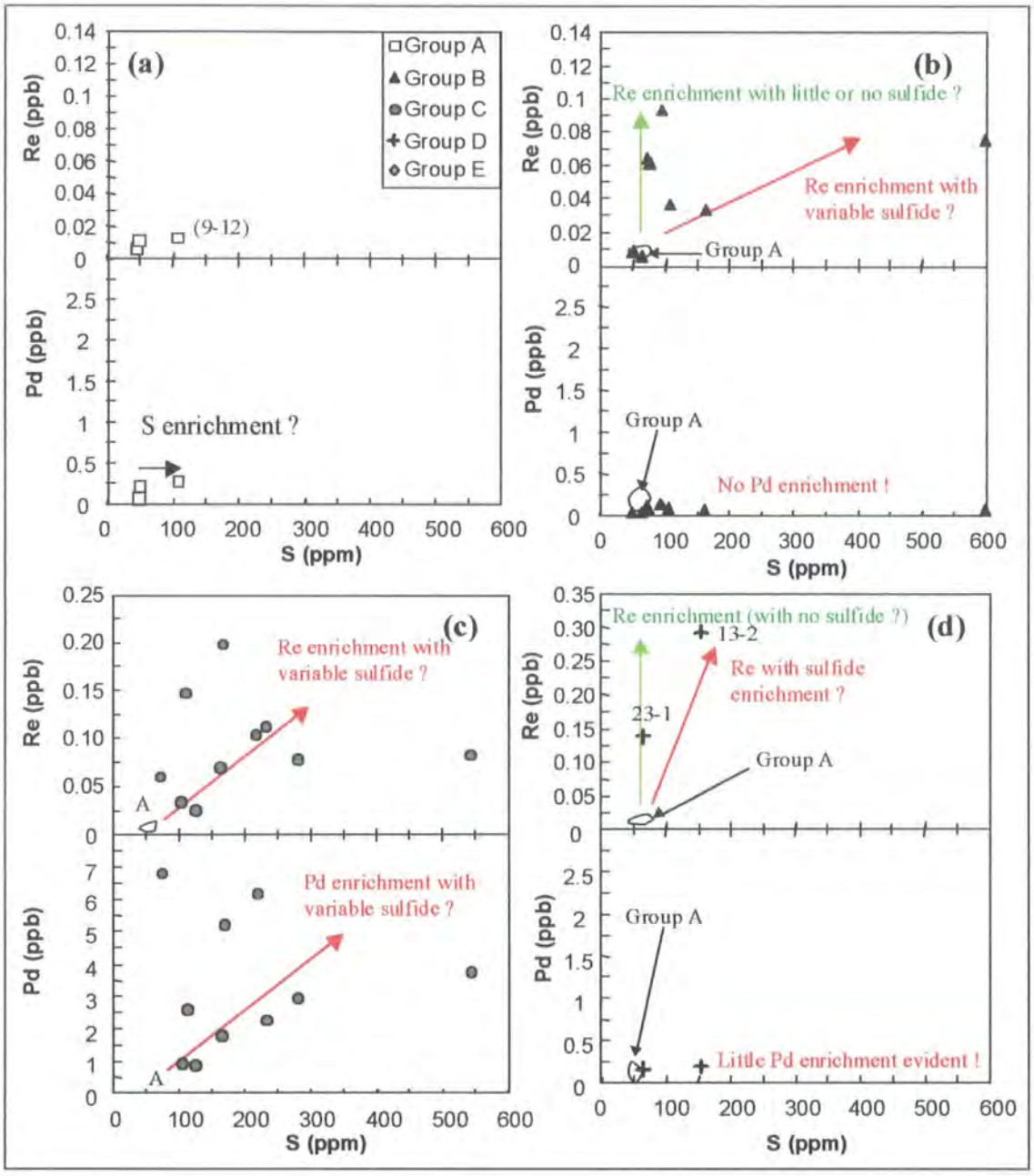

Figure 4.19 Pd and Re abundances versus S content for individual Jericho peridotite groups. (a) peridotites with highly depleted PGE patterns, (b) peridotites with Re enriched PGE patterns, (c) peridotites with Pd enriched PGE patterns, and (d) peridotites with Re and Pd enriched PGE patterns.

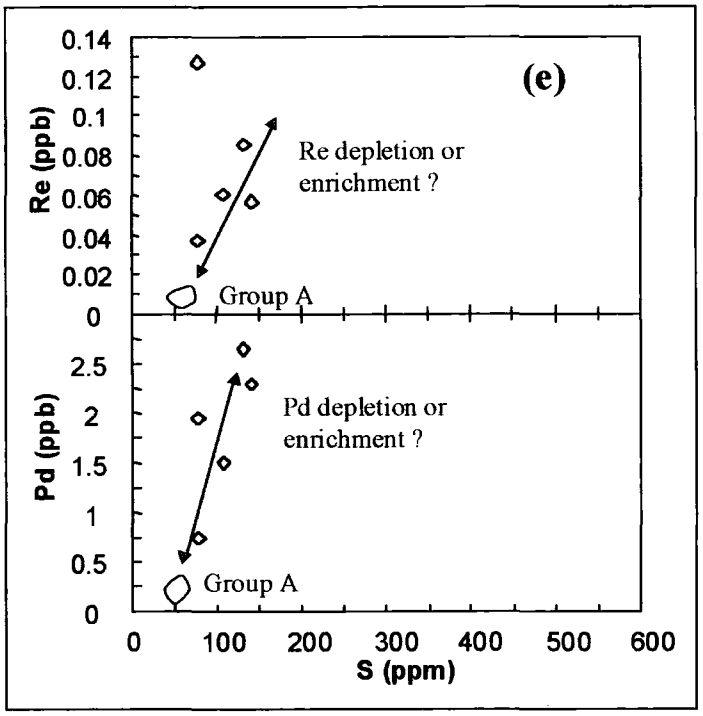

Figure 4.19 (continued) Pd and Re abundances versus S content for individual Jericho peridotite groups. (e) moderately depleted peridotites?

4.5.4.b Variation of PGEs with major elements

The Jericho peridotites display a wide range in the degree of melt extraction as evidenced by magmaphile elements such as Al_2O_3. However, no systematic correlation exists between Al_2O_3 and PGE abundance in the Jericho peridotites (Figure 4.20). Due to the highly compatible nature of IPGEs, it is not unexpected that they show no clear relationship with Al_2O_3. The moderately incompatible and depleted PPGEs within the Jericho peridotite suite however, show no distinct correlation either (Figure 4.20).

Correlations between the shape of PGE patterns and bulk rock Al_2O_3 contents of the peridotites are apparent (Figure 4.21). These trends tend to mirror the Sulfur-PGE relationships for the Jericho peridotite groups. The Group A peridotites have low Pd, Re and Al_2O_3 concentrations (Table 4.12 and 4.13). Possible Al_2O_3 addition to sample 8-7 is suggested by a slightly elevated abundance of Al_2O_3 of 0.64 wt%. A minor inflection in the chondrite normalised PGE pattern at Re may relate to Re addition associated with this, but appears to be insignificant and in general the PGE systematics are undisturbed (Figure 4.21a). The Group B peridotites show no overall systematic correlation between Re and Al_2O_3 (Figure 4.21b), but enrichment of Re is variably associated with an enrichment of Al_2O_3. Peridotites from Group C show a marked enrichment in Pd associated with Al_2O_3 enrichment (Figure 4.21c; Table 4.13), and also

show an slight enrichment in Re. Group D peridotites show a similar but higher degree of PGE enrichment with Al_2O_3 (Figure 4.21d). Group E peridotites, with moderately

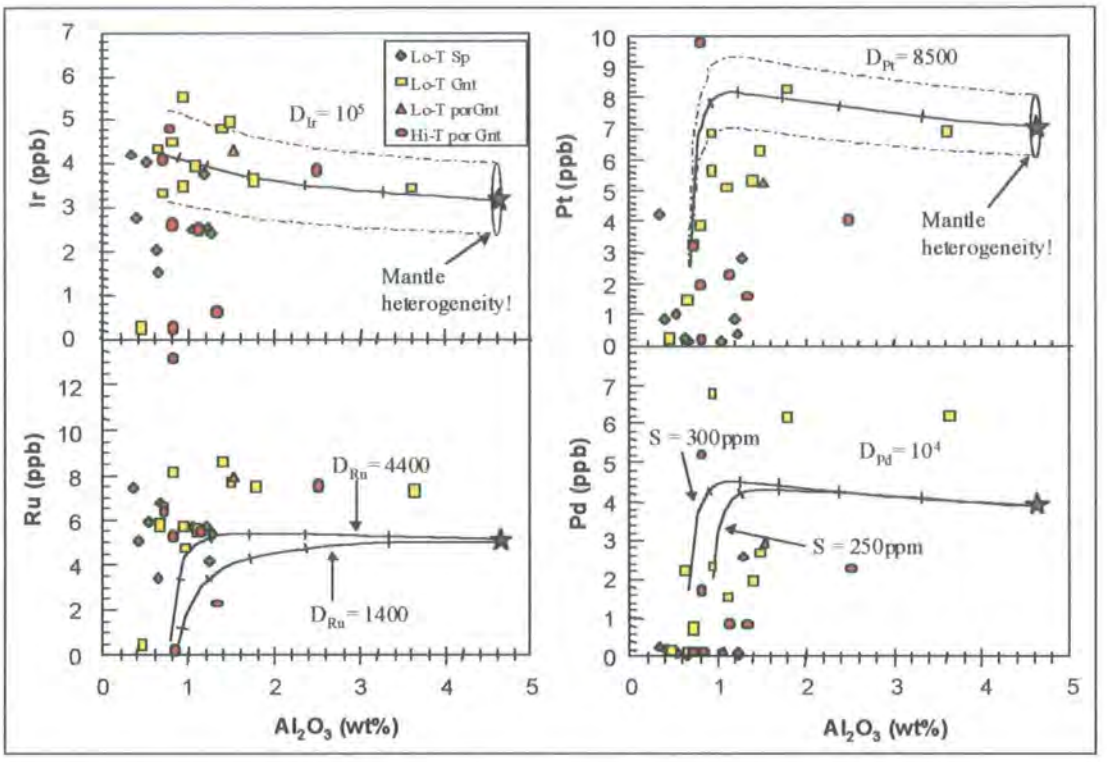

Figure 4.20 PGE abundances versus Al_2O_3 (symbols as for Figure 4.16). Predicted residue compositions are based on non-modal fractional melting models using a primitive mantle source with sulfur compositions of 300 ppm (represented by star symbol), and the extracted melts have a sulfur capacity of 1000 ppm S. The range of partition coefficients for PGEs, $D_{PGE(sulf/melt)}$ is large (Stone *et al.*, 1990; Bezmen *et al.*, 1994; Peach *et al.*, 1994; Fleet *et al.*, 1996). A value of 10^4 for D_{Pd} has been used to model Pd based upon the good correlation found by Lorand *et al.*(1999) in Pyrenean orogenic lherzolites. The value D_{Ir} was assumed to be an order of magnitude higher based upon contrasting behaviour of these two elements in the same study. D_{Ru} was modelled using values of 1400 and 4400, D_{Pt} a value of 8500. For comparison of models with xenolith data, F values were re-calculated as Al_2O_3 wt%. Varying S content of the source or S capacity of the melt does not significantly alter the melt extraction trends. Marks indicate 5% increments of melting.

fractionated PGE pattern, show a good correlation between Pd, Re and Al_2O_3 (Figure 4.21a; r = 0.74 and 0.84 for Pd and Re respectively). This may represent the removal of Pd, Re and Al_2O_3 during partial melting, and a depletion trend from a common homogeneous source, with minor perturbations. Alternatively, the correlation may simply reflect a melt addition vector.

Using the overall relationships between sulfur and PGEs and chondrite-normalised PGE patterns seen in the Jericho suite, the peridotites were constrained into five general groups. These groups are further constrained by the relationship of bulk rock Al_2O_3 and the PGEs (Table 4.13).

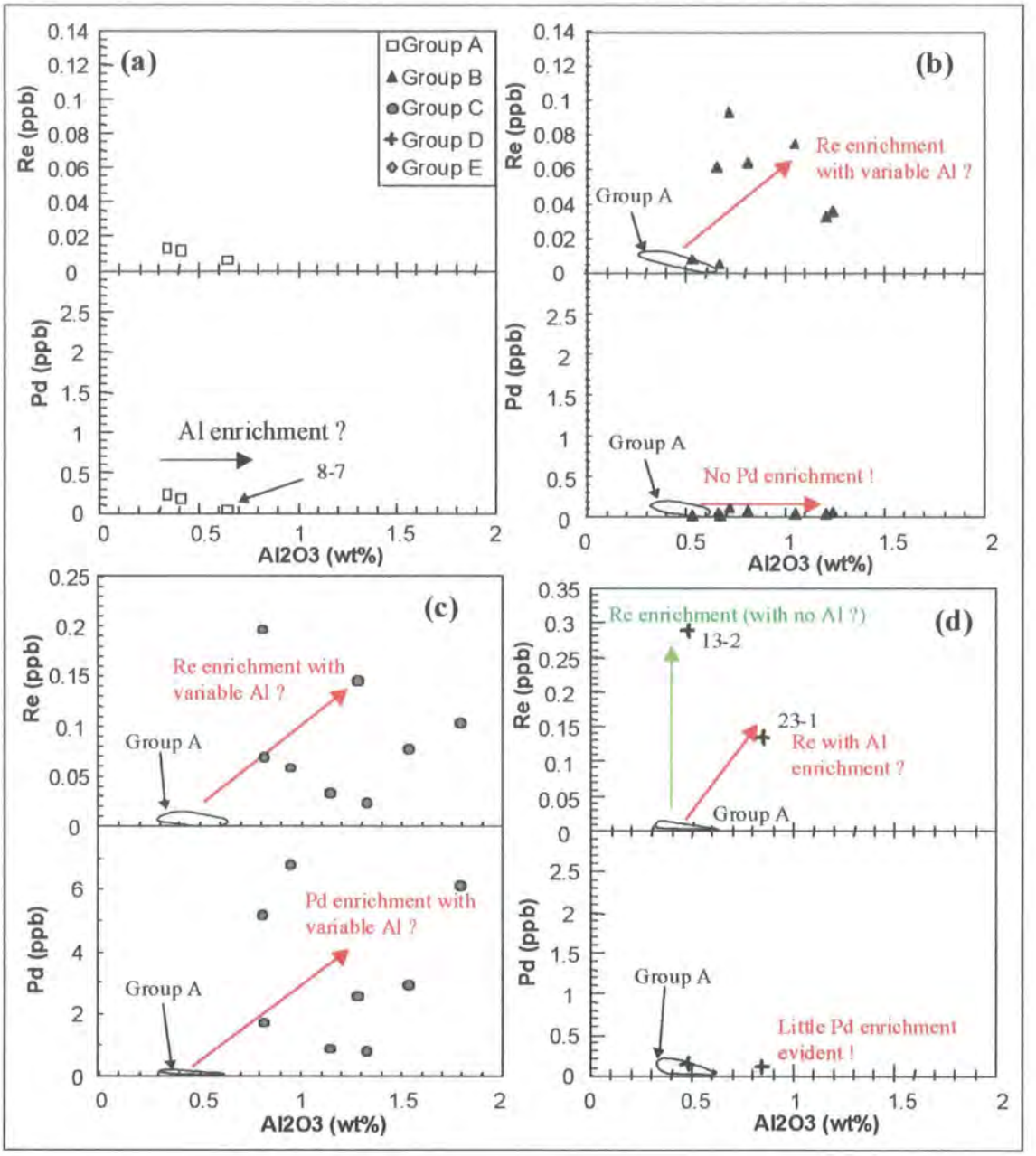

Figure 4.21 Pd and Re abundances versus Al_2O_3 content for the Jericho peridotites. (a) peridotites with highly depleted PGE patterns, (b) peridotites with Re enriched PGE patterns, (c) peridotites with Pd enriched PGE patterns, and (d) peridotites with Re and Pd enriched PGE patterns.

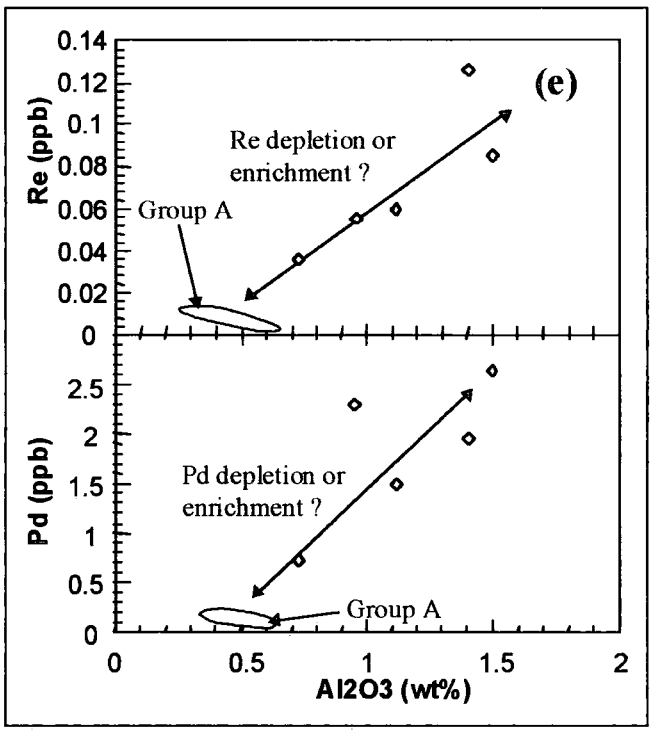

Figure 4.21 (continued) Pd and Re abundances versus Al_2O_3 content for the Jericho peridotites. (e) moderately depleted peridotites?

4.5.4.c Variation of PGEs with trace elements

IPGEs within the Jericho peridotites[b] are unfractionated and show chondritic behaviour, and therefore remain compatible even at high degrees of melting. It is therefore unsurprising that the IPGEs show no correlation with trace elements. PPGEs in contrast are incompatible and fractionate during mantle melting and subsequent metasomatism. Trace elements are therefore more likely to follow the behaviour of PPGEs and may help to constrain the relative roles of fluid enrichment versus melt depletion.

PGE variation with REE: La and Yb

The variations in PGEs within the Jericho peridotite suite are not consistent with a single stage melt-extraction event, but suggest a more complex history. The chondrite-normalised PGE patterns from most Jericho peridotites, including the disturbed samples, show vestiges of the original fractionation associated with melt extraction, noticeable by a depletion in Pd and/or Pt relative to IPGEs. Incompatible trace elements in contrast, show strong enrichment rather than depletion. Neither PGE abundances or ratios correlate with $(La/Yb)_n$ ratios suggesting that LILE-enriching processes within the Jericho peridotite suite do not significantly enrich chalcophile PGEs. This is consistent

with the consensus of other studies (Mitchell and Keays, 1981; Morgan *et al.*, 1981; Lorand, 1989).

PGE variation with hydrous fluid mobile elements

Re and Pd both show a wide scatter when plotted against Ba, with no apparent correlation. If the Jericho peridotites are separated on the basis of their chondrite-normalised PGE patterns, correlations become evident. These trends tend to mirror the relationships observed with Al_2O_3 and S. It may be surmised therefore that the fluids responsible for enriching the samples in Al_2O_3, S, Pd and Re, have also enriched Ba.

PGE variation with fluid immobile incompatible elements: Nb

Re and Pd show an overall lack of correlation with Nb. Separated on the basis of PGE patterns, the variation of Re and Pd with Nb reflects the variation of these elements with Al_2O_3 and S.

4.5.5 Re-Os and PGE systematics for Jericho peridotite xenoliths

4.5.5.a Effects of alteration on Re and Os abundances

Sulfides have been cited as the possible host for PGEs within non-cratonic peridotites (e.g. Hart and Ravizza, 1996). Lorand (1990) and Handler *et al.* (1997) have suggested that alteration of peridotites due to weathering may alter Os concentrations in peridotites, through the leaching of sulfides. However, if primary sulfides are present, this process would only tend to lower Os concentrations in the peridotites. It should be noted that the samples from Jericho are relatively fresh for cratonic peridotites, and even samples showing slightly higher degrees of alteration, such as 44-12 (Table 4.2; LOI 6.68), have Re and Os concentrations close to the average for Jericho peridotites. Similar observations have been made for Kaapvaal craton (R.W. Carlson, pers. comm., Carlson *et al.*, 1999). Lorand (1990) and Handler *et al.* (1997) suggest that oxidation of the xenoliths after eruption, would tend to remove the BMS phase. Under oxidising conditions Re and Os would be unstable as sulfide species (Burnham, 1995). ReS_2 and OsS_2 would react with oxidising fluids and release sulfur in solution as sulfate ions, resulting in the loss of Re as a solute in the oxidising fluids, whilst Os would remain as either metal or hydrated oxide grains (Burnham, 1995). This process ca not explain the scatter observed in Os abundances within the Jericho peridotites, nor does it explain the wide scatter to high Re abundances (Figure 4.15 and 4.22).

The scatter of Os abundances within the Jericho peridotite suite, as a function of major element depletion (Figure 4.22), may suggest exsolution of the element from the

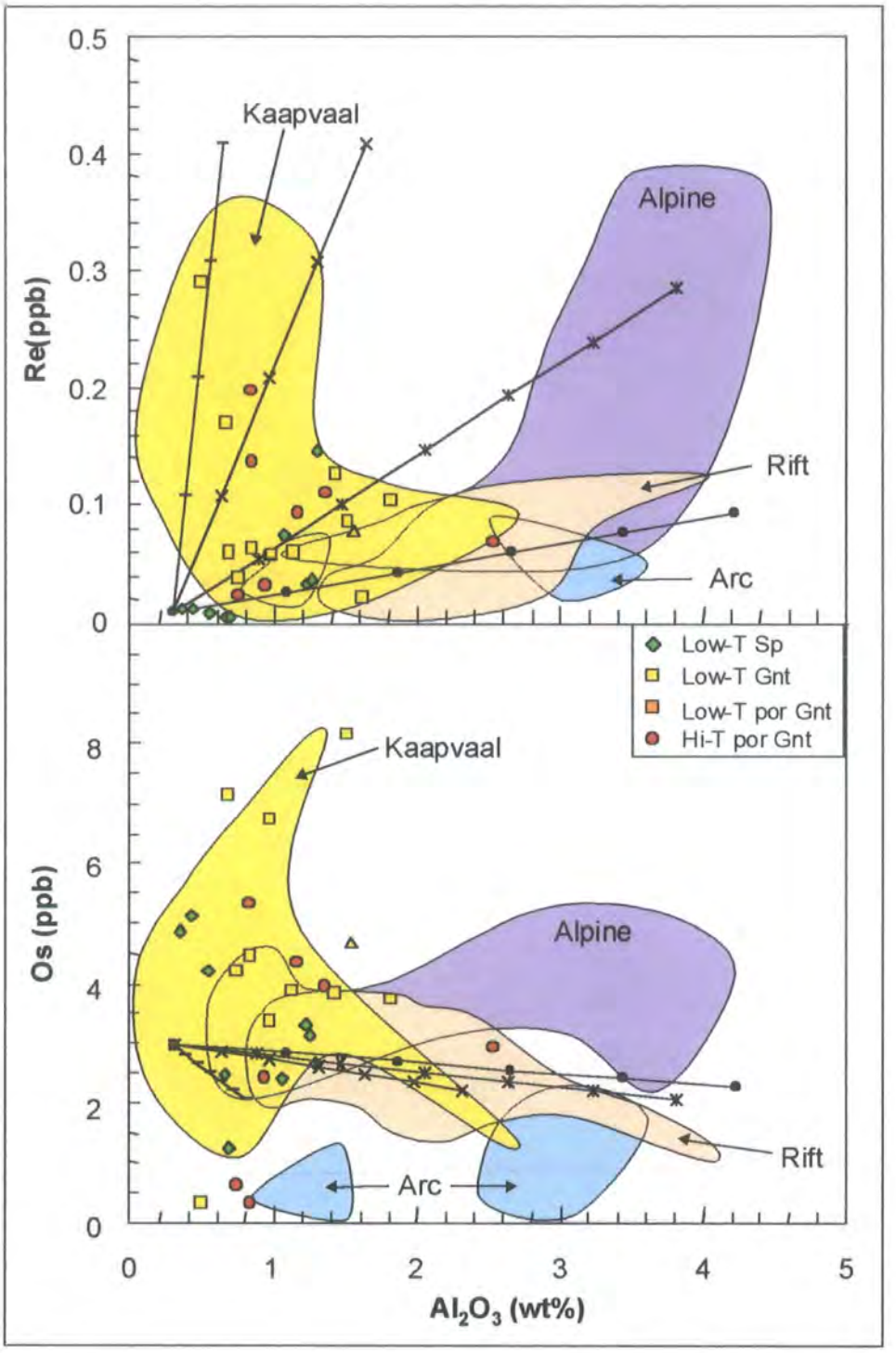

Figure 4.22 Re and Os concentrations (in ppb) plotted against Al_2O_3 content (in wt%). Cratonic peridotites from the Kaapvaal craton (Carlson *et al.*, 1999) represented by the yellow field. Alpine peridotite data (Reisberg *et al.*, 1991; Reisberg and Lorand, 1995) are shown by the purple field and rift-related spinel peridotites (Meisel *et al.*, 1996; Handler *et al.*, 1997) by the beige field. Spinel peridotites from "arc" settings are shown by the blue fields, one each for samples from the Simcoe volcano in the Cascades and the Itchinomegata volcano in the back-arc of the Japanese convergent margin (Brandon *et al.*, 1996). The lines represent model mixing lines between an end-member depleted peridotite (Al_2O_3 = 0.3%, Re = 0.01ppb, Os = 3ppb, $^{187}Os/^{188}Os$ = 0.109) and possible metasomatising magmas, marks indicate 5% increments in the addition of magma. Carbonatite (horizontal hatching; Al_2O_3 = 2%, Re = 2ppb, Os = 0.002ppb, $^{187}Os/^{188}Os$ = 0.13; Shank *et al.* (1992)), kimberlite (x; Al_2O_3 = 7%, Re = 2ppb, Os = 0.5ppb, $^{187}Os/^{188}Os$ = 0.13; Walker *et al.* (1989)), average OIB (star; Al_2O_3 = 12%, Re = 0.35ppb, Os = 0.2ppb, $^{187}Os/^{188}Os$ = 0.135; Reisberg *et al.* (1993), Roy-Barman and Allègre (1995), Hauri and Hart (1996) and Hauri *et al.* (1996)) and average MORB (circle; Al_2O_3 = 16%, Re = 0.93ppb, Os = 0.002ppb, $^{187}Os/^{188}Os$ = 0.125;], Roy-Barman and Allègre (1994) and Hauri and Hart (1996)).

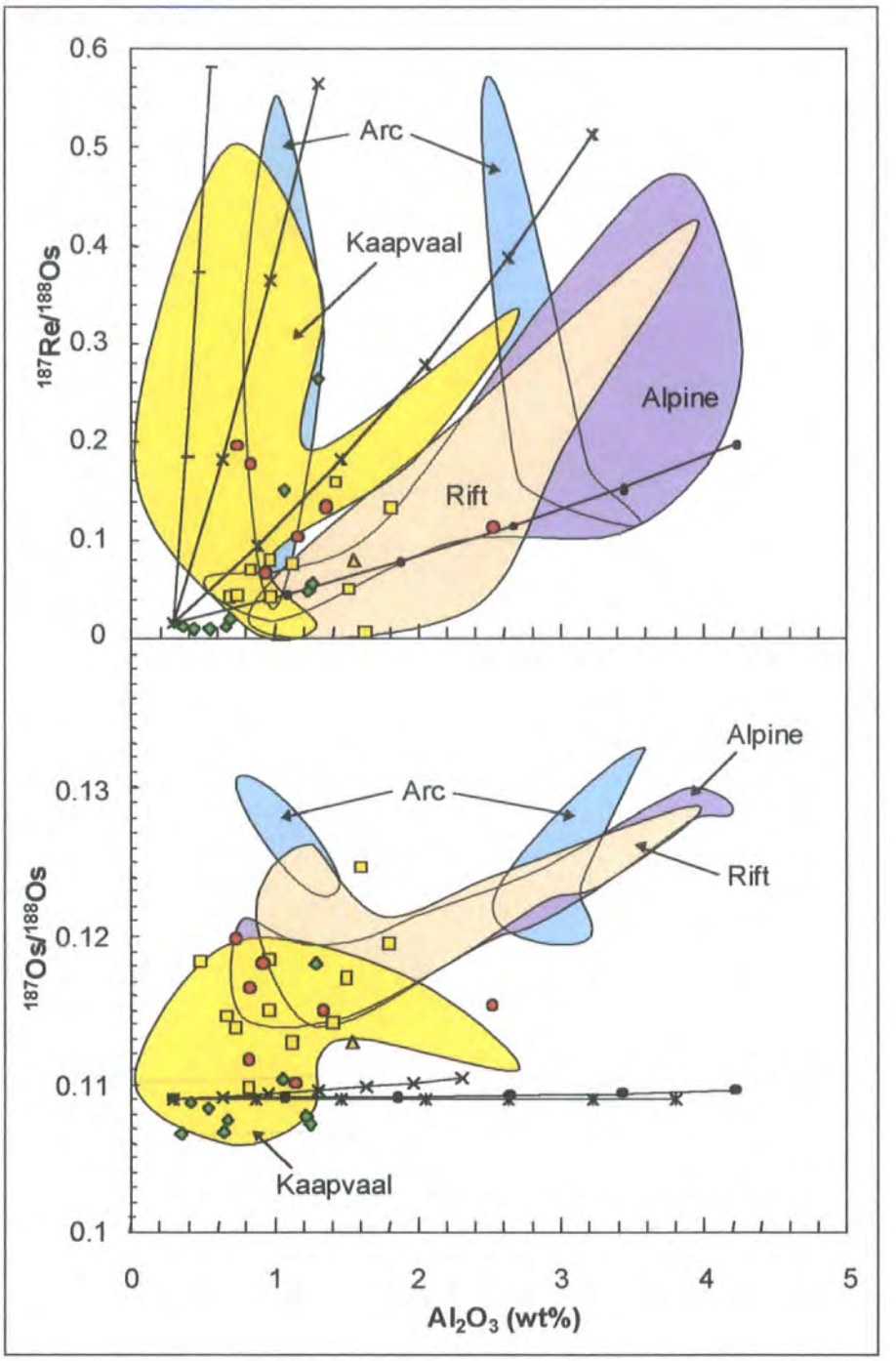

Figure 4.22 (continued) $^{187}Re/^{188}Os$ and $^{187}Os/^{188}Os$ plotted against Al_2O_3 content (in wt%).

mantle BMS phase under more reducing conditions. This would result in a heterogeneous distribution of Os-bearing minerals such as Os-Ir alloys or laurite (Burnham, 1995).

Handler *et al.* (1999) attributed the fractionation of Ir and Os within Australian alkali-basalt hosted spinel peridotites to late stage Os mobility, and loss, due to sulfide breakdown. As can be seen in Figure 4.23, the Ir/Os ratio of Jericho peridotites tends to be near-chondritic with a mean of 0.931 (std.dev. = 0.17), therefore late stage Os loss through weathering is not evident (cf. Chondritic Ir/Os = 0.95, Anders and Grevesse, 1989; Jochum, 1996).

This evidence would suggest that Os and other IPGEs may not be situated within sulfides in the Jericho suite.

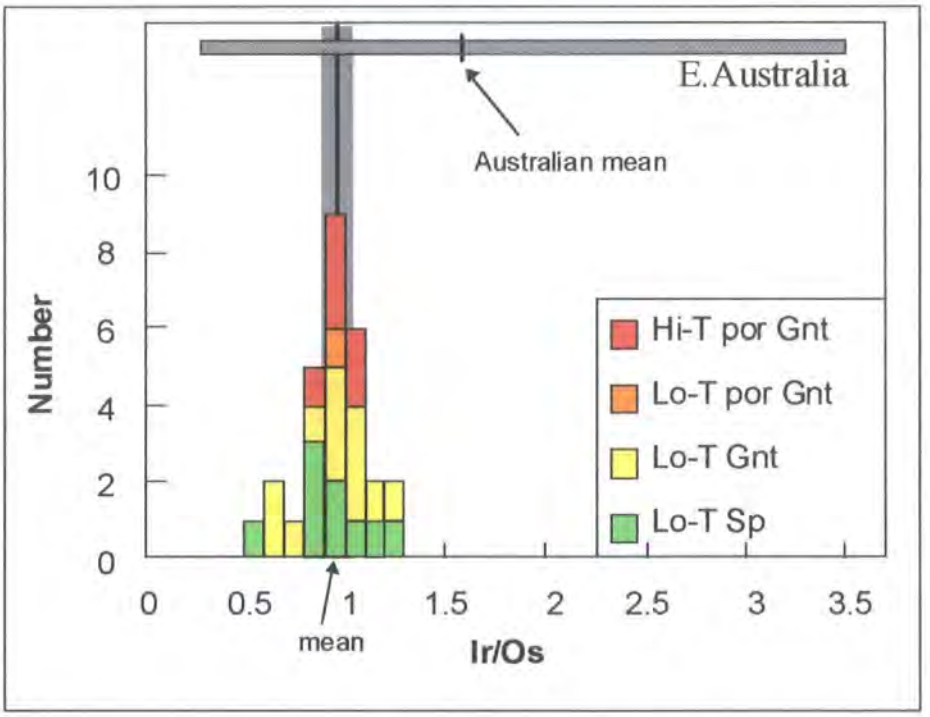

Figure 4.23 Histogram of Ir/Os ratios for Jericho peridotites. Vertical line represents CI-chondrite Ir/Os and band represents 2σ error on mean from Anders and Grevesse (1989) and Jochum (1996). Australian xenolith data from Handler *et al.* (1999).

4.5.5.b Behaviour of Re, Os and PGEs during partial melt extraction

Re behaviour during partial melt extraction

If the Re characteristics of the Jericho peridotite suite simply reflect partial-melting processes operating on a homogeneous mantle source, Re concentrations should correlate with indices of melt extraction. In previous studies of Alpine peridotites it was argued that Re partitions into melts with a distribution coefficient similar to Al

(Reisberg and Lorand, 1995), as shown by the crude correlation in Figure 4.22. Similarly correlations have been noted in spinel peridotites from rift settings, erupted in alkali basalts (e.g. Handler *et al.*, 1997). In contrast, spinel peridotites from arc settings, show little correlation between Re and Al, particularly if separated on the basis of individual localities (Brandon *et al.*, 1996). Similarly, Re concentrations in cratonic peridotite xenoliths from Jericho show no correlation with indices of melt depletion, such as Al_2O_3, confirming that Re variation is not controlled by partial melt extraction alone (Figure 4.22). Studies of cratonic peridotite xenoliths from the Kaapvaal craton show a similar lack of correlation (Pearson *et al.*, 1995a; Carlson *et al.*, 1999), and these studies have suggested that the large Re variation in cratonic peridotite xenoliths may be due to "metasomatism".

The low Re/Os of Jericho peridotites is consistent with the melt-depleted nature of both bulk-rock and mineral compositions that indicates depletion in magmaphile elements (section 4.4, Kopylova *et al.*, 1999b; Kopylova and Russell, 2000). However, the observed variation in Re/Os in the Jericho peridotites does not correlate with melt indices such as Al_2O_3, and this suggests that the variation is not due solely to single-stage isobaric melt extraction, but includes possibly an additional metasomatic or cumulate component (Figure 4.22).

Os and other PGE behaviour during partial melt extraction

It has been suggested that sulfides act as a buffer for PGEs within mantle melting residues (Lorand *et al.*, 1993; Keays, 1995; Snow and Schmidt, 1998). If we model PGEs for the Jericho suite as a function of Al_2O_3, this will allow us to investigate the buffering effect of sulfides, and the behaviour of PGEs and Re during partial melting. Lorand *et al.* (1989; 1991) argued that positive correlations between S and Al_2O_3 within unmetasomatised Pyrenean peridotites were evidence of the residual origin for sulfides. From Figure 4.24 we can see that little correlation exists between S and Al_2O_3 for the Jericho suite (r = 0.55). However, this lack of correlation may be the result of metasomatism disturbing earlier systematics.

Melt extraction model predictions fail to account for the variation in PGEs with S for the Jericho samples (Table 4.10 and 4.13), and therefore do not ascertain the role sulfides play in hosting PGEs (Figure 4.25). Some of the vertical distribution in Figure 4.25, besides that expected from simple melt-extraction alone, may be consistent with a non-homogeneous source mantle. In terms of sulfide control, the variation in sulfur distribution within Jericho samples is complex. Several samples show an enrichment in sulfur with no associated enrichment in Pd.

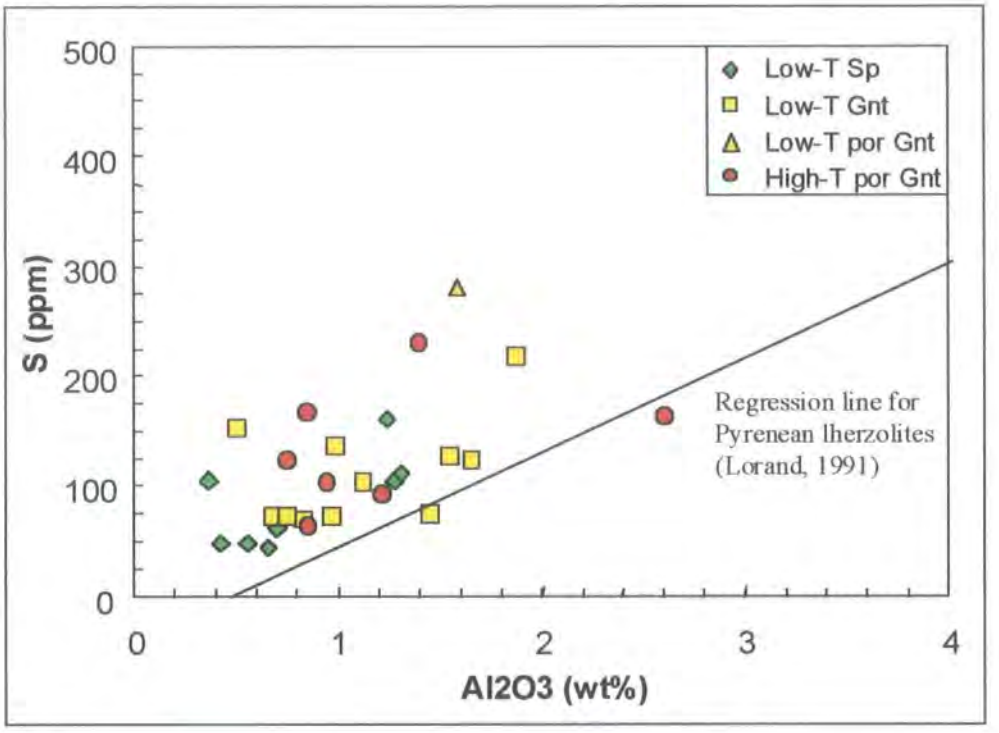

Figure 4.24 Variations of S (ppm) as a function of Al_2O_3 (wt%) in the Jericho peridotites.

Non-modal fractional melting, melt extraction models were constructed for PGEs and these are compared with the Jericho peridotite data in Figure 4.20. F values have been re-calculated as Al_2O_3 using the inverse method of Bodinier (1988). Little correlation is evident between PGEs and Al_2O_3, or with the predicted models of melt extraction (Figure 4.20 and 4.22). Only the depleted spinel peridotites and a few depleted low-T and high-T garnet peridotites seem to display correlated low Al_2O_3 and Pd, consistent with >25% melt extraction. Varying the source S content does not appreciably alter the melt extraction trends, nor does it explain the spread in data. Using varied partition coefficients ($D_{PGE(sulf/melt)}$) also fails to account for the spread in data. Osmium and Ir are compatible elements during mantle melting processes, therefore plots of Os and Ir against melt indices such as Al_2O_3 should produce sub-horizontal trends. From figure 4.22, we can see that this is the case for peridotites from most tectonic settings. Peridotites from the Jericho suite, like those from previous studies of the Kaapvaal craton (Carlson *et al.*, 1999), show an non-systematic near-vertical trend with a wide variation in Os concentration for a small variation in Al_2O_3 (wt%) content. Even the most extreme cases of melt extraction and sulfide breakdown could not produce the range of Os and Ir observed in the Jericho suite (Figure 4.20 and 4.22). With all Os remaining in the residue, the Os concentration would only increase by a factor of two for 50% melt extraction. If we assume experimental bulk partition

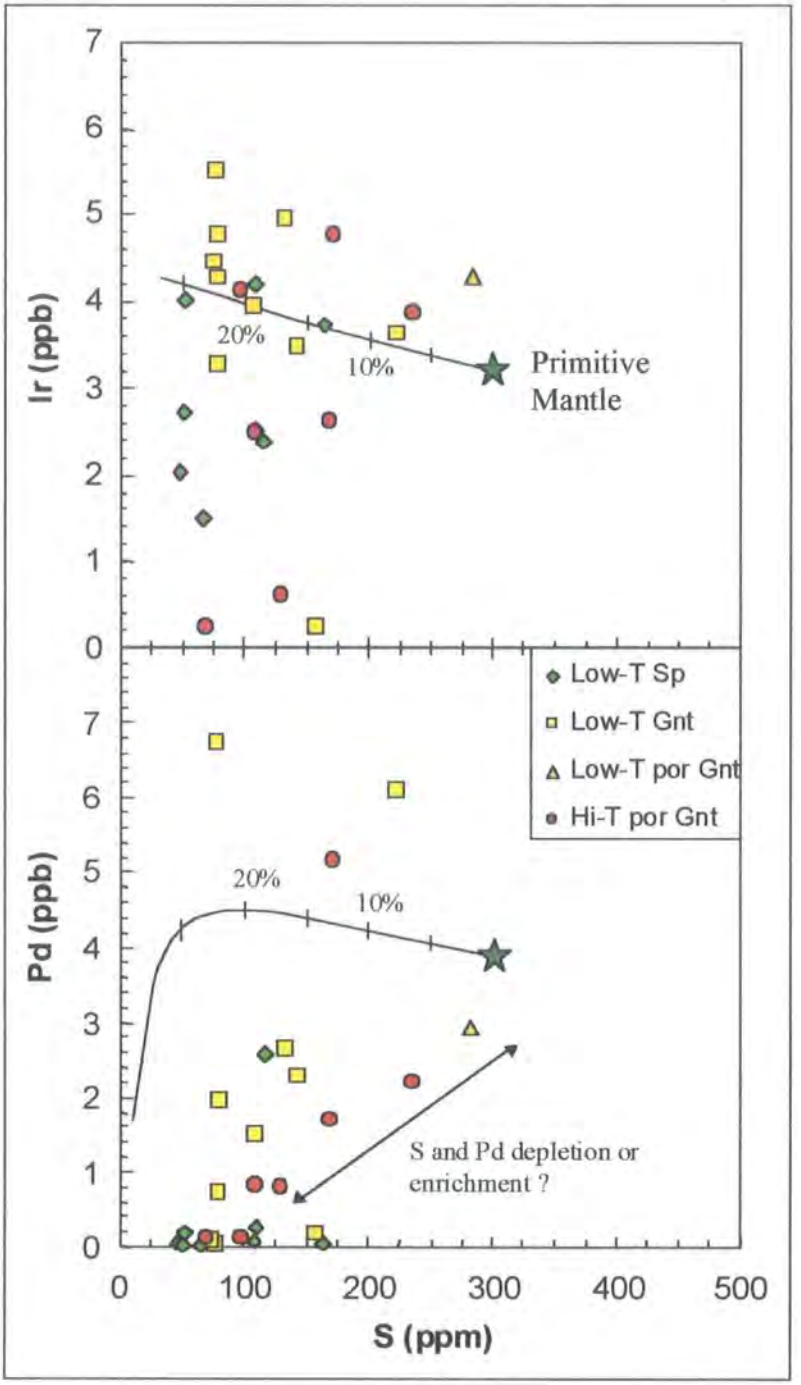

Figure 4.25 Predicted residue compositions are based on non-modal fractional melting models using a primitive mantle source with sulfur compositions of 300 ppm (represented by star symbol), and the extracted melts have a sulfur capacity of 1000 ppm S. The range of partition coefficients for PGEs, $D_{PGE(sulf/melt)}$ is large (Stone *et al.*, 1990; Bezmen *et al.*, 1994; Peach *et al.*, 1994; Fleet *et al.*, 1996). As for Figure 4.20 a value of 10^4 for D_{Pd} has been used to model Pd and the value D_{Ir} was assumed to be an order of magnitude higher based upon contrasting behaviour of these two elements. Varying S content of the source or S capacity of the melt does not significantly alter the melt extraction trends.

coefficient data ($D_{sul/sil}$) for Os and Ir are correct, some other factors must influence the variation in their concentration in the Jericho peridotites. The vertical distribution of Os and Ir in the Jericho data, over and above that expected for simple melt extraction, may be consistent with derivation from a non-homogeneous mantle source reflecting the heterogeneous distribution of sulfides or ultra-trace Os-alloys in the Slave lithospheric mantle as sampled by the Jericho kimberlite. It does not explain why this should be a feature unique to cratonic lithospheric peridotites as noted at Jericho and Kaapvaal, and not peridotites from other tectonic settings. One explanation is that the variations observed in the IPGE contents for cratonic peridotites, such as those from Jericho, are produced from some process other than melt removal. This alternative is not supported by the general features of PGE patterns of these rocks. It is possible that the variations in Ir and Os abundances are related to extreme degrees of melt depletion completely removing primary sulfides from the residue and stabilising alloy phases. The heterogeneous distribution of these alloy phases, rich in Ir and Os, may then cause substantial whole rock heterogeneity that is not encountered in peridotites from other tectonic settings.

If chondritic PGE ratios are assumed within the source mantle of all Jericho peridotite xenoliths, PGE ratios measured as a function of Al_2O_3 should negate source heterogeneities. If we consider Pd and Ir as examples of incompatible and compatible PGEs respectively, theoretical melt models should constrain the behaviour and fractionation of these groups. There is still limited correlation between PGEs and the theoretical behaviour of Pd/Ir and Al_2O_3 for melt extraction models in the Jericho peridotites (Figure 4.26), but some systematics emerge. For several of the Jericho peridotites, depleted bulk rock Al_2O_3 contents correlate well with samples showing depleted PGE signatures, i.e. low $(Pd/Ir)_n$ (Groups A and B, Table 4.13; Figures 4.17 a and b), and suggests that the PGE systematics have remained closed since the time of initial melt extraction for these samples. Other samples with less fractionated PGE patterns are consistent with a less depleted major element composition and plot on or close to an extension of the theoretical melt model, and may also represent closed systems. Displacement of other samples from the theoretical model is consistent with the disturbed PGE patterns seen, and these plot on vectors that can be attributed to sulfide or melt addition (Figure 4.26).

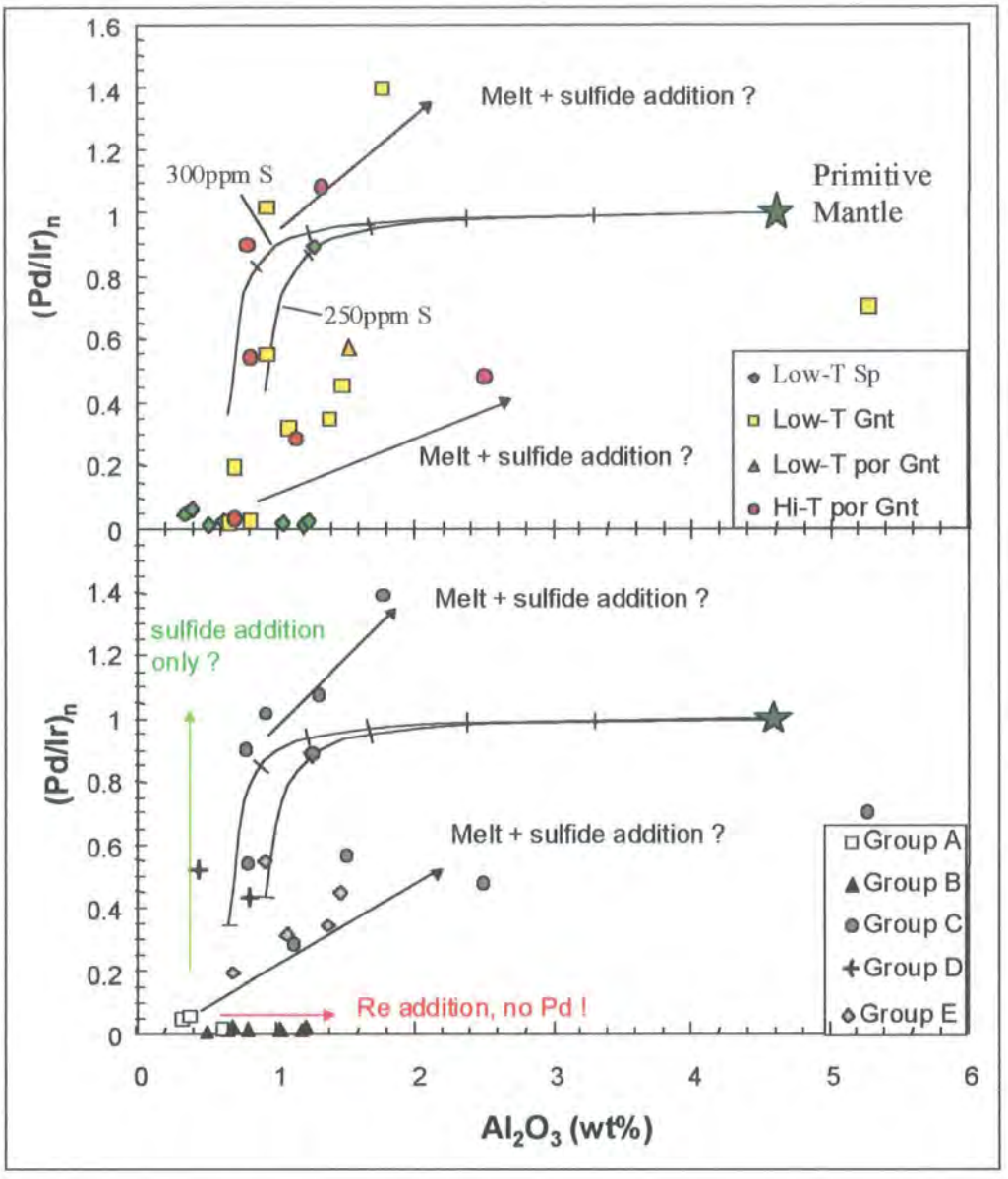

Figure 4.26 Variation of chondrite-normalised Pd/Ir as a function of whole-rock Al_2O_3 content (wt%). Lines represent the theoretical evolution of Pd/Ir in a peridotite residuum submitted to increasing degrees of equilibrium partial melting. Marks indicate 5% increments of melting. Primitive mantle represented by the star symbol. The two curves depict starting compositions with 250ppm and 300ppm total sulfur.

4.5.5.c Effects of metasomatism and melt infiltration

Metasomatism

Previous studies have shown that multiple generations of sulfide often exist within individual peridotites. The precipitation of secondary sulfide along intergranular boundaries could be responsible for the observed variation in Os abundances, PGE systematics and isotope ratios within the cratonic peridotite suite at Jericho. Samples with low Re concentrations (Group A; Table 4.13), particularly those of the spinel

peridotite suite, would suggest that they have not experienced secondary sulfide introduction, assuming the sulfide contains high abundances of both. In general sulfide and / or melt addition to Jericho peridotites associated with Re enrichment only (Group B; Table 4.13), apperars to have little effect on Os abundance or $^{187}Os/^{188}Os$ ratios (Table 4.14).

Group	Sample	S (ppm)	Os (ppb)	$(Pd/Ir)_n$	$^{187}Os/^{188}Os(i)$
A	8-7	47	2.47	0.020	0.10676
	9-12	108	4.86	0.049	0.10656
	11-18	50	5.10	0.055	0.10869
B	10-11	164	3.30	0.010	0.10784
	10-12A	109	3.10	0.024	0.10726
	10-12B	51	4.20	0.005	0.10836
	23-9	66	1.23	0.013	0.10754
	44-12	599	2.40	0.017	0.11034
	21-1	76	7.15	0.011	0.11455
	22-1	73	4.46	0.019	0.10982
	40-20	96	4.36	0.025	0.11010
C	39-23	115	2.65	0.886	0.11814
	9-2	221	3.75	1.392	0.11949
	26-11	76	6.74	1.016	0.11491
	51-2	545	3.71	0.701	0.11742
	21-3	283	4.66	0.565	0.11286
	21-2	171	5.31	0.896	0.11171
	26-9	167	2.95	0.536	0.11538
	39-3	235	3.97	0.476	0.11503
	40-9	128	0.61	1.075	0.11986
	40-21	107	2.43	0.282	0.11818
D	13-2	157	0.32	0.516	0.11821
	23-1	68	0.31	0.428	0.11650
E	10-456'	141	3.38	0.546	0.11838
	22-4	78	3.83	0.340	0.11422
	25-4	107	3.88	0.316	0.11278
	28-15	131	8.17	0.445	0.11722
	41-4	77	4.19	0.189	0.11377

Table 4.14 Summary of S and Os abundances, PGE systematics and $^{187}Os/^{188}Os$ isotope ratios for Jericho peridotites, on the basis of the PGE patterns.

Peridotites with more complex PGE patterns, showing Pd enrichment as well as Re tend to have more radiogenic $^{187}Os/^{188}Os$ ratios (Table 4.13 and 4.14), and therefore Os isotopic compositions may be a reflection of secondary sulfide addition in these samples. In terms of the abundance of Os however, there is no clear evidence of Os enrichment (Table 4.14). An alternative explanation for these samples therefore may be that the radiogenic Os isotopic compositions signify residual Re in only moderately

depleted peridotites (e.g. group E; Table 4.13), or Re addition occurred earlier in the history of the samples.

Variation in absolute and relative abundances of PGEs and their co-variation with both S and Al_2O_3 (Table 4.13) suggest that the Jericho peridotite suite have a complex history of melt extraction and post melt-extraction enrichment. The nature of PGE enrichment in the Jericho samples is variable and suggests that the peridotites may have been affected by more than one generation of fluid enrichment, or varying degrees of PGE precipitation.

Residual cratonic peridotites are susceptible to contamination by processes such as metasomatism and melt infiltration, as they have low Re abundances and Re/Os relative to mantle derived melts and fluids. However, the large range observed in Re and Os abundances, or $^{187}Re/^{188}Os$ and $^{187}Os/^{188}Os$, in the Jericho peridotites can not be attributed to any single magma or fluid type, and several types or generations of fluids may be necessary e.g. carbonatite, kimberlite, OIB or MORB (Figure 4.22).

The metasomatising fluid in general is limited by the small variation in Al_2O_3 content (Table 4.3), to a fluid with a relatively high Re/Al and Os/Al ratio (Figure 4.22). In terms of Re this would rule out basaltic fluids, and it has been proposed that either Al-poor hydrous fluids from the dewatering of subducted slabs (Brandon *et al.*, 1996), or carbonatitic and high Re kimberlitic melts may be the responsible metasomatising agents (Figure 4.22, Pearson *et al.*, 1995; Carlson *et al.*, 1999). The Jericho peridotites have mean Os abundances higher than bulk mantle in contrast to lower than bulk mantle for peridotites from arc settings. Brandon *et al.* (1996) proposed that the low Os abundances of arc peridotites were the result of metasomatism by oxidised fluids. This type of process therefore could not account for the high Os contents observed within the Jericho peridotite suite, but perhaps other fluids associated with subduction zones may have contributed.

The high SiO_2 content of cratonic peridotites from the Kaapvaal craton has been attributed to magmas such as tonalites and trondhjemites (Rudnick, 1995). These magmas have high Al and low Os compositions, and are therefore unlikely metasomatising agents. The precipitation of Os-rich alloys or sulfides from fluids or magmas percolating through the lithospheric mantle however may be responsible for raising Os concentrations (Pearson *et al.*, 1998b).

In contrast to observations from off-craton spinel lherzolite and orogenic massif suites (Pearson *et al.*, 1995a; Reisberg and Lorand, 1995; Handler *et al.*, 1997), at Jericho there is no apparent correlation between $^{187}Os/^{188}Os$ and Al_2O_3 (Figure 4.22).

This lack of correlation has also been observed in other cratonic and circum-cratonic xenolith suites (Pearson, 1999a). The mixing lines of Figure 4.22 indicate that infiltration by common magmatic fluids can account for some of the horizontal spread in the $^{187}Os/^{188}Os$ data but can not account for the vertical distribution, unless the infiltration was associated with the precipitation of Os-rich sulfides or alloys.

The scatter in Re abundance at Jericho can, in general, be accounted for by a 0-10% addition of kimberlite or carbonatite to the peridotite xenoliths. This does not account for all samples however, and the remaining samples can be accounted for by 0-10% addition of MORB or OIB melt. The addition of up to 10% carbonatite or kimberlite to the Jericho peridotites should be evident by the enrichment in elements such as Ba and Sr. From Figure 4.27 it can be seen that there is no overall systematic correlation between Re and Ba within the Jericho suite. However, the scatter in Re and Ba can be accounted for by the addition of 0-5% carbonatite, 0-10% kimberlite or 0-30% OIB, but again this does not account for all samples e.g. the apparent enrichment in Al_2O_3 in some samples. The peridotite xenoliths do not necessarily originate from a single depleted homogeneous mantle source, but may instead be sourced from a variably depleted mantle. In addition, the simplistic models proposed in Figure 4.22 and 4.27 do not account for the possibility of several generations of metasomatic alteration. These scenarios would give rise to a greater and more varied scatter of data.

Cumulate processes

The scatter of Re in the Slave cratonic lithospheric mantle could be attributed to a cumulate component (Herzberg, 1993; Pearson *et al.*, 1995a; Herzberg, 1999). Herzberg (1993) proposed that orthopyroxene cumulates crystallising from rising komatiitic magmas mixed with olivine-rich residues of komatiite extraction, producing orthopyroxene rich peridotite in the Kaapvaal craton. Though the Slave cratonic lithosphere as sampled by the Jericho kimberlite has, on average, a lower modal volume of orthopyroxene than Kaapvaal (Kopylova and Russell, 2000), this model is still relevant as low-T spinel peridotites show SiO_2 enrichments relative to melting models and experiments. It has been proposed that the range in Re and Os abundances within cratonic peridotites is related to a cumulate component (Pearson *et al.*, 1995). Hart and Ravizza (1996) suggested that the Re concentration of orthopyroxene is low, making it doubtful that orthopyroxene addition has produced the observed scatter in Re concentration seen at Jericho. If the deep crystallisation of the komatiite and cumulate component is accompanied by the precipitation of sulfides or alloys rich in Re and Os, this may contribute to the observed spread in data (Pearson *et al.*, 1998b).

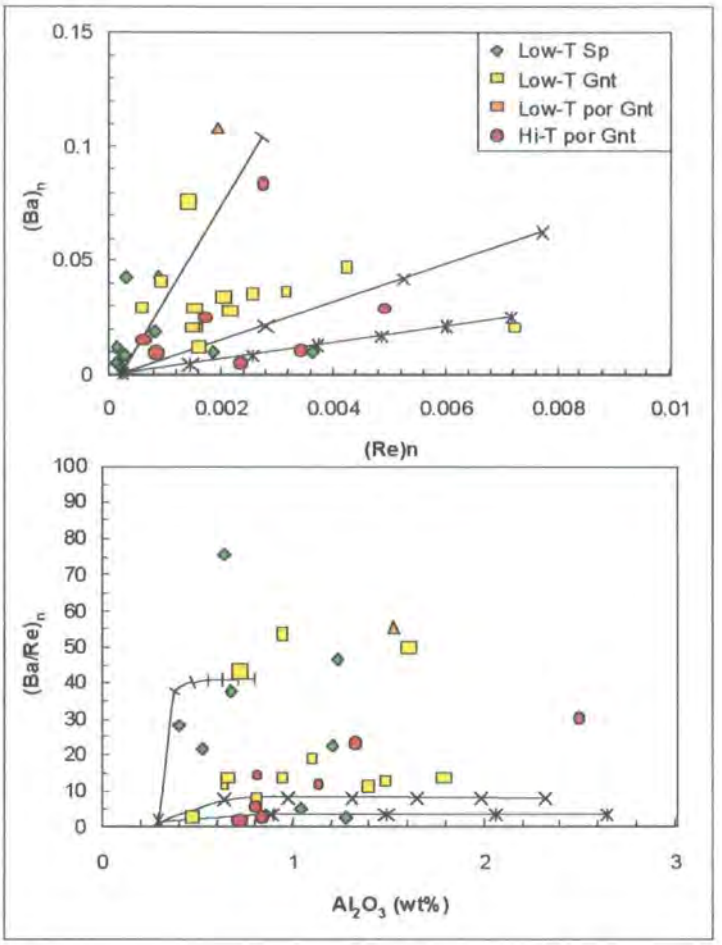

Figure 4.27 (a) Chondrite normalised plot of Ba vs. Re content for Jericho peridotites, and (b) Chondrite normalised Ba/Re ratio vs. Al_2O_3. The lines represent model mixing lines between an end-member depleted peridotite (Re = 0.01ppb, Ba = 1ppm) and possible metasomatising magmas, marks indicate 5% increments in the addition of magma. Carbonatite (hatching; Re = 2ppb, Ba = 5000ppm; Tuttle and Gittins (1966)), kimberlite (x; Re = 2ppb, Ba = 1000ppm; Bergman (1987) and Smith *et al.* (1985)), average OIB (star; Re = 0.35ppb, Ba = 200ppm; Basaltic Volcanism Studies Project (1981)).

4.6 Timing of lithospheric mantle differentiation

The rationale for Re-Os age systematics from peridotites is presented in Chapter 1.2.

4.6.1 Re-Os Isochrons

If the Slave lithospheric mantle, as sampled at Jericho, was formed from a common mantle source with constant Os isotopic composition though varying Re/Os, in a single melt extraction event, the samples would define an isochron whose slope defines the age of melt extraction. As can be seen from Figure 4.28 this is not the case, and there is a wide scatter in the data, due to the processes discussed previously in section 4.5. Reference isochrons have been added to Figure 4.28, passing through the most depleted coarse spinel peridotites, for comparative purposes. Several samples appear to lie close

to these isochrons and define linear arrays. Five samples from the Jericho kimberlite appear to define a crude linear array that corresponds to an age of 1.3 Ga with an initial Os isotopic composition of 0.108 (γOs = -9.1). From the scatter in data it is unlikely whether these isochrons have any real significance, and are probably co-incidental despite this example being close to the age of the McKenzie dyke swarm (Table 4.1).

The Jericho suite may have formed an isochron initially. The lack of any correlation and failure to produce isochrons is not unsurprising given the known variation in Re and Os and the possibility of metasomatic alteration. It also argues against the Re and Os variations resulting from cumulate processes near to the time of melt extraction, but instead suggests that fractionation of Re/Os occurred following formation, possibly on several occasions. This scenario is consistent with other studies that show evidence of recent Re addition to mantle xenoliths (Walker *et al.*, 1989; Meisel *et al.*, 1996; Chesley *et al.*, 1999) and disturbed Re/Os in massif peridotites (Reisberg *et al.*, 1991; Reisberg and Lorand, 1995).

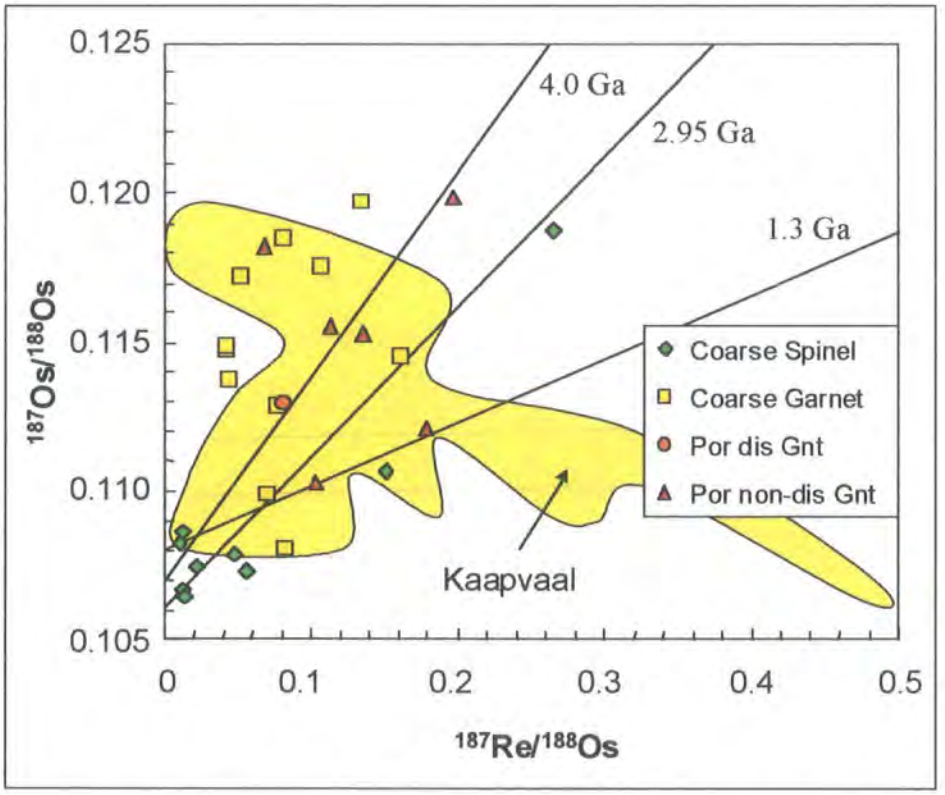

Figure 4.28 Re-Os isochron diagram for the Jericho data shown in Table 4.8. Reference isochrons passing through the Jericho data are shown. Isochrons were calculated using a decay constant (λ) of 1.666 x 10^{-11}. Kaapvaal data from Carlson *et al.* (1999).

4.6.2 Age determination from Al_2O_3 - $^{187}Os/^{188}Os$ relationships

As discussed in Chapter 3.7.2, Al - Os isotope relationships have been used to constrain peridotite ages in massifs (Reisberg *et al.*, 1991; Reisberg and Lorand, 1995). However, concerns have been raised concerning the use of this relationship; see caveats of Pearson (1999) and Pearson *et al.* (2001). As can be seen from Figure 4.29, there is no overall correlation between Al_2O_3 and $^{187}Os/^{188}Os$ for the Jericho peridotite suite. The spread in the data is too large for any practical age information to be obtained from this approach for the Jericho samples.

Given the known variations in $^{187}Os/^{188}Os$ composition over a small range in Al_2O_3 and the likely metasomatic alteration to both it is not surprising that there is an overall lack of correlation. This this illustrates the problem of using Al_2O_3 and $^{187}Os/^{188}Os$ to estimate peridotite age.

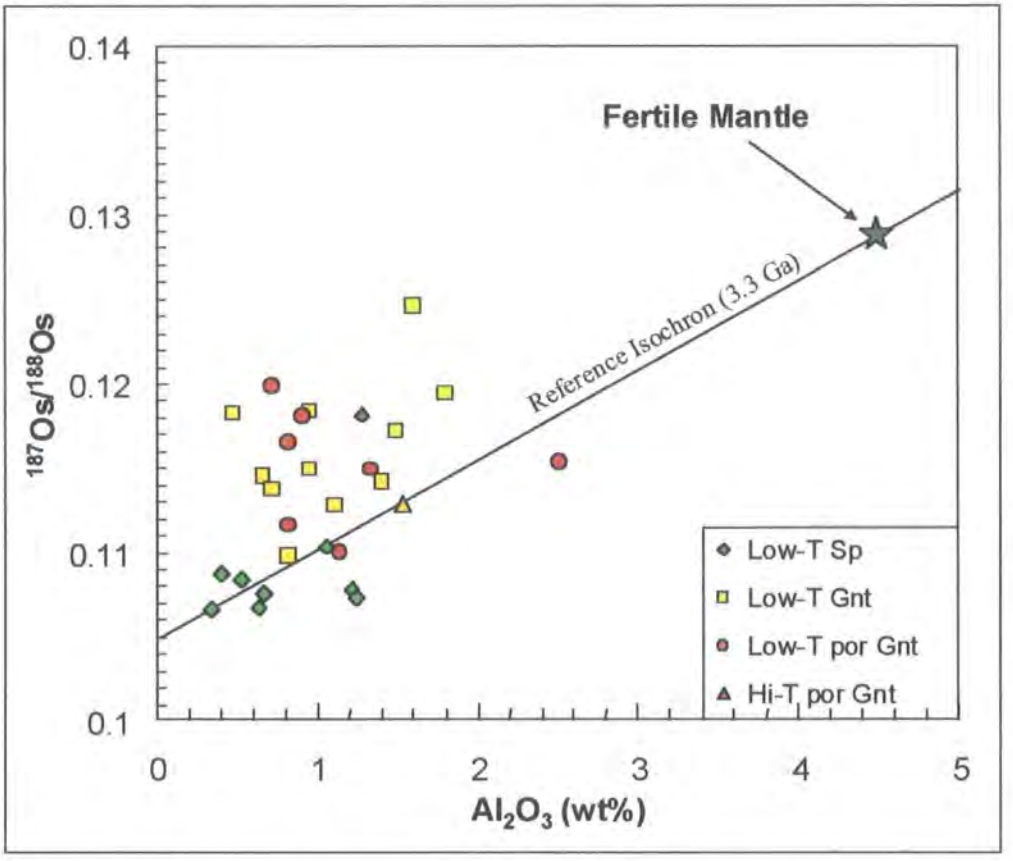

Figure 4.29 $^{187}Os/^{188}Os$ ratios plotted against Al_2O_3 content (in wt%) for low-T Jericho peridotites. Line represents a reference "isochron" passing through fertile mantle and the most depleted Jericho samples. $^{187}Os/^{188}Os(i)$ for the isochron is 0.105, which equates to an age of 3.3 Ga.

4.6.3 Model ages for Jericho peridotites

Rhenium depletion model ages (T_{RD})

The observed range in Os isotope compositions for the Jericho peridotites in (Table 4.5) equate to T_{RD} model ages of 3.1 to 0.5 Ga (Figure 4.30). Two samples have T_{RD} model ages > 3.0 Ga, nine samples between 2.5 and 3.0 Ga, and nineteen samples < 2.5 Ga. Three features are evident in the distribution of model ages shown in Figure 4.30; (i) few samples have a T_{RD} > 3 Ga, (ii) a bimodal distribution between samples with T_{RD} < 2.0 Ga and samples with T_{RD} > 2.5 Ga, and (iii) the scattering of T_{RD} to younger, post-Archean, ages. The mean T_{RD} model age for all Jericho peridotite samples in Figure 4.30 is 2.1 +/- 0.7 Ga (1 std.dev.) with a median of 2.0 Ga. This is much lower than that reported from previous studies of cratonic peridotites from the Kaapvaal craton, with a mean T_{RD} model age of 2.5 +/- 0.4 Ga and median of 2.6 Ga (Carlson *et al.*, 1999).

In order to expand from the xenolith scale to a more regional scale, the xenoliths have been placed into a mantle stratigraphy using previous geothermobarometry studies of the Jericho peridotite suite by Kopylova *et al.* (1999b). Combined P-T and Re-Os data from Jericho peridotites suggest there is a correlation between T_{RD} model ages and depth of origin (Figure 4.31; Table 4.5). If we consider coarse spinel peridotites only, these have a mean T_{RD} of 2.7 +/- 0.5 Ga with a median of 2.9 Ga, which is more comparable to previous studies of cratonic peridotites. Coarse garnet peridotites (mean T_{RD} of 1.8 +/- 0.6 Ga with a median of 1.9 Ga) and high temperature porphyroclastic non-disrupted garnet peridotites (mean T_{RD} of 1.9 +/- 0.5 Ga with a median of 1.9 Ga) generally have lower T_{RD} model ages than coarse spinel peridotites suggesting that there is either an overall younging of lithospheric mantle with depth, or a stratigraphical boundary. This is not exclusively the case for all samples. Sample 22-1, a low-T coarse garnet peridotite, and sample 40-20, a high-T garnet peridotite, produce T_{RD} model ages of 2.6 Ga. Younger Phanerozoic ages are also evident within the Jericho peridotite suite. Sample 11-22, a low-T garnet peridotite, produces a T_{RD} model age of 0.6 Ga. This is within error of the T_{RD} model ages produced by two wehrlite xenoliths from Jericho, samples 54-9 and 56-1, with T_{RD} model ages of 0.5 and 0.7 Ga respectively (Irvine *et al.*, 1999).

T_{RD} model ages reflect the minimum age of Re-depletion experienced by the Jericho samples. The range in ages of spinel peridotites from Jericho shows that at least this portion of the cratonic lithospheric keel is ancient and has persisted since the Archean. The oldest low-T garnet peridotite gives a T_{RD} age of 2.9 Ga. This is significant as it suggests that the Archean mantle now mainly restricted to the spinel facies extended

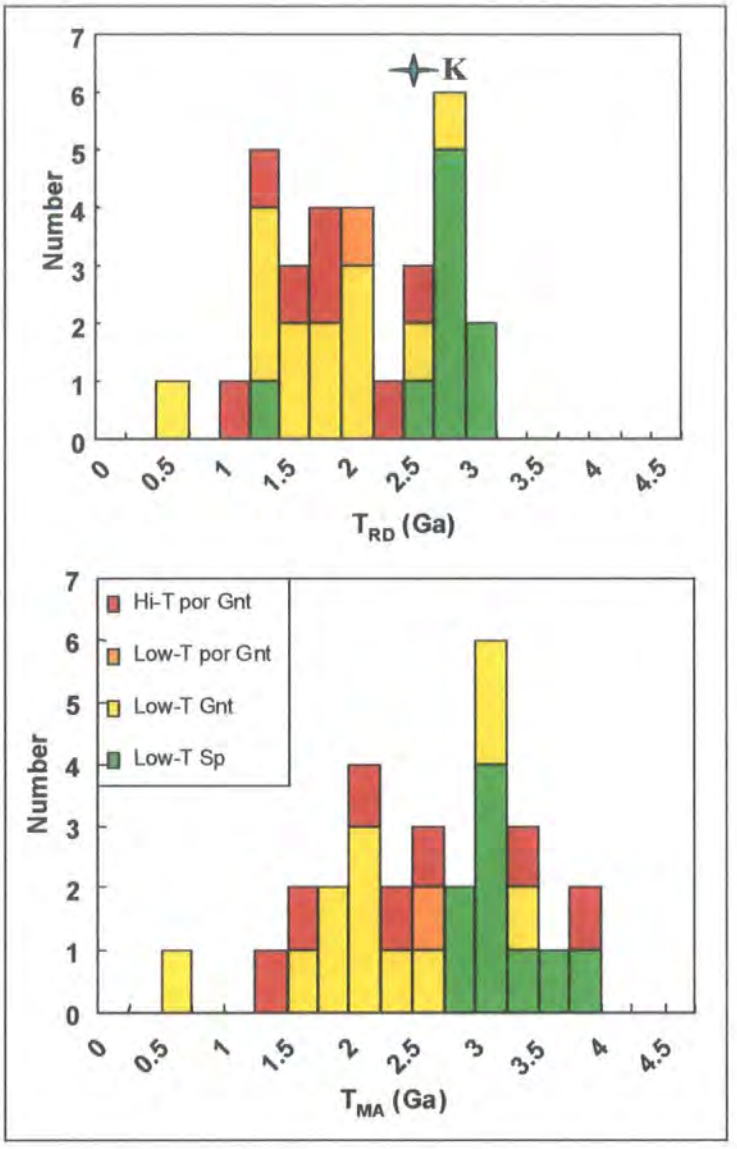

Figure 4.30 Histograms of Re-depletion (T_{RD}) and mantle extraction (T_{MA}) Re-Os model ages for Jericho peridotites. Also shown are mean T_{RD} values for K – Kaapvaal from Carlson *et al* (1999) at 2.5 Ga.

into the low-T garnet facies. The younger ages produced by the low-T and high-T garnet peridotites suggest that the lithospheric keel as a whole is still old and that it has persisted since at least the Proterozoic.

Mantle separation model ages (T_{MA})

T_{MA} ages for the Jericho peridotites in Table 4.5 equates to model ages of 3.9 - 0.6 Ga (Figure 4.30), excluding samples that produce future ages or ages greater than the age of the Earth. Twelve samples have T_{MA} model ages >3.0 Ga, five samples have T_{MA} model ages between 2.5 Ga and 3.0 Ga, and twelve samples have T_{MA} ages < 2.5 Ga. Two features are prominent in the distribution of T_{MA} model ages shown in Figure 4.30; (i) a bimodal distribution with peaks at 3.0 Ga and 2.25 Ga, and (ii) wide continuous distribution in model ages from Archean to the neo-Proterozoic. The mean

T_{MA} model age for all Jericho peridotite samples in Figure 4.30 is 2.7 +/- 0.8 Ga (1 std.dev.) with a median of 2.8 Ga.

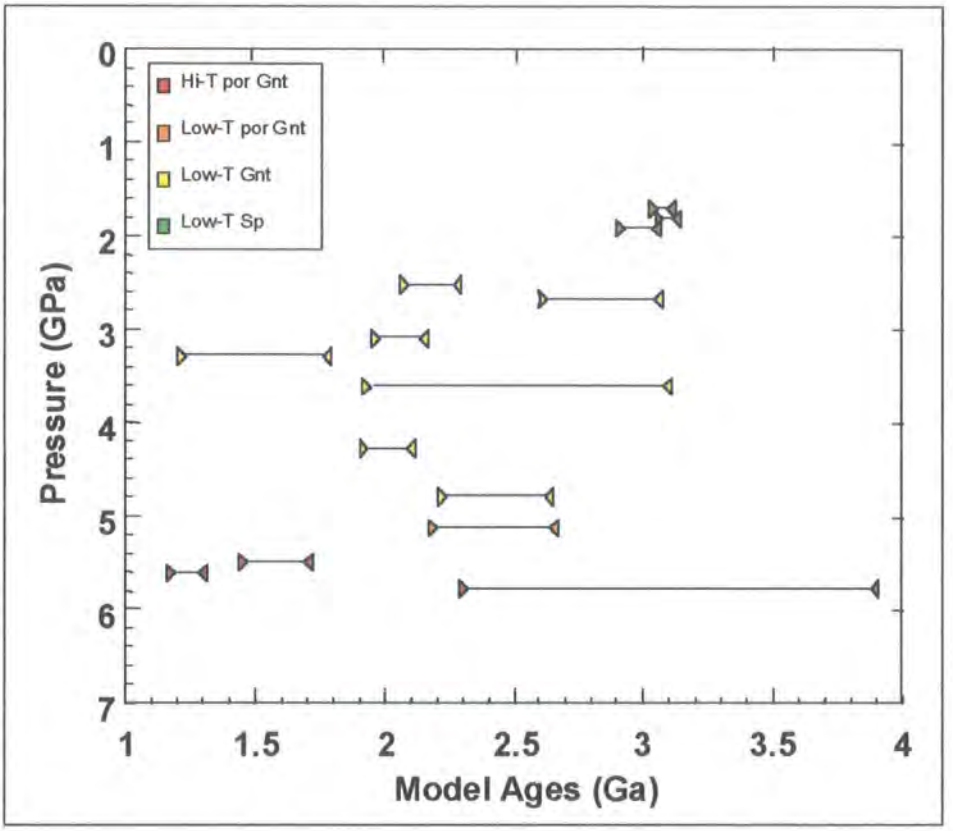

Figure 4.31 T_{RD} (right facing triangles) and T_{MA} (left facing triangles) model ages for peridotite xenoliths from individual facies plotted against the pressure of equilibration as determined by mineral geothermobarometry. All samples plotting at pressures less than 2 GPa are spinel peridotites (pressure arbitrarily assigned in 0.2 GPa increments up to 2 GPa).

Again there appears to be a correlation between T_{MA} model ages and depth of origin for the Jericho peridotites (Figure 4.31). If we consider coarse spinel peridotites only, these have a mean T_{MA} of 3.2 +/- 0.3 Ga with a median of 3.1 Ga, producing a reasonably constrained T_{MA} model age. Coarse garnet peridotites (mean T_{RD} of 2.2 +/- 0.8 Ga with a median of 2.1 Ga) and high-T porphyroclastic non-disrupted garnet peridotites (mean T_{RD} of 2.7 +/- 0.8 Ga with a median of 2.6 Ga) generally have lower model T_{MA} ages than coarse spinel peridotites and these are poorly constrained.

If the Re/Os ratio of the Jericho samples has changed at all during the evolution of the sample, this will produce spurious mantle separation ages. By way of example, if we consider infiltration by the host kimberlite (Figures 4.22), this will produce an increase in the Re/Os ratio without greatly affecting the $^{187}Os/^{188}Os$ composition. This will result in erroneous steepening of the calculated evolutionary trajectory of the Os isotopic composition through time, displacing the intercept with fertile mantle towards

higher ages thereby overestimating the true melt extraction age. In contrast, a loss of Re, possibly produced by weathering and consequent sulfide removal would result in an underestimated T_{MA}. Many T_{MA} model ages deviate greatly from their T_{RD} model ages (Figure 4.32). As expected for samples that have experienced recent Re addition with no changes in $^{187}Os/^{188}Os$, e.g. samples 13-2 and 23-1 (Table 4.5). Even though T_{MA} model ages are susceptible to Re addition, T_{MA} model ages for coarse spinel peridotites are within a few 100 Ma of their T_{RD} ages and suggest little disturbance.

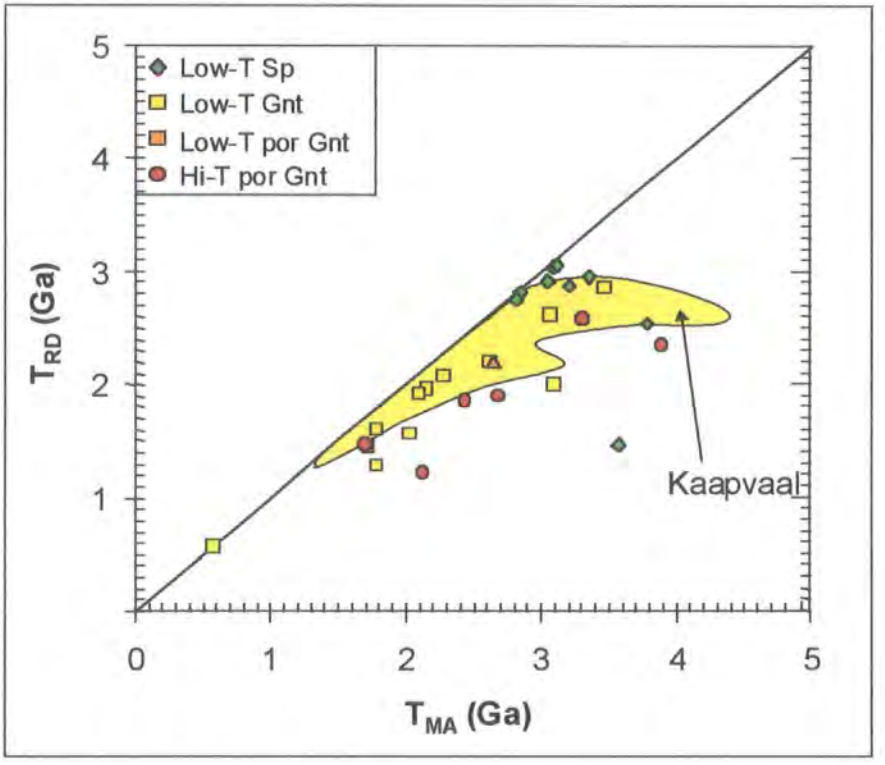

Figure 4.32 Plot of T_{RD} vs. T_{MA} model ages for individual Jericho peridotite suites. The line in the figure represents the $T_{RD} = T_{MA}$ line. Data for peridotites from the Kaapvaal craton (Carlson *et al.*, 1999).

Although there is a wide range in model ages, there is good agreement with many of the T_{RD} and T_{MA} model ages for individual samples at Jericho, e.g. sample 8-7 has a T_{RD} model age of 3.0 Ga and T_{MA} model age of 3.1 Ga. This suggests a long period of melt-residue addition to the lithospheric keel beneath Jericho since at least the late to mid-Archean. The depth extent of the Archean lithospheric keel is uncertain, as there is evidence of high-temperature peridotites with Archean model ages. If these model ages are a true reflection of formation age, the spinel facies of the lithospheric mantle is dominated by ancient Archean material, whilst the low-T garnet and high-T garnet

facies lithosphere is dominated by younger peridotite extracted from the convecting mantle in the Proterozoic.

4.6.4 Constraints from PGE systematics on the significance of model ages for the lithospheric mantle beneath Jericho

By considering the Re-Os age systematics and the behaviour of PGEs within the Jericho peridotite suite, we can constrain the age of the Slave lithospheric mantle and evaluate the significance of T_{RD} vs. T_{MA} model ages.

Three Jericho low-T spinel peridotites have extremely fractionated chondrite normalised PGE patterns with a noticeable depletion in Pt, Pd and Re (Table 4.12; Figure 4.17a). This pattern is that expected for a residue of extensive melting that has lost most of its primary sulfide (>25% melting), and this is also reflected in the depleted major element composition (Table 4.3). The very depleted Re content of these sample is reflected in the agreement between T_{RD} and T_{MA}, e.g. sample 8-7 with T_{RD} and T_{MA} of 3.0 Ga and 3.1 Ga respectively. The low bulk-rock Al_2O_3, depleted PGE profile and close agreement between T_{MA} and T_{RD} suggest that the Re-Os isotope systematics of these samples have remained closed since initial melt extraction. The REE enrichment observed in these samples (Table 4.4) suggests that they have undergone a degree of metasomatism, but this has not been accompanied by Re enrichment and therefore not disturbed the Re-Os isotope systematics. The T_{MA} of sample 8-7 is therefore likely to approximate the age of melting, and provides a maximum age for the lithospheric mantle as sampled at Jericho from the present sample suite. The small discrepancy between T_{RD} and T_{MA} model ages suggests that, although T_{RD} represents a minimum age for the sample, it would appear to be a good approximation of the actual age because the Re was mostly removed during the initial melt event.

By comparison, some samples also display highly fractionated PGE patterns but with a marked inflection at Re (Figure 4.17b). $(Pd/Ir)_n$ values for these samples are low (mean = 0.016 +/- 0.007), suggesting that they have undergone large degrees of partial melting. However the low $(Pd/Ir)_n$ gives little indication of the disturbed nature of the PGE profiles. The extended PGE pattern for sample 10-12A shows a marked inflection at Re resulting in a greater variation between T_{RD} (3.0 Ga) and T_{MA} (3.4 Ga) ages. Analysis of the PGE data suggests that the Re enrichment was accompanied by S and Al_2O_3 enrichment (Table 4.13) and the sample is displaced to the right of the theoretical (Pd/Ir)n vs. Al_2O_3 model (Figure 4.26), most likely indicating interaction with a silicate

melt with possible Re-rich sulfides. The most significant feature of the Re-Os systematics of sample 10-12A is that the T_{RD} model age is within error of the age of PPGE depleted sample 8-7, consistent with a major melt extraction event at ca. 3.0 Ga. This may suggest that Os was not transported by the infiltrating sulfide phases.

Several Jericho peridotites display moderately fractionated chondrite normalised PGE patterns (Figure 4.17e). Patterns such as those expected for peridotites that have experienced low degrees of partial melting, where Re may still be residual in the sample e.g. sample 10-456' (Table 4.12), with only moderate depletion of Pt, Pd and Re. This feature is consistent with major element data (Table 4.3), and this correlates with the model $(Pd/Ir)_n$ vs. Al_2O_3 evolution trend (Figure 4.26), where 10-456' lies on or close to an extension of the trend. The PGE profile for this sample shows little evidence of disturbance to the PPGEs, or open-system behaviour. In comparison to more depleted Jericho samples, the chondrite normalised Pd and Re abundances are almost a magnitude greater, which may suggest that primary sulfides are still resident within this section of the mantle and melting never reached the point of total sulfide breakdown. The model ages for this sample provide a T_{RD} model age of 1.4 Ga and a T_{MA} of 1.7 Ga respectively. The model ages are in close agreement, and therefore the T_{MA} model age may better reflect the true age of the sample.

Using combined PGE characteristics with Re-Os isotope systematics, and investigation of the correlation between magmaphile elements and PGEs to the Jericho peridotite suite, we can gain better insights into the age systematics of the Slave lithospheric mantle (as sampled at Jericho). This provides us with an understanding of initial formation and subsequent modification of the lithosphere. It is evident from the extended chondrite normalised PGE patterns that the majority of samples have undergone Re enrichment to a degree. T_{MA} model ages frequently produce anomalously old ages of formation compared with T_{RD} (Figure 4.32), and sometimes produce future ages. As most Jericho peridotites show vestiges of major-element and PPGE melt depletion, T_{RD} model ages might be regarded as a more reliable indicator of the age of a particular sample. The systematic behaviour of melt-depleted extended PGE patterns, agreement of $(Pd/Ir)_n$ vs. Al_2O_3 and coincidence of T_{MA} and T_{RD} ages for some of the samples give us confidence that they are recording mainly the timing of melt depletion and lithospheric formation.

4.7 Evolution of the lithospheric mantle beneath the Slave craton

Composition and stratification

The lithospheric mantle underlying the Slave craton has a long and complex history (Griffin *et al.*, 1999b; Kopylova and Russell, 2000). Unlike the cratonic mantle beneath the Kaapvaal and Siberian cratons, the lithospheric mantle sampled by the Jericho kimberlite is stratified in terms of its mineralogy and geochemistry (Kopylova and Russell, 2000). This stratification is defined by a shallow layer of depleted spinel peridotite underlain by garnet peridotite and a layer of fertile peridotite.

The bulk compositions of the spinel peridotites are consistent with an origin as residues of varying degrees of partial melting over a range of pressure, 4 to 7 GPa (Walter, 1999). The PGE patterns for these samples are consistent with a partial-melting residue. The samples are high in Si and modal OPX, similar to the Kaapvaal and Siberian cratons, which may suggest a common origin. The bulk compositions of most low-T garnet peridotites are similar to high-pressure experimental residues, consistent with pressures of 3 to 7 GPa. High-T garnet peridotite compositions though are consistent with residues of low pressure melting of undepleted mantle such as oceanic residues. This may be consistent with underplating of oceanic lithosphere during subduction events.

The Slave lithospheric mantle is not only vertically stratified, it is also laterally heterogeneous and is composed of three northeast trending domains each with differing compositions. The northern domain, which hosts the Jericho kimberlite, lacks harzburgitic garnet (Grütter *et al.*, 1999), has high CPX content, a unique garnet major element trend and the discontinuity between garnet free mantle and garnet bearing is at 80 to 100 km depth (Kopylova and Russell, 2000). The central domain has the most depleted composition as defined by garnet chemistry (Grütter *et al.*, 1999), the areal extent of which may be restricted simply to the central domain or it may coincide with the larger Archean lherzolite layer of Griffin *et al.* (1999b). A two-layer structure has been reported for this central domain and the depleted layer extends down to 150 km, though this thins to the north, south and southwest. The south-eastern domain has an intermediate depletion between that of the northern and central domains (Grütter *et al.*, 1999).

Formation of the lithospheric mantle

The oldest crustal rocks of the Slave craton, the Acasta gneiss in the Anton terrane, are dated at 3.96 to 4.0 Ga (Bowring and Housh, 1995). No peridotites as old as this have been found from the Slave craton. The spinel facies peridotites analysed from the

Jericho kimberlite suggest that the Contwoyto terrane has an Archean nucleus with a model age of at least 3.0 Ga and that this, in part, extended down into the low-T garnet facies of the lithospheric mantle. The oldest upper crustal rocks from the Contwoyto terrane, through which the Jericho kimberlite erupts, are basic volcanic and metaturbidite rocks at ca. 2.72 to 2.61 Ga. Isotope studies of the crustal rocks define a major boundary in the Slave craton between old felsic crust in the western Slave and more Juvenile crust in the East (Davis and Hegner, 1992; Thorpe *et al.*, 1992). The Jericho kimberlite lies to the East of the original Pb-isotope boundary of Thorpe *et al.* (Davis and Hegner, 1992; Thorpe *et al.*, 1992), suggesting that it is located on the younger part of the craton. However, new unpublished Pb-data from the GSC places the Pb-boundary to the east of Jericho which means it lies on the older part of the craton (Kjarsgaard, pers. comm.). It should also be noted that lower crustal xenoliths erupted in Lac de Gras kimberlites give zircon U-Pb ages of 3.02 +/- 0.04 Ga (Bleeker and Davis, 1999), providing supporting evidence for an Archean basement beneath the Contwoyto terrane. This basement may be the older CSBC over which the Contwoyto terrane has been obducted (Figure 4.33). The final stabilisation of the Slave craton, when the Anton terrane docked with the Hackett and Contwoyto terranes, was marked by the emplacement of voluminous granitoids ca. 2.62 to 2.58 Ga (Davis *et al.*, 1994, Figure 4.34). This age is co-incidental with numerous Re-Os model ages of 2.6 Ga observed within low-T spinel and garnet, and high-T garnet facies peridotites. This may indicate disruption of the PGEs and Re-Os isotope systematics, or alternatively the addition of new mantle material at this time.

Spinel, low-T garnet and high-T garnet peridotites at Jericho are stratified in terms of their geochemistry and mineralogy. Peridotites from each facies give T_{RD} model ages of 2.6 Ga, though their geochemistry is discernible from each other and fits with the stratigraphical trend seen. This would favour disruption of PGEs and Os-isotopes as an explanation of the younger model ages, but the addition of new material cannot be ruled out, if it equilibrated with pre-existing lithospheric mantle through melt-rock reactions.

Although, due to uncertainties in the initial Os isotopic composition of fertile mantle estimates, the accuracy of model ages cannot be assured, distinct peaks in the T_{RD} histogram (Figure 4.30) appear to coincide with some of the events recorded in crustal rocks.

T_{RD} model ages for peridotites, ranging between 1.8 and 2.2 Ga, are co-incident with several major tectonic and magmatic events affecting the Slave craton. During the period of 1.8 to 2.2 Ga there were several major magmatic events within the Slave

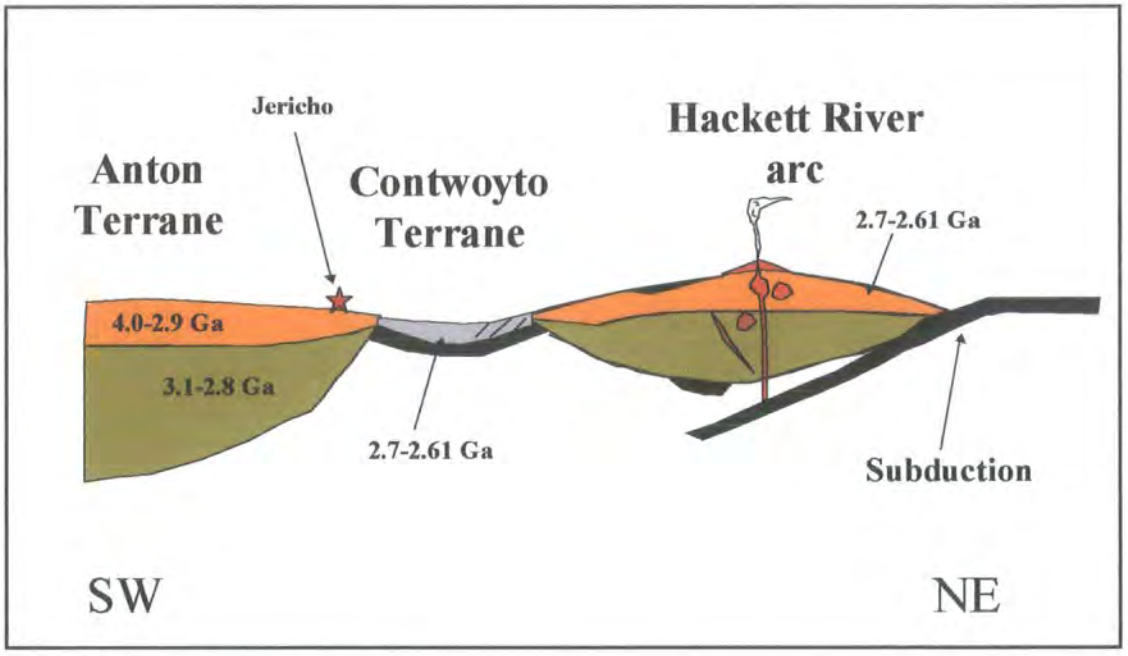

Figure 4.33 Schematic model for the formation of the Archean core of the Slave craton at Jericho.

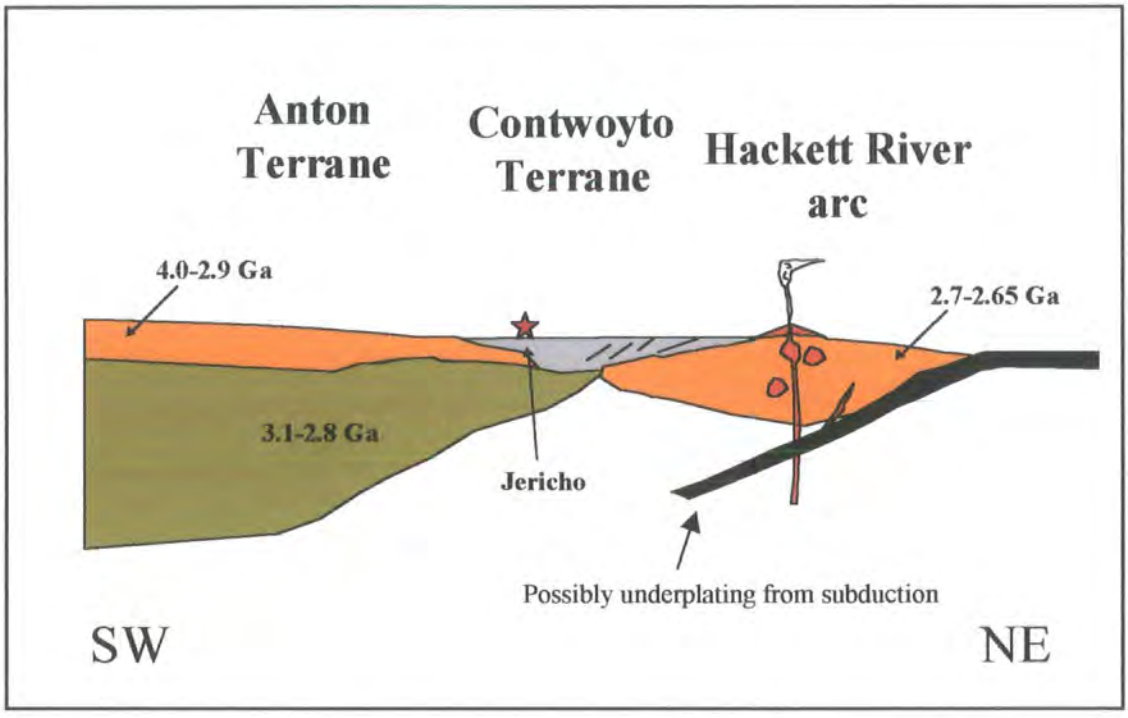

Figure 4.34 Schematic model for the formation of the lithospheric mantle as sampled by the Jericho kimberlite, and stabilisation of the Slave craton.

craton, which have been attributed to rifting, and plume events. These events produced the Malley and MacKay dyke swarms at 2.23 and 2.21 Ga respectively, and the Lac de Gras diabase dykes at 2.03 and 2.02 Ga. The Thelon Orogen (2.2 to 1.9 Ga) which bounds the Slave craton on its eastern margin was formed during the collision of the

Slave and Churchill Provinces. The Wopmay Orogen (1.97 to 1.84 Ga) bounds the Slave craton on its western margin, formed during the collision of the Nahanni continental block and accretion of the Hottah magmatic and Great Bear continental arcs (Figure 4.35). Collisional activity ended near 1.65 Ga when the Slave was incorporated into Laurentia. Model ages of 1.5 to1.6 Ga in a spinel peridotite and two low-T garnet peridotites may be coeval with the termination of collisional activity.

Model ages ranging from 1.2 to 1.4 Ga within the Jericho peridotite suite may indicate the onset of the major MacKenzie igneous event (ca. 1.27 Ga; Figure 4.3 and 4.36), which has been interpreted as a plume focused to the West of Victoria Island. Geophysical evidence suggests that the mantle beneath the northern Slave craton is seismically faster than that beneath the southern Slave (Hoffman, 1990), and this corresponds to dykes with a vertical flow regime. It has been speculated that the MacKenzie plume event has eroded the base of the lithosphere beneath the northern Slave craton (Davis, 1997). The Jericho kimberlite is situated between two MacKenzie dykes and the kimberlite precursor dyke follows the strike of these, indicating that the MacKenzie event has had a strong influence on the crustal rocks of this region. The Jericho kimberlite lies on the margin of the area of vertical flow in dykes and seismically fast mantle. The low-T and high-T garnet peridotites appear as though an event close to age of the MacKenzie plume event played a significant role in either adding new material to the lithosphere, or significantly altering the Re-Os systematics.

The youngest model age for a low-T garnet peridotite (0.6 Ga) is within error of model ages for two wehrlite xenoliths (0.5 and 0.7 Ga) from the Jericho kimberlite. These model ages are also within error of the Gunbarrel and Franklin diabase swarms at 0.78 and 0.72 Ga respectively, and similarly they are within error of the oldest kimberlite activity. The Drybones kimberlite has been dated at 440 Ma and AK5035 at 539 Ma (Davis and Kjarsgaard, 1997; Heaman *et al.*, 1997).

All of these tectonic and magmatic events could have had a profound influence on the lithospheric mantle beneath Jericho. The varied model ages of the low-T garnet and high-T garnet peridotites would suggest that they are influenced / dominated by one or all of these events. These model ages may indicate either the addition of new material to the lithosphere during the tectono-magmatic activity, or that there has been a substantial disturbance of PGEs and Os isotope systematics during the events by metasomatic type processes. Similar coincidences of peridotite xenolith Os model ages and major magmatic events are observed in the Kaapvaal craton. For instance the Premier kimberlite pipe, which erupts through the Bushveld intrusion (2.05 Ga),

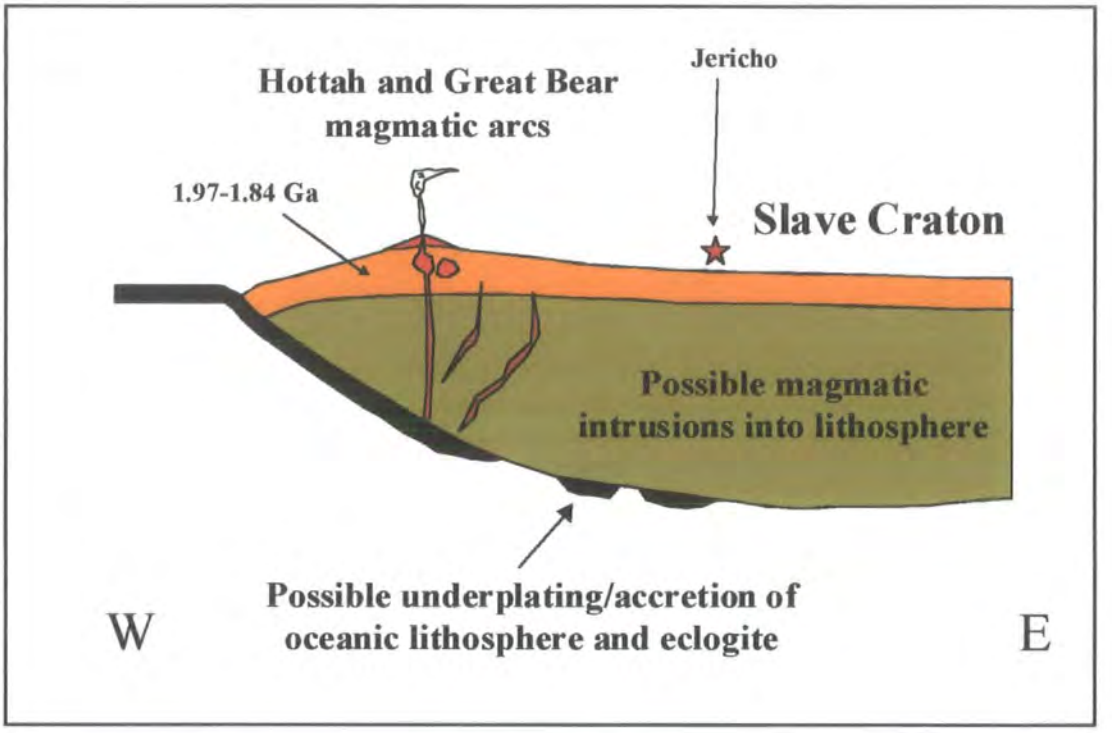

Figure 4.35 Schematic model of the Wopmay orogen and implications for the Slave lithospheric mantle.

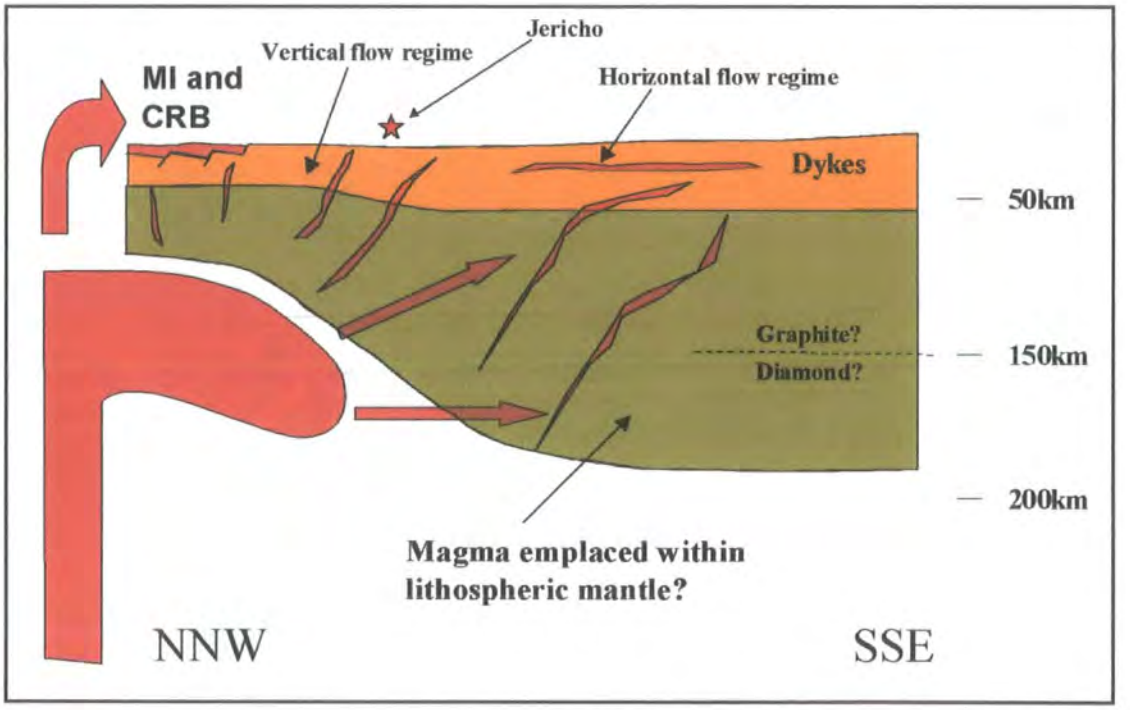

Figure 4.36 Schematic model of the Mackenzie plume event and the implications for the sub-continental lithospheric mantle beneath the Slave craton. MI – Muskox intrusion, CRB – Coppermine River Basalt.

contains a large number of peridotite xenoliths that give T_{RD} model ages of 2.0 Ga (Carlson *et al.*, 1999).

The young Proterozoic addition or modification to the lithospheric mantle beneath Jericho has important implications for the survival and age of diamonds. The cratonic lithospheric mantle beneath Jericho has either retained its diamondiferous nature throughout these events, or alternatively the diamonds from Jericho may be younger or introduced through these magmatic events (Griffin *et al.*, 1999a).

Chapter 5

Peridotite Xenoliths from the Somerset Island Kimberlite Field

5.1 Introduction

Until recently, samples of sub-cratonic mantle, erupted by kimberlitic magmatism, were dominated by xenoliths from the Kaapvaal and Siberian cratons (Boyd and Mertzman, 1987; Boyd, 1989; Griffin *et al.*, 1999). Studies of these xenoliths highlighted the refractory nature of mantle roots beneath Archean cratons i.e., residues depleted in fusible major elements from melt extraction (Nixon, 1987; Herzberg, 1993; Boyd *et al.*, 1997). The similarities between mantle samples from these two areas (Boyd *et al.*, 1997) has dominated our thinking and understanding of the evolution of cratonic lithospheric mantle. Kimberlite-hosted mantle xenoliths from Somerset Island in Arctic Canada provide us with the opportunity to place constraints on the nature of the mantle root beneath the Canadian Shield, and allows us to make comparisons with both the Kaapvaal and Siberian cratons.

Somerset Island is considered to be part of the Churchill Province, on the northern margin of the North American Craton (Figure 5.1). The presence of ultrabasic igneous breccias in Somerset Island was first recorded during the 1960's (Blackadar and Christie, 1963; Blackadar, 1967). These rocks were subsequently confirmed as kimberlites by Mitchell and Fritz (1973) and Clarke and Mitchell (1975). Subsequent exploration has resulted in the discovery of further kimberlites on Somerset Island (Figure 5.2). Mantle xenoliths have been found at a number of kimberlite locales within the Somerset Island kimberlite field of Arctic Canada and these have provided insights into the lithospheric mantle underlying the Churchill Province (Mitchell, 1976; Mitchell, 1987; Kjarsgaard and Peterson, 1992; Kjarsgaard, 1996).

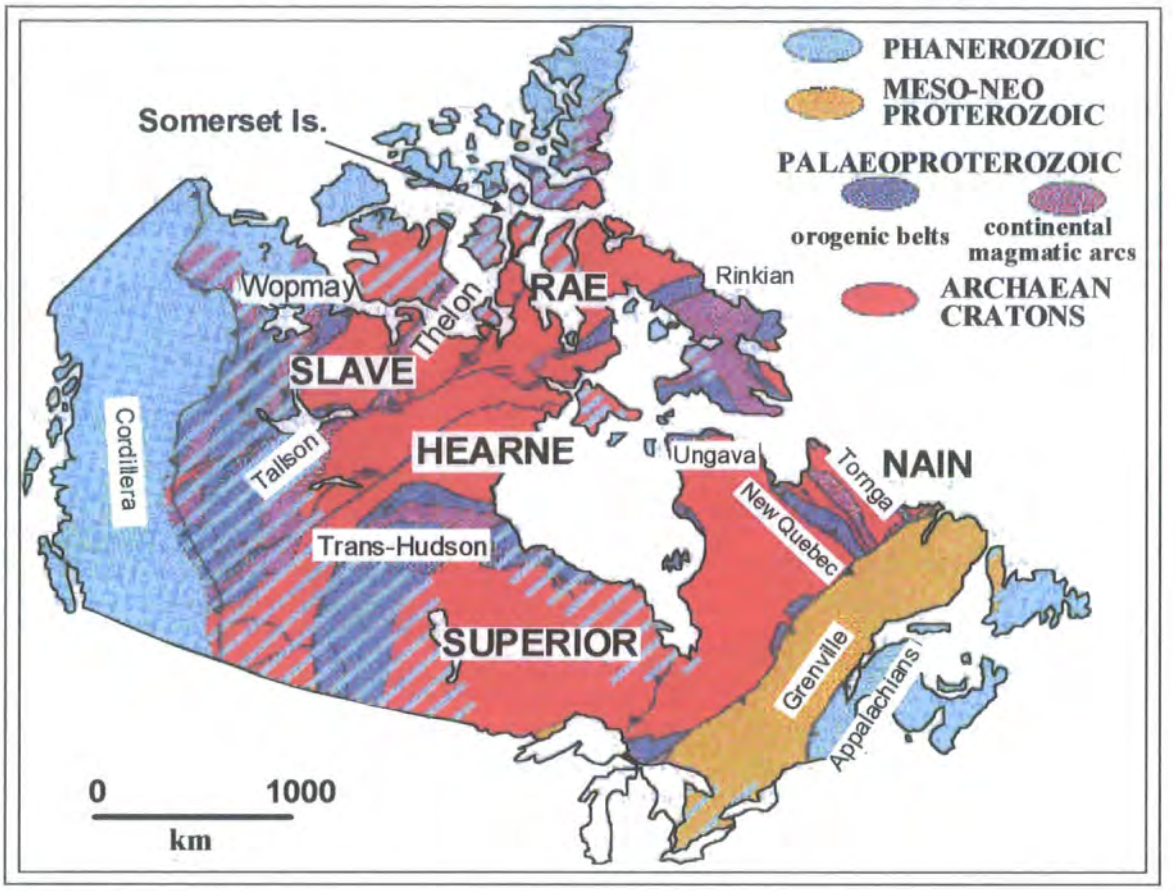

Figure 5.1 Map of Canada showing Precambrian tectonic elements, modified after Percival (1996). Blue diagonal stripes represent areas of Phanerozoic cover over Precambrian basement. Somerset Island highlighted with heavy border, forms part of the Archean NW Churchill Province. Upper case names represent Archean Provinces; lower case names represent Proterozoic and Phanerozoic orogens. Blue diagonal stripes represent areas where the Precambrian basement is covered by Phanerozoic platformal cover.

5.2 Geological Setting

5.2.1 Regional Geology

Somerset Island and the Churchill province have a long geological history, rooted in the Archean during the formation of the Canadian Shield and continuing through to the Tertiary. The geological record for Somerset Island and the Churchill province is summarised in Table 5.1.

5.2.1.a The Churchill Province

Somerset Island is located in the Churchill structural province, which Hoffman (Hoffman, 1990b) subdivided into the Rae and Hearne sub-provinces (Figure5.1). The Churchill province differs from most Archean cratonic areas in the strict sense because of its variable and widespread Paleoproterozoic reactivation (Percival, 1996). Extensive

igneous activity at 2.4 Ga (Keewatin) produced the Happytoyuk basalts, Hurwitz gabbros and Kaminak dykes (Heaman, 1994). The Churchill province was involved in collisional tectonics with the bounding Slave, Superior and Nain cratons between 2.2 and 1.82 Ga (Hoffman, 1990a). A high velocity seismic zone underlies the Churchill province; this would suggest that an Archean mantle root may have been sufficiently buoyant to survive tectonic thickening (Hoffman, 1990a), contrary to the model proposed by Ashwal and Burke (1989). Extensive alkaline mafic magmatism occurred at 1.84 Ga (Peterson *et al.*, 1994) and further voluminous crustal melting occurred at 1.76 Ga, with the production of rhyolite and rapakivi granites. Isotopic evidence to indicate whether the mantle survived this event has been lacking (Hoffman, 1990a), except that old xenoliths have now been found in magmas that erupt through the lithospheric mantle keel (Irvine *et al.*, 1999).

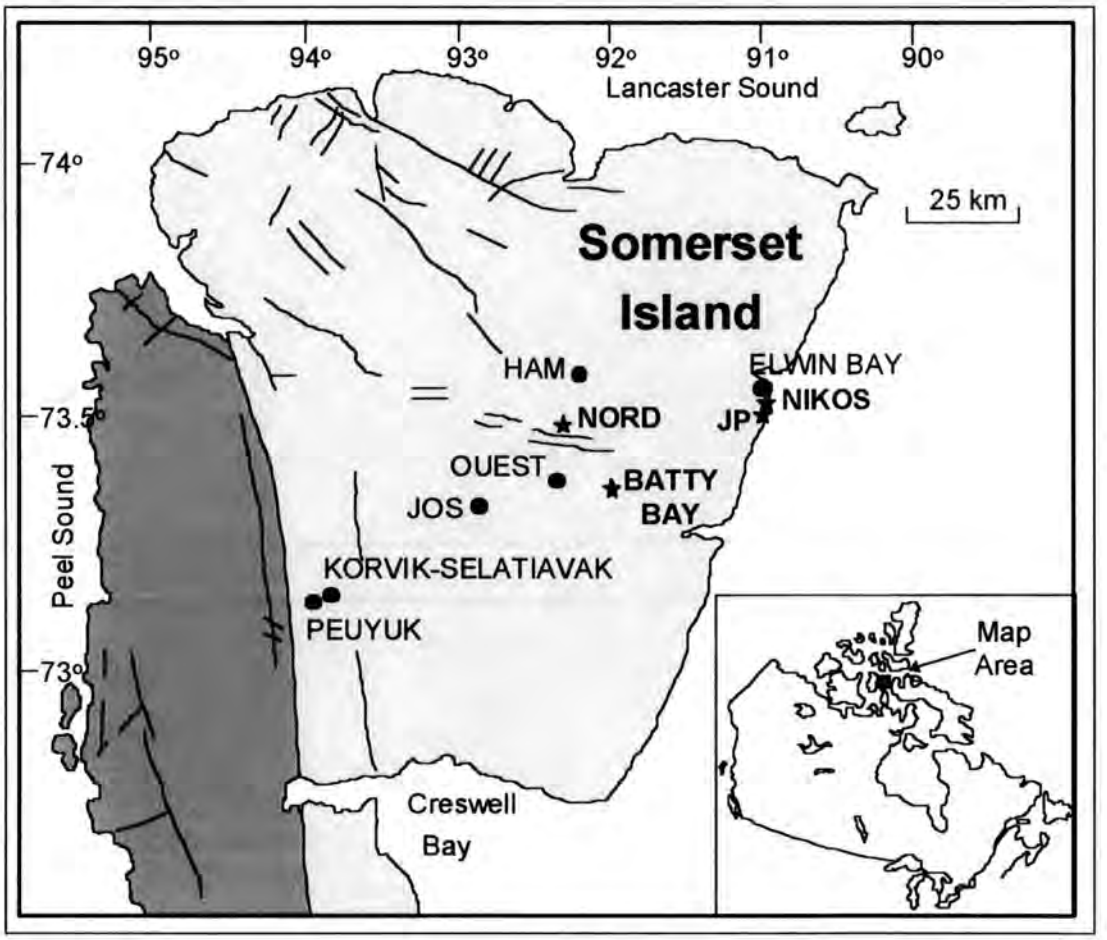

Figure 5.2 Geological map of Somerset Island (after Stewart, 1987 and Kjarsgaard, 1996) showing location of kimberlites. Peridotite xenoliths from kimberlites highlighted with stars and bold type were used in this study. Legend: light grey, Paleozoic cover; striped, late Proterozoic cover; dark grey, Precambrian basement; lines, normal faults.

Table 5.1 Summary of Geological events for Somerset Island and the Churchill Province.

Type	Geology	Age	Comments	Reference
Churchill (overview)				
Supracrustal cover rocks	Komatiites, quartzites	3.0 – 2.7 Ga		1
Volcanic rocks and associated sediments	Calc-alkaline	2.9 – 2.6 Ga		1
Mafic Igneous event	Basalts and Gabbros	2.4 Ga	Keewatin province. Happytoyuk basalts, Hurwitz gabbro and Kaminak dykes,	2
Intrusives	Granitic plutons	2.4 – 2.0 Ga		3
Collision tectonics		2.2 - 1.82 Ga	Amalgamation of Churchill, Slave, Superior and Nain cratons	4
Thelon orogen	Continental arc. Granites and diorites.	2.02 – 1.92 Ga	Continental collision with Slave. Taltson magmatic zone. Syn- and post-collision arc.	5, 6, 7
Metamorphism	Granulite		Granulite metamorphism relating to Thelon overprinting amphibolite to granulite grade Archean gneisses.	6
Alkaline magmatism	ultrapotassic	1.84 Ga		8
Intrusive	Rhyolite and rapakivi	1.76 Ga	Voluminous crustal melting.	8
Somerset Island				
Somerset Island basement rocks	Gneisses, metasediments and deformed intrusives	~ 3.0 Ga	Granulite facies	9, 10
Intrusives	Granitic plutons	2.4 – 2.0 Ga	Syenites from Cape Bird (Somerset Island) and Boothia Peninsula produce 2.4 Ga ages.	3
Metamorphism (Somerset Island basement)		2.2 Ga	U-Pb zircon ages from Somerset Island basement	11
Metamorphism (Somerset Island basement)	Granulite	1.93 Ga	U-Pb zircon from Cape Bird syenite.	10
Intrusives	Granite	~ 1.7 Ga	M'Clure Bay Granite U-Pb age of 1703 Ga.	10, 12
Tectonism	Rift basins	1400-1000 Ma		13
Sedimentary rocks	Sandstone	1400-1200 Ma	Aston formation	13
Dyke swarm	Diabase	1.27 Ga	Mackenzie dykes.	13
Sedimentary rocks	Dolomite	1200-700 Ma	Hunting formation	13

Table 5.1 (Continued) Summary of Geological events for the Somerset Island.

Type	Geology	Age	Comments	Reference
Somerset Island				
Dyke swarm	Diabase	0.72 Ga	Franklin dykes	13, 14
Sedimentary rocks	Carbonate	Ordovician to Devonian	From Silurian to Devonian clastic sediments from uplifting core become evident.	13, 15
Sedimentary rocks	Clastic sediments	Tertiary	Preserved in grabens from Tertiary rifting.	15
Kimberlites and Melnoites		105 -88 Ma	Cretaceous kimberlite magmatism. Hypabyssal / diatreme facies : present exposure suggest 1 to 2 km of erosion.	16, 17, 18

1 - Percival (1996), 2 - Heaman (1994), 3 - Bickford *et al.* (1994), 4 -Hoffman (1990a), 5 - van Breeman *et al.* (1987), 6 - Hoffman. (1988), 7 - Hanmer *et al.* (1992), 8 - Peterson *et al.* (1994), 9 - Frisch *et al.* (1987), 10 - Frisch and Sandeman. (1991), 11 - Frisch and Hunt (1993), 12 - Blackadar (1967), 13 - Okulitch *et al.* (1986), 14 - Fahrig (1987), 15 - Stewart (1987), 16 - Mitchell (1975), 17 - Smith *et al.* (1987), 18 - Heaman (1989).

The Rae sub-province is separated from the Hearne sub-province by the Snowbird line (Hoffman, 1987). This northeast trending crustal discontinuity (shear zone) extends from the edge of the Rocky Mountains, Alberta, to the Northwest Teritories, a distance of at least 1500 km (Bickford *et al.*, 1994). The Rae sub-province lies to the west of this line and the Hearne to the east. The Snowbird line has been variably interpreted as an intracontinental orogenic reactivation front (Lewry and Sibbald, 1980), and an intracontinental transcurrent fault (Bickford *et al.*, 1994). Based on geophysical evidence Hoffman (Hoffman, 1990b) has suggested that the Snowbird line represents a collisional suture between the Rae and Hearne continental plates. This collision post-dated the development of the Taltson arc (1.99-1.91 Ga) which lies to the west, and predates intrusion and sedimentation in the Baker Lake basin (~1.85 Ga). Geologic evidence in the exposed Shield is tenuous however with no evidence for a magmatic arc related to the Snowbird line (Lewry and Collerson, 1990).

5.2.1.b The Rae sub-province of the Churchill Province

The Rae sub-province is comprised predominantly of Archean rocks and is exposed in three sections; the western Northwest Territories, the Arctic Islands and Quebec-Labrador (figure 5.1). The Rae consists of Archean rocks ranging in age from 3.3 to 2.6 Ga with infolded remnants of thrusted Paleoproterozoic cover sequences. Archean rocks include 3.0 to 2.7 Ga supracrustal komatiite-quartzite sequences and 2.9 to 2.6 Ga calc-alkaline volcanic rocks and associated sediments (Percival, 1996).

The geological evolution of the Rae sub-province continued into the Proterozoic. Phases of Proterozoic granite plutonism have been documented, ranging in age from 2.4 to 2.0 Ga (Bickford *et al.*, 1994). The western margin of the Churchill province incorporates elements of a major Paleoproterozoic orogen, the Thelon orogen, between 2.02 and 1.92 Ga. This orogen formed when the craton was involved in continent-continent collision with the Slave craton in the west (van Breeman *et al.*, 1987; Hoffman, 1988; Hanmer *et al.*, 1992). The main element of this orogen is the Taltson-Thelon magmatic zone consisting of a continental arc comprising deformed dioritic and granitic plutons, and a syn- to post-collisional magmatic arc (Thériault, 1992). This developed on the leading edge of the NW Churchill province due to eastward subduction of the Slave plate. To the east of this arc, parts of the Rae sub-province have been interpreted as a Tibetan-style plateau comprising of amphibolite to granulite grade Archean gneisses overprinted by a younger granulite facies event related to the Thelon

orogen (Hoffman, 1988). Significant Proterozoic reworking is suggested by deformation effects, mid-amphibolite-facies metamorphism of cover sequences and the presence of 1.85 Ga ultrapotassic rocks and 1.76 Ga rapakivi granites (Percival, 1996; Peterson and LeCheminant, 1996).

5.2.1.c Somerset Island

Crystalline Basement Geology

The basement rocks of Somerset Island, exposed in the west side of the Island (Figure 5.2), are comprised predominantly of north-trending ortho- and para-gneisses, metamorphosed to granulite facies, and have undergone three phases of folding (Blackadar, 1967; Brown *et al.*, 1969; Kerr and deVries, 1977). The crystalline basement can be subdivided into granitoid gneisses, garnetiferous metasedimentary gneiss and marble/calc-silicate rock (Frisch *et al.*, 1987). Syenitic and mafic bodies intruded these gneisses prior to deformation. Diabase dykes from the Mackenzie and Franklin events were intruded following Archean deformation (Jones and Fahrig, 1978; Okulitch *et al.*, 1986; Fahrig, 1987). Determination of Sm-Nd radiometric ages for the Precambrian basement of Somerset Island produce T_{DM} crustal separation ages (from a depleted mantle) that range in age from 3.0 to 2.2 Ga (Frisch and Sandeman, 1991; Frisch and Hunt, 1993). U-Pb zircon ages from a granodiorite gneiss produces upper intercept ages of 2776 +67/-56 Ma and lower intercept ages of 2200 +/- 68 Ma. Two populations of zircon suggest that the gneiss represent a Proterozoic protolith with inherited late Archean zircons (Frisch and Hunt, 1993).

Sm-Nd studies of syenitic intrusive rocks from Cape Bird and northern Boothia Peninsula (just South of Somerset Island) produce ages of 2.4 Ga. A U-Pb zircon age of 1.93 Ga was determined for the Cape Bird syenite, which was suggested to be the age of granulite facies metamorphism (Frisch and Sandeman, 1991). Kimberlite derived xenocrystic zircons (assumed to derive from the lower crust) have produced U-Pb ages of 1976 +/- 5 Ma and 2500 Ma (Frisch and Sandeman, 1991). Zircons from the M'Clure Bay granite body on Somerset Island have produced a near concordant U-Pb age of 1703 +/- 2 Ma (Frisch and Sandeman, 1991), only slightly older than biotite K-Ar mineral ages reported by Blackadar (1967) at 1660 and 1670 Ma for the Boothia-Somerset Shield terrane. It appears as though the Somerset Island basement experienced a major mid-Proterozoic thermal event, but has a geologic history extending back into the Archean.

Structural Geology

The structural geology of Somerset Island is dominated by the Boothia Uplift (Kerr and Christie, 1965), a northward trending feature that appears to be controlled by the gneissic trends of its crystalline core, the Boothia Horst (Kerr, 1977). The Boothia Uplift is a major structural feature, formed during the Silurian to Early Devonian, and extends for nearly 1000 km from the Boothia Peninsula to the Grinnel Peninsula on Devon Island (Okulitch *et al.*, 1986). The Boothia Horst was raised in a series of pulses which were attributed to the Cornwallis disturbance (Kerr, 1977). The sedimentary cover rocks were consequently deformed giving rise to an anticlinorium termed the Cornwallis Fold Belt. In Somerset Island the deformed cover rocks overlap the east flank of the Boothia Uplift. The Boothia Horst and its sedimentary cover were fragmented by faulting during a Cretaceous-Tertiary event known as the Eurekan Rifting Episode (Kerr, 1977).

Sedimentary Cover

Unconformable deposition of the Proterozoic Aston sandstone formation (Helikian in age ca. 1400-1200 Ma) on the crystalline basement is the earliest record of cover on Somerset Island (Okulitch *et al.*, 1986). A period of uplift and erosion preceded the deposition of the Proterozoic Hunting dolomite formation (Neohelikian or Paleohadrynian, ca. 1200-700 Ma). This in turn was uplifted and eroded prior to deposition of younger cover rocks. Kerr (1977) attributed this to arching along the axis of the Boothia Uplift during the Proterozoic. However, coeval disconformities across the Arctic Archipelago suggest these periods of tectonism were not restricted to the region of the Boothia uplift and were probably unrelated to its genesis (Okulitch *et al.*, 1986). Proterozoic (1400 and 1000 Ma) rifting on northern Baffin Island produced several northwest trending basins and uplifts suggesting that the Aston and Hunting formations may have been deposited in the associated Borden Basin. These structures were incorporated into the younger Boothia Uplift Island (Okulitch *et al.*, 1986).

The Paleozoic history of Somerset Island begins with unconformable deposition of predominantly carbonate-rich successions in the Lower Ordovician and continued uninterrupted until the Lower Devonian (Kerr, 1977). From the Silurian through to Early Devonian clastic sediment from the uplifting Boothia crystalline core becomes evident in the sedimentary cover (Okulitch *et al.*, 1986; Stewart, 1987).

Tertiary faulting on Somerset Island produced grabens, preserving clastic Tertiary and Upper Cretaceous sediments (Stewart, 1987).

Intrusive Igneous Geology

At least two generations of Proterozoic diabase dykes are known from Somerset Island. The Proterozoic Aston formation is intruded by dykes and sills believed to be related to the MacKenzie diabase dykes (Jones and Fahrig, 1978; Okulitch *et al.*, 1986). It is suggested that this emplacement episode represents a radial dyke swarm associated with a mantle plume (Le Cheminant and Heaman, 1989). The 1.27 Ga MacKenzie plume formed dykes and gabbros, the Coppermine River flood basalts and Muskox intrusion (Le Cheminant and Heaman, 1989). Dyke rocks extend over 2300 km from a focus slightly to the west of Victoria Island, which has been interpreted as the site of the plume head (Fahrig, 1987, Figure 4.4). At distances less than 500 km from the focus, dykes have been emplaced vertically but at distances greater than 500 km they appear to be dominantly horizontal (Ernst and Baragar, 1992). On Somerset Island Mackenzie dykes intrude the crystalline basement as well as the Aston formation, but are truncated by the unconformity separating the Aston formation form the Hunting formation. The second generation of Proterozoic dykes intrudes the Hunting formation as well as the Aston and these are truncated by the unconformity at the base of the Paleozoic cover. These dykes belong to the Franklin diabase dyke swarms dated at 0.72 Ga (Jones and Fahrig, 1978; Okulitch *et al.*, 1986; Fahrig, 1987).

Kimberlite Geology

Kimberlites have intruded Somerset Island and appear to be localised, forming a belt trending northeast-southwest (Figure 5.2). The kimberlite magmatism appears to be controlled by fracture sets in the country rocks with north, northwest and northeast trends (Mitchell, 1975). These fractures can be seen as lineaments in the Precambrian Boothia terrane exposed on the west of Somerset Island and are continuous, extending from the basement into the Paleozoic cover (Blackadar, 1967). These fracture sets are believed to have developed in the Precambrian basement during three phases of Cornwallis folding (Brown *et al.*, 1969).

Cretaceous ages have been determined for the Ham kimberlite at 88 Ma (Heaman, 1989) and Georgia melnoite pipe at 105 Ma (Smith *et al.*, 1989) using U-Pb perovskite dating. The Elwin Bay kimberlite has also been dated using this method but the interpreted age of 27 to 36 Ma was considered spurious, possibly due to Pb-loss or U-gain of the perovskite (Smith *et al.*, 1989). The K10 Tunraq pipe, part of the Batty Bay kimberlite complex (Figure 5.3), gave a Rb-Sr errorchron age of ~100 Ma for phlogopite "phenocrysts" (Smith *et al.*, 1989). Additional U-Pb perovskite dating has produced ages of 98-94 Ma for six Somerset Island kimberlites (B.A. Kjarsgaard, *pers.*

comm. 2001). The Cretaceous ages of the kimberlites are consistent with their intrusion into the Paleozoic (Cambro-Ordovician to Upper Silurian) cover rocks (Stewart, 1987).

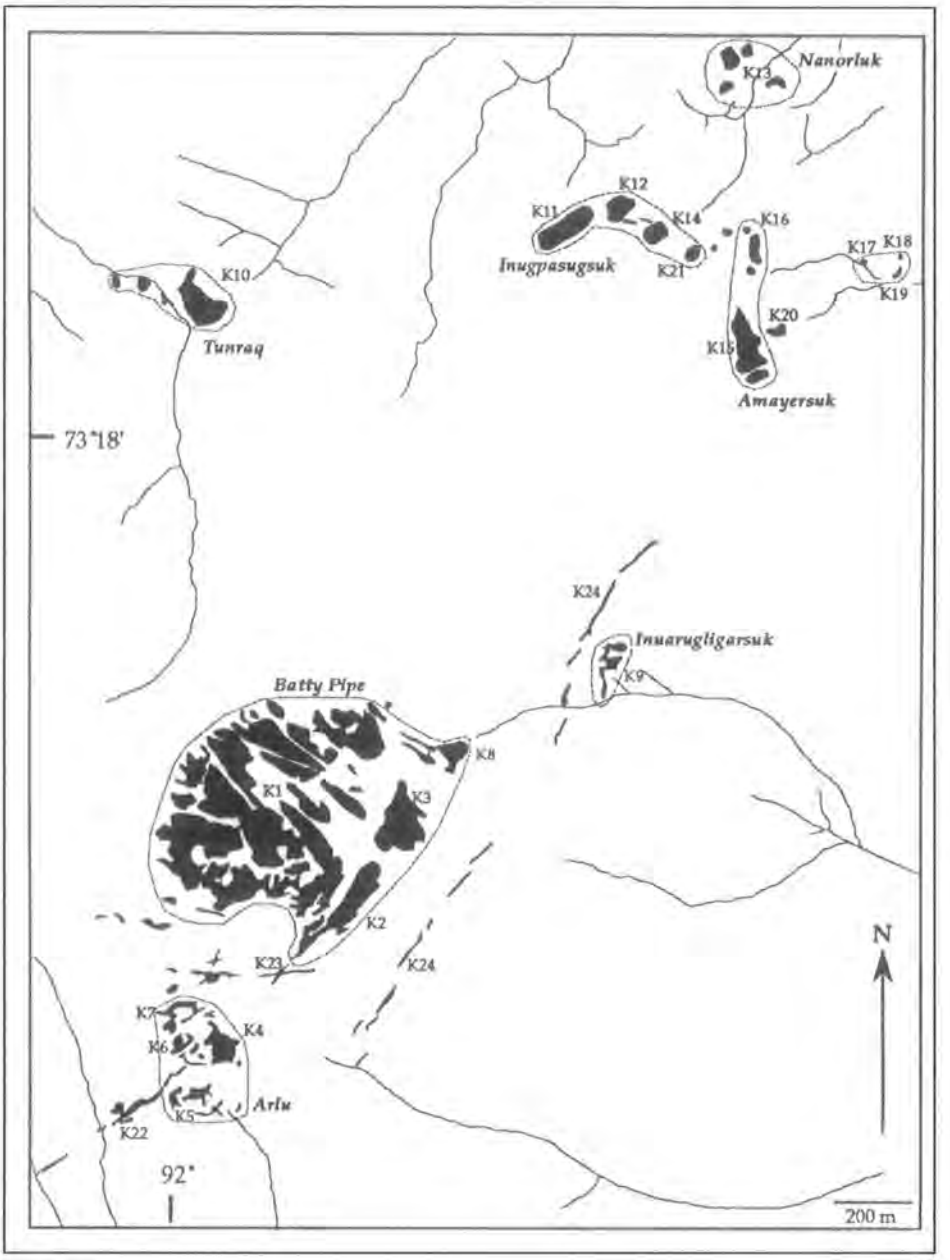

Figure 5.3 Detailed map of the surface expression of the Batty Bay kimberlite complex (Kjarsgaard and Peterson, 1992). The dashed lines group the individual kimberlites named by Mitchell (1976).

Somerset Island kimberlites are predominantly hypabyssal facies, though rare diatreme and transitional hypabyssal / diatreme occur. This suggests the current exposure level for the kimberlites is in the root zone, indicating 1 to 2 km of erosion.

5.2.2 Geological setting of the Somerset Island kimberlites

Kimberlites in Somerset Island form clusters, like in the Kaapvaal craton (Mitchell, 1986). The largest of these clusters, the Batty Bay kimberlite complex is located approximately 16 km northwest of Batty Bay, Somerset Island (73°17'N, 91°59'W; Figures 5.3 and 5.4). The Batty Bay complex consists of a series of pipes, enlarged blows and kimberlite dykes as previously discussed by Mitchell (1976; 1987), and Kjarsgaard and Peterson (1992). The Batty Bay kimberlites are predominantly hypabyssal facies though rare diatreme and transitional hypabyssal/diatreme facies occur.

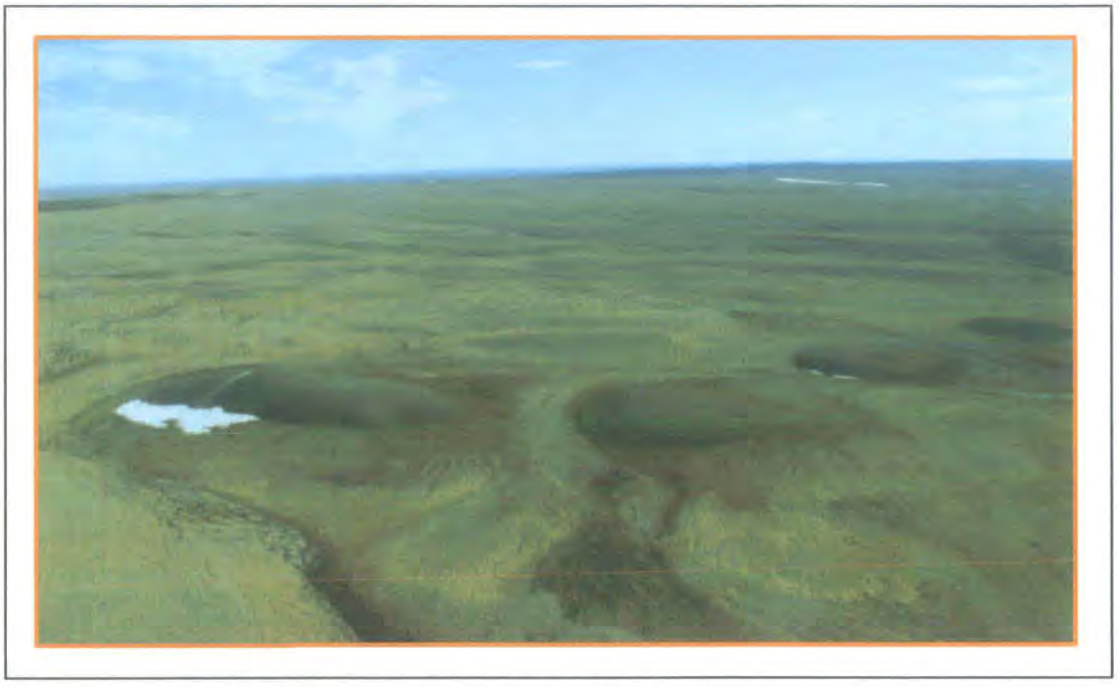

Figure 5.4 Aerial Photograph of the Batty Bay kimberlite complex.

The Nord kimberlite is located approximately 17 km northwest of the Batty Bay complex (73°27'N, 92°20'W; figure 5.3). The Nord kimberlite is of hypabyssal facies and this kimberlite forms an enlarged fissure (blow).

The JP kimberlite pipe outcrops on the eastern coast of Somerset Island (73°28'N, 90°58'W; Figure 5.3 and 5.5), approximately 7 km south of Elwin Bay. The JP kimberlite consists of three individual bodies initially discovered and described by Pell (1993). The Nikos kimberlite lies 1 km to the north of the JP kimberlite, on the coast.

The Somerset Island kimberlites examined in this study intrude the Upper Silurian Read Bay formation. This is mainly composed of thin-bedded fossiliferous limestones with argillaceous or silty partings along bedding planes. Crustal xenoliths entrained

within the kimberlites indicate that crystalline basement occurs below the Phanerozoic sedimentary cover rocks.

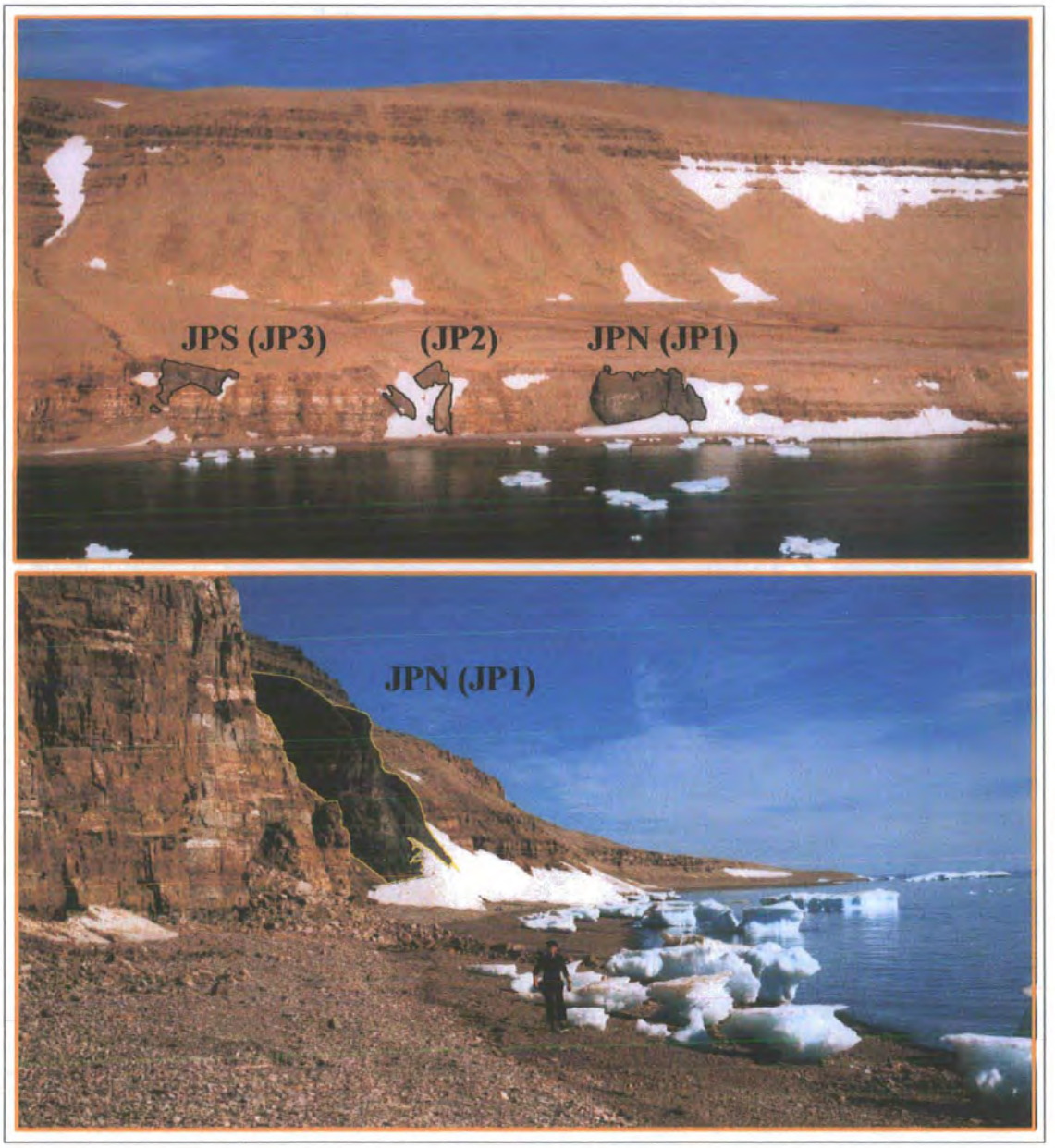

Figure 5.5 Photograph of the JP kimberlite, outcropping on the eastern coast of Somerset Island south of Elwin Bay.

5.3 Sample selection and Analytical Methods

Mantle xenoliths have been found in a number of kimberlites on Somerset Island. These are dominantly spinel, spinel-garnet and garnet lherzolites, with rare dunites and harzburgites (Mitchell, 1987; Kjarsgaard and Peterson, 1992). A representative selection of thirty three low-temperature peridotite xenoliths were chosen for this study from the various kimberlite bodies on Somerset Island. The xenoliths were chosen from

the collections of B.A. Kjarsgaard, J. Pell and Durham University, collected over several field seasons on Somerset Island. Petrological and textural summaries are provided in Appendix A.

The methods of sample preparation and whole-rock analysis are described in detail in Appendix B. All powders were prepared from at least 500g of sample (minimum). In addition, sufficient material remained to allow further petrological and geochemical studies. Large sample sizes were used to obtain representative analyses of both major and trace elements. Major elements were analysed by wavelength-dispersive X-ray fluorescence, the precision determined by replicate analysis of internal standard and reference materials. Trace elements and REE were determined by ICP-MS and INAA. The precision was estimated from duplicate analyses of rock standards.

5.3.1 Batty Bay and Nord kimberlites

The xenolith samples used in this study were donated by B.A. Kjarsgaard and are a subset of over 200 peridotite xenoliths collected from Batty Bay kimberlite bodies K11 to K16 (Figure 5.3) and the Nord kimberlite (Figure 5.2). The samples were received as polished thin-sections and coarse crush. Garnet peridotite predominates over spinel peridotite at all localities apart from K13, where there is an approximate equal abundance. Over 65% of samples collected were garnet peridotite with the remainder garnet-spinel and spinel peridotites, with minor harzburgite and dunite. Xenolith size ranges from small nodules of approximately 0.5 cm diameter up to larger ovoids 15cm by 10 cm by 8 cm. The majority of samples were rounded and 4 to 5 cm in diameter. Using the textural nomenclature of Harte (1977), most xenoliths are classified as coarse equant to coarse tabular. However, subordinate examples of porphyroclastic, mosaic porphyroclastic and disrupted porphyroclastic occur. Fifteen representative samples were chosen for different textural types, facies and degrees of alteration.

5.3.2 JP and Nikos kimberlites

The JP kimberlite hosts a well-preserved suite of, generally large ovoid (10 to 20 cm), mantle-derived xenoliths. The peridotite xenolith suite from the JP kimberlite is dominated by garnet peridotites, which account for approximately 60% of peridotite xenoliths. The remaining peridotite xenoliths are garnet-spinel (30%) and spinel (10%) peridotites. The xenoliths are mainly lherzolites and harzburgites, with minor dunite. The majority of the peridotite xenoliths have coarse equant to coarse tabular textures,

based on the textural classification of mantle-derived rocks by Harte (1977). Eighteen representative samples were selected from the different facies and textural types. Ten samples were selected from the Durham University collection of JP peridotite xenoliths, and B.A. Kjarsgaard and J.P. Armstrong donated eight samples from the J. Pell collection (four from Nikos and 4 from JP).

5.4 Petrology of Somerset Island's lithospheric mantle xenoliths

5.4.1 Xenolith Petrography

Polished thin sections were prepared for all Somerset Island peridotite samples analysed in this study. Petrographical descriptions for each sample are summarised in Appendix A.

5.4.1.a Batty Bay and Nord

Coarse Peridotite

Coarse peridotites from the Batty Bay and Nord kimberlites are composed of olivine (65-80%), and lesser amounts of clinopyroxene (0-6%), orthopyroxene (15-30%), spinel (0-3%) and/or garnet (0-6%). The predominant rock types are lherzolite and minor harzburgite. Coarse peridotite occurs in spinel, spinel-garnet and garnet facies. The coarse texture derives from early crystallisation of large subhedral olivine (up to 12 mm) and orthopyroxene (2-5 mm) and these dominate the mineral assemblage (Figure 5.6a). Clinopyroxene occurs as emerald-green anhedral equant crystals (0.5-1 mm). Reddish-brown to opaque spinel forms anhedral, irregular crystals up to 1 mm in size. These are interstitial and may show poikilitic intergrowth with olivine (Figure 5.6b). Lilac coloured garnet, 1-3 mm, is subhedral to anhedral and is variably surrounded by kelyphitic rims containing spinel and occasional phlogopite. The kelyphitic alteration rims show complex zonation patterns with various distinct zones (Figure 5.6c). Generally two kelyphite zones are apparent in the Batty Bay garnets, although these are sometimes repeated. An inner zone of fibrous or feathery aggregates, and an outer zone of small equant pyroxene crystals. Similar kelyphite coronas have been described in xenoliths from the Lashaine volcano in Tanzania (Reid and Dawson, 1970), and the Lesotho peridotite suite (Chapter 3). Rarely orthopyroxenes show exsolution lamellae of clinopyroxene aligned along the cleavage in tabular sections.

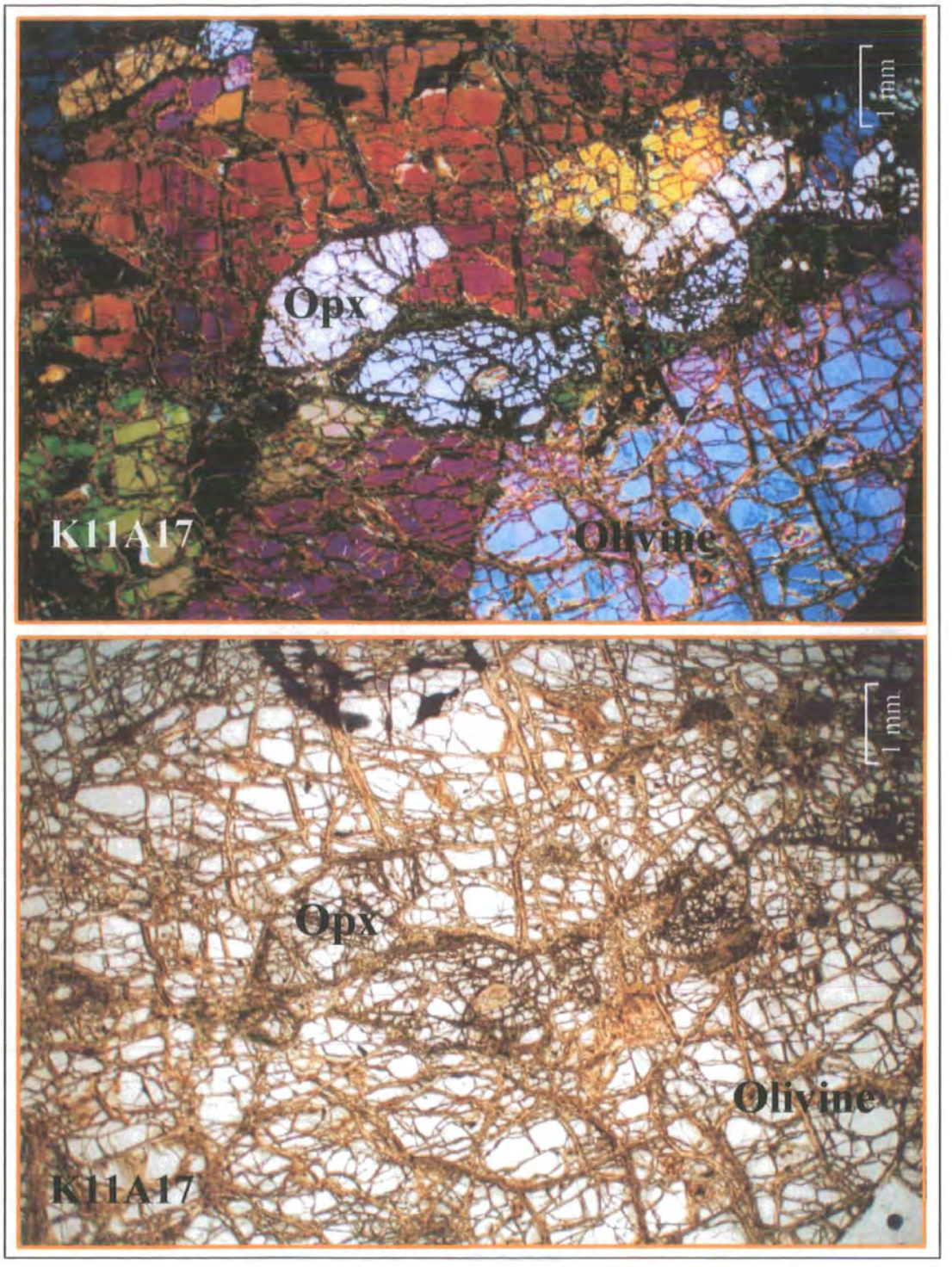

Figure 5.6 (a) Photomicrographs of peridotite xenolith from the Batty Bay kimberlite, showing coarse equant texture in peridotite.

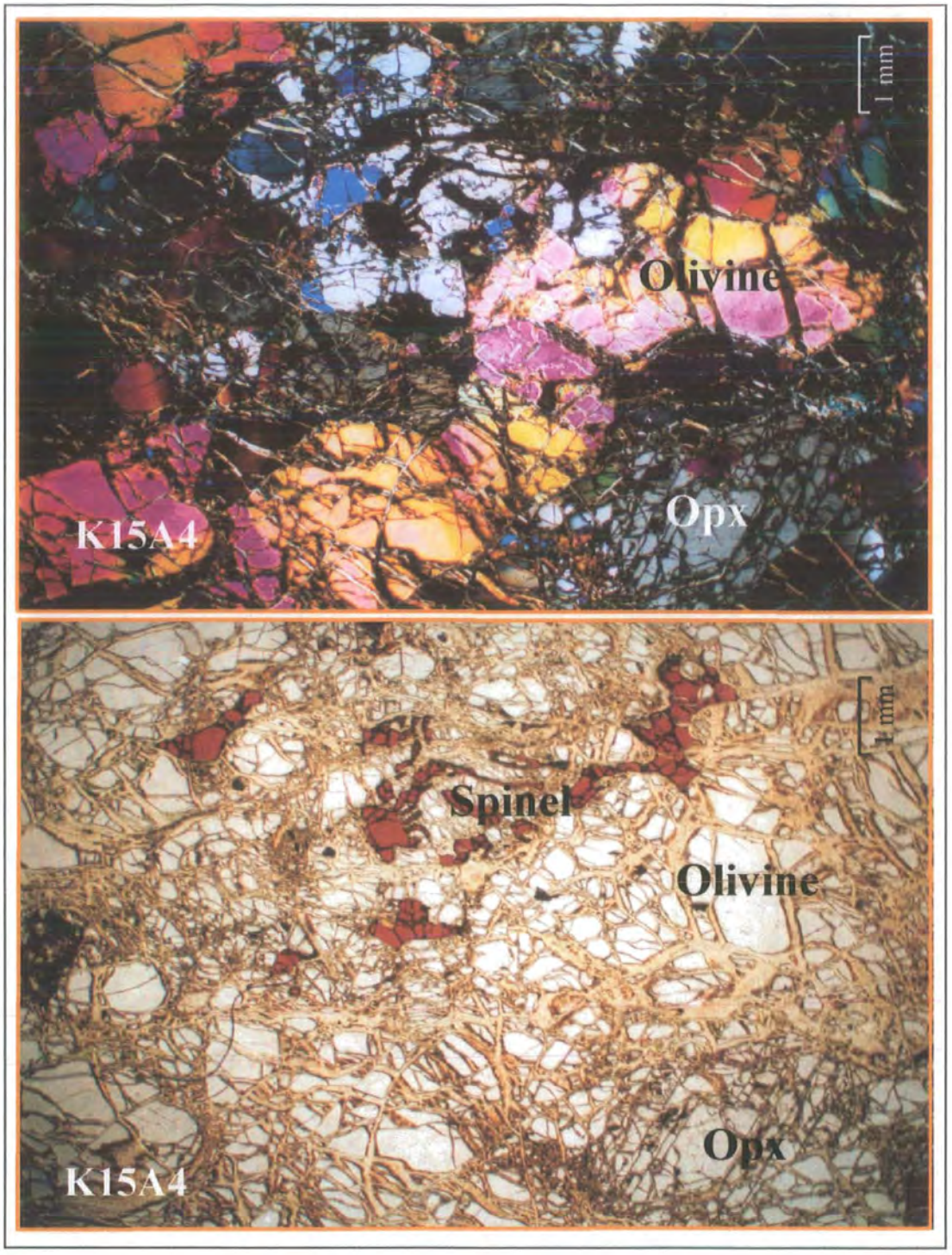

Figure 5.6 (b) Photomicrographs of peridotite xenolith from the Batty Bay kimberlite, showing late stage interstitial spinel forming poikilitic intergrowth texture with olivine.

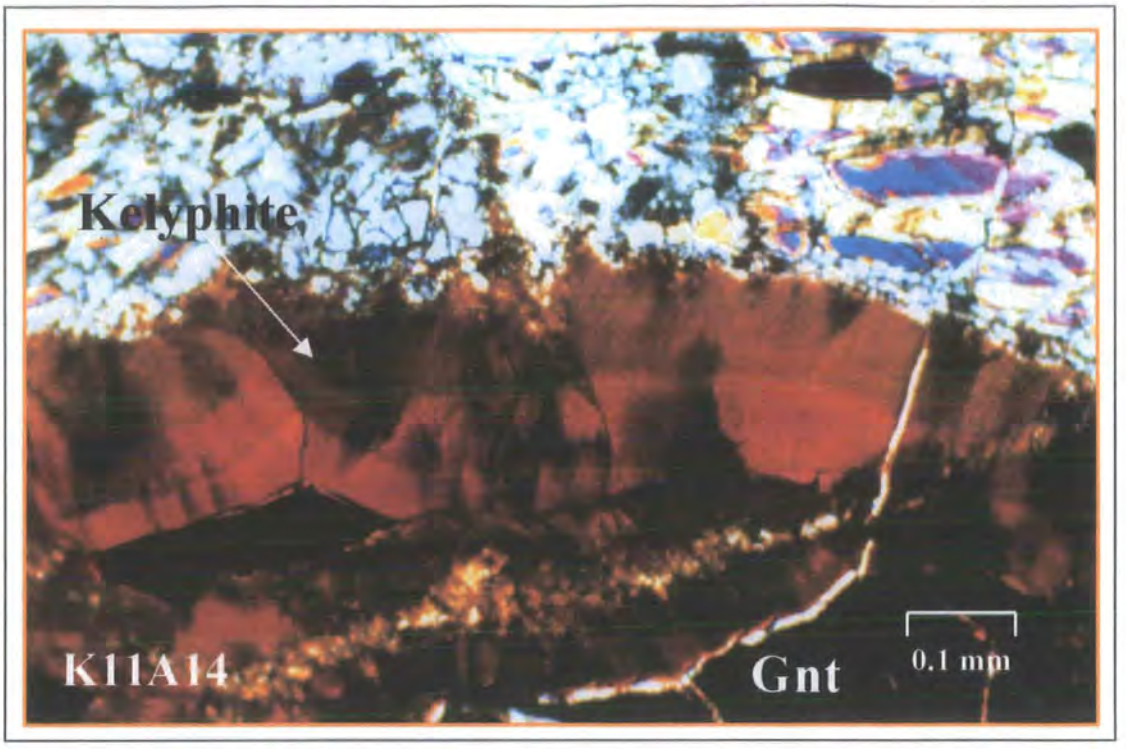

Figure 5.6 (c) Photomicrograph of peridotite xenolith from the Batty Bay kimberlite, showing zoned kelyphitic "corona" around garnet crystal.

The majority of peridotite specimens show coarse equant or coarse tabular texture (Figure 5.6a). Anhedral spinel is found in the interstices between olivine crystals or occasionally as irregular inclusions in garnet and pyroxene, which would suggest that deformation textures can be classified as primary (Mercier and Nicolas, 1975). Secondary alteration includes serpentine after olivine and orthopyroxene. Samples occasionally exhibit secondary carbonate veining.

Porphyroclastic Peridotites

Low-T peridotite xenoliths from the Batty Bay and Nord kimberlites occasionally exhibit non-fluidal porphyroclastic textures (Figure 5.6d). The porphyroclastic non-fluidal peridotites comprise olivine (72-85%), orthopyroxene (15-25%), with minor clinopyroxene (up to 3%), spinel (0-2%) and/or garnet (0-3%). Olivine porphyroclasts (5-15 mm) show undulose extinction and kink banding, and are associated with strain-free olivine neoblasts (0.1-0.5 mm). Orthopyroxene occurs as large porphyroclasts (up to 8 mm), and variably show evidence of strain. Clinopyroxene (up to 1mm), spinel (up to 3 mm) and garnet (up to 5mm) are optically similar to those found in coarse peridotites.

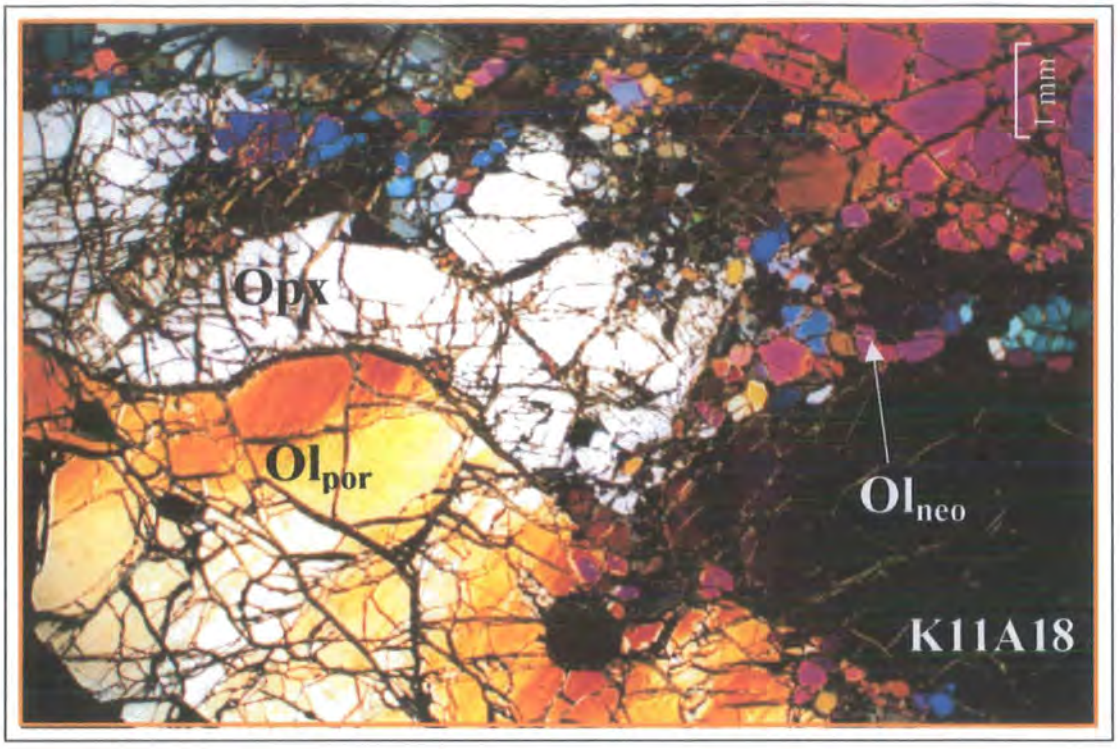

Figure 5.6 (d) Photomicrograph of peridotite xenolith from the Batty Bay kimberlite, showing porphyroclastic non-fluidal texture in peridotite.

5.4.1.b JP and Nikos

Coarse Peridotite

Xenoliths of coarse peridotite are composed of olivine (55-80%), and lesser amounts of clinopyroxene (0-8%), orthopyroxene (10-30%), spinel (0-2%) and/or garnet (0-15%). The predominant rock types are lherzolite and minor harzburgite. Coarse peridotite occurs in spinel, spinel-garnet and garnet facies. The coarse texture derives from early crystallisation of large subhedral olivine (up to 10 mm) and orthopyroxene (2-7 mm) and these dominate the mineral assemblage. Clinopyroxene occurs as emerald-green anhedral equant crystal (1-5 mm), with smooth boundaries. Clinopyroxene also occurs in some peridotites as anhedral, tabular crystals along the margins between olivine crystals. Spinel forms anhedral crystals up to 1 mm in size. Lilac coloured garnet, 1-3 mm, is subhedral to anhedral and is variably surrounded by kelyphitic rims containing phlogopite and spinel. In some instances phlogopite forms subhedral tabular crystals that may be in textural equilibrium with the primary mantle mineralogy, which would suggest a primary metasomatic origin (Winterburn *et al.*, 1990). Generally however, phlogopite is found in close relationship with garnet and

clinopyroxene. Possibly these grew from garnet during hydrous reaction, alternatively garnet may have grown from phlogopite during dehydration. Rarely orthopyroxenes show exsolution lamellae of clinopyroxene.

Generally the peridotite xenoliths are coarse equant or coarse tabular in texture, and show the same features as xenoliths from Batty Bay. Secondary alteration includes serpentine after olivine and orthopyroxene. Secondary carbonate veining is also apparent in some samples.

Porphyroclastic Peridotites

A small number of xenoliths exhibit non-fluidal porphyroclastic textures. Porphyroclastic non-fluidal peridotite comprises olivine (65-80%), orthopyroxene (15-25%), clinopyroxene (1-4%), spinel (0-2%) and/or garnet (0-9%). Olivine porphyroclasts (5-10 mm) show undulose extinction and kink banding. These are associated with strain-free olivine neoblasts (0.1-0.5 mm). Orthopyroxene occurs as large porphyroclasts (up to 4 mm) and vary between showing evidence of strain and showing none. Clinopyroxene (up to 2mm) and garnet (up to 3mm) are optically similar to those found in coarse peridotites.

5.4.2 Mineral Chemistry

Electron-microprobe analyses of olivine and garnet mineral compositions were performed at the Geological Survey of Canada using a CAMECA SX-50 microprobe, operating in a wavelength dispersion mode (see Appendix B for operating conditions). Mineral analyses are listed in Tables 5.2 and 5.3.

Garnets were analysed for trace elements using the Guelph scanning proton microprobe (Department of Physics, University of Guelph), and the data was processed via the Guelph PIXE software package (see Appendix B for operating conditions). Mineral analyses are listed in Table 5.4.

5.4.2.a Olivine

Representative olivine analyses for low-temperature Somerset Island peridotites are presented in Table 5.2. Individual olivine crystals are homogenous in thin section and show no evidence of chemical zonation. Although serpentine veins crosscut many individual olivine crystals, most grains have fresh cores.

Table 5.2 Representative olivine analyses for Somerset Island peridotites. These yield cation totals, based on 4 oxygens, between 2.996 and 3.020 (average 3.014), comparable with a theoretical 3.000 cation total. Olivines from lherzolites produce a range and average in cation totals identical to that for the whole suite. Harzburgites, however, yield cation totals consistently above the theoretical 3.000, with a range of 3.001 to 3.019 (average 3.014). Silicon per formula unit is also variable ranging from 0.979 to 1.002 (average 0.985) atoms per formula unit (AFU) in lherzolites, and 0.979 to 0.997 (average 0.985) AFU for harzburgites. The sum of octahedrally co-ordinated cations within the Somerset Island suite is approximately 2.016, close to the theoretical value of 2.

Sample	**XO4**	**XO5**	**XO6**	**XO7**	**JP1-X2**	**JP3-X1**	**JP3-X**	**JPS-1**	**JPS-2**
Type	Core	Core	Core	Core	Core	Core	Core	Core	Core
SiO_2	39.99	39.67	40.30	39.60	39.81	40.08	39.66	40.05	40.03
TiO_2	0.00	0.02	0.01	0.00	0.00	0.01	0.04	0.03	0.01
Al_2O_3	0.03	0.02	0.00	0.05	0.00	0.03	0.04	0.03	0.03
Cr_2O_3	0.00	0.04	0.02	0.05	0.00	0.06	0.08	0.02	0.05
FeO	8.09	7.85	8.00	7.22	7.69	7.52	7.56	7.45	7.43
MnO	0.11	0.11	0.11	0.11	0.07	0.16	0.10	0.09	0.14
MgO	50.94	50.68	50.37	50.90	50.75	51.31	50.41	50.83	50.89
CaO	0.04	0.04	0.02	0.04	0.01	0.07	0.04	0.00	0.04
Na_2O	0.00	0.00	0.00	0.00	0.00	0.00	0.00	0.00	0.00
NiO	0.37	0.36	0.35	0.40	0.35	0.35	0.37	0.42	0.39
Cations O =4									
Si	0.980	0.980	0.990	0.979	0.983	0.980	0.983	0.985	0.984
Al	0.001	0.000	0.000	0.001	0.000	0.001	0.001	0.001	0.001
Ti	0.000	0.000	0.000	0.000	0.000	0.000	0.001	0.001	0.000
Fe	0.166	0.162	0.164	0.149	0.159	0.154	0.157	0.153	0.153
Mn	0.002	0.002	0.002	0.002	0.002	0.003	0.002	0.002	0.003
Mg	1.861	1.866	1.845	1.876	1.867	1.870	1.862	1.864	1.865
Ca	0.001	0.001	0.001	0.001	0.000	0.002	0.001	0.000	0.001
Na	0.001	0.001	0.000	0.000	0.000	0.001	0.000	0.000	0.000
Cr	0.000	0.001	0.000	0.001	0.000	0.001	0.002	0.000	0.001
Ni	0.007	0.007	0.007	0.008	0.007	0.007	0.007	0.008	0.008
Sum	3.020	3.020	3.010	3.019	3.017	3.019	3.015	3.014	3.015
Mg#	0.918	0.920	0.918	0.926	0.922	0.924	0.922	0.924	0.924

Table 5.2 (continued) Olivine analyses.

Sample	JPS4	JPS-6A	JPS-6B	JPN-2	JPN-3A	JPN3B	JPN-4	JPN-9	JPN-11
Type	Core	Core	Core	Core	Core	Core	Core	Core	Core
SiO_2	40.94	39.73	39.36	39.84	39.96	41.57	40.07	39.83	41.26
TiO_2	0.02	0.04	0.02	0.00	0.01	0.04	0.04	0.03	0.05
Al_2O_3	0.02	0.06	0.01	0.05	0.05	0.04	0.04	0.03	0.00
Cr_2O_3	0.08	0.08	0.00	0.06	0.04	0.02	0.04	0.10	0.14
FeO	7.25	8.13	7.78	7.97	7.54	8.11	7.95	7.64	7.57
MnO	0.01	0.12	0.11	0.13	0.13	0.04	0.12	0.15	0.15
MgO	50.82	50.55	50.25	50.56	50.90	50.61	50.79	50.64	50.92
CaO	0.05	0.05	0.04	0.06	0.00	0.01	0.05	0.06	0.05
Na_2O	0.00	0.00	0.00	0.00	0.00	0.00	0.00	0.00	0.00
NiO	0.33	0.41	0.39	0.39	0.35	0.42	0.36	0.40	0.43
Cations O =4									
Si	0.997	0.979	0.980	0.981	0.983	1.002	0.983	0.982	0.997
Al	0.001	0.002	0.000	0.002	0.001	0.001	0.001	0.001	0.000
Ti	0.000	0.001	0.000	0.000	0.000	0.001	0.001	0.001	0.001
Fe	0.148	0.167	0.162	0.164	0.155	0.164	0.163	0.157	0.153
Mn	0.000	0.002	0.002	0.003	0.003	0.001	0.003	0.003	0.003
Mg	1.846	1.856	1.865	1.857	1.866	1.819	1.857	1.861	1.834
Ca	0.001	0.001	0.001	0.002	0.000	0.000	0.001	0.002	0.001
Na	0.000	0.000	0.001	0.000	0.000	0.000	0.000	0.000	0.000
Cr	0.002	0.002	0.000	0.001	0.001	0.000	0.001	0.002	0.003
Ni	0.006	0.008	0.008	0.008	0.007	0.008	0.007	0.008	0.008
Sum	3.001	3.019	3.020	3.017	3.016	2.996	3.016	3.016	3.001
Mg#	0.926	0.917	0.920	0.919	0.923	0.918	0.919	0.922	0.923

Table 5.3 Representative garnet analyses for Low-T Somerset Island peridotites.

Sample	XO4	XO5	XO6	JP1-X2	JP3-X	JPS-1	JPS-2	JPS-4	JPS-6A	JPS-6B	JPN-2	JPN-3A	JPN-3B	JPN-4	JPN-9	JPN-11
Type	Core	Core	Core	Core	Core	Core	Core	Core	Core	Core	Core	Core	Core	Core	Core	Core
SiO_2	41.09	40.70	40.45	40.52	40.32	40.54	40.27	41.62	40.80	41.00	41.15	40.87	41.56	40.95	37.00	39.99
TiO_2	0.18	0.40	0.19	0.09	0.18	0.10	0.24	0.23	0.23	0.30	0.30	0.26	0.31	0.14	0.12	0.29
Al_2O_3	21.59	20.06	21.03	20.52	18.26	18.31	18.09	18.37	20.68	20.86	17.86	19.33	19.15	19.82	20.86	17.69
Cr_2O_3	2.49	4.29	3.49	4.13	7.21	6.97	7.10	6.80	3.53	3.68	7.07	5.39	5.55	4.91	4.53	7.69
FeO	7.21	6.31	8.33	7.23	5.99	6.40	6.36	6.16	6.73	6.92	7.06	6.57	6.77	6.54	7.97	6.62
MnO	0.40	0.30	0.53	0.41	0.30	0.32	0.31	0.38	0.33	0.36	0.34	0.30	0.41	0.32	0.38	0.31
MgO	21.51	21.46	19.96	20.94	20.65	20.84	20.17	20.02	21.53	21.66	19.98	21.31	20.58	21.34	23.80	19.84
CaO	4.45	5.14	5.10	5.02	6.18	5.78	6.34	6.20	4.57	4.72	5.95	5.32	5.35	5.30	3.63	6.29
Na_2O	0.00	0.01	0.00	0.00	0.00	0.00	0.00		0.02	0.01		0.00		0.00	0.00	0.00
NiO	0.02	0.00	0.02	0.00	0.05	0.02	0.03		0.04	0.06		0.02		0.04	0.00	0.03
Si	2.948	2.941	2.933	2.933	2.935	2.944	2.943	3.004	2.948	2.935	2.985	2.946	2.991	2.948	2.706	2.938
Al	0.010	0.022	0.010	0.005	0.010	0.005	0.013	0.013	0.012	0.016	0.016	0.014	0.017	0.008	0.007	0.016
Ti	1.826	1.709	1.798	1.751	1.566	1.567	1.558	1.562	1.762	1.759	1.527	1.643	1.624	1.681	1.799	1.532
Cr	0.141	0.245	0.200	0.236	0.415	0.400	0.410	0.388	0.202	0.208	0.405	0.307	0.316	0.279	0.262	0.447
Fe3+	0.061	0.069	0.049	0.061	0.062	0.069	0.062	0.028	0.063	0.067	0.055	0.074	0.043	0.070	0.188	0.056
Fe2+	0.372	0.313	0.456	0.376	0.303	0.320	0.327	0.344	0.344	0.347	0.373	0.322	0.364	0.324	0.300	0.351
Mn	0.025	0.019	0.032	0.025	0.019	0.019	0.019	0.023	0.020	0.022	0.021	0.018	0.025	0.019	0.024	0.019
Mg	2.300	2.311	2.158	2.260	2.241	2.256	2.197	2.153	2.320	2.311	2.160	2.291	2.208	2.290	2.595	2.173
Ca	0.342	0.398	0.396	0.389	0.482	0.450	0.496	0.480	0.354	0.362	0.462	0.411	0.413	0.409	0.284	0.495
Sum	8.026	8.026	8.032	8.037	8.031	8.031	8.026	7.995	8.024	8.028	8.005	8.027	8.001	8.027	8.163	8.027
Mg#	0.842	0.858	0.810	0.838	0.860	0.853	0.850	0.853	0.851	0.848	0.835	0.853	0.844	0.853	0.842	0.842
Almandine	9.54	7.24	11.84	8.84	3.16	2.69	4.27	5.92	8.63	8.16	3.98	5.41	7.14	7.26	0.00	3.77
Andradite	3.11	1.02	2.50	1.17	0.00	0.00	0.00	0.00	1.74	1.70	0.00	0.00	0.00	0.00	0.00	0.00
Grossular	1.30	0.00	0.77	0.00	0.00	0.00	0.00	0.00	0.00	0.00	0.00	0.00	0.00	0.00	0.00	0.00
Pyrope	78.02	78.60	73.56	77.04	79.16	80.55	77.54	76.27	78.68	78.75	78.47	79.66	77.51	78.13	89.49	77.81
Spessartine	0.83	0.63	1.10	0.86	0.66	0.69	0.67	0.81	0.68	0.74	0.76	0.63	0.87	0.66	0.00	0.69
Uvarovite	7.20	12.52	10.23	12.09	17.02	16.06	17.51	16.99	10.27	10.65	16.79	14.30	14.48	13.95	10.51	17.73

Table 5.4 Trace element composition of peridotitic garnet (ppm) and estimated Ni-in-garnet temperatures. Pressures estimated from the steady state geotherm of Somerset Island lithospheric mantle (44mW/m^2, Kjarsgaard and Peterson, 1992)

Sample	XO4	XO5	XO6	JP1-X2	JP3-X	JPS-1	JPS-2	JPS-4	JPS-6A
Trace Elements (ppm)									
Zn	11.8	7.6	8.1	7.3	12.2	11.6	10.6	6.9	13.7
Ga	10.3	5.6	6.3	9.2	8	0	3.9	5.3	10.2
Y	19.4	19.3	9.1	16.5	9.1	5.7	5.5	7	19.5
Zr	20.7	50.6	7.5	15.1	28.4	128.2	86	80.8	60.3
Ni	32.5	71.4	22.4	24.2	68.4	69.4	54.1	55.2	53
Ni temperatures									
T (oC)	**951**	**1226**	**865**	**884**	**1200**	**1152**	**1093**	**1155**	**1066**
P (GPa)	3.36	5.1	2.94	3.06	4.89	4.57	4.1	4.59	4.03

Sample	JPS-6B	JPN-2	JPN-3A	JPN-3A	JPN-3B	JPN-4	JPN-9	JPN-11	JPN-11
Trace Elements (ppm)									
Zn	14.2	12.5	11.3	10.6	8.5	11.3	10.6	13	9.3
Ga	8.8	5.8	5.3	2.5	3.2	5.3	3.9	1.2	4.5
Y	13.3	18	8.1	12.9	9	8.4	14.6	21.6	13.4
Zr	59.2	60.9	31.6	34.3	36	47.9	53	101	100.4
Ni	80.8	59.2	65.9	74.8	59.6	73.8	23.9	74.9	60
Ni temperatures									
T (oC)	**1242**	**1204**	**1140**	**1262**	**1097**	**1241**	**850**	**1190**	**1089**
P (GPa)	5.3	4.97	4.88	5.8	4.2	5.3	2.88	4.56	4.05

Olivine in Somerset Island peridotites is magnesium rich and ranges in magnesium number ($Mg^{\#}$ = Mg/{Mg+Fe}) from 0.917 to 0.926 (average 0.921). This is comparable to the reported range of 0.913 to 0.927, from previous studies of Somerset Island peridotite xenoliths by Kjarsgaard and Peterson (1992). The most magnesian olivine (Fo_{92-93}) occurs in harzburgites (Figure 5.7) and ranges in $Mg^{\#}$ from 0.922 to 0.926 (average 0.924). The $Mg^{\#}$ for lherzolites ranges from 0.917 to 0.923 (average 0.920).

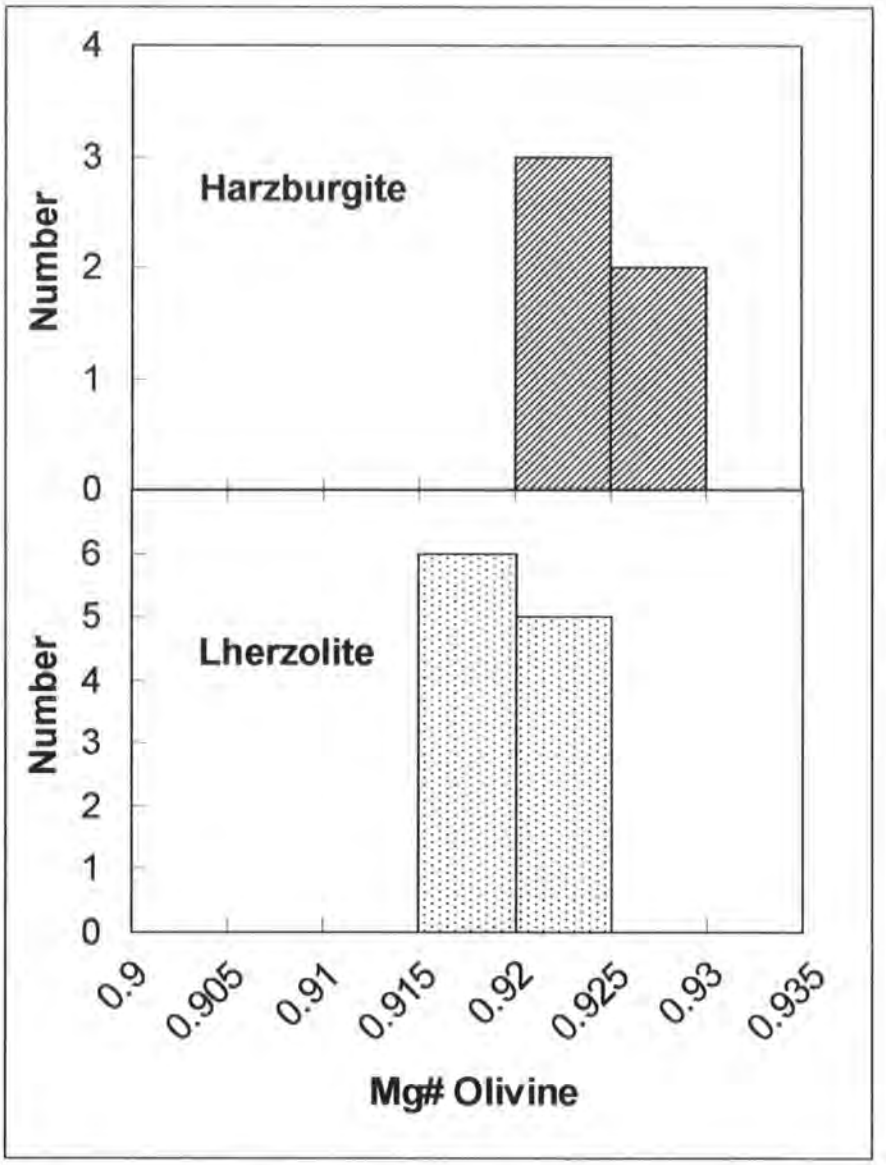

Figure 5.7 Histograms of $Mg^{\#}$ of olivine {Mg/(Mg+Fe)} for Somerset Island peridotites.

This suggests that higher values of $Mg^{\#}$ occur in the more refractory harzburgitic peridotites. The dataset is small however and this may be an artefact of sample selection. If we consider the xenoliths in terms of facies, coarse peridotites from the spinel-garnet facies are slightly more magnesian rich (0.918-0.926, average 0.923) than

those from garnet facies (0.915-0.923, average 0.920). Only two low-T porphyroclastic samples were analysed and these lie within the range for coarse peridotites at a $Mg^{\#}$ of 0.919, suggesting that there is no compositional difference between textural types. The average Somerset Island olivine $Mg^{\#}$ for this study at 0.921 +/- 0.003 is slightly lower, but within error of that reported by Schmidberger *et al* (1999) at 0.923. Concentrations of Ni in olivine range from 0.33 to 0.43 wt% (average 0.38 wt% NiO). Ni concentrations in olivines from lherzolites and harzburgites span similar ranges as do spinel-garnet and garnet facies. Olivines from Somerset Island peridotites have slightly elevated levels of Cr (0-0.13 wt% Cr_2O_3), Ca (0-0.07 wt% CaO) and Ti (0-0.05 wt% TiO_2). No systematic variation was observed for these values in relation to other oxide components within the mineral.

5.4.2.a Garnet

The garnet from Somerset Island peridotites is a chromium pyrope with high MgO, low CaO and $Mg^{\#}$ ranging from 0.81 to 0.86 (Table 5.3). The pyrope content of the garnet ranges from 74 to 90%. A summary of the end-member compositions is given in Table 5.3. The garnets are homogeneous and exhibit no chemical zoning on a thin-section scale. The Cr_2O_3 content within the garnets ranges from 2.5 to 7.7 wt%. On average, garnet from harzburgites is more Cr_2O_3 rich (6.58 +/- 0.82 wt%) than garnet from lherzolites (4.67 +/- 1.57 wt%). Very little variation is observed between garnet from peridotites of different facies or textures. The garnets can generally be classified as group 9 (G9) garnets in the statistical classification scheme of Dawson and Stephens (1975), in agreement with previous studies of Somerset Island peridotite xenoliths (Mitchell, 1978; Jago and Mitchell, 1987; Mitchell, 1987; Kjarsgaard and Peterson, 1992; Schmidberger and Francis, 1999). Plotted as Cr_2O_3 vs. CaO (Figure 5.8), pyrope compositions define a common lherzolitic trend parallel to the G9-G10 boundary.

Trace elements were measured in the garnets and these contain 22-81 ppm Ni, 0-10.3 ppm Ga, 6-22 ppm Y, and 8-128 ppm Zr (Table 5.4). More than half of the Somerset Island peridotitic garnet show Y concentration exceeding 10 ppm, and Zr exceeding 30 ppm. This is similar to that reported for peridotite xenoliths from the Jericho kimberlite (Kopylova *et al.*, 1999b). Elevated levels of Y and Zr are considered to represent high-temperature and low-temperature metasomatic enrichment respectively (Griffin and Ryan, 1995; Griffin *et al.*, 1996). The link between temperature and enrichment of Y and Zr is therefore not evident at Somerset Island. No correlation exists between Y and

Zr concentration and Ni content. Here, as at the Jericho kimberlite (Kopylova *et al.*, 1999b), the cryptic metasomatism was not associated with any particular range of temperature.

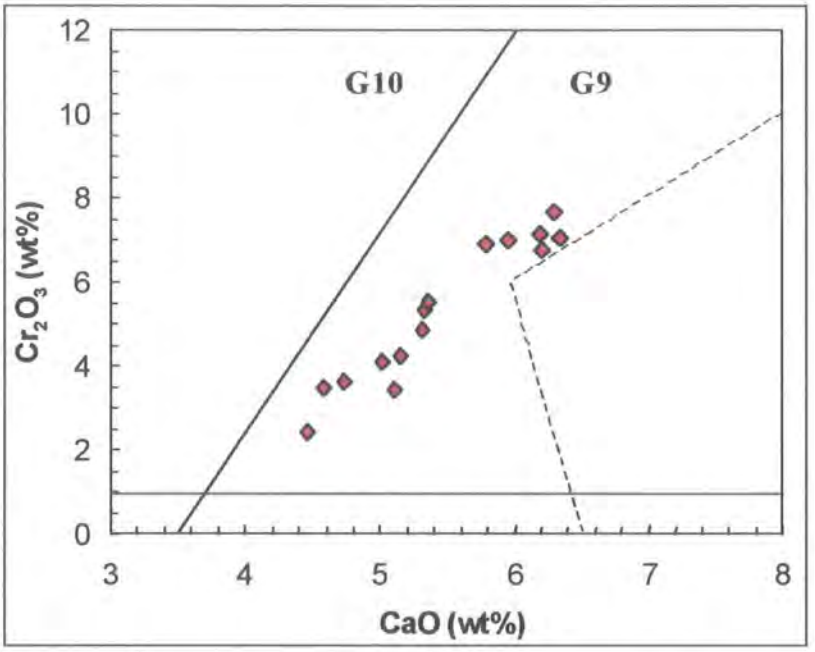

Figure 5.8 A Cr_2O_3 vs. CaO plot for garnet in Somerset Island peridotites. Fields shown for garnets (G9, G10 and all non-peridotitic garnets) are from Dawson and Stephens (Dawson and Stephens, 1975).

5.4.3 Pressure-Temperature Calculations

In the absence of full microprobe data on all phases, in all the rocks analysed, temperatures of equilibration for Somerset Island peridotites were calculated using a geothermometric method (see Appendix F), based on the partitioning of Ni between chrome-pyrope and olivine (Griffin *et al.*, 1989; Kjarsgaard, 1992; Ryan *et al.*, 1996). This was done so that a stratigraphy could be constructed for the lithospheric mantle beneath Somerset Island based on model age determinations.

Temperatures were calculated for the xenoliths (Table 5.4) using measured Ni concentrations in olivine, which are commonly higher than the fixed value of 2900 ppm used by Ryan *et al* (1996). Previous studies of Somerset Island peridotites (Kjarsgaard and Peterson, 1992; Schmidberger and Francis, 1999), using standard three and four-phase geothermobarometers, have defined a steady-state geotherm for the lithospheric mantle beneath Somerset Island of 44 mW/m^2 (Figure 5.9).

The temperature of equilibration for the Somerset Island peridotites in this study were cross-correlated with the steady state geotherm of Somerset Island lithospheric

mantle to calculate equivalent pressures of formation. Temperatures within the Somerset Island suite range from 850 to 1260 °C, and corresponding pressure range from 2.9 to 5.8 GPa.

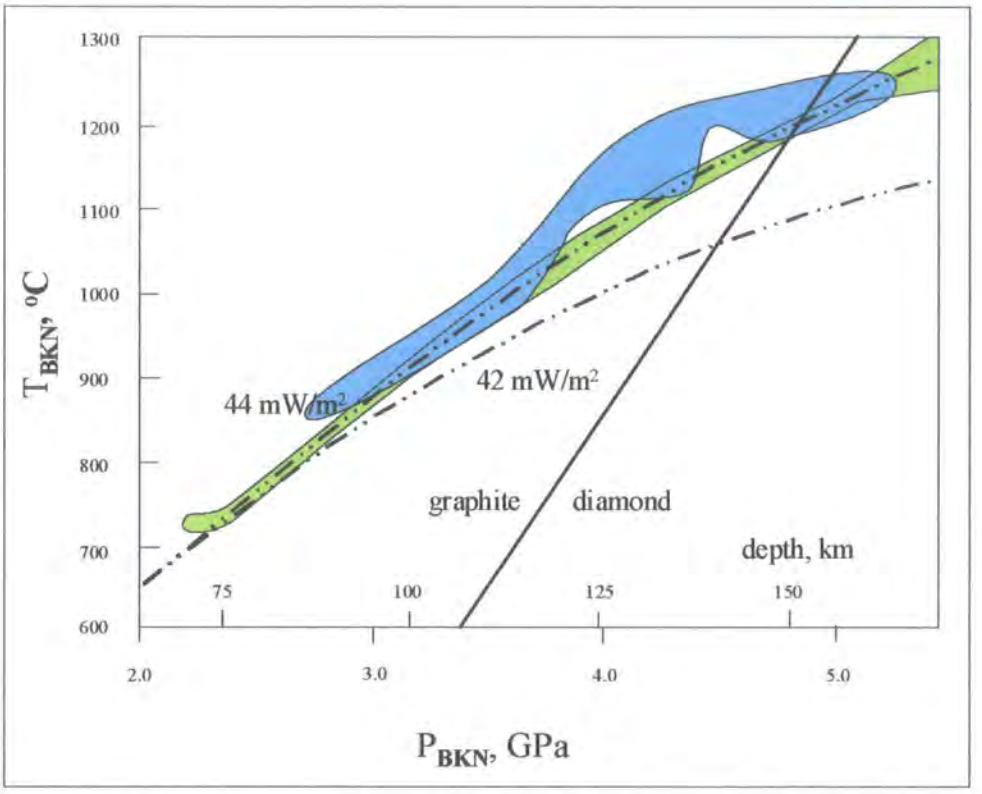

Figure 5.9 Steady state geotherm for Somerset Island peridotites (44 mW/m^2), calculated by Kjarsgaard and Peterson (1992) and Schmidberger and Francis (1999) using the experimentally calibrated thermobarometers of Brey *et al* (1990). Data from Kjarsgaard and Peterson (1992) represented by the blue field, Schmidberger and Francis (1999) by the green field.

High-temperature porphyroclastic peridotites from the Kaapvaal craton have been interpreted as representing the asthenospheric mantle, whereas coarse peridotites in contrast have been interpreted as representing lithospheric mantle (Boyd, 1987). Similar relationships have been reported from the Slave craton, and peridotite xenoliths from the Jericho kimberlite (Kopylova *et al.*, 1999b). No correlation exists between texture and equilibration conditions observed in the Somerset Island peridotites, consistent with the findings from previous studies of xenoliths from the Batty Bay (Kjarsgaard and Peterson, 1992), and Nikos kimberlites (Schmidberger and Francis, 1999).

5.4.4 Discussion of mineral textures and chemistry

The mantle beneath Somerset Island has many features that are common to cratonic mantle elsewhere. The peridotites are mostly coarse textured and rarely display disrupted textures. The dominant rock type is peridotite, with Mg-enriched mineral compositions, similar to that reported for the Kaapvaal and Siberian cratons (Nixon, 1987a; Boyd *et al.*, 1997). Somerset Island peridotites are depleted in fusible elements compared to primitive mantle (McDonough, 1990). The xenoliths from this study of Somerset Island are generally equivalent to the low temperature suites from other cratons. A similarity in olivine composition between Somerset Island and other cratonic settings indicates a comparable degree of depletion. The range in $Mg^{\#}$ of olivine (0.92 to 0.93) parallels the average range for peridotites from Kaapvaal, Siberian (Udachnaya) and the Slave cratons (Boyd and Canil, 1997; Boyd *et al.*, 1997; MacKenzie and Canil, 1998; Kopylova *et al.*, 1999b), and reflect the highly refractory nature of the Somerset Island peridotite.

The compositional range found in the peridotitic garnet at Somerset Island, like those of the Kaapvaal craton, lie predominantly within the G9 field with a general lack of G10 sub-calcic garnet compositions, even within Somerset Island harzburgites. This is a feature shared by the Somerset Island, Jericho and Lesotho peridotite suites (Chapters 3 and 4). The scarcity of G10 garnets within the Somerset Island peridotites may be attributable to equilibration of harzburgite assemblages with lherzolite-dominated mantle (Boyd and Nixon, 1978), but alternatively it may indicate the disruption of low-Ca rocks in the presence of carbonate (Canil, 1990). Garnet within harzburgites is saturated in Ca despite an absence of clinopyroxene.

The Somerset Island xenoliths record a wide range of equilibration conditions in the lithospheric mantle, indicating a derivation from depths of 90 to 190 km. Although the pressure and temperature estimates for harzburgites and lherzolites overlap, the harzburgites tend to lie towards the higher end of the P-T range for the xenoliths. This would suggest that the upper section of the lithospheric mantle sampled by the kimberlite was more fertile than the lower section. Schmidberger and Francis (1999) made a similar observation for xenoliths from the Nikos kimberlite.

5.5 Xenolith whole-rock Major and Trace element geochemistry

5.5.1 Introduction

The peridotitic mantle underlying cratons has long been known to be chemically distinct by comparison to mantle from younger sub-continental and sub-oceanic settings (Boyd, 1989). Studies of cratonic peridotites indicate that they have undergone a history of melt extraction resulting in the depletion of fusible elements such as Fe, Al and Ca (Nixon, 1987a; Herzberg, 1993; Boyd *et al.*, 1997). The depletion in fusible elements compared to fertile mantle (Boyd and Mertzman, 1987), produces a buoyant low-density mantle-root that contributes to the stability of Archean continental lithosphere (Boyd and McCallister, 1976; Jordan, 1979). Shallow cratonic lithospheric mantle, although depleted in major elements, is enriched in light rare earth elements (LREE) and modal orthopyroxene (Menzies *et al.*, 1987; Boyd, 1989; McDonough, 1990). Enrichment in LREE has been interpreted as the interaction of lithospheric mantle with metasomatising, percolating fluids (Hawkesworth *et al.*, 1983; Menzies *et al.*, 1987).

It is important to assess the role of these processes on the formation of the lithospheric mantle, prior to applying the Re-Os isotope system. Using elemental data the chemical composition of the Somerset Island peridotites will be discussed, and models proposed for the observed range in compositions.

In order to compare major element analyses, the data was recalculated as anhydrous compositions to correct for serpentinisation, and normalised to 100%. Uncorrected major element data are presented in Table 5.5, and corrected anhydrous data in Table 5.6. Trace and rare earth element data are presented in Table 5.7.

5.5.2 Whole-Rock Elemental Data

5.5.2.a Major element composition

Whole-rock analyses for Somerset Island peridotites indicate that they are strongly depleted in fusible elements such as Ti, Ca, Al and Na compared to estimates of fertile mantle composition (Nixon and Boyd, 1973; McDonough, 1990), and generally depleted in FeO, in keeping with the magnesian nature of their olivines. Removal of a basaltic fraction from fertile mantle depletes magmaphile elements such as Al, but Mg remains primarily in the residue. A plot of Mg/Si vs Al/Si gives a strongly anti-correlated trend indicative of the degree of depletion (Figure 5.10).

Table 5.5 Major element compositions for Somerset Island peridotites. LOI: loss on ignition. Total Fe given as FeO. Lherz: lherzolite, Harz: harzburgite.

Sample	K11A14	K11A15	K11A16	K11A17	K11A18	K12A1	K13A1	K13A3	K13A4	K13A5	K13B4	K15A4	N1C	N2B	XO4
Major Elements in wt%															
SiO_2	42.40	41.30	41.60	41.20	41.10	42.00	38.60	43.50	38.80	41.40	44.10	41.70	41.50	42.40	44.30
TiO_2	0.04	0.08	0.03	0.06	0.04	0.01	0.02	0.04	0.04	0.23	0.08	0.02	0.11	0.09	0.09
Al_2O_3	1.10	1.00	1.30	0.90	0.80	0.90	0.90	0.40	1.40	1.10	0.80	0.90	0.80	0.70	2.30
FeO	7.20	7.02	6.57	6.93	6.93	7.02	7.02	6.75	7.02	6.93	6.93	6.84	7.56	7.29	7.02
MnO	0.12	0.11	0.10	0.11	0.11	0.11	0.10	0.11	0.09	0.19	0.10	0.09	0.26	0.11	0.12
MgO	44.72	43.47	43.27	43.27	45.44	44.85	38.84	44.96	34.41	39.50	43.96	43.11	44.32	45.93	39.90
CaO	0.73	1.10	1.22	0.93	0.47	0.60	1.37	0.50	2.90	0.82	0.63	0.30	0.69	0.72	2.28
Na_2O	0.00	0.00	0.10	0.00	0.00	0.00	0.00	0.00	0.00	0.00	0.00	0.00	0.00	0.00	0.10
K_2O	0.22	0.22	0.26	0.21	0.10	0.06	0.06	0.05	0.03	0.08	0.09	0.05	0.14	0.24	0.10
P_2O_5	0.03	0.03	0.04	0.04	0.02	0.01	0.03	0.02	0.03	0.04	0.02	0.04	0.03	0.02	0.02
Cr_2O_3	0.37	0.41	0.55	0.46	0.68	0.46	0.54	0.22	0.42	0.38	0.37	0.39	0.46	0.27	0.41
LOI	3.80	5.20	5.30	5.80	4.90	4.20	12.30	3.60	14.60	9.70	3.20	6.60	4.20	2.60	3.00
Total	100.73	99.94	100.34	99.91	100.59	100.22	99.78	100.15	99.74	100.37	100.28	100.04	100.07	100.37	99.64

Sample	XO5	XO6	XO7	JP1-X2	JP2-X2	JP3-X1	JP3-X	JPS-1	JPS-6A	JPS-6B	JPN-2	JPN-3A	JPN-3B	JPN-4	JPN-9	JPN-11
Major Elements in wt%																
SiO_2	42.70	41.10	44.40	43.00	42.20	41.50	41.50	42.30	41.50	41.30	41.40	44.00	43.70	43.40	42.30	44.60
TiO_2	0.05	0.07	0.03	0.04	0.08	0.04	0.06	0.05	0.06	0.05	0.13	0.08	0.07	0.10	0.02	0.03
Al_2O_3	1.60	3.10	0.20	1.30	0.60	0.10	0.80	0.60	1.40	1.60	0.70	1.10	1.10	1.70	0.70	0.70
FeO	7.47	7.20	6.84	7.29	6.75	7.29	7.02	6.75	7.29	7.29	8.01	6.84	6.75	7.02	7.38	7.11
MnO	0.11	0.13	0.10	0.21	0.10	0.10	0.08	0.09	0.10	0.10	0.10	0.15	0.10	0.11	0.10	0.11
MgO	42.46	39.16	44.80	43.58	43.22	45.72	44.20	43.20	43.17	42.68	44.59	42.74	42.13	42.84	44.44	43.05
CaO	1.23	1.68	0.24	1.32	0.95	0.40	0.47	0.98	1.28	1.65	0.52	0.76	1.18	0.98	0.74	0.85
Na_2O	0.00	0.00	0.00	0.00	0.00	0.00	0.00	0.00	0.00	0.00	0.00	0.00	0.00	0.00	0.00	0.00
K_2O	0.07	0.20	0.04	0.04	0.37	0.03	0.04	0.10	0.06	0.06	0.35	0.14	0.13	0.22	0.04	0.07
P_2O_5	0.01	0.03	0.01	0.03	0.02	0.01	0.01	0.02	0.02	0.02	0.02	0.02	0.02	0.02	0.02	0.02
Cr_2O_3	0.43	0.56	0.25	0.40	0.23	0.28	0.37	0.38	0.34	0.40	0.32	0.36	0.38	0.42	0.26	0.38
LOI	3.80	7.00	3.40	3.40	5.20	4.60	5.40	5.20	4.90	5.20	3.90	4.70	4.80	4.00	4.50	3.50
Total	99.93	100.23	100.31	100.61	99.72	100.07	99.95	99.67	100.12	100.35	100.04	100.89	100.36	100.81	100.50	100.42

Table 5. 6 Anhydrous major element data for low-T Somerset Island peridotites. $Mg^{\#}$ = Mg/(Mg+Fe). Modes were calculated using whole-rock compositions and converting to an equivalent modal mineralogy using mass balance relationships implied by observed mineralogy in Somerset Island peridotites. Additional mineral data from Mitchell (1977).

Sample	K11A14	K11A15	K11A16	K11A17	K11A18	K12A1	K13A1	K13A3	K13A4	K13A5	K13B4	K15A4	N1C	N2B	XO4
Major Elements in wt%															
SiO_2	43.74	43.59	43.77	43.78	42.95	43.74	44.12	45.05	45.57	45.66	45.43	44.63	43.29	43.37	45.84
TiO_2	0.04	0.08	0.03	0.06	0.04	0.01	0.02	0.04	0.05	0.25	0.08	0.02	0.11	0.09	0.09
Al_2O_3	1.13	1.06	1.37	0.96	0.84	0.94	1.03	0.41	1.64	1.21	0.82	0.96	0.83	0.72	2.38
FeO	7.43	7.41	6.91	7.36	7.24	7.31	8.02	6.99	8.24	7.64	7.14	7.32	7.88	7.46	7.26
MnO	0.12	0.12	0.11	0.12	0.11	0.11	0.11	0.11	0.11	0.21	0.10	0.10	0.27	0.11	0.12
MgO	46.14	45.88	45.53	45.98	47.49	46.71	44.40	46.57	40.42	43.57	45.28	46.14	46.23	46.98	41.29
CaO	0.75	1.16	1.28	0.99	0.49	0.62	1.57	0.52	3.41	0.90	0.65	0.32	0.72	0.74	2.36
Na_2O	0.00	0.00	0.11	0.00	0.00	0.00	0.00	0.00	0.00	0.00	0.00	0.00	0.00	0.00	0.10
K_2O	0.23	0.23	0.27	0.22	0.10	0.06	0.07	0.05	0.04	0.09	0.09	0.05	0.15	0.25	0.10
P_2O_5	0.03	0.03	0.04	0.04	0.02	0.01	0.03	0.02	0.04	0.04	0.02	0.04	0.03	0.02	0.02
Cr_2O_3	0.38	0.43	0.58	0.49	0.71	0.48	0.62	0.23	0.49	0.42	0.38	0.42	0.48	0.28	0.42
Ca/Al	0.97	1.49	1.27	1.40	0.79	0.90	2.06	1.69	2.80	1.01	1.06	0.45	1.16	1.39	1.34
Mg No	0.92	0.92	0.92	0.92	0.92	0.92	0.91	0.92	0.90	0.91	0.92	0.92	0.91	0.92	0.91
Trace Elements in ppm															
Ni	2380	2441	2435	2188	2408	2350	2407	2468	2128	2170	2519	2441	2495	2550	2034
Cr	2414	3542	4234	3502	2549	3409	3067	1203	3060	2247	2893	3054	3298	1598	3063
Co	107	111	100	100	102	102	103	107	100	96	105	103	109	108	95
V	28	32	40	34	21	26	28	17	56	63	27	30	24	22	50
Calculated modes in wt%															
Ol	75.24	77.43	74.43	76.73	83.18	76.18	67.88	73.07	52.6	59.19	67.25	73.13	77.53	80.83	56.49
OPX	17.14	14.32	15.06	16.19	12.89	19.01	21.86	24.15	27.81	33.75	27.53	23	15.67	14.04	23.91
CPX	1.28	4.01	3.89	3.37	1.47	2.4	6.28	1.9	13.9	3.36	1.09	0.27	2.1	2.5	7.38
Sp		0.06		0.11	0.01	2.4	3.98	0.88	5.63	3.7		0.01	1.05	0.01	
Gnt	6.34	4.19	6.63	3.6	2.45						4.14	3.6	3.65	2.62	12.22

Table 5.6 (continued) Anhydrous major element and selected trace element data for low-T Somerset Island peridotites.

Sample	XO5	XO6	XO7	JP1-X2	JP2-X2	JP3-X1	JP3-X	JPS-1	JPS-6A	JPS-6B	JPN-2	JPN-3A	JPN-3B	JPN-4	JPN-9	JPN-11
Major Elements in wt%																
SiO_2	44.42	44.09	45.82	44.23	44.65	43.47	43.89	44.78	43.58	43.41	43.06	45.74	45.73	44.83	44.06	46.02
TiO_2	0.05	0.08	0.03	0.04	0.08	0.04	0.06	0.05	0.06	0.05	0.14	0.08	0.07	0.10	0.02	0.03
Al_2O_3	1.66	3.33	0.21	1.34	0.63	0.10	0.85	0.64	1.47	1.68	0.73	1.14	1.15	1.76	0.73	0.72
FeO	7.77	7.72	7.06	7.50	7.14	7.63	7.42	7.14	7.65	7.66	8.33	7.11	7.06	7.25	7.69	7.33
MnO	0.11	0.14	0.10	0.22	0.11	0.10	0.08	0.10	0.11	0.11	0.10	0.16	0.10	0.11	0.10	0.11
MgO	44.17	42.00	46.23	44.83	45.73	47.89	46.75	45.73	45.34	44.86	46.38	44.43	44.09	44.25	46.29	44.42
CaO	1.28	1.80	0.25	1.36	1.01	0.42	0.50	1.04	1.34	1.73	0.54	0.79	1.23	1.01	0.77	0.88
Na_2O	0.00	0.00	0.00	0.00	0.00	0.00	0.00	0.00	0.00	0.00	0.00	0.00	0.00	0.00	0.00	0.00
K_2O	0.07	0.21	0.04	0.04	0.39	0.03	0.04	0.11	0.06	0.06	0.36	0.15	0.14	0.23	0.04	0.07
P_2O_5	0.01	0.03	0.01	0.03	0.02	0.01	0.01	0.02	0.02	0.02	0.02	0.02	0.02	0.02	0.02	0.02
Cr_2O_3	0.45	0.60	0.26	0.41	0.24	0.29	0.39	0.40	0.36	0.42	0.33	0.37	0.40	0.43	0.27	0.39
Ca/Al	1.04	0.73	1.62	1.37	2.14	5.40	0.79	2.21	1.23	1.39	1.00	0.93	1.45	0.78	1.43	1.64
Mg No	0.91	0.91	0.92	0.91	0.92	0.92	0.92	0.92	0.91	0.91	0.91	0.92	0.92	0.92	0.91	0.92
Trace Elements in ppm																
Ni	2303	1793	2722	2351	2367	2566	2439	2648	2498	2516	2455	2267	2309	2107	2619	2529
Cr	3099	4120	1024	2354	1525	2023	2860	2132	2314	2679	1760	2127	2660	2902	1421	2568
Co	105	84	109	104	100	108	104	106	106	108	111	96	96	96	111	107
V	37	42	14	32	19	16	23	26	36	41	24	26	33	36	21	27
Calculated modes in wt%																
Ol	67.8	64.2	69.75	72.06	71.93	81.84	76.25	73.11	74.45	74.32	78.1	63.67	63.78	66.02	75.1	63.33
OPX	19.65	16.39	29.38	17.4	22.49	15.37	18.56	20.97	13.46	10.79	15.73	29.26	27.01	23.23	18.47	30.49
CPX	2.9	0.1	0.85	4.41	3.99	1.55	0.4	4	3.76	5.46	1.29	1.26	3.6	1.57	1.84	2.21
Sp		trace	0.01	0.37	1.6	1.24		0.01			1.31					
Gnt	9.65	15.43	0.01	5.75			4.78	1.91	8.33	9.42	3.58	5.81	5.62	9.17	4.58	3.98

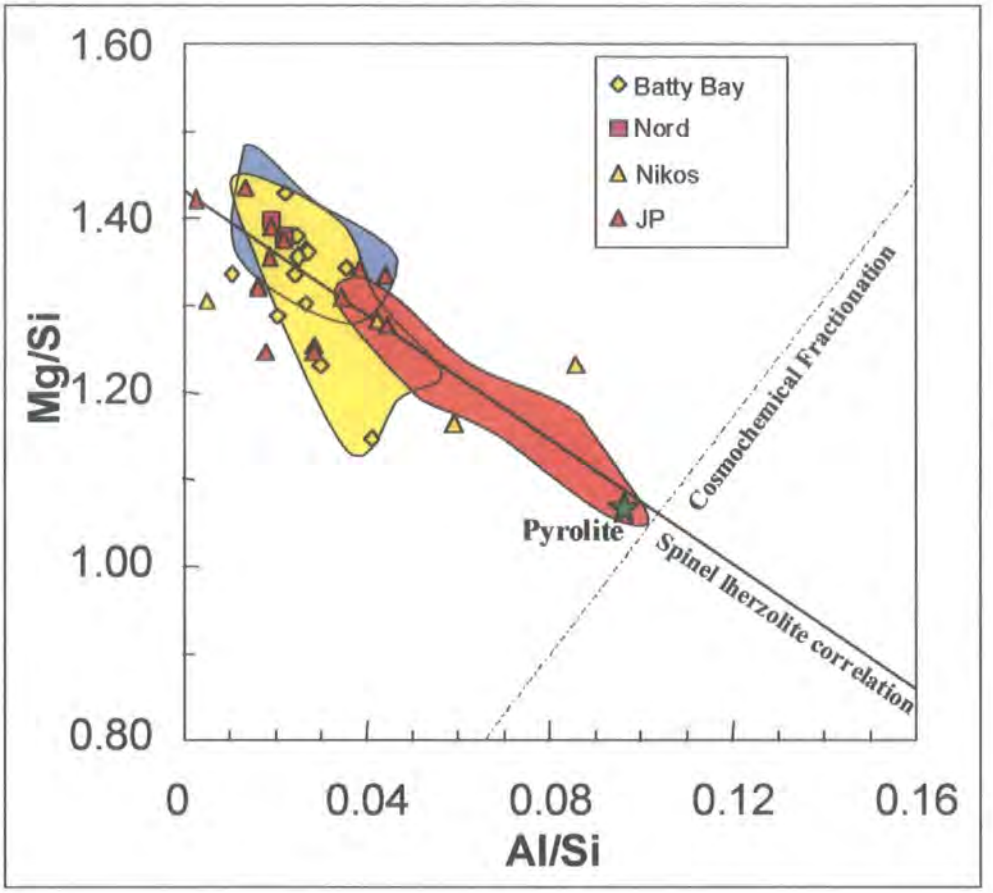

Figure 5.10 Mg/Si vs. Al/Si wt% ratios of low-T Somerset Island peridotites compared to the range for primitive spinel lherzolites erupted off craton (Morgan, 1986), represented by the red field. Kaapvaal low-T peridotites represented by yellow field, Siberian by the blue-grey field. Kaapvaal and Siberian data from Boyd and Mertzman (1987) and Boyd *et al* (1997). Additional data from Jagoutz (1979).

Off-craton spinel peridotites show a linear depletion trend on such a plot (Morgan, 1986), that intersects the cosmochemical fractionation line of Jagoutz (1979) near to the value for pyrolite (Ringwood, 1975). The Somerset Island low-T peridotites are in general highly depleted in Al and enriched in Mg (Figure 5.10). A secondary, overlying trend of Mg depletion relative to Al, or Si enrichment, causes some samples to deviate from the spinel lherzolite array, similar to that observed in peridotite xenoliths from the Kaapvaal craton (Pearson *et al.*, 1995a). MgO content of the peridotites ranges from 40.4 to 47.9 wt%. Whole rock magnesium numbers $Mg^{\#}$ for lherzolites (average 0.914) and harzburgites (average 0.918) indicate a shift towards higher values in the more refractory peridotites (Figure 5.11). The average whole rock $Mg^{\#}$ for Somerset Island peridotite suite is 0.915. This is lower than the average olivine $Mg^{\#}$ (0.921) for the peridotite suite and may suggest whole-rock enrichment in Fe, lowering bulk $Mg^{\#}$.

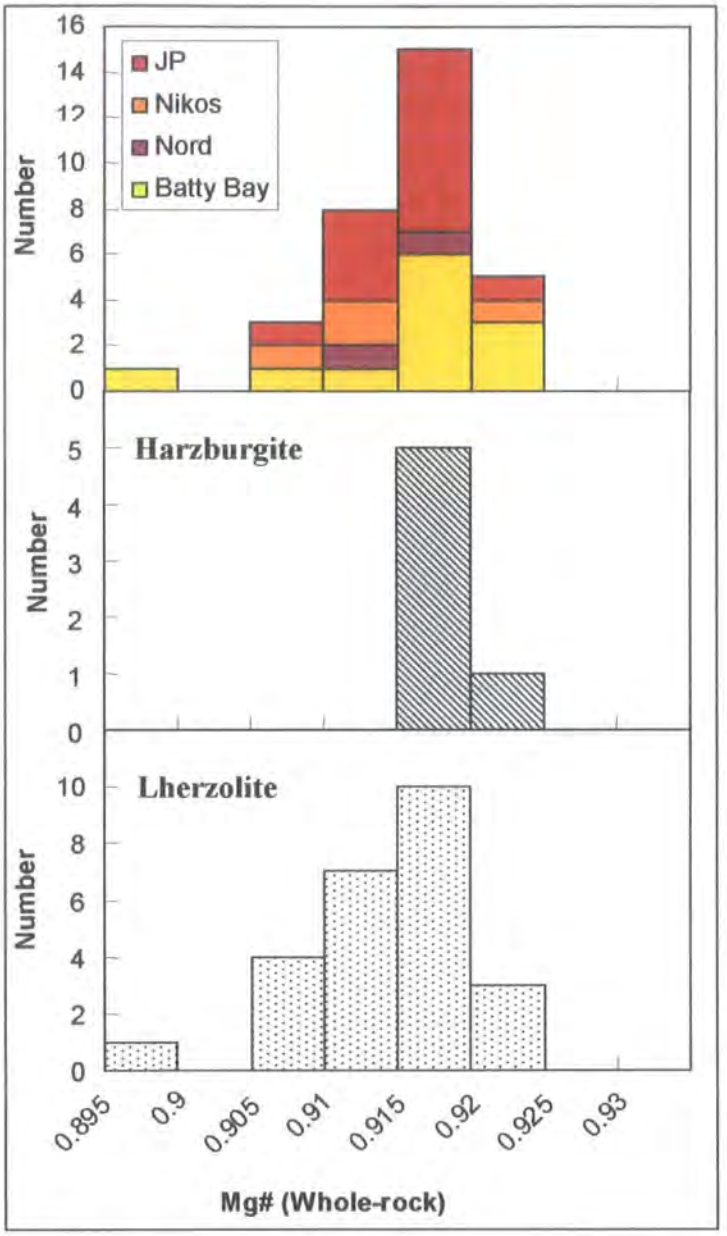

Figure 5.11 Histogram of whole rock $Mg^{\#}$ of Somerset Island peridotites.

When plotted on bivariate oxide-MgO plots, the major element compositions display several systematic trends. As MgO content increases, Al_2O_3 and CaO contents are shown to decrease (Figure 5.12). No systematic correlation appears to exist between MgO and FeO. However, FeO and TiO_2 may have initially formed a better correlation with MgO, with later scattering of data from metasomatic alteration. SiO_2 displays a negative trend with MgO, however several samples are enriched relative to primitive mantle compositions (Figure 5.12).

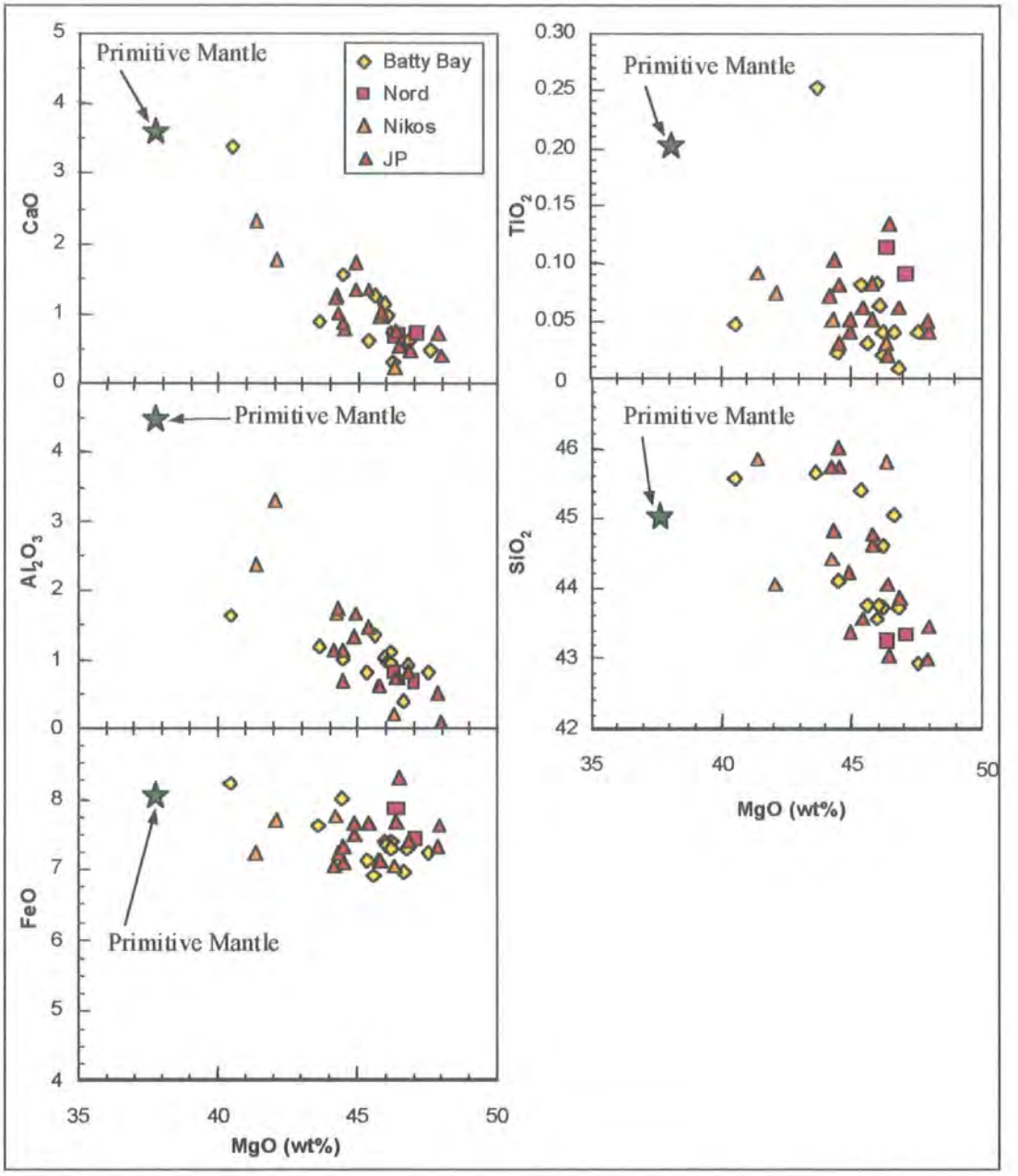

Figure 5.12 Variation of major elements with MgO (wt%) for Somerset Island peridotites. Primitive mantle, denoted by the star, after McDonough (1990).

The Somerset Island peridotites range in composition from depleted harzburgites to compositions more fertile than abyssal peridotites (Figure 5.13). Several peridotite samples show compositions as fertile as pyrolite, though with different Ca/Al ratios. In general the Somerset Island peridotites lie along the oceanic trend and therefore have higher Ca/Al values (0.73 to 2.8, mean = 1.46; Table 5.6) than reported for the Kaapvaal craton (average 0.73 Boyd, 1989). No systematic variation exists between peridotites from different facies or textural types for the Somerset Island suite.

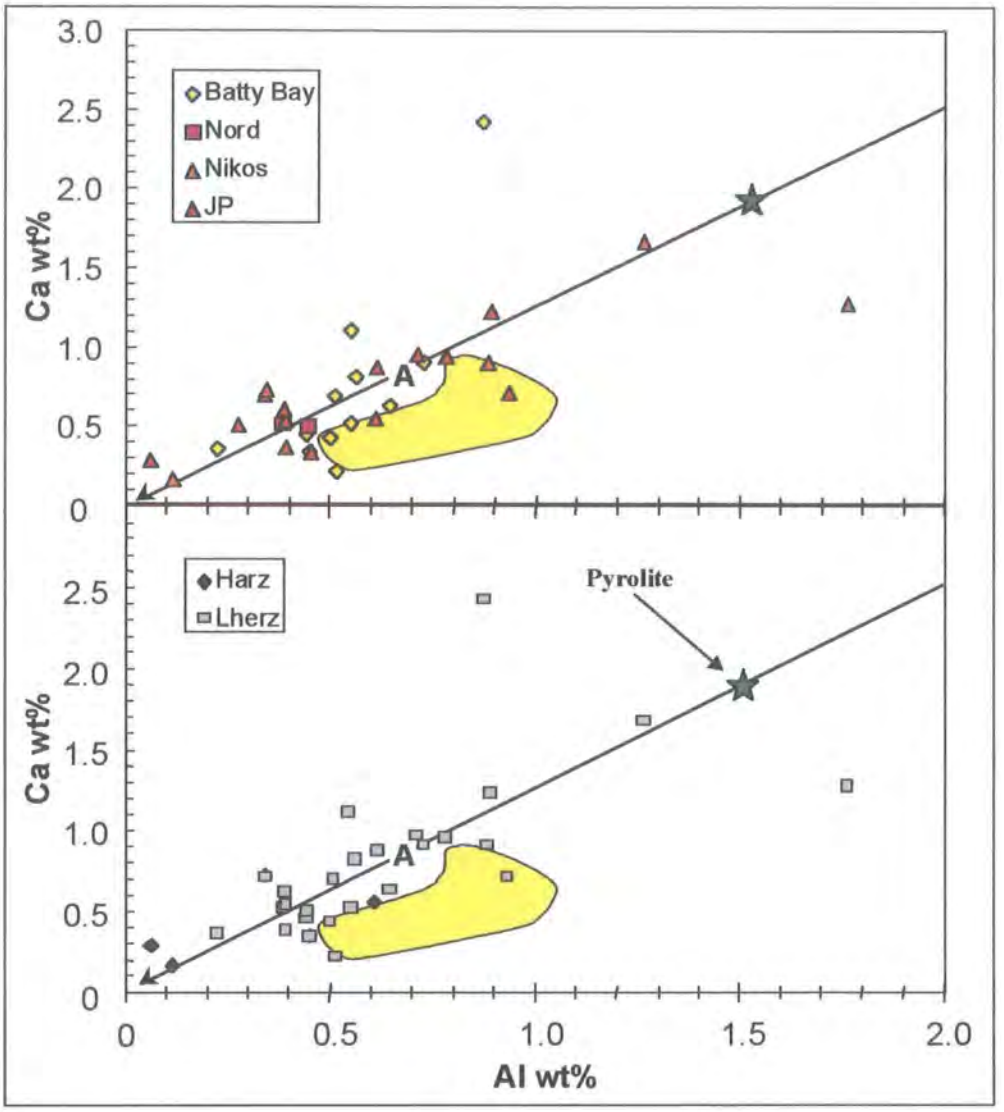

Figure 5.13 Composition of Somerset Island peridotites as wt% Ca vs. wt% Al. Line represents overall trend expected for the depletion of oceanic peridotite (Boyd, 1989). Also shown are average compositions for abyssal peridotite (Dick *et al.*, 1984), indicated by the letter A and pyrolite (Ringwood, 1979), indicated by star. Field represents low-T Kaapvaal peridotite (Boyd, 1989).

5.5.2.b Mineral Modes

The modal mineral proportions of Somerset Island xenoliths were calculated using whole rock compositions and converting to an equivalent modal mineralogy using mass balance relationships implied by observed mineralogy in Somerset Island peridotites (Table 5.6). The method is described in more detail in Appendix D. Mineral compositions from Mitchell (1977) were used along with data from this study during the calculations.

Somerset Island peridotites contain higher modal abundances of olivine (average 71%) than peridotites from Kaapvaal (61%, Boyd, 1989), and appear more similar to spinel peridotites from the Jericho kimberlite (72%, Kopylova and Russell, 2000). The

high modal olivine content is indicative of the highly refractory nature of the Somerset Island lithospheric mantle and suggests they are residues of high degrees of partial melting. The chemical signatures of the Somerset Island peridotites are similar to compositions reported for low-temperature peridotites from the Archean Kaapvaal and Siberian cratons but clearly distinct from oceanic domains when plotted as olivine $Mg^{\#}$ vs. modal olivine content (Figure 5.14).

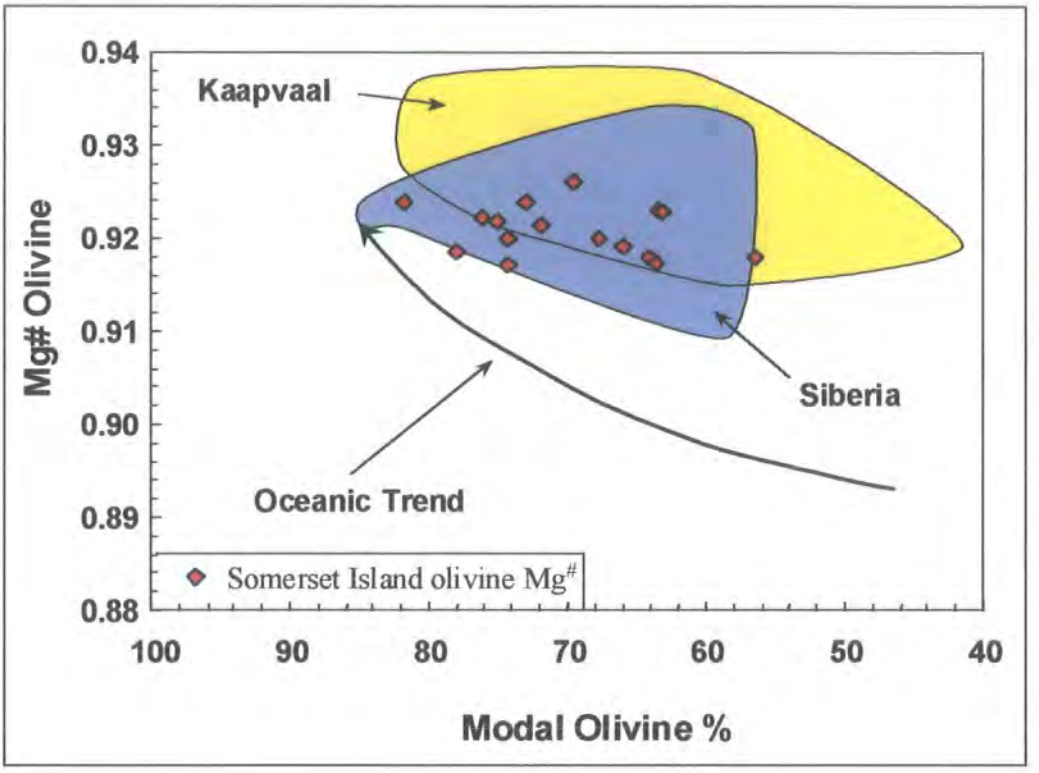

Figure 5.14 Olivine $Mg^{\#}$ vs. modal olivine content (%) for Somerset Island peridotites. Fields for Low-T peridotites from the Kaapvaal and Siberian cratons (Boyd, 1989; Boyd *et al.*, 1997). Trend defined by oceanic peridotites after Boyd (1989).

The average modal orthopyroxene content of Somerset Island peridotites is 20% (range of 11 to 34%). This is similar to that reported for peridotite xenoliths from the Siberian craton (Boyd *et al.*, 1997) and Jericho kimberlite (Kopylova and Russell, 2000). The Kaapvaal craton in contrast has an average orthopyroxene mode of 31% (Boyd, 1989).

The average modal clinopyroxene content of Somerset Island peridotites (3%) is slightly higher than that observed in Kaapvaal cratonic peridotites (1.8%, Boyd, 1989). This may account for the higher Ca/Al ratios seen within the Somerset Island peridotite suite.

5.5.2.c Trace elements

Transition metal trace elements

Both Ni and Co behave compatibly in the Somerset Island peridotites, showing a positive correlation with MgO (Figure 5.15). Vanadium abundances are inversely correlated demonstrating their incompatibility in the peridotites, with vanadium content decreasing as clinopyroxene and spinel are removed with the melt (Canil, 1997). The contrasting behaviour of these elements agree with previously observed compatibilities from melt systems (Frey and Prinz, 1978), and peridotites from Lesotho and Jericho (Chapters 3 and 4).

The overall variation in Ni within the peridotite suite is from 1793 to 2722 ppm, and the variation of Ni with MgO is large, up to 400ppm (20%). The scatter in data and lack of tight correlation may be indicative of a cumulate component within the peridotites rather than solely a residue of partial melting (Pearson, 1989). Alternatively, scatter in Ni concentration may be due to the effects of cryptic metasomatism from melts passing through the peridotite, patent metasomatism as clinopyroxene and garnet introduced (Pearson *et al.*, 2001), or serpentinisation (Coleman, 1977).

Cr abundances are highly variable and show no systematic variation. A similar lack of correlation has been observed in spinel peridotites from continental basalts (Maaloe and Aoki, 1977). Frey *et al* (1985) attributed incoherent Cr-MgO relationships in peridotites from the Ronda massif to heterogeneous Cr distribution (mainly within spinels). Elthon (1992) explained the lack of variation as a partition coefficient $K_D \sim 1$ for Cr, no variation with melting.

Rare earth elements

All samples of Somerset Island peridotite show a similar trace element character (Table 5.7). The chondrite normalised whole-rock REE abundances for Somerset Island peridotites are shown in Figure 5.16. The chondrite normalised REE patterns for Somerset Island peridotites are strikingly similar. Generally they show subchondritic HREE values ranging from 0.03 to 0.9 x chondrite, with flat Ho to Lu profiles showing little evidence of fractionation or enrichment. All samples have high chondrite normalised La/Yb (3 to 140, mean = 29.7) and Sm/Yb (1 to 24, mean = 5.5) ratios, suggesting equilibration of the source of incompatible elements with garnet. The subchondritic nature of HREE is characteristic of melt depletion completely removing residual garnet, or melt removal at shallower depth in the absence of residual garnet. Three samples from Nikos are an exception to this and they show HREE values of 1 to

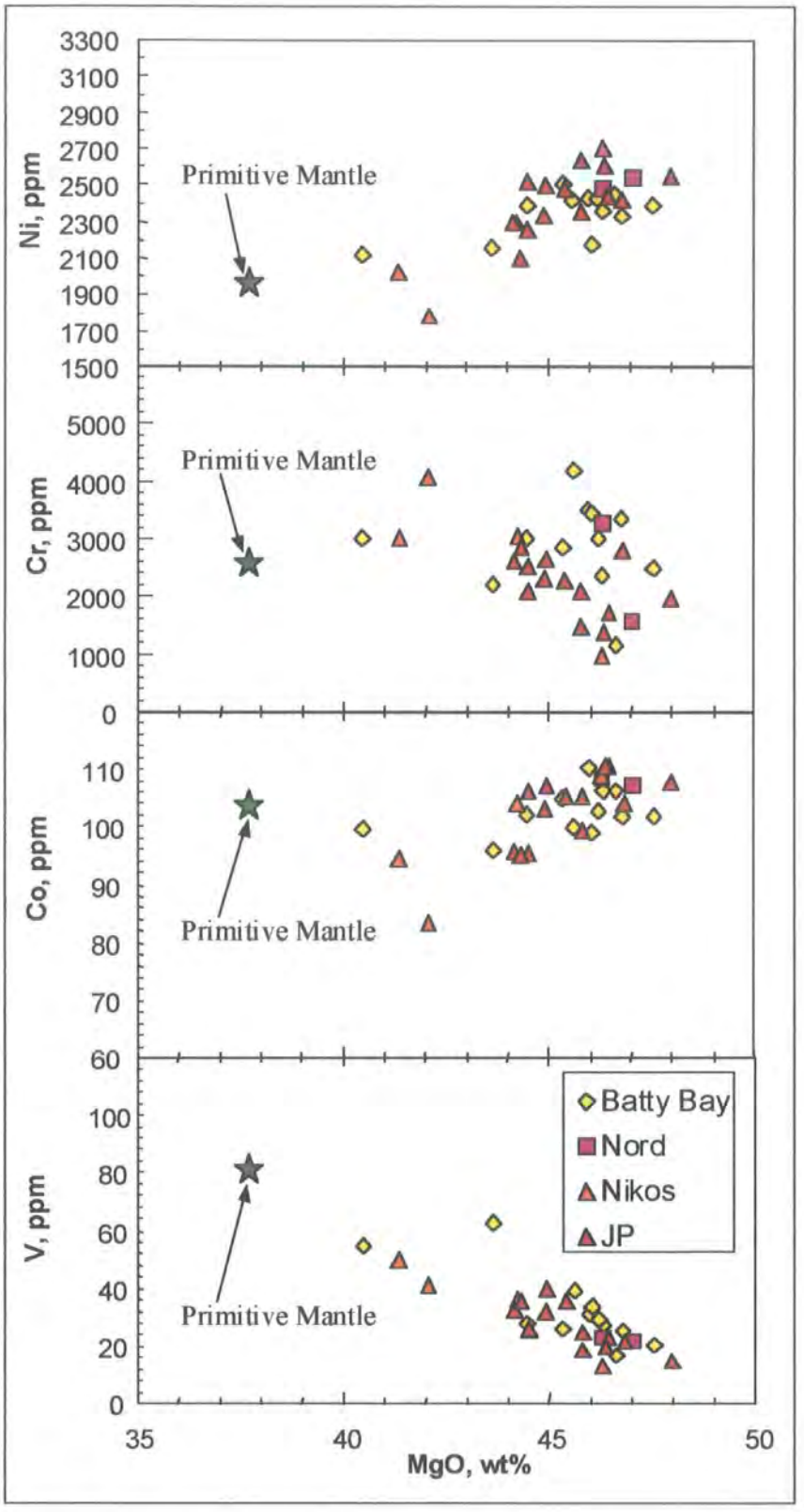

Figure 5.15 Variations of trace elements (ppm) with MgO (wt%) for the low-T Somerset Island peridotites. Primitive mantle after McDonough and Sun (1995).

Table 5.7 Rare earth element data for low-T Somerset Island peridotites. Chondrite normalised using normalisation values of M^{c}Donough and Sun (1995).

Sample	K11A14	K11A15	K11A16	K11A17	K11A18	K12A1	K13A1	K13A3	K13A4	K13A5	K13B4	K15A4	N1C	N2B	X04	X05
REE concentrations in ppm																
La	1.53	1.82	2.55	1.83	0.77	0.52	1.51	2.09	0.56	2.25	3.34	1.52	3.14	2.82	2.09	0.83
Ce	2.43	3.24	4.19	3.03	1.48	0.99	2.48	3.51	0.91	3.92	6.35	2.52	4.98	4.85	4.58	1.63
Pr	0.26	0.38	0.47	0.34	0.19	0.11	0.26	0.37	0.12	0.40	0.72	0.29	0.54	0.55	0.64	0.22
Nd	0.91	1.47	1.75	1.22	0.75	0.35	0.90	1.29	0.50	1.42	2.56	1.17	1.88	1.91	2.62	0.89
Sm	0.15	0.29	0.34	0.21	0.17	0.05	0.13	0.16	0.12	0.22	0.37	0.22	0.28	0.26	0.50	0.20
Eu	0.05	0.09	0.10	0.07	0.05	0.02	0.04	0.04	0.04	0.07	0.10	0.07	0.08	0.08	0.32	0.07
Gd	0.15	0.26	0.29	0.21	0.12	0.05	0.10	0.11	0.16	0.22	0.25	0.19	0.24	0.21	0.48	0.23
Tb	0.02	0.03	0.04	0.03	0.01	0.01	0.01	0.01	0.03	0.04	0.03	0.02	0.03	0.03	0.07	0.04
Dy	0.13	0.14	0.17	0.17	0.04	0.05	0.07	0.06	0.19	0.22	0.12	0.11	0.15	0.12	0.44	0.24
Ho	0.03	0.02	0.03	0.03	0.01	0.01	0.01	0.01	0.04	0.04	0.02	0.02	0.03	0.02	0.09	0.05
Er	0.08	0.05	0.06	0.08	0.01	0.03	0.04	0.03	0.12	0.10	0.03	0.05	0.06	0.05	0.27	0.15
Tm	0.01	0.01	0.01	0.01	0.00	0.01	0.01	0.00	0.02	0.02	0.00	0.01	0.01	0.01	0.05	0.03
Yb	0.08	0.05	0.05	0.07	0.01	0.04	0.05	0.02	0.13	0.10	0.03	0.04	0.06	0.05	0.29	0.17
Lu	0.01	0.01	0.01	0.01	0.00	0.01	0.01	0.00	0.02	0.01	0.00	0.01	0.01	0.01	0.05	0.03
Chondrite normalised REE																
La	6.43	7.69	10.76	7.72	3.25	2.18	6.37	8.82	2.37	9.50	14.11	6.42	13.26	11.89	8.81	3.52
Ce	3.96	5.29	6.83	4.94	2.42	1.62	4.05	5.73	1.48	6.40	10.36	4.11	8.13	7.91	7.47	2.66
Pr	2.79	4.12	5.03	3.62	2.02	1.16	2.85	4.02	1.26	4.28	7.76	3.14	5.82	5.90	6.89	2.32
Nd	2.00	3.21	3.82	2.68	1.64	0.78	1.98	2.82	1.08	3.12	5.59	2.57	4.12	4.18	5.73	1.95
Sm	1.03	1.95	2.27	1.40	1.13	0.33	0.85	1.09	0.78	1.48	2.48	1.49	1.91	1.78	3.35	1.37
Eu	0.88	1.55	1.80	1.24	0.89	0.29	0.71	0.76	0.79	1.29	1.82	1.17	1.48	1.36	5.71	1.19
Gd	0.74	1.28	1.44	1.03	0.58	0.26	0.50	0.53	0.78	1.12	1.26	0.93	1.19	1.03	2.43	1.14
Tb	0.60	0.82	0.98	0.86	0.26	0.19	0.35	0.32	0.76	1.02	0.79	0.60	0.79	0.69	2.06	1.05
Dy	0.53	0.58	0.71	0.69	0.15	0.20	0.29	0.25	0.76	0.88	0.48	0.46	0.61	0.49	1.81	0.98
Ho	0.49	0.43	0.49	0.59	0.10	0.20	0.25	0.17	0.77	0.78	0.28	0.36	0.46	0.36	1.73	0.98
Er	0.47	0.34	0.38	0.51	0.08	0.20	0.24	0.16	0.73	0.65	0.22	0.29	0.40	0.32	1.68	0.97
Tm	0.49	0.32	0.36	0.53	0.08	0.24	0.28	0.14	0.81	0.65	0.18	0.24	0.43	0.30	1.88	1.15
Yb	0.50	0.30	0.32	0.46	0.08	0.23	0.30	0.15	0.82	0.59	0.19	0.28	0.36	0.29	1.81	1.08
Lu	0.51	0.37	0.33	0.53	0.10	0.28	0.35	0.16	0.91	0.57	0.18	0.30	0.37	0.28	2.01	1.24
Chondrite nomalised REE ratios																
La/Yb	13.24	26.06	33.63	16.74	38.80	9.31	21.38	59.77	2.90	16.02	74.48	23.09	36.65	40.52	4.86	3.26
Sm/Yb	2.12	6.61	7.10	3.03	13.46	1.41	2.85	7.40	0.95	2.49	13.12	5.37	5.27	6.07	1.85	1.27
Dy/Yb	1.23	1.98	2.22	1.50	1.79	0.86	0.98	1.71	0.93	1.48	2.53	1.65	1.69	1.69	1.00	0.91

Table 5.7 (continued) REE data for low-T Somerset Island peridotites

Sample	X06	X07	JP1X2	JP2X2	JP3X	JP3X1	JPN2	JPN3A	JPN3B	JPN4	JPN9	JPN11	JPS1	JPS4	JPS6A	JPS6B
REE concentrations in ppm																
La	2.02	0.65	2.35	0.71	1.08	0.75	1.33	1.45	1.44	1.39	1.40	1.01	1.81	2.15	1.93	2.05
Ce	3.48	1.10	4.97	1.45	1.59	1.08	2.37	2.53	2.69	2.56	2.70	1.59	2.62	3.17	2.60	2.89
Pr	0.40	0.13	0.64	0.19	0.17	0.11	0.27	0.30	0.33	0.31	0.36	0.19	0.29	0.36	0.30	0.34
Nd	1.45	0.50	2.27	0.78	0.63	0.39	1.02	1.12	1.27	1.14	1.47	0.65	1.04	1.23	1.13	1.32
Sm	0.23	0.07	0.32	0.13	0.10	0.05	0.14	0.17	0.22	0.22	0.29	0.12	0.16	0.20	0.22	0.26
Eu	0.08	0.02	0.09	0.04	0.04	0.02	0.04	0.05	0.07	0.08	0.08	0.04	0.06	0.06	0.08	0.09
Gd	0.25	0.04	0.22	0.11	0.09	0.04	0.11	0.15	0.19	0.24	0.23	0.14	0.17	0.18	0.25	0.27
Tb	0.04	0.00	0.03	0.01	0.01	0.00	0.01	0.02	0.02	0.04	0.03	0.02	0.02	0.02	0.04	0.04
Dy	0.26	0.02	0.16	0.06	0.07	0.02	0.05	0.10	0.12	0.19	0.16	0.11	0.11	0.12	0.23	0.26
Ho	0.05	0.00	0.03	0.01	0.02	0.00	0.01	0.02	0.02	0.04	0.03	0.02	0.02	0.02	0.05	0.05
Er	0.15	0.00	0.09	0.02	0.04	0.01	0.02	0.04	0.05	0.10	0.07	0.04	0.04	0.05	0.12	0.14
Tm	0.02	0.00	0.02	0.00	0.01	0.00	0.00	0.01	0.01	0.02	0.01	0.01	0.01	0.01	0.02	0.02
Yb	0.16	0.00	0.10	0.01	0.05	0.01	0.02	0.04	0.05	0.10	0.07	0.03	0.03	0.04	0.12	0.14
Lu	0.03	0.00	0.02	0.00	0.01	0.00	0.00	0.01	0.01	0.02	0.01	0.01	0.01	0.01	0.02	0.02
Chondrite normalised REE																
La	8.53	2.72	9.90	3.01	4.55	3.15	5.60	6.11	6.07	5.85	5.91	4.26	7.64	9.08	8.16	8.66
Ce	5.67	1.80	8.11	2.36	2.59	1.76	3.86	4.12	4.39	4.17	4.41	2.59	4.28	5.17	4.24	4.71
Pr	4.29	1.40	6.85	2.07	1.82	1.23	2.93	3.23	3.59	3.35	3.93	2.02	3.15	3.85	3.24	3.68
Nd	3.18	1.09	4.96	1.70	1.38	0.86	2.22	2.45	2.79	2.50	3.21	1.43	2.27	2.70	2.47	2.89
Sm	1.52	0.46	2.14	0.90	0.71	0.31	0.92	1.15	1.50	1.51	1.93	0.83	1.11	1.36	1.52	1.78
Eu	1.46	0.32	1.53	0.72	0.67	0.29	0.73	0.91	1.15	1.35	1.50	0.72	0.99	1.02	1.36	1.55
Gd	1.28	0.19	1.13	0.55	0.45	0.18	0.57	0.75	0.94	1.20	1.14	0.72	0.85	0.91	1.27	1.36
Tb	1.14	0.10	0.84	0.35	0.33	0.08	0.30	0.50	0.66	1.05	0.87	0.62	0.62	0.68	1.09	1.23
Dy	1.04	0.06	0.66	0.24	0.30	0.08	0.22	0.40	0.50	0.78	0.64	0.45	0.45	0.50	0.94	1.06
Ho	0.98	0.03	0.58	0.16	0.27	0.05	0.15	0.31	0.38	0.66	0.57	0.35	0.35	0.38	0.86	0.99
Er	0.91	0.02	0.58	0.10	0.25	0.03	0.12	0.28	0.32	0.60	0.45	0.25	0.26	0.33	0.77	0.90
Tm	0.97	0.04	0.63	0.10	0.30	0.02	0.12	0.28	0.28	0.61	0.49	0.24	0.24	0.32	0.81	0.93
Yb	0.97	0.02	0.62	0.08	0.28	0.04	0.10	0.26	0.32	0.62	0.43	0.21	0.21	0.27	0.76	0.88
Lu	1.06	0.00	0.69	0.06	0.35	0.04	0.08	0.28	0.37	0.77	0.49	0.20	0.28	0.28	0.81	0.89
Chondrite nomalised REE ratios																
La/Yb	8.81	140.38	15.96	38.83	16.12	78.07	56.34	23.44	18.79	9.42	13.63	20.60	36.42	33.81	10.70	9.84
Sm/Yb	1.58	23.63	3.45	11.60	2.50	7.66	9.28	4.40	4.64	2.43	4.45	4.02	5.29	5.05	1.99	2.02
Dy/Yb	1.08	3.19	1.06	3.15	1.06	2.04	2.17	1.53	1.54	1.25	1.48	2.16	2.13	1.85	1.23	1.20

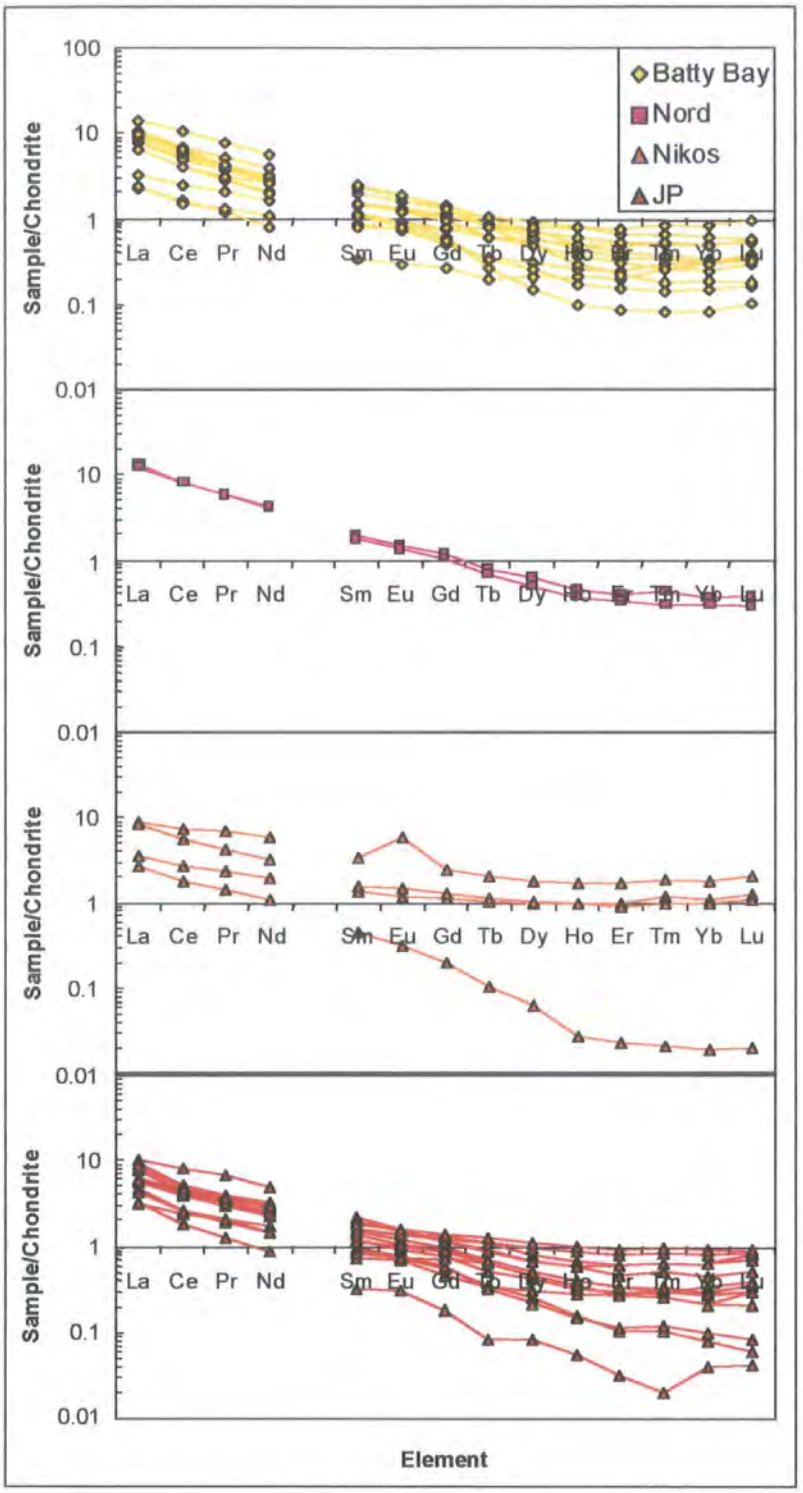

Figure 5.16 Chondrite normalised REE profiles for Somerset Island peridotites using normalisation values of M^{c}Donough and Sun (1995).

2 x chondrite, suggesting that parts of the lithospheric mantle may be enriched relative to ordinary chondrites, or that melting was in the presence of residual garnet. These samples have major element chemistry very similar to all other samples. All samples show enrichment in LREE, from 2 to 14 x chondrite for La. The overall LREE enrichment seen in Somerset Island peridotites is similar to that previously reported for

low-T peridotites from other cratons, such as the Kaapvaal craton (Nixon *et al.*, 1981) and Slave craton (Kopylova and Russell, 2000). LREE enrichment within the Somerset Island peridotites is inconsistent with the major element depletion recorded in the xenoliths, suggesting they are decoupled (Nixon *et al.*, 1981). This possibly represents melt addition in LREE or cryptic metasomatism from fluids passing through the mantle.

5.5.3 Interpretation of whole-rock major element data

By comparing compositional data for naturally occurring residual peridotite samples with residues of experimental melting, pressure and temperature conditions for the melt depletion events can be inferred (Walter, 1999). For such a comparison on dry melting $FeO_{(T)}$, SiO_2, MgO and Al_2O_3 contents have been used (Figure 5.17). The parameters inferred for dry melting are also applicable to high pressure melting in the presence of 4-5 wt% H_2O (Walter, 1999).

The majority of Somerset Island compositions can be explained by dry 20-40% batch melting of pyrolite at pressures of 1-4 GPa (Figure 5.17). Some of the peridotite samples appear to have $FeO_{(T)}$ contents higher than experimental residues of experimental melting at 1GPa which may result from metasomatism re-enriching the sample in Fe, as proposed for other peridotite suites (Harte and Hawkesworth, 1989). Several samples are too rich in Si and modal orthopyroxene, and too low in olivine to be comparable to high-pressure experimental residues. This inconsistency is also apparent in low-temperature peridotites from the Kaapvaal and Siberian cratons, which have high modal orthopyroxene concentrations (Maaloe and Aoki, 1977; Boyd and Mertzman, 1987).

5.5.4 Melt extraction

5.5.4.a Major element modelling of melt residues

As discussed above the Somerset Island peridotite suite may have experienced some disturbance to its major element systematics through metasomatic processes. However, if we are mindful of the disturbance, it can still be useful to compare the xenolith data to melting models. The depleted nature of the Somerset Island lithospheric mantle can be attributed to varying, but large, degrees of melting of a primitive mantle source, and the variation observed in major element trends may be the result of varying degrees of melt extraction.

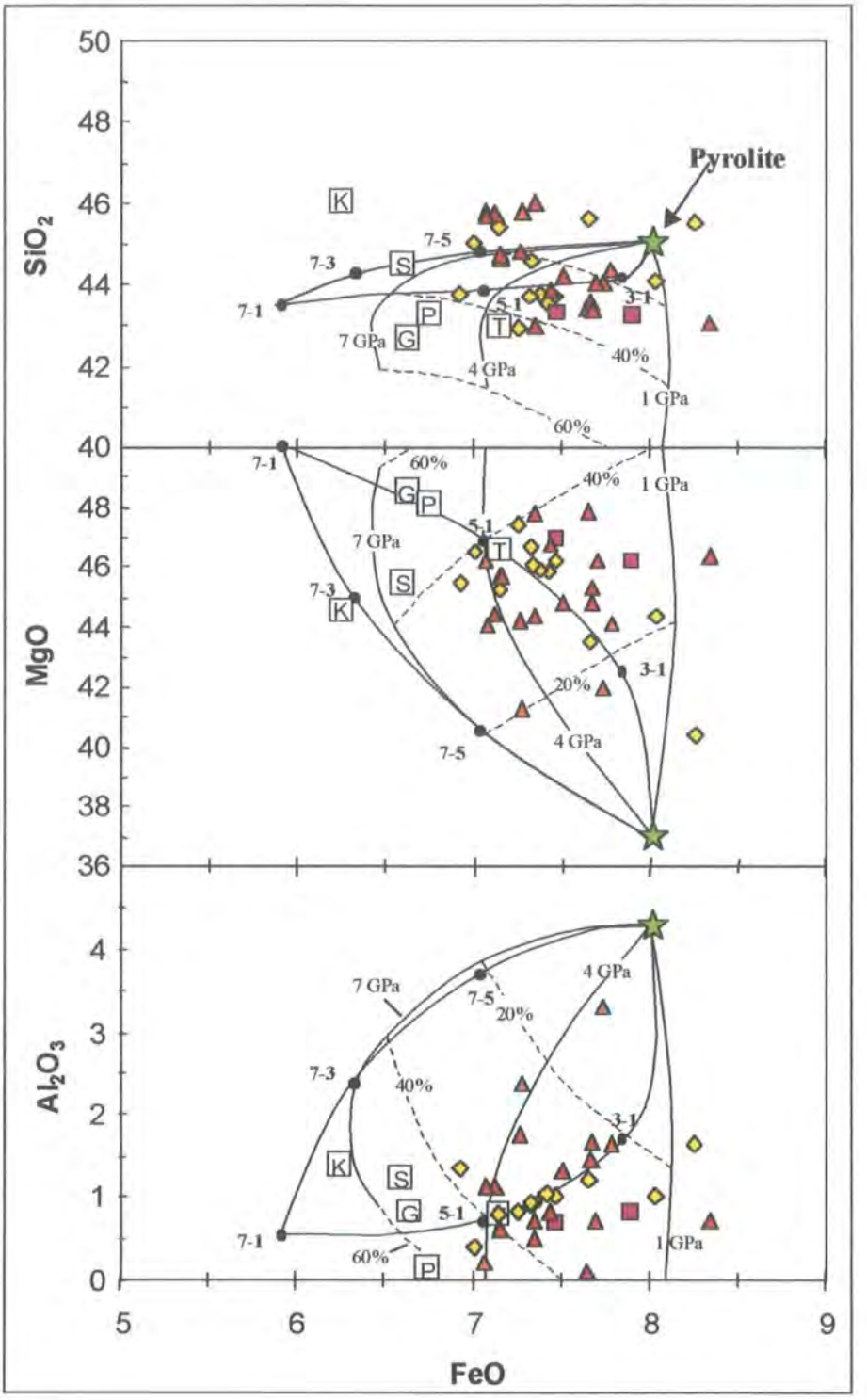

Figure 5.17 Oxide variation diagrams (wt%) for residues of batch and polybaric near-fractional melt extraction, after the method of Walter (1999). Thin solid lines are isobaric batch melt extraction contours and dashed lines give percent batch melt extraction. The filled circles connected by thick solid contours are residues of polybaric near-fractional melt extraction and are labelled according to the pressure range of melt extraction (see Appendix E). Open squares show average low-temperature cratonic peridotites from Kaapvaal (K), Siberia (S), Tanzania (T), Papua New Guinea (P) and East Greenland (G). Additional data from Walter (1999). Fertile mantle denoted by star symbol.

Using geochemical modelling techniques such as those developed by Hanson and Langmuir (1978), this hypothesis can be tested (see Appendix E for details). To estimate the degree of melt extraction experienced by the Somerset Island peridotites, it is assumed that they formed from partial melting of a pyrolitic source (MgO = 47.8 mol%, FeO = 5.35 mol%; (Ringwood, 1975). Partition coefficient data of Bickle *et al* (1977) at 3.0 GPa were used in conjunction with the equations of Hanson and Langmuir (1978) to produce a residue grid (Figure 5.18).

From this type of modelling the Somerset Island peridotites could represent ~20 to 35% batch melting of a pyrolitic mantle source (Figure 5.18). A degree of spatial variation may be apparent, with xenoliths from the JP kimberlite showing a generally lower degree of partial melting (~25%) compared to xenoliths from Batty Bay (~30-35%). However, the overall ranges for xenoliths from both kimberlites are approximately equal, and the difference may be an artefact of sample selection. No overall correlation appears to exist between facies and degree of melt but the harzburgites from the JP kimberlite display higher degrees of melt (30-35%) than lherzolites from the JP kimberlite (~25%). Thompson (1984) noted that the liquidus temperature of 4-phase lherzolite increases with pressure. If this is combined with the pressure dependence of K_D, high-pressure residues will be shifted to the left (lower mol% FeO) on Figure 5.18, whilst low-pressure residues will be shifted to the right (higher mol% FeO). The temperature at which the melt-residues formed will vary with pressure, but the degree of melting remains approximately the same (Hanson and Langmuir, 1978). From Figure 5.18 it is also apparent that some peridotites have anomalously high FeO contents. This could indicate that these samples represent a low-pressure melt residue, or alternatively it may represent later enrichment of Fe after melt extraction. Trace element data for these samples does not appear to deviate from that seen for other peridotite samples.

From Figure 5.18 it would appear as though Somerset Island peridotites represent lower degrees of melt at lower temperature than Kaapvaal and Siberian peridotites. However, many of the samples have FeO contents as low as Siberian low-T peridotites. Boyd *et al* (1997) found clear indication of late-stage introduction of Ca and Fe to the Siberian suite, which may suggest that the Somerset Island peridotites have been similarly affected.

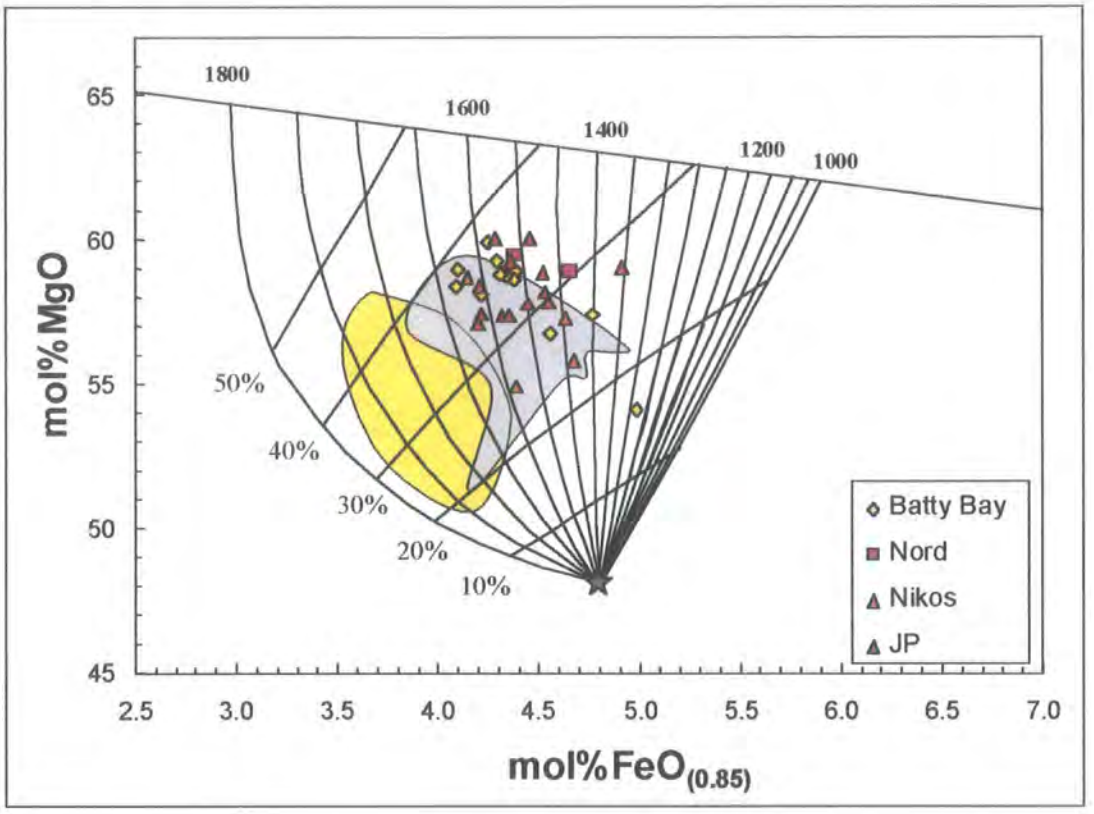

Figure 5.18 FeO-MgO diagram for Somerset Island peridotites. The diagram is contoured for temperature and degree of batch melting of pyrolitic mantle (Ringwood, 1975) at 3 GPa using method described by Hanson and Langmuir (1978). Field for Kaapvaal and Siberian peridotites from Pearson *et al* (1995a). Kaapvaal low-T peridotites represented by yellow field, Siberian by the blue-grey field. Pyrolite denoted by star symbol.

5.5.4.b HREE modelling

Although REE abundances in the Somerset Island whole-rock peridotites are obviously disturbed (Figure 5.16), the low HREE abundances may be indicative of the melt depletion event rather than later melt addition. The degree of melting may be estimated by plotting fractionation of the HREE as a function of HREE abundances (Figure 5.19), after the method of Bodinier *et al* (1988). In addition to providing evidence for the degree of melt, the fractionation of HREE can distinguish between the presence and absence of garnet, due to the buffering of HREE by garnet.

On a plot of Dy/Yb ratio against Yb (Figure 5.19), calculated ratios for model melting of a peridotite source of variable garnet content are presented for up to 20% batch and fractional melting, after Burnham (1995). See Appendix E for a detailed explanation of modelling parameters. The data for Somerset Island peridotites show no decrease in Dy/Yb for a decrease in Yb, but instead show an increase in the Dy/Yb ratio for a given Yb abundance. The Somerset Island peridotites do not match the trajectories of the model melts, and this would suggest that the samples have undergone Dy addition

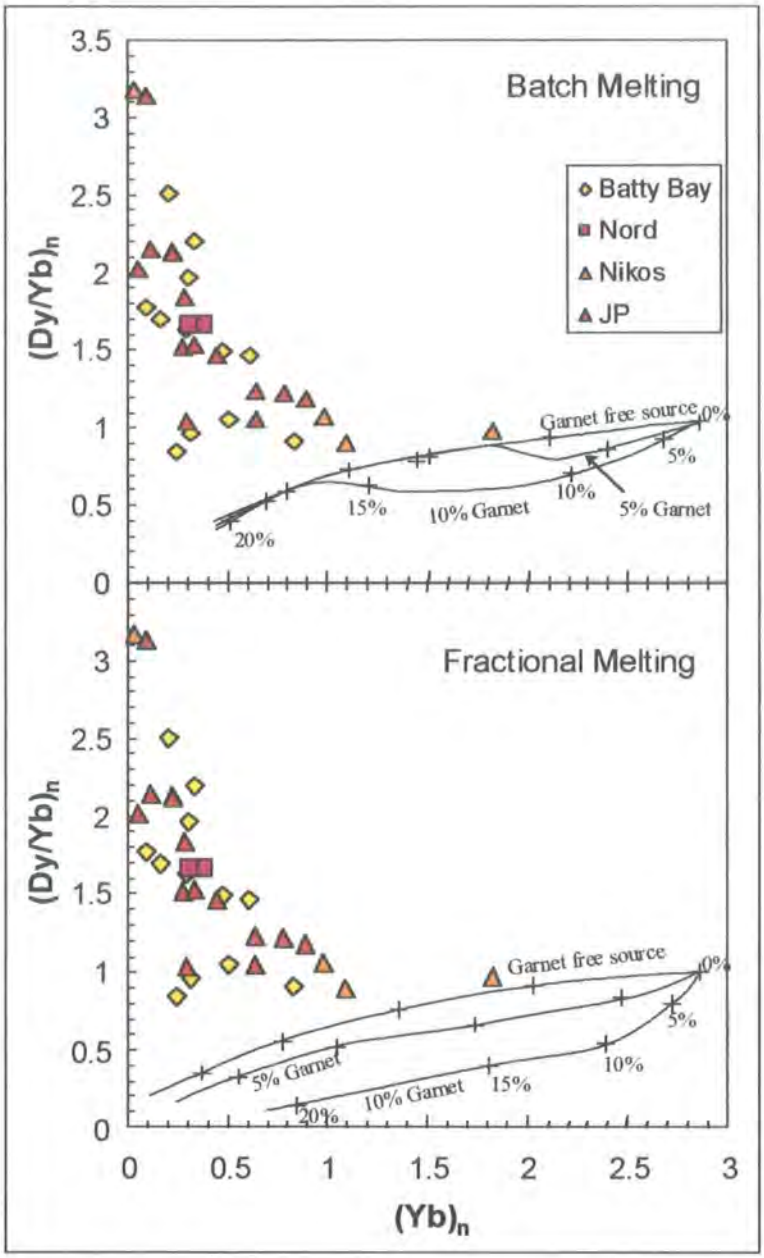

Figure 5.19 Variation of Dy/Yb ratio with Yb abundances in peridotites from Somerset Island, superimposed on calculated variations of Dy/Yb ratios with Yb calculated for up to 25% melting of a peridotite source containing variable quantities of garnet, after Burnham (1995). Crosses at 5% melting intervals.

after the melt depletion event. The modelling of REEs therefore provide no evidence of the initial melt depletion event or the composition of the source mantle, but appear to be overprinted by later metasomatic events. Absolute Yb abundances for the Somerset Island peridotites are generally sub-chondritic however (Figure 5.16), and this suggests that melting occurred either within spinel facies, or was sufficient to remove all garnet from the residue.

5.5.5 Summary of peridotite petrogenesis

A general model for the origin of the cratonic mantle underlying Somerset Island is illustrated in Figure 5.20, based on experimental models of Walter (1999). Primary melt extraction from a pyrolitic source produces a harzburgitic lithosphere (melt extraction vector of Figure 5.20). The average values illustrated for Greenland, Tanzania and Papua New Guinea approximate a residue of 40 to 50% melt extraction at an average of 3-4 GPa (Walter, 1999). Several Somerset Island samples appear to be as depleted as peridotites from Tanzania, but in general they appear to be more fertile than peridotites from Greenland, Tanzania and Papua New Guinea. This would suggest that they formed from lower degrees of melt. The modal mineralogy and $Mg^{\#}$ of olivine in Somerset Island peridotites would suggest however that the lithospheric mantle underlying Somerset Island is more depleted than the relationship of major elements would indicate. Subsequent to melt extraction, the addition of secondary SiO_2, manifested as orthopyroxene, moves the average composition of Kaapvaal and Siberian cratonic peridotites along the vector shown in Figure 5.20. This may be the result of melt-mantle reaction (Keleman *et al.*, 1998), cumulate mixing (Herzberg, 1993; Herzberg, 1999) or both. From Figure 5.20 it is not apparent whether the Somerset Island peridotites have been enriched in SiO_2. However, from Figure 5.20 it would appear as though the Somerset Island samples have been enriched in FeO. Several Somerset Island peridotites have FeO contents higher than the model pyrolitic source. Somerset Island peridotites may therefore have suffered Fe metasomatism, as previously noted from studies of other cratonic peridotite suites (Harte and Hawkesworth, 1989). Possible Fe enrichment from metasomatism, if Fe is preferentially mobilised relative to Mg and Al, would shift the sample to the right on Figure 5.20, and therefore mask the relationship with SiO_2. This could explain the inconsistency between modal mineralogy, mineral chemistry and whole-rock major element modelling. The Fe enrichment appears to be unrelated to REE enrichment and no systematic relationship is seen between Fe enrichment and trace elements.

Trace element enrichment in the peridotite xenoliths is not systematically related to major-element chemistry within the Somerset Island peridotites. Subsequent to melt depletion however, all Somerset Island samples have undergone consistent LREE enrichment. This may suggest that the lithospheric mantle has undergone episodic and variable metasomatism from varying metasomatic fluids of different character (cf. Menzies and Hawkesworth, 1987).

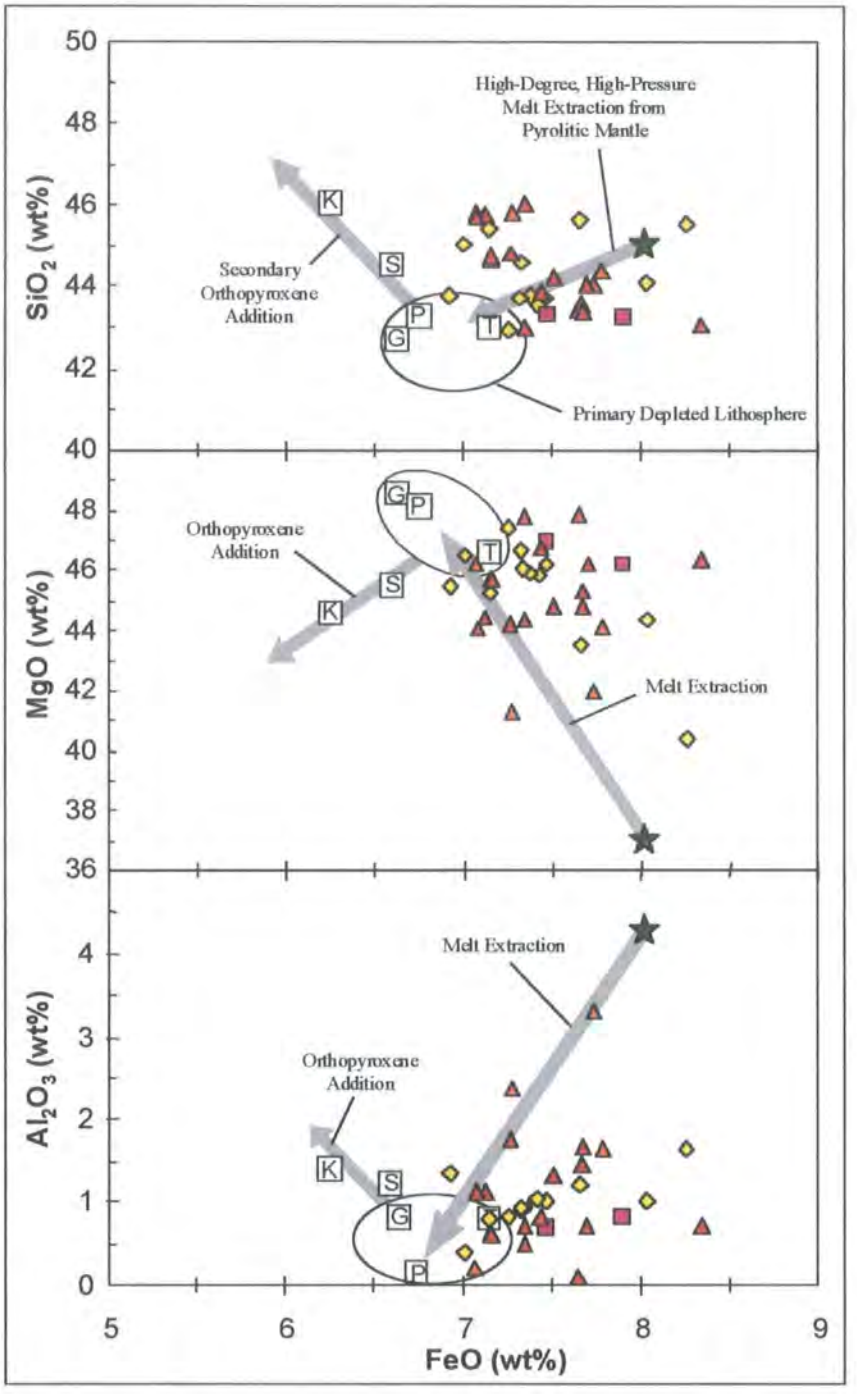

Figure 5.20 Oxide variation diagrams (wt%) showing a general model for the origin of cratonic lithosphere, after Walter (1999). Primary melt extraction from pyrolitic mantle (star symbol) of about 40-50% melt at pressures of 3-4 GPa produce a residue with compositions within a field encompassing Tanzania, Greenland and Papua New Guinea. Addition of OPX to Siberian and Kaapvaal lithosphere has caused enrichment in SiO_2 and Al_2O_3, and depletion in MgO and FeO.

5.6 Re-Os Isotopic Study of Somerset Island Peridotite Xenoliths

5.6.1 Introduction

To form an understanding of the generation and evolution of the cratonic lithospheric mantle beneath Somerset Island requires knowledge of the age, time-scale of formation and the relationship between the crustal and mantle section of the lithosphere.

It has been shown that the continental lithosphere underlying Somerset Island has a complex history involving melt depletion with refertilisation or metasomatism associated with the passage of later mantle-derived melts/fluids. Previous isotopic studies of Somerset Island peridotite xenoliths from the Nikos kimberlite have shown that due to this complex history Nd model ages mainly reflect younger metasomatic events (Schmidberger *et al.*, 2000), and as a consequence provide little information on the earliest events in the evolution of the continental lithospheric mantle. These studies suggested that the Lu-Hf isotope systematics appeared to be less affected by metasomatic events and provided a correlation on a Lu-Hf isochron diagram of 2.5 Ga (on a limited sample set, n = 3) relative to a chondritic reservoir. This was interpreted as a late Archean age for the stabilisation of the lithospheric mantle beneath the Canadian Arctic.

During partial melting of the mantle, Os is a compatible element and consequently the Os content of most magmatic fluids are low. Metasomatism of the mantle by these magmatic fluids should in turn have a negligible effect on $^{187}Os/^{188}Os$ ratios. The Re-Os isotope system therefore provides the opportunity to help constrain the timing and processes involved in the formation of the Somerset Island continental lithospheric mantle, which should be free from the effects of metasomatism and alteration processes which obscure the results of other isotope systems. The extraction of melt from the lithospheric mantle is a critical step in producing the compositional buoyancy, vital for lithosphere formation and craton stabilisation (Walker *et al.*, 1989; Pearson, 1999b).

5.6.2 Re and Os Abundances and Isotopic Compositions

5.6.2.a Re variation

Re contents in the Somerset Island peridotite xenoliths (Table 5.8) show a considerable scatter (0.012 ppb to 2.58 ppb), extending over a larger range than that reported from other studies of Archean (Walker *et al.*, 1989; Pearson *et al.*, 1995a; Pearson *et al.*, 1995b; Carlson *et al.*, 1999) and post-Archean (Carlson and Irving, 1994;

Table 5.8 Re-Os Isotopic data for Somerset Island peridotites. γOs, T_{RD} and T_{MA} calculated with respect to chondrite ($^{187}Os/^{188}Os = 0.3972$ and $^{187}Re/^{188}Os = 0.1276$; Walker *et al.*, 1989) and fertile mantle ($^{187}Os/^{188}Os = 0.4243$ and $^{187}Re/^{188}Os = 0.1287$; Meisel *et al.*, 1996) with ^{187}Re decay constant of 1.666×10^{-11} yr^{-1}. γOs is the difference (in %) in $^{187}Os/^{188}Os$ between the sample and fertile mantle/chondrite at the eruption age of the kimberlite. Errors are 2σ within run. T_{RD} and T_{MA} expressed in Ga.

Samples	Re (ppb)	Os (ppb)	$^{187}Re/^{188}Os$	$^{187}Os/^{188}Os(m)$	+/-	$^{187}Os/^{188}Os(i)$	γOs	T_{RD}	T_{MA}	$^{187}Os/^{188}Os(i)$	γOs	T_{RD}	T_{MA}
						Chondrite				*Fertile Mantle*			
(Batty Bay)													
K11A6	0.023	4.57	0.0245	0.10968	8	0.10964	-13.65	2.65	2.82	0.10964	-14.34	2.64	2.79
K11A14	0.026	3.61	0.0351	0.11291	9	0.11285	-11.11	2.18	2.38	0.11285	-11.83	2.20	2.39
K11A15	0.019	1.74	0.0519	0.11431	14	0.11422	-10.04	1.98	2.26	0.11422	-10.76	2.01	2.28
K11A16	0.048	4.57	0.0503	0.11227	10	0.11218	-11.64	2.28	2.59	0.11218	-12.35	2.29	2.58
K11A17	0.019	2.38	0.0375	0.11157	16	0.11151	-12.17	2.38	2.61	0.11151	-12.88	2.38	2.60
K11A18	0.012	0.55	0.1096	0.11493	15	0.11475	-9.62	1.91	2.58	0.11475	-10.35	1.94	2.57
K12A1	0.052	3.42	0.0732	0.11460	15	0.11448	-9.84	1.95	2.36	0.11448	-10.56	1.98	2.36
K13A1	0.129	4.32	0.1440	0.11113	12	0.11089	-12.66	2.47	3.78	0.11089	-13.36	2.47	3.65
K13A3	0.025	3.80	0.0314	0.11100	13	0.11095	-12.61	2.46	2.66	0.11095	-13.31	2.46	2.64
K13A4	0.034	1.89	0.0875	0.11955	18	0.11941	-5.95	1.22	1.53	0.11941	-6.71	1.30	1.61
K13A5	0.197	3.15	0.3004	0.11279	10	0.11229	-11.56	2.27	8.53	0.11229	-12.27	2.28	
K13B4	0.012	3.21	0.0182	0.10940	12	0.10937	-13.86	2.69	2.81	0.10937	-14.55	2.67	2.79
K15A4	1.402	1.08	6.2295	0.11871	10	0.10836	-14.65	2.84		0.10836	-15.34	2.81	
(Nord)													
N1C	0.194	3.15	0.2957	0.11448	11	0.11399	-10.22	2.02		0.11399	-10.94	2.05	
N2B	0.034	1.42	0.1140	0.11348	16	0.11329	-10.77	2.12	2.91	0.11329	-11.49	2.14	2.87

Table 5.8 (continued) Re-Os Isotopic data for Somerset Island peridotites.

Samples	Re (ppb)	Os (ppb)	$^{187}Re/^{188}Os$	$^{187}Os/^{188}Os(m)$	+/-	$^{187}Os/^{188}Os(i)$	γOs	T_{RD}	T_{MA}	$^{187}Os/^{188}Os(i)$	γOs	T_{RD}	T_{MA}
						Chondrite				*Fertile Mantle*			
(Nikos)													
X04	0.229	3.31	0.3335	0.11644	16	0.11589	-8.72	1.74		0.11589	-9.46	1.79	
X05	0.386	3.23	0.5750	0.11474	16	0.11378	-10.38	2.05		0.11378	-11.10	2.07	
X06	0.126	2.76	0.2190	0.11393	27	0.11356	-10.55	2.08	4.43	0.11356	-11.27	2.10	4.17
X07	0.066	5.95	0.0534	0.10973	12	0.10964	-13.64	2.65	3.04	0.10964	-14.34	2.64	2.99
(JP)													
JP1-X2	0.111	3.41	0.1565	0.11339	12	0.11313	-10.89	2.14	3.44	0.11313	-11.61	2.16	3.34
JP2-X2	0.029	4.07	0.0342	0.11150	11	0.11145	-12.22	2.39	2.60	0.11145	-12.93	2.39	2.59
JP3-X	0.046	2.60	0.0857	0.11388	10	0.11374	-10.42	2.06	2.58	0.11374	-11.14	2.08	2.57
JP3-X1	0.974	3.30	1.4201	0.11135	27	0.10899	-14.16	2.74		0.10899	-14.85	2.73	
JPN2	0.058	4.91	0.0563	0.11086	12	0.11077	-12.76	2.49	2.87	0.11077	-13.46	2.48	2.84
JPN3A	0.079	6.70	0.0564	0.11274	10	0.11265	-11.27	2.21	2.56	0.11265	-11.99	2.23	2.55
JPN3B	0.159	5.81	0.1319	0.11445	11	0.11423	-10.03	1.98	2.90	0.11423	-10.75	2.01	2.86
JPN4	0.027	2.91	0.0439	0.11593	10	0.11586	-8.75	1.74	1.95	0.11586	-9.48	1.79	1.98
JPN9	0.092	4.25	0.1040	0.11256	12	0.11238	-11.48	2.25	3.00	0.11238	-12.20	2.27	2.95
JPN11	0.033	2.77	0.0572	0.11487	14	0.11477	-9.60	1.90	2.20	0.11477	-10.33	1.94	2.22
JPS1	1.646	6.07	1.3031	0.11092	9	0.10875	-14.34	2.78		0.10875	-15.03	2.76	
JPS4	0.449	3.48	0.6196	0.11036	10	0.10933	-13.89	2.69		0.10933	-14.58	2.68	
JPS6A	2.585	4.43	2.8043	0.11410	11	0.10945	-13.80	2.68		0.10945	-14.49	2.66	
JPS6B	1.989	3.97	2.4060	0.11390	10	0.10990	-13.44	2.61		0.10990	-14.14	2.60	

Meisel *et al.*, 1996; Handler *et al.*, 1997; Peslier *et al.*, 2000) cratonic peridotite xenoliths.

The mean Re concentration for all Somerset Island peridotite xenoliths in this study is 0.343 ppb (std.dev. = 0.637) with a median of 0.066 ppb (n = 33), compared to an estimated 0.26 ppb for fertile mantle (Morgan, 1986). This illustrates that peridotite xenoliths from Somerset Island are, in general, highly depleted in Re relative to fertile mantle compositions (Figure 5.21) but also that a few samples are highly enriched in Re. If we consider the samples depleted relative to fertile mantle alone the mean Re content is then 0.072 ppb (std.dev. = 0.063) with a median of 0.047 ppb (n = 26). This is comparable to the mean Re concentration of 0.084 ppb (std.dev. = 0.078) and median of 0.072 ppb for Kaapvaal peridotites (Carlson *et al.*, 1999).

Location	Mean (ppb)	+/-	Median (ppb)	n
Somerset Island	0.343	0.637	0.066	33
Somerset Island†	0.072	0.063	0.047	26
Batty Bay	0.154	0.379	0.026	13
Batty Bay†	0.05	0.056	0.026	12
Nord	0.114	0.114	0.114	2
Nikos	0.202	0.14	0.178	4
JP	0.591	0.862	0.102	14
JP†	0.07	0.045	0.058	9

Table 5.9 Summary of the mean and Median Re concentrations in peridotites from the Somerset Island suite and individual Somerset Island kimberlite locations.
† calculated mean and median for peridotite xenoliths depleted in Re relative to fertile mantle compositions (0.26 ppb, Morgan, 1986).

A summary of mean and median Re concentrations is presented in Table 5.9. Peridotite xenoliths from the Batty Bay kimberlite complex and Nord kimberlite generally have the lowest Re contents of all Somerset Island samples, compared to those from Nikos and JP. If samples enriched in Re relative to fertile mantle estimates are excluded, Batty Bay remains the most depleted. However, samples from the JP kimberlite now appear to be much more depleted in Re (Table 5.9), and more similar to typical values reported for Archean and post Archean peridotite xenoliths (Handler *et al.*, 1997; Carlson *et al.*, 1999). This suggests that the continental lithospheric mantle beneath Somerset Island is depleted in Re as typically seen in Archean and post-Archean regions but has possibly undergone localised Re enrichment.

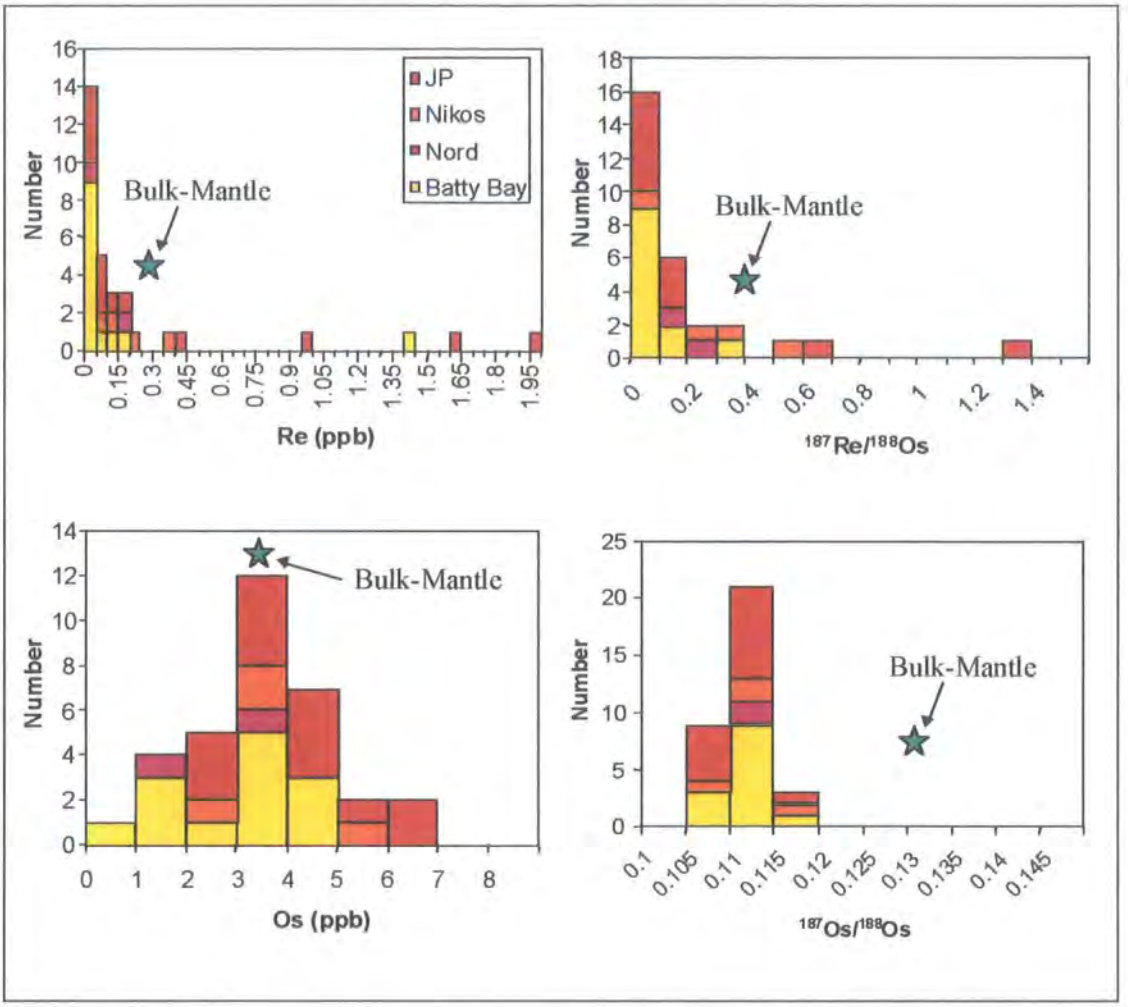

Figure 5.21 Histograms of Re and Os concentration (ng/g or ppb), $^{187}Re/^{188}Os$ and $^{187}Os/^{188}Os$ for low-T Somerset Island peridotite xenoliths. Bulk-Mantle after Morgan (1986).

5.6.2.b Os variation

Measured Os concentrations for the Somerset Island peridotites (Table 5.8) show considerable scatter (0.55 ppb to 6.7 ppb) and span a similar range to that reported for Kaapvaal and Siberian peridotites (Walker *et al.*, 1989; Pearson *et al.*, 1995a; Pearson *et al.*, 1995b; Carlson *et al.*, 1999). On average (mean = 3.54 ppb; Table 5.10) the Os content of Somerset Island peridotites is slightly higher than estimates for fertile mantle (3.4 ppb, Morgan, 1986), as would be expected for a residue of partial melting, consistent with the depleted nature of the xenoliths (Figure 5.21). Os concentrations reported for Kaapvaal peridotite xenoliths (mean = 4.61 ppb, median = 4.05 ppb, Carlson *et al.*, 1999) and Alpine peridotites (mean = 3.74 ppb, median = 3.84 ppb, Reisberg and Lorand, 1995) are also higher than fertile mantle. The Os content of Somerset Island xenolith peridotites, although spanning a similar range to both these

groups, tends to be lower on average and tends more towards that of fertile mantle. In contrast, rift related spinel peridotite xenoliths (McBride *et al.*, 1996; Meisel *et al.*, 1996; Handler *et al.*, 1997; Chesley *et al.*, 1999; Peslier *et al.*, 2000), arc related spinel peridotite xenoliths (Brandon *et al.*, 1996) and Abyssal peridotites (Snow and Reisberg, 1995) have Os contents lower than fertile mantle estimates.

The Os concentrations for peridotite xenoliths from the Batty Bay kimberlite complex and Nord kimberlite are generally similar to those reported for rift related spinel peridotite xenoliths (Handler *et al.*, 1997; Peslier *et al.*, 2000), and lower than fertile mantle estimates (Table 5.10). The Os content of peridotite xenoliths from the JP and Nikos kimberlites however are higher than fertile mantle and therefore more comparable to Kaapvaal peridotite xenoliths and Alpine peridotites. This may indicate a possible spatial distribution in differences within the Os systematics of the Somerset Island continental lithospheric mantle (Figure 5.2).

Location	Mean (ppb)	+/-	Median (ppb)	n
Somerset Island	3.54	1.41	3.41	33
Batty Bay	2.95	1.32	3.21	13
Nord	2.28	1.23	2.28	2
Nikos	3.81	1.44	3.27	4
JP	4.19	1.28	4.02	14

Table 5.10 Summary of the mean and Median Os concentrations in peridotites from the Somerset Island suite and individual Somerset Island kimberlite locations.

5.6.2.c Re/Os isotopic variation

Cratonic peridotites generally have amongst the lowest $^{187}Re/^{188}Os$ ratios of any peridotite suites, though most peridotites worldwide have $^{187}Re/^{188}Os$ ratios less than that of fertile mantle estimates ($^{187}Re/^{188}Os = 0.4243$, Meisel *et al.*, 1996). The range in Re and Os concentrations of the Somerset Island peridotite xenolith suite (Table 5.8) results in a large range in $^{187}Re/^{188}Os$ ratios from 0.018 to 6.23 (subchondritic to suprachondritic), with a mean of 0.548 (std.dev. = 1.22) and a median of 0.104 (Table 5.11). This is higher than $^{187}Re/^{188}Os$ ratios reported for cratonic peridotites from the Kaapvaal craton (mean $^{187}Re/^{188}Os = 0.109$, Carlson *et al.*, 1999) and Alpine peridotites (mean $^{187}Re/^{188}Os = 0.207$, Reisberg and Lorand, 1995), but similar to that seen in spinel peridotite xenoliths from the Northern Canadian Cordillera (mean $^{187}Re/^{188}Os = 0.537$, Peslier *et al.*, 2000). Of the 33 Somerset Island samples analysed (Table 5.8), seven have $^{187}Re/^{188}Os$ ratios greater than fertile mantle. If we exclude these seven

samples, the average $^{187}Re/^{188}Os$ ratio is reduced considerably to 0.072 (std.dev. = 0.063) with a median of 0.047. This is even lower than seen in previous studies of Kaapvaal peridotites and is consistent with the moderately incompatible nature of Re during partial melting.

Location	Mean	+/-	Median	n
Somerset Island	0.548	1.22	0.104	33
Somerset Island†	0.072	0.063	0.047	26
Batty Bay	0.553	1.71	0.052	13
Batty Bay†	0.08	0.079	0.051	12
Nord	0.205	0.129	0.205	2
Nikos	0.295	0.219	0.276	4
Nikos†	0.202	0.141	0.219	3
JP	0.663	0.948	0.118	14
JP†	0.081	0.042	0.057	9

Table 5.11 Summary of the mean and Median $^{187}Re/^{188}Os$ concentrations in peridotites from the Somerset Island suite and individual Somerset Island kimberlite locations.
† calculated mean and median for peridotite xenoliths with $^{187}Re/^{188}Os$ ratios lower than fertile mantle estimates only (0.4243, Meisel *et al.*, 1996).

The mean $^{187}Re/^{188}Os$ ratio for peridotite xenoliths from the Nikos and Nord kimberlites are similar to those reported for Alpine peridotites. The $^{187}Re/^{188}Os$ ratios of peridotite xenoliths from the JP and Batty Bay kimberlites however are higher than fertile mantle estimates. If samples with $^{187}Re/^{188}Os$ ratios higher than fertile mantle are excluded, the peridotite xenoliths from the Batty Bay and JP kimberlites are lower than those from Nikos and Nord. This would support the observation that the lithospheric mantle beneath Somerset Island is depleted relative to fertile mantle, as typically seen in Archean and post-Archean regions but with localised enrichment.

5.6.2.d Os isotopic variation

The clearest distinction between cratonic peridotites and peridotites from other tectonic settings is provided by Os isotopic composition. The Os isotopic composition of Somerset Island peridotite xenoliths ranges from $^{187}Os/^{188}Os$ of 0.1084 to 0.1194 (Table 5.8; Figure 5.21), comparable to the range for Kaapvaal and Siberian peridotite xenolith suites (Pearson *et al.*, 1995a; Pearson *et al.*, 1995b; Carlson *et al.*, 1999). Although the range in Re/Os for Somerset Island peridotites overlaps that of peridotites from other tectonic settings, the low unradiogenic $^{187}Os/^{188}Os$ values present at

Somerset Island are distinctive from these other peridotite groups (Figure 5.21). The Somerset Island peridotites are highly unradiogenic relative to both chondritic and fertile mantle estimates (Table 5.8). The unradiogenic isotopic characteristic of the Somerset Island peridotites, comparable to other cratonic peridotites, is indicative of long-term Re depletion and isolation from the convecting mantle, and so must have occurred much earlier than in the non-cratonic peridotite groups plotted in Figure 5.21.

Location	Mean	+/-	Median	N
Kaapvaal†	0.1115	0.0032	0.1105	38
Somerset Island	0.1123	0.0025	0.1124	33
Batty Bay	0.1124	0.0029	0.1122	13
Nord	0.1136	0.0005	0.1136	2
Nikos	0.1132	0.0026	0.1137	4
JP	0.1118	0.0023	0.1119	14

Table 5.12 Summary of the mean and Median $^{187}Os/^{188}Os$ ratios in peridotites from the Somerset Island suite and individual Somerset Island kimberlite locations.
† Mean and median $^{187}Os/^{188}Os$ ratios for Kaapvaal craton from Carlson *et al* (1999).

The $^{187}Os/^{188}Os$ isotopic composition of peridotite xenoliths from Somerset Island are on average slightly more radiogenic than those from the Kaapvaal (Table 5.12). The $^{187}Os/^{188}Os$ isotopic composition of peridotites from the JP kimberlite are on average the most unradiogenic Somerset Island peridotites, and are comparable with the Kaapvaal craton. The average $^{187}Os/^{188}Os$ compositions of peridotites from the Batty Bay, Nikos and Nord kimberlites being only slightly less unradiogenic.

5.6.3 PGE geochemistry of the Somerset Island peridotites

5.6.3.a Whole-rock PGE abundances

The Somerset Island peridotite suite considered shows a large variation in PGE and Re abundances (Table 5.13). This range in PGE concentration is much larger than has been observed for Pyrenean orogenic lherzolites (Lorand *et al.*, 1999), or alkali basalt hosted spinel peridotites (Morgan *et al.*, 1981; Handler and Bennett, 1999). On average, IPGE (Ir, Os, Ru) abundances for Somerset Island peridotites are similar to primitive mantle (McDonough and Sun, 1995, Table 5.13), whilst the PPGE (Pt, Pd) abundances are generally depleted, consistent with their major-element depleted nature. In comparison to peridotites from other tectonic settings, the IPGEs from the Somerset Island peridotites have similar abundances to that observed in orogenic massifs (Pattou *et al.*,

Table 5.13 PGE, Re and selected major and trace element abundances for Somerset Island peridotites. CI chondrite values from McDonough and Sun (1995). Primitive mantle values taken as 0.007 x CI chondrite after method of McDonough and Sun (1995).

Samples	S (ppm)	Al2O3 (wt%)	(La/Yb)n	Ba (ppm)	Nb (ppm)	Os (ppb)	Ir (ppb)	Ru (ppb)	Pt (ppb)	Pd (ppb)	Re (ppb)
Batty Bay											
K11A14	101	1.03	12.95	73.41	2.53	2.39	2.20	4.43	1.98	1.42	0.03
K11A15	68	1.06	26.06	68.57	3.76	2.35	2.50	5.40	1.11	6.89	0.02
K11A16	126	1.37	33.63	97.90	4.11	3.25	3.66	6.64	4.21	1.40	0.05
K11A17	157	0.96	16.74	69.06	3.87	2.58	2.75	6.02	1.25	0.96	0.02
K11A18	108	0.84	38.80	25.64	1.34	0.62	0.64	1.23	0.09	0.41	0.01
K12A1	78	0.94	9.31	16.22	0.77	3.60	2.56	4.53	2.82	1.44	0.05
K13A1	40	1.03	21.38	73.40	2.03	4.49	4.42	9.81	7.54	1.77	0.13
K13A3	171	0.41	59.77	50.05	2.22	4.20	3.97	7.19	2.08	0.58	0.03
K13A4	93	1.64	16.02	56.64	0.48	2.25	3.32	6.19	5.24	3.95	0.04
K13A5	68	1.21	2.90	58.76	3.37	3.73	4.66	8.67	2.81	1.72	0.22
K13B4	73	0.82	74.48	60.79	5.76	4.18	4.25	6.14	8.32	0.46	0.01
K15A4	43	0.96	23.09	43.88	3.03	1.80	2.20	7.52	2.92	0.69	1.50
Nord											
N1C	194	0.83	36.65	63.45	5.20	3.38	3.31	6.31	2.19	1.22	0.21
N2B	123	0.72	40.52	109.27	5.24	1.74	1.87	3.85	1.59	0.91	0.03
Nikos											
X04	2544	2.38	4.86	34.12	2.70	3.31	3.10	5.28	3.86	3.38	0.23
X05	2741	1.66	3.26	15.33	1.53	3.23	2.97	6.78	1.93	1.34	0.39
X06	369	3.33	8.81	132.93	5.09	2.87	2.66	6.12	2.40	1.64	0.14
X07	190	0.21	140.38	15.32	1.19	5.95	5.93	10.81	5.35	1.50	0.07

Table 5.13 (continued) PGE, Re and selected major and trace element abundances for Somerset Island peridotites.

Samples	S (ppm)	Al2O3 (wt%)	(La/Yb)n	Ba (ppm)	Nb (ppm)	Os (ppb)	Ir (ppb)	Ru (ppb)	Pt (ppb)	Pd (ppb)	Re (ppb)
JP											
JP1-X2	260	1.34	15.96	26.05	2.67	3.41	3.21	5.61	3.07	2.43	0.11
JP2-X2	277	0.63	38.83	24.25	2.28	3.58	3.18	5.57	2.90	0.16	0.03
JP3-X	275	0.85	16.12	10.25	1.50	2.89	2.82	5.13	2.27	1.37	0.05
JP3-X1	177	0.10	78.07	11.42	1.10	2.65	2.65	3.42	1.12	0.27	1.09
JPN2	339	0.73	56.34	43.18	2.43	4.91	4.61	9.12	4.01	2.48	0.06
JPN3A	268	1.14	23.44	28.55	2.43	6.70	6.52	12.38	7.52	4.20	0.08
JPN3B	407	1.15	18.79	29.53	2.38	5.81	5.78	9.77	5.78	3.82	0.16
JPN4	298	1.76	9.42	36.52	2.54	2.91	2.59	4.77	1.93	1.43	0.03
JPN9	471	0.73	13.63	19.91	2.13	4.25	3.79	6.87	2.85	1.89	0.09
JPN11	236	0.72	20.60	18.75	1.46	2.77	2.93	5.17	1.47	0.08	0.03
JPS1	1702	0.64	36.42	66.61	2.72	6.07	5.63	10.88	4.43	1.18	1.65
JPS4	1484		33.81	75.86	2.57	3.48	4.04	7.40	2.42	1.47	0.45
JPS6A	1006	1.47	10.70	47.63	1.76	4.43	4.15	7.80	3.71	2.28	2.58
JPS6B	1028	1.68	9.84	38.59	1.93	3.97	3.90	7.42	4.17	2.59	1.99
Primative mantle	250	4.44	1.47	6.6	0.658	3.4	3.2	5	7.1	3.9	0.28
CI chondrite	54,000	1.62	1.47	2.41	0.24	490	455	710	1,010	550	40

	Os	Ir	Ru	Pt	Pd	Re
Somerset Island Range	0.623-6.7	0.636-6.52	1.23-12.4	0.094-8.32	0.080-6.89	0.013-2.59
Somerset Island Average	3.55	3.52	6.69	3.29	1.79	0.36

1996; Lorand *et al.*, 1999), but higher than those observed for spinel peridotites (Morgan *et al.*, 1981; Handler and Bennett, 1999). However, PPGEs within the Somerset Island peridotites are depleted relative to both orogenic massifs and alkali basalt hosted spinel peridotites.

5.6.3.b Covariation of PGEs in Somerset Island peridotites

Osmium and Ru show good positive correlations with Ir, with close to chondritic ratios (Figure 5.22). The overall correlation coefficients between Os, and Ru, with Ir for the entire Somerset Island suite are r = 0.95 and 0.93 respectively. Peridotites from individual kimberlite pipes show different levels of correlation (Table 5.14).

Location	*Correlation coefficients*		
	Os-Ir	***Ru-Ir***	***n***
Somerset Island	0.95	0.93	33
Batty Bay	0.89	0.84	13
Nikos	0.98	0.89	4
JP	0.98	0.98	14

Table 5.14 Summary of correlation coefficients for IPGEs within the Somerset Island low-T peridotite suite, and individual kimberlites locations.

Xenoliths from the JP kimberlite show the best correlation (Table 5.14), whereas xenoliths from Batty Bay show a much poorer correlation which may be related to the generally smaller size of the Batty Bay xenoliths and greater degree of weathering. The mean chondrite normalised Os/Ir ratio, $(Os/Ir)_n$, for Somerset Island peridotites is slightly subchondritic at 0.94 whilst $(Ru/Ir)_n$ is superchondritic at 1.24 (Table 5.15). In contrast to the IPGEs, the PPGEs show poor systematic correlations with Ir overall (Figure 5.22). The Ir-Pt variation has a correlation coefficient of r = 0.74. Both Pd and Re show very little correlation. Mean chondrite normalised ratios for Pt and Pd with Ir, $(Pt/Ir)_n$ and $(Pd/Ir)_n$, are subchondritic, whilst $(Re/Ir)_n$ is suprachondritic (Table 5.15). The $(Re/Ir)_n$ is heavily biased by four very high Re values and if these are excluded the mean is subchondritic.

5.6.3.c PGE patterns of Somerset Island peridotites

For the Somerset Island peridotites, IPGEs range between 0.001 and 0.017 x CI chondrite (mean = 0.008 x CI chondrite) and generally show a flat chondrite normalised pattern with very little intra-element fractionation.

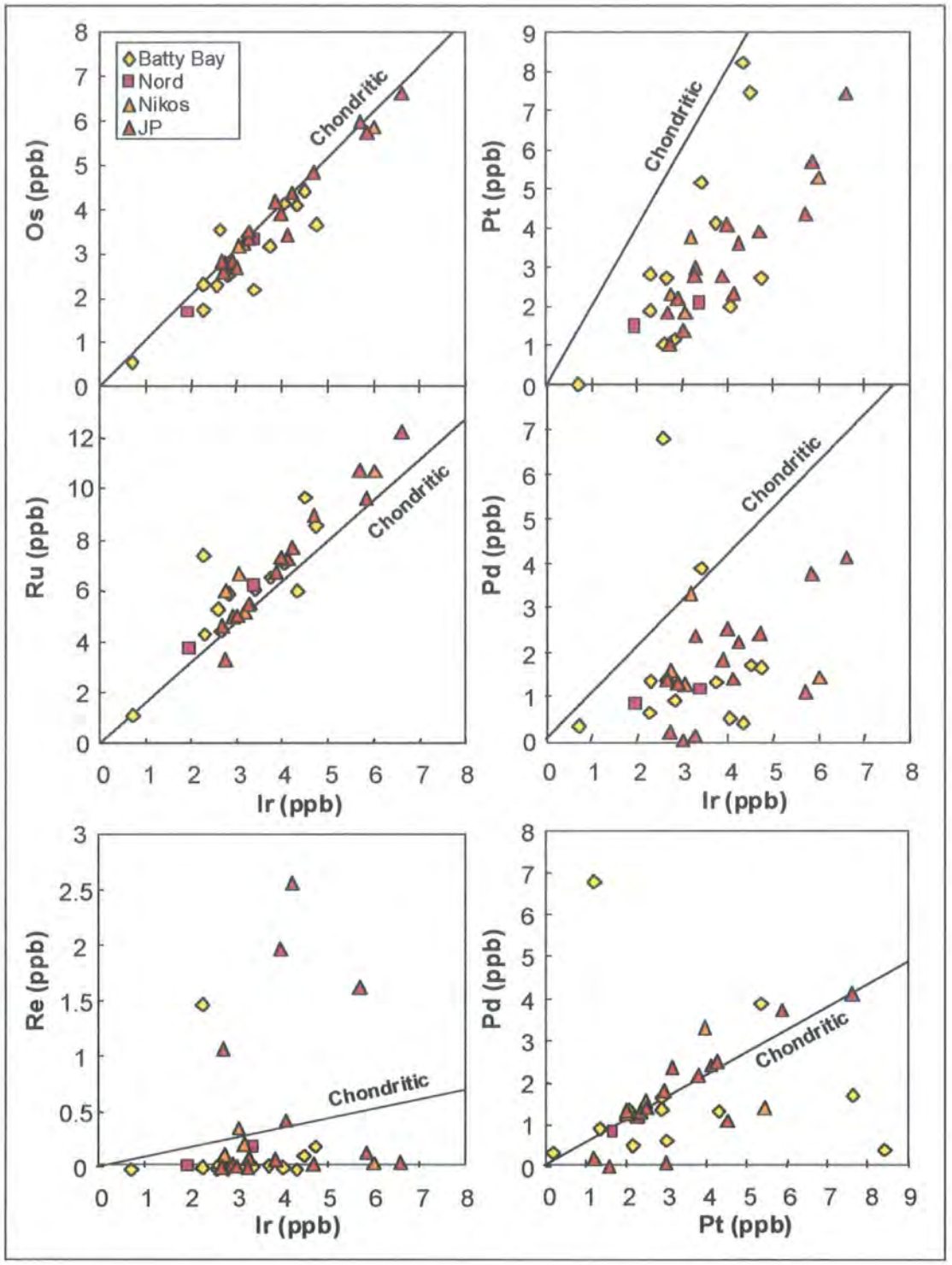

Figure 5.22 Bivariate PGE abundance plots for the Somerset Island peridotite suite. The positive correlation between Os, Ru and Ir (r = 0.95 and 0.93 respectively), may suggest these elements are controlled by the same phases in the xenoliths. None of the remaining PGEs or Re correlate with Ir or each other.

Table 5.15 CI-chondrite normalised PGEs and PGE ratios for the Somerset Island peridotite suite. Chondrite normalised using normalisation values of M^{c}Donough and Sun (1995).

Samples	Os	Ir	Ru	Pt	Pd	Re	(Os/Ir)n	(Ru/Ir)n	(Pt/Ir)n	(Pd/Ir)n	(Re/Ir)n
Batty Bay											
K11A14	0.0049	0.0048	0.0062	0.0020	0.0026	0.0007	1.01	1.29	0.41	0.53	0.14
K11A15	0.0048	0.0055	0.0076	0.0011	0.0125	0.0005	0.87	1.38	0.20	2.28	0.09
K11A16	0.0066	0.0080	0.0094	0.0042	0.0025	0.0013	0.82	1.16	0.52	0.32	0.16
K11A17	0.0053	0.0060	0.0085	0.0012	0.0018	0.0004	0.87	1.40	0.21	0.29	0.06
K11A18	0.0013	0.0014	0.0017	0.0001	0.0007	0.0003	0.91	1.24	0.07	0.53	0.25
K12A1	0.0074	0.0056	0.0064	0.0028	0.0026	0.0012	1.31	1.13	0.50	0.46	0.21
K13A1	0.0092	0.0097	0.0138	0.0075	0.0032	0.0033	0.94	1.42	0.77	0.33	0.34
K13A3	0.0086	0.0087	0.0101	0.0021	0.0011	0.0007	0.98	1.16	0.24	0.12	0.08
K13A4	0.0046	0.0073	0.0087	0.0052	0.0072	0.0009	0.63	1.20	0.71	0.99	0.12
K13A5	0.0076	0.0102	0.0122	0.0028	0.0031	0.0054	0.74	1.19	0.27	0.31	0.53
K13B4	0.0085	0.0093	0.0086	0.0082	0.0008	0.0003	0.91	0.92	0.88	0.09	0.04
K15A4	0.0037	0.0048	0.0106	0.0029	0.0012	0.0375	0.76	2.19	0.60	0.26	7.75
Nord											
N1C	0.0069	0.0073	0.0089	0.0022	0.0022	0.0053	0.95	1.22	0.30	0.31	0.73
N2B	0.0035	0.0041	0.0054	0.0016	0.0016	0.0008	0.86	1.32	0.38	0.40	0.20
Nikos											
X04	0.0068	0.0068	0.0074	0.0038	0.0061	0.0057	0.99	1.09	0.56	0.90	0.84
X05	0.0066	0.0065	0.0096	0.0019	0.0024	0.0097	1.01	1.46	0.29	0.37	1.48
X06	0.0059	0.0059	0.0086	0.0024	0.0030	0.0034	1.00	1.47	0.41	0.51	0.58
X07	0.0121	0.0130	0.0152	0.0053	0.0027	0.0017	0.93	1.17	0.41	0.21	0.13

Table 5.15 (continued) CI-chondrite normalised PGEs and PGE ratios for the Somerset Island peridotite suite.

Samples	Os	Ir	Ru	Pt	Pd	Re	(Os/Ir)n	(Ru/Ir)n	(Pt/Ir)n	(Pd/Ir)n	(Re/Ir)n
JP											
JP1-X2	0.0070	0.0071	0.0079	0.0030	0.0044	0.0028	0.99	1.12	0.43	0.63	0.39
JP2-X2	0.0073	0.0070	0.0078	0.0029	0.0003	0.0008	1.05	1.12	0.41	0.04	0.11
JP3-X	0.0059	0.0062	0.0072	0.0022	0.0025	0.0013	0.95	1.17	0.36	0.40	0.22
JP3-X1	0.0054	0.0058	0.0048	0.0011	0.0005	0.0272	0.93	0.83	0.19	0.08	4.69
JPN2	0.0100	0.0101	0.0128	0.0040	0.0045	0.0014	0.99	1.27	0.39	0.45	0.14
JPN3A	0.0137	0.0143	0.0174	0.0074	0.0076	0.0020	0.95	1.22	0.52	0.53	0.14
JPN3B	0.0119	0.0127	0.0138	0.0057	0.0069	0.0040	0.93	1.08	0.45	0.55	0.31
JPN4	0.0059	0.0057	0.0067	0.0019	0.0026	0.0007	1.04	1.18	0.33	0.46	0.12
JPN9	0.0087	0.0083	0.0097	0.0028	0.0034	0.0023	1.04	1.16	0.34	0.41	0.28
JPN11	0.0057	0.0064	0.0073	0.0015	0.0001	0.0008	0.88	1.13	0.23	0.02	0.13
JPS1	0.0124	0.0124	0.0153	0.0044	0.0021	0.0411	1.00	1.24	0.35	0.17	3.32
JPS4	0.0071	0.0089	0.0104	0.0024	0.0027	0.0112	0.80	1.17	0.27	0.30	1.26
JPS6A	0.0090	0.0091	0.0110	0.0037	0.0041	0.0646	0.99	1.20	0.40	0.45	7.08
JPS6B	0.0081	0.0086	0.0104	0.0041	0.0047	0.0497	0.95	1.22	0.48	0.55	5.80
Mean	0.0073	0.0077	0.0094	0.0033	0.0033	0.0090	0.94	1.24	0.40	0.45	1.18

Such behaviour reflects the nature of Os, Ir and Ru in mantle melting processes (Barnes *et al.*, 1985; Brügmann *et al.*, 1987; Barnes and Picard, 1993; Reisberg and Lorand, 1995) and is considered to be characteristic of PGE patterns for upper-mantle peridotites (cf. O'Neill, 1991). The overall range in IPGE abundances shown by the Somerset Island peridotites may reflect a heterogeneous distribution of PGEs.

PPGEs in the Somerset Island suite in contrast are highly variable, with samples showing strongly fractionated, rather than flat chondritic patterns. This behaviour is essentially consistent with their moderately incompatible nature. On the basis of PPGEs, four distinct groups of peridotites have been ascertained in the Somerset Island peridotites (Figure 5.23a-e) which will be outlined below.

5.6.3.d Fractionation of PGEs within the Somerset Island peridotites

Despite showing some IPGE abundance variation, the Somerset Island peridotites show very limited inter-element fractionation (Figs 5.22 and 5.23a-e). In contrast, PPGEs show considerable and varied inter-element fractionation.

PPGE depleted peridotites (Group A)

Four samples from Somerset Island have highly fractionated PPGEs (Figure 5.23a), with marked depletions in Pd and Re, and intermediate depletion in Pt. This pattern is generally what would be expected for a peridotite that has undergone varying but extensive degrees of melt extraction, and in the Somerset Island suite this depletion is more evident than in harzburgitic residues from Pyrenean orogenic massifs (Lorand *et al.*, 1999). Chondrite normalised Pd/Ir ratios for these samples range from $(Pd/Ir)_n$ of 0.09 to 0.32 (Tables 5.15 and 5.16). The depleted PGE pattern of these samples would suggest that the system has remained closed since the time of melt extraction.

PPGE depleted peridotites with Re enrichment (Group B)

This group of samples also has marked depletion in PPGEs (Figure 5.23b), but has variable Re contents with a marked upwards inflection in the extended PGE pattern. This may reflect secondary, post-melt extraction, addition of Re to the peridotite. Low $(Pd/Ir)_n$ of 0.02 to 0.33 support the notion that these samples represent variably but extensively depleted peridotites and hence suggests the notion that the samples have experienced later Re introduction.

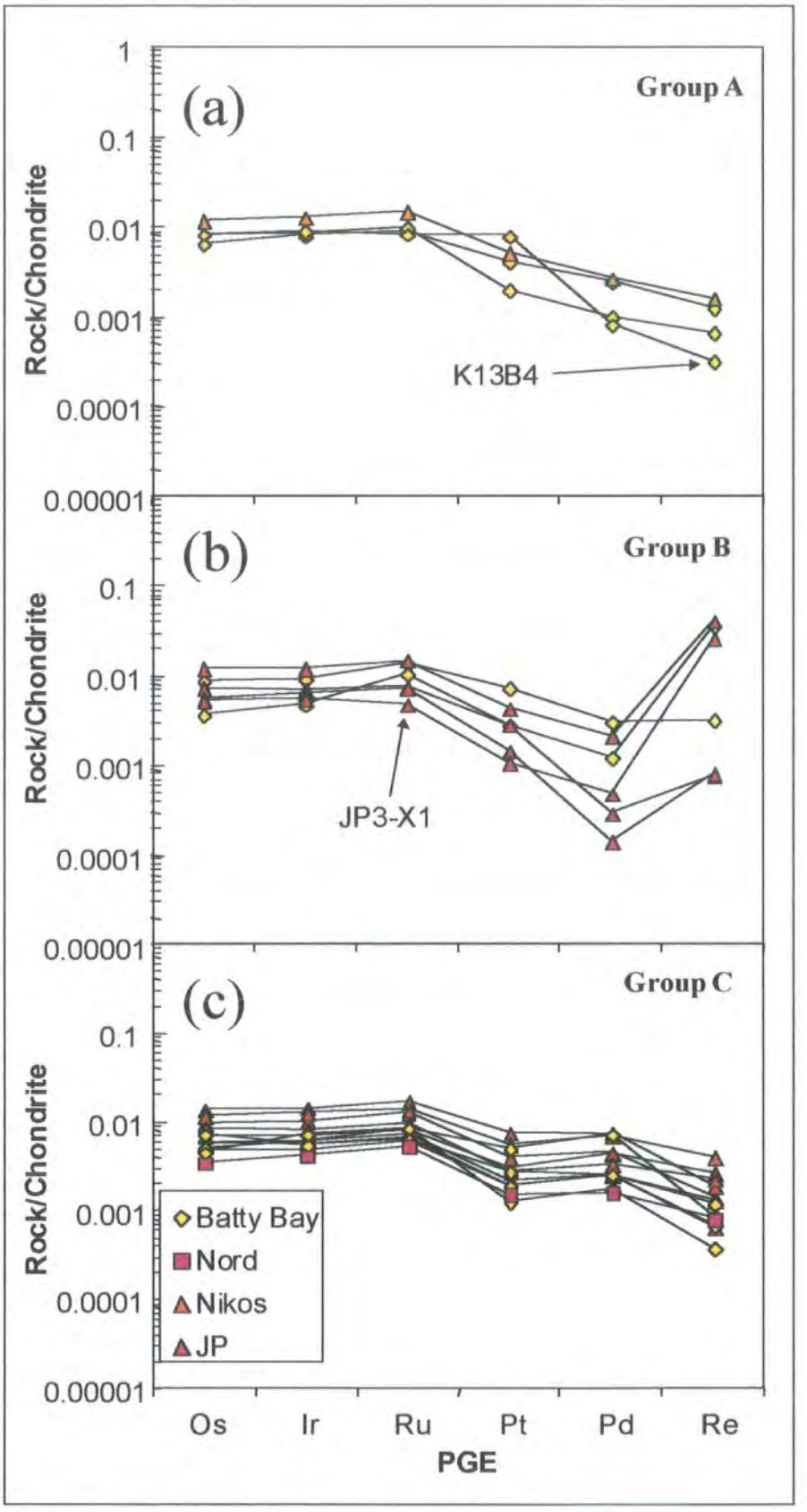

Figure 5.23 CI-chondrite normalised PGE abundances for the Somerset Island peridotite suite. (a) PPGE depleted pattern, (b) PPGE depleted pattern with Re enrichment, (c-d) PPGE depleted pattern with Pd and possible Re enrichment, and (e) PPGE depleted pattern with Pd and Re enrichment. CI chondrite values from McDonough and Sun (1995).

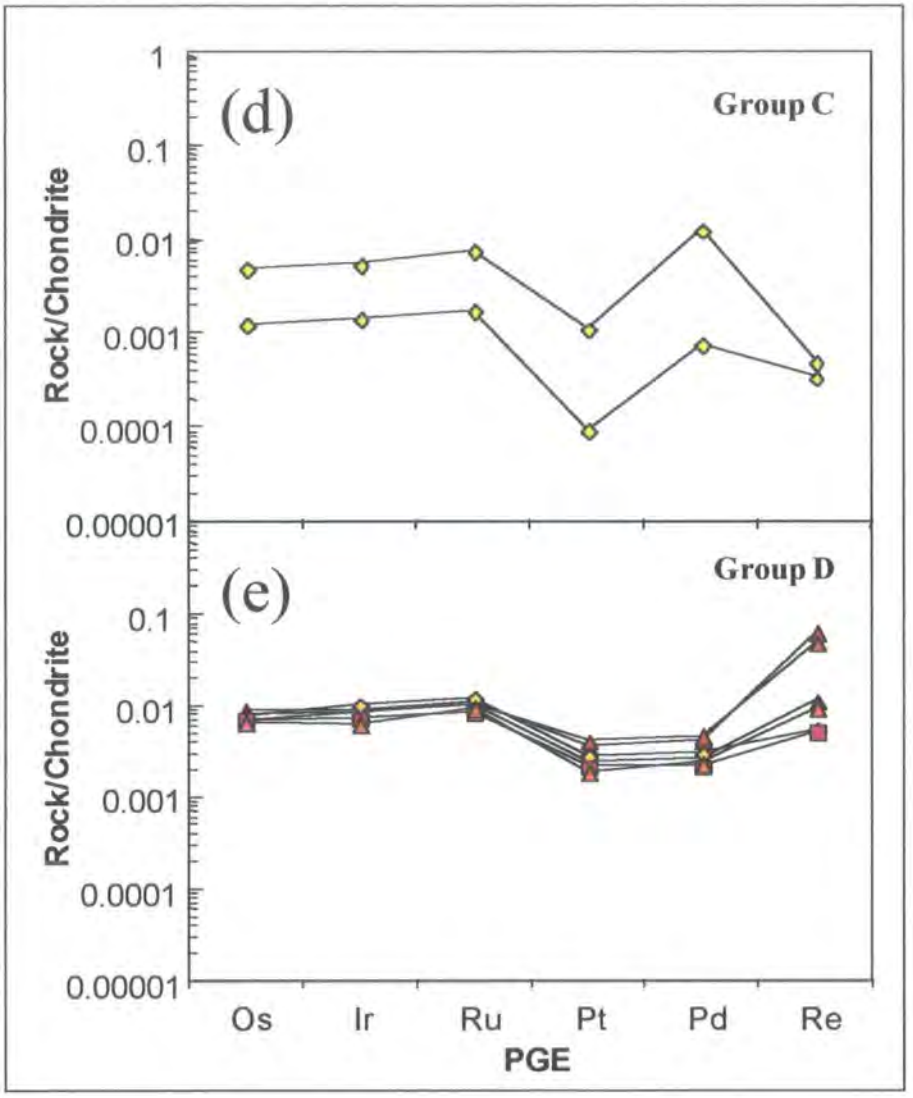

Figure 5.23 (continued) Cl-chondrite normalised PGE abundances for the Somerset Island peridotite suite. (a) PPGE depleted pattern, (b) PPGE depleted pattern with Re enrichment, (c-d) PPGE depleted pattern with Pd and possible Re enrichment, and (e) PPGE depleted pattern with Pd and Re enrichment.

PPGE depleted peridotites with Pd enrichment (Group C)

This group of Somerset Island samples (Figure 5.23c) show a noticeable depletion in Pt similar to that seen in groups A and B, but is considerably more enriched in Pd. This may be an indication that Pd has been re-introduced to the peridotites after the melt extraction event. The wide variation in Re abundance, and Re/Pt of group though suggests some Re mobility may have occurred also. Two samples from the Batty Bay kimberlite (K11A15 and K11A18) show an extreme variation of this trend (Figure 5.23d).

PPGE depleted peridotites with Pd and Re enrichment (Group D)

This group of samples (Figure 5.23e) again show a noticeable depletion in Pt, as seen for all Somerset Island peridotites, but both Re and Pd are clearly enriched and all have $(Re/Pt)_n > 1$ (Table 5.16).

Table 5.16 Summary of PGE behaviour within the Somerset Island peridotites, on the basis of the shape of the PPGE part of the PGE patterns. Average whole-rock elemental abundances and PGE ratios on the basis of PPGE determined groups.

Group	PGE Pattern	Pd (ppb)	Re (ppb)	S (ppm)	Al_2O_3 (wt%)	Ba (ppm)	Nb (ppm)	$(Pd/Ir)_n$	$(Re/Ir)_n$	$(Re/Pt)_n$
A	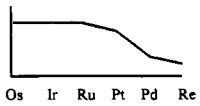	0.98	0.04	140	0.70	56.02	3.32	0.18	0.10	0.25
B	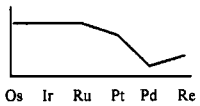	0.69	0.74	155	0.69	39.72	2.10	0.15	2.72	8.04
C	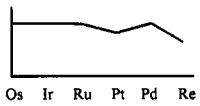	2.27	0.06	236	1.10	46.21	2.50	0.52	0.19	0.47
D	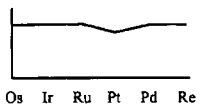	1.77	0.97	1087	1.37	49.94	2.73	0.38	2.81	7.30

PGE fractionation

The depletion of PPGEs is consistent with the major-element depleted nature of Somerset Island peridotites and would suggest that the PGEs have been fractionated during melt extraction. Relative compatibility during the fractionation of PGEs, through melt extraction, based on the evidence from the chondrite-normalised patterns of peridotites from Somerset Island, is in the order Os ~ Ir ~ Ru > Pt > Pd ≥ Re. This is consistent with evidence from Lesotho and Jericho, and with the order of fractionation seen in melts derived from the mantle (Barnes *et al.*, 1985; Woodland, 2000).

5.6.4 PGE variation with whole-rock chemistry

5.6.4.a Variation of PGEs with sulfur

The control of sulfides on PGEs within the Somerset Island peridotites can be considered through comparison of PGE and S abundances. Sulfur is a moderately incompatible element in the mantle and behaves coherently during mantle melting processes (Lorand, 1989; Lorand, 1991). PGEs however, have high partition coefficients into sulfides and unless all sulfide within the mantle is consumed (~25% melting) and the melt nears saturation (Keays, 1995), no correlation of S with PGEs should necessarily exist.

Estimates for the S content of fertile mantle vary but are generally less than 300 ppm (Peach and Mathez, 1996). The S contents within Somerset Island peridotites range from 40 ppm to 2741 ppm, i.e. from depleted to highly enriched relative to fertile mantle source. Little overall correlation exists between PGEs and S within the Somerset Island peridotites (Figure 5.24).

The Somerset Island kimberlites are emplaced in carbonate sequences, which contains gypsum deposits. It is possible that the kimberlites and peridotite xenoliths have experienced enrichment in sulfur from leaching of the host rock by groundwater. Although the Somerset Island peridotites show flat chondritic IPGE patterns, they show varying absolute abundances in individual peridotites. If the peridotites were not derived from the same homogeneous source mantle, it would not be surprising that they show no positive correlations with sulfur overall. Alternatively the poor PGE-S correlations may be a reflection of metasomatism, as observed in the Pyrenees massif by Lorand *et al* (1999). However, IPGEs appear to be less susceptible to melt-related metasomatism than PPGEs on the basis of their compatibilities.

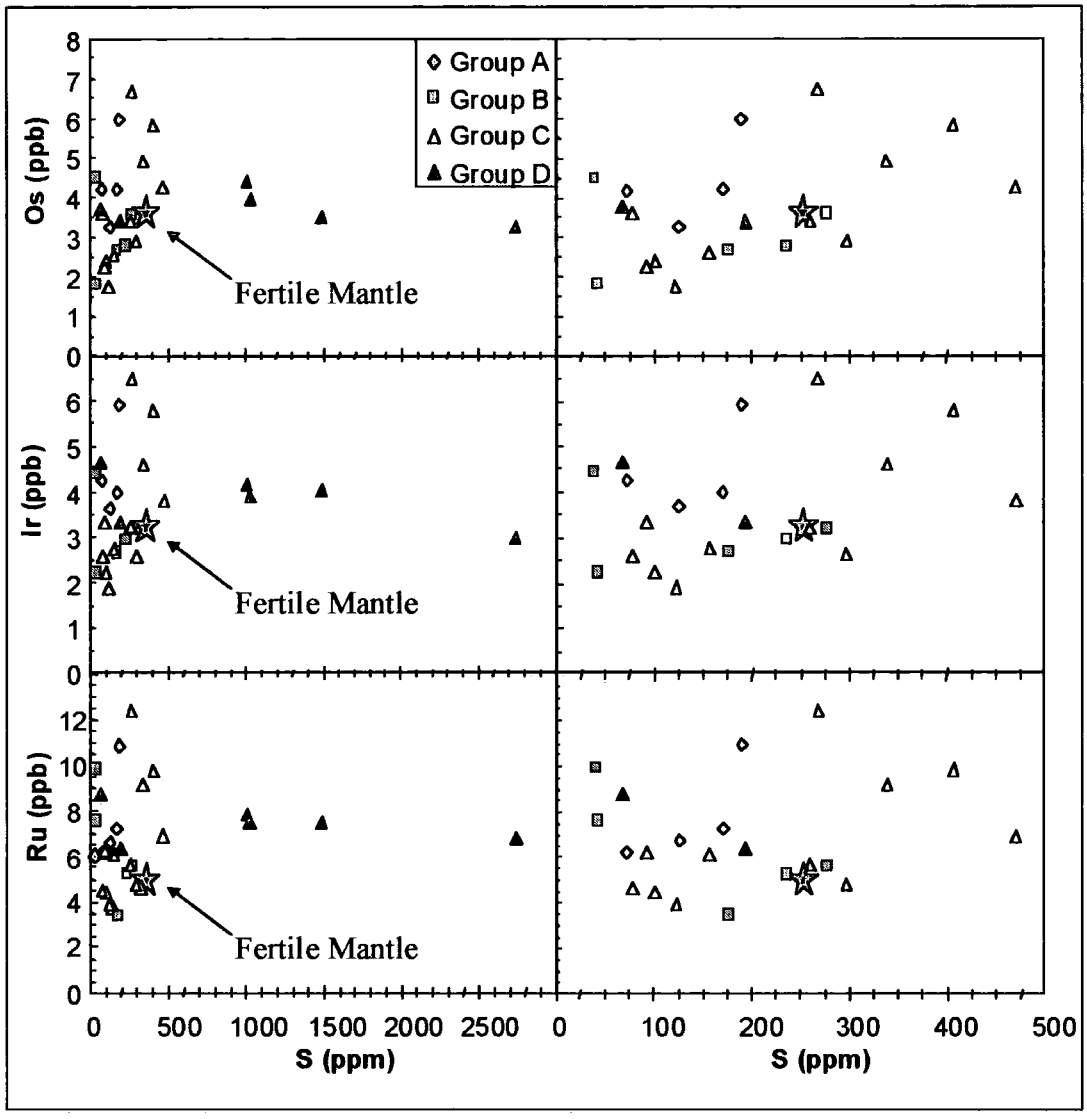

Figure 5.24 PGE and Re abundances versus S content for the Somerset Island peridotite suite. Primitive mantle, represented by star, after McDonough and Sun (1995).

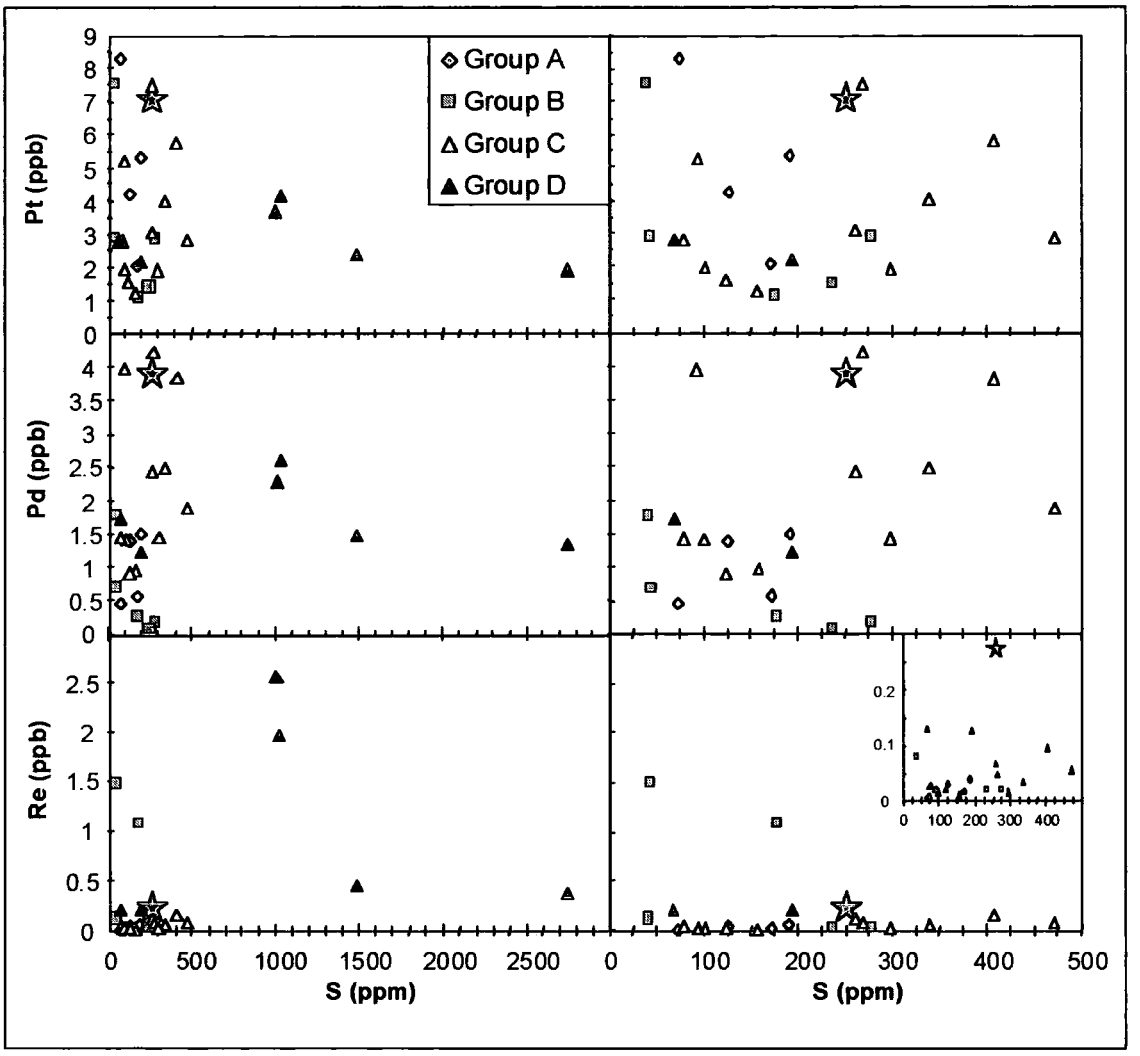

Figure 5.24 (continued) PGE and Re abundances versus S content for the Somerset Island peridotite suite. Primitive mantle, represented by star, after McDonough and Sun (1995).

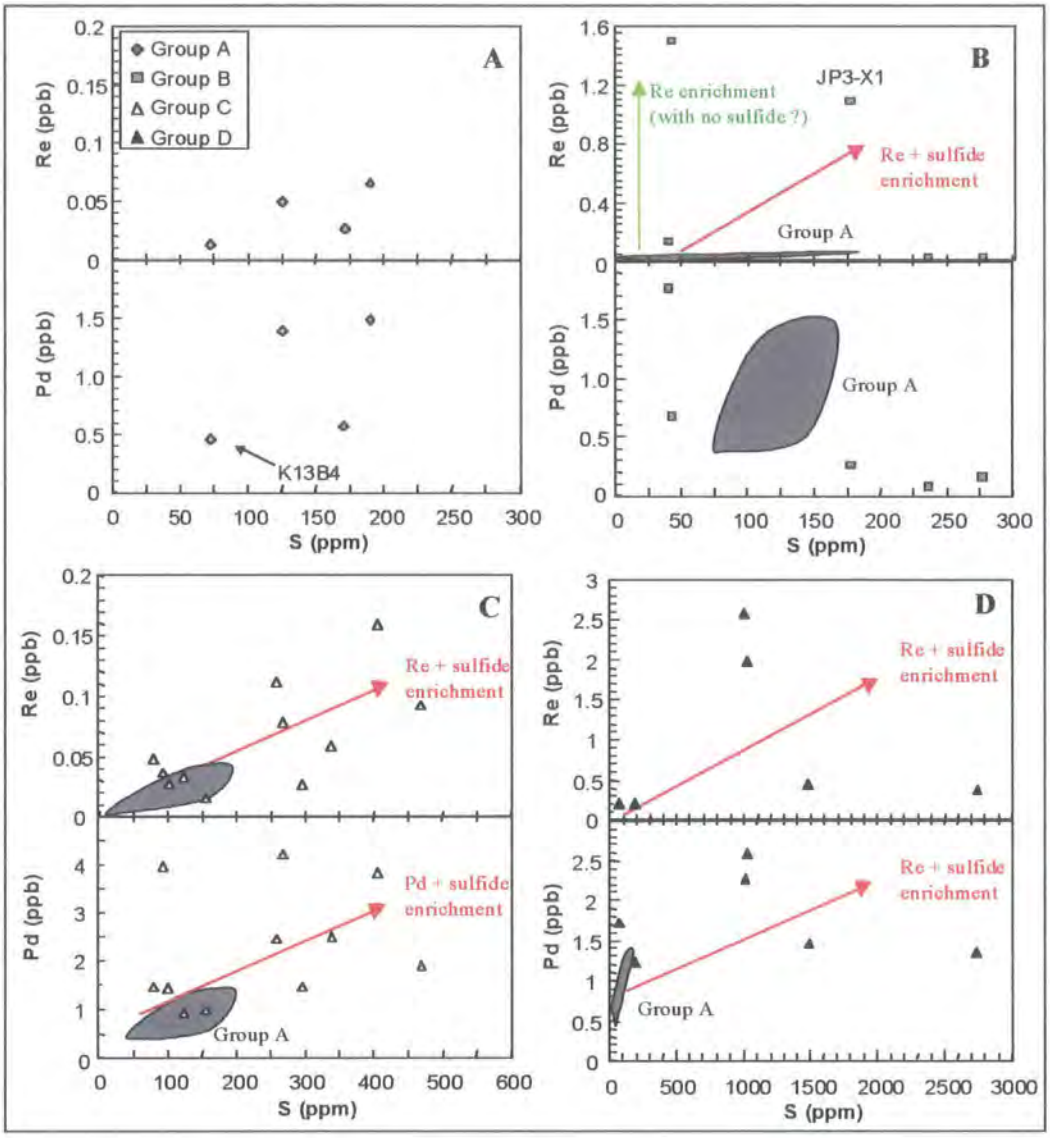

Figure 5.25 Pd and Re abundances versus S content for individual Somerset Island peridotite groups. (a) peridotites with depleted PGE patterns, (b) peridotites with Re enriched PGE patterns, (c) peridotites with Pd enriched PGE patterns, and (d) peridotites with Re and Pd enriched PGE patterns.

In detail, systematic correlations between PPGE variations and S exist in the Somerset Island peridotites if considered in terms of their chondrite normalised PGE patterns. The group A peridotites tend to have low Re and Pd concentrations (Figure 5.25a). Possible sulfide addition is suggested by elevated abundances of S up to 190 ppm. Slightly higher Pd abundances in some of the samples may relate to Pd addition, but alternatively it may just represent residual Pd from lower degrees of melt extraction. The group B peridotites show no overall systematic correlation between Re and S (Figure 5.25b), although some samples appear to be enriched in S and Re. Group C peridotites show enrichment in Pd associated with S enrichment (Figure 5.25c). These samples also appear to have elevated Re abundances also associated with S enrichment. The fourth group of peridotites, showing Pd enrichment, but also a much more

pronounced Re enrichment (group D) associated with higher degrees of S enrichment (Figure 5.25d).

5.6.4.b Variation of PGEs with major elements

No systematic variation is observed between PGE abundance and major elements for the Somerset Island peridotites, despite the large range in Al_2O_3 (Figure 5.26; Table 5.13).

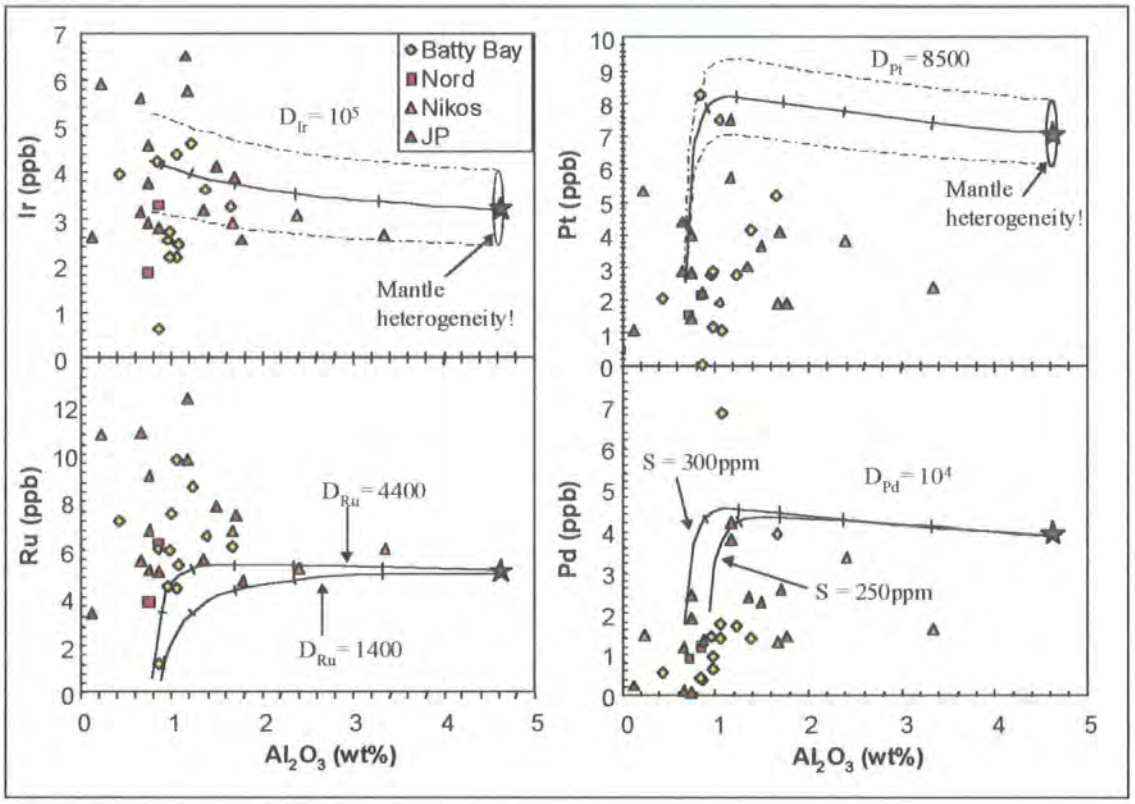

Figure 5.26 PGE abundances versus Al_2O_3. Predicted residue compositions are based on non-modal fractional melting models using a primitive mantle source ppm (represented by star symbol) with sulfur compositions of 250-300ppm, and the extracted melts have a sulfur capacity of 1000 ppm S. The range of partition coefficients for PGEs, $D_{PGE(sulf/melt)}$ is large (Stone *et al.*, 1990; Bezmen *et al.*, 1994; Peach *et al.*, 1994; Fleet *et al.*, 1996). A value of 10^4 for D_{Pd} has been used to model Pd based upon the good correlation found by Lorand *et al*(1999) in Pyrenean orogenic lherzolites. The value D_{Ir} was assumed to be an order of magnitude higher based upon contrasting behaviour of these two elements in the same study. D_{Ru} was modelled using values of 1400 and 4400, D_{Pt} a value of 8500. For comparison of models with xenolith data, F values were re-calculated as Al_2O_3 wt%. Varying S content of the source or S capacity of the melt does not significantly alter the melt extraction trends. Marks indicate 5% increments of melting.

It is not surprising that IPGEs, due to their highly compatible nature, show no clear relationship with Al_2O_3. The PPGEs, which are moderately incompatible and depleted within the Somerset Island suite however show no distinct correlations either (Figure

5.26). Correlations between the shape of PGE patterns and bulk-rock Al_2O_3 content however are evident (Figure 5.27).

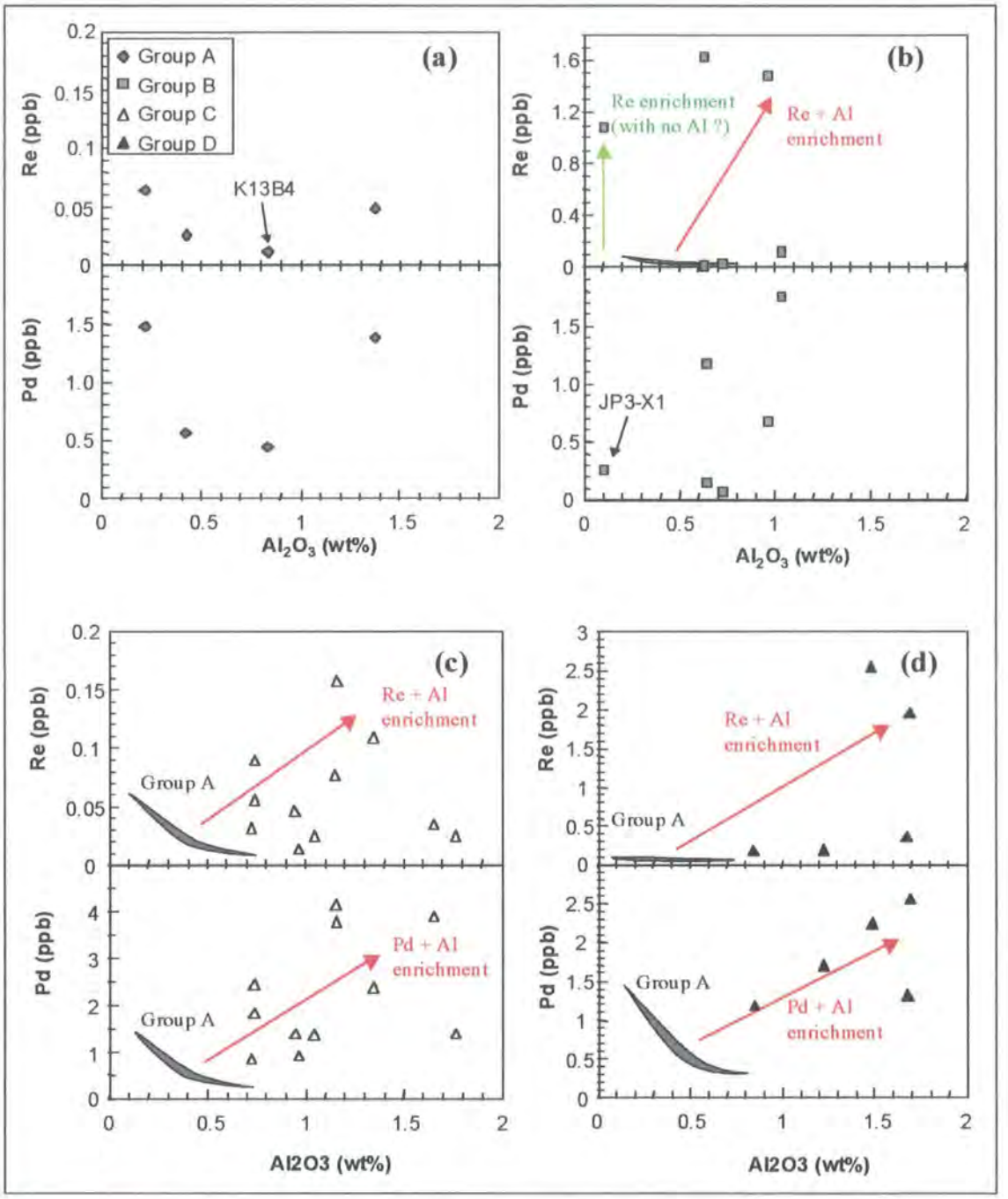

Figure 5.27 Pd and Re abundances versus Al_2O_3 content for the Somerset Island peridotites. (a) peridotites with depleted PGE patterns, (b) peridotites with Re enriched PGE patterns, (c) peridotites with Pd enriched PGE patterns, and (d) peridotites with Re and Pd enriched PGE patterns.

Group A peridotites tend to have low Re and Pd concentrations (Tables 5.13 and 5.16). Possible Al_2O_3 addition is suggested in some samples by enhanced abundances for its sulfur content. Slightly higher Pd abundances in some of the group A samples

may relate to Pd addition, but alternatively may just represent higher initial abundances in the source rock. This is supported by the fact that high Pd abundances in these samples do not necessarily correlate with high Al_2O_3. The group B peridotites show no overall systematic correlation between Re and Al_2O_3 (Figure 5.27b; Table 5.16), though many samples show an enrichment in Al_2O_3 associated with enrichment in Re. Peridotites from group C show enrichment in Pd associated with Al_2O_3 enrichment (Figure 5.27c), with an associated enrichment in Re. Group D peridotites also show a similar but higher degree of PGE enrichment associated with Al_2O_3 enrichment (Figure 5.27d).

5.6.4.c Variation of PGEs with trace elements

PPGEs are incompatible and fractionate during mantle melting and subsequent metasomatism. Trace elements are therefore more likely to track the behaviour of PPGEs and may help to constrain relative roles of fluid enrichment versus melt depletion.

PGE variation with REE: La and Yb

As discussed above, the variation of PGEs within the Somerset Island peridotite suite is not consistent with a single stage melt-extraction event, but indicates a rather more complex history. CI-chondrite normalised PGE trends from most Somerset Island peridotites display vestiges of the original fractionation associated with melt extraction, manifested in depleted Pt and Pd abundances relative to IPGEs. In contrast, incompatible trace elements show strong enrichment rather than depletion. Neither abundances or ratios of PGEs correlate with (La/Yb)n ratios. This is consistent with observations from Lesotho and Jericho (Chapters 3 and 4), and consensus in the literature that LILE-enriching processes do not significantly enrich chalcophile PGEs (Mitchell and Keays, 1981; Morgan *et al.*, 1981; Lorand, 1989).

PGE variation with hydrous fluid mobile elements

Both Re and Pd show a wide scatter when plotted against Ba, with no discernible systematics or correlations. If the Somerset Island peridotites are separated on the basis of CI-chondrite normalised PGE patterns the correlations are still generally poor, but it is possible to derive some systematics from the data. The variation in Pd and Re with Ba tends to mirror the variation of Pd and Re with Al_2O_3 content.

PGE variation with fluid immobile incompatible elements: Nb

Re and Pd show a lack of correlation with high field strength elements such as Nb, even when separated on the basis of CI-chondrite normalised PGE patterns.

5.6.5 Re-Os and PGE systematics for Somerset Island peridotite xenoliths

5.6.5.a Effects of alteration on Re and Os abundances

It has been suggested that the weathering of peridotites may alter their Os concentrations, by the leaching of sulfides (Lorand, 1990; Handler *et al.*, 1997), if these exist as primary phases. This process, if it occurs, is only likely to reduce Os concentrations within the peridotites. The Somerset Island peridotites are in general relatively fresh for cratonic peridotites and even samples showing high degrees of alteration, such as K13A1 (up to 50% serpentinisation), have Re and Os concentrations close to the average for Somerset Island peridotites (Table 5.8). As suggested by Lorand (1990) and Handler *et al* (1997) post-eruptive oxidation of peridotite xenoliths would tend to remove the base metal sulfide (BMS) phase. Under these oxidising conditions both Re and Os would be unstable as sulfide species (Burnham, 1995). This would result in the loss of Re, which should be soluble in the oxidising fluids, with Os remaining as either metal or hydrated oxide grains (Burnham, 1995). This process cannot therefore explain the scatter seen in Os abundances within the Somerset Island peridotites, nor can it explain the wide scatter to high Re abundances.

The scatter in Os abundance as a function of major element depletion (Figure 5.28) may reflect exsolution of the element from the mantle BMS phase under reducing conditions, resulting in heterogeneously distributed Os-bearing minerals such as Os-Ir alloys or laurite (Burnham, 1995).

Handler *et al* (1999) found that Ir and Os fractionated within alkali-basalt hosted spinel peridotites, from Australia, which was attributed to late stage Os mobility and loss due to the breakdown of sulfides (Handler *et al.*, 1999). From figure 5.29 it can be seen that the Ir/Os ratio of Somerset Island peridotites tends to be near-chondritic with a mean of 1.01 +/- 0.13 (cf. Chondritic Ir/Os = 0.95, Anders and Grevesse, 1989; Jochum, 1996), and there is little evidence for late stage Os loss through weathering in this suite.

These lines of evidence would suggest that Os and other IPGEs are not situated in sulfides, in the Somerset Island peridotites.

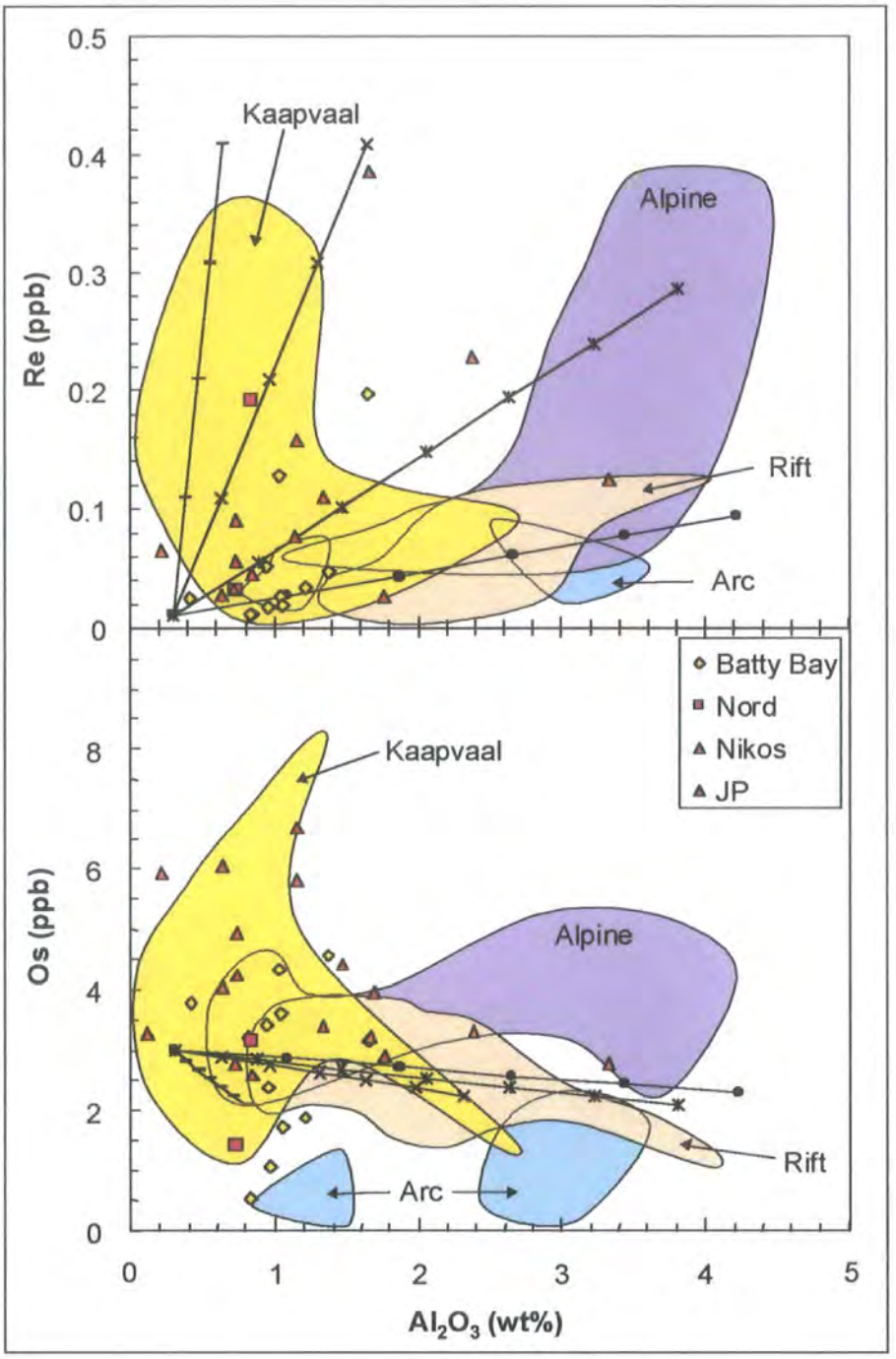

Figure 5.28 Re and Os concentrations (in ppb) against Al_2O_3 content (in wt%). Cratonic peridotites from the Kaapvaal craton (Carlson *et al.*, 1999) represented by the yellow field. Alpine peridotite data (Reisberg *et al.*, 1991; Reisberg and Lorand, 1995) are shown by the purple field and rift-related spinel peridotites (Meisel *et al.*, 1996; Handler *et al.*, 1997) by the beige field. Spinel peridotites from "arc" settings are shown by the blue fields, one each for samples from the Simcoe volcano in the Cascades and the Itchinomegata volcano in the back arc of the Japanese convergent margin (Brandon *et al.*, 1996). The lines represent model mixing lines between an end-member depleted peridotite (Al_2O_3 = 0.3%, Re = 0.01ppb, Os = 3ppb, $^{187}Os/^{188}Os$ = 0.109) and possible metasomatising magmas, marks indicate 5% increments in the addition of magma. Carbonatite (horizontal hatching; Al_2O_3 = 2%, Re = 2ppb, Os = 0.002ppb, $^{187}Os/^{188}Os$ = 0.13; Shank *et al* (1992)), kimberlite (x; Al_2O_3 = 7%, Re = 2ppb, Os = 0.5ppb, $^{187}Os/^{188}Os$ = 0.13; Walker *et al* (1989)), average OIB (star; Al_2O_3 = 12%, Re = 0.35ppb, Os = 0.2ppb, $^{187}Os/^{188}Os$ = 0.135; Reisberg *et al* (1993), Roy-Barman and Allègre (1995), Hauri and Hart (1996) and Hauri *et al* (1996)) and average MORB (circle; Al_2O_3 = 16%, Re = 0.93ppb, Os = 0.002ppb, $^{187}Os/^{188}Os$ = 0.125;], Roy-Barman and Allègre (1994) and Hauri and Hart (1996)).

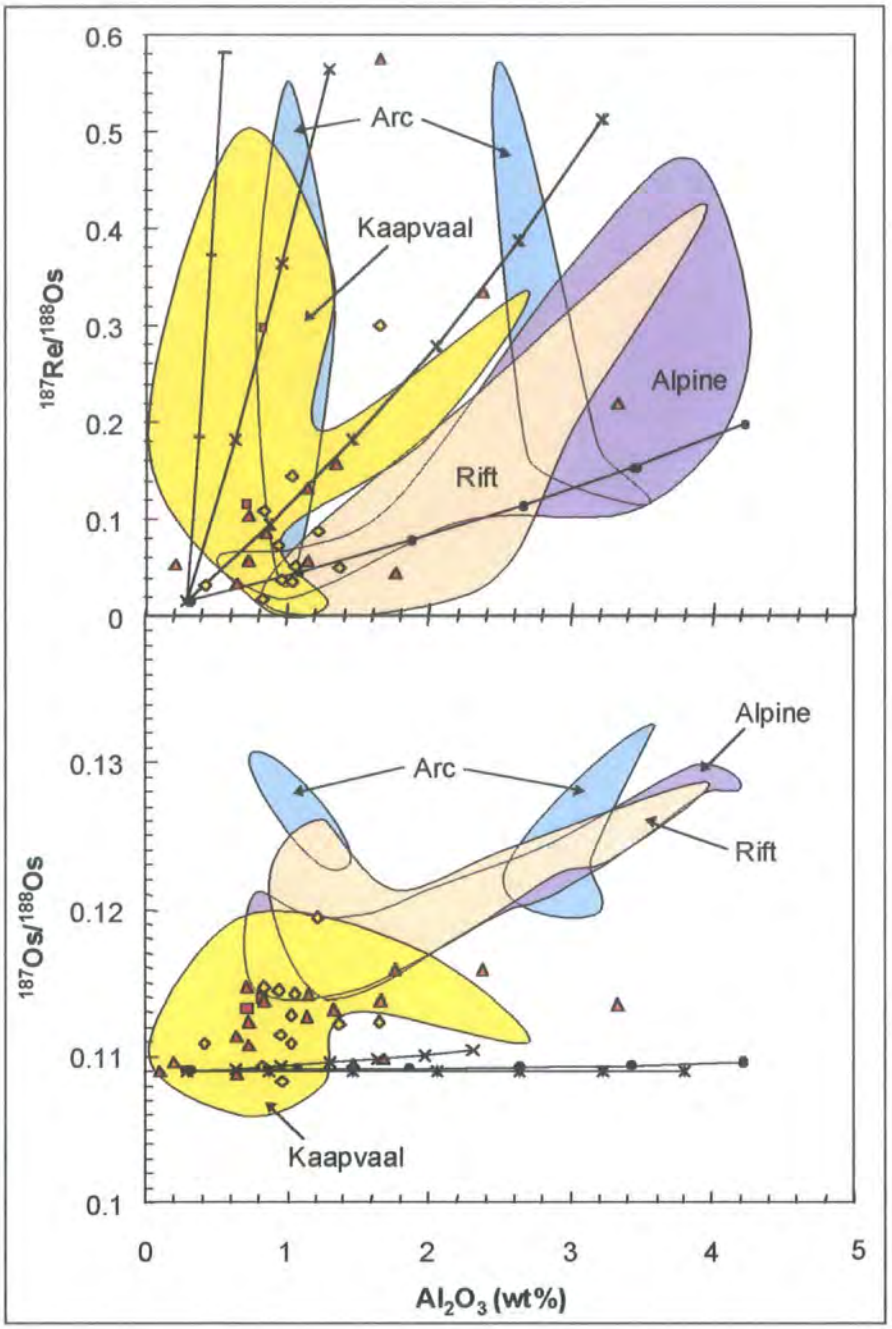

Figure 5.28 $^{187}Re/^{188}Os$ and $^{187}Os/^{188}Os$ plotted against Al_2O_3 content (in wt%). Cratonic peridotites from the Kaapvaal craton (Carlson *et al.*, 1999) represented by the yellow field. Alpine peridotite data (Reisberg *et al.*, 1991; Reisberg and Lorand, 1995) are shown by the purple field and rift-related spinel peridotites (Meisel *et al.*, 1996; Handler *et al.*, 1997) by the beige field. Spinel peridotites from "arc" settings are shown by the blue fields, one each for samples from the Simcoe volcano in the Cascades and the Itchinomegata volcano in the back arc of the Japanese convergent margin (Brandon *et al.*, 1996). The lines represent model mixing lines between an end-member depleted peridotite (Al_2O_3 = 0.3%, Re = 0.01ppb, Os = 3ppb, $^{187}Os/^{188}Os$ = 0.109) and possible metasomatising magmas, marks indicate 5% increments in the addition of magma. Carbonatite (horizontal hatching; Al_2O_3 = 2%, Re = 2ppb, Os = 0.002ppb, $^{187}Os/^{188}Os$ = 0.13; Shank *et al* (1992)), kimberlite (x; Al_2O_3 = 7%, Re = 2ppb, Os = 0.5ppb, $^{187}Os/^{188}Os$ = 0.13; Walker *et al* (1989)), average OIB (star; Al_2O_3 = 12%, Re = 0.35ppb, Os = 0.2ppb, $^{187}Os/^{188}Os$ = 0.135; Reisberg *et al* (1993), Roy-Barman and Allègre (1995), Hauri and Hart (1996) and Hauri *et al* (1996)) and average MORB (circle; Al_2O_3 = 16%, Re = 0.93ppb, Os = 0.002ppb, $^{187}Os/^{188}Os$ = 0.125;], Roy-Barman and Allègre (1994) and Hauri and Hart (1996)).

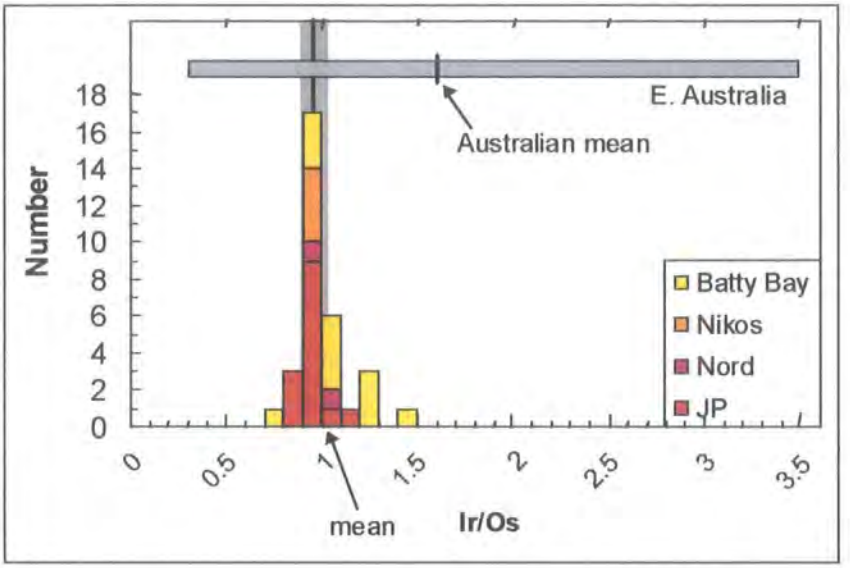

Figure 5.29 Histogram of Ir/Os ratios for Somerset Island peridotites. Vertical line represents CI-chondrite Ir/Os ratio and band represents 2σ error on mean from Anders and Grevesse (1989) and Jochum (1996). Australian xenolith data from Handler *et al* (1999).

5.6.5.b Behaviour of Re, Os and PGEs during partial melt extraction

Re behaviour during partial melt extraction

If the Re characteristics of the Somerset Island xenoliths reflect partial melting processes operating on a homogeneous mantle source, Re concentrations should correlate with indices of melt extraction. Studies on Alpine peridotites have suggested that Re partitions into melts with a distribution coefficient similar to that of Al (Reisberg and Lorand, 1995). This can be seen by the simple correlation in Figure 5.28. Similar correlations have been reported for rift-related spinel peridotites erupted in alkali basalts (Meisel *et al.*, 1996; Handler *et al.*, 1997). In contrast, arc-related spinel peridotites show little correlation between Re and Al (Brandon *et al.*, 1996). Peridotite xenoliths from Somerset Island show no overall correlation between Re and indices of melt depletion, such as Al_2O_3, suggesting that Re variation is not exclusively controlled by partial melt extraction (Figure 5.28). Studies of cratonic peridotite xenoliths from the Kaapvaal craton (Pearson *et al.*, 1995a; Carlson *et al.*, 1999) also found no correlation between Re and melt-extraction indices and these studies suggested that the large variation in Re could be attributed to "metasomatism".

The generally low Re/Os of Somerset Island peridotites is consistent with the melt-depleted nature of both bulk-rock and mineral compositions that indicate depletion in magmaphile elements (Sections 5.4 and 5.5, Kjarsgaard and Peterson, 1992).

Os and other PGE behaviour during partial melt extraction

Modelling PGEs as a function of Al_2O_3 allows us to investigate the buffering effect of sulfides (Lorand *et al.*, 1993; Keays, 1995; Snow and Schmidt, 1998), and the behaviour of PGEs and Re during partial melting. Positive correlations between S and Al_2O_3 within unmetasomatised peridotites from the Pyrenees massif were offered as evidence of a residual origin for sulfides (Lorand *et al.*, 1989). From Figure 5.30 it can be seen that little correlation exists between S and Al_2O_3 for the Somerset Island peridotites, though this lack of correlation may be the result of metasomatism disrupting any original systematics.

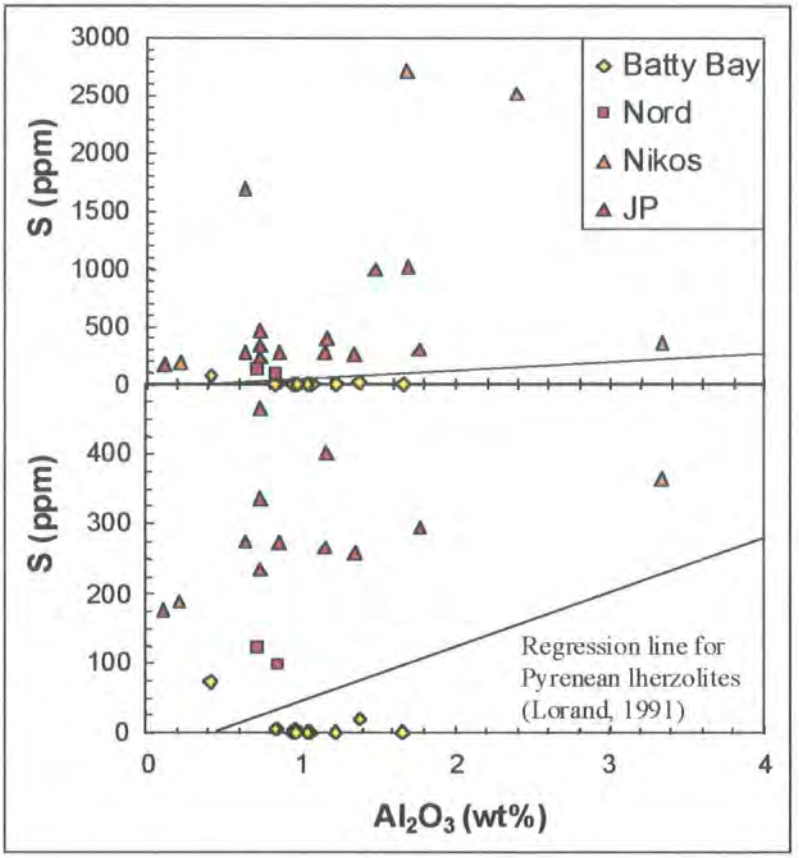

Figure 5.30 Variations of S (ppm) as a function of Al_2O_3 (wt%) in the Somerset Island peridotites.

Melt extraction models fail to account for the variation in PGEs with S for the Somerset Island samples (Tables 5.13 and 5.16), and therefore do not help to constrain the role of sulfides in hosting PGEs (Figure 5.31). Some of the vertical spread in Figure 5.31, over and above that expected for simple melt extraction, may be consistent with a non-homogeneous or non-common source. The distribution of S within the Somerset Island samples however is more complex. Several samples with very low-level Pd samples are enriched in sulfur for no accompanying enrichment in Pd.

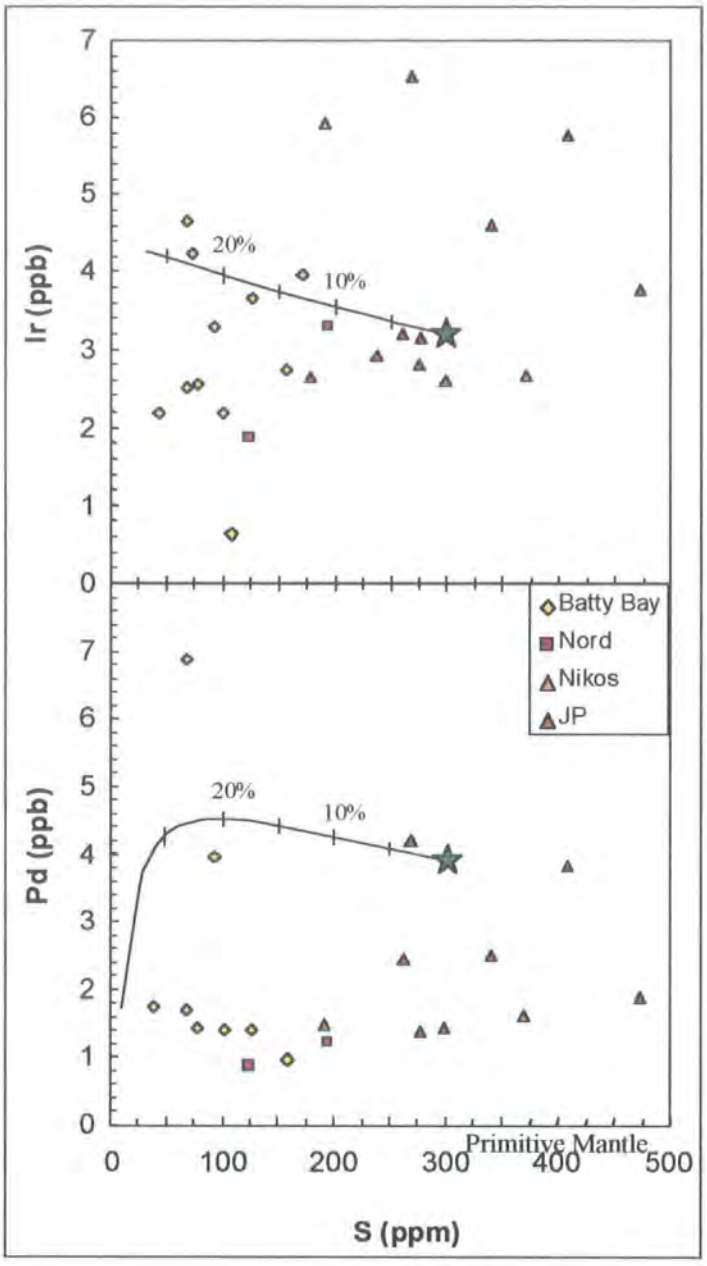

Figure 5.31 Predicted residue compositions are based on non-modal fractional melting models using a primitive mantle source with sulfur compositions of 300 ppm (represented by star symbol), and the extracted melts have a sulfur capacity of 1000 ppm S. The range of partition coefficients for PGEs, $D_{PGE(sulf/melt)}$ is large (Stone *et al.*, 1990; Bezmen *et al.*, 1994; Peach *et al.*, 1994; Fleet *et al.*, 1996). As for Figure 5.26 a value of 10^4 for D_{Pd} has been used to model Pd and the value D_{Ir} was assumed to be an order of magnitude higher based upon contrasting behaviour of these two elements. Varying S content of the source or S capacity of the melt does not significantly alter the melt extraction trends.

Non-modal fractional melting melt extraction models were created for PGEs for comparison to the Somerset Island peridotites (Figure 5.26). Values of F for the models were recalculated as Al_2O_3 using the inverse method of Bodinier (1988). Little correlation exists between PGEs and Al_2O_3, or the predicted models of melt extraction (Figure 5.26 and 5.28). However, several samples appear to display both low Pd and Al_2O_3 abundances and are consistent with >25% melt extraction. Varying the S content

of the source does not significantly alter the melt extraction trends for the models and cannot explain the spread in data. Altering partition coefficients, $D_{PGE(sulf/melt)}$, also fails to account for the spread in data. Os and Ir are compatible during mantle melting and therefore plots of Os and Ir against melt-indices such as Al_2O_3 should produce sub-horizontal trends. This is the case for peridotites from most tectonic settings (Figure 5.28). Peridotites from Somerset Island together with cratonic peridotites from the Kaapvaal craton (Pearson *et al.*, 1995a; Carlson *et al.*, 1999) show a wide, non-systematic variation in Os concentrations with a near vertical trend for a low Al_2O_3 (wt%) content. The reason for this observed trend is not known and even extreme cases of melt extraction could not produce this range in Os content (Figure 5.28). The scatter in Os concentration may reflect the heterogeneous distribution of sulfides or ultra-trace Os-alloys within the Somerset Island lithospheric mantle. It is unclear why this feature appears to be exclusive to cratonic lithospheric peridotites such as seen at Somerset Island and Kaapvaal, and not peridotites from other tectonic settings. It is possible that the variations observed in the IPGE contents for cratonic peridotites are produced from process other than melt removal. This is not supported by the general features of PGE patterns from Somerset Island peridotites. The variations in Ir and Os abundances may be related to extreme degrees of melt depletion, greater than experienced by peridotites from other tectonic settings, removing primary sulfides completely from the residue and stabilising alloy phases, resulting in substantial whole rock heterogeneity.

If PGE ratios are considered as a function of Al_2O_3, this should negate source heterogeneities, assuming chondritic ratios are present initially. If Pd and Ir are considered as incompatible and compatible PGEs respectively, theoretical models of melt extraction should constrain the behaviour and fractionation of these groups. There is still limited correlation between PGEs and the theoretical behaviour of Pd/Ir and Al_2O_3 for melt extraction models in Somerset Island peridotites (Figure 5.32), but some systematics do emerge. For several of the Somerset Island peridotites, depleted bulk-rock Al_2O_3 contents correlate well with samples showing depleted PGE signatures, i.e. low $(Pd/Ir)_n$ (Group A and B; Table 5.16; Figure 5.23a and b). This suggests that the PGE systematics for these samples have remained closed since the time of initial melt extraction. In contrast, displacement of other samples from the theoretical model trends on a Pd/Ir vs. Al_2O_3 plot is consistent with their disturbed PGE patterns. These samples plot on vectors that may be attributed to sulfide or melt addition (Figure 5.32).

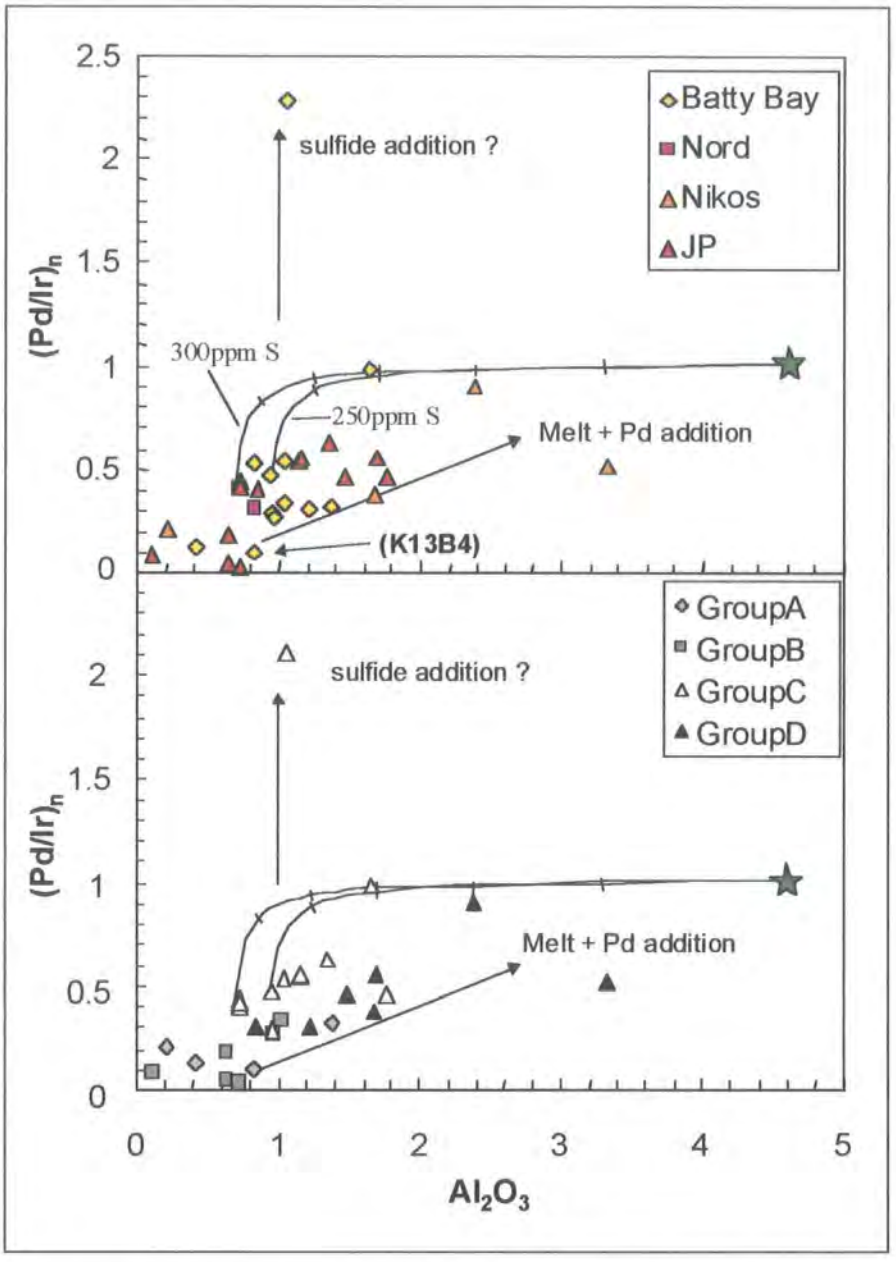

Figure 5.32 Variation of chondrite-normalised Pd/Ir as a function of whole-rock Al_2O_3 content (wt%). Lines represent the theoretical evolution of Pd/Ir in a peridotite residuum submitted to increasing degrees of equilibrium partial melting. Marks indicate 5% increments of melting. Primitive mantle represented by the star symbol. The two curves depict starting compositions with 250ppm and 300ppm total sulfur.

5.6.5.c Effects of metasomatism and melt infiltration

Metasomatism

Multiple generations of sulfides can exist within individual peridotites (Burton *et al.*, 1999; Alard *et al.*, 2000; Pearson *et al.*, 2000). The precipitation of secondary sulfide along intergranular boundaries may account for the spread seen in Os concentrations, PGE systematics and Os isotope ratios within the Somerset Island peridotite suite. Samples with low Re abundances (Group A, Table 5.16) would suggest that they have little secondary sulfide introduction, assuming the sulfide contains high abundances of

Re. In general, sulfide and/or melt addition to Jericho peridotites associated with Re enrichment only (Group B; Table 5.16), apperars to have little effect on Os abundance or $^{187}Os/^{188}Os$ ratios (Table 5.17).

Group	Sample	S (ppm)	Os (ppb)	$(Pd/Ir)_n$	$^{187}Os/^{188}Os(i)$
A	K11A16	126	3.25	0.31627	0.11218
	K13A3	171	4.20	0.12076	0.11095
	K13B4	73	4.18	0.09034	0.10937
	X07	190	5.95	0.20894	0.10964
B	K13A1	40	4.49	0.33144	0.11089
	K15A4	43	1.80	0.25819	0.10836
	JP2-X2	277	3.58	0.04229	0.11145
	JP3-X1	177	2.65	0.08295	0.10899
	JPN11	236	2.77	0.02268	0.11477
	JPS1		6.07	0.17316	0.10875
C	K11A14	101	2.39	0.53349	0.11285
	K11A17	157	2.58	0.29025	0.11151
	K12A1	78	3.60	0.46432	0.11448
	K13A4	93	2.25	0.9856	0.11941
	N2B	123	1.74	0.39982	0.11329
	JP1-X2	260	3.41	0.62718	0.11313
	JPN2	339	4.91	0.4455	0.11077
	JPN3A	268	6.70	0.53323	0.11265
	JPN3B	407	5.81	0.54735	0.11423
	JPN4	298	2.91	0.45706	0.11586
	JPN9	471	4.25	0.41186	0.11238
D	K13A5	68	3.73	0.30518	0.11229
	N1C	194	3.38	0.305	0.11399
	X05	2741	3.23	0.37402	0.11378
	JPS4	1484	3.48	0.30009	0.10933
	JPS6A	1006	4.43	0.45318	0.10945
	JPS6B	1028	3.97	0.54944	0.10990

Table 5.17 Summary of S and Os abundances, PGE systematics and $^{187}Os/^{188}Os$ isotope ratios for low-T Somerset Island peridotites, on the basis of the PGE patterns.

Peridotites with more complex PGE patterns, showing Pd enrichment as well as Re tend to have more radiogenic $^{187}Os/^{188}Os$ ratios (Table 5.16 and 5.17), and therefore Os isotopic compositions may be a reflection of secondary sulfide addition in these samples. In terms of the abundance of Os however, there is no clear evidence of Os enrichment (Table 5.17). An alternative explanation for these samples therefore may be that the radiogenic Os isotopic compositions signify residual Re in only moderately depleted peridotites, or Re addition occurred earlier in the history of the samples.

Variation of PGEs in terms of their absolute and relative abundances, and co-variation with S and Al_2O_3 suggest that the Somerset Island peridotites have a complex history of melt extraction with post melt-extraction enrichment. The nature of

enrichment of PGEs is variable suggesting that the peridotites may have been affected different generations of fluid enrichment.

The high Re and Re/Os of mantle derived melts and fluids, relative to residual peridotite, makes the peridotite susceptible to contamination by processes such as metasomatism and melt infiltration. No single magma or fluid type can be invoked to produce the wide scatter seen within the Somerset Island peridotites (Figure 5.28). Due to the relatively small variation in Al_2O_3 content seen within the Somerset Island peridotites (Table 5.8), the metasomatising fluid is limited to one with a relatively high Re/Al and Os/Al ratio. This would generally rule out basaltic fluids (Figure 5.28). Possible metasomatising fluids include Al-poor hydrous fluids from the de-watering of subducted slabs (Brandon *et al.*, 1996), or carbonatitic and high Re kimberlitic melts (Pearson *et al.*, 1995a; Carlson *et al.*, 1999). The Somerset Island peridotites have an average Os concentration higher than bulk-mantle compared to lower than bulk-mantle for peridotites from arc settings. Brandon *et al* (1996) attributed the low Os contents of arc peridotites to oxidation by hydrous fluids anf therefore this process could not account for the generally high Os content within Somerset peridotites, though perhaps another type of fluid associated with subduction zones may be responsible.

Correlations have been observed between $^{187}Os/^{188}Os$ and Al_2O_3 in off-craton spinel lherzolite and orogenic massif suites (Reisberg and Lorand, 1995; Handler *et al.*, 1997). In contrast the Somerset Island peridotites show no correlation (Figure 5.28). This lack of correlation has also been observed in other cratonic and circum-cratonic xenoliths suites such as Namibia and East Griqualand (Pearson, 1999a). The mixing lines in Figure 5.28 suggest that infiltration by common magmatic fluids could account for the horizontal distribution in $^{187}Os/^{188}Os$ data, but not the vertical, unless the infiltration of metasomatising fluids was accompanied by precipitation of Os-rich sulfides or alloys.

The scatter in Re content in the Somerset Island peridotites can be generally accounted for by a 0-10% addition of kimberlite or 0-5% carbonatite to the lithospheric peridotites, but this does not account for all samples. The remaining scatter in Re data can be accounted for by the addition of 0-20% OIB or MORB. The addition of up to 10% carbonatite and kimberlite should be apparent from enrichment in elements such as Ba and Sr. From Figure 5.33 we can see that there is no overall systematic correlation between Re and Ba. The scatter in Re and Ba can be variously accounted for by the addition of 0-5% carbonatite, 0-15% kimberlite or 0-25% OIB, but again this does not account for all samples and does not account for all samples, e.g. the enrichment in Al_2O_3. If the composition of the end-member depleted peridotite in Figure 5.28 is

sequentially modified, the model mixing lines can be seen to correspond better with some of the scattered data. One explanation for this is the peridotites are not sourced from a single depleted homogeneous mantle source. This simplistic model however does not account for the possibility of several generations of metasomatic alteration.

Rb-Sr, Sm-Nd and U-Th-Pb isotope studies on mantle peridotites corroborate the idea of pervasive metasomatism, to the degree that metasomatic signatures dominate and little information can be gained about the initial melt extraction event (Stosch *et al.*, 1980; Richardson *et al.*, 1985, Carlson, 1994 ; Pearson *et al.*, 1995a).

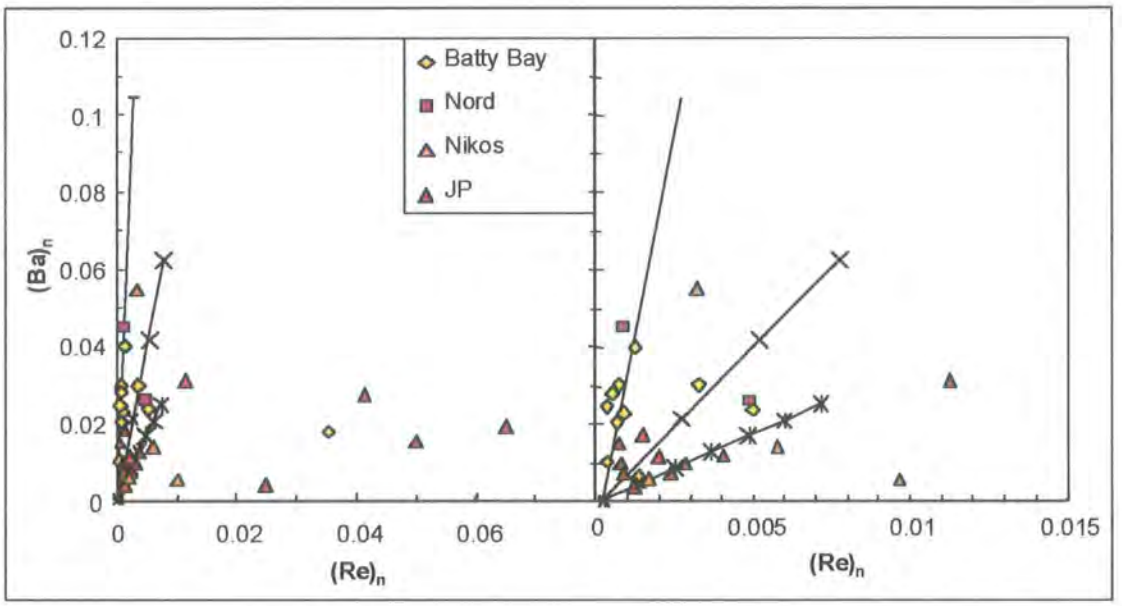

Figure 5.33 A) Chondrite normalised plot of Ba vs. Re content for Somerset Island peridotites. The lines represent model mixing lines between an end-member depleted peridotite (Re = 0.01ppb, Ba = 1ppm) and possible metasomatising magmas, marks indicate 5% increments in the addition of magma. Carbonatite (hatching; Re = 2ppb, Ba = 5000ppm; Tuttle and Gittins (1966)), kimberlite (x; Re = 2ppb, Ba = 1000ppm; Bergman (1987) and Smith *et al* (1985)), average OIB (star; Re = 0.35ppb, Ba = 200ppm; Basaltic Volcanism Studies Project (1981)).

Cumulate processes

An alternative mechanism to explain the scatter in Re and Os concentrations is that they contain a cumulate component (Herzberg, 1993; Pearson *et al.*, 1995a; Herzberg, 1999). Herzberg (1993) suggested that the orthopyroxene rich nature of cratonic peridotites in the Kaapvaal craton could be explained by the crystallisation of orthopyroxene cumulates from the mixing of ascending komatiitic magmas and olivine-rich residues of komatiite extraction. Although the Somerset Island lithospheric mantle has on average a lower modal volume of orthopyroxene than that of the Kaapvaal craton (Table 5.6) this model may still be applicable, as many of the peridotites show SiO_2 enrichment relative to melting models and experiments. It has been proposed that the

Re content within orthopyroxene is low, therefore making it unlikely that the addition of orthopyroxene could produce the observed scatter in Re concentration (Hart and Ravizza, 1996). However, if the deep crystallisation of the komatiite and cumulate component is accompanied by the precipitation of sulfides or alloys rich in Re and Os, this could contribute to the scatter observed (Pearson *et al.*, 1998b).

5.7 Timing of lithospheric mantle differentiation

5.7.1 Re-Os Isochrons

If the Somerset Island peridotites were formed from a common source with constant isotopic composition but varying Re/Os, in a single melt-extraction event, the samples would define an isochron whose slope defines the age of melt extraction. As can be seen from Figure 5.34 this is not the case with the Somerset Island peridotites and the data are widely scattered, due to the processes discussed previously.

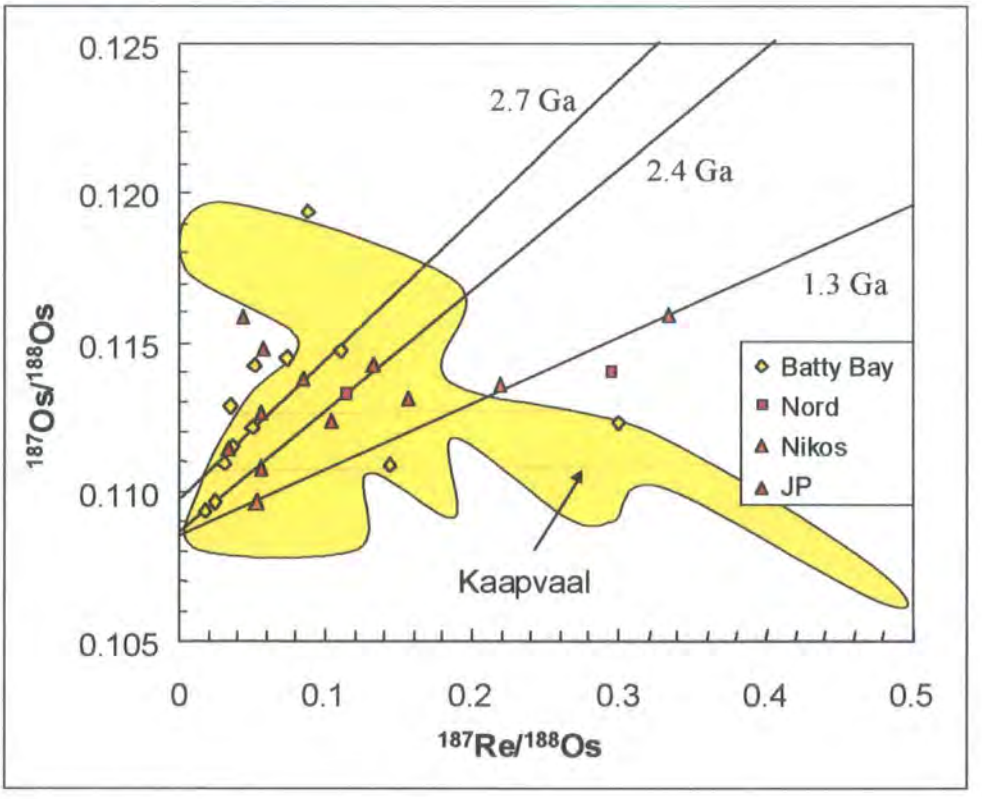

Figure 5.34 Re-Os isochron diagram for the Somerset Island data shown in Table 5.8. Reference isochrons passing through the Somerset Island data are shown. Isochrons were calculated using a decay constant (λ) of 1.666×10^{-11}. Kaapvaal data from Carlson *et al* (1999).

Reference isochrons have been added to Figure 5.34 for comparative purposes. Some samples lie close to these isochrons and define linear arrays. Three of the four

samples from the Nikos kimberlite appear to define a linear array that corresponds to an age of 1.3 Ga with an initial Os isotopic composition of 0.1085 (γOs = -9.1). From the overall scatter in data it is doubtful whether this has any real significance, and is probably coincidental despite being close to the age of the McKenzie dykes.

The peridotites may have formed an isochron initially, but the lack of correlation is not surprising given the known variations in Re and Os contents and possible metasomatic alteration. This lack of isochronous behaviour argues against the variation in Re and Os simply from cumulate processes close to the time of melt extraction and suggests instead that Re/Os was fractionated, possibly more than once, following initial formation. This is consistent with other studies that show evidence of recent Re addition in mantle xenoliths (Walker *et al.*, 1989; Meisel *et al.*, 1996; Chesley *et al.*, 1999) and disturbed Re/Os in massif peridotites (Reisberg *et al.*, 1991; Reisberg and Lorand, 1995).

5.7.2 Age determination from Al_2O_3 - $^{187}Os/^{188}Os$ relationships

As discussed in Chapter 3.7.2, Al - Os isotope relationships have been used to constrain peridotite ages in massifs (Reisberg *et al.*, 1991; Reisberg and Lorand, 1995). There is a general lack of correlation between Al_2O_3 and $^{187}Os/^{188}Os$ for the Somerset Island peridotites (Figure 5.35). The dispersion of the data is too great for any useful age information to be obtained from this diagram for the Somerset Island samples.

The lack of correlation is not surprising given the known variations in $^{187}Os/^{188}Os$ composition over a small range in Al_2O_3 and likely metasomatic alteration to both.

5.7.3 Model ages for Somerset Island peridotites

Rhenium depletion model ages

The observed range in Os isotopic compositions for the Somerset Island peridotites (Table 5.8) equate to T_{RD} model ages of 2.8 to 1.3 Ga (Figure 5.36). Nine samples have T_{RD} model ages between 2.5 Ga and 3.0 Ga, and 24 samples have T_{RD} ages < 2.5Ga.

Three features are prominent in the distribution of T_{RD} model ages shown in Figure 5.36; (i) no samples with T_{RD} > 3.0 Ga, (ii) a prominent peak in samples between 2.0 and 2.25 Ga, and (iii) broad distribution of T_{RD} model ages to older Archean ages. The mean T_{RD} model age for all Somerset Island peridotite samples shown in Figure 5.36 is 2.3 +/- 0.3 Ga (1 std.dev.) with a median of 2.3 Ga. This is lower than the mean T_{RD} model age reported by Carlson *et al* (1999) for cratonic peridotites from the Kaapvaal

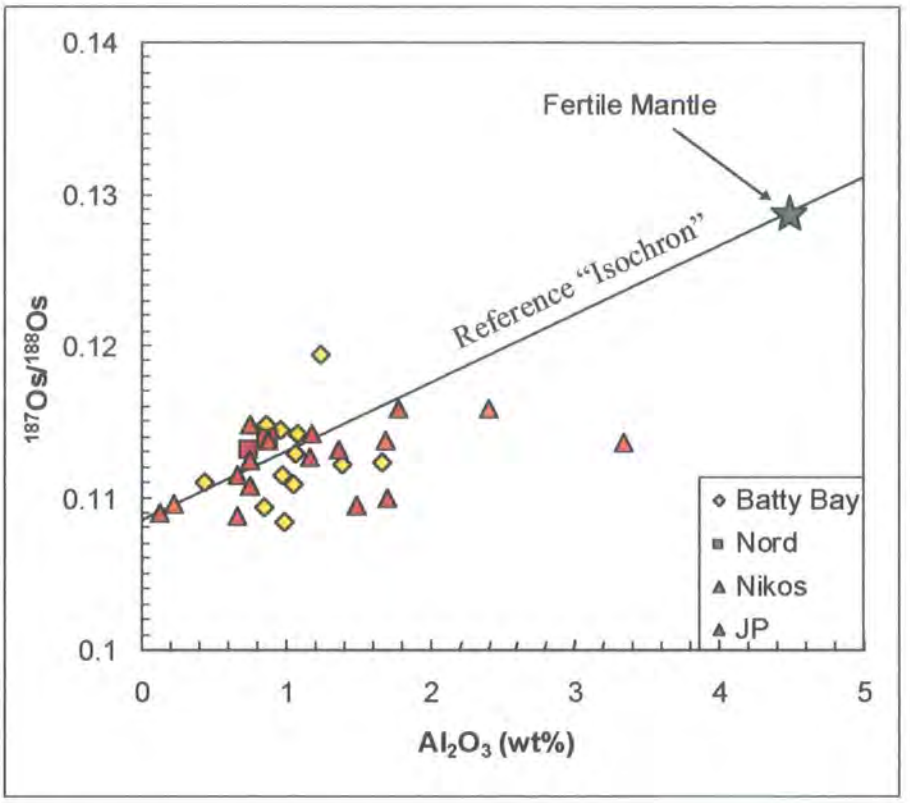

Figure 5.35 $^{187}Os/^{188}Os$ concentration plotted against Al_2O_3 content (in wt%). Line represents a reference "isochron" passing through fertile mantle and the most depleted Somerset Island samples. $^{187}Os/^{188}Os(i)$ for the isochron is 0.1085, which equates to an age of 2.8Ga.

craton (mean = 2.5 +/- 0.4 Ga, median =2.6 Ga). In general, peridotites from individual kimberlite localities on Somerset Island show a similar distribution in T_{RD} ages compared to the overall distribution seen in Figure 5.36. Peridotites from Batty Bay have a mean T_{RD} model age of 2.3 +/- 0.4 Ga with a median of 2.3 Ga and peridotites from JP have a mean of 2.3 +/- 0.3 Ga with a median of 2.3 Ga. Peridotites from Nikos and Nord have a slightly lower mean T_{RD} model age, at 2.2 +/- 0.3 Ga for Nikos and 2.1 +/- 0.1 Ga for Nord.

There is no clear overall correlation between T_{RD} and depth of origin for the Somerset Island peridotites (Figure 5.37), although there may be a weak correlation at the JP kimberlite where there appears to be a possible younging with depth. If we consider spinel peridotites alone, these have a mean T_{RD} of 2.2 +/- 0.5 Ga with a median of 2.4 Ga, which is comparable to the overall mean for Somerset Island. The mean for garnet-spinel peridotites is 2.4 +/- 0.3 Ga with a median of 2.4 Ga, and garnet peridotites 2.2 +/- 0.3 Ga with a median of 2.2 Ga. The age of the Somerset Island lithospheric mantle within the individual facies would therefore appear to be the same, within error, though the overall range of ages within the spinel facies appears to be

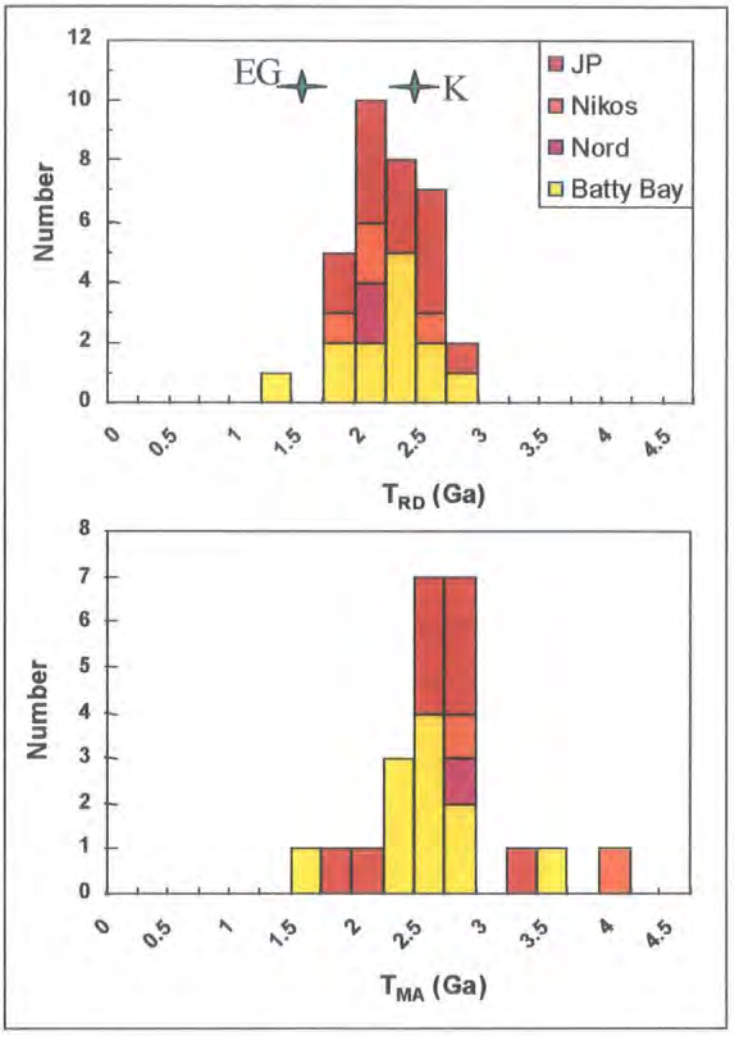

Figure 5.36 Histograms of Re-depletion (T_{RD}) and mantle extraction (T_{MA}) model ages for Somerset Island peridotites. Also shown are mean T_{RD} values for K – Kaapvaal from Carlson *et al* (1999) at 2.5 Ga, and EG - East Griqualand from Pearson *et al* (1998a) at 1.5 Ga.

larger. The maximum T_{RD} model age for spinel peridotites at Somerset Island is 2.7 Ga, garnet-spinel peridotites 2.8 Ga, and garnet peridotites 2.7 Ga. It would therefore suggest that ancient Archean lithospheric mantle persists to depth at Somerset Island, but either this has been modified by reworking at a later stage or younger mantle has been added to the lithospheres stratigraphic column. The overall range in T_{RD} ages for the Somerset Island lithospheric mantle indicates that it has persisted since at least the Early Proterozoic.

Mantle separation model ages

The observed range in Os isotopic compositions for the Somerset Island peridotites (Table 5.8) equate to T_{MA} model ages of 4.2 to 1.6 Ga (Figure 5.36), excluding those that produce future ages or ages greater than the age of the Earth. Three samples have T_{MA} ages >3.0 Ga, fourteen samples have T_{MA} model ages between 2.5 Ga and 3.0 Ga, and six samples have T_{MA} ages < 2.5Ga. Two features are prominent in the distribution

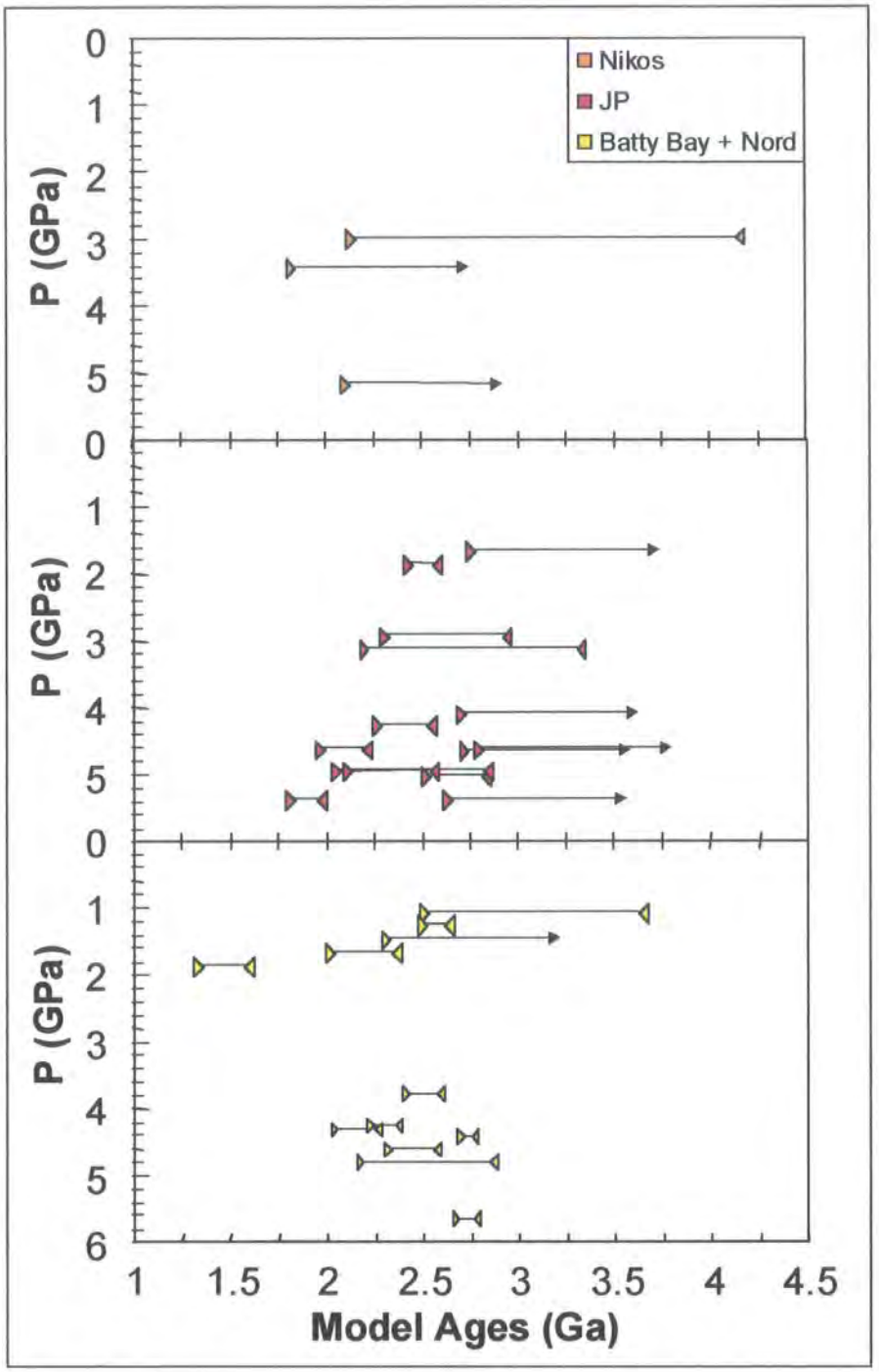

Figure 5.37 T_{RD} (right facing triangles) and T_{MA} (left facing triangles) model ages for peridotite xenoliths from individual kimberlite pipes plotted against the pressure of equilibration as determined by mineral geothermobarometry. All samples plotting at pressures less than 2 GPa are spinel peridotites (pressure arbitrarily assigned in 0.2 GPa increments up to 2 GPa). Samples with arrows have T_{MA} ages in excess of the age of the Earth.

of T_{MA} model ages shown in Figure 5.36; (i) few samples with T_{MA} > 3.0 Ga, and (ii) main peak in samples between 2.5 and 3.0 Ga. The mean T_{MA} model age for all Somerset Island peridotite samples shown in Figure 5.36 is 2.7 +/- 0.5 Ga (1 std.dev.) with a median of 2.6 Ga. In general, peridotites from individual kimberlite localities on

Somerset Island show a similar distribution in T_{MA} ages compared to the overall distribution seen in Figure 5.36. Peridotites from JP have a mean T_{MA} model age of 2.7 +/- 0.4 Ga with a median of 2.6 Ga and peridotites from Batty Bay have a mean of 2.6 +/- 0.5 Ga with a median of 2.6 Ga.

Again there is no clear correlation between T_{MA} model ages and depth of origin for the Somerset Island peridotites (Figure 5.37). If we consider spinel peridotites alone, these have a mean T_{MA} of 2.6 +/- 0.7 Ga with a median of 2.6 Ga, which is comparable to the overall mean for Somerset Island. The mean for garnet-spinel peridotites is 2.9 +/- 0.5 Ga with a median of 2.8 Ga, and garnet peridotites 2.5 +/- 0.3 Ga with a median of 2.6 Ga. The maximum T_{MA} model age for spinel peridotites at Somerset Island is 3.6 Ga, garnet-spinel peridotites 4.2 Ga, and garnet peridotites 3.0 Ga. This would suggest that the lithospheric mantle beneath Somerset Island has persisted since the Archean, throughout its stratigraphic column.

5.7.4 Constraints from PGE systematics on the significance of model ages for the lithospheric mantle beneath Somerset Island

By considering the PGE systematics of Somerset Island peridotites in conjunction with the Re-Os age systematics we can evaluate the significance of T_{RD} vs. T_{MA} model ages and hence better constrain the age of the lithospheric mantle beneath Somerset Island, part of the Churchill province.

A few Somerset Island peridotites have extremely fractionated CI-chondrite normalised PGE patterns (Figure 5.23a). Patterns such as those expected for a residues of extensive melting where loss of most of the primary sulfide has occurred (>25% melting). This is also reflected in the depleted major element compositions (Table 5.6). The very depleted Re content of a number of Somerset Island samples is reflected in the close agreement seen between T_{RD} and T_{MA} model ages, for example sample K13B4 with T_{RD} and T_{MA} of 2.7 and 2.8 Ga respectively. The low bulk-rock Al_2O_3, low $(Pd/Ir)_n$ of 0.09, depleted PGE profile and close agreement in model ages suggest that the Re-Os isotope systematics for at least some of the Somerset Island peridotites have remained closed since initial melt extraction. REE enrichment of these samples (Table 5.7) indicates that the they have undergone a degree of metasomatism, but this is not accompanied by significant Re enrichment and hence has not disturbed the Re-Os isotope systematics. The T_{MA} model age of sample K13B4 therefore is a likely approximation of the age of melting and provides a maximum age for the lithospheric

mantle as sampled by the Somerset Island kimberlites from the present sample suite. The small difference between T_{RD} and T_{MA} model ages shows that in this case, although T_{RD} represents the minimum age of the sample, it would appear to be a good approximation of the actual age for PPGE depleted samples.

In contrast, some Somerset Island samples also display highly fractionated PGE patterns but with marked inflection in the Re abundance (Figure 5.23b). (Pd/Ir)n values for these samples (mean = 0.15 +/- 0.12) suggest they have undergone melt extraction and give little indication of the disturbed nature of the PGE profiles. The extended PGE pattern for samples such as JP3-X1 shows a Re inflection, and this leads to a considerable difference between T_{RD} (2.7 Ga) and T_{MA} (future) model ages. The Re enrichment was accompanied by S enrichment, but no enrichment in Al_2O_3 (Table 5.16). This most likely indicates enrichment by sulfides with no addition of any silicate phases. Sample JP3-X1 has a similar T_{RD} model age to sample K13B4, consistent with a major melt extraction event at 2.7 Ga and may suggest that Os was not transported by the infiltrating sulfide phases.

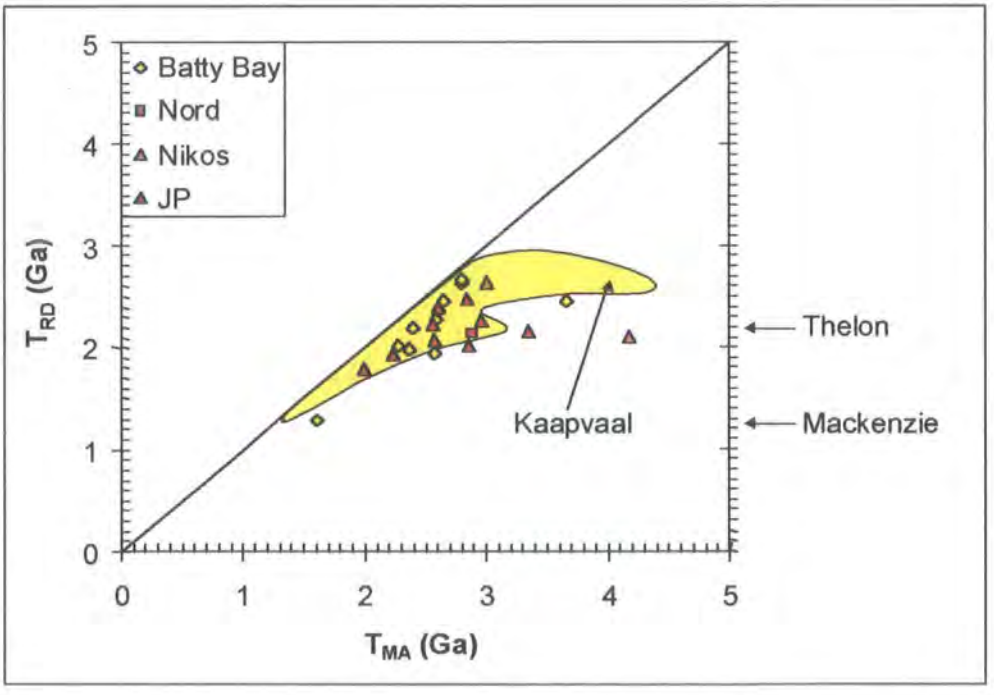

Figure 5.38 Plot of T_{RD} vs. T_{MA} model ages for individual Somerset Island peridotite suites. The line in the figure represents the $T_{RD} = T_{MA}$ line. Data for peridotites from the Kaapvaal craton (Carlson *et al.*, 1999).

Using combined PGE characteristicss with Re-Os isotope systematics and the correlation between PGEs and magmaphile elements to Somerset Island peridotites we gain better insights into the age systematics of the Somerset Island lithospheric mantle.

This allows us to improve our understanding of initial differentiation and subsequent modification of the Somerset Island lithosphere. From the extended CI-chondrite normalised PGE patterns it is evident that the majority of samples have undergone Re enrichment to a degree. T_{MA} model ages quite often produce anomalously old ages of formation compared with T_{RD} (Figure 5.38), and frequently produce anomalously old ages. As all Somerset Island peridotite samples show vestiges of major-element and PPGE melt depletion, T_{RD} model ages might be regarded as the more reliable indicator of the age of a particular sample. The systematic behaviour of melt-depleted extended PGE patterns, agreement of $(Pd/Ir)_n$ vs. Al_2O_3 and coincidence of T_{MA} and T_{RD} ages for some of the samples give us confidence that they are recording mainly the timing of melt depletion and lithospheric formation.

5.8 Evolution of the lithospheric mantle beneath the Churchill Province

Radiometric age determination of the Precambrian basement of Somerset Island produces Sm-Nd T_{DM} crustal separation ages of 3.0 to 2.2 Ga (Frisch and Sandeman, 1991; Frisch and Hunt, 1993), providing the earliest possible stabilisation of the craton. No peridotites in this study were found to be as old as 3.0 Ga, although the error on the model age calculation is ~200 Ma. The Re-Os age systematics of the Somerset Island peridotites suggest that the oldest remnant lithospheric mantle is 2.8 +/- 0.2 Ga.

New data from lower crustal xenoliths from the Kaapvaal craton indicate a very widespread, craton-wide differentiation event that affected the entire crustal thickness at ca. 3.1 Ga (Moser *et al.*, 2001). Such a widespread crustal differentiation event is inconsistent with the presence of a thick (>150 km), protective lithospheric mantle keel beneath the entire craton at this time, and Moser *et al* (2001) suggested that this 3.1 Ga event represents a maximum age for the establishment of a protective lithospheric mantle root. This argument may also apply to Somerset Island and the northern Churchill province, and a crustal age of 3.0 Ga (Hoffman, 1989; Frisch and Sandeman, 1991; Percival, 1996) could represent the maximum age for the establishment of a lithospheric keel. This does not preclude the possibility of older lithospheric mantle beneath Somerset Island that has not been sampled by the kimberlite.

Within the Somerset Island peridotite suite there appears to be two significant groups of T_{RD} model ages. The first group ranges from a T_{RD} model age of 2.8 to 2.6 Ga, and these peridotites may represent the initial formation and stabilisation of the

lithospheric keel beneath Somerset Island. The second group ranges in from T_{RD} model ages of 2.3 to 1.8 Ga with a prominent peak at 2.0 to 2.25 Ga. This coincides with a period of intense tectonic activity within the Churchill province (Table 5.1) related to collision with the Slave, Superior and Nain cratons (Hoffman, 1990a). The Thelon orogen (2.2 to 1.9 Ga) is of particular importance to the NW Churchill province and Somerset Island. This orogen produced the eastward subduction of the Slave craton beneath the Churchill province, followed by continent-continent collision. A consequence of the Thelon orogen was the uplift of the granulite terrane (Queen Maud uplift) in the eastern hinterland of the orogen, interpreted as an eroded Tibetan-type plateau (Hoffman, 1987). The model ages of the peridotites may therefore represent either the addition of new material to the lithosphere during this tectono-magmatic activity, or that there has been a substantial disturbance of PGE and Os isotope systematics during this event.

The Churchill province was also subjected to a major igneous event at 2.4 Ga, the Keewatin, producing the Kaminak dykes, Hurwitz gabbros and Happytoyuk basalts (Heaman, 1994), though no evidence of these event exists in the crustal rocks of Somerset Island.

Subsequent tectonic activity related to the NW Churchill province and Somerset Island in particular, do not appear to have disturbed the lithospheric mantle. In contrast to the continental lithospheric mantle beneath the Jericho kimberlite, there appears to be little evidence of the McKenzie Plume event, except for perhaps sample K13A4 (a spinel lherzolite from Batty Bay) with a T_{RD} model age of 1.3 Ga. The Boothia uplift and Tertiary rifting recorded in the geology of Somerset Island, are not manifested in the mantle sample as recorded by the Re-Os systematics.

From the Re-Os isotope systematics it is clearly evident that depleted late Archean mantle is present beneath Somerset Island, but also that younger Proterozoic lithospheric mantle is much evident. The mantle does not appear to be stratified with respect to age. The ages of lithospheric mantle beneath Somerset Island are significant with respect to stabilisation or major tectonomagmatic events. The young Proterozoic addition or modification to the lithospheric mantle beneath Somerset Island has important implications for the survival and age of diamonds. Initial exploration of the Somerset Island kimberlite field have found sub-economic diamond grades, and this may suggest that the Proterozoic tectono-magmatic events had a detrimental effect to the long-term survivability of diamonds in the lithospheric keel beneath Somerset Island. Alternatively, this edge of craton area did not experience diamond growth,

though previous studies have suggested that peridotite xenoliths from Somerset Island originate in the diamond stability field (Kjarsgaard and Peterson, 1992; Schmidberger and Francis, 1999).

Chapter 6

SUMMARY AND CONCLUSION

6.1 Introduction

In this project, the Re-Os isotope and PGE systematics of three peridotite suites, derived from kimberlites in Lesotho and northern Canada, have been investigated with the aims of:

i. Constraining the timing of formation and stabilisation of the sub-cratonic lithospheric mantle beneath the Kaapvaal (Lesotho), Slave (Jericho kimberlite) and Churchill (Somerset Island) cratons.
ii. Assessing the proposed models of craton formation (based on the Kaapvaal and Siberian cratons) with new evidence from other cratons (e.g. Slave).
iii. Investigating the link between stabilisation of the lithospheric mantle and the formation of the overlying crust.

Before discussing the Re-Os isotope and PGE systematics of the peridotite suites, the whole-rock compositions were examined, enabling the processes affecting the peridotites, either in the mantle or during emplacement, to be investigated. The observed range of whole-rock major element compositions in the peridotite suites was attributed to two processes; depletion of a fertile mantle source by the extraction of partial melts, and in several cases the refertilisation of refractory peridotites by metasomatic alteration.

6.2 Petrogenesis of the Lithospheric Mantle

The peridotite suites from Lesotho, Jericho and Somerset Island share many features in common, but also slight differences related to their evolutionary history.

6.2.1 Mantle Petrography

The mantle xenolith suites from Lesotho and Somerset Island are dominated by coarse textured peridotites, with lesser numbers of porphyroclastic peridotites, a feature common to most cratonic peridotite collections. The xenolith suite from Jericho,

although dominated by coarse peridotites, also contains an abundance of porphyroclastic peridotites, pyroxenites and eclogites (Kopylova *et al.*, 1999). This feature of the Jericho kimberlite is not unique, and several kimberlite localities in South Africa and Lesotho (Kaapvaal craton) are known for their "unusual" mantle xenolith assemblages, e.g. Thaba Putsoa (High-T porphyroclastic peridotites), Roberts Victor (eclogites) and Matsoku (pyroxenites).

In studies of cratonic peridotites it has been observed that mineral compositions of low-T peridotites are generally Mg-enriched, e.g. Olivine $Mg^{\#}$ for Kaapvaal craton ranges from 0.92 to 0.93 with an average of 0.926 (Boyd, 1989). Mineral compositions for peridotites from the Lesotho (mean $Mg^{\#}$ = 0.928), Jericho (mean $Mg^{\#}$ = 0.92) and Somerset Island (mean $Mg^{\#}$ = 0.921) suites are also Mg-enriched. The olivines from Somerset Island peridotites are slightly less Mg-rich than from Lesotho or the Kaapvaal craton as a whole, however, the olivine $Mg^{\#}$ from Somerset Island peridotites in this study are slightly lower than those previously reported (e.g. 0.923, Schmidberger and Francis, 1999). The low olivine $Mg^{\#}$ may reflect the slightly younger age of the Somerset Island lithospheric mantle. Similar correlations between low $Mg^{\#}$ and young ages have been observed at East Griqualand and Namibia (Pearson *et al.*, 1994; Pearson *et al.*, 1998; Pearson, 1999)

Garnet compositions from Lesotho, Jericho and Somerset Island peridotites are generally classified as G9 in the classification of Dawson and Stephens (1975), with few examples of sub-calcic G10 garnets even in harzburgites. This suggests that the lithospheric mantle beneath all three study locations shares this common feature, and may be attributed to the equilibration of harzburgites with a predominantly lherzolitic mantle (Boyd and Nixon, 1978) or disruption of low-Ca rocks due to the presence of carbonate during eruption (Canil, 1990).

6.2.2 Melt depletion

Previous studies of cratonic peridotite suites indicate a depletion in fusible elements such as Fe, Al and Ca (Nixon, 1987; Herzberg, 1993; Boyd *et al.*, 1997) suggesting that they have experienced a history of melt extraction. This depletion in fusible elements, compared to fertile mantle (Boyd and Mertzman, 1987), produces a buoyant low-density mantle-root and contributes to the stability of Archean continental lithosphere (Boyd and McCallister, 1976; Jordan, 1979). The whole-rock composition of

peridotites from Lesotho, Jericho and Somerset Island also indicate a similar history of melt depletion;

- Peridotites from the three xenolith suites are strongly depleted in Ti, Ca and Al relative to fertile mantle, in keeping with their Mg enriched composition.
- The Lesotho and Jericho low-T spinel peridotites are in general strongly depleted in Fe relative to fertile mantle. Somerset Island and Jericho low-T garnet peridotites are also depleted in Fe but not so strongly.
- Ni behaves compatibly relative to Mg in the all three suites but the correlations are poorly defined. The scatter in Ni data may indicate a cumulate component in the peridotites (Pearson, 1989).
- In general the HREEs (Yb to Ho) in the Lesotho, Jericho and Somerset Island suites are subchondritic. This would suggest that the suites represent either melt extraction at shallow depths in the presence of spinel, the complete removal of garnet from the residue, or melting of a peridotite where all garnet is dissolved in a high-T OPX, i.e. garnet absent lithology (Cox *et al.*, 1987).

Although all three peridotite suites exhibit evidence of melt depletion, differences are apparent between the three that may relate to the degree of melt extraction, or alternatively to the subsequent evolution of the lithospheric mantle after melt extraction.

- The average mineral modal abundance for peridotites from the low-T Lesotho peridotite (Table 6.1) suite mirrors that previously reported for low-T Kaapvaal peridotites by Boyd (1989). In contrast, the mineral modal abundance for Somerset Island and Jericho low-T peridotites are more olivine rich and OPX poor (Table 6.1), similar to the Siberian craton (Boyd *et al.*, 1997). The high olivine modes of Somerset Island and Jericho peridotites are indicative of the highly refractory nature of these suites. This higher OPX mode in Lesotho peridotites is a reflection of the higher Si content.

- The ratio of Ca/Al in the Somerset Island and Jericho peridotites is, on average, higher than the Lesotho suite.
- Modelling the peridotite suites after the method of Walter (1999), in terms of isobaric batch melting the Lesotho peridotites can be explained by 40-60% at 4 to > 7 GPa, Somerset Island peridotites by 20-40% at 1-4 GPa, and Jericho peridotites by 20-60% at 1 to > 7 GPa.
- Modelling the three suites after the method of Hanson and Langmuir (1978) at 3 GPa, the Lesotho suite can be explained by 35-50% batch melting, Jericho low-T

spinel peridotites 35-45%, Jericho low-T garnet peridotites 20-30 % and the Somerset Island peridotites 20-35%.

Location	LREE $(La/Yb)_n$	Mineral Modes		
		Olivine	OPX	CPX
Kaapvaal		61%	31%	1.8%
Lesotho	41.70	60%	33%	1.85%
Somerset Island	29.75	71%	20%	3%
Jericho	124.21	67-72%	19-26%	1.5-7.1%

Table 6.1 Mineral modes and REE ratios for the Lesotho, Somerset Island and Jericho peridotite suites. Kaapvaal data from Boyd (1989), and Jericho data from Kopylova and Russell (2000).

We must be aware of the fact that late-stage introduction of diopside and some garnet (Simon *et al.*, 2001) may have altered bulk-rock FeO and Al_2O_3 contents, and therefore these estimates will not be accurate. Even though peridotites from the three suites may have experienced some disturbance to their major element compositions, it can be useful to compare the xenolith data to melting models. It can be observed that many samples from the peridotite suites are too rich is Si and modal OPX to be comparable to high-pressure experimental residues. It should also be noted that many spinel peridotites suggest melting at pressures greater than 3 GPa, above which spinel is not stable unless Cr-rich. In contrast, the depleted nature of HREE suggested that melting might have occurred at low-pressures in the presence of spinel. The major-element chemistry of the peridotite suites however suggest that melting occurred at higher pressures and was therefore sufficient to remove all garnet from the residue, or at high pressure with no garnet present.

6.2.3 Metasomatic History

Peridotites from the Lesotho, Jericho and Somerset Island suites show evidence of post-melt extraction metasomatic alteration, possibly in multiple events.

- Si-enrichment, evident in peridotites from Lesotho and Jericho and several samples from Somerset Island, may be the result of melt-mantle reaction (Keleman *et al.*, 1998) or cumulate mixing (Herzberg, 1993; Herzberg, 1999) and is reflected in high OPX modes.
- The mean CPX modes for Somerset Island Jericho low-T garnet peridotites (Table 6.1), in conjunction with high olivine $Mg^{\#}$, suggest that much of the CPX present in the samples may be attributable to late-stage metasomatism (Menzies

and Murthy, 1980a; Boyd and Mertzman, 1987; Shimizu, 1999; Simon *et al.*, 2001).

- Late stage secondary Na, Al and Cr rich CPX occurs in the Lesotho and Jericho peridotites as fine-grained veins at grain boundaries within the xenoliths. This feature has also been observed in peridotites from Siberia (Boyd *et al.*, 1997), and has been attributed to secondary crystallisation during eruption (Boyd *et al.*, 1997; Kopylova *et al.*, 1999).
- The scatter in Ni data in all three suites, and the lack of a well defined correlation with Mg, may be the result of later metasomatism from melts passing through the peridotite, or patent metasomatism as CPX and some garnet is introduced (Pearson *et al.*, 2001).
- Fe enrichment has been observed in several peridotite xenolith suites, and has been attributed to mantle metasomatism (Harte *et al.*, 1987; Harte and Hawkesworth, 1989). Fe enrichment is apparent in peridotites from Jericho and Somerset Island, though several samples from Lesotho also appear to be enriched. Whole-rock $Mg^{\#}$ are in general lower than olivine $Mg^{\#}$, providing supporting evidence for Fe enrichment of whole-rocks after melt-extraction.
- LREE enrichment is ubiquitous in cratonic peridotite suites and has been noted previously in the Kaapvaal (Nixon *et al.*, 1981) and Slave cratons (Kopylova and Russell, 2000). This has been attributed to the interaction of metasomatising fluids with lithospheric mantle by Hawkesworth *et al* (1983) and Menzies *et al* (1987). The Lesotho, Jericho and Somerset Island peridotites all show enrichment in LREE (Table 6.1).

6.3 Age of the Continental Lithospheric Mantle

The primary aim of this project was to constrain the age and time-scale of formation of the lithospheric mantle underlying the three study areas of Lesotho, Jericho and Somerset Island. The compatible nature of Os during partial melting of the mantle and its low abundance in mantle melts makes it less subject to metasomatism and alteration processes, and therefore provides the opportunity to constrain the timing of formation.

6.3.1 Re-Os Systematics

The Re-Os data from Lesotho, Jericho and Somerset Island peridotites illustrate many differences in the evolutionary history of the three regions, but also certain similarities.

The mean Re content of peridotites from the Jericho suite is comparable to that previously reported from peridotites of the Kaapvaal craton (Table 6.2). The Re content of peridotites from Lesotho and more particularly Somerset Island are, in contrast, much higher. On average, peridotites from Lesotho and Jericho are depleted in Re relative to fertile mantle estimates. The mean Re abundance of Somerset Island peridotites however is higher than fertile mantle estimates, and suggests that the Re-Os systematics of these peridotites has been disturbed (Table 6.2).

In terms of mean Os concentrations, Jericho peridotites again show similarities to the observed abundances in Kaapvaal peridotites (Table 6.2). The Lesotho peridotite suite, although it shows slightly lower Os abundances, is within error of the Kaapvaal dataset. The mean for Somerset Island peridotites is much lower, but this may be an artefact of sample selection, and is still within error of Kaapvaal. In all three peridotite suites from this study the mean Os abundances are higher than fertile mantle estimates, as expected for residues of partial melting. In terms of the Somerset Island samples, particularly those from Batty Bay and Nord where alteration was more apparent, the low Os values may relate to weathering. However, the spread in Os abundances from Somerset Island peridotites is much lower than that observed in the other peridotite suites (Table 6.2).

Location	Mean Re (ppb)	Mean Os (ppb)	Mean $^{187}Re/^{188}Os$	Mean $^{187}Os/^{188}Os$
Fertile mantle	0.26 [a]	3.4 [a]	0.4243 [b]	0.1287 [b]
Kaapvaal	0.084 ± 0.078	4.61 ± 2.11	0.109 ± 0.11	0.1115 ± 0.0032
Lesotho	0.141 ± 0.128	4.27 ± 2.5	0.233 ± 0.28	0.1106 ± 0.0040
Jericho	0.077 ± 0.064	4.65 ± 3.86	0.292 ± 0.85	0.1135 ± 0.0050
Somerset Island	0.343 ± 0.637	3.54 ± 1.41	0.548 ± 1.22	0.1123 ± 0.0025

Table 6.2 Mean Re-Os data for peridotite suites in this study. Kaapvaal data from Carlson *et al* (1999). Fertile mantle estimates from [a] Morgan (1986) and [b] Meisel *et al* (1996).

In general the mean $^{187}Re/^{188}Os$ ratio of cratonic peridotite suites, as seen at Lesotho and Jericho, are lower than fertile mantle estimates. The mean $^{187}Re/^{188}Os$ ratio of peridotites from Somerset Island however is higher than fertile mantle estimates reflecting the observed enrichment in Re and disturbance to the Re-Os systematics. In all three suites from this study the $^{187}Re/^{188}Os$ ratios are higher than those reported for the Kaapvaal craton (Table 6.2).

If samples with Re abundances or $^{187}Re/^{188}Os$ ratios higher than fertile mantle are discounted from all three peridotite suites however, the mean Re abundances and $^{187}Re/^{188}Os$ ratios are lowered significantly to values more similar to, or lower than, those reported for the Kaapvaal craton (Chapters 3 to 5).

The clearest distinction between the three suites of cratonic peridotites studied is in their Os isotopic characteristics. The Lesotho peridotites are on average the most unradiogenic of the three suites studied, even more so than previous studies of Kaapvaal peridotites (Table 6.2), and particularly if separated on the basis of kimberlite location (Table 3.14). This is notable because they have higher Re/Os ratios than average Kaapvaal, and this means elevated Re/Os is a recent feature. Somerset Island peridotites by comparison, are on average slightly more radiogenic than the mean for Lesotho peridotites or the Kaapvaal craton. If separated into specific kimberlite localities however, peridotites from the JP and Nikos kimberlites are more comparable to the Kaapvaal craton average (Table 5.12). These samples are larger and fresher than those from Batty Bay or Nord. Similarly, for the Jericho suite, the mean $^{187}Os/^{188}Os$ is more radiogenic than Lesotho or Somerset Island peridotites, but if separated into facies, the low-T spinel peridotites are more unradiogenic than the average for the Lesotho suite (Table 4.9) and clearly indicate the presence of Archean mantle beneath this region.

The clearest distinction between cratonic peridotites and those from other tectonic settings is provided by Os isotopic compositions. It is clear that the Lesotho, Jericho and Somerset Island peridotite suites mostly have very low $^{187}Os/^{188}Os$, indicating long-term Re-depletion and isolation from the convecting mantle. This Re-depletion clearly occurred earlier than in peridotites from non-cratonic settings e.g. Namibia (Pearson *et al.*, 1994). It is also apparent from this study that the three peridotite suites have experienced very different post-melt extraction histories, with possible Re enrichment and modification of the mantle or the addition of new material to the lithospheric mantle, particularly at Jericho and Somerset Island.

6.3.2 PGE Systematics

In fertile peridotites, sulfides contain the majority of Re and Os. Detailed studies of mineral separates (Burton *et al.*, 1999), and in-situ analysis of sulfides (Alard *et al.*, 2000; Pearson *et al.*, 2000) in non-cratonic peridotites have indicated the presence of several generations of sulfide. Introduced intergranular sulfides may account for the

spread in Re-Os systematics from the Lesotho, Jericho and Somerset Island peridotites. Whole rock Re-Os analyses may therefore produce an integration of various generations of sulfides. Given the observed metasomatic alteration in cratonic peridotites suites (Menzies and Murthy, 1980b; Hawkesworth *et al.*, 1984; Harte *et al.*, 1987; Simon *et al.*, 2001) including this study, and the presence of multiple generations of sulfides in some mantle peridotites, it is necessary to evaluate the significance of the Re-Os isotope systematics. Most cratonic peridotites are the residues of large degrees of melting. The removal of > 30% partial melt will act towards removing all primary *mss* from the residue, breaking it down into minor sulfides (e.g. laurite) or alloy phases (e.g. Ir-Os) with higher solidi (Brennan and Andrews, in press). Osmium and associated IPGEs remain within the peridotite as finely dispersed grains and the PGE patterns of whole-rocks and sulfides become highly fractionated.

The whole-rock PGE behaviour of peridotites from Lesotho, Jericho and Somerset Island indicate a similar history of melt depletion, and in many cases subsequent enrichment (see summary Table 6.3).

IPGEs display flat chondrite normalised PGE patterns with little inter-element fractionation, consistent with their compatible nature. The depletion of PPGEs in the Lesotho, Jericho and Somerset Island peridotite suites is consistent with their major-element-depleted nature, and suggests that the PGEs have been fractionated during melt extraction. Relative compatibility of PGEs during fractionation, through melt extraction, based on the evidence from the chondrite-normalised patterns of peridotites from all three suites, is in the order Os ~ Ir ~ Ru < Pt < Pd ≤ Re. In contrast to the ubiquitous enrichment of LREEs in whole-rock peridotites, PGEs invariably have PPGE depleted patterns, generally retaining some vestiges of a depleted character with sub-chondritic abundances of Pt and/or Pd, i.e. the incompatible PGEs.

Subsequent to melt depletion, all three suites show evidence of enrichment in Re and/or Pd. Peridotites from all three cratonic suites can be consistently subdivided on the basis of PPGE fractionation into five groups (Table 6.3). This indicates that all three peridotite suites have undergone similar enrichment processes, though to variable degrees (Table 6.3). All three suites show evidence of peridotites with undisturbed, depleted PGE patterns, and are thought to represent primary PGE signatures of residues from large degrees of melt extraction. These samples are often associated with unradiogenic $^{187}Os/^{188}Os$ ratios. Many samples from all three peridotite suites show PGE patterns with inflections in the Re abundance (Table 6.3). Often these samples have unradiogenic $^{187}Os/^{188}Os$ ratios and are thought to represent recent Re addition,

Table 6.3 Summary of PGE behaviour within the Lesotho, Jericho and Somerset Island peridotite suites, on the basis of the shape of the PPGE part of the PGE patterns. Numbers in brackets indicate the number of samples from each suite with corresponding PGE patterns.

Group	PGE Pattern	Lesotho	Jericho	Somerset Island	Features
A	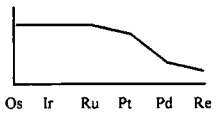	√ (1)	√ (3)	√ (4)	Depleted in Pd and Re. Low $(Pd/Ir)_n$. Depleted in S and Al_2O_3. Depleted in Ba and Nb.
B_i	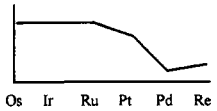	√ (8)	√ (2)	√ (2)	Depleted in Pd but enriched in Re. Low $(Pd/Ir)_n$. Associated enrichment in S and Al_2O_3. Variable enrichment in Ba and Nb.
B_{ii}	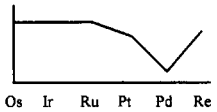	√ (12)	√ (7)	√ (3)	Essentially a sub-group of B with more prominent Re enrichment. Low $(Pd/Ir)_n$.
B_{iii}	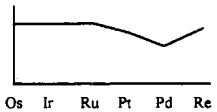	√ (4)		√ (1)	Essentially a sub-group of B with more prominent Re enrichment and possible enrichment of Pd. Moderate $(Pd/Ir)_n$. Enriched in S, Al_2O_3, variably in Ba and Nb.
C	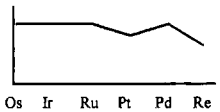	√ (1)	√ (10)	√ (11)	Noticeable depletion in Pt and Re, but enriched in Pd. High $(Pd/Ir)_n$. Enriched in S and Al_2O_3. Enriched in Ba and Nb. Enriched in S, Al_2O_3, variably in Ba and Nb.
D	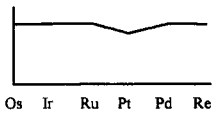	√ (2)	√ (2)	√ (6)	Noticeable depletion in Pt and Re, but enriched in Pd. High $(Pd/Ir)_n$. Enriched in S, Al_2O_3, variably in Ba and Nb.
E	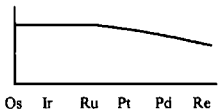	√ (4)	√ (5)		Noticeable depletion in Pt and Re, but enriched in Pd. High $(Pd/Ir)_n$. Enriched in S and Al_2O_3. Enriched in Ba and Nb. Enriched in S, Al_2O_3, variably in Ba and Nb.

possibly associated with the host kimberlite or associated precursor fluids. The number of peridotites from Jericho and Somerset Island that are enriched in Pd is greater than that observed at Lesotho. Lesotho samples tend to be enriched in Re only. Complex PGE patterns with enrichment in Pd, and corresponding high $(Pd/Ir)_n$ ratios, in all three suites appears to be consistently associated with more radiogenic $^{187}Os/^{188}Os$ ratios (see Tables 3.19, 4.14 and 5.17). Os isotopic compositions in these samples may therefore be a reflection of secondary sulfide addition to these samples. However, in terms of Os abundances there is no clear evidence from any of the suites to suggest that Os has been enriched. An alternative explanation for the radiogenic Os isotopic compositions may be the in-growth of radiogenic Os from Re addition occurring earlier in the history of the sample.

The timing of metasomatism is important, to understand the nature of the metasomatising fluid responsible for the observed variation in the Re-Os systematics. For samples with highly radiogenic $^{187}Os/^{188}Os$ ratios, if metasomatism occurred earlier in the history of the sample, the metasomatising fluid need only have had a high Re/Al ratio. If the metasomatism is more recent the metasomatising agent must also have had a high Os/Al ratio. Generally fluids / melts have low Os contents, due to the compatible nature of Os, and therefore the former argument may seem the more likely.

6.3.3 Lithospheric Mantle Formation

The observed range in Os isotopic compositions from Lesotho, Jericho and Somerset Island peridotites produce a wide range in T_{RD} model ages for all three suites (Table 6.4). Pearson *et al* (1995) attributed a similar spread in T_{RD} model ages for peridotites from the Kaapvaal craton to disturbance of the primary Re-Os isotope systematics, and suggested that the oldest ages represented the likely formation of much of the lithosphere. From the variation in PGE systematics of the Lesotho, Jericho and Somerset Island suites we know that the PGE and Re-Os systematics for many samples from these suites are disturbed, and these disturbed samples produce younger T_{RD} model ages.

To place constraints on the original depletion ages we consider samples from each of the peridotite suites with undisturbed PGE systematics representing residues of large degrees of melt extraction, with low Re and low $(Pd/Ir)_n$. The very low Re content of these samples means that the T_{RD} and T_{MA} model ages agree very closely (Table 6.4),

since the T_{RD} is calculated assuming Re = 0 and the T_{MA} uses the measured very low Re/Os ratio of the sample.

		Examples			
Location	**T_{RD} range (Ga)**	**Sample**	**$(Pd/Ir)_n$**	**T_{RD} (Ga)**	**T_{MA} (Ga)**
Lesotho	2.9 to 0.8	LQ8	0.037	2.9	2.9
Jericho	3.1 to 0.5	8-7	0.02	3.0	3.1
Somerset Island	2.8 to 1.3	K13B4	0.09	2.7	2.8

Table 6.4 Summary of Re-Os model ages for the Lesotho, Jericho and Somerset Island peridotite suites. Examples are given for each suite, of a peridotite with an undisturbed PGE pattern reflecting the primary PGE and Re-Os systematics related to melt depletion.

The low Re and low $(Pd/Ir)_n$ are both indication of undisturbed melt residues. This highlights the fact that, for residues of large degrees of melt extraction with undisturbed PGE patterns, the T_{RD} model age is a good approximation for the age of formation. In all three peridotite suites there are many samples with unradiogenic $^{187}Os/^{188}Os$ ratios identical to the undisturbed samples, but with high Re/Os ratios due to recent Re addition. For these samples there is a substantial variation between T_{RD} and T_{MA} model ages. The close agreement between T_{RD} and T_{MA} model ages in depleted samples suggests that the T_{RD} model age is a good approximation to the age of formation for these samples. Samples showing evidence of recent Re enrichment produce anomalous T_{MA} model ages. However, the agreement between T_{RD} model ages in Re-enriched samples, with T_{RD} model ages in Re-depleted samples suggests that the T_{RD} model age is a good approximation for their age of formation.

Samples from Lesotho, Jericho and Somerset Island that exhibit more complex PGE patterns with Pd enrichment tend to have more radiogenic $^{187}Os/^{188}Os$ ratios and therefore produce younger T_{RD} model ages. These often cluster in groups, representing younger, significant modification to the lithospheric mantle either by metasomatism or the addition of new material.

6.4 Inter-relationship of Crust and Lithospheric Mantle

Moser *et al* (2001) suggested that the ca. 3.1 Ga crustal differentiation event that affected the Kaapvaal craton was inconsistent with the presence of a thick lithospheric mantle keel at this time and therefore this should represent the maximum age for the establishment of a protective root. This argument may also apply to the Slave and Churchill cratons. The oldest ages of the lithospheric mantle at Lesotho, Jericho and Somerset Island tend to post-date the last major differentiation events recorded within

the overlying crust of the Kaapvaal, Slave and Churchill cratons. This may indicate that the waning of major crustal differentiation and the onset of more stable continental conditions coincide with the stabilisation of a thick protective lithosphere mantle keel.

T_{RD} model ages of the more disturbed peridotites, from all three peridotite suites, generally correspond to younger ages and thermal/magmatic disturbances recorded in the overlying crust, however this may be coincidental. Many uncertainties are involved regarding the $^{187}Os/^{188}Os$ ratio of these samples. If Re has been introduced to the sample earlier in its history, the $^{187}Os/^{188}Os$ ratio will begin to evolve. This evolution will be complex and related the amount of Re introduced, and the time of introduction. Alternatively, if Os has been introduced to the sample, the $^{187}Os/^{188}Os$ ratio will reflect an amalgamation of different sulfide generations, and therefore the T_{RD} model age will be an artefact of the combined $^{187}Os/^{188}Os$ ratios. However, the correspondence between T_{RD} model ages in the mantle and tectono-magmatic events in the crust, in all three peridotite suites would suggest that the lithosphere has been modified by the events recorded in the crust.

The Jericho and Somerset Island peridotite suites are more disturbed than the Lesotho peridotite suite, and this may relate to their location relative to major tectono-magmatic events. The Jericho kimberlite is located on the proposed margin of the plume head of the Mackenzie dyke swarm. Modification of the lithospheric mantle by this plume at 1.27 Ga and subsequent isotopic evolution may explain the increasing disturbance of the PGE systematics with depth beneath Jericho. The Somerset Island kimberlites are located on the margin of the Churchill craton near the Queen Maud uplift and Thelon front, related to the Thelon orogeny. The addition of variable quantities of Re or new material during these events would be consistent with the younger T_{RD} model ages seen at these localities. However, it should be noted that the Lesotho peridotite suite is sourced from a mantle that experienced an influx of melt during the voluminous Karroo rifting event ca. 190 Ma, 100 Myr before kimberlite magmatism. This event does not appear to have disturbed the lithospheric mantle as sampled by the Lesotho peridotite suite. Although the Lesotho peridotite suite is less disturbed than both Jericho and Somerset Island, the few disturbed samples produce T_{RD} model ages consistent with tectono-magmatic events recorded in the crust related to events such as the Namaqua-Natal orogeny (Schmitz and Bowring, 1999; Irvine *et al.*, 2001).

6.5 Conclusion

This project has provided the first detailed study of PGE systematics on the cratonic mantle since the pioneering study of Morgan (1991). The study has shown how PGEs are systematically fractionated within the cratonic lithospheric mantle during mantle melting processes and subsequent modification during metasomatic alteration.

Overall the results from this study have illustrated the potential for combined PGE and Re-Os isotope studies in evaluating the significance of Re-Os model ages in peridotite suites. When combined with major-element studies, the coherence of major-elements with PGE fractionation trends, e.g. $(Pd/Ir)_n$ vs. Al_2O_3, provide a firm basis for evaluating the oldest T_{RD} and T_{MA} model ages in a given suite. Evaluation of these systematics also allows for more confident assessment of younger T_{RD} model ages in peridotites that exhibit PGE - major element chemistry expected of residues.

New age constraints are provided for peridotite suites from beneath the Slave craton and Churchill Province lithosphere to aid our understanding of cratonic root evolution. In addition Re-Os and PGE data from this study indicate the modification of lithospheric mantle beneath these regions associated with tectono-magmatic events. This is comparable to the reported modification or addition of new material to the lithospheric mantle beneath the Premier kimberlite in South Africa, related to the Bushveld event (Pearson *et al.*, 1995; Carlson *et al.*, 1999). This would suggest that, although lithospheric mantle keels persist beneath Archean cratons, they are subject to modification by major thermal events which may overprint the primary PGE and Re-Os systematics.

Extensive studies of xenolith suites reveal significant trends in the composition of lithospheric mantle through time (Boyd, 1989; Menzies, 1990). The symmetry between apparent ages from on- and off-craton, with Archean crust underlain by Archean mantle, and Proterozoic crust underlain by Proterozoic mantle shows the long-term coupling of crust and lithospheric mantle in continental plates over billions of years (Pearson *et al.*, 2001). Only near the margins do cratons seem susceptible to substantial disruption or reworking. Where post-Archean effects are seen inside cratons, these may be manifest at suture lines where discrete blocks joined initially to form the craton. Archean mantle roots clearly exist beneath the Slave craton and Churchill province but these have been substantially modified by Proterozoic reworking / disturbance. In fact the peridotite suite form Somerset Island show that the lithospheric mantle below what is now recognised as the Churchill Province appears to have formed in the Archean and along with the crust has experienced substantial Proterozoic re-

working. The Slave lithospheric mantle as sampled at Jericho has been affected by major tectonomagmatic events such as the Mackenzie plume ca. 1.27 Ga. The Jericho kimberlite is also located near the margin of the Central Slave basement complex, possibly close to a suture with the younger Archean Contwoyto and Hackett terranes. Somerset Island is located on the margin of the Churchill province, close to the Thelon orogeny ca. 2.2 – 1.9Ga. This event, reflected in granulite metamorphism in the Somerset Island crust (Frisch and Sandeman, 1991), appears to have significantly reworked the Archean lithospheric mantle.

No systematic Re-Os model age differences were observed between Lesotho peridotites from the margin of the Kaapvaal craton, and those from previous studies of peridotites from more central locations in the craton. Comparison of Re-Os model age systematics with equilibration pressures for the Lesotho peridotite suite reveal no significant correlation between depth and age. The predominant mode in T_{RD} model ages at 2.7 Ga for the Kaapvaal peridotite suite in general post-dates the last significant period of crustal differentiation.

This Re-Os study of Lesotho, Jericho and Somerset Island peridotites indicate that the lithospheric mantle beneath continents generally began to form in the Mesoarchean, but continued into the Neoarchean when, in the case of Lesotho, significant volumes of lithospheric mantle formed. Major magmatic events have substantially modified the lithospheric mantle and crust at Jericho and Somerset Island, but the cratons have retained their integrity for another 2 Gyr.

References

Alard, O., Griffin, W.L., Lorand, J.P., Jackson, S.E., and O'Reilly, S.Y. (2000) Non-chondritic distribution of the highly siderophile elements in mantle sulphides, *Nature,* **407**, 891-894.

Anbar, A.D., Papanastassiou, D.A., and Wasserburg, G.J. (1997) Determination of iridium in natural waters by clean chemical extraction and negative thermal ionisation mass spectrometry, *Analytical Chemistry,* **69**, 2444-2450.

Anders, E. and Grevesse, N. (1989) Abundances of the elements: Meteoritic and solar, *Geochimica et Cosmochimica Acta,* **53**, 197-214.

Armstrong, R.A., Compston, W., deWit, M.J., and Williams, I.S. (1990) The stratigraphy of the 3.5-3.2 Ga Barberton Greenstone Belt revisited: a single zircon ion microprobe study, *Earth and Planetary Science Letters,* **101**, 90-106.

Armstrong, R.A., Compston, W., Retief, E.A., Williams, I.S., and Welke, H.J. (1991) Zircon Ion Microprobe Studies Bearing on the Age and Evolution of the Witwatersrand Triad, *Precambrian Research,* **53**(3-4), 243-266.

Ashwal, L.D. and Burke, K. (1989) African lithospheric structure, volcanism, and topography, *Earth and Planetary Science Letters,* **96**, 8-14.

Barnes, S.J., Naldrett, A.J., and Gorton, M.P. (1985) The origin and fractionation of platinum-group elements in terrestrial magmas, *Chemical Geology,* **53**, 303-323.

Barnes, S.J. and Picard, C.P. (1993) The behaviour of platinum-group elements during partial melting, crystal fractionation and sulfide segregation: an example from the Cape Smith Fold Belt, Northern Quebec, *Geochimica et Cosmochimica Acta,* **57**, 79-87.

Basaltic Volcanism Studies Project (1981). *Basaltic volcanism on the terrestrial planets*, Pergamon Press, New York, pp. 1286.

Bergman, S.C. (1987). Lamproites and other potassium-rich igneous rocks: a review of their occurrence, mineralogy and geochemistry. In: J.G. Fitton and B.G.J. Upton (Eds.), *Alkaline Igneous Rocks, Geological Society Special Publication No 30*, pp. 103-190.

Bezmen, N.I., Asif, M., Brügmann, G.E., Romanenko, I.M., and Naldrett, A.J. (1994) Distribution of Pd, Ru, Rh, Ir, Os and Au between sulfide and silicate melts, *Geochimica et Cosmochimica Acta,* **58**, 1251-1260.

Bickford, M.E., Collerson, K.D., and Lewry, J.F. (1994) Crustal history of the Rae and Hearne provinces, southwestern Canadian Shield, Saskatchewan: constraints from geochronologic and isotopic data, *Precambrian Research,* **68**, 1-21.

Bickle, M.J., Ford, C.E., and Nisbet, E.G. (1977) The petrogenesis of peridotitic komatiites: evidence from high-pressure melting experiments, *Earth and Planetary Science Letters,* **37**, 97-106.

Blackadar, R.G. (1967). Precambrian geology of the Boothia Peninsula, Somerset Island, and the Prince of Wales Island, District of Franklin., *Geological Survey of Canada. Bulletin*, **151**, pp. 62.

Blackadar, R.G. and Christie, R.L. (1963). Geological reconnaissance, Boothia Peninsula and Somerset, King William and Prince of Wales Islands, District of Franklin, *Geological Survey of Canada. Paper*, **63-19**, pp. 15.

Bleeker, W. and Davis, W.J. (1999) The 1991-1996 NATMAP Slave Province Project: Introduction, *Canadian Journal of Earth Sciences,* **36**, 1033-1042.

Bleeker, W., Ketchum, J.W.F., Jackson, V.A., and Villeneuve, M. (1999a) The Central Slave Basement Complex. Part I: It's structural topology and autochthonous core, *Canadian Journal of Earth Sciences,* **36**, 1083-1109.

Bleeker, W., Ketchum, J.W.F., and Davis, W.J. (1999b) The Central Slave Basement Complex. Part II: age and tectonic significance of high-strain zones along the basement-cover contact, *Canadian Journal of Earth Sciences,* **36**, 1111-1130.

Bloomer, A.G. and Nixon, P.H. (1973). The Geology of Letseng-la-terae Kimberlite Pipes. In: P.H. Nixon (Ed.), *Lesotho Kimberlites*, Cape and Transvaal, Cape Town, pp. 20-38.

Bodinier, J.L. (1988) Geochemistry and petrogenesis of the Lanzo peridotite body, western Alps, *Tectonophysics,* **149**, 67-88.

Bodinier, J.L., Dupuy, C., and Dostal, J. (1988) Geochemistry and petrogenesis of Eastern Pyrenean peridotites, *Geochimica et Cosmochimica Acta,* **52**, 2893-2907.

Bowie, C. (1994). Slave NATMAP; digital release of preliminary datasets on CD-ROM media. In: R. Kusick and S.P. Goff (Eds.), *Exploration overview 1994; Northwest Territories; Mining, Exploration and Geological Investigations.*, Yellowknife, NWT: Geological Survey of Canada, Northern Affairs Program, NWT Geology Division, pp. 25.

Bowring, S.A. and Grotzinger, J.P. (1992) Implications of new chronostratigraphy for tectonic evolution of the Wopmay orogen, *American Journal of Science,* **292**, 1-20.

Bowring, S.A. and Housh, T. (1995) The Earth's early evolution, *Science,* **269**, 1535-1540.

Bowring, S.A., Housh, T.B., and Isachsen, C.E. (1990). The Acasta gneisses; remnant of Earth's early crust. In: H.E. Newsom and J.H. Jones (Eds.), *The Origin of the Earth*, Oxford University Press, New York, pp. 319-343.

Boyd, F.R. (1970) Garnet Peridotites and the System $CaSiO_3$ - $MgSiO_3$ - Al_2O_3, *Mineralogical Society of America, Special Paper,* **3**, 63-75.

Boyd, F.R. (1987). High- and low temperature garnet peridotite xenoliths and their possible relation to the lithosphere-asthenosphere boundary beneath southern Africa. In: P.H. Nixon (Ed.), *Mantle Xenoliths*, John Wiley & Sons, New York, pp. 403-412.

Boyd, F.R. (1989) Compositional distinction between oceanic and cratonic lithosphere, *Earth and Planetary Science Letters,* **96**, 15-26.

Boyd, F.R. and McCallister, R.H. (1976) Densities of fertile and sterile garnet peridotites, *Geophysical Research Letters,* **3**, 509-512.

Boyd, F.R. and Nixon, P.H. (1978) Ultramafic nodules from the Kimberley pipes, South Africa, *Geochimica et Cosmochimica Acta,* **42**, 1367-1382.

Boyd, F.R. and Gurney, J.J. (1986) Diamonds and the African lithosphere, *Science,* **232**, 472-477.

Boyd, F.R. and Mertzman, S.A. (1987). Composition and structure of the Kaapvaal lithosphere, Southern Africa. In: B.O. Mysen (Ed.), *Magmatic Processes: Physicochemical Principles*, The Geochemical Society, pp. 3-12.

Boyd, F.R., Pearson, D.G., Nixon, P.H., and Mertzman, S.A. (1993) Low Ca garnet harzburgites from southern Africa: their relation to craton structure and diamond crystallisation, *Contributions to Mineralogy and Petrology,* **113**, 352-366.

Boyd, F.R. and Canil, D. (1997) Peridotite xenoliths from the Slave craton, Northwest Territories, *Seventh Annual V.M. Goldschmidt Conf.,* **LPI Cont. 921**, 34-35.

Boyd, F.R., Pokhilenko, N.P., Pearson, D.G., Mertzman, S.A., Sobolev, N.V., and Finger, L.W. (1997) Composition of the Siberian cratonic mantle: evidence from Udachnaya peridotite xenoliths, *Contributions to Mineralogy and Petrology,* **128**, 228-246.

Brandon, A.D., Creaser, R.A., Shirey, S.B., and Carlson, R.W. (1996) Os Recycling in Subduction Zones, *Science,* **272**, 861-825.

Brennan, J.M. and Andrews, D. (in press) High temperature stability of laurite and Ru-Os-Ir alloy and their role in PGE fractionation in mafic magmas, *Canadian Mineralogist.*

Brey, G.P. and Kohler, T. (1990) Geothermobarometry in four-phase lherzolites II. New thermobarometers, and practical assessment of existing thermobarometers, *Journal of Petrology,* **31**, 1353-1378.

Brey, G.P., Kohler, T., and Nickel, K.G. (1990) Geothermobarometry in four-phase lherzolites I. Experimental results from 10 to 60 kb, *Journal of Petrology*, **31**, 1313-1352.

Brown, R.L., Dalziel, I.W.D., and Rust, B. (1969) The structure, metamorphism and development of the Boothia arch, Arctic Canada, *Canadian Journal of Earth Science,* **6**, 525-534.

Brügmann, G.E., Arndt, N.T., Hofmann, A.W., and Tobschall, H.J. (1987) Noble Metal Abundances in Komatiite Suites from Alexo, Ontario, and Gorgona Island, Columbia, *Geochimica et Cosmochimica Acta,* **51**, 2159-2169.

Burnham, O.M. (1995) The Geochemistry of Re and Os in Ultramafic Rocks from the Pyrenees and Massif Central, France. PhD, Open University.

Burton, K.W., Schiano, P., Birk, J.L., and Allegre, C.J. (1999) Osmium isotope disequilibrium between mantle minerals in a spinel-lherzolite, *Earth and Planetary Science Letters,* **172**, 311-322.

Campbell, J.L., Teesdale, W.J., Kjarsgaard, B.A., and Cabri, L.J. (1996) Micro-PIXE Analysis of Silicate Reference Standards for Trace Ni, Cu, Zn, Ga, Ge, As, Rb, Sr, Y, Zr, Nb, Mo and Pb, with Emphasis on Ni for Application of the Ni-Garnet Geothermometer, *The Canadian Mineralogist,* **34**, 37-48.

Canil, D. (1990) Experimental study bearing on the absence of carbonate in mantle-derived xenoliths, *Geology,* **18**, 1011-1013.

Canil, D. (1994) An experimental calibration of the "Nickel in Garnet" geothermometer with applications, *Contributions to Mineralogy and Petrology,* **117**, 410-420.

Canil, D. (1997) Vanadium partitioning and the oxidation state of Archaean komatiite magmas, *Nature,* **389**, 842-845.

Carlson, R.W. and Irving, A.J. (1994) Depletion and enrichment history of subcontinental lithospheric mantle: Os, Sr, Nd and Pb evidence for xenoliths from the Wyoming Craton, *Earth and Planetary Science Letters,* **126**, 457-472.

Carlson, R.W., Pearson, D.G., Boyd, F.R., Shirey, S.B., Irvine, G., Menzies, A.H., and Gurney, J.J. (1999). Re-Os Systematics of Lithospheric Peridotites: Implications for Lithosphere Formation and Preservation. In: J.J. Gurney, J.L. Gurney, M.D. Pascoe, and S.H. Richardson (Eds.), *Proceedings of the VIIth International Kimberlite Conference, Vol. 1*, Red Roof Design, Cape Town, pp. 99-108.

Carney, J.N., Aldiss, D.T., and Lock, N.P. (1994). The Geology of Botswana, *Geological Survey Department. Bulletin,* **37**.

Cheney, E.S. and Winter, H.d.l.R. (1995) The late Archean to Mesoproterozoic major unconformity-bounded units of the Kaapvaal Province of Southern Africa, *Precambrian Research,* **74**, 203-223.

Chesley, J.T., Rudnick, R.L., and Lee, C.T. (1999) Re-Os systematics of mantle xenoliths from the East African Rift: Age, structure and history of the Tanzanian craton., *Geochimica et Cosmochimica Acta,* **63**(7/8), 1203-1217.

Chicowich, A. and Green, R.W.E. (1992) Tomographic study of upper mantle structure to the South African Continent, using wave form inversion., *Physics of Earth and Planetary Interiors,* **72**, 276-285.

Clarke, D.B. and Mitchell, R.H. (1975) Mineralogy and petrology of the kimberlite from Somerset Island, *Physics and Chemistry of the Earth,* **9**, 123-135.

Coleman, R.G. (1977) Ophiolites, Springer Verlag, Berlin, pp. 229.

Cohen, A.S. and Waters, F.G. (1996) Separation of osmium from geological materials by solvent extraction for analysis by thermal ionisation mass spectrometry, *Anal. Chim. Acta,* **332**, 269-275.

Compston, W. and Kröner, A. (1988) Multiple zircon growth within early Archaean tonalitic gneiss from the Ancient Gneiss Complex, Swaziland, *Earth and Planetary Science Letters,* **87**, 13-28.

Cookenboo, H.O. (1998), Emplacement history of the Jericho kimberlite pipe, northern Canada. In: *Extended Abstracts of the 7th International Kimberlite Conference, Cape Town,* 13-18 April, pp. 161-163.

Cookenboo, H.O. (1999). History and Process of Emplacement of the Jericho (JD-1) Kimberlite Pipe, Northern Canada. In: J.J. Gurney, J.L. Gurney, M.D. Pascoe, and S.H. Richardson (Eds.), *Proceedings of the VIIth International Kimberlite Conference, Vol. 1,* Red Roof Designs, Cape Town, pp. 125-133.

Corner, B. (1991). Crustal architecture of the Precambrian of the Kaapvaal province from geophysical data. In: P.G. Eriksson (Ed.), *Precambrian Sedimentary Basins of southern Africa. Terra Nova 3: 5,* Blackwell, Oxford,

Cox, K.G., Gurney, J.J., and Harte, B. (1973). Xenoliths from the Matsoku Pipe. In: P.H. Nixon (Ed.), *Lesotho Kimberlites,* Cape and Transvaal, Cape Town, pp. 76-100.

Cox, K.G., Smith, M.R., and Beswetherick, S. (1987). Textural studies of garnet lherzolites: evidence of exsolution from high-temperature harzburgites. In: P.H. Nixon (Ed.), *Mantle Xenoliths,* Wiley, New York, pp. 537-550.

Creaser, R.A., Papanastasio, D.A., and Wasserburg, G.J. (1991) Negative thermal ion mass spectrometry of osmium, rhenium and iridium, *Geochimica et Cosmochimica Acta,* **55**, 397-401.

Davis, G.L. (1977) The ages and uranium contents of zircons from kimberlites and associated rocks, *Carnegie Institution of Washington Yearbook.,* **76**, 631-635.

Davis, W.J. (1997) U-Pb zircon and rutile ages from granulite xenoliths in the Slave province: Evidence for mafic magmatism in the lower crust coincident with Proterozoic dike swarms, *Geology,* **25**(4), 343-346.

Davis, W.J., Fryer, B.J., and King, J.E. (1994) Geochemistry and evolution of Late Archean plutonism and its significance to the tectonic development of the Slave craton, *Precambrian Research,* **67**, 207-241.

Davis, W.J. and Hegner, E. (1992) Neodymium isotopic evidence for the tectonic assembly of Late Archean crust in the Slave Province, Northwest Canada, *Contributions to Mineralogy and Petrology,* **111**, 493-504.

Davis, W.J. and Kjarsgaard, B.A. (1997) A Rb-Sr Isochron Age for a Kimberlite from the Recently Discovered Lac de Gras Field, Slave Province, Northwest Canada, *The Journal of Geology,* **105**, 503-509.

Dawson, J.B. (1968) Recent researches on kimberlite and diamond geology, *Economic Geology,* **63**, 504-511.

Dawson, J.B. and Stephens, W.E. (1975) Statistical classification of garnets from kimberlites and associated xenoliths, *Journal of Geology,* **83**, 589-607.

Dawson, J.B., Harley, S.L., Rudnick, R.L., and Ireland, T.R. (1997) Equilibration and reaction in Archaean quartz-sapphirine granulite xenoliths from the Lace kimberlite pipe, South Africa, *Journal of Metamorphic Geology,* **15**, 253-266.

de Wit, M.J. (1991) Archaean Greenstone Belt Tectonism and Basin Development - Some Insights from the Barberton and Pietersburg Greenstone Belts, Kaapvaal Craton, South-Africa, *Journal of African Earth Science,* **13**(1), 45-63.

de Wit, M.J., Roering, C., Hart, R.J., Armstrong, R.A., Ronde, C.E.d., Green, R.W.E., Tredueaux, M., Peberdy, E., and Hart, R.A. (1992) Formation of an Archaean continent, *Nature,* **357**, 553-562.

Dempster, A.N. and Richard, R. (1973). Regional Geology and Structure. In: P.H. Nixon (Ed.), *Lesotho Kimberlites*, Cape and Transvaal, Cape Town, pp. 1-19.

Dick, H.J.B., Fisher, R.L., and Bryan, W.B. (1984) Mineralogical variability of the uppermost mantle along mid-ocean ridges, *Earth and Planetary Science Letters,* **69**, 88-106.

Doyle, B.J., Kivi, K., and Scott-Smith, B.H. (1999). The Tli Kwi Cho (DO27 and DO18) Diamondiferous Kimberlite Complex, Northwest Territories, Canada. In: J.J. Gurney, J.L. Gurney, M.D. Pascoe, and S.H. Richardson (Eds.), *Proceedings of the VIIth International Kimberlite Conference, 1*, Red Roof Designs, Cape Town, pp. 194-204.

Dreibus, G., Palme, H., Spettel, B., Zipfel, J., and Wänke, H. (1995) Sulfur and selenium in chondritic meteorites, *Meteoritics,* **30**, 439-445.

Eales, H.V. and Cawthorn, R.G. (1996). The Bushveld Complex. In: R.G. Cawthorn (Ed.), *Layered Intrusions*, Elsevier, Amsterdam, pp. 181-229.

Elthon, D., Stewart, M., and Ross, D.K. (1992) Compositional trends of minerals in oceanic cumulates, *Journal of Geophysical Research,* **97**, 15189-15199.

Encarnacion, J., Fleming, T.H., Elliot, D.H., and Eales, H.V. (1996) Synchronous emplacement of Ferrar and Karoo dolerites and the early breakup of Gondwana, *Geology,* **24**, 535-538.

Enzweiller, J., Potts, P.J., and Jarvis, K.E. (1995) Determination of Pt, Pd, Ru and Ir in Geological Samples by Isotope Dilution Inductively Coupled Plasma Mass Spectrometry Using a Sodium Peroxide Fusion and Tellurium Coprecipitation, *Analyst,* **120**, 1391-1396.

Eriksson, P.G., Schweitzer, J.K., Bosch, P.J.A., Schereiber, U.M., vanDeventer, J.L., and Gatton, C.J. (1993) The Transvaal sequence; an overview, *Journal of African Earth Science,* **16**, 25-51.

Ernst, R.E. and Baragar, W.R.A. (1992) Evidence from magnetic fabric for the flow pattern of magma in the Mackenzie giant radiating dyke swarm, *Nature,* **356**, 511-513.

Fahrig, W.F. (1987). The tectonic setting of the continental mafic dyke swarms: Failed arm and early passive margins. In: H.C. Halls and W.F. Fahrig (Eds.), *Mafic dike swarms*, Geological Association of Canada, Paper, **34**, pp. 331-348.

Finnerty, A.A. and Boyd, F.R. (1987). Thermobarometry for garnet peridotite xenoliths: a basis for upper mantle stratigraphy. In: P.H. Nixon (Ed.), *Mantle Xenoliths*, Wiley, London, pp. 381-402.

Fleet, M.E., Crocket, J.H., and Stone, W.E. (1996). Partitioning of platinum-group elements (Os, Ir, Ru, Pt, Pd) and gold between sulfide liquid and basalt melt, *Geochimica et Cosmochimica Acta,* **60**, 2397-2412.

Frey, F.A. and Prinz, M. (1978). Ultramafic inclusions from San Carlos, Arizona: petrological and geochemical data bearing on their petrogenesis, *Earth and Planetary Science Letters,* **38**, 129-176.

Frey, F.A., Suen, J., and Stockman, H.W. (1985) The Ronda high temperature peridotite: Geochemistry and petrogenesis, *Geochimica et Cosmochimica Acta,* **49**, 2469-2491.

Frisch, T., Digel, M.R., and Williams, E.J. (1987). Precambrian Shield of the Boothia Uplift, southern Somerset Island and northern Boothia Peninsula, District of Franklin, *Geological Survey of Canada. Current Research Part A, Paper*, **87-1A**, pp. 429-434.

Frisch, T. and Hunt, P.A. (1993). Reconnaissance U-Pb geochronology of the crystalline core of the Boothia Uplift, District of Franklin, Northwest Territories, *Geological Survey of Canada. Paper*, **93-2**, pp. 3-22.

Frisch, T. and Sandeman, H.A.I. (1991). Reconnaissance geology of the Precambrian Shield of the Boothia Uplift, northwestern Somerset Island and eastern Prince of Wales Island, District of Franklin, *Geological Survey of Canada. Current Research Part C, Paper*, **91-1C**, pp. 173-178.

Fryer, B.J. and Greenough, J.D. (1992) Evidence for Mantle Heterogeneity from PGE abundances in Indian Ocean Basalts, *Canadian Journal of Earth Science,* **29**, 2329-2340.

Fyson, W.K. and Helmstaedt, H. (1988) Structural patterns and tectonic evolution of supracrustal domains in the Archean Slave Province, Canada, *Canadian Journal of Earth Sciences,* **25**, 301-315.

Garuti, G., Oddone, M., and Torres-Ruiz, J. (1997) Platinum-group-element distribution in the sub-continental mantle: Evidence from the Ivrea Zone (Italy) and the Betic-Rifean cordillera (Spain and Morocco), *Canadian Journal of Earth Science,* **34**, 444-463.

Grand, S.P. (1994) Mantle shear structure beneath the Americas and surrounding oceans, *Journal of Geophysical Research,* **99**, 11591-11621.

Gregoire, D.C. (1990) Sample introduction techniques for the determination of osmium isotope ratios by inductively coupled plasma mass spectrometry, *Analytical Chemistry,* **62**, 141-146.

Griffin, W.L., Cousens, D.R., Ryan, C.G., Sie, S.H., and Suter, G.F. (1989) Ni in chrome-pyrope garnets: a new geothermobarometer, *Contributions to Mineralogy and Petrology,* **103**, 199-202.

Griffin, W.L. and Ryan, C.G. (1995) Trace elements in indicator minerals: Area selection and target evaluation in diamond exploration, *Journal of Geochemical Exploration,* **53**, 311-337.

Griffin, W.L., Doyle, B.J., Ryan, C.G., Pearson, N.J., O'Reilly, S.Y., Davies, R., Kivi, K., van Achterbergh, E., and Natapov, L.M. (1999a) Layered Mantle Lithosphere in the Lac de Gras Area, Slave craton: Composition, Structure and Origin, *Journal of Petrology,* **40**(5), 705-727.

Griffin, W.L., Doyle, B.J., Ryan, C.G., Pearson, N.J., O'Reilly, S.Y., Davies, R., Kivi, K., van Achterbergh, E., and Natapov, L.M. (1999b). Lithosphere Structure and Mantle Terranes: Slave Craton, Canada. In: J.J. Gurney, J.L. Gurney, M.D. Pascoe, and S.H. Richardson (Eds.), *Proceedings of the VIIth International Kimberlite Conference, Vol. 1*, Red Roof Designs, Cape Town, pp. 299-306.

Grütter, H.S., Apter, D.B., and Kong, J. (1999). Crust-Mantle coupling: Evidence from mantle-derived xenocrystic garnets. In: J.J. Gurney, J.L. Gurney, M.D. Pascoe, and S.H. Richardson (Eds.), *Proceedings of the VIIth International Kimberlite Conference, 1*, Red Roof Design, Cape Town, pp. 307-312.

Hall, G.E.M. and Pelchat, J.C. (1994) Analysis of Geological Materials for Au, Pt and Pd at Low ppb Levels by Fire Assay-ICP Mass Spectrometry, *Chemical Geology,* **115**, 61-72.

Handler, M.R., Bennett, V.C., and Esat, T.Z. (1997) The persistence of off-cratonic lithospheric mantle: Os isotopic systematics of variably metasomatised southeast Australian xenoliths, *Earth and Planetary Science Letters,* **151**, 61-75.

Handler, M.R. and Bennett, V.C. (1999) Behaviour of Platinum-group elements in the subcontinental mantle of Eastern Australia during variable metasomatism and melt depletion, *Geochimica et Cosmochimica Acta,* **63**(21), 3597-3618.

Handler, M.R., Bennett, V.C., and Dreibus, G. (1999) Evidence from correlated Ir/Os and Cu/S for late-stage Os mobility in peridotite xenoliths: Implications for Re-Os systematics, *Geology,* **27**(1), 75-78.

Hanmer, S., Bowring, S., vanBreeman, O., and Parrish, R. (1992) Great Slave Lake shear zone, NW Canada: mylonitic record of early Proterozoic continental convergence, collision and indentation, *Journal of Structural Geology,* **14**, 757-773.

Hanson, G.N. and Langmuir, C.H. (1978) Modelling of major elements in mantle-melt systems using trace element approaches, *Geochimica et Cosmochimica Acta,* **42**, 725-741.

Hart, S.R. and Ravizza, G.E. (1996). Os partitioning between phases in lherzolite and basalt. In: A. Basu and S.R. Hart (Eds.), *Earth processes: reading the isotopic code, Geophysical Monograph 95*, American Geophysical Union, Washington, pp. 123-134.

Harte, B. (1977) Rock nomenclature with particular relation to deformation and recrystallisation textures in olivine-bearing xenoliths, *Journal of Geology,* **85**, 279-288.

Harte, B. and Hawkesworth, C.J. (1989). Mantle domains and mantle xenoliths. In: J. Ross, A.L. Jaques, J. Ferguson, D.H. Green, S.Y. O'Reilly, R.V. Danchin, and A.J. Janse (Eds.), *Kimberlites and related rocks*, Special Publication of the Geological Society of Australia, **14**, pp. 649-686.

Harte, B., Winterburn, P.A., and Gurney, J.J. (1987). Metasomatic and enrichment phenomena in garnet peridotite facies mantle xenoliths from the Matsoku kimberlite pipe, Lesotho. In: C.J. Hawkesworth and M.A. Menzies (Eds.), *Mantle Metasomatism*, Academic Press, London, pp. 145-220.

Hauri, E. and Hart, S.R. (1993) Re-Os isotope systematics in HIMU and EMII ocean island basalts, *Earth and Planetary Science Letters,* **114**, 253-271.

Hauri, E.H. and Hart, S.R. (1996) Rhenium abundances and systematics in oceanic basalts, *Chemical Geology,* **139**, 185-205.

Hauri, E.H., Lassiter, J.C., and Depaolo, D.J. (1996) Osmium isotope systematics of drilled lavas from Mauna Loa, Hawaii, *Journal of Geophysical Research,* **101**, 11793-11806.

Hawkesworth, C.J., Erlank, A.J., Marsh, J.S., Menzies, M.A., and Calsteren, P.v. (1983). Evolution of the continental lithosphere: evidence from volcanics and xenoliths from southern Africa. In: C.J. Hawkesworth and M.J. Norry (Eds.), *Continental basalts and mantle xenoliths*, Shiva, Nantwich, pp. 111-138.

Hawkesworth, C.J., Rogers, N.W., Calsteren, P.W.C.v., and Menzies, M.A. (1984) Mantle enrichment processes, *Nature,* **311**, 331-335.

Heaman, L.M. (1989) The nature of the subcontinental mantle from Sr-Nd-Pb isotopic studies on kimberlitic perovskite, *Earth and Planetary Science Letters,* **92**, 323-334.

Heaman, L.M. (1994) 2.45 Ga global mafic magmatism: Earths oldest superplume, *8th International Conference of Geochronology, Cosmochronology and Isotope Geology, Program with Abstracts, US Geological Survey Circular 1107*, 132.

Heaman, L.M., Kjarsgaard, B., Creaser, R.A., Cookenboo, H.O., and Kretschmar, U. (1997). Multiple episodes of kimberlite magmatism in the Slave Province, North America, *University of Calgary. LITHOPROBE Report*, **56**, pp. 14-17.

Helmstaedt, H.H. and Gurney, J.J. (2001), Formation of the Archean Kaapvaal Province revisited: Implications for the birth and growth of its diamondiferous root. In: *The Slave-Kaapvaal Workshop, Merrickville, Ontario, Canada.*

Herzberg, C.T. (1993) Lithosphere peridotites of the Kaapvaal craton, *Earth and Planetary Science Letters,* **120**, 13-29.

Herzberg, C.T. (1999). Phase equilibrium constraints on the formation of cratonic mantle. In: Y. Fei, C.M. Bertka, and B.O. Mysen (Eds.), *Mantle Petrology: Field observations and high pressure experimentation. A tribute to Francis R. (Joe) Boyd, Special Publication No. 6*, The Geochemical Society, Houston, pp. 241-257.

Heumann, K.G. (1988). Isotope dilution mass spectrometry. In: F. Adams (Ed.), *Inorganic mass spectrometry*, Wiley, New York, pp. 301-376.

Hoffman, E.L., Naldrett, A.J., Van Loon, J.C., Hancock, R.G.V., and Mason, A. (1978) The determination of all the platinum group elements and gold in rocks and ore by neutron activation analysis after preconcentration by a nickel sulfide fire-assay technique of large samples, *Anal. Chim. Acta,* **102**, 157-166.

Hoffman, P.F. (1987) Continental transform tectonics: Great Slave Lake shear zone (c. 1.9 Ga), northwest Canada, *Geology,* **15**, 785-788.

Hoffman, P.F. (1988) United plates of America, the birth of a continent: Early Proterozoic assembly and growth of Laurentia, *Annual Reviews Earth and Planetary Science Letters,* **16**, 543-603.

Hoffman, P.F. (1989). Precambrian geology and tectonic history of North America. In: A.W. Bally and A.R. Palmer (Eds.), *The Geology of North America - An Overview*, GSA, Boulder, VA, pp. 447-512.

Hoffman, P.F. (1990a) Geological constraints on the origin of the mantle root beneath the Canadian shield, *Philosophical Transactions of the Royal Society London,* **A 331**, 523-532.

Hoffman, P.F. (1990b) Subdivision of the Churchill province and extent of the Trans-Hudson Orogen. In: J.F. Lewry and M.R. Stauffer (Eds.), *The Early Proterozoic Trans-Hudson Orogen of North America*, Vol. 37, Geological Society of Canada Special Paper, pp. 15-39.

Hunter, D. (1991) Crustal processes during Archaean evolution of the Southeastern Kaapvaal Province, *Journal of African Earth Science,* **13**, 13-26.

Irvine, G.J., Kopylova, M.G., Carlson, R.W., Pearson, D.G., Shirey, S.B., and Kjarsgaard, B.A. (1999) Age of the lithospheric mantle beneath and around the Slave craton: a Rhenium-Osmium isotopic study of peridotite xenoliths from the Jericho and Somerset Island kimberlites., *Ninth Annual V.M. Goldschmidt Conf.*, **LPI Cont. 971**, 134-135.

Irvine, G.J., Pearson, D.G., and Carlson, R.W. (2001) Lithospheric mantle evolution of the Kaapvaal Craton: A Re-Os isotope study of peridotite xenoliths from Lesotho kimberlites, *Geophysical Research Letters,* **28**(13), 2505-2508.

Isachsen, C.E. and Bowring, S.A. (1994) Evolution of the Slave craton, *Geology,* **22**, 917-920.

Isachsen, C.E. and Bowring, S.A. (1997) The Bell group and Anton Complex: a basement-cover sequence beneath the Archean Yellowknife greenstone belt revealed and implicated in greenstone belt formation, *Canadian Journal of Earth Sciences,* **34**, 169-189.

Jago, B.C. and Mitchell, R.H. (1987) Ultrabasic xenoliths from the Ham kimberlite, Somerset Island, Northwest Territories, *Canadian Mineralogist,* **25**, 515-525.

Jagoutz, E., Palme, H., Baddenhausen, H., Blum, K., Cendales, M., Dreibus, G., Spettel, B., Lorenz, V., and Wanke, H. (1979) The abundances of major, minor and trace elements in the Earth's mantle as derived from primitive ultramafic nodules, *Proc. Lunar Sci. Conf.,* **10th**, 2031-2050.

Jahn, B.M., Bertrand-Sarfati, J., Morin, N., and Mace, J. (1990) Direct dating of stromatilitic carbonates from the Schmidtsdrif Formation (Transvaal Dolomite), South Africa, with implications on the age of the Ventersdorp Supergroup, *Geology,* **18**, 1211-1214.

James, D.E., Fouch, M.J., VanDecar, J.C., and vanderLee, S. (2001) Tectospheric structure beneath southern Africa, *Geophysical Research Letters,* **28**(13), 2485-2488.

Janney, P.E., Carlson, R.W., Shirey, S.B., Bell, D.R., and leRoex, A.P. (1999) Temperature,, pressure, and rhenium-osmium age systematics of off-craton peridotite xenoliths from the Namaqua-Natal belt, western South Africa, *Ninth Annual V.M. Goldschmidt Conf.*, **LPI Cont. 971**, 139.

Jarvis, I., Totland, M.M., and Jarvis, K.E. (1997a) Assessment of Dowel 1-X8 based anion-exchange resin procedures for the separation and determination of ruthenium, rhodium, palladium, iridium, platinum and gold in geological samples by inductively coupled plasma mass spectrometry, *Analyst,* **122**, 19-26.

Jarvis, I., Totland, M.M., and Jarvis, K.E. (1997b) Determination of the platinum-group elements in geological materials by ICP-MS using microwave digestion, alkali fusion and cation-exchange chromatography, *Chemical Geology,* **143**, 27-42.

Jochum, K.P. (1996) Rhodium and other PGEs in Carbonaceous Chondrites, *Geochimica et Cosmochimica Acta,* **60**, 3353-3357.

Jones, D.L. and Fahrig, W.F. (1978) Paleomagnetism and age of the Aston dykes and Savage Point sills of the Boothia Uplift, Canada, *Canadian Journal of Earth Science,* **15**, 1605-1612.

Jordan, T.H. (1979). Mineralogies, densities and seismic velocities of garnet lherzolites and their geophysical implications. In: F.R. Boyd and H.O.A. Meyer (Eds.), *The Mantle Sample: Inclusions in Kimberlites and Other Volcanics*, American Geophysical Union, Washington, pp. 1-13.

Jordan, T.H. (1988) Structure and formation of the continental tectosphere, *Journal of Petrology,* **Special Lithospheric Issue**, 11-37.

Keays, R.R. (1995) The role of komatiitic and picritic magmatism and S-saturation in the formation of ore-deposits, *Lithos,* **34**, 1-18.

Keays, R.R., Sewell, D.K.B., and Mitchell, R.H. (1981) Platinum and palladium minerals in upper mantle-derived lherzolites, *Nature,* **294**, 646-648.

Keleman, P.B., Dick, H.J.B., and Quick, J.E. (1992) Formation of harzburgite by pervasive melt/rock reaction in the upper mantle, *Nature,* **358**, 635-641.

Keleman, P.B., Hart, S.R., and Bernstein, S. (1998) Silica enrichment in the continental upper mantle via melt/rock reaction, *Earth and Planetary Science Letters,* **164**, 387-406.

Kerr, J.W. (1977) Cornwallis Fold Belt and the mechanism of basement uplift, *Canadian Journal of Earth Science,* **14**, 1374-1401.

Kerr, J.W. and Christie, R.L. (1965) Tectonic history of Boothia Uplift and Cornwallis Fold Belt, Arctic Canada, *A.A.P.G. Bulletin,* **49**, 905-926.

Kerr, J.W. and deVries, C.D.S. (1977). Structural Geology of Somerset Island and Boothia Peninsula, District of Franklin, *Geological Survey of Canada. Report of Activities Part A, Paper*, **77-1A**, pp. 107-112.

King, J.I., Davis, W.J., and Relf, C. (1992) Late Archean tectono-magmatic evolution of the central Slave Province, NWT, *Canadian Journal of Earth Sciences,* **29**, 2156-2170.

Kjarsgaard, B.A. (1992). Is Ni in pyrope garnet a valid diamond exploration tool?, *Geological Survey of Canada. Paper*, **92-1E**, pp. 315-322.

Kjarsgaard, B.A. (1996). Slave Province kimberlites, NWT. In: A.N. LeCheminant, D.G. Richardson, R.N.W. DiLabio, and K.A. Richardson (Eds.), *Searching for diamonds in Canada, 3228*, Geological Survey of Canada, Open File, pp. 55-60.

Kjarsgaard, B.A. and Peterson, T.D. (1992) Kimberlite-derived ultramafic xenoliths from the diamond stability field: a new Cretaceous geotherm for Somerset Island, Northwest Territories, *Current Research, Part B; Geological Survey of Canada. Paper,* **92-1B**, 1-6.

Kopylova, M., Russell, J.K., and Cookenboo, H. (1998a), Petrography and chemistry of the Jericho kimberlite (Slave craton, Northern Canada). In: *Extended Abstracts of the 7th International Kimberlite Conference, Cape Town*, 13-18 April, pp. 449-451.

Kopylova, M., Russell, J.K., and Cookenboo, H. (1998b), Unique chemical features of the peridotitic mantle below the Jericho kimberlite (Slave craton, Northern Canada). In: *Extended Abstracts of the 7th International Kimberlite Conference, Cape Town*, 13-18 April, pp. 455-457.

Kopylova, M., Russell, J.K., and Cookenboo, H. (1998c), Upper mantle stratigraphy and thermal regime of the north-central Slave craton, Canada. In: *Extended Abstracts of the 7th International Kimberlite Conference, Cape Town,* 13-18 April, pp. 452-454.

Kopylova, M.G., Russell, J.K., and Cookenboo, H. (1999a). Mapping the Lithosphere beneath the North Central Slave Craton. In: J.J. Gurney, J.L. Gurney, M.D. Pascoe, and S.H. Richardson (Eds.), *Proceedings of the VIIth International Kimberlite Conference, Vol. 1,* Red Roof Design, Cape Town, pp. 468-479.

Kopylova, M.G., Russell, J.K., and Cookenboo, H. (1999b) Petrology of Peridotite and Pyroxenite Xenoliths from the Jericho Kimberlite: Implications for the Thermal State of the Mantle beneath the Slave Craton, Northern Canada, *Journal of Petrology,* **40**(1), 79-104.

Kopylova, M.G. and Russell, J.K. (2000) Chemical stratification of cratonic lithosphere: constraints from the Northern Slave craton, Canada, *Earth and Planetary Science Letters,* **181**, 71-87.

Korkisch, J. and Klakl, H. (1989) Anion-exchange behaviour of the platinum metals and gold in hydrochloric acid - organic solvent media, *Talanta,* **15**, 339-346.

Kröner, A. and Layer, P.W. (1992) Crust formation and plate motion in the early Archean, *Science,* **256**, 1405-1412.

Kusky, T.M. (1989) Accretion of the Archean Slave province, *Geology,* **17**, 63-67.

Le Cheminant, A.N. and Heaman, L.M. (1989) Mackenzie igneous events, Canada: Middle Proterozoic hotspot magmatism associated with ocean opening, *Earth and Planetary Science Letters,* **96**, 38-48.

Le Cheminant, A.N., Heaman, L.M., van Breeman, O., Ernst, R.E., Baragar, W.R.A., and Buchan, K.L. (1996). Mafic magmatism, mantle roots and kimberlites in the Slave craton. In: A.N. LeCheminant, D.G. Richardson, R.N.W. DiLabio, and K.A. Richardson (Eds.), *Searching for diamonds in Canada, 3228,* Geological Survey of Canada, Open File, pp. 161-169.

Lewry, J.F. and Collerson, K.D. (1990) The Trans-Hudson Orogen: extent, subdivisions and problems. In: J.F. Lewry and M.R. Stauffer (Eds.), *The Early Proterozoic Trans-Hudson Orogen of North America,* Vol. 37, Geological Society of Canada Special Paper, pp. 1-14.

Lewry, J.F. and Sibbald, T.I.L. (1980) Thermotectonic evolution of the Churchill province in northern Saskatchewan, *Tectonophysics,* **68**, 45-82.

Lindner, M., Leich, D.A., Borg, R.J., Russ, G.P., Bazan, J.M., Simons, D.S., and Date, A.R. (1986) Direct laboratory determination of the 187Re half-life, *Nature,* **320**, 246-247.

Lindner, M., Leich, D.A., Russ, G.P., Bazan, J.M., and Borg, R.J. (1989) Direct determination of the half-life of 187Re, *Geochimica et Cosmochimica Acta,* **53**, 1597-1606.

Lorand, J.P. (1989) Abundances and distribution of Cu-Fe-Ni sulfides, sulfur, copper and platinum-group elements in orogenic-type spinel peridotites of Ariege (Northeastern Pyrenees, France), *Earth and Planetary Science Letters,* **93**, 50-64.

Lorand, J.P. (1990) Are spinel lherzolite xenoliths representative of the abundance of sulphur in the upper mantle?, *Geochimica et Cosmochimica Acta,* **54**, 1487.

Lorand, J.P. (1991) Sulphide petrology and sulphur geochemistry of orogenic lherzolites: A comparative study of the Pyrenean bodies (France) and the Lanzo Massif (Italy), *Journal of Petrology,* **Special Lherzolites Issue**, 77-95.

Lorand, J.P., Keays, R.R., and Bodinier, J.L. (1993) Copper and noble metal across the lithosphere-asthenosphere boundary of mantle diapirs: Evidence from the Lanzo lherzolite massif, *Journal of Petrology,* **34**, 1111-1140.

Lorand, J.P., Pattou, L., and Gros, M. (1999) Fractionation of Platinum-group Elements in the Upper Mantle: a Detailed Study in Pyrenean Orogenic Lherzolites, *Journal of Petrology,* **40**(6), 957-981.

Luck, J.-M. and Allègre, C.-J. (1983) ^{187}Re-^{186}Os systematics in meteorites and cosmochemical consequences, *Nature,* **302**, 130-132.

Luck, J.-M., Birck, J.-L., and Allègre, C.-J. (1980) ^{187}Re-^{187}Os systematics in meteorites; Early chronology of the solar system and age of the galaxy, *Nature,* **283**, 256-259.

Maaloe, S. and Aoki, K. (1977) The major element composition of the upper mantle estimated from the composition of lherzolites, *Contributions to Mineralogy and Petrology,* **63**, 161-173.

MacGregor, I.D. (1974) The system MgO-Al2O3-SiO2: solubility of Al2O3 in enstatite for spinel and garnet peridotite compositions., *American Mineralogist,* **59**, 110-119.

MacKenzie, J.M. and Canil, D. (1998). Composition and thermal evolution of the upper mantle beneath the Archean Slave Province: evidence from xenolith studies. In: F. Cook and P. Erdmer (Eds.), *Slave-Northern Cordillera Lithospheric Evolution (SNORCLE) Transect and Cordilleran Tectonics Workshop Meeting (6-8 March)*, Simon Fraser University, pp. 37-38.

Martin, C.E. (1990) Rhenium-Osmium Isotope Geochemistry of the Mantle. Ph.D., Yale University.

Martin, C.E. (1991) Osmium isotopic characteristics of mantle-derived rocks, *Geochimica et Cosmochimica Acta,* **55**, 1421-1434.

Maxwell, J.A., Campbell, J.L., and Teesdale, W.J. (1989) The Guelph PIXE software package, *Nucl. Instrum. Methods Phys. Res.,* **B43**, 172-179.

Maxwell, J.A., Teesdale, W.J., and Campbell, J.L. (1995) The Guelph PIXE software package II, *Nucl. Instrum. Methods Phys. Res.,* **B95**, 407-421.

McBride, J.S., Lambert, D.D., Greig, A., and Nicholls, I.A. (1996) Multi-stage evolution of Australian subcontinental mantle: Re-Os isotopic constraints from Victorian mantle xenoliths, *Geology,* **24**, 631-634.

McDonald, I. (1998) The need for a common framework for collection and interpretation of data in Platinum-Group Element Geochemistry, *Geostandards Newsletter,* **22**, 85-91.

McDonald, I., Hart, R.J., and Tredoux, M. (1994) The analysis of the platinum group elements in South African and kimberlites by nickel sulphide fire assay and neutron activation analysis, *Anal. Chim. Acta.,* **289**, 237-247.

McDonough, W.F. (1990) Constraints on the composition of the continental lithospheric mantle, *Earth and Planetary Science Letters,* **101**, 1-18.

McDonough, W.F. and Sun, S.S. (1995) The composition of the Earth, *Chemical Geology,* **120**, 223-253.

Meisel, T., Walker, R.J., and Morgan, J.W. (1996) The osmium isotopic composition of the Earth's primitive upper mantle, *Nature,* **383**, 517-520.

Menzies, A.H., Shirey, S.B., Carlson, R.W., and Gurney, J.J. (1999). Re-Os isotope systematics of diamond-bearing eclogites and peridotites from Newlands kimberlite. In: J.J. Gurney, J.L. Gurney, M.D. Pascoe, and S.H. Richardson (Eds.), *Proceedings of the VIIth International Kimberlite Conference, Vol. 2*, Red Roof Design, Cape Town, pp. 579-581.

Menzies, M.A. (1990). Archaean, proterozoic and phanerozoic lithospheres. In: M.A. Menzies (Ed.), *Continental mantle*, Clarendon Press, Oxford, pp. 67-86.

Menzies, M.A. and Murthy, V.R. (1980a) Nd and Sr isotope geochemistry of hydrous mantle nodules and their host alkali basalts; implications for local heterogeneities in metasomatically veined mantle, *Earth and Planetary Science Letters,* **46**, 323-334.

Menzies, M.A. and Murthy, V.R. (1980b) Mantle metasomatism as a precursor to the genesis of alkaline magmas- Isotopic evidence, *American Journal of Science,* **280A**, 622-638.

Menzies, M.A. and Hawkesworth, C.J. (1987) Mantle Metasomatism, Academic Press, New York, pp. 472.

Menzies, M.A., Rogers, N., Tindle, A., and Hawkesworth, C.J. (1987). Metasomatic and enrichment processes in the lithospheric peridotites, an effect of asthenosphere-lithosphere interaction. In: M.A. Menzies and C.J. Hawkesworth (Eds.), *Mantle Metasomatism*, Academic Press, London, pp. 313-361.

Mercier, J.C.C. and Nicolas, A. (1975) Textures and fabrics of upper-mantle peridotites as illustrated by xenoliths from basalts, *Journal of Petrology,* **16**, 454-487.

Meyer, H.O.A., Waldman, M.A., and Garwood, B.L. (1994) Mantle xenoliths from kimberlite near Kirkland Lake, Ontario., *Canadian Mineralogist,* **32**, 295-306.

Mitchell, R.H. (1975) Geology, magnetic expression, and structural control of the central Somerset Island kimberlites, *Canadian Journal of Earth Science,* **12**, 757-764.

Mitchell, R.H. (1976). Kimberlites of Somerset Island, District of Franklin, *Geological Survey of Canada. Paper*, **76-1A**, pp. 501-502.

Mitchell, R.H. (1977) Ultramafic xenoliths from the Elwin Bay kimberlite: the first Canadian paleogeotherm, *Canadian Journal of Earth Science,* **14**, 1202-1210.

Mitchell, R.H. (1978) Garnet lherzolites from Somerset Island, Canada and aspects of the nature of perturbed geotherms, *Contributions to Mineralogy and Petrology,* **67**, 341-347.

Mitchell, R. (1986) Kimberlites: Mineralogy, Geochemistry and Petrology, Plenum Press, New York.

Mitchell, R.H. (1987). Mantle-derived xenoliths in Canada. In: P.H. Nixon (Ed.), *Mantle Xenoliths*, John Wiley & Sons, Cichester, pp. 33-40.

Mitchell, R.H. and Fritz, P. (1973) Kimberlite from Somerset Island, District of Franklin, NWT, *Can. J. Earth Sci.,* **10**, 384-393.

Mitchell, R.H. and Keays, R.R. (1981) Abundance and distribution of gold, palladium and iridium in some spinel and garnet lherzolites: Implications for the nature and origin of precious metal-rich intergranular components in the upper mantle, *Geochimica et Cosmochimica Acta,* **45**, 2425-2442.

Morgan, J.W. (1986) Ultramafic xenoliths: Clues to earth's late accretionary history, *Journal of Geophysical Research,* **91**(B12), 12375-12387.

Morgan, J.W., Wandless, G.A., Petrie, R.K., and Irving, A.J. (1981) Composition of the Earth's upper mantle - I. Siderophile trace elements in ultramafic nodules, *Tectonophysics,* **75**, 47-67.

Morgan, J.W., Golightly, D.W., and Dorrzapf, A.F. (1991) Methods for the separation of rhenium, osmium and molybdenum applicable to isotope geochemistry, *Talanta,* **38**, 259-265.

Moser, D.E., Flowers, R.M., and Hart, R.J. (2001) Birth of the Kaapvaal Tectosphere 3.08 Billion Years Ago, *Science,* **291**, 465-468.

Naldrett, A.J. and Duke, J.M. (1980) Pt Metals in Magmatic Sulfide Ores; The Occurrence of these Metals is Discussed in Relation to the Formation and Importance of these Ores, *Science,* **208**, 1417-1424.

Nelson, D.R., Trendal, A.F., DeLaeter, J.R., Grobler, N.J., and Fletscher, I.R. (1992) A comparative study of the geochemical and isotope systematics of Late Archean flood basalts from the Pilbara and Kaapvaal cratons, *Precambrian Research,* **54**, 231-256.

Nier, A.O. (1950) A redetermination of the relative abundances of the isotopes of carbon, nitrogen, oxygen, argon and potassium, *Phys. Rev.,* **77**, 789-793.

Nixon, P.H. (1973a). The Geology of Mothae, Solane, Thaba Putsoa and Blow 13. In: P.H. Nixon (Ed.), *Lesotho Kimberlites*, Cape and Transvaal, Cape Town, pp. 39-47.

Nixon, P.H. (1973b) Lesotho Kimberlites, Cape and Transvaal, Cape Town, pp. 350.

Nixon, P.H. (1987a). Kimberlitic xenoliths and their cratonic setting. In: P.H. Nixon (Ed.), *Mantle Xenoliths*, John Wiley & Sons, Chichester, pp. 215-239.

Nixon, P.H. (1987b) Mantle Xenoliths, John Wiley & Sons, Chichester.

Nixon, P.H., Knorring, O.v., and Rooke, J.M. (1963) Kimberlites and associated inclusions: a mineralogical and geochemical study, *American Mineralogist,* **48**, 1060-1132.

Nixon, P.H. and Boyd, F.R. (1973a). The discrete nodule association in kimberlites in northern Lesotho. In: P.H. Nixon (Ed.), *Lesotho Kimberlites*, Cape and Transvaal, Cape Town, pp. 67-75.

Nixon, P.H. and Boyd, F.R. (1973b). The Liqhobong Intrusions and Kimberlitic Olivine Composition. In: P.H. Nixon (Ed.), *Lesotho Kimberlites*, Cape and Transvaal, Cape Town, pp. 141-148.

Nixon, P.H. and Boyd, F.R. (1973c). Petrogenesis of the granular and sheared ultrabasic nodule suite in kimberlite. In: P.H. Nixon (Ed.), *Lesotho Kimberlites*, Cape and Transvaal, Cape Town, pp. 48-56.

Nixon, P.H., Rogers, N.W., Gibson, I.L., and Grey, A. (1981) Depleted and fertile mantle xenoliths from southern African kimberlites, *Annual Review Earth and Planetary Science Letters,* **9**, 285-309.

Nixon, P.H., Calsteren, P.v., Boyd, F.R., and Hawkesworth, C.J. (1987). Harzburgites with garnets of diamond facies from Southern Africa. In: P.H. Nixon (Ed.), *Mantle Xenoliths*, Wiley, U.K., pp. 523-533.

Okulitch, A.V., Packard, J.J., and Zolnai, A.I. (1986) Evolution of the Boothia Uplift, Arctic Canada, *Canadian Journal of Earth Science,* **23**, 350-358.

O'Neill, H.S.C. (1980) An experimental study of the iron-magnesium partitioning between garnet and olivine and it's calibration as a geothermometer: corrections, *Contributions to mineralogy and petrology,* **72**, 337.

O'Neill, H.S.C. (1991) The origin and the early history of the Earth - a chemical model. Part 2: The Earth, *Geochimica et Cosmochimica Acta,* **55**, 1159-1172.

O'Neill, H.S.C. and Wood, B.J. (1979) An experimental study of the iron-magnesium partitioning between garnet and olivine and it's calibration as a geothermometer, *Contributions to mineralogy and petrology,* **70**, 59-70.

Padgham, W.A. and Fyson, W.K. (1992) The Slave Province: a distinct Archean craton, *Canadian Journal of Earth Sciences,* **29**, 2072-2086.

Pattou, L., Lorand, J.P., and Gros, M. (1996) Non-chondritic platinum-group element ratios in the Earth's mantle, *Nature,* **379**, 712-715.

Peach, C.L., Mathez, E.A., Keays, R.R., and Reeves, S.J. (1994) Experimentally Determined Sulfide Melt-Silicate Melt Partition Coefficients for Ir and Pd, *Chemical Geology,* **117**, 361-377.

Peach, C.L. and Mathez, E.A. (1996) Constraints on the formation of PGE deposits in igneous rocks, *Economic Geology,* , 439-450.

Pearson, D.G. (1989) The petrogenesis of pyroxenites containing octahedral graphite and associated mafic and ultramafic rocks of the Beni Bousera peridotite massif, N. Morocco. PhD, Leeds.

Pearson, D.G. (1999a) The age of continental roots, *Lithos, special edition,* **48**, 171-194.

Pearson, D.G. (1999b). Evolution of cratonic lithospheric mantle: an isotopic perspective. In: Y. Fei, C.M. Bertka, and B.O. Mysen (Eds.), *Mantle Petrology: Field observations and high pressure experimentation. A tribute to Francis R. (Joe) Boyd, Special Publication No. 6*, The Geochemical Society, Houston, pp. 57-78.

Pearson, D.G., Boyd, F.R., Hoal, K.E.O., Hoal, B.G., Nixon, P.H., and Rogers, N.W. (1994) A Re-Os isotopic and petrological study of Namibian peridotites: contrasting petrogenesis and composition of on- and off-craton lithospheric mantle., *Mineralogical Magazine,* **58A**, 703-704.

Pearson, D.G., Carlson, R.W., Shirey, S.B., Boyd, F.R., and Nixon, P.H. (1995a) The stabilisation of Archaean lithospheric mantle: A Re-Os isotope study of peridotite xenoliths from the Kaapvaal craton, *Earth and Planetary Science Letters,* **134**, 341-357.

Pearson, D.G., Shirey, S.B., Carlson, R.W., Boyd, F.R., Pokhilenko, N.P., and N.Shimizu. (1995b) Re-Os, Sm-Nd & Rb-Sr isotope evidence for thick Archaean lithospheric mantle beneath the Siberia craton modified by multi-stage metasomatism., *Geochimica et Cosmochimica Acta,* **59**, 959-977.

Pearson, D.G., Carlson, R.W., Boyd, F.R., Shirey, S.B., and Nixon, P.H. (1998a), Lithospheric mantle growth around cratons: A Re-Os isotope study of peridotite xenoliths from East Griqualand. In: *Extended Abstracts of the 7th International Kimberlite Conference, Cape Town.*

Pearson, D.G., Shirey, S.B., Harris, J.W., and Carlson, R.W. (1998b) Sulfide inclusions in diamonds from the Koffiefontein kimberlite, S. Africa: Constraints on diamond ages and mantle Re-Os systematics., *Earth and Planetary Science Letters,* **160**, 311-326.

Pearson, D.G. and Woodland, S.J. (2000) Solvent extraction/anion exchange separation and determination of PGEs (Os, Ir, Pt, Pd, Ru) and Re-Os isotopes in geological samples by isotope dilution ICP-MS, *Chemical Geology,* **165**, 87-107.

Pearson, D.G., Irvine, G.J., Carlson, R.W., Kopylova, M.G., and Ionov, D.A. (2001). The development of lithospheric keels beneath the earliest continents: time constraints using PGE and Re-Os systematics, *The Early Earth, Special Publication*, Geological Society of London, London.

Pearson, N.J., Allard, O., Griffin, W.L., Graham, S., and Jackson, S.E. (2000) LAM-MC-ICPMS analysis of mantle derived sulfides: the key to Re-Os systematics of mantle peridotites, *Journal of Conference Abstracts,* **5(2)**, 777.

Pearson, N.J., Griffin, W.L., Doyle, B.J., O'Reilly, S.Y., van Achterbergh, E., and Kivi, K. (1999). Xenoliths from Kimberlite Pipes of the Lac de Gras Area, Slave Craton, Canada. In: J.J. Gurney, J.L. Gurney, M.D. Pascoe, and S.H. Richardson (Eds.), *Proceedings of the VIIth International Kimberlite Conference, Vol. 2*, Red Roof Design, Cape Town, pp. 644-658.

Pell, J.P. (1993). New kimberlite discoveries on Somerset Island. In: S.P. Goff (Ed.) *Exploration Overview 1993*, NWT Geology Division, Department of Indian and Northern Affairs, Yellowknife, pp. 47.

Pell, J.A. (1997) Kimberlites in the Slave craton, Northwest Territories, Canada., *Geoscience Canada,* **24**, 77-91.

Percival, J.A. (1996). Archean cratons. In: A.N. Le Cheminant, D.G. Richardson, R.N.W. DiLabio, and K.A. Richardson (Eds.), *Searching for diamonds in Canada, 3228*, Geological Survey of Canada, Open File, pp. 161-169.

Peslier, A.H., Reisberg, L., Ludden, J., and Francis, D. (2000) Re-Os constraints on harzburgite and lherzolite formation in the lithospheric mantle: A study of Northern Cordillera xenoliths, *Geochimica et Cosmochimica Acta,* **64**(17), 3061-3071.

Peterson, T.D., Esperança, S., and LeCheminant, A.N. (1994) Geochemistry and origin of the Proterozoic ultrapotassic rocks of the Churchill Province, Canada, *Mineralogy and Petrology,* **51**, 251-276.

Peterson, T.D. and LeCheminant, A.N. (1996). Ultrapotassic rocks of the Dubawnt Supergroup, District of Keewatin, N.W.T. In: A.N. Le Cheminant, D.G. Richardson, R.N.W. DiLabio, and K.A. Richardson (Eds.), *Searching for diamonds in Canada, 3228*, Geological Survey of Canada, Open File, pp. 97-100.

Poujol, M. and Anhaeusser, C.R. (2001) The Johannesburg Dome, South Africa: new single zircon U-Pb isotopic evidence for early Archean granite-greenstone development within the central Kaapvaal craton, *Precambrian Research,* **108**, 139-157.

Poujol, M., Anhaeusser, C.R., and Armstrong, R.A. (2000). Episodic Archean granitoid emplacement in the Amalia-Kraaipan terrane, South Africa: new evidence from single zircon chronology with implications for the age of the Western Kaapvaal Craton, *Economic Geology Research Institute. Information Circular*, **346**, pp. 21.

Ravizza, G. and Pyle, D. (1997) PGE and Os isotopic analyses of single sample aliquots with NiS fire assay preconcentration, *Chemical Geology,* **141**, 251-268.

Rehkämper, M. and Halliday, A.N. (1997) Development and application of new ion-exchange techniques for the separation of the platinum group and other siderophile elements from geological samples, *Talanta,* **44**, 663-672.

Rehkämper, M., Halliday, A.N., Alt, J., Fitton, J.G., Zipfel, J., and Takazawa, E. (1999a) Non-chondritic platinum-group element ratios in oceanic mantle lithosphere: petrogenetic signature of melt percolation?, *Earth and Planetary Science Letters,* **172**, 65-81.

Rehkämper, M., Halliday, A.N., Fitton, J.G., Lee, D.-C., Wieneke, M., and Arndt, N.T. (1999b) Ir, Ru, Pt and PD in basalts and komatiites: New constraints for the geochemical behaviour of the platinum-group elements in the mantle, *Geochimica et Cosmochimica Acta,* **63**, 3915-3934.

Reid, A.M. and Dawson, J.B. (1970) Olivine-garnet reaction in peridotites from Tanzania, *Lithos,* **5**, 115-124.

Reisberg, L. and Lorand, J.P. (1995) Longevity of sub-continental mantle lithosphere from osmium isotope systematics in orogenic peridotite massifs, *Nature,* **376**, 159-162.

Reisberg, L.C., Allegre, C.J., and Luck, J.-M. (1991) The Re-Os systematics of the Ronda ultramafic complex in southern Spain, *Earth and Planetary Science Letters,* **105**, 196-213.

Reisberg, L., Zindler, A., Marcantonio, F., White, W., Wyman, D., and Weaver, B. (1993) Os isotope systematics in ocean island basalts, *Earth and Planetary Science Letters,* **120**, 149-167.

Relf, C., Villeneuve, M., and Helmstaedt, H. (1995). Discovery of an Archean carbonatite-bearing alkaline complex in the Northern Slave Province: Tectonic and economic implications, *Exploration overview 1994: Northwest Territories Mining*, Exploration and Geological Investigations, pp. 53-54.

Reid, A.M. and Dawson, J.B. (1970) Olivine-garnet reaction in peridotites from Tanzania, *Lithos,* **5**, 115-124.

Richardson, S.H., Gurney, J.J., Erlank, A.J., and Harris, J.W. (1984) Origin of diamonds in old enriched mantle, *Nature,* **310**, 198-202.

Richardson, S.H., Erlank, A.J., and Hart, S.R. (1985) Kimberlite-borne garnet peridotite xenoliths from old enriched subcontinental lithosphere, *Earth and Planetary Science Letters,* **75**, 116-128.

Ringwood, A.E. (1975) Composition and petrology of the Earth's mantle, McGraw-Hill, New York, pp. 618.

Ringwood, A.E. (1979) Origin of the Earth and Moon, Springer-Verlag, New York, pp. 295.

Roy-Barman, M. and Allegre, C.J. (1994) 187Os/186Os ratios of mid-ocean ridge basalts and abyssal peridotites, *Geochimica et Cosmochimica Acta,* **58**, 5043-5054.

Roy-Barman, M. and Allegre, C.J. (1995) 187Os/186Os in oceanic island basalts: tracing oceanic crust recycling in the mantle, *Earth and Planetary Science Letters,* **129**, 145-161.

Rudnick, R.L. (1995) Making continental crust, *Nature,* **378**, 571-578.

Ryan, C.G., Griffin, W.L., and Pearson, N.L. (1996) Garnet geotherms: pressure-temperature data from Cr-pyrope garnet xenocrysts in volcanic rocks, *Journal of geophysical research,* **101(B3)**, 5611-5625.

Sautter, V. and Harte, B. (1988) Diffusion gradients in an eclogite xenolith from Roberts Victor kimberlite pipe: 1. Mechanism and evolution of garnet exsolution in Al_2O_3 -rich clinopyroxene, *Journal of Petrology,* **29**, 1325-1352.

Schmidberger, S., Simonetti, A., and Francis, D. (2000) Lu-Hf Isotope Systematics for Peridotite Xenoliths from Somerset Island Kimberlites: Evidence for Archean Lithosphere beneath Arctic Canada, *Journal of Conference Abstracts,* **5(2)**, 890.

Schmidberger, S.S. and Francis, D. (1999) Nature of the mantle roots beneath the North American craton: mantle xenolith evidence from Somerset Island kimberlites, *Lithos,* **48**, 195-216.

Schmitz, M.D., Bowring, S.A., and Robey, J.v.A. (1998), Constraining the thermal history of an Archean craton: U-Pb thermochronology of lower crustal xenoliths from the Kaapvaal craton, southern Africa. In: *Extended Abstracts of the 7th International Kimberlite Conference, Cape Town,* pp. 766-768.

Schmitz, M.D. and Bowring, S.A. (1999) The evolution of cratonic geotherms: U-Pb thermochronometric constraints from lower crustal xenoliths, Lesotho, southern Africa, *Ninth Annual V.M. Goldschmidt Conf.,* **LPI Cont. 971**, 263.

Schmitz, M.D. and Bowring, S.A. (2000) The significance of U-Pb zircon ages from lower crustal xenoliths of the southwestern margin, Kaapvaal craton, southern Africa, *Chemical Geology,* **172**, 59-76.

Shank, S.G., Carlson, R.W., and Eggler, D.H. (1992) Source of potassic and carbonatite magmas in the Rocky Boy Stock, Bearpaw Mountains, Montana, *Trans. American Geophysical Union,* **73**, 339.

Shaw, D.M. (1970) Trace element fractionation during anatexis, *Geochimica et Cosmochimica Acta,* **34**, 237-243.

Shimizu, N. (1999). Young geochemical features in cratonic peridotites from southern Africa and Siberia. In: Y. Fei, C.M. Bertka, and B.O. Mysen (Eds.), *Mantle Petrology: Field observations and high pressure experimentation. A tribute to Francis R. (Joe) Boyd, Special Publication No. 6,* The Geochemical Society, Houston, pp. 47-55.

Shirey, S.B. (1997) Re-Os isotopic compositions of Mid-continent rift system picrites: implications for plume-lithosphere interaction and enriched mantle sources, *Canadian Journal of Earth Science,* **34**, 489-503.

Shirey, S.B. (1997) Initial osmium isotopic composition of Munro Township, Ontario, komatiites revisited: Additional evidence of near-chondritic late-Archean convecting mantle beneath the Superior Province, *Seventh Annual V.M. Goldschmidt Conf.,* **LPI Cont. 921**, 193.

Shirey, S.B. and Walker, R.J. (1994) Carius tube digestions for Re-Os chemistry: An old technique applied to new problems, *EOS,* **75**, 355-356.

Shirey, S.B. and Walker, R.J. (1995) Carius tube digestions for low-blank rhenium-osmium chemistry analysis, *Analytical Chemistry,* **67**, 2136-2141.

Shirey, S.B. and Walker, R.J. (1998) The Re-Os isotope system in cosmochemistry and high-temperature geochemistry, *Annual Reviews Earth and Planetary Science Letters,* **26**, 423-500.

Simon, N.S.C., Pearson, D.G., Carlson, R.W., and Davies, R.W. (2001), Origin of garnet and clinopyroxene in Kaapvaal low-T peridotite xenoliths: implications from secondary ionisation mass spectrometry (SIMS) data. In: *The Slave-Kaapvaal Workshop, Merrickville, Ontario, Canada.*

Smith, C.B., Gurney, J.J., Skinner, E.M.W., Clement, C.R., and Ebrahim, N. (1985) Geochemical character of southern African kimberlites: A new approach based on isotopic constraints, *Trans. Geological Society of South Africa,* **88**, 267-280.

Smith, C.B., Allsopp, H.L., Garvie, O.G., Kramers, J.D., Jackson, P.F.S., and Clement, C.R. (1989) Note on the U-Pb perovskite method for dating kimberlites: examples from the Wesselton and DeBeers mines, South Africa, and Somerset Island, Canada, *Chemical Geology (Isotope Geoscience Section),* **79**, 137-145.

Smith, D. and Boyd, F.R. (1987). Compositional heterogeneity in high-temperature lherzolite nodule and implications for mantle processes. In: P.H. Nixon (Ed.), *Mantle Xenoliths*, John Wiley & Sons, New York, pp. 551-561.

Smoliar, M.I., Walker, R.J., and Morgan, J.W. (1996) Re-Os ages of Group IIA, IIIA, IVA and IVB iron meteorites., *Science,* **271**, 1099-1102.

Snow, J.E. and Reisberg, L. (1995) Os Isotope Systematics of the MORB Mantle: Results from Altered Abyssal Peridotites, *Earth and Planetary Science Letters,* **133**, 411-421.

Snow, J.E. and Schmidt, G. (1998) Constraints on Earth accretion deduced from noble metals in the oceanic mantle, *Nature,* **391**, 166-169.

Stewart, W.D. (1987). Late Proterozoic to Early Tertiary stratigraphy of Somerset Island and northern Boothia Peninsula, District of Franklin, *Geological Survey of Canada. Paper*, **83-26**, pp. 78.

Stone, W.E., Crocket, J.H., and Fleet, M.E. (1990) Partitioning of palladium, iridium, platinum and gold between sulfide liquid and basalt melts at 1200^{o}C, *Geochimica et Cosmochimica Acta,* **54**, 2341-2344.

Stosch, H.G., Carlson, R.W., and Lugmair, G.W. (1980) Episodic mantle differentiation: Nd and Sr isotopic evidence, *Earth and Planetary Science Letters,* **47**, 263-271.

Thompson, R.N. (1984) Dispatches from the basalt front: I. experiments, *Proceedings of the Geological Association,* **249**.

Thériault, R.J. (1992) Nd isotopic evolution of the Taltson Magmatic Zone, Northwest Territories, Canada: Insights into Early Proterozoic accretion along the western margin of the Churchill province, *J. Geology,* **100**, 465-475.

Thorpe, R.I., Cumming, G.L., and Mortensen, J.K. (1992). A significant Pb isotope boundary in the Slave province and its probable relation to ancient basement in the western Slave province, *Geological Survey of Canada. Open File Report*, **2484**, pp. 179-184.

Tirrul, R. and Grotzinger, J.P. (1990) Early Proterozoic collisional orogeny along the northern Thelon tectonic zone, Northwest Territories, Canada: evidence from the foreland, *Tectonics,* **9**, 1015-1036.

Turner, B.R. (1972) Revision of the stratigraphic position of cynodonts from the upper part of the Karroo (Gondwana) System in Lesotho, *Geological Magazine,* **109**(4), 349-360.

Tuttle, O.F. and Gittins, J. (1966) Carbonatites, Interscience Publishers, London, pp. 591.

van Breeman, O., King, J.E., and Davis, W.J. (1989). U-Pb zircon and monazite ages from plutonic rocks in the Contwoyto-Nose Lakes map area, central Slave province, District of Mackenzie, *Radiogenic age and isotopic studies*, Geological Survey of Canada, **Report 3**, Paper 89-2, pp. 29-38.

van Loon, J.C. and Barefoot, R.R. (1991) Determination of the Precious Metals, Wiley, Chichester, pp. 276.

Völkening, J., Walczyk, T., and Heumann, K.G. (1991) Osmium isotope ratio determinations by negative thermal ionization mass spectrometry, *International Journal of Mass Spectrometry and Ion Processes,* **105**, 147-159.

Walczyk, T. and Heumann, K.G. (1993) Iridium isotope measurements by negative thermal ionisation mass spectrometry and atomic weight of iridium, *International Journal of Mass Spectrometry and Ion Processes,* **123**, 139-147.

Walker, R.J., Carlson, R.W., Shirey, S.B., and Boyd, F.R. (1989) Os, Sr, Nd, and Pb isotope systematics of southern African peridotite xenoliths: Implications for the chemical evolution of subcontinental mantle, *Geochimica et Cosmochim Acta,* **53**, 1583-1595.

Walter, M.J. (1998) Melting of garnet peridotite and the origin of komatiite and depleted lithosphere, *Journal of Petrology,* **39**, 29-60.

Walter, M.J. (1999). Melting residues of fertile peridotite and the origin of cratonic lithosphere. In: Y. Fei, C.M. Bertka, and B.O. Mysen (Eds.), *Mantle Petrology: Field observations and high pressure experimentation. A tribute to Francis R. (Joe) Boyd, Special Publication No. 6*, The Geochemical Society, Houston, pp. 225-239.

Windley, B.F. (1995) The Evolving Continents, John Wiley & Sons, Chichester, pp. 526.

Winterburn, P.A., Harte, B., and Gurney, J.J. (1990) Peridotite xenoliths from the Jagersfontein kimberlite: I. Primary and primary-metasomatic mineralogy, *Geochimica et Cosmochimica Acta,* **54**, 329-341.

Woodland, S.J. (2000) Development of ICP-MS Isotope Dilution Preconcentration Techniques for Determination of Platinum Group Elements in Volcanic Rocks. PhD, University of Durham.

Woodland, S.J. and Pearson, D.G. (1999). Analysis of PGEs by ICP-MS: a comparison between fire-assay and carius-tube anion-preconcentration methods. In: J.G. Holland and S.D. Tanner (Eds.), *Plasma Source Mass Spectrometry - New Developments and Applications, Special Publication 234*, Royal Society of Chemistry, pp. 267-276

Yamashita, K., Creaser, R., and Heaman, M.L. (1998). Geochemical and isotopic constraints for tectonic evolution of the Slave province, northwest Canadian Shield, *SFU. Lithoprobe report*, **64**, pp. 11-14..

Appendix A

SAMPLE LIST, TEXTURAL SUMMARIES AND PETROGRAPHY

A.1 Lesotho Low-Temperature Peridotite Suite

University of Durham Lesotho peridotite collection collected during the 7th International Kimberlite Conference Lesotho field trip (1998). Textural classifications after Harte (1977).

Sample	Location	Rock Type	Texture
LET2	Letseng	Gnt Harz	Coarse Tabular
LET6	Letseng	Sp Lherz	Porphyroclastic non-fluidal
LET8	Letseng	Sp Harz	Coarse Tabular
LET12	Letseng	Gnt Harz	Coarse Tabular
LET13	Letseng	Gnt-Sp Lherz	Coarse Tabular
LET14	Letseng	Gnt-Sp Harz	Coarse Tabular
LET25	Letseng	Sp Lherz	Coarse Tabular
LET27	Letseng	Gnt Lherz	Coarse Tabular/Equant
LET28	Letseng	Sp Harz	Coarse Tabular
LET29	Letseng	Gnt Lherz	Coarse tabular/Porphyroclastic
LET30	Letseng	Gnt Lherz	Coarse Tabular/Equant
LET31	Letseng	Gnt Lherz	Coarse Tabular
LET38	Letseng	Gnt Lherz	Coarse Tabular
LET47	Letseng	Gnt-Sp Lherz	Coarse Equant
LET48	Letseng	Gnt Lherz	Coarse tabular/Porphyroclastic
LET49	Letseng	Gnt Lherz	Coarse Tabular
LET58	Letseng	Gnt Lherz	Coarse Tabular
LET64	Letseng	Gnt Lherz	Coarse Tabular
TP6	Thaba Putsoa	Gnt-Sp Lherz	Coarse Tabular
TP7	Thaba Putsoa	Gnt-Sp Harz	Porphyroclastic non-fluidal
TP9	Thaba Putsoa	Gnt-Sp Lherz	Coarse Tabular
LQ1	Liqhobong	Gnt Lherz	Coarse Tabular
LQ5	Liqhobong	Gnt Lherz	Coarse Tabular
LQ6	Liqhobong	Gnt Lherz	Coarse Tabular
LQ8	Liqhobong	Gnt Lherz	Coarse tabular/Porphyroclastic
LQ9	Liqhobong	Gnt Harz	Coarse Tabular
M1	Matsoku	Gnt-Sp Harz	Porphyroclastic non-fluidal
M5	Matsoku	Sp Lherz	Coarse Equant
M6	Matsoku	Sp Lherz	Coarse Equant
M8	Matsoku	Gnt-Sp Lherz	Coarse Tabular/Equant
M9	Matsoku	Gnt Lherz	Coarse tabular/Porphyroclastic
M11	Matsoku	Gnt Lherz	Coarse Tabular
M13	Matsoku	Gnt-Sp Lherz	Coarse Tabular

A.2 Somerset Island Low-Temperature Peridotite Suite

Low-T peridotite xenoliths from the collections of B.A. Kjarsgaard, J. Pell and Durham University collected over several field seasons on Somerset Island.

Sample	Location	Rock Type	Texture
K11A14	Batty Bay	Gnt lherz	Coarse equant
K11A15	Batty Bay	Gnt-Sp lherz	Coarse equant
K11A16	Batty Bay	Gnt lherz	Coarse equant
K11A17	Batty Bay	Gnt-Sp lherz	Coarse equant
K11A18	Batty Bay	Gnt-Sp lherz	Coarse equant/Porphyroclastic
K12A1	Batty Bay	Sp lherz	Porphyroclastic non-fluidal
K13A1	Batty Bay	Sp lherz	Coarse tabular
K13A3	Batty Bay	Sp lherz	Coarse tabular/Porphyroclastic
K13A4	Batty Bay	Sp lherz	Coarse tabular
K13A5	Batty Bay	Sp lherz	Coarse tabular
K13B4	Batty Bay	Gnt perid	Coarse tabular
K15A4	Batty Bay	Gnt-Sp lherz	Coarse tabular
N1C	Nord	Gnt-Sp lherz	Coarse tabular/Porphyroclastic
N2B	Nord	Gnt-Sp lherz	Coarse tabular/Porphyroclastic
XO4	Nikos	Gnt lherz	Coarse equant
XO5	Nikos	Gnt lherz	Coarse equant
XO6	Nikos	Gnt-Sp lherz	Coarse equant
XO7	Nikos	Gnt-Sp harz	Coarse tabular
JP1-X2	JP North	Gnt-Sp lherz	Coarse equant
JP2-X2	JP Central	Sp lherz	Coarse tabular/Porphyroclastic
JP3-X1	JP South	Sp harz	Coarse tabular
JP3-X	JP South	Gnt harz	Coarse tabular
JPS-4	JP South	Gnt-Sp harz	Coarse tabular
JPS-6A	JP South	Gnt lherz	Coarse tabular
JPS-6B	JP South	Gnt lherz	Coarse tabular
JPN-2	JP North	Gnt-Sp lherz	Coarse tabular/Porphyroclastic
JPN-3A	JP North	Gnt harz	Coarse tabular
JPN-3B	JP North	Gnt perid	Coarse tabular
JPN-4	JP North	Gnt lherz	Coarse tabular/Porphyroclastic
JPN-9	JP North	Gnt lherz	Coarse equant
JPN-11	JP North	Gnt lherz	Coarse equant

A.3 Jericho Peridotite Suite

The Jericho peridotite xenoliths were kindly donated from the collection of Maya G. Kopylova at the University of British Columbia. The suite has been well characterised in terms of both petrology (Kopylova *et al.*, 1999) and major-element chemistry (Kopylova and Russell, 2000).

Sample	Facies	Texture	Rock Type
Low-T			
8-7	Spinel	Coarse	dunite
9-12	Spinel	Coarse	dunite
10-11	Spinel	Coarse	lherzolite
10-12A	Spinel	Coarse	dunite
10-12B	Spinel	Coarse	dunite
11-18	Spinel	Coarse	lherzolite
23-9	Spinel	Coarse	dunite
39-23	Spinel	Coarse	lherzolite
44-12	Spinel	Coarse	dunite
9-2	Spinel-Garnet	Coarse	peridotite
22-1	Spinel-Garnet	Coarse	peridotite
25-4	Spinel-Garnet	Coarse	peridotite
26-11	Spinel-Garnet	Coarse	peridotite
10-456'	Garnet	Coarse	lherzolite
11-22	Garnet	Coarse	lherzolite
13-2	Garnet	Coarse	Lherzolite-dunite
21-1	Garnet	Coarse	peridotite
22-4	Garnet	Coarse	peridotite
28-15	Garnet	Coarse	dunite
41-4	Garnet	Coarse	peridotite
51-2	Garnet	Coarse	harzburgite
53-10	Garnet	Coarse	harzburgite
21-3	Garnet	Porphyroclastic	peridotite
High-T			
21-2	Garnet	Porphyroclastic	lherzolite
23-1	Garnet	Porphyroclastic	dunite
26-9	Garnet	Porphyroclastic	fluidal peridotite
39-3	Garnet	Porphyroclastic	fluidal peridotite
40-9	Garnet	Porphyroclastic	peridotite
40-20	Garnet	Porphyroclastic	lherzolite
40-21	Garnet	Porphyroclastic	peridotite

A.4 Petrography of Lesotho and Somerset Island peridotites

Representative thin sections were made for all samples analysed in this study. Ol = olivine, OPX = orthopyroxene, CPX = clinopyroxene, Sp = spinel, Gnt = garnet and Ph = phlogopite. Minerals estimated from thin section are expressed as %; tr = trace, por = porphyroclast, neo = neoblast. Mineral size is maximum evident in thin section.

Lesotho peridotites:

Sample	Ol	OPX	CPX	Sp	Gnt	Petrography
LET2	70	25	2		3	Ol 11mm, OPX 6mm, Gnt 4mm. Trace Ph and Sp associated with Gnt. Ol strained. Gnt with zoned kelyphite.
LET6	65	30	4	1		Ol por 7mm, Ol neo 0.5mm, OPX 3mm, CPX 1mm, Sp 0.5mm. Ol por strained. Exsolution lamellae in OPX. Ph associated with CPX.
LET8	65	31	3	1		Ol 7mm, OPX 4mm, Sp 2mm. Symplectic intergrowth of Sp and OPX. Serpentine up to 20%.
LET12	55	38	2		5	Ol 7mm, OPX 4mm, Gnt 4mm. Exsolution lamellae in OPX. Gnt with zoned kelyphite.
LET13	60	34	1	tr	5	Ol 12mm, OPX 7mm, Sp 1mm, Gnt 5mm. Gnt with zoned kelyphite.
LET14	57	38	1	tr	4	Ol 7mm, OPX 7mm, Sp 0.5mm, Gnt 8mm. Gnt with zoned kelyphite. Exsolution lamellae in OPX. Slight straining observed.
LET25	70	28	1	1		Ol 6mm, OPX 2mm, Sp 1mm. Exsolution lamellae in OPX. Slight straining observed. Sp dark brown.
LET27	55	36	2		7	Ol 7mm, OPX 6mm, CPX 1.5mm, Gnt 6mm. Gnt with zoned kelyphite. Slight straining observed. Serpentine up to 30%. Ph in kelyphite rims.
LET28	63	35	1	1		Ol 10mm, OPX 5mm, Sp 0.5mm. Straining observed, Ol may be disaggregating. Exsolution lamellae in OPX.
LET29	62	32	3		3	Ol por 6mm, Ol neo 0.25mm, OPX 6mm, CPX 3mm, Gnt 5mm. Ol por highly strained. Gnt with zoned kelyphite.
LET30	61	32	1		6	Ol 5mm, OPX 5mm, CPX 1mm, Gnt 6mm. Exsolution lamellae in OPX. Gnt with zoned kelyphite. CPX associated with Gnt.
LET31	56	37	2		5	Ol 4mm, OPX 5mm, CPX 1mm, Gnt 5mm. Exsolution lamellae in OPX. Gnt with zoned kelyphite, sometimes completely altered. CPX rare and associated with Gnt.
LET38	53	40	1		6	Ol 5mm, OPX 5mm, CPX 2mm, Gnt 3mm. Slight straining observed. Gnt with zoned kelyphite, sometimes completely altered.
LET47	60	35		tr	5	Ol 5mm, OPX 3mm, CPX 1mm, Sp 1mm, Gnt 5mm. Straining evident. Gnt with zoned kelyphite, sometimes completely altered. Ol displays triple-point mosaic texture.

Sample	Ol	OPX	CPX	Sp	Gnt	Petrography
LET48	60	35	2		3	Ol 7mm, OPX 5mm, CPX 2mm. Ol and OPX highly strained. Gnt completely kelyphitised, and/or replaced with Sp.
LET49	70	20	2		8	Ol 6mm, OPX 4mm. Ol and OPX highly strained. Gnt in general completely kelyphitised, but occasional fresh core. Traces of Ph.
LET58	65	27	3		5	Ol 5mm, OPX 3mm, CPX3mm. Ol OPX and CPX highly strained. Gnt completely kelyphitised,
LET64	50	40	2		8	Ol 10mm, OPX 8mm, CPX 4mm, Gnt 3mm. Exsolution lamellae in OPX. Gnt with zoned kelyphite. Ph <1mm, Sp < 0.5mm associated with Gnt. CPX both discrete and associated with Gnt.
TP6	68	28	1	tr	3	Ol 8mm, OPX 4mm, CPX 1mm, Sp 2mm, Gnt 2mm. Exsolution lamellae in OPX. Gnt with zoned kelyphite. Ph and Sp associated with Gnt. Fresh Gnt cores contain Ph an Sp.
TP7	61	30	1	1	7	Ol por 3mm, Ol neo 0.5mm, OPX 3mm, Sp 1mm, Gnt 4mm. Ol por strained. Gnt with zoned kelyphite.
TP9	65	30	1	tr	4	Ol 7mm, OPX 7mm, CPX 1.5mm, Sp 1mm, Gnt 1.5mm. Exsolution lamellae in OPX. Gnt with zoned kelyphite and associated Sp.
LQ1	70	24	1		5	Ol 9mm, OPX 3mm, CPX 0.5mm, Gnt 3mm. Exsolution lamellae in OPX. Gnt with zoned kelyphite and associated Sp. Gnt associated with CPX and with Sp and OPX inclusions.
LQ5	50	41	2		7	Ol 6mm, OPX 5mm, CPX 3mm, Gnt 4mm. Gnt with minor kelyphite rims and some associated Sp and Ph.
LQ6	55	36	3		6	Ol 4mm, OPX 4mm, CPX 1mm, Gnt 4mm, Ph 2mm. Straining, with Ol disaggregating. In places equant mosaic and others tabular. Minor kelyphite rims on Gnt.
LQ8	55	40	1		4	Ol por 7mm, Ol neo 0.3mm, OPX 6mm, CPX 2mm, Gnt 4mm. Ol por strained. Gnt with zoned kelyphite and associated CPX.
LQ9	51	40	2		7	Ol 5mm, OPX 5mm, Gnt 3mm. Straining, with Ol disaggregating. Gnt with zoned kelyphite and associated Ph and Sp.
M1	65	30	1	1	3	Ol por 2mm, Ol neo 0.1mm, OPX 3mm, Sp 0.5mm, Gnt 0.8mm. Ol por and OPX strained. Exsolution lamellae in OPX.
M5	59	36	4	1		Ol 5mm, OPX 4mm, CPX 2mm, Sp 1mm, Ph 2.5mm. Ol and OPX strained.
M6	62	33	4	1		Ol 5mm, OPX 5mm, CPX 1.5mm, Sp 1mm. Ol strained. Exsolution lamellae in OPX.
M8	59	35	3	tr	3	Ol 3mm, OPX 2.5mm, CPX 1.5mm, Sp 1mm, Ph 1.5mm. Ol slightly strained.
M9	55	40	2		3	Ol 3mm, OPX 4mm, CPX 2mm, Gnt 5mm, Ph 1.5mm. Ol strained with some disaggregation. CPX and Ph associated with Gnt.
M11	58	35	2		5	Ol 4mm, OPX 5mm, CPX 1mm, Gnt 2mm. Ol strained with some disaggregation. Gnt with zoned kelyphite. CPX and Ph associated with Gnt.
M13	65	30	3	1	1	Ol 3mm, OPX 5mm, CPX 0.5mm, Gnt 3.5mm. Ol strained with some disaggregation. Gnt with zoned kelyphite. CPX, Sp and Ph associated with Gnt.

Somerset Island peridotites:

Sample	Ol	OPX	CPX	Sp	Gnt	Petrography
K11A14	75	18	1	tr	6	Ol 10mm, OPX 3mm, Gnt 4mm. Ol and OPX occasionally strained. Gnt with zoned kelyphite.
K11A15	77	15	4	tr	4	Ol 10mm, OPX 2mm, CPX < 1mm, Gnt 1mm. Ol and OPX occasionally strained. Gnt kelyphitised.
K11A16	75	15	4	tr	6	Ol 3mm, OPX 2mm, Gnt 1mm. Ol and OPX occasionally strained.
K11A17	80	15	3	tr	2	Ol 12mm, OPX 3mm, Gnt 2mm. Ol and OPX occasionally strained.
K11A18	80	15	2	tr	1	Ol 16mm, OPX 8mm, Gnt 3mm. Ol strained with some disaggregation. OPX strained, and exsolution lamellae. Sp dark brown.
K12A1	75	20	3	2		Ol por 4mm, Ol neo 0.2mm, OPX 2mm, CPX 2mm, Sp 3mm. Ol por and OPX strained. OPX strained and exsolution lamellae || cleavage. Sp dark brown and long axis aligned with OPX cleavage.
K13A1	69	22	6	3		Serpentine up to 60%. Remaining olivine fresh but slightly strained. Sp dark brown.
K13A3	72	25	2	1		Ol por 14mm, Ol neo 0.5mm, OPX 5mm, Sp 1mm. Ol por and OPX strained. OPX strained, with exsolution lamellae. Sp dark brown. OPX cleavage aligned.
K13A4						Serpentine up to 90%. Ol were 5mm, OPX 2mm, CPX 2mm. Sp dark brown 1mm.
K13A5						Serpentine up to 50%. Ol were 5mm, OPX 3mm, CPX 2mm. Sp dark brown 1mm. Remaining Ol strained. OPX with exsolution lamellae.
K13B4	65	30	1	tr	4	Ol 10mm, OPX 5mm, Gnt 3mm. Ol strained. Gnt with zoned kelyphite.
K15A4	72	25	tr	tr	3	Up to 30% serpentinisation. Ol 10mm, OPX 3mm, Sp 3mm, Gnt 3mm. Ol strained.
N1C	78	16	2	1	3	Ol por 8mm, Ol neo 0.1mm, OPX 3mm, Gnt 5mm. Ol por strained. OPX appears to be strung out in lenses. Sp dark brown. Gnt highly kelyphitised. Ph associated with Gnt.
N2B	80	15	3	tr	2	Ol por 12mm disaggregating to Ol neo 2mm, OPX 3mm, Sp 0.5mm, Gnt 2mm. Ol por and OPX strained. Sp dark brown.
JP1-X2	70	20	5	tr	5	Ol 10mm, OPX 7mm, CPX 5mm, Gnt 3mm. OPX strained. CPX forms small clusters. Gnt with small kelyphite rims.
JP2-X2	72	23	4	1		Ol por 5mm, Ol neo 0.5mm, OPX 4mm, CPX 1.5mm, Ph 3mm. Ol por highly strained. Ph and CPX closely associated.
JP3-X1	80	17	2	1		Ol 15mm, OPX 4mm, Sp 1mm. Ol slightly strained. OPX appears to be strung out in lenses.
JP3-X	75	19	1	tr	5	Ol 10mm, OPX 2mm, Gnt 2mm. Ol strained with evidence of disaggregation.
JPS-6A	74	14	4	tr	8	Ol 10mm, OPX 4mm, CPX 1mm, Gnt 5mm, Ph 2mm. Ol strained. Intergrowth between Ol and OPX at margins.
JPS-6B	75	10	5	tr	10	Ol 8mm, OPX 3mm, CPX 1.5mm, Gnt 5mm, Ph 2mm. Ol strained. Minor Ph at margins of Gnt.

Sample	Ol	OPX	CPX	Sp	Gnt	Petrography
JPN-2	80	15	1	2	2	Ol 6mm, OPX 4mm, CPX 2mm, Ph 4mm. Ol strained with some disaggregation. OPX strained.
JPN-3A	64	30	1	tr	5	Ol 5mm, OPX 2.5mm, Gnt 3mm, Ph 2mm. Ol strained with some disaggregation. OPX with exsolution lamellae. Small kelyphite rims on Gnt. Ph closely associated with Gnt.
JPN-3B	63	28	4	tr	5	Ol 5mm, OPX 3mm,CPX 1mm, Gnt 2mm, Ph 2mm. Ol slightly strained. OPX with exsolution lamellae. Kelyphite rims on Gnt.
JPN-4	65	25	1	tr	9	Ol 10mm, OPX 4mm, CPX 2mm, Gnt 3mm, Ph 2mm. Ol highly strained with some disaggregation. OPX slightly strained. Kelyphite rims on Gnt.
JPN-9	75	19	2	tr	4	Ol 10mm, OPX 5mm, CPX 4mm, Gnt 4mm, Ph 2mm. Ol strained. OPX with exsolution lamellae. Intergrowth between Ol and OPX at margins. Small kelyphite rims on Gnt.
JPN-11	63	32	2	tr	3	Ol 10mm, OPX 4mm, CPX 2mm, Gnt 5mm, Ph 2mm. Ol strained. OPX, and possibly CPX, with exsolution lamellae. Intergrowth between Ol and OPX at margins. Zoned kelyphite rims on Gnt.

Appendix B

SAMPLE PREPARATION AND WHOLE-ROCK ANALYSIS

B.1 Sample Preparation

Whole rock powders: All samples from Lesotho and Somerset Island weighed at least 500g minimum, but many samples were larger. Hand specimens were initially cut with a steel-bladed, rotary saw, such that fresh specimens were selected. Surfaces with saw-marks were thoroughly scrubbed and washed in MQ. Samples were lapped on a diamond table to remove all saw marks. The samples were reduced to rock-chips with a stainless steel, Fritsch Pulverisette jaw crusher. These chips were then ground to a fine powder in a Fritsch Pulverisette agate ball-mill. The mills were thoroughly cleaned between each sample, by grinding with high-purity silica sand. Tungsten carbide mills were deliberately avoided to ensure that there was no contamination of the PGE-signatures in the low-abundance samples.

B.2 Major-element Analysis by XRF

B.2.1 Sample preparation

All surface moisture is driven off the rock powders to be analysed by drying in an oven overnight (~100°C). Approximately 2g of dry powder is weighed into a ceramic crucible and the weight recorded. The crucible is placed in a furnace for 2 hours at a temperature of 900°C to remove the water of crystallisation. The 'ignited' rock powders are then re-weighed to determine the loss on ignition.

The ignited powders and lithium tetraborate fusion flux are dried prior to use. The flux and sample powders are weighed accurately and combined, in the ratio of 0.45g sample: 2.25g flux ± 0.001g, in an agate mill to ensure thorough mixing. This charge is fused in a Pt crucible at a temperature of 1050°C for 20 minutes. The sample is homogenised by swirling the contents of the hot crucible. The charge is poured into a

graphite mould whilst molten and pressed with an aluminium plunger to produce the final fusion disc.

B.2.2 Instrument and operating parameters

The fusion discs were analysed at the University of Durham using a Phillips PW1400 XRF Spectrometer fitted with a Pwa500/10 automatic sample changer, and a Rh tube X-ray source. The operating conditions were 80Kv and 35mA for all the major elements. Calibration and correction factors were calculated using Phillips X40 software. Machine drift was corrected by reference to internal standards. Reproducibility is generally better than 1% for elemental oxides in excess of 5%, and 1-2% for element oxide abundances of 0.5 to 5%.

B.3 Trace-element Analysis by ICP-MS

B.3.1 Sample preparation

Sample powders are dried overnight in an oven at ~105°C. Teflon vials are pre-cleaned by refluxing with Analar HNO_3 for 24 hours and rinsing with MQ before use. Rock powders are weighed into the Teflon vial (0.1 ± 0.001g). Four mls of HF and 1 ml of HNO_3 are added to the samples and the teflon vial is sealed. The rock powders are digested on a hotplate (~150°C) for 48hrs. After digestion the samples are evaporated to a moist residue in the teflon vials, ensuring they do not drydown completely. Samples are re-dissolved in HNO_3 (1mls), and evaporate twice to remove fluoride precipitates. 2.5mls of HNO_3 are added to the samples and this is diluted to ~10mls with MQ. These samples are spiked with an internal standard (-1.25mls; typically contains 2ppm Re and Rh). The sample is further diluted to 50mls with MQ. To prepare this solution for the ICP-MS 1ml of this solution is further diluted by the addition of 10mls of MQ to final dilution factor of 1/5000.

B.3.2 Instrument and operating parameters

The dissolved samples were analysed at the University of Durham using a Perkin-Elmer Sciex Elan 6000 ICP-MS, equipped with a cross-flow nebuliser and an auto-sampler with an uptake rate of 1ml/min. The plasma is operated at 1100 to 1300 W.

Analytical results are processed on-line using the Sciex software supplied with the Elan 6000. The instrument is optimised and performance monitored by a daily check solution from which oxide production and machine sensitivity is assessed.

Data quality is ensured by:

- Procedural blanks are analysed to ensure samples were not contaminated during preparation.
- Internal standards are analysed which compensate for sample loss during dilution and fluctuations in machine sensitivity during an analytical session
- International standards with different levels of trace elements are analysed, and the unknown samples are calibrated against these. The standards used were AGV-1, BCR-1, W-2 and X-108. Sample GP13, the Durham in-house peridotite standard was also used and compared to isotope dilution trace element data (Pearson, 1989).
- Wash-out times of 3 minutes using diluent (3.5% HNO_3) was allowed between each sample to eliminate memory effects.

B.4 Sulfur Analysis

The peridotite samples were analysed for sulfur at the Max-Planck-Institut für Chemie using a Carbon and Sulfur analyser (CSA 2002). Approximately 50mg to 100mg of rock sample were analysed using commercially available apparatus consisting of an induction furnace and infrared-detection system.

The accuracy of this method is checked by analysing standards (Dreibus *et al.*, 1995). The standards used are (a) BAM, a steel-standard containing 0.152 wt% S. Repeat analysis of this standard produces a 1σ standard deviation of ±3%. (b) Carbonaceous chondrites Murchison (CM) 3.03%, and Allende (CV3) 2.06%. Repeat analysis of this standard produces a 1σ standard deviation of ±3% (Dreibus *et al.*, 1995).

Repeat analyses were made for the peridotites using several aliquots to account for heterogeneous sulfide distribution. The accuracy for S measurement in the range observed in the peridotite suites is between 10% and 15%, but rises to 20% for samples with < 40 ppm S content. The detection limit is 10 ppm. The generally low S concentrations in the peridotites required continuous background measurement and

calibration checks. Small uncertainties below 40 ppm are artefacts; the actual uncertainty due to the blank value is in the range of 40 to 50 ppm.

The results of S analysis for the Lesotho, Somerset Island and Jericho peridotite suites are given in Tables B.1, B.2 and B.3 respectively.

Table B.1 Summary of sulfur data for the Lesotho peridotite suite.

Location	Sample	S (ppm)	±
Lesotho			
Letseng-la-terae	LET 2	202.75	12
Letseng-la-terae	LET 6	345	21
Letseng-la-terae	LET 8	161	10
Letseng-la-terae	LET 12	188	12
Letseng-la-terae	LET 13	158	13
Letseng-la-terae	LET 14	130.25	6
Letseng-la-terae	LET 25	350.5	8
Letseng-la-terae	LET 27	273.75	10
Letseng-la-terae	LET 28	380.75	19
Letseng-la-terae	LET 29	380.75	19
Letseng-la-terae	LET 30	145	16
Letseng-la-terae	LET 31	266	13
Letseng-la-terae	LET 38	84.2	16
Letseng-la-terae	LET 47	101.75	15
Letseng-la-terae	LET 48	48.75	2
Letseng-la-terae	LET 49	196.8	15
Letseng-la-terae	LET 58	91.75	7
Letseng-la-terae	LET 63	332.5	27
Letseng-la-terae	LET 64	121	4
Thaba Putsoa	TP 5	14.5	3
Thaba Putsoa	TP 6	< 10	
Thaba Putsoa	TP 7	37	7
Thaba Putsoa	TP 9	15	3
Liqhobong	LQ 1	294.75	13
Liqhobong	LQ 5	28	4
Liqhobong	LQ 6	36.2	4
Liqhobong	LQ 8	19	5
Liqhobong	LQ 9	31	5
Matsoku	M 1	122	6
Matsoku	M 3	274.5	13
Matsoku	M 5	60	6
Matsoku	M 6	42.5	7
Matsoku	M 8	41.5	2
Matsoku	M 9	22.25	3
Matsoku	M 11	17.8	3
Matsoku	M 13	14.25	6

Table B.2 Summary of sulfur data for the Somerset Island peridotite suite.

Location	Sample	S (ppm)	±
Somerset Island			
Nikos	XO 4	2543.5	17
Nikos	XO 5	2740.75	49
Nikos	XO 6	369	28
Nikos	XO 7	190.25	10
JP	JP 1 - X 2	260.4	12
JP	JP 2 - X 2	277.2	8
JP	JP 3 - X	275	65
JP	JP 3 - X 1	177	77
JP	JPN 2	339.25	17
JP	JPN 3 A	268	5
JP	JPN 3B	407.17	18
JP	JPN 4	297.75	9
JP	JPN 9	471.17	20
JP	JPN 11	236.4	9
JP	JPS 1	1701.75	24
JP	JPS 4	1484.4	20
JP	JPS 6A	1006.25	20
JP	JPS 6B	1028.2	14
Batty Bay	K11A14	101	31
Batty Bay	K11A15	68	29
Batty Bay	K11A16	126	50
Batty Bay	K11A17	157	56
Batty Bay	K11A18	108	69
Batty Bay	K12A1	78	19
Batty Bay	K13A1	40	27
Batty Bay	K13A3	171	14
Batty Bay	K13A4	93	57
Batty Bay	K13A5	68	42
Batty Bay	K13B4	73	19
Batty Bay	K15A4	43	30
Nord	N1C	194	44
Nord	N2B	123	62

Table B.3 Summary of sulfur data for the Jericho peridotite suite.

Location	Sample	S (ppm)	±
Slave			
Jericho	8-7	47	30
Jericho	9-12	108.44	16
Jericho	10-11	164	56
Jericho	10-12A	108.6	9
Jericho	10-12B	51	1
Jericho	11-18	50.17	7
Jericho	23-9	66	3
Jericho	39-23	114.5	6
Jericho	44-12	599.33	19
Jericho	9-2	221.14	16
Jericho	10-456'	140.5	8
Jericho	11-22	128	9
Jericho	13-2	156.5	7
Jericho	21-1	76.33	6
Jericho	22-1	73.4	3
Jericho	22-4	77.5	4
Jericho	25-4	106.6	7
Jericho	26-11	76	4
Jericho	28-15	131.2	13
Jericho	41-4	76.75	7
Jericho	51-2	545	42
Jericho	53-10	790.75	39
Jericho	54-9	445.67	5
Jericho	56-1	610.6	25
Jericho	21-3	282.75	7
Jericho	21-2	170.5	11
Jericho	23-1	67.5	4
Jericho	26-9	167	15
Jericho	39-3	234.5	9
Jericho	40-9	128	8
Jericho	40-20	96	41
Jericho	40-21	106.75	11

Appendix C

INSTRUMENT OPERATING CONDITIONS

C.1 JEOL JXA-8900L Microprobe Analysis

Mineral analyses of olivine, OPX, CPX and garnet, from the Lesotho peridotite suite, were determined using the JEOL JXA-8900L electron microprobe at the Carnegie Institution of Washington. The microprobe beam had an accelerating voltage of 15kV and current of 3nA. Count times were approximately 200 seconds. Individual mineral analyses tabulated in this thesis are an average of a minimum of ~10 analyses. Prior to mineral analyses, standards were analysed to calibrate the microprobe (Table C.1).

Element	Standard	Crystal
Na_2O	DJ35	TAP
MgO	P140	TAP
Al_2O_3	DJ35/ENAL20	TAP
SiO_2	P140/DJ35	TAP
CaO	DJ35	PETJ
TiO_2	Di2Ti	PETJ
Cr_2O_3	52NL11	LIF
MnO	Ddiopside	LIFH
FeO	P140	LIFH
NiO	Ddiopside	LIF

Table C.1 Element calibration standards and crystals

ZAF corrections were calculated "on-line" by the JEOL software. Only totals > 99.0 and <100.9 % were accepted for single analyses. An average of 16 analyses of olivine cores from peridotite LET2 gave the following 2σ errors of the total value: SiO_2 = 0.46%, FeO = 1.5%, MgO = 0.7%. The errors for elements with abundance below 1% were considerably higher, and were commonly 30% of the total value.

C.2 Cameca SX50 Microprobe Analysis

Electron microprobe analyses of olivine and garnet mineral compositions from the Somerset Island peridotites were performed with a fully automated Cameca SX50 microprobe at the Geological Survey of Canada (Ottawa). The microprobe operated with four wavelength dispersion spectrometers. Operating parameters and standard analyses are summarised in Table C.2.

Minerals were analysed using the GSC major element analysis scheme "SILPYROX". Peak overlap corrections were available at the time of analysis, to compensate for elemental interferences.

C.3 Proton Microprobe Analysis

Garnets from Somerset Island peridotites were analysed for trace elements with the Guelph scanning proton microprobe (Department of Physics, University of Guelph). The energy of the proton beam was 3 MeV, I was ~10nA, and spot size ~ 15μm^2. The 80 mm^2 Oxford Instrument Si(Li) detector is placed 25 mm from the specimen to provide the most efficient geometry (Campbell *et al.*, 1996), and the energy resolution of the detector (full width and half height of the Mn$K\alpha$ line) is 145 eV. Spectra were recorded for an average of 10 spots per sample, and each spectrum was measured over a period of 3 to 5 minutes.

Data was processed via the Guelph GUPIX software package developed for PIXE analysis (for further detail see Maxwell *et al.*, 1989; and Maxwell *et al.*, 1995). The process involves comparing the measured spectrum with the model spectrum, to ascertain peak areas. These are converted to elemental concentrations using the measured instrumental constant (based on detector and absorber characteristics), and matrix corrections (based on the attenuation of emitted x-rays by major elements). The detection limit for Ni using this technique is approximately 5 ppm. The analysis of silicate reference standards for trace elements using the Guelph proton microprobe is reviewed by Campbell *et al* (1996).

Table C.2 Analytical conditions and standards for the major elements scheme "SILPYROX" in conjunction with the CAMECA SX50.

Instrument Calibration parameters:

CALIBRATION DATA											
ELEMENT	SPC	XTAL	POS.	+BG OFFSET	-BG OFFSET	BG SLOPE	PK-BG C/s/nA	SIGMA	PK_TIM sec.	%REQ. ACCUR.	BG_TIM ms
Na	1	PCO	26651	2000	-2000	0	1414.96	0.8	20	0.1	10000
K	3	PET	42746	512	0	1	193.63	0.1	20	0.1	10000
Fe	4	LIF	48082	512	0	1	146.12	0.6	20	0.1	10000
Mg	2	TAP	38506	912	0	1	943.54	0.2	20	0.1	10000
Si	2	TAP	27737	1531	0	1	972.57	0.1	10	0.1	5000
Ca	3	PET	38379	531	0	1	213.78	0.3	10	0.1	5000
w	4	LIF	52204	631	0	1	47.54	3.1	10	0.1	5000
Ti	3	PET	31427	831	0	1	414.45	0.3	10	0.1	5000
Cr	4	LIF	56876	531	0	1	41.64	0.4	10	0.1	5000
Al	2	TAP	32467	1431	0	1	1064.4	0.4	10	0.1	5000
Ni	4	LIF	41167	531	0	1	116.95	6.3	10	0.1	5000

Abbreviations:
SPC = spectrometer number; XTAL = spectrometer crystal; POS. = position of spectrometer; +BG OFFSET = positive background offset; -BG OFFSET = negative background offset; BG SLOPE = background slope; PK-BG C/s/nA = peak minus background in counts/second/nanoamperes; PK_TIM Sec. = peak counting time in seconds; % REQ. ACCUR. = percent required accuracy for peak counting time; BG_TIM ms = background counting time in milliseconds.

Table C.2 (contd.) Standard Compositions and Analysis

STANDARD DATA					
ELEMENT	STANDARD	WEIGHT FRACTION	LINE	kV	Beam Current nA
Na	NACL7	0.3930	Ka	15.0	10.0
K	KBR7	0.3290	Ka	15.0	10.0
Fe	MAGI	0.7236	Ka	15.0	10.0
Mg	MG01	0.6032	Ka	15.0	10.0
Si	QTZl	0.4674	Ka	15.0	30.0
Ca	WOLl	0.3432	Ka	15.0	30.0
w	RHOD1	0.2854	Ka	15.0	30.0
Ti	RUTI	0.5895	Ka	15.0	30.0
C r	CHR1	0.2504	Ka	15.0	30.0
Al	CORI	0.5290	Ka	15.0	30.0
Ni	NIS4	0.6457	Ka	15.0	30.0

STANDARD COMPOSITION												
Standard	Element	WEIGHT FRACTION	Element	WEIGHT FRACTION	Element	WEIGHT FRACTION	Element	WEIGHT FRACTION	Element	WEIGHT FRACTION	Element	WEIGHT FRACT10N
NACL7	Na	0.3930	Cl	0.607								
KBR7	K	0.3290	Br	0.671								
MAGI	Fe	0.7236	O	0.2764								
MG01	Mg	0.6032	O	0.3968								
QTZ1	Si	0.4674	O	0.5326								
WOL1	Ca	0.3432	Fe	0.003	Mn	0.0012	Si	0.2399	O	0.4127		
RHOD1	Mn	0.2854	Al	0.0003	Fe	0.0131	Si	0.2178	Mg	0.0052	Ca	0.0469
	Na	0.0010	K	0.0007	Zn	0.0574	O	0.3722				
RUT1	Ti	0.5895	Fe	0.0050	Nb	0.0050	O	0.4005				
CHRl	Cr	0.2504	Al	0.0762	Fe	0.2985	Mg	0.0434	Ti	0.0054	V	0.0012
	Mn	0.0015	Ni	0.0012	Si	0.0011	O	0.3211				
CORI	Al	0.5290	O	0.4710								
NIS4	Ni	0.6457	Fe	0.0010	S	0.3533						

Appendix D

MINERAL MODES

D.1 Computed Modal Mineralogy

The modal mineralogy of all peridotite samples from Lesotho and Somerset Island were calculated using a spreadsheet developed by Maya G. Kopylova at the University of British Columbia.

The mineral modes of peridotite samples are calculated from the chemical composition of the samples using mass balance relationships inferred from the observed mineralogy. The mode is calculated by solving a system of linear equations (Kopylova and Russell, 2000). The following function is minimised:

$$RMS = \sum_{i}^{n} \sum_{k}^{p} [[M_k \times C_i] - x_i]^2$$

where M_k is mol% of the kth mineral in the rock, C_i is the mole fraction of the ith oxide in the mineral, x_i is the concentration of the ith oxide in the peridotite, p is the number of minerals in the rock, and n is the number of elements (Kopylova and Russell, 2000). Solving for this minimisation returns an estimate of mineral mode and a degree of misfit expressed as a root mean square. The degree of misfit quantitatively assesses how well the mineral mode agrees with the whole rock chemical composition.

For values of C_i the average mineral compositions found in the different facies of the Lesotho and Somerset Island peridotite suites were used. The solutions were based on SiO_2, Al_2O_3, Cr_2O_3, FeO, MgO and CaO. Other oxides are excluded as their concentrations are near to the minimum detection levels. All Fe is considered as ferrous Fe, as mineral compositions used in the model assemblages don't accommodate significant quantities of ferric Fe (Kopylova and Russell, 2000).

Appendix E

MAJOR AND TRACE-ELEMENT MODELLING

E.1 Major-element Modelling

E.1.1 Major-elements in mantle-melt systems (Hanson and Langmuir, 1978)

Hanson and Langmuir (1978) proposed that major elements could be modelled numerically, similar to the quantitative petrogenetic modelling approach for trace elements. The modelling is constrained by the stoichiometry of solid phases and the K_d for Mg and Fe between olivine and melt ($K_{d\,MgO}^{Ol/L}$ and $K_{d\,FeO}^{Ol/L}$) as a function pressure, temperature and composition. These data can be applied to calculate the MgO and FeO contents of peridotite residues from varying degrees of melting of a uniform source.

The equations of Hanson and Langmuir (1978) were used in conjunction with Mg-Fe partition coefficient data of Bickle *et al* (1977) at 3GPa (Table E.1) to calculate a "residue" grid from various degrees of melting of a pyrolitic source (Ringwood, 1975) at varying temperatures.

	Melt			**Olivine**		
RUN	MB33	MB32	MB46	MB33	MB32	MB46
P (GPa)	3	3	3	3	3	3
T (°C)	1700	1775	1800	1700	1775	1800
MgO (wt%)	24.35	28.18	31.81	50.04	50.79	52.24
FeO (wt%)	11.39	10.79	10.62	8.26	7.13	6.02
MgO (mol%)	33.84	38.37	42.37	60.87	61.40	62.47
FeO (mol%)	8.88	8.24	7.93	5.64	4.83	4.04
RUN	**MB33**		**MB32**		**MB46**	
T (°C)	1700		1775		1800	
Kd(MgO)	1.80		1.60		1.47	
Kd(FeO)	0.63		0.59		0.51	

Table E.1 Summary of experimental data from Bickle *et al* (1977) at 3 GPa, for the partition of Mg and Fe between olivine and melt.

Partition coefficients form MgO and FeO, based upon the experimental data of Bickle *et al* (1977), can be calculated using the following equations:

$$\log_{10} K_{d(MgO)} = \frac{2410}{T} - 0.97 \qquad \text{(Eqn. E1.1)}$$

$$\log_{10} K_{d(FeO)} = \frac{2678}{T} - 1.55 \qquad \text{(Eqn. E1.2)}$$

The molar concentration of MgO and FeO in olivine is given by the equation:

$$C_O = MgO + FeO = 47.8 + 5.35 = 66.67\% \qquad \text{(Eqn. E1.3)}$$

For the composition of the initial melt (F = 0), the bulk partition coefficient

$$D = \frac{C_S}{C_L} = \frac{C_S C_{ol}}{C_{ol} C_L} = \frac{C_S}{C_{ol}} K_d^{ol/L} \qquad \text{(Eqn. E1.4)}$$

where C_S is the original composition of the mantle, i.e. C_O, in this case pyrolite (Eqn. E1.3). The olivine composition is estimated for the initial mantle composition ($Fo_{89.5}$)

$$C_{L(MgO)} = 20.04 \qquad C_{L(FeO)} = 6.30$$

$$D_{MgO} = 2.39 \qquad D_{FeO} = 0.85$$

The maximum extent of permissible melting at a given temperature occurs when only olivine exists as the residual phase. At this point the bulk distribution coefficient, $D = K_d^{Ol/L}$, and the composition of the liquid (C_L) and solid (C_S) are given by:

$$C_L = \frac{C_O}{K_d(1-F) + F} \qquad \text{(Eqn. E1.5)}$$

$$C_S = C_L K_d \qquad \text{(Eqn. E1.6)}$$

There are two such equations for both Mg and Fe, and in addition to equation (E1.3) these five equations relate the five unknowns of F, and the abundance of Fe and Mg in both liquid and solid. The calculation for maximum extent of partial melting is independent of olivine composition and therefore the unknowns can be determined.

As an example of how the composition of melts and residues, between minimum and maximum melting are calculated, detailed calculations for determining MgO and FeO

for 30% melting (F = 0.3) of pyrolite at 1400 °C for the MgO-FeO "residue grid" are presented here. Maximum melting at 1400 °C is 32.8%.

The pyrolite parent composition, C_O, is:

MgO = 47.8 mol% FeO = 5.35 mol%

From equations (E1.1) and (E1.2) the values of D for MgO and FeO, for the maximum extent of melting at 1400°C are

$$D_{MgO} = K_{d\,MgO}^{Ol/L} = 2.98 \qquad D_{FeO} = K_{d\,FeO}^{Ol/L} = 1.11$$

It is possible to start with any value of D, but quicker to begin with an appropriately chosen value between the maximum and minimum. Here we will select values of

$$D_{MgO} = 2.93 \qquad D_{FeO} = 1.09$$

The melt composition can now be calculated

$$C_L = \frac{C_O}{D(1-F)+F} \qquad \text{(Eqn. E1.7)}$$

$$C_{L(MgO)} = \frac{47.8}{2.93\times(1-0.3)+0.3} = 20.35\%$$

$$C_{L(MgO)} = \frac{5.35}{1.09\times(1-0.3)+0.3} = 5.04\%$$

The residue can also be calculated

$$C_S = DC_L \qquad \text{(Eqn. E1.8)}$$

$$C_{S(MgO)} = 2.93\times 20.35 = 59.56\%$$

$$C_{S(MgO)} = 1.09\times 5.04 = 5.48\%$$

This residue is plotted on an MgO-FeO diagram (see Hanson and Langmuir, 1978, for further details). From the position of the residue on this plot, the composition of the coexisting olivine can be estimated.

$$C_{ol(MgO)} = 61.15\% \qquad C_{ol(FeO)} = 5.53\%$$

New values of D can be calculated using equation (E1.4), and new values of C_L and C_S from equation (E1.7) and (E1.8). The method of reiteration is repeated until the D's calculated are the same, reflecting a convergence of the solution.

The results can be assessed, by ensuring the liquid is in equilibration with olivine using the relationship

$$C_{ol} = C_L K_d^{ol/L}$$

After six reiterations this yields

$$C_{ol}^{MgO} = 61.07\% \qquad C_{ol}^{FeO} = 5.60\%$$

which gives a sum of 66.67%, showing that stoichiometrically the mineral is olivine. As the olivine is the same as the estimated olivine the results are internally consistent and the unique solution with olivine, residue and melt in equilibrium has been reached (Hanson and Langmuir, 1978).

E.1.2 Melting residues of fertile peridotite (Walter, 1999)

Walter (1999) used experimentally determined melt compositions, from fertile "pyrolitic" peridotite, to predict major element compositions of melt extraction residues as a function of pressure, degree of melting and melting processes (isobaric batch and polybaric near-fractional melt extraction).

Table E.2 (Walter, 1999), gives melt and residue compositions for polybaric near-fractional melting of fertile mantle. Five separate models, comprising melting between 1 and 7 GPa with variable initial and final pressures of melting, are listed (see Walter, 1999, for further details).

P Range[1]	7 – 1.1		5 – 1.1		3 – 1.1		7 – 3.1		7 – 5.1	
Ave P[2]	4		3		2		5		6	
Melt %[3]	60		40		20		40		20	
	Melt	**Residue**	**Melt**	**Residue**	**Melt**	**Residue**	**Melt**	**Residue**	**Melt**	**Residue**
SiO_2	46.8	43.7	47.2	44.0	48.3	44.2	46.0	44.5	45.0	45.0
Al_2O_3	9.0	0.6	11.8	0.6	15.6	1.7	8.2	2.4	6.5	3.8
FeO	10.3	5.9	9.8	7.1	8.5	7.9	11.2	6.3	12.6	7.0
MgO	22.1	50.0	17.9	46.9	13.2	42.7	21.9	45.0	22.4	40.7
$Mg^{\#}$ [4]	79.3	93.8	76.5	92.2	73.5	90.6	77.7	92.7	76.0	91.2

Table E.2 Melt and residue compositions (wt%) in polybaric near-fractional melting models (from Walter, 1999). [1] Pressure range in GPa; [2] average pressure; [3] aggregate melt %; [4] $Mg^{\#}$ = (Mg/Mg+Fe) in moles, all Fe is Fe^{2+}.

E.2 Trace-element Modelling

The degree of melting can be estimated from the fractionation of HREE as a function of HREE abundances, following the method of Bodinier *et al* (1988). This method also distinguishes between the presence and absence of garnet, owing to the buffering of HREE by garnet.

Calculations for batch and fractional melting are made using the equations

$$C_R = \frac{C_O D^{s/l}}{D^{s/l}(1-F)+F} \qquad \text{(Eqn. E2.1)}$$

$$C_R = C_O(1-F)^{(1/D^{s/l}-1)} \qquad \text{(Eqn. E2.2)}$$

where $D^{s/l}$ is the bulk distribution coefficient, C_R the residue composition and C_O the original composition. For modelling HREEs, melting paths are calculated using the non-modal melting equations of Shaw (1970). The bulk distribution coefficient is given by

$$D = \frac{(D_O - PF)}{(1-F)} \qquad \text{(Eqn. E2.3)}$$

where D_O is the initial bulk distribution coefficient and P is the distribution coefficient of the phase assemblage. Substituting Equation E2.3 into equations for batch (Eqn. E2.1) and fractional (Eqn. E2.2) melting will produce equations that define the residue compositions of melt extraction (Eqn. E2.4 and E2.5).

$$C_R = \frac{DC_O}{D_O + F(1-P)} \qquad \text{(Eqn. E2.4)}$$

$$C_R = \frac{DC_O}{D_O}\left(1-\frac{PF}{D_O}\right)^{(1/P-1)} \qquad \text{(Eqn. E2.5)}$$

The parameters used in the calculations, from Burnham (1995), are given in Table E.3. To simplify the model it was assumed that the proportion of minerals entering the melt remained constant until exhausted (Burnham, 1995, and references therein).

Mineral	D Values		Initial Modal Composition (%)			Melt Proportion (%)	
	Dy	Yb	A	B	C	Sp. Lherz.	Gnt. Lherz.
CPX	0.51	0.52	17	12.5	10	71	41
OPX	0.05	0.11	30	22.5	20	38	9
Olivine	0.004	0.023	50	60	60	-22	-13
Garnet	1.27	4.2	0	5	10	0	63
Spinel	0.0015	0.0045	3	0	0	13	0

Table E.3 Parameters used for the modelling of HREE abundances during the melting of a fertile lherzolite source (Burnham, 1995, and references therein). Negative proportions indicate the production of olivine during the melting reaction.

The melting trajectories produced by batch and fractional melting processes in garnet free rocks are virtually indistinguishable. In the presence of garnet however the processes produce trends that are significantly different:

i. Garnet is exhausted after 10-15% batch-melting, and HREE are no longer buffered, therefore the garnet signature of the host is lost. At higher degrees of batch melting the residual peridotite should follow the same path as a garnet-free source.

ii. For fractional melting, the initial HREE fractionation created by the presence of garnet remains even after garnet is exhausted and HREE fractionation remains in the residue during further melting.

Appendix F

Ni IN OLIVINE THERMOMETRY

F.1 Partitioning of Ni between Cr-pyrope and olivine

The work of Griffin *et al* (1989), Canil (1994) and Ryan *et al* (1996) have resulted in the development of an empirical geothermometer. The method of Griffin *et al* (1989) assumes a constant Ni content of 2900 ppm in mantle olivine, and the "nickel thermometer" estimates the equilibration temperature on the basis of measured Ni abundance in garnet. As noted by Kjarsgaard (1992) application of Ni concentration data requires the calibration of the Ni thermometer to be well constrained. The published calibrations of Canil (1994), Griffin and Ryan (1995) and Ryan *et al* (1996) produce comparable results within the given calibration range for single spot analyses, but widely diverging results at high and low Ni abundances; producing temperature differences greater than the measurement error (see review in Campbell *et al.*, 1996).

Measured Ni concentrations in olivine from the Somerset Island peridotites were variable, and were commonly both higher and lower than 2900 ppm. Temperatures were calculated using the following parameters and equation:

$$T = \left(\frac{1000}{-0.428 \times \log_{10}\left(100 \times K_d^{gt/ol}\right) + 0.84} \right) - 273.3$$

The Somerset Island garnets were analysed for Ni at the University of Guelph using their proton microprobe and PIXE analysis techniques (see Appendix C). Olivines from the Somerset Island peridotites were analysed at the Geological Survey of Canada using their CAMECA SX50 microprobe. The Ni concentrations for olivine and garnet, and calculated equilibration temperatures are given in Table F.1.

Sample	Ni in Gt. (ppm)	Ni in Ol (wt%)	Ni in Ol (ppm)	$K_d^{gt/ol}$	T (°C)
JPN9	23.9	0.399	3133	0.0076	**850**
X06	22.4	0.350	2750	0.0081	**865**
JP1-X2	24.2	0.351	2757	0.0088	**884**
X04	32.5	0.366	2873	0.0113	**951**
JPS6A	53	0.409	3211	0.0165	**1066**
JPS2	54.1	0.385	3029	0.0179	**1093**
JPN3B	59.6	0.419	3295	0.0181	**1097**
JPN11	67.5	0.420	3301	0.0204	**1141**
JPS1	69.4	0.419	3293	0.0211	**1152**
JPS4	55.2	0.331	2603	0.0212	**1155**
JPN3A	70.5	0.378	2973	0.0237	**1198**
JP3-X	68.4	0.365	2871	0.0238	**1200**
JPN2	59.2	0.313	2461	0.0241	**1204**
X05	71.4	0.358	2812	0.0254	**1226**
JPN4	73.8	0.357	2805	0.0263	**1241**
JPS6B	80.8	0.391	3069	0.0263	**1242**

Table F.1 Summary of Ni concentrations in olivine and garnet from Somerset Island peridotites, and calculated temperatures